NASA
CP
2108-
pt.1
c.1

NASA Conference Publication 2108

LOAN COPY: R
AFWL TECHNI
KIRTLAND AF
0099732
TECH LIBRARY KAFB, NM

Supersonic Cruise Research '79

Part 1

Proceedings of a conference
held at Langley Research Center
Hampton, Virginia
November 13-16, 1979

NASA

FOR U.S. GOVERNMENT AGENCIES
AND THEIR CONTRACTORS ONLY

Date for general release March 1981.

TECH LIBRARY KAFB, NM
0099732

NASA Conference Publication 2108

Supersonic Cruise Research '79

Part 1

Proceedings of a conference
held at Langley Research Center
Hampton, Virginia
November 13-16, 1979

National Aeronautics
and Space Administration

**Scientific and Technical
Information Office**

1980

PREFACE

Since 1972 the Supersonic Cruise Research (SCR) Program has provided an accelerated and focused technology effort which has resulted in development of improved analytical techniques, design procedures, and an expanded experimental data base. Progress made in the first 4 years was highlighted in a conference at Langley Research Center in 1976 (see NASA CP-001, Parts 1 and 2).

Subsequent to the 1976 conference, NASA had conducted and monitored additional supersonic cruise vehicle studies and enhanced the advanced supersonic technology data base through further tests. Significant achievements in the interim since the previous conference were reported to the technical community at the SCR '79 Conference held at Langley Research Center, November 13-16, 1979. This document is a compilation of papers, authored by representatives of airframe and engine manufacturers, the Federal Aviation Administration, three NASA research centers, and the Office of Technology Assessment (Congress of the United States), which were presented at the latter Conference.

The Conference was organized in six sessions as follows:

I. Aerodynamics
II. Stability and Control
III. Propulsion
IV. Environmental Factors
V. Airframe Structures and Materials
VI. Systems Integration and Economics

Papers and the authors thereof are grouped by session and identified in the CONTENTS. The order of papers is the actual order of speaker appearance at the Conference.

The size of the compilation necessitated publication in two parts (Parts 1 and 2). A list of attendees, by organizational affiliation, is included at the back of Part 2.

We would like to express appreciation to session chairmen and speakers whose efforts contributed to the technical excellence of the Conference.

Use of trade names or names of manufacturers in this report does not constitute an official endorsement of such products or manufacturers, either expressed or implied, by the National Aeronautics and Space Administration.

C. Driver
Hal T. Baber, Jr.

Conference Cochairmen

CONTENTS

Part 1

PREFACE iii

SCR PROGRAM OVERVIEW 1
Vincent R. Mascitti

SESSION I - AERODYNAMICS
Chairman: Robert E. Bower

INTRODUCTORY REMARKS 9
Robert E. Bower

1. OVERVIEW OF THE LANGLEY SUBSONIC RESEARCH EFFORT ON SCR CONFIGURATIONS 13
Paul L. Coe, Jr., James L. Thomas, Jarret K. Huffman, Robert P. Weston, Ward E. Schoonover, Jr., and Garl L. Gentry, Jr.

2. RESULTS OF A LOW-SPEED WIND TUNNEL TEST OF THE MDC 2.2M SUPERSONIC CRUISE AIRCRAFT CONFIGURATION 35
R. L. Roensch, J. E. Felix, H. R. Welge, L. P. Yip, and L. P. Parlett

3. THE PREDICTION OF PRESSURE DISTRIBUTIONS ON AN ARROW-WING CONFIGURATION INCLUDING THE EFFECT OF CAMBER, TWIST, AND A WING FIN 59
Marjorie E. Manro, Percy J. Bobbitt, and Robert M. Kulfan

4. EXPLORATORY SUBSONIC INVESTIGATION OF VORTEX-FLAP CONCEPT ON ARROW WING CONFIGURATION 117
Dhanvada M. Rao

5. WIND TUNNEL TEST RESULTS OF A NEW LEADING EDGE FLAP DESIGN FOR HIGHLY SWEPT WINGS - A VORTEX FLAP 131
L. James Runyan, Wilbur D. Middleton, and John A. Paulson

6. A STUDY OF WING BODY BLENDING FOR AN ADVANCED SUPERSONIC TRANSPORT . . 149
T. P. Goebel, E. Bonner, and D. A. Robinson

7. PREDICTION OF NACELLE AERODYNAMIC INTERFERENCE EFFECTS AT LOW SUPERSONIC MACH NUMBERS 171
Robert M. Kulfan

8. ANALYTIC DEVELOPMENT OF AN IMPROVED SUPERSONIC CRUISE AIRCRAFT BASED ON WIND TUNNEL DATA 205
R. L. Roensch and G. S. Page

9. SUPERSONIC WINGS WITH SIGNIFICANT LEADING-EDGE THRUST AT CRUISE 229
A. Warner Robins, Harry W. Carlson, and Robert J. Mack

SESSION II - STABILITY AND CONTROL
Chairman: Seth B. Anderson

INTRODUCTORY REMARKS 249
Seth B. Anderson

10. FLYING QUALITIES DESIGN CRITERIA APPLICABLE TO SUPERSONIC CRUISE AIRCRAFT 251
Charles R. Chalk

11. ADVANCED SUPERSONIC TRANSPORT FIXED-BASE SIMULATOR EVALUATIONS AT LANDING APPROACH 269
John B. Feather

12. SIMULATOR INVESTIGATION OF ARROW-WING LOW-SPEED HANDLING QUALITIES . . 285
Ben T. Averett

13. DEVELOPMENT OF SCR AIRCRAFT TAKEOFF AND LANDING PROCEDURES FOR COMMUNITY NOISE ABATEMENT AND THEIR IMPACT ON FLIGHT SAFETY 299
William D. Grantham and Paul M. Smith

SESSION III - PROPULSION
Chairman: Warner L. Stewart

INTRODUCTORY REMARKS 337
Warner L. Stewart

14. SUPERSONIC CRUISE RESEARCH PROPULSION SYSTEM STUDIES - SLIDE PRESENTATION (Text not available for publication) 339
R. D. Allan and J. E. Johnson

15. VCE TEST BED ENGINE FOR SUPERSONIC CRUISE RESEARCH 347
J. W. Vdoviak and J. A. Ebacher

16. VARIABLE STREAM CONTROL ENGINE FOR ADVANCED SUPERSONIC AIRCRAFT DESIGN UPDATE 357
Richard B. Hunt and Robert A. Howlett

17. PROGRESS WITH VARIABLE CYCLE ENGINES 371
John S. Westmoreland

18. EFFECTS OF INLET TECHNOLOGY ON CRUISE SPEED SELECTION 391
L. H. Bangert, D. M. Santman, G. Horie, and L. D. Miller

SESSION IV - ENVIRONMENTAL FACTORS
Chairman: R. W. Schroeder

INTRODUCTORY REMARKS 415
R. W. Schroeder

19. VCE EARLY ACOUSTIC TEST RESULTS OF GENERAL ELECTRIC'S HIGH-RADIUS RATIO COANNULAR PLUG NOZZLE 417
Paul R. Knott, J. F. Brausch, P. K. Bhutiani, R. K. Majjigi, and V. L. Doyle

20. FLIGHT AND TUNNEL TEST RESULTS OF THE MDC MECHANICAL JET NOISE SUPPRESSOR NOZZLE 453
R. D. FitzSimmons, R. A. McKinnon, and E. S. Johnson

21. EFFECTS OF NOZZLE DESIGN ON THE NOISE FROM SUPERSONIC JETS 479
John M. Seiner, Thomas D. Norum, and Lucio Maestrello

22. STATUS OF NOISE TECHNOLOGY FOR ADVANCED SUPERSONIC CRUISE AIRCRAFT . . 493
James R. Stone and Orlando A. Gutierrez

23. ENVIRONMENTAL EFFECTS OF AIRCRAFT AT CRUISE: AN UPDATE 519
N. Sundararaman

24. ADVANCED TECHNOLOGY FOR CONTROLLING POLLUTANT EMISSIONS FROM SUPERSONIC CRUISE AIRCRAFT 535
Robert A. Duerr and Larry A. Diehl

Part 2*

SESSION V - AIRFRAME STRUCTURES AND MATERIALS
Chairman: R. R. Heldenfels

INTRODUCTORY REMARKS 553
R. R. Heldenfels

25. STRUCTURAL CONCEPT TRENDS FOR COMMERCIAL SUPERSONIC CRUISE AIRCRAFT DESIGN 563
I. F. Sakata, G. W. Davis, and B. Saelman

26. OPPORTUNITIES FOR STRUCTURAL IMPROVEMENTS FOR AN ADVANCED SUPERSONIC TRANSPORT VEHICLE 589
J. E. Fischler

27. SUPERSONIC CRUISE RESEARCH AIRCRAFT STRUCTURAL STUDIES: METHODS AND RESULTS 617
J. Sobieszczanski-Sobieski, David Gross, William Kurtze, Jerry Newsom, Gregory Wrenn, and William Greene

*Papers 25 to 43 are presented under separate cover.

28. COMPRESSION PANEL STUDIES FOR SUPERSONIC CRUISE VEHICLES
(To be published as NASA TP-1617)
Robert R. McWithey, Dick M. Royster, and William L. Ko

29. FABRICATION DEVELOPMENT AND EVALUATION OF ADVANCED TITANIUM AND COMPOSITE STRUCTURAL PANELS (To be published as NASA TP-1616)
Thomas T. Bales, Edward L. Hoffman, Lee Payne, and Lawrence F. Reardon

30. AN ASSESSMENT OF BUFFER STRIPS FOR IMPROVING DAMAGE TOLERANCE OF COMPOSITE LAMINATES 657
C. C. Poe, Jr., and John M. Kennedy

31. EVALUATION OF HIGH-TEMPERATURE STRUCTURAL ADHESIVES FOR EXTENDED SERVICE 675
Carl L. Hendricks and Sylvester G. Hill

32. ADVANCED MATERIALS AND FABRICATION PROCESSES FOR SUPERSONIC CRUISE AIRCRAFT 687
Marlon K. Guess, Russell S. Kaneko, and George G. Wald

33. EFFECTS OF AN AST PROGRAM ON U.S. TITANIUM STORY 713
Richard D. Fitzsimmons

SESSION VI - SYSTEMS INTEGRATION AND ECONOMICS
Chairman: G. G. Kayten

INTRODUCTORY REMARKS 739
G. G. Kayten

34. CONCORDE WITH THE AIRLINES 741
Clive S. Leyman

35. LONG-RANGE AIRPLANE STUDY - THE CONSUMER LOOKS AT SST TRAVEL 759
Karyl H. Landes and J. A. Matter

36. ASSESSMENT OF THE IMPACT OF ADVANCED AIR-TRANSPORT TECHNOLOGY 805
R. L. Maxwell and L. V. Dickinson, Jr.

37. OVERVIEW OF BOEING SUPERSONIC TRANSPORT EFFORTS - 1971-1979 821
A. Sigalla

38. A FAMILY OF SUPERSONIC AIRPLANES - TECHNICAL AND ECONOMIC FEASIBILITY 833
Frank D. Neumann and Jerry W. Whitten

39. IMPACT OF CHANGING FUEL CHARACTERISTICS ON SUPERSONIC CRUISE AIRPLANE 855
O. J. Hadaller, J. E. Schmidt, A. M. Momenthy, and P. E. Johnson

40. TECHNOLOGY DEVELOPMENT STATUS AT McDONNELL DOUGLAS 873
William T. Rowe

41. SUPERSONIC MARKET AND ECONOMIC ANALYSES 889
Lucian S. Rochte

42. THE IMPACT OF MATERIALS TECHNOLOGY AND OPERATIONAL CONSTRAINTS ON THE ECONOMICS OF CRUISE SPEED SELECTION 909
J. S. Clauss, Jr., F. A. Bruckman, D. L. Horning, R. H. Johnston, and J. V. Werner

43. SUPERSONIC CRUISE VEHICLE RESEARCH/BUSINESS JET 935
Robert Kelly

ATTENDEES 951

SCR PROGRAM OVERVIEW

Vincent R. Mascitti
NASA Langley Research Center

Since the last Conference in 1976, the name of the program has changed from the Supersonic Cruise Aircraft Research (SCAR) program to the Supersonic Cruise Research (SCR) program as shown in figure 1. The deletion of the "A" is very significant as it emphasizes the fact that this is not an aircraft program but a research program. Focused research efforts are being carried out in Propulsion, Structures and Materials, Aerodynamic Performance, and Stability and Control as shown in figure 2. In each of these research areas, improved solutions to known supersonic problems are being sought. Consequently the SCR data base has been enhanced. This was shown very adequately by all the wind tunnel tests and experiments depicted in the multimedia presentation.

There are complex interdisciplinary relationships in the evolution of a supersonic cruise aircraft. The SCR program has adopted the Systems Integration Studies approach to sort out these interdisciplinary relationships and assess the impact of various disciplinary technology advances. As illustrated in figure 2, disciplinary results are fed to Systems Integration Study teams which consider the impact on baseline supersonic cruise aircraft concepts.

A break-out of the total program R&D funding to date ($86.2 million) is shown in figure 3. Figure 4 presents an eight year history of the R&D funding trends. Aside from the Lewis Research Center managed VCE test bed program, the funding has remained approximately constant at an average of eight million dollars per year. Figure 5 presents the SCR R&D funding distribution for FY 1980 and highlights the fact that the largest portion of funding is for Systems Integration Studies. This has grown somewhat over the years, seemingly at the expense of other disciplinary areas, however, a different picture emerges if the effort carried on under the Systems Studies is broken down by discipline. Figure 6 shows that multi-disciplinary efforts are also performed under these studies and the cross-hatched region emphasizes that industry is matching the government funding dollar for dollar.

In summary, (figure 7), the SCR program is a technology program, the systems integration studies are augmented by industry funding, and at the current time both NASA and industry prefer an integrated team approach. This Conference will provide examples of the research accomplishments obtained under sponsorship of the SCR program.

SCAR

Figure 1.- Program title change.

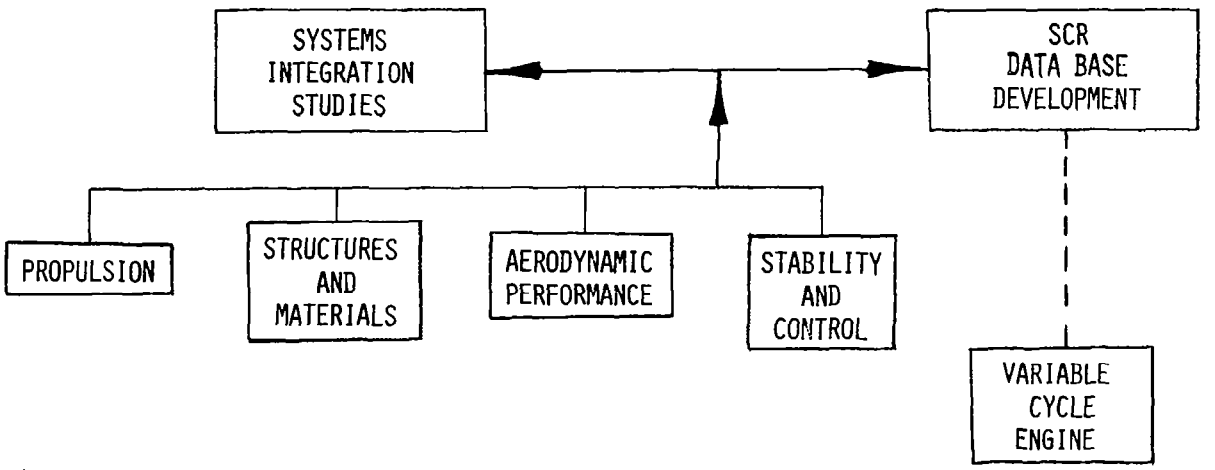

Figure 2.- Supersonic cruise research.

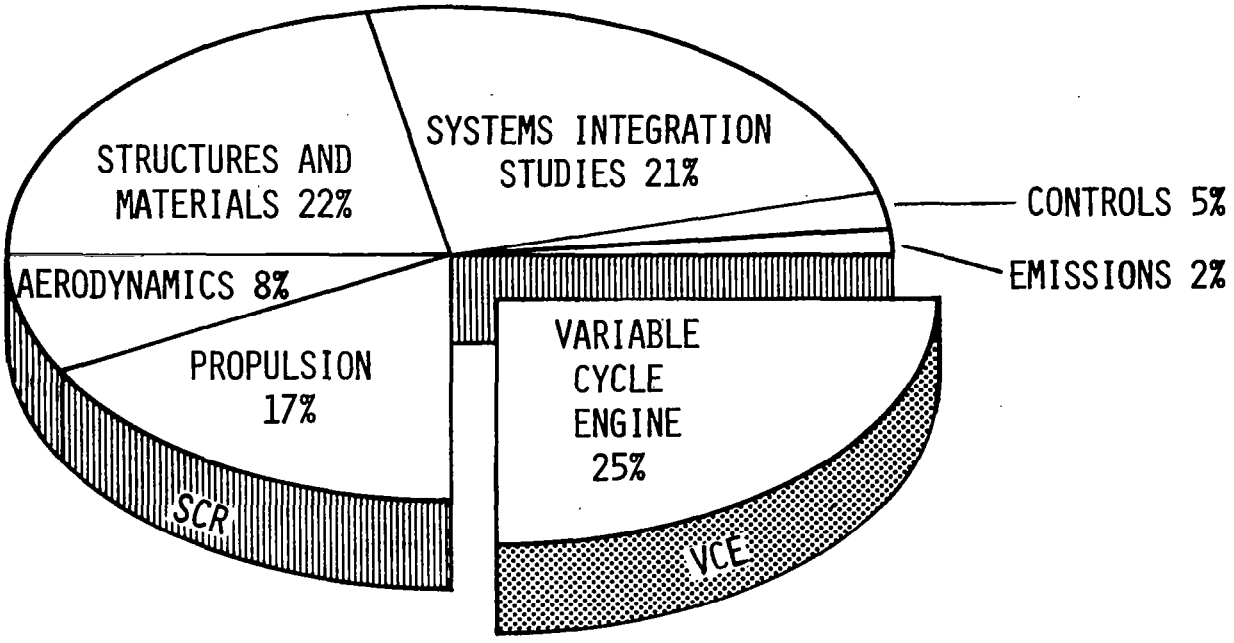

Figure 3.- Distribution of SCR and VCE R&D funding (total R&D funds to date ($86.2M)).

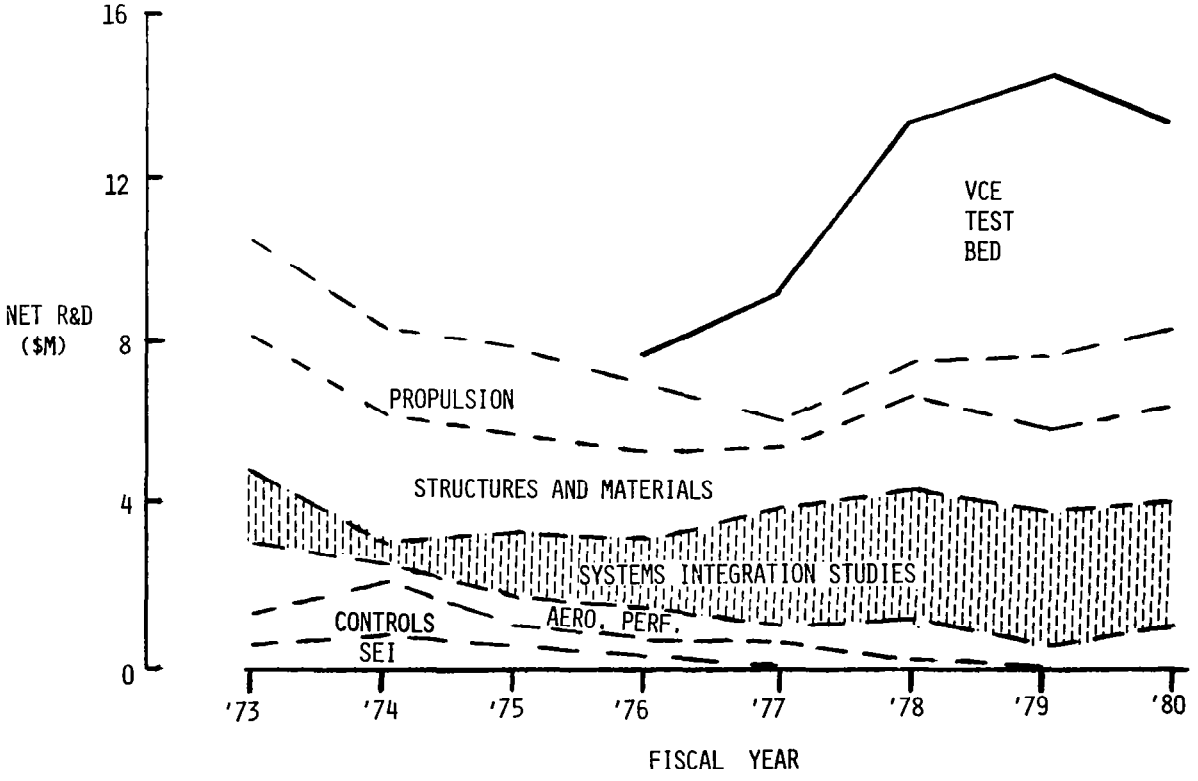

Figure 4.- SCR funding trends.

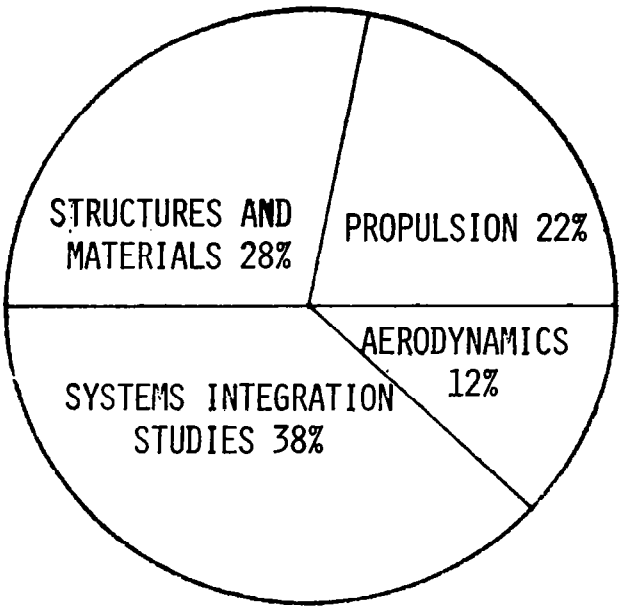

Figure 5.- Distribution of SCR FY 1980
R&D effort ($8.2M).

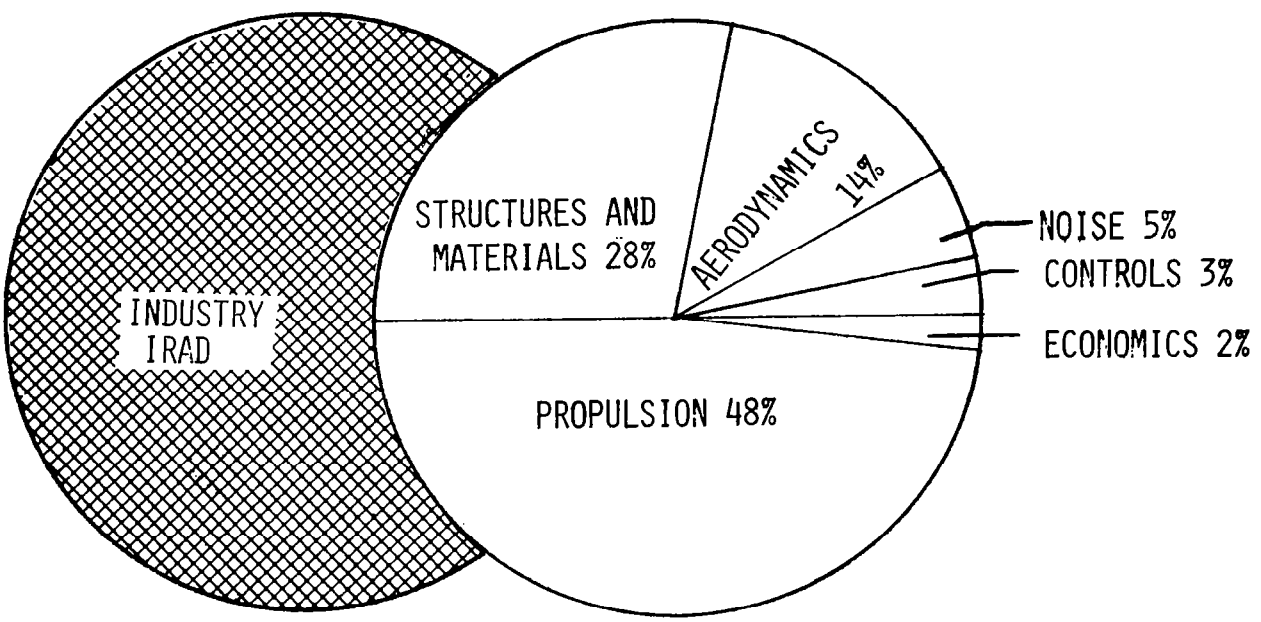

Figure 6.- 1980 systems integration studies by
discipline ($3.0M).

- SCR IS A TECHNOLOGY PROGRAM
- SCR SYSTEMS INTEGRATION STUDIES ARE AUGMENTED BY INDUSTRY
- INDUSTRY PREFERS INTEGRATED TEAM APPROACH

Figure 7.- Summary.

SESSION I - AERODYNAMICS

INTRODUCTORY REMARKS

Robert E. Bower
NASA Langley Research Center

This session consists of nine papers which summarize recent advances in low-speed and high-speed aerodynamics of supersonic cruise configurations.

Low-Speed Aerodynamics

The low-speed aerodynamics of highly swept slender wings has continued to receive attention because of the serious performance and stability and control problems caused by leading-edge flow separation and the resulting vortices. At the time of the 1976 Supersonic Cruise Aircraft Research (SCAR) Conference, these aerodynamic deficiences dominated aircraft sizing studies to the extent that wing loading and thrust-to-weight ratios were determined by the low-speed operational constraints. A considerable effort has been expended during these past three years to eliminate or minimize these deficiencies. Figure 1 shows the extensive amount of low-speed experimental data recently obtained on various supersonic cruise configurations by NASA and industry. The most significant advance has been leading-edge flap deflection concepts which effectively reduce leading-edge flow separation. Figure 2 presents the improvements in lift-to-drag ratio that have been achieved with these new concepts.

The paper by Coe (paper no. 1) will report on the Langley low-speed research program for supersonic cruise configurations and describe the theoretical and experimental studies that will form the basis of future research in this area. Recent experimental results obtained by industry and NASA with various leading-edge flap designs provide the focus for three papers to be presented by Roensch (paper no. 2), Rao (paper no. 4), and Runyan (paper no. 5).

Predicting aerodynamic pressure distributions on highly swept wings at moderate to high angles of attack is by no means a new problem. A program has been underway for the past five years to examine the state-of-the-art and advanced theoretical methods to predict aeroelastic loads on highly swept wings. Progress in this area will be the subject of the paper by Manro (paper no. 3). Recent experimental results obtained on a cambered-twisted wing and some new developments in separated-vortex and attached-flow advanced-panel methods will be presented.

High Speed Aerodynamics

Analytical design methods were emphasized in the 1976 SCAR Conference. In the last three years, these design methods have been exercised and both industry and NASA have constructed high speed wind tunnel models to verify the

design methods. Figure 3 shows the configurations that have been designed and the current status of the planned test programs. The predicted performance for the first five configurations depicted in figure 3 is shown in figure 4. The predicted performance range discussed during the last conference is represented by the shaded band. Predicted cruise lift-to-drag ratios above the band are a result of improved wing/body blending and nacelle integration methods.

The theoretical and analytical development of the Rockwell and Douglas configurations that are to be tested in the near future is the subject of two papers to be presented by Goebel (paper no. 6) and Roensch (paper no. 8). A paper by Kulfan (paper no. 7) will present results of a current effort to assess the accuracy of analytical predictions of nacelle aerodynamic interference effects at low supersonic speeds by means of test versus theory comparisons. A final paper by Robins (paper no. 9) will report on the results of a recently developed method for calculating and designing for leading-edge thrust at cruise.

		BOEING	DOUGLAS	LOCKHEED	NASA
PERFORMANCE:	LEADING EDGE DEVICES	●	●		●
	HIGH LIFT DEVICES		●		●
STABILITY:	LONGITUDINAL		●	●	○
	LATERAL-DIRECTIONAL		●	●	●
CONTROL:	LONGITUDINAL		●	●	
	LATERAL-DIRECTIONAL		●	●	○

○ TEST PLANNED
● TEST COMPLETED

Figure 1.- Experimental low speed SCR effort.

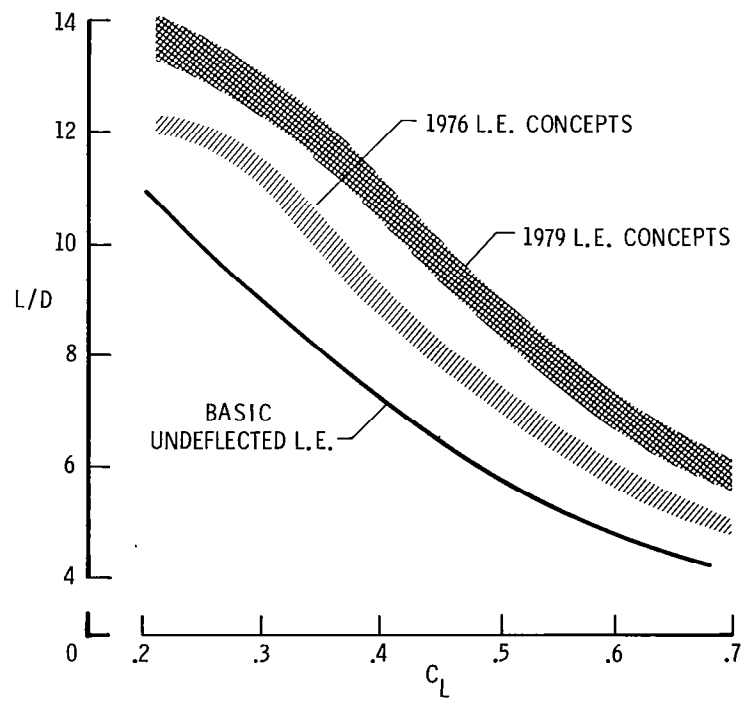

Figure 2.- Progress in low speed leading edge research.

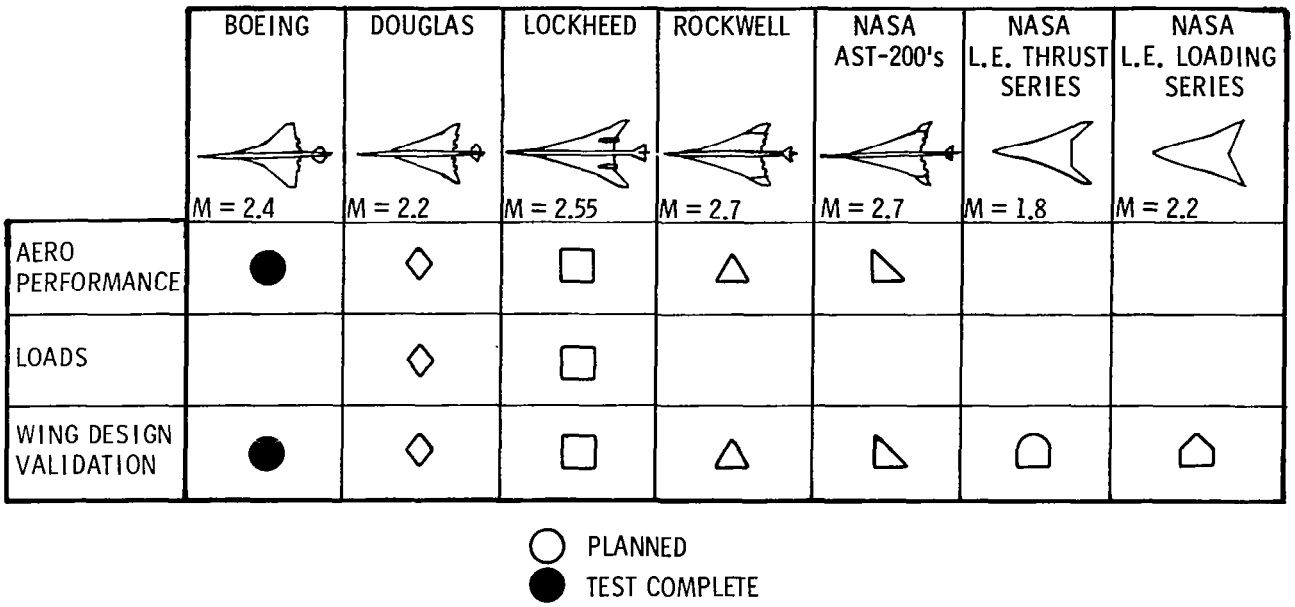

Figure 3.- High speed test matrix.

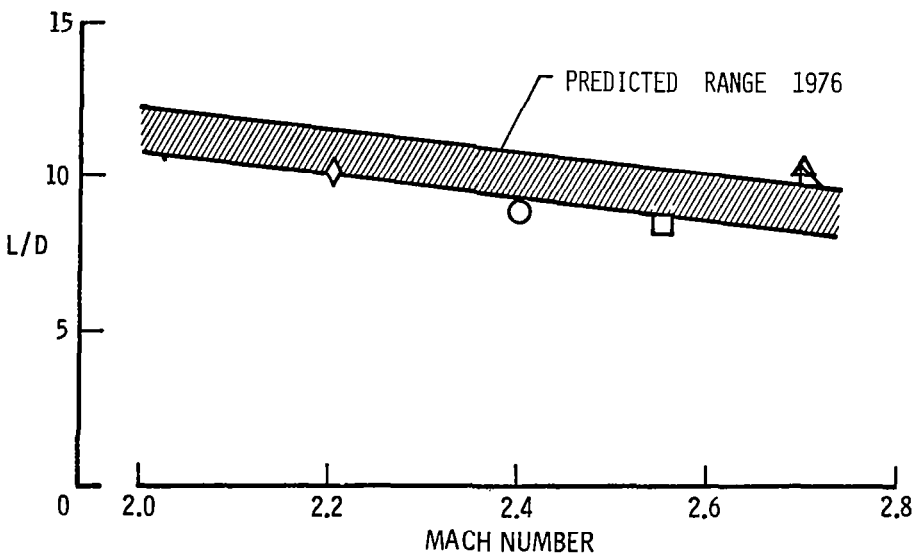

Figure 4.- Predicted aero performance for high speed configurations.

OVERVIEW OF THE LANGLEY SUBSONIC RESEARCH EFFORT ON SCR CONFIGURATIONS

Paul L. Coe, Jr., James L. Thomas, Jarrett K. Huffman, Robert P. Weston,
Ward E. Schoonover, Jr., and Garl L. Gentry, Jr.
NASA Langley Research Center

SUMMARY

The National Aeronautics and Space Administration is currently investigating the aerodynamic characteristics of advanced aircraft concepts which are capable of cruising efficiently at supersonic speeds. These conceptual designs are representative of future generation commercial and military vehicles and incorporate wing sweeps on the order of 70° to 80°. Unfortunately, owing to the high wing sweeps, such configurations exhibit deficiencies in the area of subsonic performance, stability, and control.

The present paper summarizes recent advances achieved by the NASA Langley Research Center in the subsonic aerodynamics of highly swept-wing designs. The most significant of these advances has been the development of leading-edge deflection concepts which effectively reduce leading-edge flow separation. The improved flow attachment results in substantial improvements in low-speed performance, significant delay of longitudinal pitch-up, increased trailing-edge flap effectiveness, and increased lateral-control capability.

The paper also considers various additional theoretical and/or experimental studies which, in conjunction with continued leading-edge deflection studies, forms the basis for Langley's future subsonic research effort.

INTRODUCTION

The National Aeronautics and Space Administration is currently investigating the aerodynamic characteristics of advanced aircraft concepts which are capable of cruising efficiently at supersonic speeds. These conceptual designs are representative of future generation commercial and military vehicles and incorporate wing sweeps on the order of 70° to 80°. (See, for example, refs. 1 and 2.) Unfortunately, owing to the high wing sweeps, such configurations exhibit deficiencies in the area of subsonic performance, stability, and control. The present paper is intended to provide a brief overview of the NASA Langley subsonic research effort which is intended to eliminate or minimize these above-mentioned deficiencies.

SYMBOLS

The longitudinal data are referred to the stability system of axes with the moment reference center being located at 59.16 percent of the reference mean aerodynamic chord. The reference wing area and chord are based on the wing planform which results from extending the inboard (74°) leading-edge sweep angle and the outboard (41.457°) trailing-edge sweep angle to the model center line. (See fig. 1.)

AR	aspect ratio
b	wing span, m (ft)
C_D	drag coefficient, Drag/qS_{ref}
$C_{D,sym}$	drag coefficient of equivalent symmetric configuration (without twist or camber) at zero lift
C_L	lift coefficient, Lift/qS_{ref}
C_{L_α}	lift-curve slope, $\partial C_L/\partial\alpha$, per deg
C_l	rolling-moment coefficient, Rolling moment/$qS_{ref}b$
C_{l_β}	lateral-stability derivative, $\partial C_l/\partial\beta$, per deg
C_m	pitching-moment coefficient, Pitching moment/$qS_{ref}c$
c	local chord, m (ft)
$\bar{c}$	reference mean aerodynamic chord, m (ft)
h	height of moment reference center above ground plane, m (ft)
q	free-stream dynamic pressure, Pa (lbf/ft^2)
R_N	Reynolds number
S_{ref}	reference wing area, m^2 (ft^2)
s	leading-edge suction parameter
$\bar{s}$	streamwise distance measured from wing leading edge
α	angle of attack, deg
β	angle of sideslip, deg
Γ	geometric anhedral, deg
δ_f	trailing-edge flap deflection normal to hinge line, positive when trailing edge is down, deg
δ_{l_e}	leading-edge deflection normal to hinge line, positive when leading edge is down, deg

DISCUSSION

Figure 1 presents a three-view sketch of the Langley SCR baseline concept (ref. 3) which has served as the focal point for the research effort summarized in figure 2. It should be noted that while much of the research has been

conducted for a particular conceptual design, the results are considered to be applicable to the generic class of highly swept-wing configurations. Recent results obtained for the areas of research indicated in figure 2 are presented in detail in references 4 through 7 and are summarized herein.

Effects of Leading-Edge Devices

As is well known, the previously mentioned deficiencies in low-speed performance, stability, and control are largely attributable to the problem of leading-edge flow separation. Consequently, Langley has concentrated its subsonic research on devising a satisfactory solution to that problem. The means considered include: deflection of the leading edge in an attempt to achieve attached flow (which is discussed in the present paper) and attempts to provide a controlled flow separation with vortex flap concepts as will be discussed in subsequent papers. (See refs. 8 and 9.)

Effect of leading-edge deflection on performance.- Figure 3 presents the drag polar for the configuration with undeflected leading edges. Also presented, for purposes of comparison, are drag polars approximating the condition of fully attached flow and the condition of fully separated flow with no subsequent reattachment. Expressions for the drag polars representing these conditions are given for fully attached flow as

$$C_D = C_{D_{sym}} + C_L^2/\pi AR \tag{1}$$

and for fully separated flow as

$$C_D = C_{D_{sym}} + C_L \tan (C_L/C_{L_\alpha}) \tag{2}$$

where $C_{D_{sym}}$ represents the drag coefficient of the untwisted, uncambered, wing-body combination at zero lift. Consideration of the experimental data of figure 3 indicates that with undeflected leading edges the flow is only partially attached for the range of lift cofficients of interest, i.e., $C_L > 0.3$. Smoke and oil flow visualization studies have identified flow separation on the outboard wing panel for $\alpha > 2^\circ$ and flow separation at the wing apex and 70.5° wing crank for $\alpha > 5^\circ$.

Figure 4 presents photographs of the wind-tunnel models used to investigate leading-edge deflection concepts intended to alleviate leading-edge flow separation. The rationale for these leading-edge concepts is discussed in detail in references 4, 6, and 10. The underlying consideration, however, is simply one of attempting to align the leading edge with the incoming flow field. The figure of merit customarily selected for such studies has been the effective leading-edge suction parameter, s, which is defined as illustrated in figure 5. (See ref. 11 for additional discussion of s.) Inasmuch as this parameter is intended to serve as an indicator of total wing efficiency, it has become customary to incorporate the influence of trailing-edge flap deflection in the calculation of s. This is accomplished by determining the envelope of the drag polar for the configuration with varying trailing-edge flap deflection

as illustrated in figure 5(b). It is, of course, acknowledged that by so doing the value of s, based on the polar envelope, is greatly influenced by the effectiveness of the trailing-edge flap system.

An initial study (ref. 4) in which an attempt was made to qualitatively evaluate the leading-edge upwash has shown that, for highly swept wings, theoretical estimates of the upwash are significantly greater than experimentally observed values. The results of that study led NASA to explore a uniform 30° leading-edge deflection, where 30° was selected as it was considered to represent an average value of the upwash along the span. The initial uniform 30° deflection studied resulted from "on-site" modifications to the wind-tunnel model shown on the left in figure 4. There was an inadequate wedge fairing between the deflected leading-edge segments and the main wing structure which resulted in a short bubble separation at the shoulder of the leading-edge flap. A more recent study, in which a circular arc fairing was introduced, has been found to eliminate this problem. Figure 6 presents the values of s calculated from the polar envelopes as a function of C_L for the uniform 30° deflected leading edges with both fairings. Also shown, for purposes of comparison, are comparable results for the configuration with an undeflected leading edge. As can be seen, both of the uniform 30° leading-edge configurations provided significant increases in s when compared with the undeflected leading edge. Furthermore, the circular arc leading-edge fairing provides about 5 to 10 percent higher values of s than the wedge fairing. It must be recalled that 30° represents an average value of the leading-edge upwash, and as such, this 30° leading edge is overdeflected at inboard span locations while being underdeflected at outboard span locations.

Additional studies in which the leading-edge deflection was contoured to more nearly align the leading edge with the incoming flow along the entire span have been conducted. The particular concepts studied are referred to as the NASA continuously warped leading edge (ref. 6) and the Boeing variable camber leading edge (ref. 10). Figure 7 presents the schedule for the leading-edge deflection angle as a function of the nondimensional semispan for these concepts. Experimental values of leading-edge suction are presented as a function of C_L in figure 8 for the Boeing variable camber concept (based on the polar envelope). Also presented for purposes of comparison are the corresponding results for the NASA uniform 30° deflected leading edge. As can be seen, the Boeing variable camber leading-edge concept results in a small increase in s for a given C_L. The NASA continously warped leading edge was unfortunately tested on a model which did not incorporate a trailing-edge flap system, and hence, a direct comparison with the values of s presented for the other concepts (based on the polar envelope) is not appropriate. Furthermore, inasmuch as the Boeing variable camber design process was conducted for conditions with $\delta_f = 5^{\circ}$, a comparison of results for conditions with $\delta_f = 0^{\circ}$ is not appropriate.

In order to provide a basis for comparison and some insight into the effect of trailing-edge flaps, figure 9 presents s versus α for the configuration with the Boeing variable camber leading-edge with several values of trailing-edge flap deflection. Also presented in figure 9 is the variation of s with respect to α for the configuration with the continously warped leading edge and $\delta_f = 0^{\circ}$. As can be seen, the continuously warped leading edge results in values of s which are equivalent to those acheived with the

variable camber leading edge for a given angle of attack; however, without the trailing-edge flap system, a higher α is required to obtain a given C_L. Additional tests are planned for the NASA continuously warped leading edge in conjunction with a trailing-edge flap system. Based on the trends observed from figure 9, it is anticipated that levels of leading edge suction higher than those presently achieved are obtainable.

It should be noted that the marked reduction in leading-edge suction, which occurs with increasing angle of attack, indicates that even with the deflected leading edges, flow separation persists at higher angles of attack. This result has been confirmed by smoke flow visualization studies which showed that, for angles of attack on the order of 8° to 10°, leading-edge separation originates at the 70.5° wing crank and on the 60° swept outboard panel. Inasmuch as the leading-edge deflection outboard of the 70.5° wing crank is largely constrained by a relatively short chord, a revised leading-edge hinge line, providing an increased chord for the leading-edge segment (as suggested in ref. 4), may aid in producing attached flow. It is further anticipated that the improvement provided by the revised hinge line would be enhanced upon the elimination of the 70.5° wing crank.

Although studies have shown that a large chord Krueger flap is effective in providing attached flow on the outboard panel, such a device may be impractical. Langley Research Center is, therefore, studying outboard panel twist and sweep in conjunction with revised outboard panel leading edges in an attempt to define alternate solutions to the problem of outboard panel flow separation.

Effect of leading-edge deflection on longitudinal stability.- In addition to improved low-speed performance, leading-edge deflection would be expected to improve longitudinal stability. Experimental results are presented in figure 10 in the form of C_m versus C_L and C_m versus α. The symbols presented in figure 10 represent the onset of pitch-up for the respective conditions. As can be seen, with undeflected leading edges, the configuration exhibits a marked pitch-up characteristic for $C_L > 0.3$ or $\alpha > 5^\circ$. The onset of this pitch-up characteristic is coincident with the formation of wing apex vortices and separation of the outboard wing panel. As expected, deflecting the wing leading edge, thereby postponing the angle of attack at which leading-edge separation occurs, results in a postponement of the pitch-up characteristic. The mild but persistent pitch-up characteristic exhibited by the configuration with deflected leading edges is considered to be a result of flow separation on the outboard wing panel. While additional research is planned to define the outboard panel geometry required to further postpone this characteristic, recent studies indicate that the linearity of C_m versus C_L, as provided by the present leading-edge devices, may be satisfactory with the introduction of α-limiting concepts.

Effect of leading-edge deflection on high lift.- The influence of leading-edge deflection on trailing-edge flap effectiveness is summarized in figure 11. As would be expected, the incremental lift provided by deflecting the plain trailing-edge flap system is markedly increased by the improved flow attachment obtained through leading-edge deflection. For values of $\delta_f < 20^\circ$, the results indicate a level of trailing-edge effectiveness which is equivalent to that

predicted by simple vortex-lattice potential-flow theory (ref. 12). Although a slotted trailing-edge system may provide increased flap effectiveness for $\delta_f > 20^\circ$, at lower flap deflections it would not increase the lifting capability above that which is available through use of appropriate leading-edge deflection.

Effect of leading-edge deflection on lateral control.- Consistent with the increased trailing-edge flap effectiveness, figure 12 shows that leading-edge deflection also provides a marked increase in the roll control provided by the outboard ailerons. Owing to the excessively high level of effective dihedral, which accompanies highly swept wings, improved roll control is particularly critical for this class of vehicle. When considering the current 30 knot crosswind landing criteria, the present level of effective dihedral requires that the configuration achieve a lateral-control capability on the order of $C_l = 0.04$. It is anticipated that increased lateral control will result from additional studies intended to further improve the flow over the outboard wing panel.

Effect of Reynolds Number

It should be noted that the data presented in the preceding section were obtained from tests conducted for values of R_N on the order of 2.5×10^6; hence, the results may not be directly applicable to aircraft concepts which operate at values of R_N on the order of 100×10^6. An illustration of R_N effects is provided by consideration of the pressure distribution over the leading edge of the 70° swept glove of an F-111 airplane. These data were obtained during joint NASA-Air Force flight tests. Figure 13 shows the aircraft in flight and illustrates the configuration cross section at the particular span station or which the data were measured. Figure 14 presents the experimental variation of C_p with the nondimensional distance from the leading edge, $\bar{s}/c$, at values of $R_N = 20 \times 10^6$ and 40×10^6. Data obtained at $R_N = 20 \times 10^6$ indicate the presence of a vortex core passing about 3 percent aft of the leading edge. In contrast to this result, data obtained at $R_N = 40 \times 10^6$ are indicative of attached flow conditions. The preceding result serves to illustrate the need for wind-tunnel tests conducted at representative values of flight R_N.

Additional Studies and Future Plans

Although the development of leading-edge deflection concepts has been the recent emphasis of the subsonic SCR effort, other aspects of the conceptual design are being actively studied (see fig. 2). These theoretical and/or experimental studies, in conjunction with the previously discussed leading-edge deflection studies, form the basis for Langley's future subsonic research effort. This future research effort is summarized in figures 15 and 16. Highlights of various isolated research efforts are summarized in the following discussion.

Leading-edge upwash.- As mentioned in a previous section, initial attempts to qualitatively evaluate the leading-edge upwash (ref. 4) have shown that for highly swept wings, theoretical estimates of the upwash are significantly greater than experimentally observed values. In order to quantatively define

the leading-edge upwash, laser velocimeter techniques will be used to measure the flow field. It is anticipated that these studies will provide the information necessary to develop optimum leading-edge deflection concepts.

Inboard wing leading-edge sweep and hinge line.- Low-speed experimental studies (see, for example, refs. 4 and 6) have shown that flow separation originates at the mid-span wing crank. These studies have shown that, while postponed, this separation pheneomena persists even with the deflected leading-edge concepts considered to date. In an attempt to quantatively define the potential benefits of eliminating this inboard sweep break, experimental studies will be conducted with a constant sweep inboard leading edge, as sketched in figure 16. These studies will further consider a revised leading-edge hinge line, also sketched in figure 16. The revised hinge line, which is discussed in reference 4, is intended to provide an increased leading-edge flap chord outboard (where it is most needed) while reducing the chord inboard, where leading-edge deflection is less critical.

Outboard panel twist and sweep.- As noted in a previous section, providing attached flow on the 60° outboard wing panel at moderate to high angles of attack remains a challenge. Consequently, tests are planned to determine the effect of outboard panel twist and sweep on low-speed performance, longitudinal stability, and lateral control. Increased twist (washout) of the outboard panel would, of course, degrade the span-load distribution and hence would have a detrimental effect on supersonic performance. However, if all movable wing tips are considered, increased washout may be a means for promoting attached flow. Reduced sweep of the outboard panel (in contrast to increased washout) may represent a more viable solution to the problem. Recent in-house studies have indicated that reduced outboard panel sweep would not significantly degrade supersonic performance.

The intent of the above low-speed study is to determine the twist and sweep of the outboard panel (in conjunction with revised outboard panel leading-edge treatment) required to provide attached flow and to determine the magnitude of the resulting improvements in the low-speed aerodynamic charactersitics so that a detailed trade study can be conducted.

Outboard vertical-fin position and orientation.- A theoretical study presented in reference 7 has shown that increasing the inwardly directed load on the outboard vertical fin results in an improved span-load distribution, and therefore, improved low-speed performance. The study has shown that such an increase in load may be accomplished by moving the outboard vertical fin forward or by toeing the vertical fin inwardly. Inasmuch as the present position and orientation of the outboard vertical fin is based on supersonic performance considerations, such changes may be inappropriate. However, an alternate means of increasing the vertical fin load would be to produce an effective camber surface by introducing a vertical fin rudder. Such a system may also require some form of vertical fin leading-edge treatment to prevent flow separation. Wind-tunnel tests are planned to determine if the improvement in low-speed performance predicted by theory can be achieved.

Geometric anhedral.- As noted in a previous section, the excessively high level of effective dihedral, which is associated with high wing sweep, is found

to require relatively high levels of lateral control to meet the current 30 knot crosswind landing criteria. These values of C_{l_β}, however, are based on test data for the cruise shape wing. Recent structural analysis has shown that in the landing condition the wing assumes a shape which is somewhat different from the cruise shape. The difference in wing shape results in the configuration having an increased geometric anhedral for the landing condition.

Recent wind-tunnel tests (see ref. 6) have determined the variation of C_{l_β} with respect to geometric anhedral and have further shown that the increment in C_{l_β} due to anhedral can be approximated with the use of simple vortex-lattice theory (see fig. 17). Based on the anticipated shape of the wing in the landing condition, and the results obtained from reference 5, it is considered that the values of C_{l_β} (as predicted by wind-tunnel tests of the cruise shape wing) are about 10 percent high. This value will be refined with subsequent wind-tunnel tests of the configuration employing the assumed landing geometry.

Leading-edge optimization for high-lift condition.- As noted previously, the NASA continuously warped leading edge has provided higher levels of leading-edge suction than the other concepts considered. However, this concept was tested on a model which did not incorporate trailing-edge flaps, and hence, its high-lift characteristics are not well defined. Experimental studies will be conducted for the continuously warped leading edge in conjunction with a trailing-edge flap system. Preliminary evidence indicates that the increased circulation provided by the trailing-edge flap system may require the leading-edge deflection schedule to be optimized as a function of trailing-edge flap deflection.

Ground effects.- Recent studies of ground effects (ref. 5), conducted using a vortex-lattice theoretical model (with ground-plane image) and experimentally with a moving ground belt, have shown that the configuration, as expected, experiences an increase in lift, a reduction in induced drag, and an increase in longitudinal stability when in ground effect (see fig. 18). The study has shown that the effects are generally more pronounced than previous estimates had indicated and result in a greater reduction in vertical descent rate than initially anticipated. The study, however, did not address the possible power-induced effects and, as such, remains incomplete. Current plans include additional tests to define the influence of thrust on ground effects while simultaneously exploring the magnitude and extent of the trailing vortex phenomena as it exists for the present SCR concept.

Reynolds number effects.- Limited available data indicate that significant Reynolds number effects may exist for highly swept wing concepts. Langley Research Center is, therefore, in the process of defining a highly swept wing, general research model capable of being tested at values of R_N on the order of 100×10^6 and a corresponding Mach number of 0.3. These tests will be possible in the National Transonic Facility and are tentatively scheduled for 1982.

CONCLUDING REMARKS

The present paper has been intended to briefly summarize recent advances achieved by the NASA Langley Research Center in the subsonic aerodynamics of low-aspect-ratio, highly swept-wing designs. The most significant of these advances has been the development of leading-edge deflection concepts which effectively reduce leading-edge flow separtion. The improved flow attachment results in substantial improvements in low-speed performance, significant delay of longitudinal pitch-up, increased trailing-edge flap effectiveness, and increased lateral-control capability.

The paper also considers various additional theoretical and/or experimental studies which, in conjunction with the continued leading-edge deflection studies, forms the basis for Langley's future subsonic research effort.

REFERENCES

1. Robins, A. Warner; Morris, Odell A.; and Harris, Roy V., Jr.: Recent Results in the Aerodynamics of Supersonic Vehicles. J. Aircraft, vol. 3, 1966, pp. 573-577.

2. Robins, A. Warner; Lamb, Milton; and Miller, David S.: Aerodynamic Characteristics at Mach Numbers of 1.5, 1.8, and 2.0 of a Blended Wing-Body Configuration With and Without an Integrand Canard. NASA TP 1427, 1979.

3. Staff, Hampton Technical Center, LTV Aerospace Corporation: Advanced Supersonic Technology Concept Study Reference Characteristics. NASA CR 132374, 1973.

4. Coe, Paul L., Jr.; and Weston, Robert P.: Effects of Wing Leading-Edge Deflection on the Low-Speed Aerodynamic Characteristics of a Low-Aspect-Ratio Highly Swept Arrow-Wing Configuration. NASA TP 1434, 1979. (Supercedes NASA TM 78787, 1978.)

5. Coe, Paul L., Jr.; and Thomas, James L.; Theoretical and Experimental Investigation of Ground Induced Effects for a Low-Aspect-Ratio Highly Swept Arrow-Wing Configuration. NASA TP 1508, 1979. (Supercedes NASA TM 80041, 1979.)

6. Coe, Paul L., Jr.; and Huffman, Jarrett K.: Influence of Optimized Leading-Edge Deflection and Geometric Anhedral on the Low-Speed Aerodynamic Characteristics of a Low-Aspect-Ratio Highly Swept Arrow-Wing Configuration. NASA TM 80083, 1979.

7. Johnson, Vicki S.; and Coe, Paul L., Jr.: Effect of Outboard Vertical Fin Position and Orientation on the Low-Speed Aerodynamic Performance of Highly Swept Wings. NASA TM 80142, 1979

8. Rao, D. M.: Exploratory Subsonic Investigation of Vortex-Flap Concept on Arrow Wing. Supersonic Cruise Research '79, NASA CP-2108, 1980. (Paper no. 4 of this compilation.)

9. Runyan, L. J.; Middleton, W. D.; and Paulson, J. A.: Wind Tunnel Test Results of a New Leading Edge Flap Design for Highly Swept Wings--A Vortex Flap. Supersonic Cruise Research '79, NASA CP-2108, 1980. (Paper no. 5 of this compilation.)

10. Paulson, J. A.; Boctor, M. L.; Maier, R. E.; Middleton, W. D.; and Vachal, J. D.: Leading-Edge Flap Design for an Arrow-Wing Configuration. NASA CR 145273, 1978.

11. Henderson, William P.: Studies of Various Factors Affecting Drag Due to Lift at Subsonic Speeds. NASA TN D-3584, 1966.

12. Tulinius, J.: Unified Subsonic, Transonic, and Supersonic NAR Vortex Lattice. Rep. TFD-72-253, Rockwell International Corporation, 1972

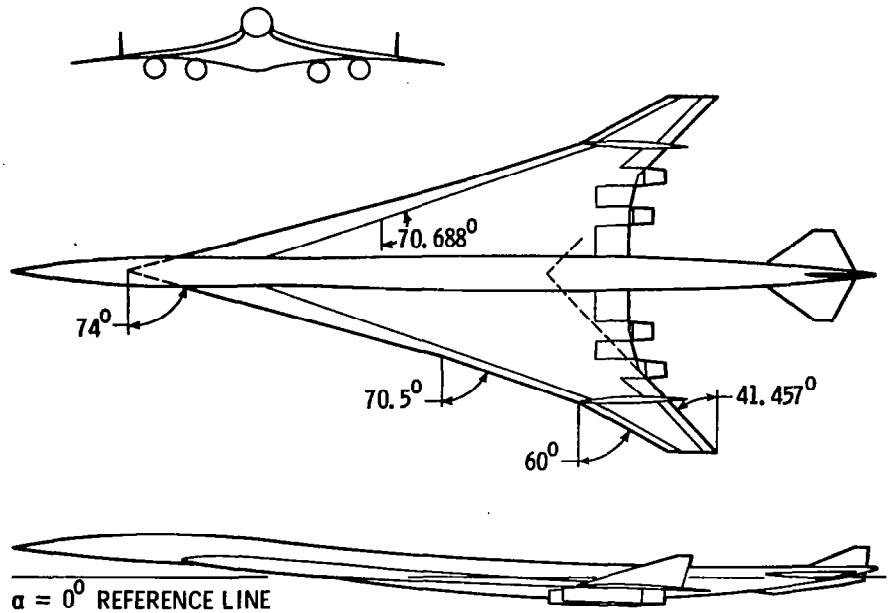

Figure 1.- Three-view sketch of Langley SCR baseline concept.

RESEARCH AREAS	OPPORTUNITIES FOR IMPROVEMENT: PERFORMANCE	LONGITUDINAL STABILITY	HIGH LIFT	LATERAL STABILITY	LATERAL CONTROL
• LEADING-EDGE DEVICES	X	X	X		X
- ATTACHED FLOW					
- VORTEX FLAP CONCEPTS					
• OUTBOARD PANEL TWIST AND SWEEP	X	X			X
• OUTBOARD VERTICAL FIN POSITION AND ORIENTATION	X				
• GEOMETRIC ANHEDRAL				X	
• GROUND EFFECTS	X	X			

Figure 2.- Summary of the NASA-LRC subsonic SCR program.

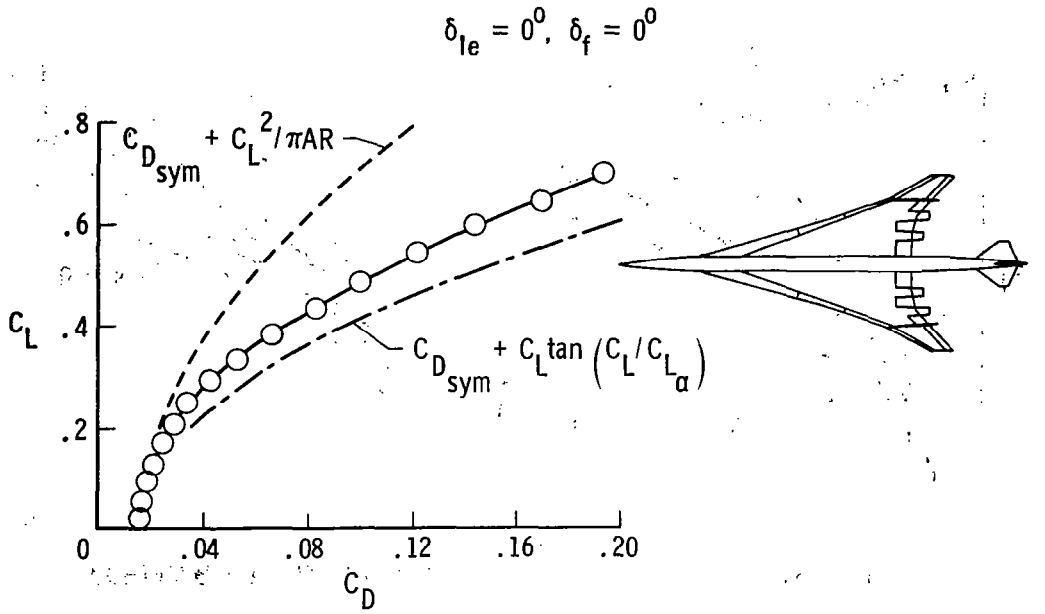

Figure 3.- Drag polar for baseline configuration.

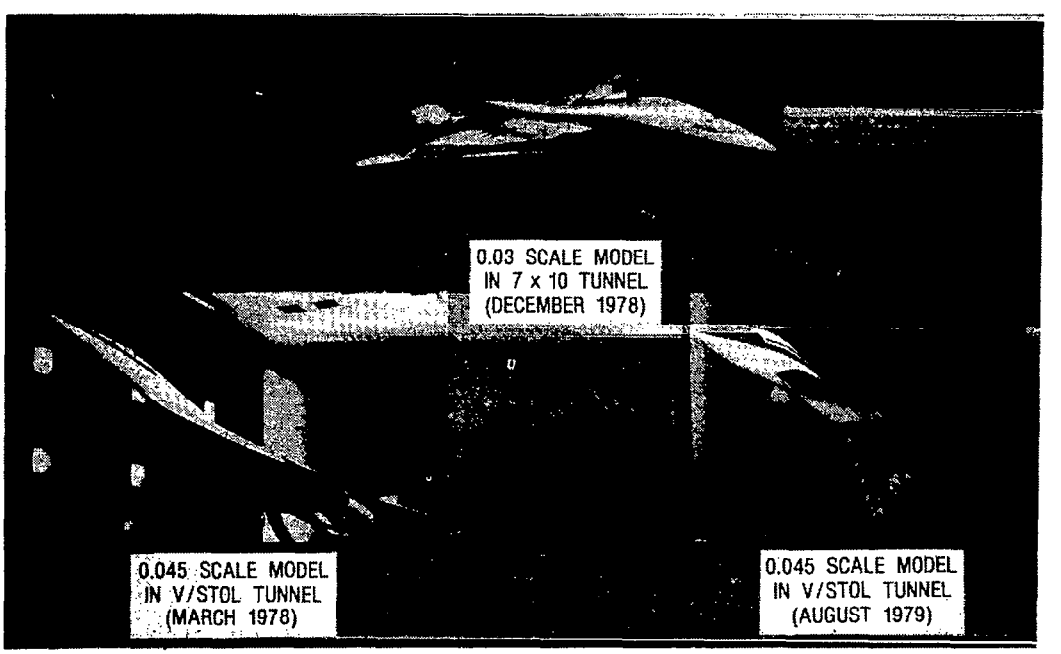

Figure 4.- Photographs of models used in leading-edge deflection studies.

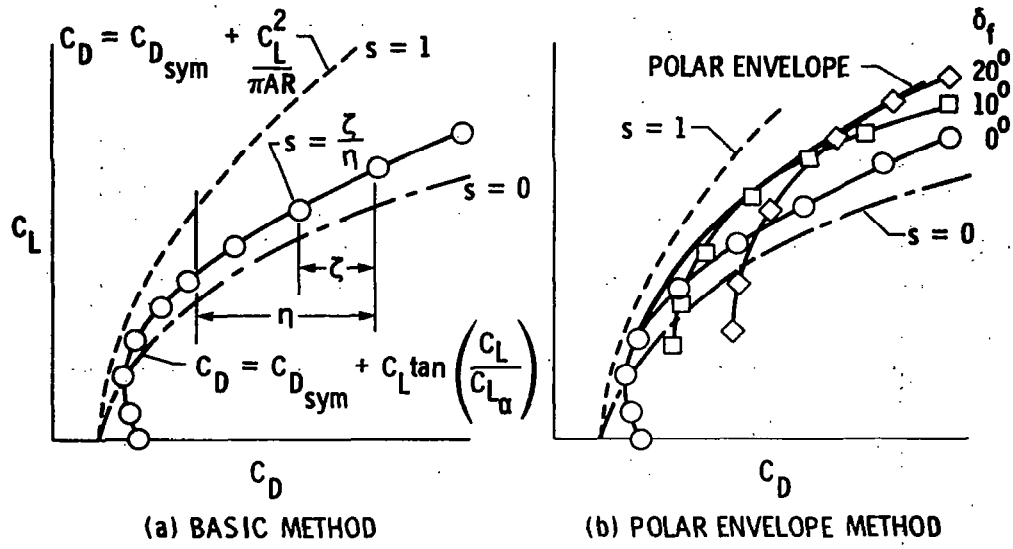

Figure 5.- Illustration of leading-edge suction determination.

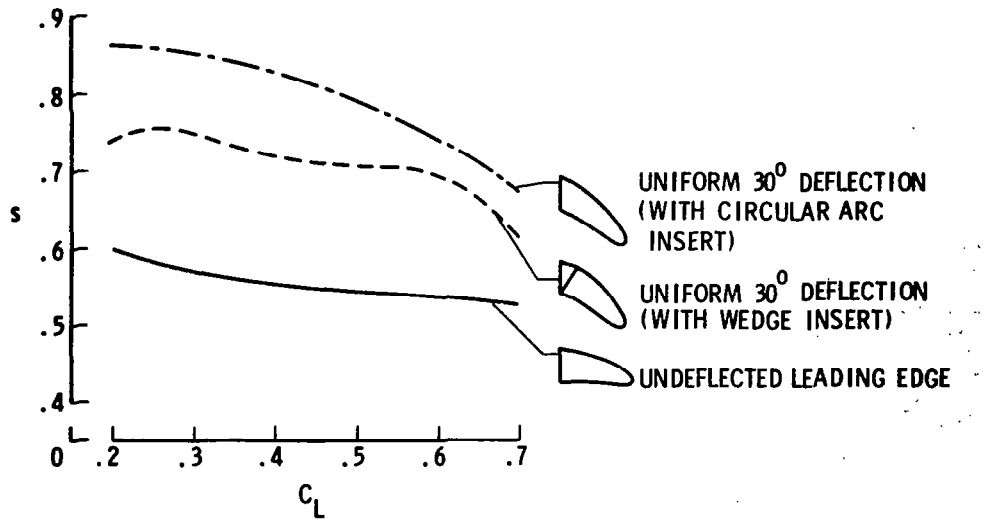

Figure 6.- s versus C_L for baseline configuration with uniformly deflected leading edge. (Polar envelope method.)

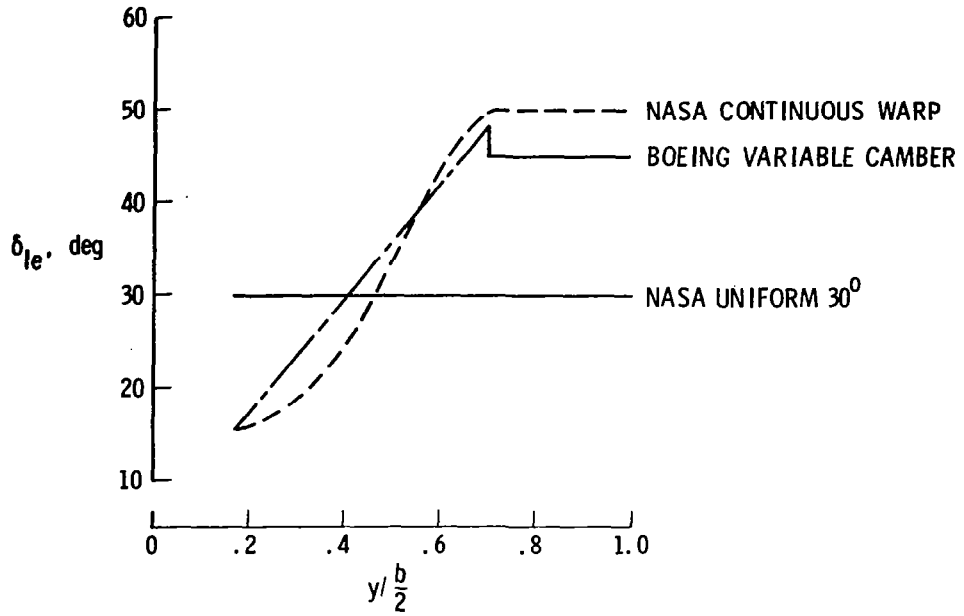

Figure 7.- Leading-edge deflection schedule for concepts studied.

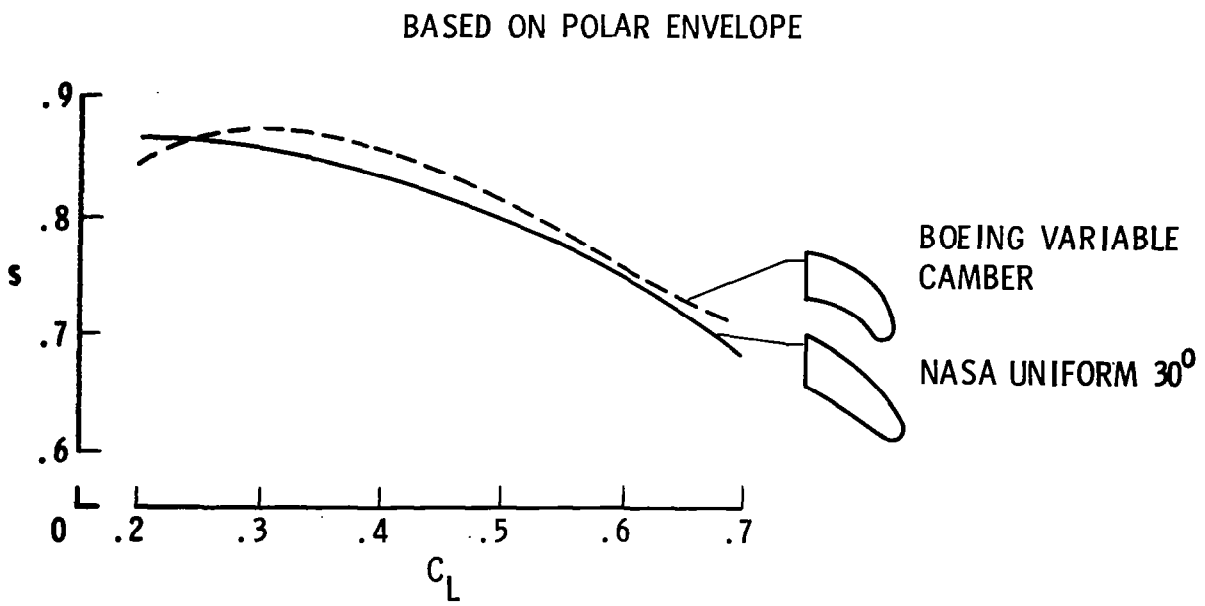

Figure 8.- s versus C_L for configuration with uniformly deflected leading edge and Boeing variable camber leading edge.

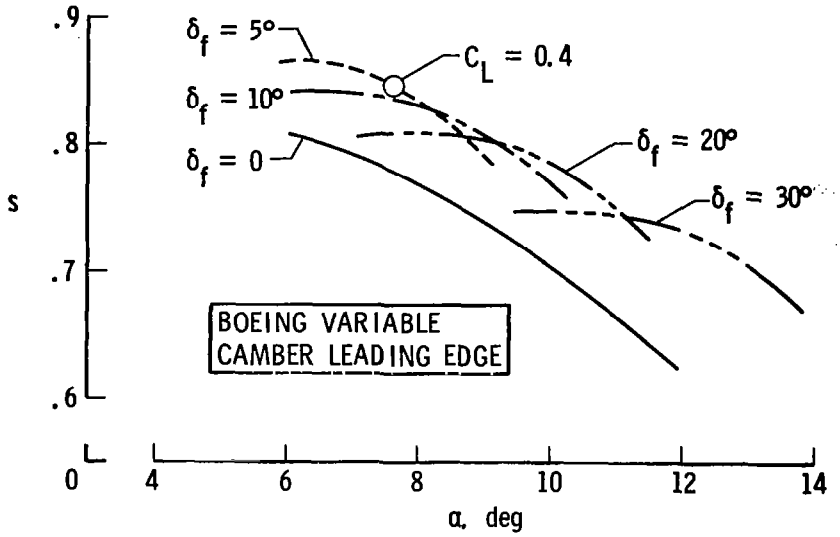

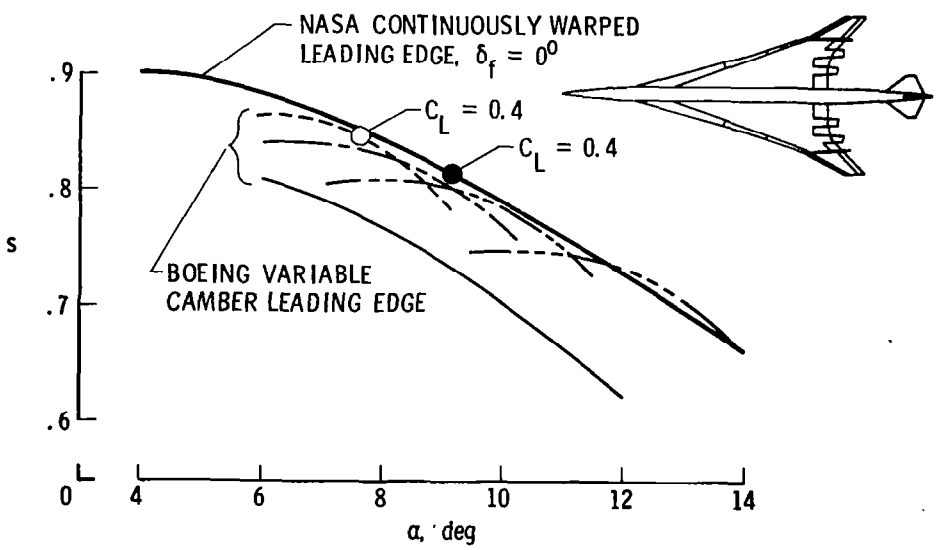

Figure 9.- Comparison of leading-edge suction for Boeing variable camber and NASA continuously warped leading edges.

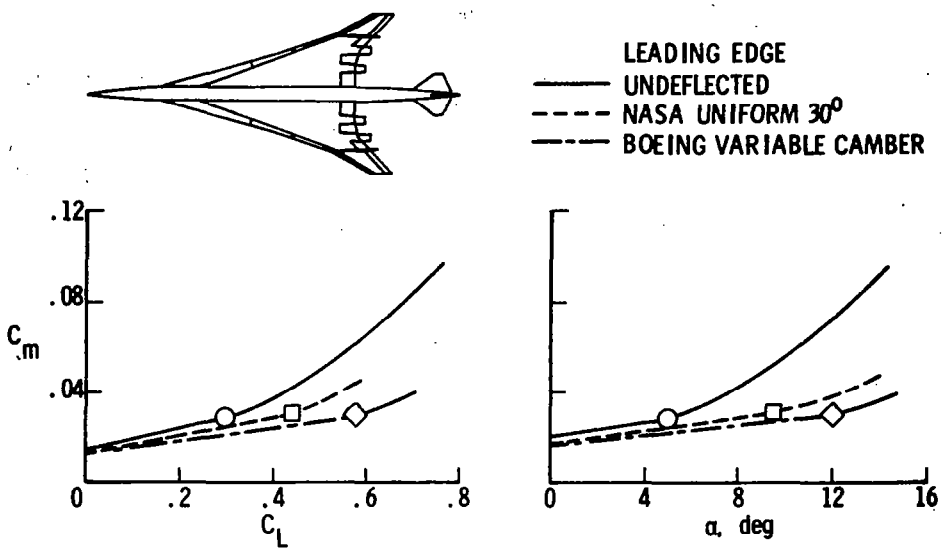

Figure 10.- Effect of leading-edge deflection on longitudinal stability. (Symbols represent the onset of pitch-up.)

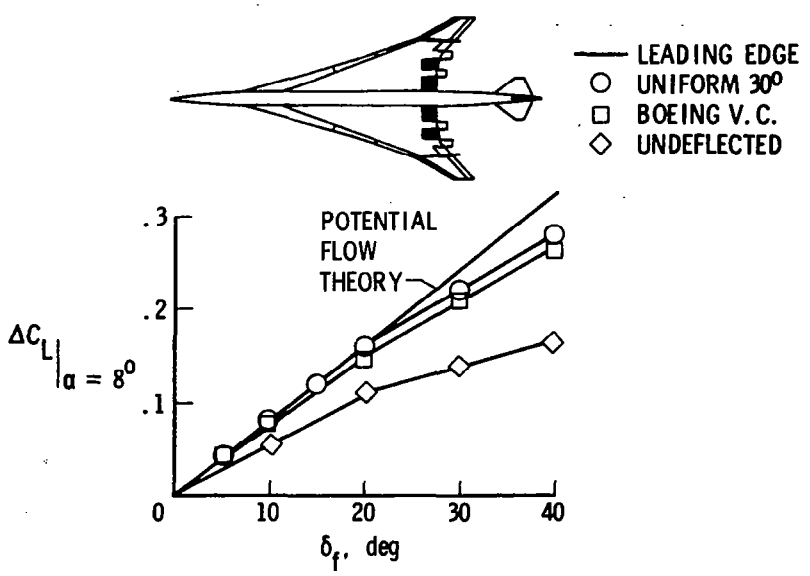

Figure 11.- Effect of leading-edge deflection on trailing-edge flap effectiveness.

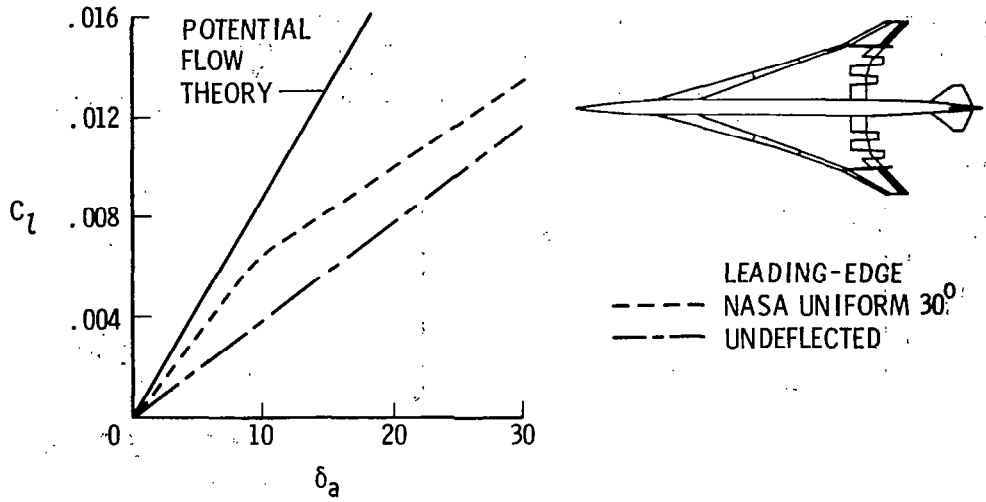

Figure 12.- Effect of leading-edge deflection on aileron effectiveness.

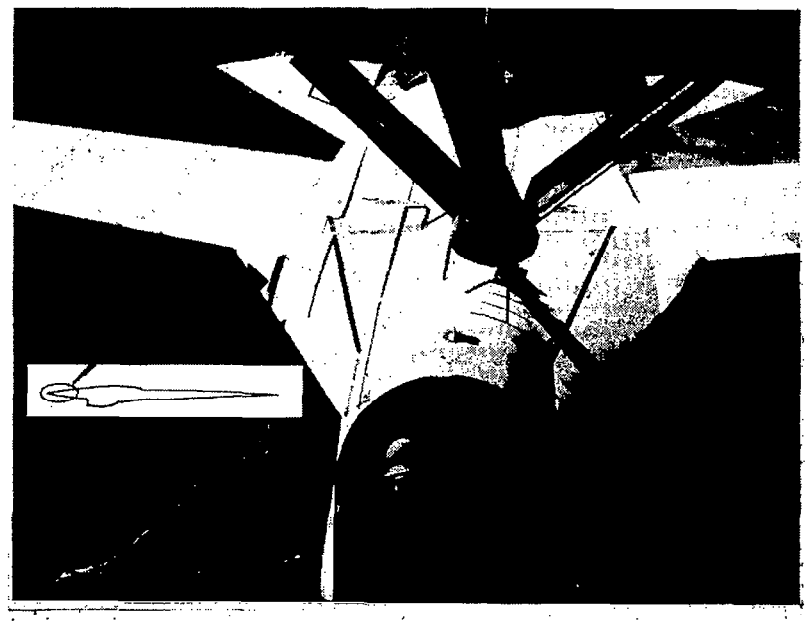

Figure 13.- F-111 during joint NASA-Air Force flight tests.

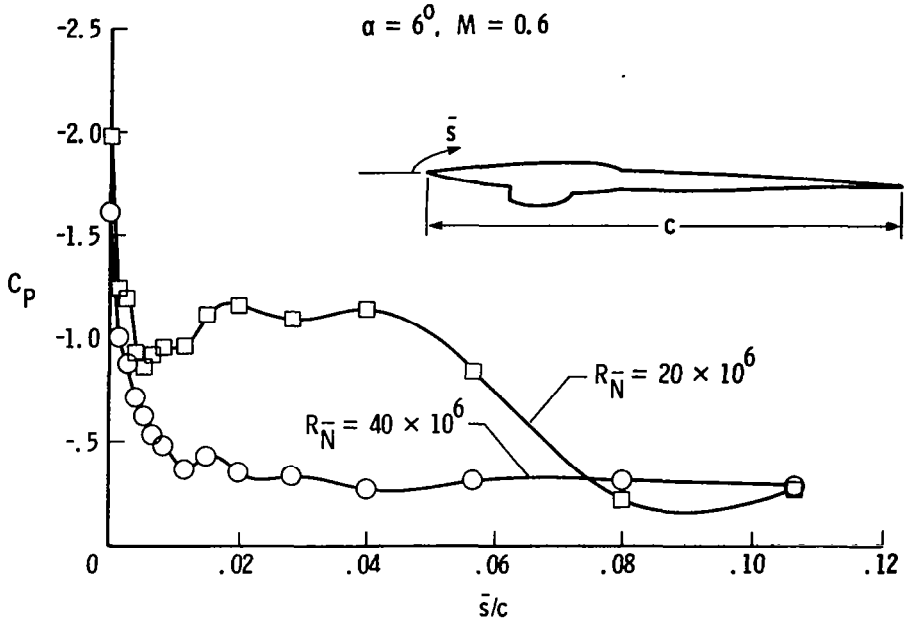

Figure 14.- Influence of R_N on leading-edge pressure distribution.

- DETERMINE LEADING EDGE UPWASH USING L.V. TECHNIQUES
- DETERMINE AERODYNAMIC IMPROVEMENTS WITH MODIFIED GEOMETRY
- OPTIMIZE LEADING EDGE FOR HIGH-LIFT CONDITION
- DETERMINE INFLUENCE OF THRUST ON GROUND EFFECTS
- DEFINE TRAILING VORTEX PHENOMENON
- DETERMINE R_N EFFECTS

Figure 15.- Summary of NASA-LRC future subsonic research effort.

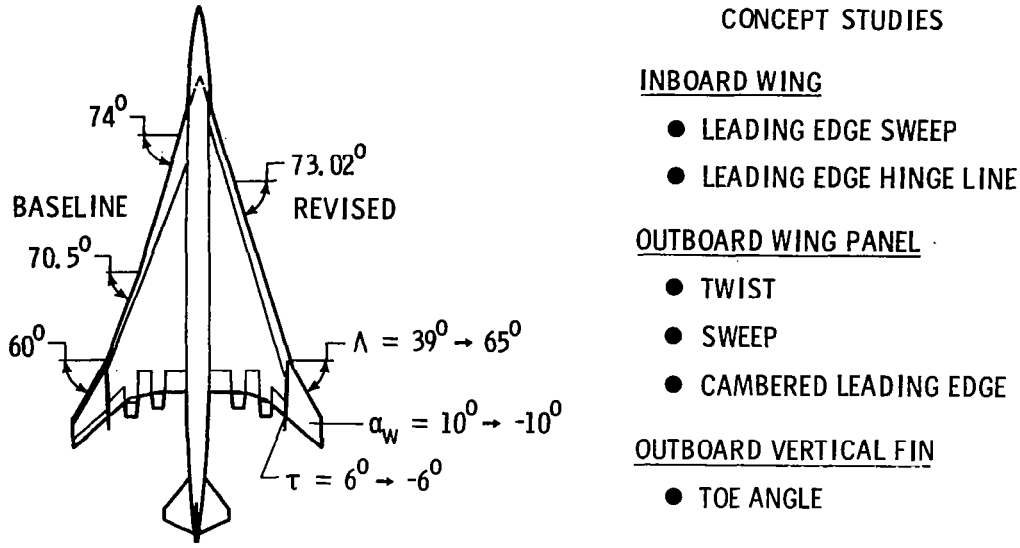

Figure 16.- SCR concept modification studies.

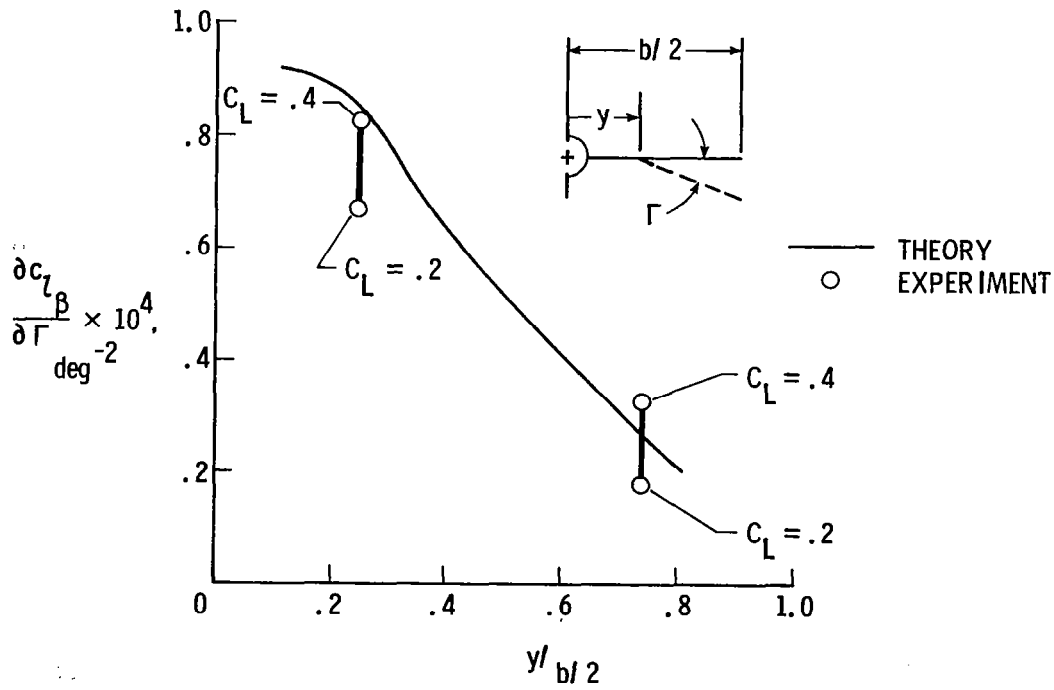

Figure 17.- Values for $\partial C_{l_\beta}/\partial \Gamma$ obtained by inclusion of additional geometric anhedral at span station $\frac{y}{b/2}$.

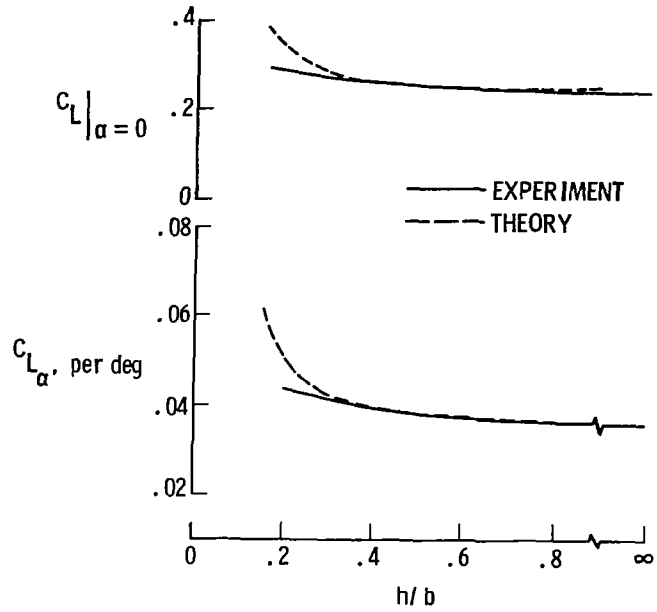

(a) Influence of ground effects on $C_L|_{\alpha=0}$ and C_{L_α}.

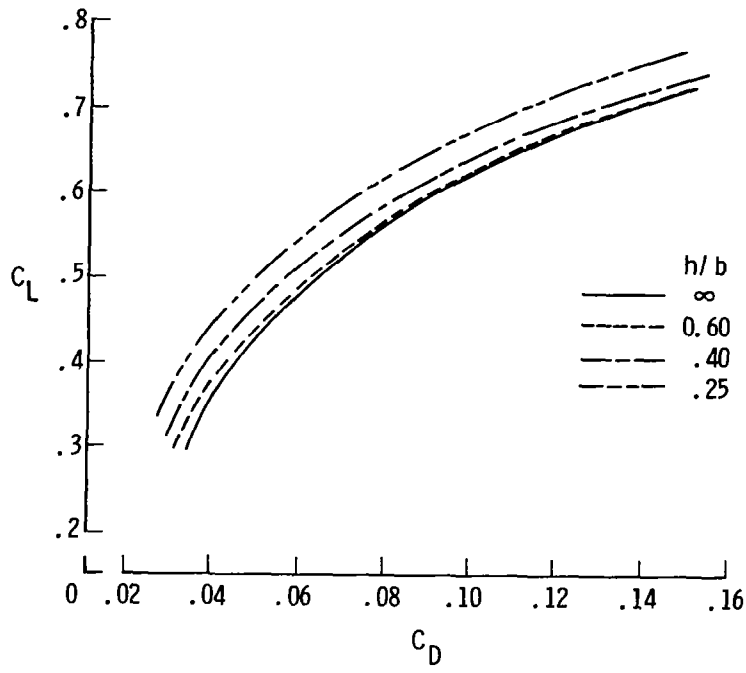

(b) Influence of ground effects on drag polar.

Figure 18.- Influence of ground effects on longitudinal aerodynamic characteristics. $\delta_f = 20^\circ$; $\delta_{LE} = 30^\circ$.

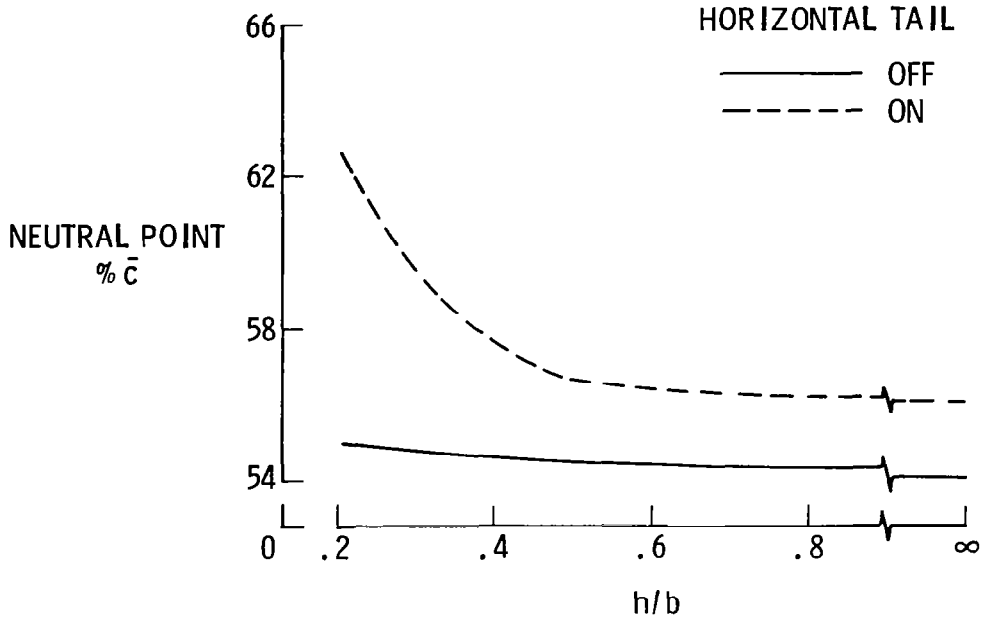

(c) Influence of ground effects on longitudinal stability.

Figure 18.- Concluded.

RESULTS OF A LOW-SPEED WIND TUNNEL TEST OF THE MDC 2.2M SUPERSONIC CRUISE AIRCRAFT CONFIGURATION*

R.L. Roensch, J.E. Felix, and H.R. Welge
Douglas Aircraft Company
McDonnell Douglas Corporation

L.P. Yip and L.P. Parlett
Langley Research Center

SUMMARY

Results of a low-speed test conducted in the Full Scale Tunnel at NASA Langley using an advanced supersonic cruise vehicle configuration are presented. These tests were conducted using a ten-percent scale model of a configuration developed by McDonnell Douglas that had demonstrated high aerodynamic performance at Mach 2.2 during a previous test program. The low-speed model has leading- and trailing-edge flaps designed to improve low-speed lift-to-drag ratios at high lift and includes devices for longitudinal and lateral/directional control.

The results obtained during the low-speed test program have shown that full-span leading-edge flaps are required for maximum performance. The amount of deflection of the leading-edge flap must increase with C_L to obtain the maximum benefit. Over eighty percent of full leading-edge suction was obtained up to lift-off C_L's of 0.65.

A mild pitch-up occurred at about 6° angle of attack with and without the leading-edge flap deflected. The pitch-up is controllable with the horizontal tail. Spoilers were found to be preferable to spoiler/deflectors at low speeds. The vertical tail maintained effectiveness up to the highest angle of attack tested but the tail-on directional stability deteriorated at high angles of attack. Lateral control was adequate for landing at 72 m/sec (140 knots) in a 15.4 m/sec (30 knot) crosswind.

It is recommended that in the future the drag-due-to-lift characteristics be validated at higher Reynolds numbers. Also fuselage strakes to improve directional stability and leading-edge slats to improve low speed lift-to-drag ratios should be considered for future testing. The impact of recent wing modifications developed for high-speed drag improvement need to be assessed at low speed.

INTRODUCTION

McDonnell Douglas (MDC) and NASA have been working jointly on the development of technology for Advanced Supersonic Cruise vehicles over the past several years. As part of this development a 1.5-percent scale high-speed wind tunnel test program was run at the NASA Ames Research Center in 1975 (ref. 1) which demonstrated that, for the configuration designed by MDC, high aerodynamic performance levels were achieved. To supplement these high-speed data, a

*This work was performed under NASA Contract NAS1-14621

ten-percent scale model of the same configuration for test at low speed was constructed by NASA using inputs from MDC for the geometry of the high-lift and low-speed control devices. These tests would measure force data and surface pressures as in the previous high speed tests, and would give a complete data base on one configuration for Mach numbers from near zero (0.09) to M = 2.4.

This low speed ten-percent scale model was tested by NASA in the Full Scale Tunnel at the Langley Research Center. This paper presents a summary of the current status of the analysis of these test results.

SYMBOLS

AR	wing aspect ratio
C_D	drag coefficient
C_{D_o}	minimum clean (no leading- or trailing-edge deflection) configuration drag coefficient
C_L	lift coefficient
C_M	pitching moment coefficient about the quarter chord
ΔC_ℓ	incremental rolling moment coefficient
C_{N_β}	variation of yawing moment coefficient with sideslip angle
ΔC_{N_v}	change in yawing moment coefficient due to vertical tail
C_p	pressure coefficient
i_H	incidence of horizontal tail relative to fuselage reference system, degrees
L/D	lift-to-drag ratio
M_o	free stream Mach number
S	leading edge suction parameter
α or alpha	fuselage reference system angle of attack, degrees
β	angle of sideslip, degrees
δ_a	aileron deflection angle, degrees
δ_F	trailing edge flap deflection angle, degrees
δ_{LE}	leading edge flap deflection angle normal to the leading edge, degrees
η	percent wing semispan

DESCRIPTION OF THE MODEL

The dimensional characteristics of the ten-percent scale model are shown in figure 1. A photograph of the model mounted in the Langley Full Scale Tunnel is shown in figure 2. The model was constructed of fiberglass over an aluminum frame and was essentially rigid for this test.

The wing consisted of an arrow planform with an inboard leading-edge sweep angle of 71 degrees and an outboard sweep angle of 57 degrees with a leading edge break at 63 percent of the semi-span. The wing was constructed with four segments of leading-edge flaps inboard of the leading-edge break and two segments outboard of the leading-edge break. The wing had an inboard and outboard single-slot trailing-edge flap system. The model had the inboard and mid slotted spoiler/deflectors installed on the right hand wing, and the outboard inverted spoiler/deflector installed on the left hand wing. They were only tested asymmetrically for their effect on roll control. The model was instrumented with 270 pressure orifices distributed among five spanwise rows over the wing. The pressures were obtained using scanivalve transducers. A schematic drawing of the leading- and trailing-edge flaps, and the spoiler/deflector system, and the spanwise location of the pressure rows are shown on figure 3 and the variable geometry features of the model are illustrated in figure 4. Indicated are the available deflections of the leading-edge flaps (measured normal to the leading edge) and the letter code designation of the combinations of deflections for which data are presented in this paper.

TESTS AND CORRECTIONS

Tests were made in the Langley Full Scale Tunnel at a freestream dynamic pressure of q = 575 Pa (12 psf or M_o = 0.09). The tests were conducted over an angle of attack range from about -6 degrees to 23 degrees and over a sideslip range from -15 degrees to 20 degrees. The Reynolds number based on the mean aerodynamic chord of 1.975 m (6.48 ft) was 4.18×10^6.

The model was tested upright and inverted with a single dummy strut, (figure 5) to evaluate the flow angularity and strut tares which were applied to the data. Buoyancy corrections were computed and applied to the data. Blockage corrections were applied based on tunnel surveys from previous tests of similar size models. Wall corrections were not applied based on previous tests (ref. 2 and 3).

RESULTS

WING-BODY LONGITUDINAL FORCE DATA

Prior to obtaining the basic aerodynamic characteristics of the configuration, an initial study was conducted to determine the best leading-edge flap deflection. The effect of deflecting the leading-edge flaps over only part of the span is shown on figure 6. Selectively eliminating leading-edge deflections over the inner, middle or outer wing panel produce higher drags at lift coefficients greater than 0.4 than full-span leading-edge deflections. No advantages were found in the lift or pitching moment to warrant part span leading-edge flap deflection.

The aerodynamic characteristics for increasing amounts of full-span leading-edge flap deflection are shown in figures 7 through 12 for zero and 30 degrees of trailing-edge flaps. For the case of zero flaps, the lift-curve break at about 5 degrees ($C_L \approx 0.2$) indicates the condition where a leading-edge vortex begins to form. The smallest angle of deflection for the leading-edge flaps tested results in a nearly linear lift curve which implies elimination of the leading-edge vortex. Significant reductions in the drag are also obtained for this deflection. The inception of the non-linear nose-up pitching-moment break at about six degrees angle of attack is not affected by deflecting the leading-edge flaps, although the magnitude of the pitch-up is reduced. Further deflection of the leading-edge flaps has little effect on the drag and lift with a small effect on pitching moments.

With the trailing-edge flaps deflected, the smallest leading-edge flap deflection also eliminates the break in the lift curve and leading-edge vortex. In this case, because the deflection of trailing-edge flaps cause more leading-edge load for a given angle of attack, the breakdown in the lift curve occurs at two degrees angle of attack. However, because of the lift the flap produces, the break in the lift curve occurs at a C_L of 0.3 instead of 0.2 with the flaps up. With the trailing-edge flaps down there is less effect of the leading-edge flap deflection on drag or pitching moments than with the flaps up.

Based on the above results, the longitudinal, lateral-directional and tail effectiveness characteristics were conducted with leading-edge flap deflection R.

The lift and pitching moment characteristics for the clean configuration (leading- and trailing-edge flaps retracted) are compared in figures 13 and 14 to the Douglas 3-D Neumann Potential Flow Program (ref. 4) results run at $M_o = 0$ and to previous data obtained on a 1.5-percent scale high-speed model (ref. 1) at $M_o = 0.5$. Adjustments to the data have not been made to correct for the Mach number difference between the two tests. The characteristics of the ten-percent low-speed model lift and pitching moment results agree very well with the previous test results except for a one degree shift in the angle of attack for zero lift. The 3-D Neumann lift-curve slope agrees with the data prior to the inception of vortex lift but the angle of attack for zero lift is shifted by about two degrees.

The drag results are compared to full and zero leading-edge suction calculations in addition to the 3-D Neumann results (which have been shifted to agree with the test data at minimum drag) and the previous 1.5-percent scale data in figure 15. The data show that 60 to 40 percent of full leading edge suction is obtained for a C_L range of 0.2 to 0.8. The Neumann results are close to full leading-edge suction as expected and do not agree well with the data. The previous 1.5 percent scale results were obtained at about the same Reynolds number based on the mean aerodynamic chord (4×10^6) and the agreement with the low speed data is within acceptable limits.

The results with deflected leading-edge flaps and zero deflection of the trailing-edge flaps are shown in figures 16 through 18. These results are also compared to the Neumann and full and zero leading-edge suction. Similar

comments as before apply to the lift and moment comparison with the Neumann results. Drag results indicate that leading edge suction is nearly 100 percent at low C_L's diminishing to about 40 percent as the C_L is increased.

Drag results with the leading- and trailing-edge flaps deflected are shown on figure 19. The Neumann results are not yet available for this case. About 80 percent of full leading-edge suction is obtained over a wide range of C_L's.

A summary of the leading-edge suction results are shown on figure 20. Seventy- to eighty-percent full leading-edge suction is obtained with the trailing-edge flaps deflected 30 degrees with or without the leading-edge flaps deflected. For the optimum trailing-edge flap setting as a function of C_L, leading-edge suction over 80 percent is achieved up to the lift-off C_L of 0.65. These data also indicate that higher leading-edge flap deflections are required as the C_L is increased. Recent results obtained by Coe (ref. 5) for a wing with higher sweep and lower aspect ratio (SCAT 15) are slightly below the current results. Recent additional data by Coe (ref. 6) have shown that further improvements are possible.

The untrimmed lift-to-drag (L/D) ratio results are shown on figure 21 for several leading- and trailing-edge deflections. These results have been corrected to the full scale Reynolds number. L/D's slightly over ten were obtained in the C_L range for climb-out ($C_L \approx 0.3$) dropping off to about 5.5 at the lift-off C_L's near 0.65. Also shown are the previous 1.5 percent scale high speed model test data, estimates made prior to the test, and recent test data from Coe (ref. 5). The 1.5 percent scale model results show slightly higher L/D's than the low speed model at C_L's in the 0.2 range with the agreement improving as the C_L is increased. The relatively small drag differences shown earlier (fig. 15) produce this discrepency. The pre-test estimates, which are indicative of the levels used to calculate the low-speed performance of the aircraft, where made without the benefit of any data-base on leading-edge devices of this type and are higher than the measured values. Recent data from Coe (ref. 5), had it been available, would have been valuable in improving these estimates. The configuration L/D obtained by Coe agrees with the current results if adjusted for aspect ratio.

WING-BODY PRESSURE DATA

The experimental upper surface pressure distributions for the clean configuration at three angles of attack are shown on figure 22. The increase of the pressure peak near the leading edge and the shape of the pressure distribution illustrates the formation of the leading-edge vortex. The aft movement of the vortex is evident at the 64 percent semi-span station as the negative pressures move progressively aft as the angle of attack is increased. At 13 degrees angle of attack, there appears to be a second vortex present as illustrated by the second negative pressure peak between 50 and 70 percent chord at the 49 percent semi-span station.

The pressure peak on the inner panel with its rounded leading edge continues to increase with angle of attack. In contrast, the constant C_P level of 0.5 to 0.75 at the leading edge of the outer panel at all angles suggests that,

because of the sharp leading edge, the outer panel vortex forms at very low angles of attack.

The experimental pressure distributions are compared to the 3-D Neumann results at an angle of attack of one degree ($C_L \approx 0.05$) prior to the inception of vortex lift on figure 23. The agreement is reasonable on the rounded leading edge inner panel but agreement deteriorates on the sharp leading edge outer panels. This confirms the fact that the sharp outer panel leading edge cannot carry the loads required to produce a potential flow, i.e., no vortex, at essentially any C_L.

Comparisons with and without the leading-edge flaps deflected are shown in figure 24 at a higher C_L of 0.35 ($\alpha = 9^o$) after the inception of vortex lift. The general character of the experimental pressure distribution is represented by the theory with the leading-edge flaps deflected but there is some disagreement in level. The data at 49-percent semi-span station illustrates the effect of the leading-edge vortex on the potential pressures without leading-edge flap deflection.

HORIZONTAL TAIL EFFECTIVENESS

Effectiveness of the horizontal tail for the landing configuration is shown in figure 25. At low angles of attack, (below 5 deg) the tail contributes to the longitudinal stability of the airplane, shifting the neutral point aft by 5% of the MAC. At angles of attack above 5 degrees, the aircraft pitches up and the tail-off neutral point shifts forward. The tail contribution to longitudinal stability is close to zero at angles of attack above 5 degrees. Tail effectiveness for pitch control is maintained to the highest angles tested. The reduced stability contribution without loss of effectiveness is attributed to a strong downwash gradient at the location of the horizontal tail.

DIRECTIONAL STABILITY AND VERTICAL TAIL EFFECTIVENESS

Directional stability of the aircraft tail-on and tail-off is illustrated in figure 26 and the contribution of the vertical tail to directional stability is shown in figure 27. Directional stability without leading- or trailing-edge flaps deflected is maintained at a reasonably constant level at angles of attack up to about 12½ degrees (fig. 26) and is gradually reduced at higher angles until neutral stability is reached at about 20 degrees. The reduced stability at high angles of attack is due to a combination of reduced tail-off stability which begins at 12½ degrees and reduced tail effectiveness (fig. 27) which begins at about 15 degrees.

In the landing configuration the tail-off stability (fig. 26) is reduced at lower angles of attack (5 degrees) while the tail contribution is maintained effective to higher angles (17½ degrees, fig. 27). The resulting airplane stability goes from an acceptable level at 5 degrees angle of attack to neutral stability at 20 degrees angle of attack.

LATERAL CONTROL SYSTEM EFFECTIVENESS

Effectiveness of various components of the lateral control system is shown in figure 28 for both clean and landing configurations. The clean aircraft control effectiveness is shown for a typical angle of attack of 5 degrees. Deflection of the inboard spoiler produces a small positive contribution to lateral control. However no rolling moment develops when the mid spoiler is deflected together with the inboard spoiler, indicating a negative contribution due to the mid spoiler. Reversed roll effectiveness of the mid spoiler is confirmed by the increase in total lift when the spoiler is extended, and by pressure data which indicates increased lift. The outboard inverted spoiler/deflector is more effective than the other spoilers and provides roll in the proper direction. The deflectors when used with the mid and inboard spoilers cause increased roll in the wrong direction.

Airplane control effectiveness in the landing configuration is presented at a typical 10 degrees angle of attack. Spoiler effectiveness is satisfactory with the mid and inboard spoilers deflected. The deflectors, which are designed to increase spoiler effectiveness at high speed, have a slight negative effect when used with flaps down. The outboard, inverted spoiler deflector, again intended for high speed use, also has a small negative contribution to rolling moment.

The aileron effectiveness is close to estimated values for both the clean airplane and the landing configuration.

CROSSWIND LANDING CAPABILITY

Crosswind landing capability of the present configuration at a gross weight of 204,117 kg (450,000 pounds) is illustrated in figure 29. At a typical landing speed of 72 m/sec (140 knots) the crosswind component is limited to 15.4 m/sec (30 knots) by maximum roll control. A more conservative limitation of 75 percent of maximum roll control would still allow over 10.8 m/sec (21 knots) of crosswind component.

CONCLUSIONS

Based on the results obtained from the test program the following conclusions are drawn.

- A full-span leading-edge device is required to maximize performance
- 80-percent leading-edge suction is obtained during climb-out after takeoff
- to maximize leading-edge suction with increasing C_L requires increasing leading-edge flap deflection.
- spoilers are preferred over spoiler/deflectors at low-speeds
- pitching moments are nonlinear with a mild pitch-up at 6-degrees angle of attack and are not significantly changed with leading-edge flap deflection

- pitch-up is controllable with horizontal tail
- the vertical tail maintains effectiveness up to highest angle of attack tested (21 degrees)
- tail-on directional stability deteriorates at high angles of attack
- lateral control appears to be adequate for landing at 72 m/sec (140 knots) in a 15.4 m/sec (30 knot) crosswind.

In addition the following low-speed testing requirements for technology readiness are recommended:

- validate drag-due-to-lift characteristics with a high Reynolds number test
- establish that fuselage strakes can improve directional stability
- evaluate suitability of leading-edge slats instead of leading-edge flaps
- evaluate effect on low-speed characteristics of latest configuration changes developed by MDC (increased outer panel sweep)

REFERENCES

1. Radkey, R.L., Welge, H.R., and Felix, J.E.: Aerodynamic Characteristics of a Mach 2.2 Advanced Supersonic Cruise Aircraft Configuration at Mach Numbers from 0.5 to 2.4. NASA CR-145094, 1977.

2. Coe, P.L. and Graham, A.B.: Results of Recent NASA Research on Low-Speed Aerodynamic Characteristics of Supersonic Cruise Aircraft. Proceedings of the SCAR Conference, CP-001, 1977.

3. Shivers, J.P., McLeneore, H.C., and Coe, P.L.: Low-Speed Wind-Tunnel Investigation of a Large-Scale Advanced Arrow Wing Supersonic Transport Configuration With Engines Mounted Above the Wing for Upper-Surface Blowing. NASA TN D-8350, 1976.

4. Friedman, D.M.: A Three-Dimensional Lifting Potential Flow Program. McDonnell Douglas Report MDC J6182, 1974.

5. Coe, P.L. and Weston, R.P.: Effects of Wing Leading-Edge Deflection on the Low-Speed Aerodynamic Characteristics of a Low-Aspect-Ratio Highly Swept Arrow-Wing Configuration. NASA TM 78787, 1978.

6. Coe, P.L., Huffman, J.K.: Influence of Optimized Leading-Edge Deflection and Geometric Anhedral on the Low Speed Aerodynamic Characteristics of a Low-Aspect-Ratio Highly Swept Arrow-Wing Configuration. NASA TM 80083, 1979.

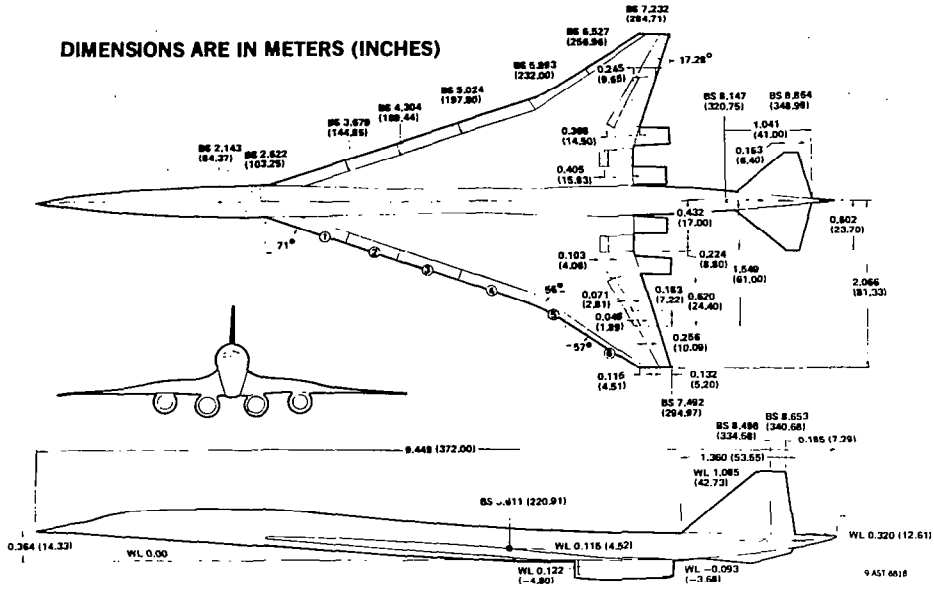

Figure 1.- Three-view drawing of 1/10-scale model.

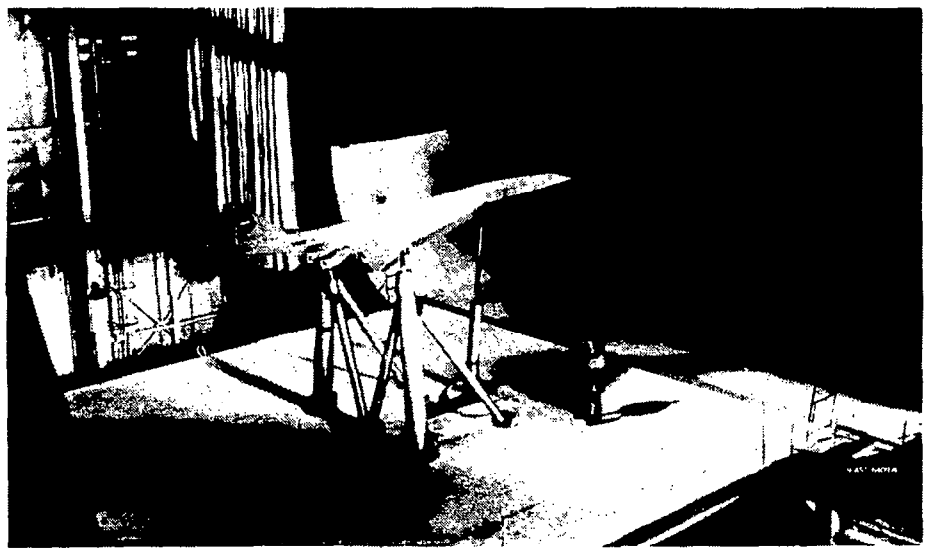

Figure 2.- 1/10-scale low-speed model in Langley 30- by 60-ft tunnel.

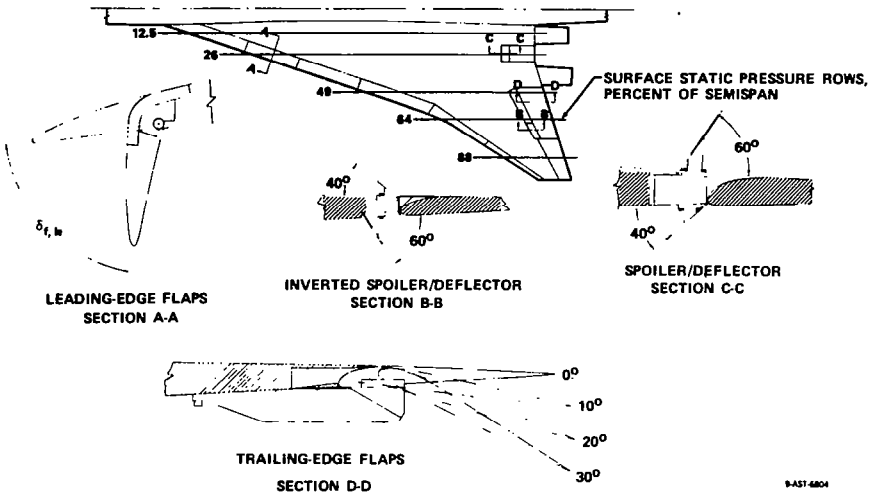

Figure 3.- Schematic drawings of leading- and trailing-edge flaps, spoiler/deflector, and inverted spoiler/deflector.

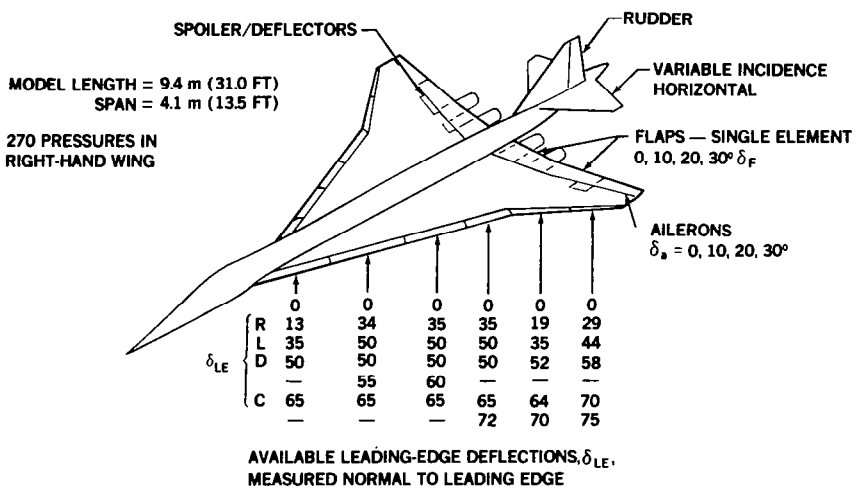

Figure 4.- Variable geometry features of 1/10-scale low-speed model.

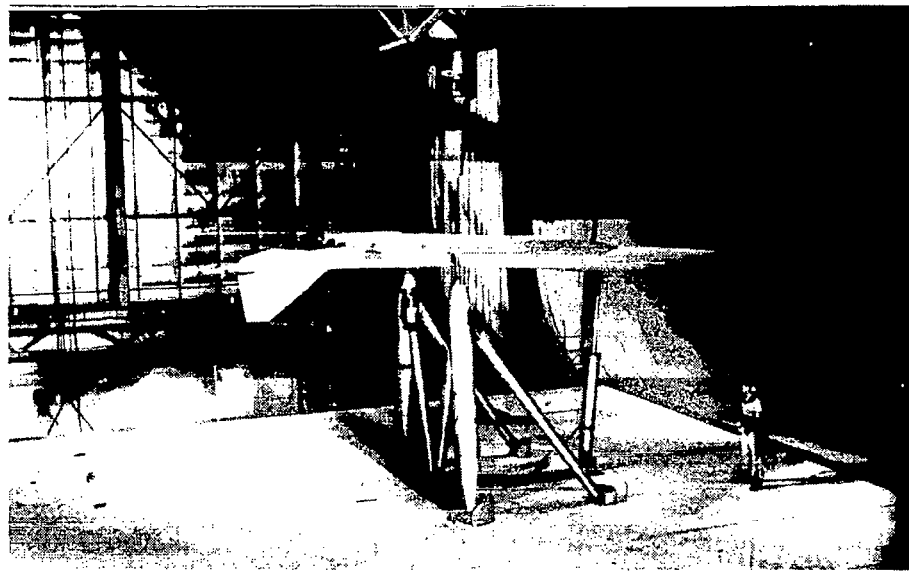

Figure 5.- Inverted model installation with dummy strut.

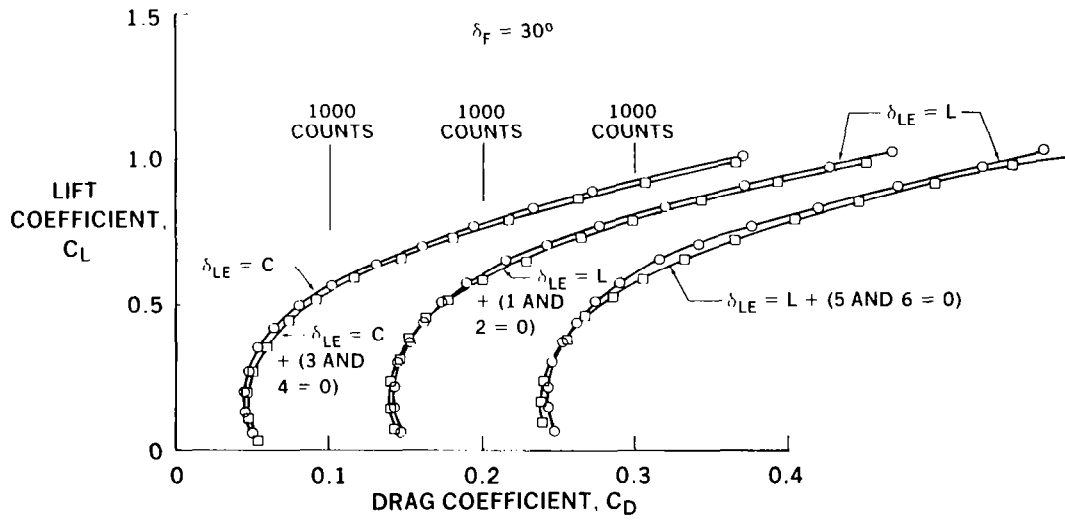

Figure 6.- Drag comparison of full and partial leading edge deflections.

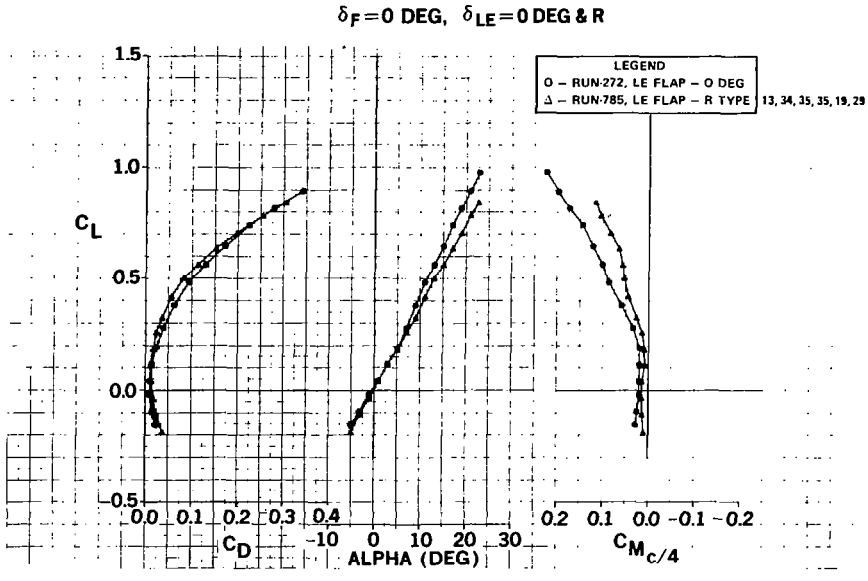

Figure 7.- Leading edge flap effectiveness.

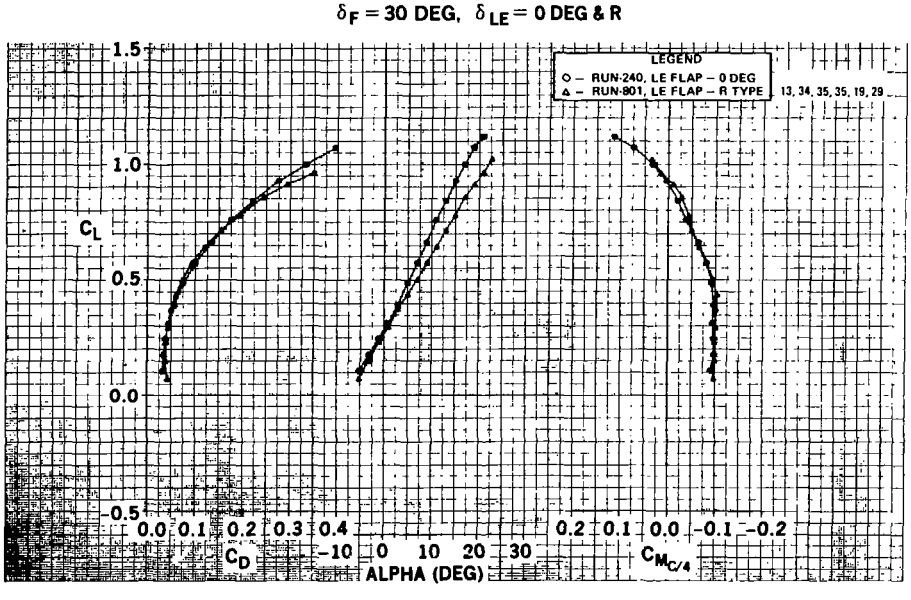

Figure 8.- Leading edge flap effectiveness.

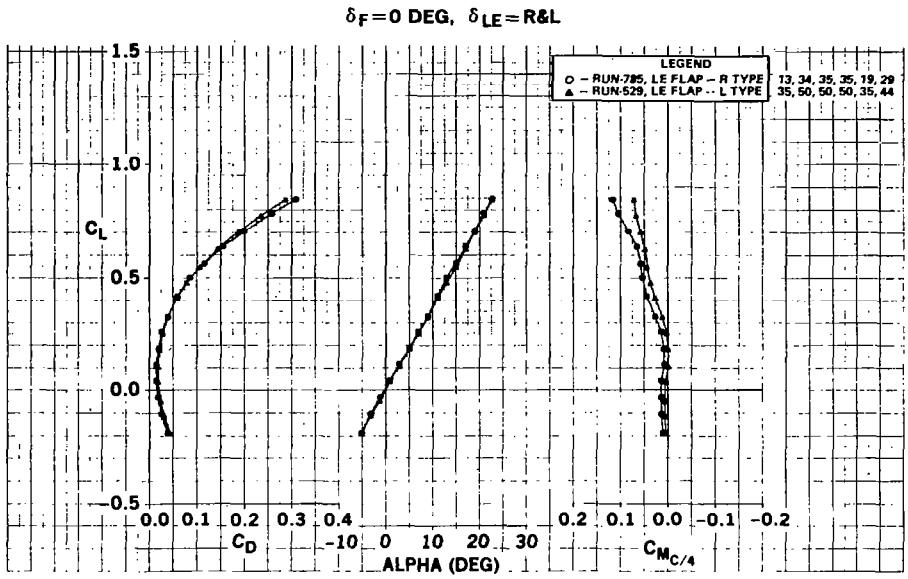

Figure 9.- Leading edge flap effectiveness.

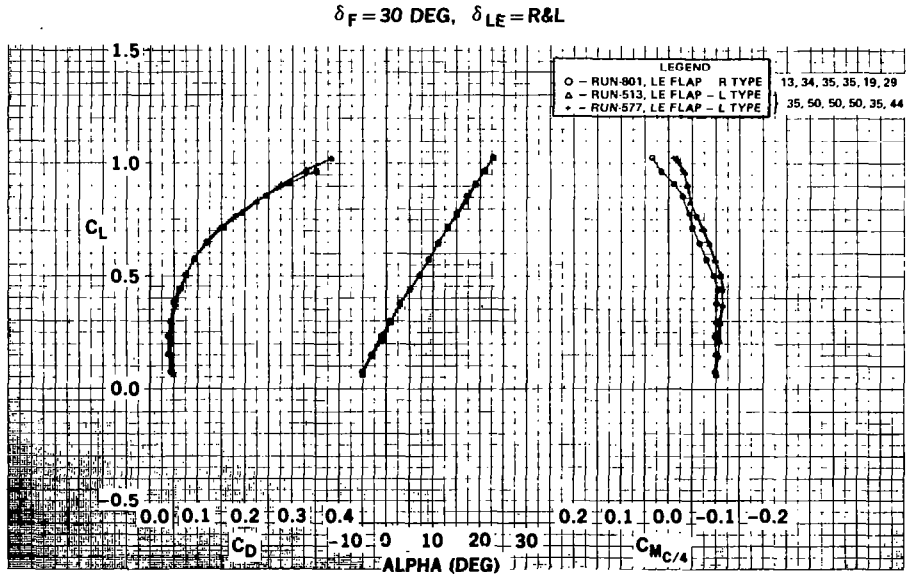

Figure 10.- Leading edge flap effectiveness.

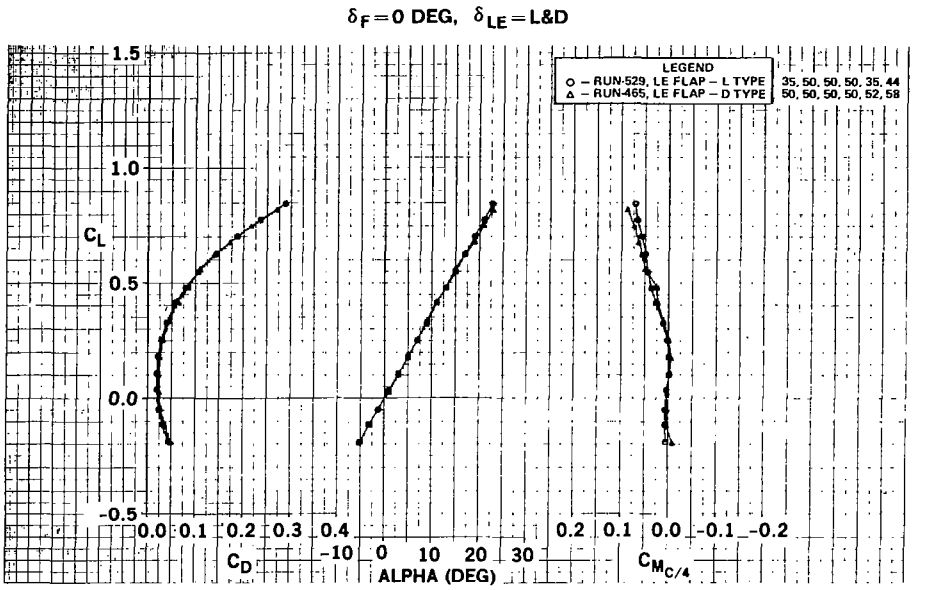

Figure 11.- Leading edge flap effectiveness.

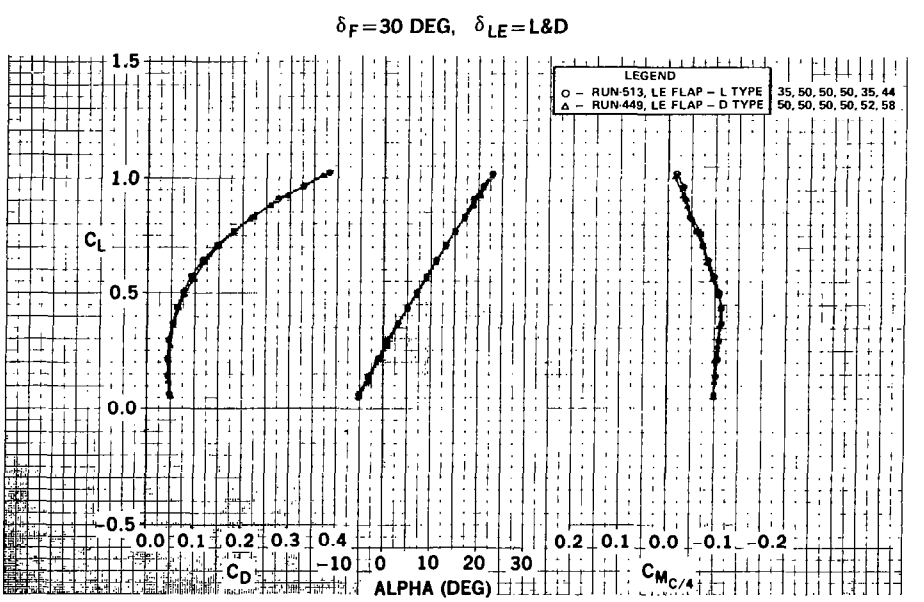

Figure 12.- Leading edge flap effectiveness.

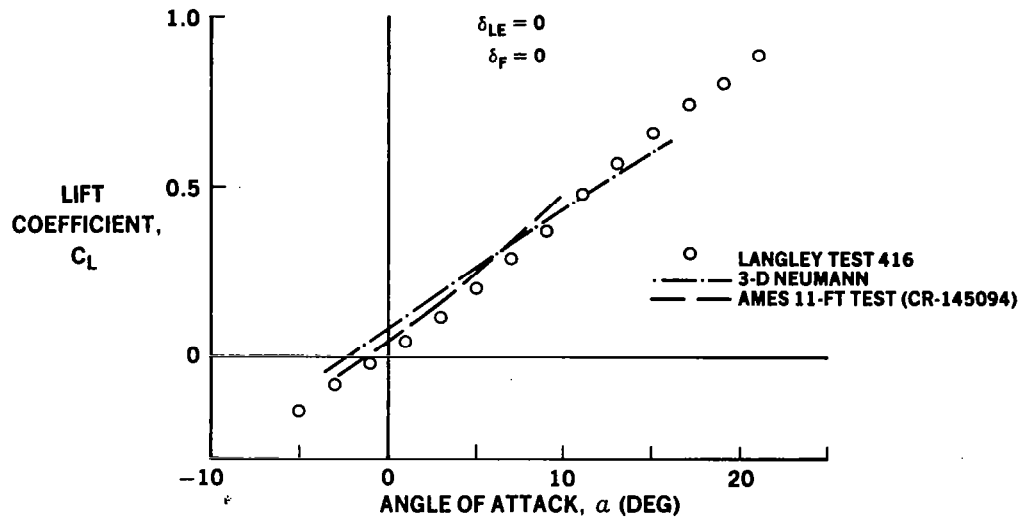

Figure 13.- Comparison of clean wing lift characteristics.

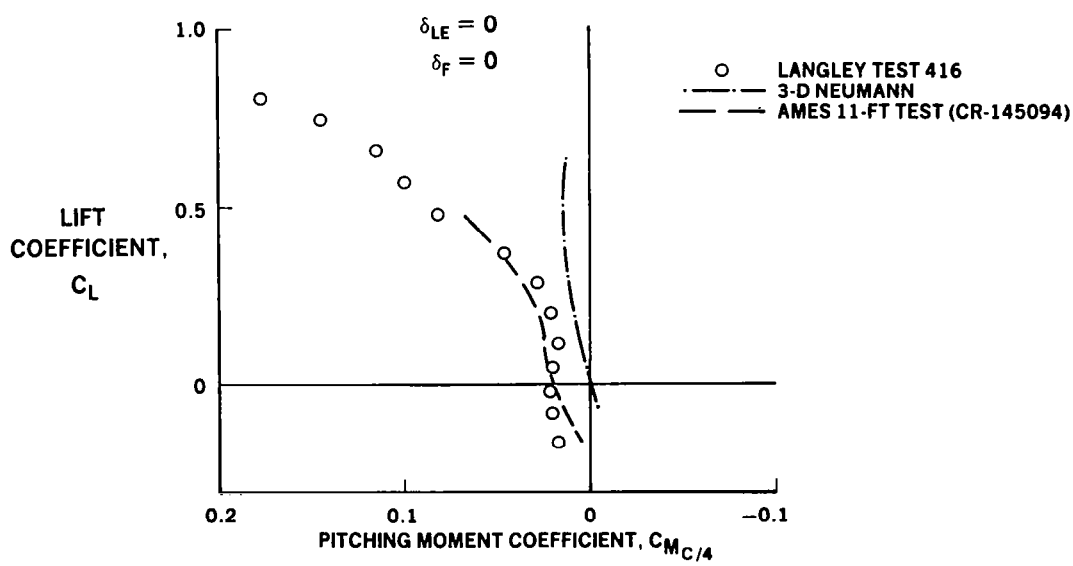

Figure 14.- Comparison of clean wing pitching moment characteristics.

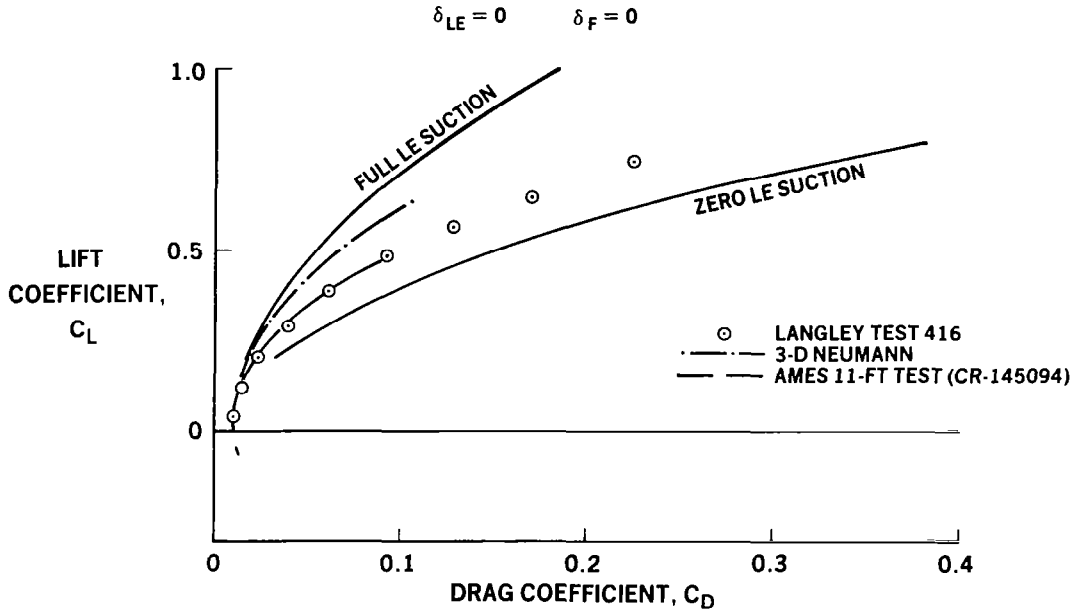

Figure 15.- Comparison of clean wing drag polars.

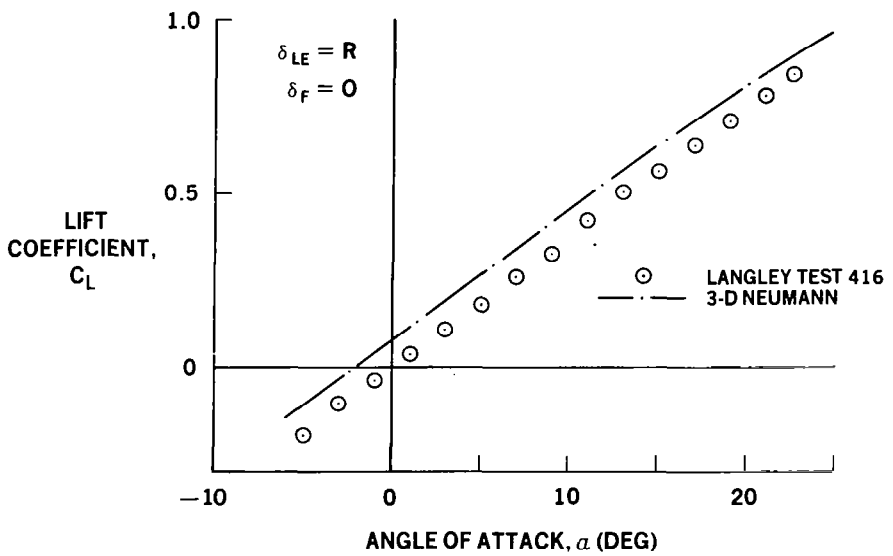

Figure 16.- Lift characteristics with leading edge deflected.

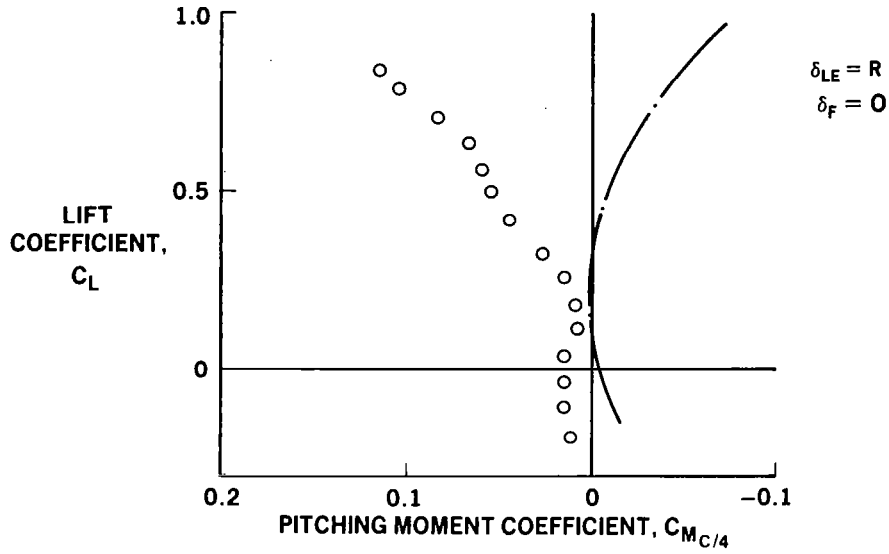

Figure 17.- Pitching moments with leading edge deflected.

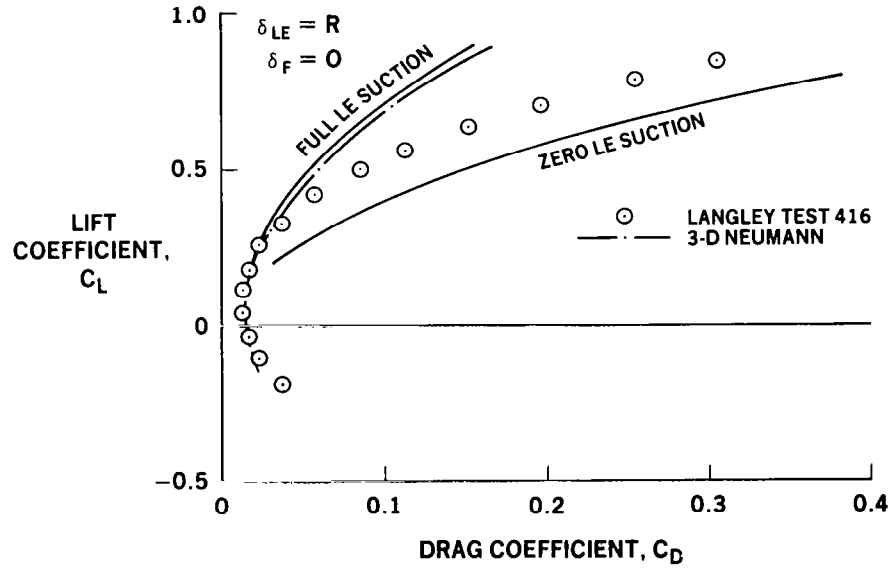

Figure 18.- Drag polars with leading edge deflected.

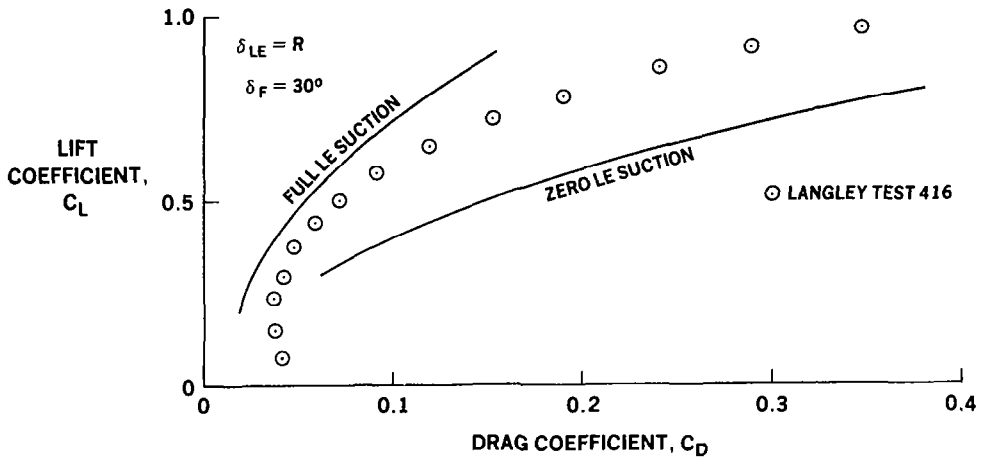

Figure 19.- Drag polar with leading and trailing edge deflected.

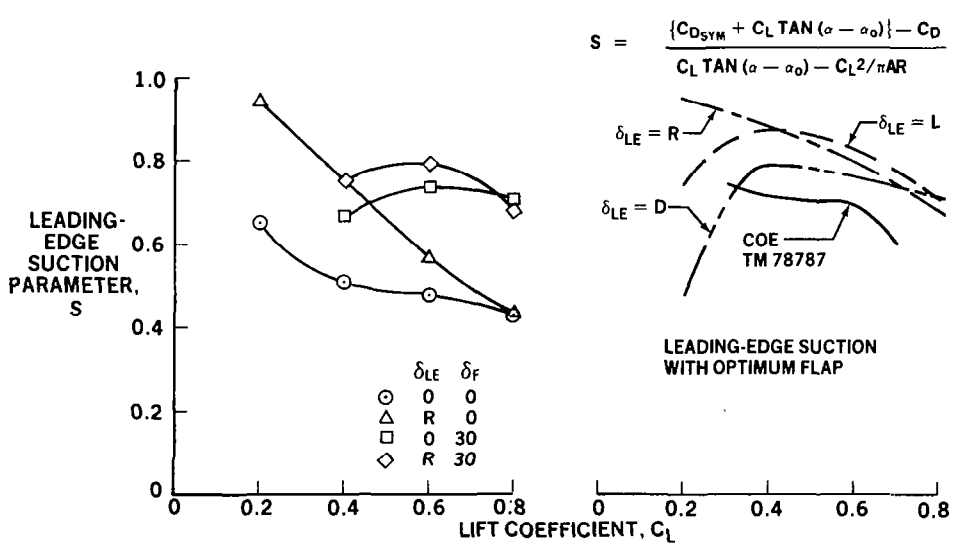

Figure 20.- Leading-edge suction characteristics.

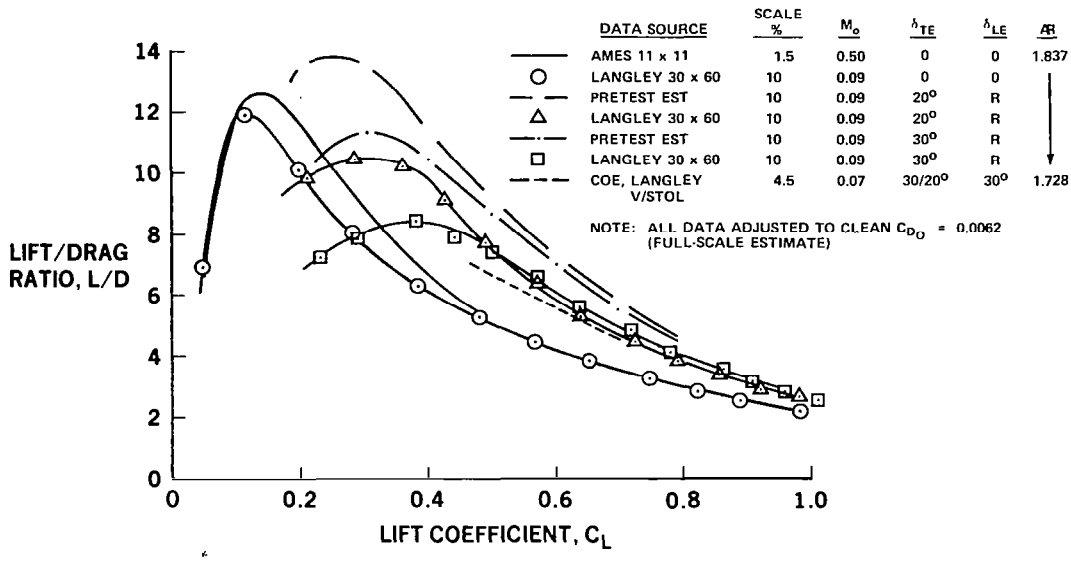

Figure 21.- Low-speed L/D summary, untrimmed.

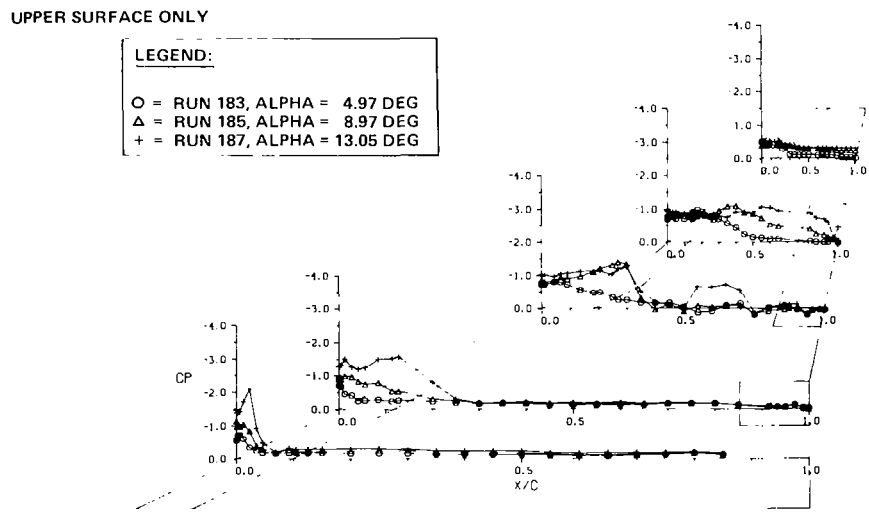

Figure 22.- Effect of angle of attack on clean wing pressure distribution.

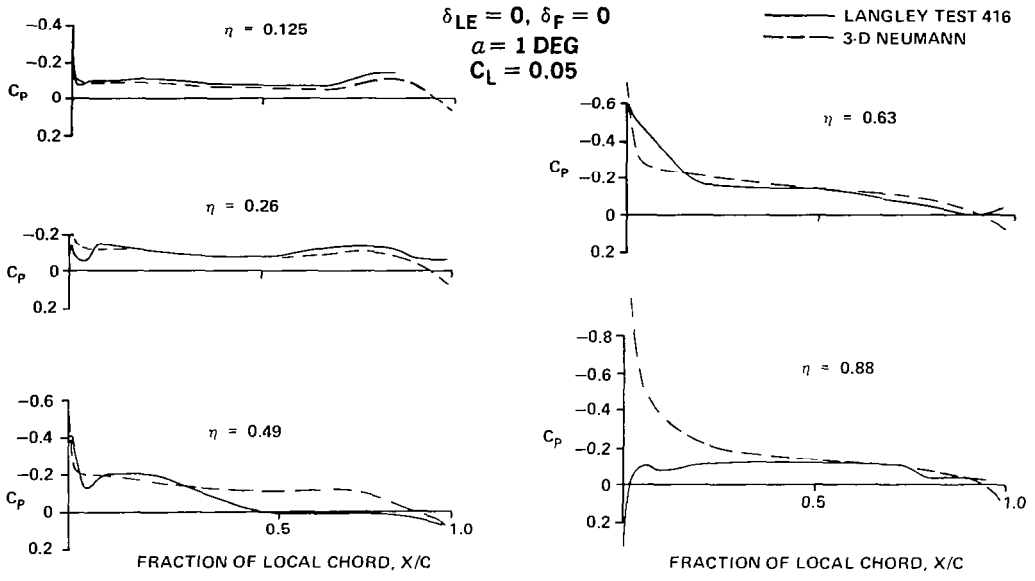

Figure 23.- Comparison of experimental upper surface pressures with theory.

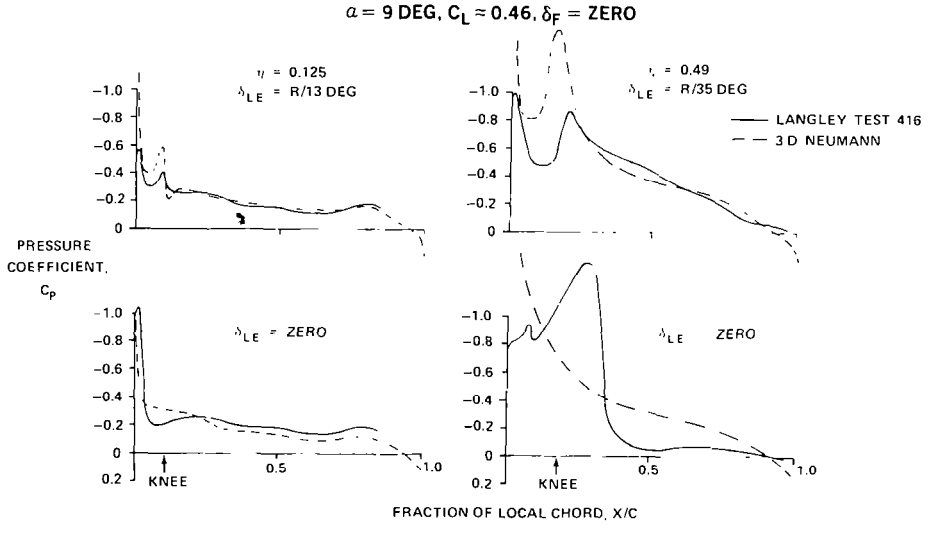

Figure 24.- Comparison of Neumann pressure distributions with data, with and without leading edge deflected.

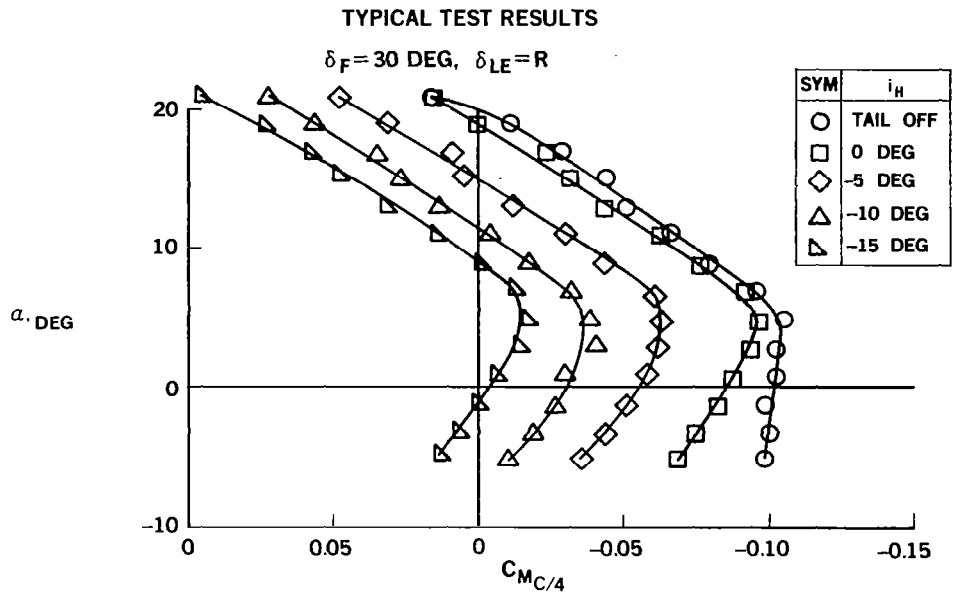

Figure 25.- Horizontal tail effectiveness.

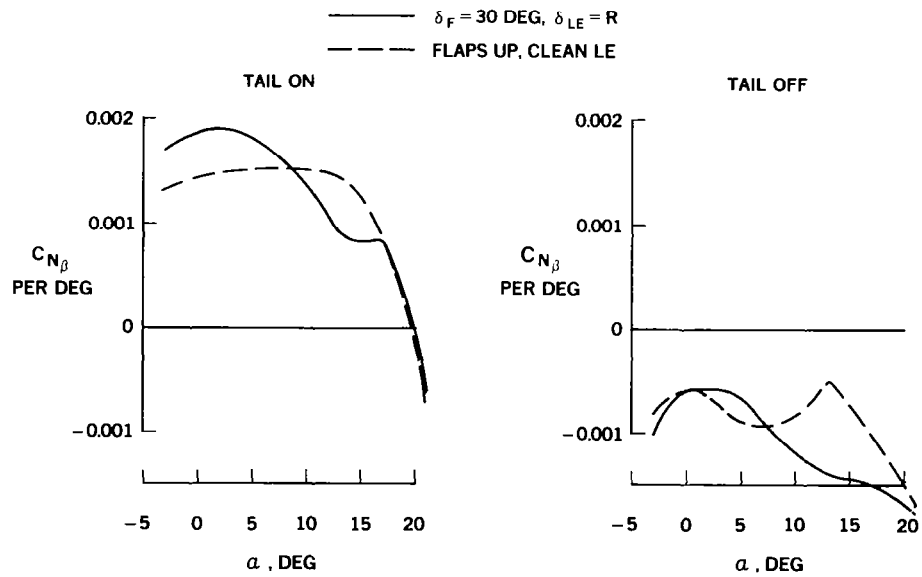

Figure 26.- Directional stability.

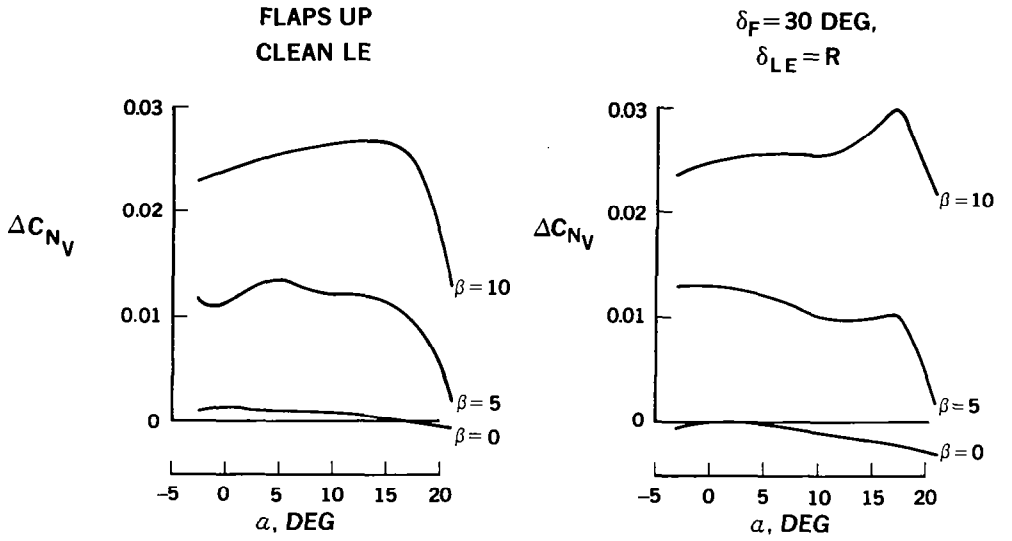

Figure 27.- Vertical tail effectiveness.

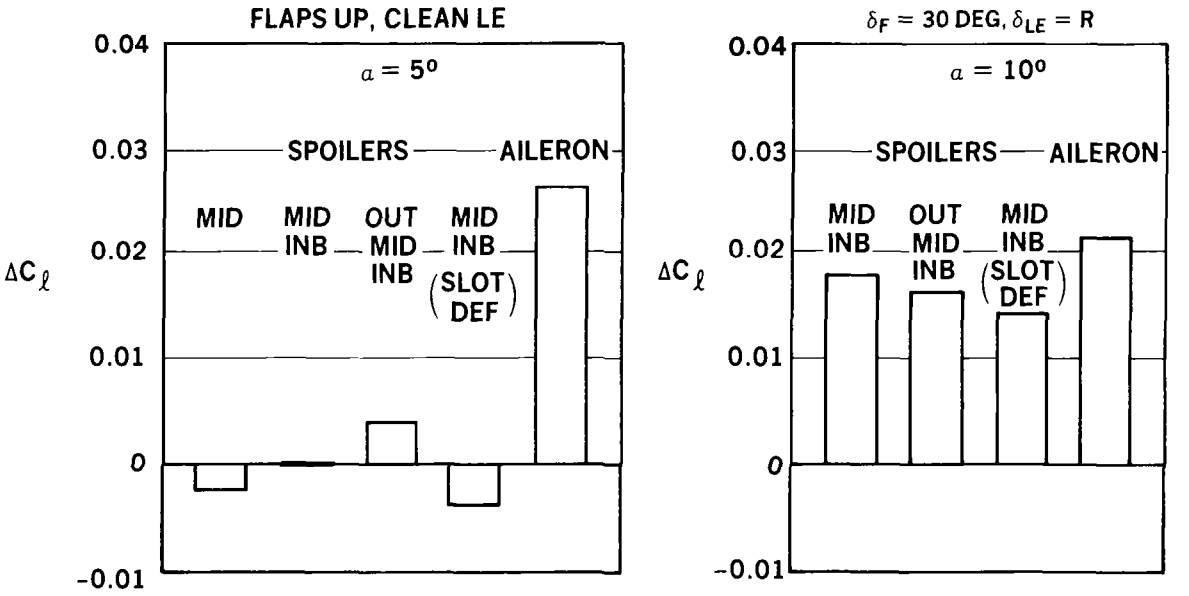

Figure 28.- Lateral control system effectiveness.

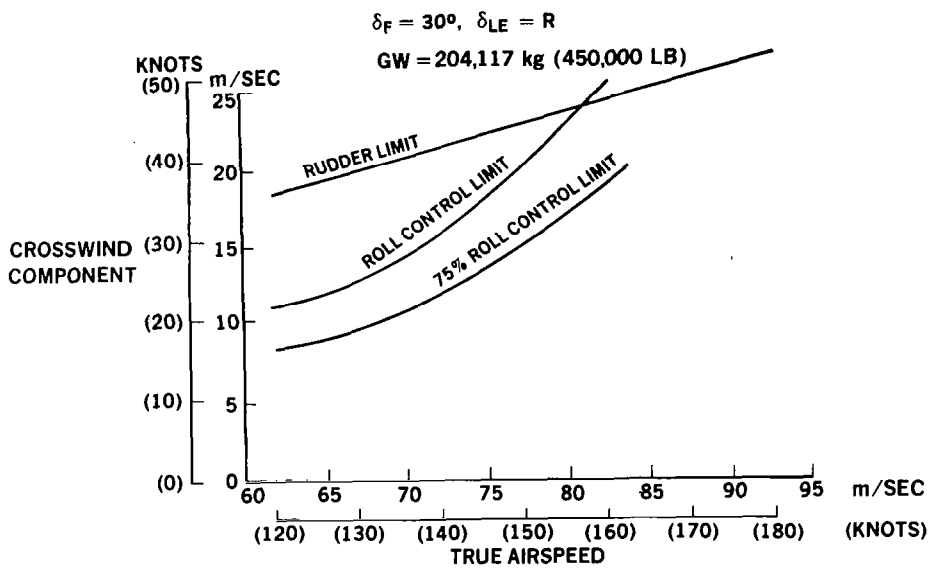

Figure 29.- Estimated cross-wind landing capability.

THE PREDICTION OF PRESSURE DISTRIBUTIONS ON AN ARROW-WING CONFIGURATION INCLUDING THE EFFECT OF CAMBER, TWIST, AND A WING FIN*

Marjorie E. Manro
Boeing Commercial Airplane Company

Percy J. Bobbitt
NASA Langley Research Center

Robert M. Kulfan
Boeing Commercial Airplane Company

SUMMARY

Wind-tunnel tests of an arrow-wing body configuration consisting of flat, twisted, and cambered-twisted wings have been conducted at Mach numbers from 0.40 to 2.50 to provide an experimental data base for comparison with theoretical methods. A variety of leading- and trailing-edge control-surface deflections were included in these tests, and in addition, the cambered-twisted wing was tested with an outboard vertical fin to determine its effect on wing and control-surface loads. Theory-to-experiment comparisons of detailed pressure distributions have been made using current state-of-the-art attached-flow methods, as well as newly developed attached- and separated-flow methods. The purpose of these comparisons was to delineate conditions under which these theories can provide accurate basic and incremental aeroelastic loads predictions. Special emphasis is given to a new procedure developed by Robert Kulfan which shows promise of being able to predict the onset of a leading-edge vortex on thick and/or warped wings. Knowledge of the onset and position of vortices could be most valuable in conjunction with separated-flow methods to predict pressure distributions.

Theory-experiment comparisons show that current state-of-the-art linear and nonlinear attached-flow methods were adequate at small angles of attack typical of cruise conditions. The incremental effects of outboard fin, wing twist, and wing camber are most accurately predicted by the advanced-panel method PANAIR. Results of the advanced-panel separated-flow method, obtained with an early version of the program, show promise that accurate detailed pressure predictions may soon be possible for an aeroelastically deformed wing at high angles of attack.

---

*This work was performed under contracts NAS1-12875, NAS1-14141, NAS1-14962, and NAS1-15678 for the NASA Langley Research Center; and supplemented by the Boeing Commercial Airplane Company Independent Research and Development Program.

INTRODUCTION

A program has been under way for the past five years to examine the ability of state-of-the-art and advanced theoretical methods to predict aeroelastic loads on highly swept wings. A parallel objective has been to obtain an experimental data base of the type best suited for such a task. Three wing models were chosen for the test program; all had the same planform and airfoil section but one was flat, one twisted, and one had both camber and twist. With this combination, the incremental effects of twist, camber, and camber-twist, as predicted by theory, could be correlated with experiment. Other geometric variables included in the program are wing leading-edge radius, leading- and trailing-edge control-surface deflections, and an outboard fin. Most of the data obtained has been at subsonic and transonic speeds in the Boeing Transonic Wind Tunnel; however, the flat and twisted wings were also tested in the 9 by 7-foot supersonic portion of the Ames Unitary Wind Tunnel in order to fully examine existing and newly formulated panel methods, which apply for both subsonic and supersonic flows.

The present paper will concentrate mainly on the data obtained in recent wind-tunnel tests of the cambered-twisted wing and some new developments in separated-vortex methods and an attached-flow advanced-panel method. With the aid of the newly acquired data the incremental effects of twist, twist and camber, control-surface deflection, and outboard fin on wing pressure distributions may be illustrated. The improved separated-flow methodology permits some new insights into the conditions necessary for the formation of, and the prediction of the point of origin of, a leading-edge vortex.

Results of the subsonic-transonic program for the flat and twisted wings are summarized in NASA SP-347 (ref. 1) and discussed in more detail in references 2 through 5. The supersonic data for these two wings are available in references 6 through 8.

PANAIR advanced-panel attached-flow method calculations used in this paper were obtained with the assistance of James L. Thomas of the NASA Langley Research Center and Forrester Johnson and Edward Tinoco of the Boeing Military Airplane Company.

SYMBOLS AND ABBREVIATIONS

BL	buttock line, cm
b	wingspan, cm
$C_{L,V}$	vortex lift coefficient increment
C_M	pitching moment coefficient (moments about $0.25\bar{c}$)
C_N	normal force coefficient
C_n	section normal force coefficient
C_p	surface pressure coefficient

$C_{p,net}$	lifting pressure coefficient
C_s	suction force coefficient
c	local chord length, cm
$\bar{c}$	mean aerodynamic chord, cm
c_r	root chord, cm
L.E.	leading edge
M	Mach number
MS	model station, cm
T.E.	trailing edge
x,y,z	orthogonal coordinates
WRP	wing reference plane
α	angle of attack, deg
$\delta_{T.E.}$	trailing-edge control-surface deflection, deg
ϕ	velocity potential, cm/sec

MODELS

The wind-tunnel-model configuration selected for this study is a highly-swept (71.2°) thin wing (3.36-percent maximum thickness) of aspect ratio 1.65, mounted on the bottom of a slender body. The planform and basic geometry of the model are shown in figure 1. Three complete wings were constructed: one with no camber or twist, one with no camber but a spanwise twist variation (fig. 1), and one with both camber and twist. The twist of this third wing was the same as the plain twisted wing. The camber is a combination of a typical cruise airfoil camber and an estimate of the aeroelastic deformation at a moderate positive angle of attack. The resulting camber at the tip is approximately a 6° arc of a circle with the leading and trailing edges up. Sections at the root, mid-span, and tip (fig. 2) show not only the camber but the position of the sections of the cambered-twisted wing and the twisted wing, relative to the wing reference plane (flat wing).

All wings were designed to permit deflection of either partial- or full-span, 25-percent chord, trailing-edge control surfaces, with brackets, to allow streamwise deflections of ±4.1°, ±8.3°, ±17.7°, and ±30.2°, as well as 0°. In addition, the flat wing was provided with removable leading-edge segments that extended over 15 percent of the streamwise chord. These segments permitted testing of the leading edge drooped 5.1° and 12.8°, as well as undeflected. To

examine the effects of leading-edge shape, a segment with a sharp leading edge was constructed for the flat wing. Figure 1 shows the basic rounded leading edge with the sharp leading edge superimposed. A streamwise fin located at 72.5-percent semispan was provided for the cambered-twisted wing. The apex of the 71.2° sweep fin was located at 15-percent local chord of the wing (fig. 1) and has a 3-percent biconvex airfoil section.

The capability to measure the detailed load distribution on the wing and body of this configuration was provided by distributing 300 pressure orifices on the model. Each wing had 217 pressure orifices, equally divided into 7 streamwise sections on the left half. Pressure taps were located on both the top and bottom surfaces at the chordwise locations shown in figure 3. Pressure orifices we · located on the body in 5 streamwise rows of 15 orifices each. An additional 8 orifices in the area of the wing-body junction made a total of 83 orifices on the left side of the body.

To ensure close control of the model dimensions, a computerized lofting program was used to provide data for machining the model components using numerically controlled operations. The model was constructed of steel to minimize aeroelastic deflections.

WIND-TUNNEL TESTS

The model was tested in the Boeing Transonic Wind Tunnel (BTWT) and in the supersonic 9- by 7-foot leg of the NASA Ames Unitary Wind Tunnel. The former is a continuous-flow, closed-circuit, atmospheric facility with a 12.5-percent porosity test section measuring 8 by 12 by 14.5 feet; the latter is a continuous-flow, closed-circuit, variable-density facility with a test section measuring 7 by 9 by 18 feet. Seven Mach numbers from 0.40 to 1.11 were tested in the BTWT, with angle of attack varying from -8° to +16°. In the Ames facility, data were obtained primarily at Mach numbers of 1.7, 2.1, and 2.5. The major configurations tested are shown in tables I and II. Photographs of the model installed in the test sections are shown in figures 4 through 7.

FLOW PHENOMENA

Before assessing the ability of theoretical methods to predict the experimental pressure distributions, it is useful to understand the characteristics of the experimental flow field. This can be facilitated by looking at some pressure distributions at Mach number 0.40 for the rounded-leading-edge flat wing shown in figures 8 and 9. It should be noted, in the figures of pressure distributions, that symbols were generally omitted for clarity. At 16° angle of attack, however, the symbols were included to show the density of the available experimental data. At the low angles of attack, the flow is still attached, except for the station nearest the tip at 4° angle of attack. The fact that the vortex has started to form is indicated by the reduction in the peak pressure in the chordwise pressure distribution (fig. 8), and by the closeness of the constant-pressure lines in the isobars (fig. 9). The vortex is well developed

on the outboard half of the wing at 8°, and by 10° the vortex flow is affecting the entire wing.

The development of the vortex is modified by the shape of the leading edge as can be seen by comparing figures 8 and 9 with figures 10 and 11, which are for the sharp-leading-edge flat wing. The vortex develops much more rapidly for the sharp-leading-edge wing and is established over most of the wing at 4° angle of attack. At the higher angles of attack the leading-edge shape seems to lose importance as the flow at 16° is quite similar for both the sharp and rounded leading edges.

The effect of aeroelastic deformation is of prime interest in this study. Aeroelastic deformation is idealized in this study as a combination of pure twist and incremental camber. The camber that was used on this model is a combination of cruise camber and an aeroelastic camber, calculated for an arrow-wing similar to the one used in this study. The models with twist and camber-twist are assumed to be aeroelastically deformed versions of the flat wing. On the wing with twist only (figs. 12 and 13), the vortex formation is delayed until 8° angle of attack and then develops rapidly. At 12° the vortex flow affects the entire wing just as on the flat wing. The twisted wing is washed out 4.5° at the tip so that the local angles of attack at the tip of the flat and twisted wings are similar when vortex flow starts. The available models do not have camber alone, so the effect seen in figures 14 and 15 is for the cambered-twisted wing. The camber is leading and trailing edges up, so that the local leading-edge angle of attack is more like the flat wing, even though the twist is the same as that of the twisted wing. The formation of the vortex flow indicates that the local leading-edge angle of attack is the controlling feature.

Another geometric feature of interest for current low-aspect-ratio configurations is a wing fin. Pressure distributions and isobars on the cambered-twisted wing with an outboard fin are shown in figures 16 and 17. The pressures seem little affected by the fin at 4° and 6° angle of attack, but at 8° the pressure just outboard of the fin indicates that the fin has reduced the influence of the vortex off the wing apex in this area. There is some indication, however, that a second vortex is forming off the apex of the fin. This blocking effect is even more pronounced at the higher angles. Inboard of the fin the pressures are very similar to those with the fin off except at the station closest to the fin. Clearly, the effect of a fin needs to be studied in more detail to assess the effect of position and cant angle as well as whether the same interference effects are obtained on wings with different camber or twist.

The trends shown here are typical of the higher Mach numbers as well.

THEORETICAL METHODS

Theoretical calculations carried out in this study for both attached and detached flows (table III) are based on potential-flow theories. Results from three attached-flow panel methods which satisfy the classical Prandtl-Glauert equation for linearized compressible flow are presented. The first method uses

the constant-pressure-panel formulation, is valid for both supersonic and subsonic analysis, and satisfies only planar boundary conditions. The second method is a lower order panel method (constant strength sources and doublets) which is limited to subsonic flow but can satisfy boundary conditions on the exact configuration surface. The third method is a higher order panel method using bi-quadratic doublet and bi-linear source panels, valid for both supersonic and subsonic flow, and capable of satisfying exact boundary conditions.

The separated-flow method is an extension of the third attached-flow theory, based on distributions of quadratically varying doublet and linearly varying source panels. Since this approach is still under development and only preliminary results are available, it must be considered an advanced rather than a state-of-the-art method. As the older separated-flow methods capable of giving detailed pressure distributions can handle only simple wing geometries (straight leading-edge deltas), theory-experiment comparisons for an arrow wing would be of limited usefulness.

One of the most successful methods for the prediction of forces and moments produced by wings with leading edge separation is the Polhamus suction analogy. R. M. Kulfan's recent extensions to this method, to account for the effects of wing thickness and warp on the development of the vortex, are outlined. Additional details of the analytical methods are discussed below.

Attached-Flow Theories

The primary analysis method used for pressure calculations in this study was the unified subsonic/supersonic panel technique of FLEXSTAB, which was developed by Boeing under NASA Ames sponsorship (ref. 9). The FLEXSTAB system of digital computer programs uses linear theory to evaluate the static and dynamic stability, the inertial and aerodynamic loading, and the resulting elastic deformations of aircraft configurations. The aerodynamic module contained in the FLEXSTAB system is based on the constant-pressure-panel method developed by Woodward (refs. 10 through 12) to solve the linearized potential-flow equations for supersonic and subsonic speeds with planar boundary conditions. The method can also produce answers for transonic speeds, although the nonlinear terms not accounted for become important as sonic speed is approached.

Figure 18 shows the distribution of panels used in this analysis. Line sources and doublets are distributed along the longitudinal axis of the body to simulate its thickness and lifting effects. Similarly, source and vortex panels are placed in the plane of the wing to simulate its thickness and lifting effects. To account for the interference effects between the wing and body, constant-pressure vortex panels are placed on a shell around the body. This "interference" shell serves to cancel the normal velocity components on the body that are induced by the wing.

At subsonic Mach numbers and the high supersonic Mach numbers, 50 line singularities, 168 interference panels, and 160 wing panels were used to represent the configuration. For the very low supersonic Mach numbers (1.05 and 1.11), the number of interference panels had to be greatly increased (to 330) to overcome instabilities associated with the solution. The edges of the wing

panels were chosen to coincide with the control-surface hinge lines and break lines. Note on figure 18 that the panels are of nearly equal width and, in the chordwise direction, panel edges are at constant percent chord with closer spacing at the leading edge and the hinge lines.

The second attached-flow method used was the general method of Rubbert and Saaris (refs. 13 through 15) for the numerical solution of nonplanar, three-dimensional boundary-value problems. The method solves the exact incompressible potential-flow equation (Laplace's equation), with compressibility effects incorporated via the Gothert rule. In contrast to FLEXSTAB, the Rubbert-Saaris solution (hereafter referred to as TEA-230) is not encumbered by the small perturbation approximation and is capable of treating problems of far more detail and generality than the linearized theories.

Figure 19 shows a typical paneling scheme used for the TEA-230 representation of the arrow-wing body model. The source panels are placed on the configuration surface; consequently, new paneling was required for each configuration. The linearly varying internal and trailing vortex panel networks are not shown.

The third and most recently developed attached-flow method is the higher-order panel method developed by Ehlers, Epton, Johnson, Magnus, and Rubbert (refs. 16 through 20) which uses bi-quadratic doublet and bi-linear source panels. This method, known as PANAIR (Panel Aerodynamics), is still under development; therefore, the current predictions were made using the pilot code. The method will solve a variety of boundary value problems in steady subsonic and supersonic inviscid flow. The solutions are governed by the classical Prandtl-Glauert equation for linearized compressible flow. Boundary conditions are satisfied on the configuration surface so that new paneling is required for each configuration. Figure 20 shows the paneling for the cambered-twisted wing with the fin attached. The wing was represented by 476 panels, the body by 232, and the fin by 60. In addition, wake networks shed from all trailing edges extend more than 56 meters behind the configuration, but for clarity are not shown.

Detached-Flow Theory

The method chosen to predict the effect on wing pressures of the leading-edge spiral vortex was that of Weber, Brune, Johnson, Lu, and Rubbert (refs. 21 through 27). This leading-edge vortex (LEV) method is capable of predicting forces, moments, and detailed surface pressures on thin wings of arbitrary planform. The wing geometry is arbitrary in the sense that leading and trailing edges may be swept, as well as curved or kinked, provided that a single vortex describes the flow and the origin can be specified. The method does not represent the secondary vortices that often form under the primary leading-edge vortex.

The governing equations are the linear flow differential equation and nonlinear boundary conditions, which require that the flow be parallel to the wing surface and that the free vortex sheet, springing from the leading and trailing edges, be aligned with the local flow and support no pressure jump.

The Kutta condition is imposed and satisfied along all wing edges. This problem is solved numerically by an aerodynamic panel method. The configuration is represented by quadilateral panels on all surfaces, with quadratically varying doublet singularities distributed on the panels. The vortex core is modeled as a simple line vortex that receives vorticity from the free sheet through a connecting kinematic sheet. The set of nonlinear equations is solved by an iterative procedure, starting with an assumed initial geometry.

The example calculations using this method were obtained with an early version of the program which handled only thin flat wings. Figure 21 shows the paneling arrangement used on the wing. Note that the leading and trailing edges are extended to a point, rather than chopped off to form a tip with a finite chord. This should have only a trivial effect on the answers obtained. The fuselage was not a part of the current model; instead, the wing external to the body was moved inboard to obtain a more realistic model of the wing alone. A total of 212 panels were used for this solution: 63 panels to describe the wing, 108 panels to describe the rolled-up vortex, and 41 panels to describe the wake. This version of the program was restricted to incompressible flow.

Although the separated-flow computer program described above is still in development, the capability for handling wing thickness, camber, and twist, as well as a fuselage representation, have recently been added. In addition, the effects of compressibility, and many improvements on the numerics in order to facilitate convergence of the solution, have been incorporated since this prediction was made.

Leading-Edge Suction Analogy

The Polhamus leading-edge suction analogy, first published in 1966 (ref. 28), was initially developed to predict lift and pitching moment on thin, sharp-leading-edge delta wings. Subsequent developments (refs. 29 through 35) have extended the method to more arbitrary thin wing planforms. The suction analogy does not predict pressure distributions, but has been shown to provide accurate estimates of lift and pitching moment for a wide range of thin sharp-leading-edge flat wing configurations. Because configurations of interest have pointed or rounded rather than sharp leading edges, have camber and twist, and also deform aeroelastically, the previously mentioned analogy does not apply as orginally formulated. R. M. Kulfan has developed extensions to the suction analogy which overcome these limitations (refs. 36 and 37). Kulfan has observed, as have many others, that wing thickness has a retarding effect on the growth of leading-edge vortices. The experimental results indicate that, because of thickness, the vortex forms at an angle of attack greater than zero degrees. The vortex then grows with reduced strength, relative to a very thin wing, at the same angles of attack. The retarding effect depends not only on the thickness distribution, but also on whether the airfoil nose is pointed or rounded.

The formation of the leading-edge vortex is associated with the very high negative pressure and subsequent steep adverse pressure gradient near the leading edge of a highly swept wing at an angle of attack. The steep adverse pressure gradient can readily cause the three-dimensional boundary layer to

separate. When separation occurs, the boundary layer leaves the wing surface along the leading edge and rolls up into a region of concentrated vorticity. This is the leading-edge vortex.

The basic features of the suction analogy are depicted in figure 22. The bottom left-hand side of the figure depicts the attached-flow situation where linear theory predicts a square root singularity in the pressure at the leading edge. This singularity in turn produces a suction force in the plane of the wing. In practice, the flow at moderate angles of attack becomes like that depicted on the right-hand panel of the wing in figure 22. The flow separates off the leading edge, a vortex forms above the wing, and the flow reattaches inboard of the leading edge. The suction analogy assumes that the force required to make the flow over the vortex attach on the upper surface is the same as the leading-edge suction force necessary to produce the attached-flow condition. For attached flow, the suction force acts in the chord plane of the wing. The suction force for vortex flow acts normal to the plane of the wing, producing vortex lift.

The leading-edge vortex springs uniformly from the full leading edge of thin sharp-edge flat wings. Pointed- and rounded-nose airfoils, however, reduce the adverse pressure near the leading edge of highly swept wings. This effect is greatest over the inboard portion of the wing. Leading-edge separation in this case starts near the wing tip and moves progressively inboard with increasing angle of attack.

The suction analogy, previously applied only to thin sharp-leading-edge wings, has been extended by Kulfan to account for the effects of wing airfoil shape and thickness on the progressive growth of leading-edge vortices on flat wings. The qualitative effects of pointed- and rounded-nose airfoil thickness on vortex lift can be understood by applying the suction analogy reasoning to these airfoils as shown in figure 23. On the pointed-nose airfoil, the flow forward of the lower surface dividing streamline has a smaller turn around the leading edge to the upper surface than on the thin sharp-leading-edge airfoil, and on the rounded-nose airfoil, a smaller, smoother turn. Hence, the net centrifugal force necessary to turn the attached flow is less than that required for a thin sharp-leading-edge wing. The assumption is now made that the pressure required to produce reattached vortex flow on the thick wing is again equal to that necessary to produce attached flows. This reduced force is called the effective suction force. The start of the vortex is delayed to a higher angle of attack for these leading edges. For the pointed nose, the angle at which vortex lift starts is related to the angle at which the upper surface attains a positive angle of attack. The vortex lift on the rounded nose airfoil starts when the suction coefficient becomes greater than the parabolic nose drag. The method to obtain the suction force and the resulting vortex lift is described in reference 36 and includes many comparisons to experimental data.

The elegance of the Polhamus suction analogy approach is that linear theory is used to successfully predict the nonlinear forces associated with leading-edge vortices. The nonlinearity in the suction analogy occurs because the leading-edge suction depends on $\sin^2\alpha$. An additional nonlinearity was introduced by the methods previously discussed, to account for the retarding effects

of pointed-nose and rounded-nose airfoils on the progressive development of the leading-edge vortex.

Since the essential element in this calculation is the linear theory calculation of the leading-edge suction, the method for predicting rounded-nose airfoil effects on vortex development can be extended readily to arbitrary highly-swept warped wings to account for the effects of camber, twist, control-surface deflections, or aeroelastic distortions. This extension is discussed in reference 37.

THEORY-TO-EXPERIMENT COMPARISONS

The usefulness of any aerodynamic theory is determined by its ability to accurately predict flight or wind-tunnel results. The predictive methods available as production tools, as well as newly developed methods, must be tested against experimental data for those configurations and flight conditions which will figure in the design analysis. With this in mind, and recognizing the limited amount of detailed pressure data available for arrow-wing configurations over the entire subsonic-supersonic speed regimes, the present experimental and associated theoretical-methods evaluation were undertaken.

Attached-Flow Methods

Theory-to-experiment comparisons were made over a range of Mach numbers from 0.40 to 2.50 using the FLEXSTAB system, at Mach numbers of 0.40 and 0.85 with the TEA-230 program, and at Mach numbers of 0.40, 0.85, and 1.05 using the PANAIR pilot code. All configurations (except the cambered-twisted wing with fin on), including deflected control surfaces, were analyzed with FLEXSTAB. The flat and twisted wings, including some deflected control-surfaces, were analyzed using TEA-230. The three wings without deflected control-surfaces, but including the effect of the wing fin, were analyzed using PANAIR. The comparisons discussed in this paper will be limited to configurations with the control surfaces undeflected, although experimental control surface data will be shown.

Initial trade studies in the process of designing aircraft are often limited to experimental force data only, if in fact any experimental data is available at this stage. Even with the availability of pressure data, force and moment data are required for performance and stability evaluations. Forces and moments presented in subsequent figures are obtained by integrating the pressure data. Figures 24 through 26 show comparisons of attached-flow method predictions of wing normal force and pitching moment coefficients to the experimental data for three Mach numbers. At low and moderate angles of attack the predictions are quite good. At the higher angles of attack, FLEXSTAB appears to be better than the other methods - TEA-230 and PANAIR both underpredict normal force - although as we have seen in figures 8 through 17 there is strong vortex flow at these angles and FLEXSTAB does not include this phenomena. This apparent agreement is fortuitous, and detailed comparisons of surface pressures are necessary to evaluate the adequacy of these theoretical solutions in describing the load distribution.

A good test of a theoretical tool is whether or not the pressure change due to a change in twist and/or camber can be accurately predicted. Figures 27 through 34 show comparisons of experimental data with results from the theoretical methods at an angle of attack of 0° and Mach numbers of 0.40 and 1.05. The predictions for the flat wing (figs. 27 and 28) are quite good for all theories, although PANAIR is definitely better at the leading edge at Mach 1.05. Figures 29 and 30 show the twisted wing where it is clear that PANAIR (and TEA-230 at Mach 0.40) is much better than FLEXSTAB. The cambered-twisted wing, fin off and on, are shown in figures 31 through 34. The predictions are again very good, except at the outboard station at Mach 1.05 where the pressures on the lower surface are overpredicted. It seems as if the change in pressures for this smooth continuous type of deformation are adequately predicted in the region where the flow is still attached.

Comparisons of experimental and theoretical surface pressure distributions at a Mach number of 0.40 and angle of attack of 4° are shown in figures 35 through 38 for the four configurations. The predictions of all methods shown seem quite good, PANAIR and TEA-230 being somewhat better than FLEXSTAB at the leading edge. Figures 39 through 42 show a similar comparison at 8° angle of attack. The comparison on the twisted wing is still quite good, although a vortex has started to form outboard of the last section shown. On the other wings the vortex is developed on the upper surface, so that the predictions are poor. The lower surface predictions, however, are still quite acceptable.

Comparisons at a Mach number of 1.05 and an angle of attack of 4° are shown in figures 43 through 46. Although the predictions are good inboard, there is vortex development outboard on all but the twisted wing (fig. 44). It is interesting to note the difference in the vortex position at the tip section between the fin-off and fin-on data (figs. 45 and 46). With the fin off, the vortex is at mid chord, whereas with the fin on the vortex is near the leading edge. As the vortex moves inboard with increasing angle of attack, the predictions at 8° (not shown) are not as good as at 4°.

As attached-flow theories are inadequate to predict the pressure distributions at moderate angles of attack, it is important to determine whether theory could be used to predict the aeroelastic increment, to use in combination with rigid experimental data. Figures 47 through 58 show the incremental distributions due to change in shape at angles of attack of 0° and 8° and Mach numbers of 0.40 and 1.05.

The data for figures 47 through 50 were obtained by subtracting the flat wing data from the twisted wing data at each combination of angle of attack and Mach number. For this increment at $M = 0.40$, all three attached-flow theories can be evaluated. At $\alpha = 0^{\circ}$ they all predict the increment very well. FLEXSTAB, being a line[illegible] theory, predicts the same increment at all angles of attack, which is not the [illegible] in the experimental data, even on the lower surface. PANAIR and TEA-230, with their exact on-the-surface boundary conditions, predict the lower surface pressure increments quite well at all angles of attack shown. The difference in the position of the vortex on the upper surface of the two wing shapes is apparent in the incremental experimental data; none of the attached-flow theories predict this.

The increment due to camber alone is obtained by subtracting the data for the twisted wing from that of the cambered-twisted wing. These data are shown in figures 51 through 54. FLEXSTAB and PANAIR predict the increment very well at $\alpha = 0^{\circ}$, as would be expected from examining figures 29 through 32 (data at $\alpha = 0^{\circ}$). At $\alpha = 8^{\circ}$, although the lower surface predictions are good, the shift in vortex position on the upper surface is not predicted.

Figures 55 through 58 are the combined camber-twist increment (subtracting flat wing data from cambered-twisted wing data). The predictions at $\alpha = 0^{\circ}$ are again good. The mid-span station at $\alpha = 8^{\circ}$ tends to look a little better for the combined increment than it did for either twist or camber alone. This is because the position of the vortex on both the flat and cambered-twisted wings is more nearly the same, while the position on the twisted wing is shifted.

In addition to the increments due to change in wing shape, the effect of adding a vertical fin to the cambered-twisted wing is shown in figures 59 through 64. Theoretical predictions of the pressures with the fin on are limited to the PANAIR method. These figures show only the three outboard pressure stations; there is no change in pressure on the inboard portion of the wing due to adding the fin, either experimentally or as shown by PANAIR. For the Mach number angle-of-attack combinations where the flow is still attached, PANAIR predicts the increment well. The fin, however, has a large effect on the position and strength of the vortex. It is evident from figure 61 ($M = 0.40$, $\alpha = 8^{\circ}$) and figure 63 ($M = 1.05, \alpha = 4^{\circ}$) that the vortex has started and that the predictions would no longer be useful at these or larger angles of attack.

It is evident that the attached-flow methods are no better at predicting incremental pressures due to aeroelastic deformation when the flow is separated than they are in predicting the absolute pressure level. The use of attached-flow methods is clearly restricted to conditions, or at least regions of the wing, where attached flow exists.

Detached-Flow Method

It is obvious that as a vortex forms at moderate angles of attack on this configuration, attached-flow theories deteriorate in their ability to predict detailed pressures. Unfortunately this type of flow may exist at various points in the flight envelope and must be assessed in structural design. The advanced-panel leading-edge vortex method previously described is being developed to provide this capability. Results of this new procedure are shown in figure 65. These data are for 12° angle of attack and include a typical FLEXSTAB prediction for comparison. The LEV results are surprisingly good, especially considering the absence of the body in the theoretical model. The level of the peak lifting pressure is generally overpredicted, which at the apex may be because the vortex is actually further from the surface than the theory predicts, and for the outboard wing because there is a secondary vortex. Predictions for the other wings, for which experimental data are available, are planned for the near future. These solutions will also examine the effect of including the body and wing thickness in the model.

Leading-Edge Suction Analogy

The Polhamus leading-edge-suction analogy, as expanded by Kulfan, still does not predict pressure distributions, but accounts for wing thickness and warp in predicting the region over which the vortex exists. The insert in figure 66 shows a typical plot of experimental net pressure coefficient as a function of angle of attack. The angle of attack at which the pressure coefficients deviate from a linear relationship is the start of vortex flow. In the composite plots in this figure, the linear part of the $C_{p,net}$ vs. α curve at each spanwise location (at $x/c = 0.025$) is shown by the open squares; the nonlinear, or separated portion, is shown by the filled-in squares. The start of vortex flow, as predicted by the Kulfan method, is indicated by the solid lines. Figure 66 also illustrates the effect of wing warp on the progressive development of the leading-edge vortex. For a sharp thin airfoil the vortex would start on the appropriate surface midway between the boundaries shown (at $\alpha = 0^{\circ}$ for the flat wing). Using the information provided by the Kulfan method to predict the vortex location, the LEV code can be executed with the vortex restricted to that location. This procedure will be tried in the near future. If one's interest is only inboard of the vortex, the attached-flow theories can be used to predict pressures quite well, although, as can be seen in figure 66, the LEV code also provides excellent agreement with the experimental data in this area.

EXPERIMENTAL EFFECTS OF CONTROL-SURFACE DEFLECTION AND FIN

Experimental data were obtained for a wide range of configurations (see table I). One particularly interesting aspect is the effect of full- and partial-span trailing-edge control-surface deflections. Figure 67 shows span-load distributions on the flat wing at Mach 0.40. At all three angles of attack shown, the effect on the inboard wing loads is almost all due to the deflection of the inboard portion of the control surface. On the outboard wing the incremental load is just as great, or greater, when only the inboard portion is deflected, as it is when only the outboard control surface is deflected. This effect is noticeably greater at 12° angle of attack.

Similar data for the twisted wing are shown in figure 68. The increments are very similar, with only the total load level changing due to the locally lower angle of attack outboard and the resulting position of the vortex. Figures 69 and 70 show the effect of trailing-edge control surface deflection on the cambered-twisted wing with the fin off and fin on respectively. The incremental control-surface data for fin off are again very similar to the previous wings. Comparing the fin-on data (fig. 70) to the fin-off data (fig. 69) shows that although the increment for full-span deflection is much the same, the deflection of the outboard portion has a larger effect on the outboard wing with the fin on - both inboard and outboard of the fin (located at $2y/b = 0.725$).

The effect of angle of attack on the spanload distribution for both fin off and fin on is shown in figures 71 through 74 for the four deflected trailing-edge control-surface configurations. Figure 71 is for the undeflected case. The spanwise loading at 4° angle of attack is the same for both fin off and fin

on, as is the loading on the inboard 70 percent of the wing at 8°. At higher angles of attack, when the fin is off, the load on the outboard quarter of the wing remains the same as it was at 8°, while the load inboard increases. With the fin on, however, it is only directly inboard of the fin ($2y/b = 0.65$) that the load remains at the 8° angle of attack level. The load increases as angle of attack increases on the rest of the wing. Figures 72, 73, and 74, which are respectively outboard only, inboard only, and full-span control-surface deflection, illustrate this same phenomena. The placement and orientation of the fin clearly needs further study to obtain the maximum benefit in a control effectiveness sense.

Theoretical pressure predictions made for the configuration with deflected trailing edge are not shown here, but have been previously reported in detail (refs. 2 and 5). The pressures at the hinge line are typically overpredicted, especially by FLEXSTAB and to some degree by TEA-230. PANAIR has not been used on this configuration to predict pressures for the deflected trailing edge.

CONCLUDING REMARKS

The previous discussion has shown that the arrow-wing configuration of this study is dominated by leading-edge vortex flow at moderate and high angles of attack. Attached-flow methods are very good at low angles of attack typical of cruise conditions (load factor one). At critical structural and control design conditions, which involve large angles of attack and/or large control-surface deflections, the attached-flow theories are inadequate. Examination of the theoretical incremental load caused by a change in shape, shows that attached-flow theories can be used to provide an aeroelastic increment to the rigid experimental data only at small angles of attack.

The one example of a separated flow method indicates much better agreement with experiment than do the attached-flow theories. If attempts to use it in conjunction with the Kulfan method to predict the location of the vortex are successful, an investigation must be made into the possibilities of including the aeroelastic effects in this procedure. At this time, this seems to be the best hope for predicting the aeroelastic loads on highly-swept, low-aspect-ratio, flexible airplanes with the accuracy required.

REFERENCES

1. Manro, Marjorie E.; Tinoco, Edward N.; Bobbitt, Percy J.; and Rogers, John T.: Comparisons of Theoretical and Experimental Pressure Distributions on an Arrow-Wing Configuration at Transonic Speeds. Aerodynamic Analyses Requiring Advanced Computers - Part II, NASA SP-347, 1975, pp. 1141-1188.

2. Manro, Marjorie E.; Manning, Kenneth J. R.; Hallstaff, Thomas H.; and Rogers, John T.: Transonic Pressure Measurements and Comparison of Theory to Experiment for an Arrow-Wing Configuration - Summary Report. NASA CR-2610, 1976.

3. Manro, Marjorie E.; Manning, Kenneth J. R.; Hallstaff, Thomas H.; and Rogers, John T.: Transonic Pressure Measurements and Comparison of Theory to Experiment for an Arrow-Wing Configuration, Volume I: Experimental Data Report - Base Configuration and Effects of Wing Twist and Leading-Edge Configuration. NASA CR-132727, 1975.

4. Manro, Marjorie E.; Manning, Kenneth J. R.; Hallstaff, Thomas H.; and Rogers, John T.: Transonic Pressure Measurements and Comparison of Theory to Experiment for an Arrow-Wing Configuration, Volume II: Experimental Data Report - Effects of Control Surface Deflection. NASA CR-132728, 1975.

5. Manro, Marjorie E.; Manning, Kenneth J. R.; Hallstaff, Thomas H.; and Rogers, John T.: Transonic Pressure Measurements and Comparison of Theory to Experiment for an Arrow-Wing Configuration, Volume III: Data Report - Comparison of Attached Flow Theories to Experiment. NASA CR-132729, 1975.

6. Manro, Marjorie E.; Bobbitt, Percy J.; and Rogers, John T.: Comparisons of Theoretical and Experimental Pressure Distributions on an Arrow-Wing Configuration at Subsonic, Transonic and Supersonic Speeds. Prediction of Aerodynamic Loading, AGARD-CP-204, Feb. 1977, pp. 11-1 - 11-14.

7. Bobbitt, Percy J.; and Manro, Marjorie E.: Theoretical and Experimental Pressure Distributions for a 71.2° Swept Arrow-Wing Configuration at Subsonic, Transonic, and Supersonic Speeds. Proceedings of the SCAR Conference - Part I, NASA CP-001, 1977, pp. 85-122.

8. Manro, M. E.: Supersonic Pressure Measurements and Comparison of Theory to Experiment for an Arrow-Wing Configuration. NASA CR-145046, 1976.

9. Tinoco, E. N.; and Mercer, J. E.: FLEXSTAB - A Summary of the Functions and Capabilities of the NASA Flexible Airplane Analysis Computer System. NASA CR-2564, 1975.

10. Woodward, F. A.; Tinoco, E. N.; and Larsen, J. W.: Analysis and Design of Supersonic Wing-Body Combinations, Including Flow Properties in the Near Field, Part 1 - Theory and Application. NASA CR-73106, 1967.

11. Woodward, Frank A.: Analysis and Design of Wing-Body Combinations at Subsonic and Supersonic Speeds. J. Aircr., vol. 5, no. 6, Nov.-Dec. 1968, pp. 528-534.

12. Dusto, A. R., et al.: A Method for Predicting the Stability Characteristics of an Elastic Airplane, Volume 1,- FLEXSTAB Theoretical Description. NASA CR-114712, 1974.

13. Rubbert, P. E.; Saaris, G. R.; Scholey, M. B.; Standen, N. M.; and Wallace, R. E.: A General Method for Determining the Aerodynamic Characteristics of Fan-in-Wing Configurations. Vol. I - Theory and Application. USAAVLABS Tech. Rep. 67-61A, U.S. Army, Dec. 1967.

14. Rubbert, P. E.; and Saaris, G. R.: A General Three-Dimensional Potential-Flow Method Applied to V/STOL Aerodynamics. SAE J., vol. 77, September 1969.

15. Rubbert, P. E.; and Saaris, G. R.: Review and Evaluation of a Three-Dimensional Lifting Potential Flow Analysis Method for Arbitrary Configurations. AIAA Paper No. 72-188, 1972.

16. Ehlers, F. E.; Epton, M. A.; Johnson, F. T.; Magnus, A. E.; and Rubbert, P. E.: An Improved Higher Order Panel for Linearized Supersonic Flow. AIAA Paper No. 78-15, January 1978.

17. Moran, Jack; and Tinoco, E. N.: User's Manual - Subsonic/Supersonic Advanced Panel Pilot Code. NASA CR-152047, 1978.

18. Ehlers, F. Edward; Epton, Michael A.; Johnson. Forrester T.; Magnus, Alfred E.; and Rubbert, Paul E.: A Higher Order Panel Method for Linearized Supersonic Flow. NASA CR-3062, 1979.

19. Johnson, Forrester T.; and Rubbert, Paul E.: Advanced Panel-Type Influence Coefficient Methods Applied to Subsonic Flows. AIAA Paper No. 75-50, January 1975.

20. Tinoco, E. N.; Johnson, F. T.; and Freeman, L. M.: The Application of a Higher Order Panel Method to Realistic Supersonic Configurations. AIAA Paper No. 79-274, January 1979.

21. Weber, James A.; Brune, Guenter W.; Johnson, Forrester T.; Lu, Paul; and Rubbert, Paul E.: A Three-Dimensional Solution of Flows Over Wings With Leading Edge Vortex Separation. Aerodynamic Analyses Requiring Advanced Computers - Part II, NASA SP-347, 1975, pp. 1013-1032.

22. Brune, G. W.; Weber, J. A.; Johnson, F. T.; Lu, P.; and Rubbert, P. E.: A Three-Dimensional Solution of Flows Over Wings With Leading-Edge Vortex Separation. Part 1 - Engineering Document. NASA CR-132709, 1975.

23. Brune, G. W.; and Rubbert, P. E.: Boundary Value Problems of Configurations With Compressible Free Vortex Flow. AIAA Journal, vol. 15, no. 10, October 1977, pp. 1521-1523.

24. Gloss, Blair B.; and Johnson, Forrester, T.: Development of an Aerodynamic Theory Capable of Predicting Surface Loads on Slender Wings With Vortex Flow. Proceedings of the SCAR Conference - Part I, NASA CP-001, 1977, pp. 55-67.

25. Johnson, F. T.; Tinoco, E. N.; Lu, P.; and Epton, M. A.: Recent Advances in the Solution of Three-Dimensional Flow over Wings with Leading Edge Vortex Separation. AIAA Paper 79-282, January 1979.

26. Johnson, F. T.; Lu, P.; Tinoco, E. N.; and Epton, M. A.: An Improved Panel Method For the Solution of Three-Dimensional Leading-Edge Vortex Flows, Volume I, Theory Document. NASA CR-159173, 1980.

27. Tinoco, E. N.; Lu, P.; and Johnson, F. T.: An Improved Panel Method For the Solution of Three-Dimensional Leading-Edge Vortex Flows, Volume II, Users Guide and Programmers Document. NASA CR-159174, 1980.

28. Polhamus, Edward C.: A Concept of the Vortex Lift of Sharp-Edge Delta Wings Based on a Leading-Edge-Suction Analogy. NASA TN D-3767, 1966.

29. Polhamus, Edward C.: Application of the Leading-Edge-Suction Analogy of Vortex Lift to the Drag Due to Lift of Sharp-Edge Delta Wings. NASA TN D-4739, 1968.

30. Polhamus, Edward C.: Predictions of Vortex-Lift Characteristics by a Leading-Edge Suction Analogy. J. Aircr., vol. 8, no. 4, Apr. 1971, pp. 193-199.

31. Snyder, Melvin H., Jr.; and Lamar, John E.: Application of the Leading-Edge-Suction Analogy to Prediction of Longitudinal Load Distribution and Pitching Moments for Sharp-Edged Delta Wings. NASA TN D-6994, 1972.

32. Lamar, John E.: Extension of Leading-Edge-Suction Analogy to Wings With Separated Flow Around the Side Edges at Subsonic Speeds. NASA TR R-428, 1974.

33. Lamar, John E.: Some Recent Applications of the Suction Analogy to Vortex-Lift Estimates. Aerodynamic Analyses Requiring Advanced Computers - Part II, NASA SP-347, 1975, pp. 985-1011.

34. Lamar, J. E.: Subsonic Vortex-Flow Design Study for Slender Wings. AIAA Paper 78-154, January 1978.

35. Lamar, J. E.: Strake-Wing Analysis and Design. AIAA Paper 78-1201, July 1978.

36. Kulfan, R. M.: Wing Airfoil Shape Effects on the Development of Leading-Edge Vortices. AIAA Paper No. 79-1675, August 1979.

37. Kulfan, R. M.: Wing Geometry Effects on Leading-Edge Vortices. AIAA Paper No. 79-1872, August 1979.

TABLE I.- SUMMARY OF CONDITIONS TESTED IN THE BOEING TRANSONIC WIND TUNNEL

WING	TRAILING EDGE	LEADING-EDGE DEFLECTION, DEGREES	TRAILING-EDGE DEFLECTION, DEGREES
ROUNDED-LEADING-EDGE FLAT WING	FLAT	0.	0., ± 4.1, ± 8.3, ± 17.7, ± 30.2
			PARTIAL SPAN + 8.3, + 17.7
		PARTIAL SPAN 5.1	PARTIAL SPAN ± 8.3, ± 17.7
		5.1, 12.8	0., + 4.1, ± 8.3, ± 17.7
	TWISTED	0.	0., + 4.1, ± 8.3, ± 17.7
SHARP-LEADING-EDGE FLAT WING	FLAT	0.	0.
ROUNDED-LEADING-EDGE TWISTED WING	TWISTED	0.	0., + 4.1, ± 8.3, ± 17.7, + 30.2
			PARTIAL SPAN + 8.3
ROUNDED-LEADING-EDGE CAMBERED-TWISTED WING (VERTICAL FIN OFF AND ON)	CAMBERED-TWISTED	0.	0., + 8.3
			PARTIAL SPAN + 8.3

MACH NUMBERS: 0.40, 0.70, 0.85, 0.95, 1.00, 1.05, 1.11
ANGLE OF ATTACK: -8° TO + 16° (2° INCREMENTS)

TABLE II.- SUMMARY OF CONDITIONS TESTED IN THE NASA AMES UNITARY WIND TUNNEL

WING	TRAILING EDGE	LEADING EDGE DEFLECTION, DEGREES	TRAILING-EDGE DEFLECTION, DEGREES
ROUNDED-LEADING-EDGE FLAT WING	FLAT	0.	0., ± 4.1, +8.3
			PARTIAL SPAN +4.1, +8.3
		5.1	0.
SHARP-LEADING-EDGE FLAT WING	FLAT	0.	0.
		5.1	0.
ROUNDED-LEADING-EDGE TWISTED WING	TWISTED	0.	0., + 8.3

MACH NUMBERS: 1.70, 2.10, 2.50
ANGLE OF ATTACK: -8° TO + 14° (2° INCREMENTS) + 15°

TABLE III.- THEORETICAL PANEL METHODS

$$(\beta^2 \phi_{xx} + \phi_{yy} + \phi_{zz} = 0 \quad \beta^2 = 1 - M_\infty{}^2)$$

METHOD	BOUNDARY CONDITIONS	COMMENTS
FLEXSTAB	LINEARIZED	
TEA-230	'EXACT' ON THE SURFACE	
PAN AIR	'EXACT' ON THE SURFACE	
LEADING-EDGE VORTEX (LEV)	'EXACT' ON THE SURFACE SATISFIES BOTH NONLINEAR $\Delta C_p = 0$ AND STREAM SURFACE CONDITIONS	ITERATIVE SOLUTION

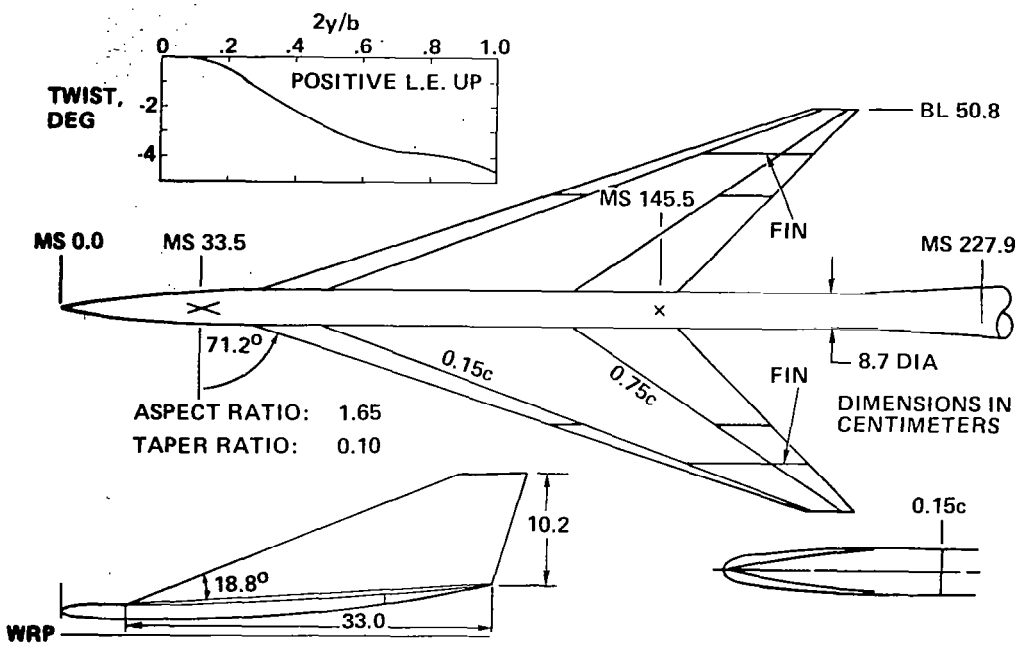

Figure 1.- General arrangement and characteristics.

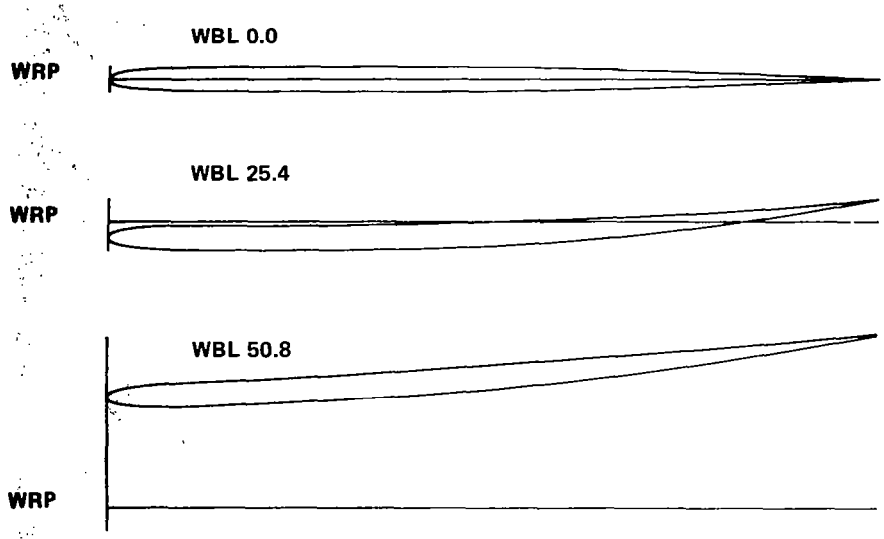

Figure 2.- Cambered-twisted wing section geometry.

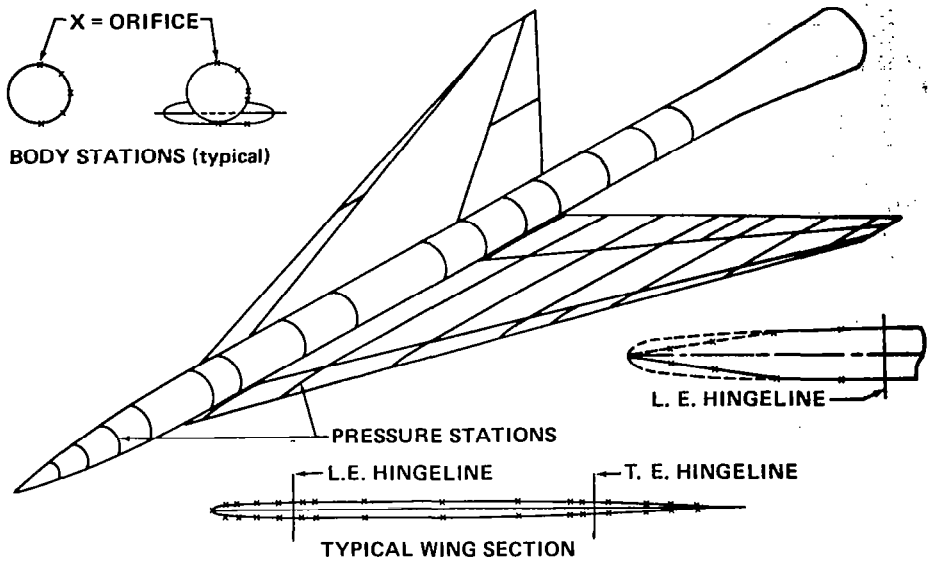

Figure 3.- Pressure orifice locations.

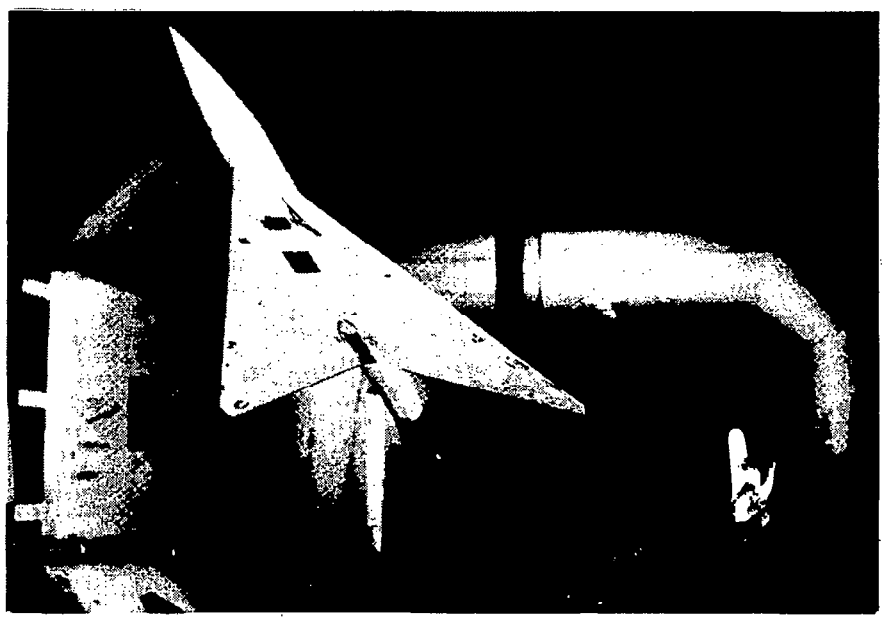

Figure 4.- Flat wing in Boeing Transonic Wind Tunnel.

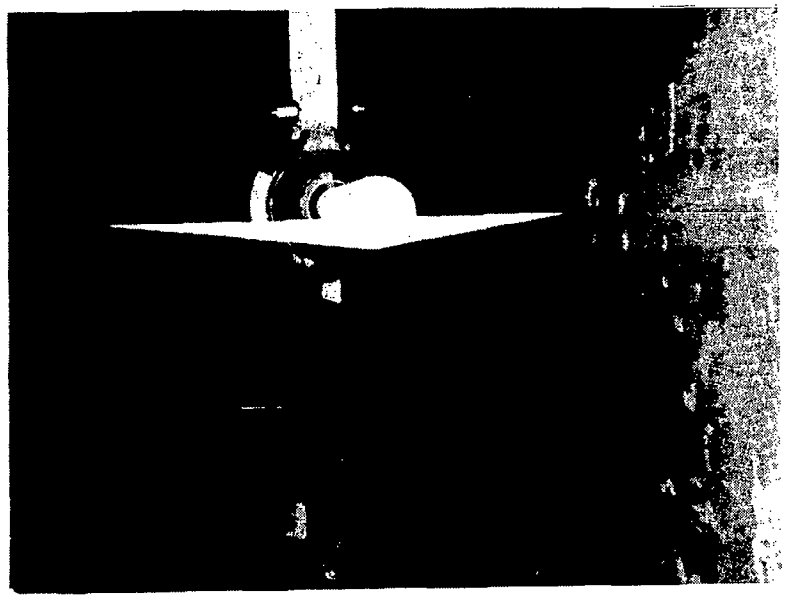

(a) Flat wing.

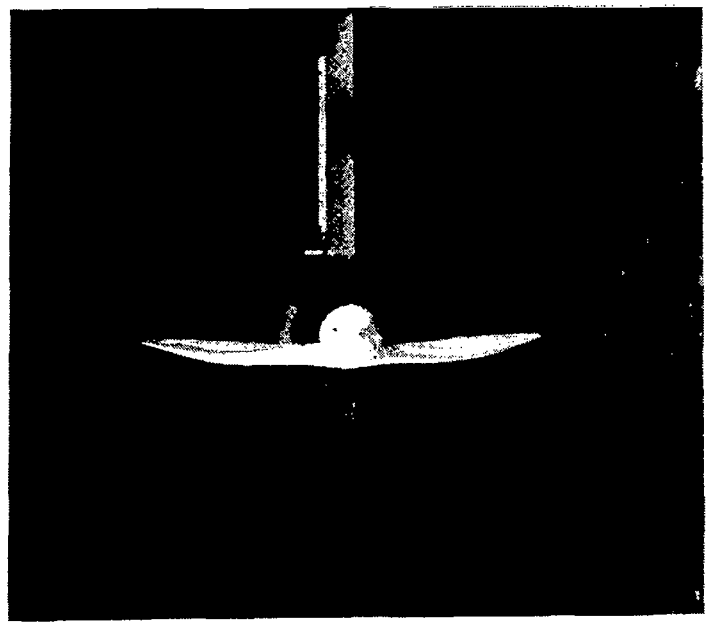

(b) Twisted wing.

Figure 5.- Flat and twisted wings in the 9- by 7-foot leg of the Ames Unitary Wind Tunnel.

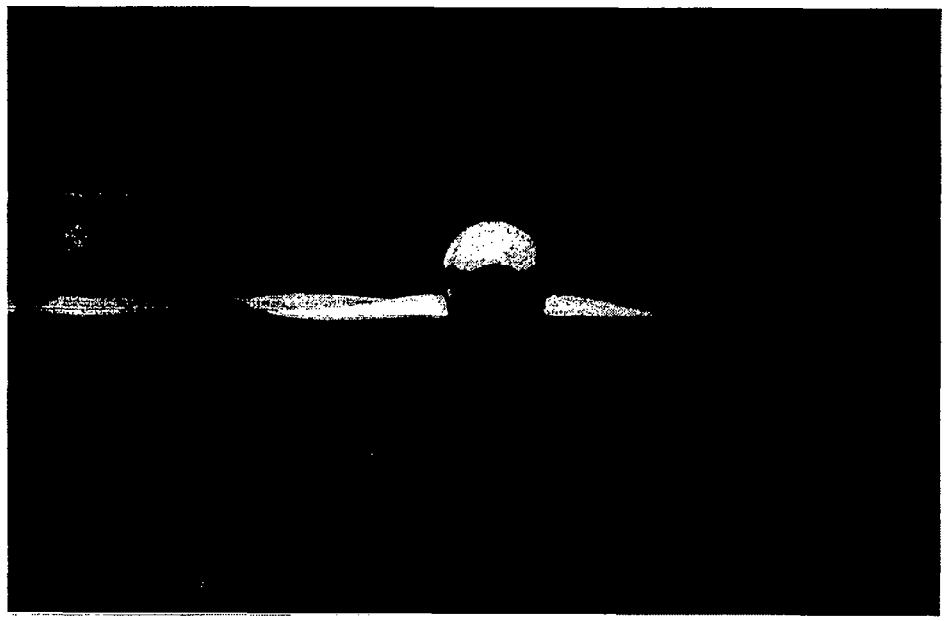

Figure 6.- Cambered-twisted wing without fin in the Boeing Transonic Wind Tunnel.

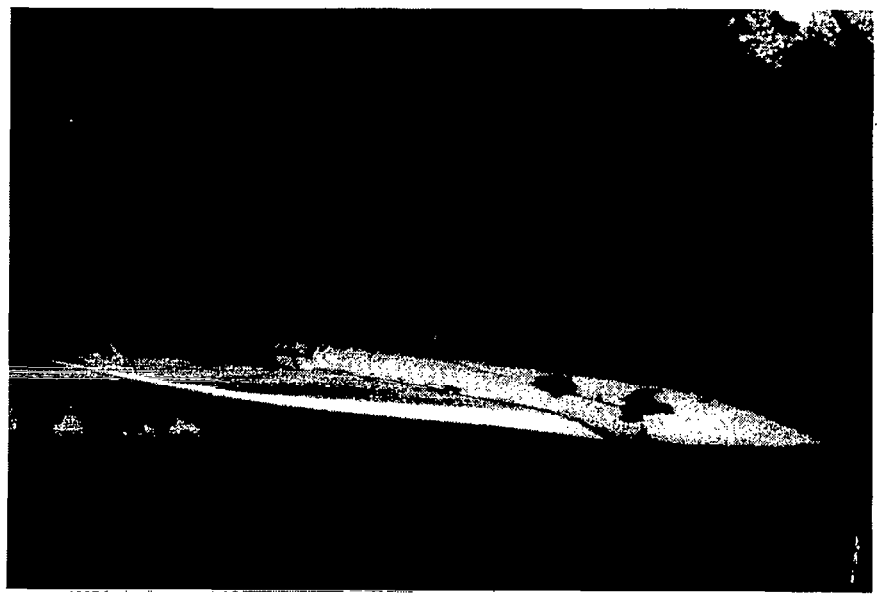

Figure 7.- Cambered-twisted wing with fin in the Boeing Transonic Wind Tunnel.

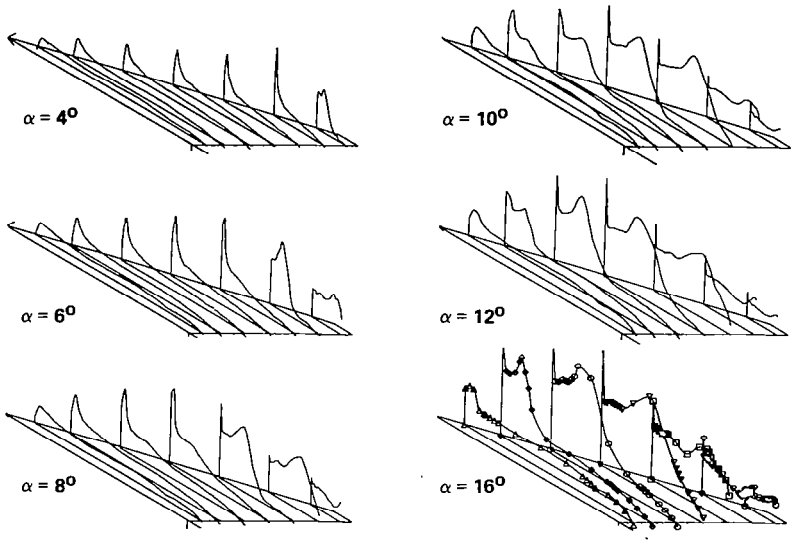

Figure 8.- Upper surface pressure distributions, rounded-leading-edge flat wing, M = 0.40.

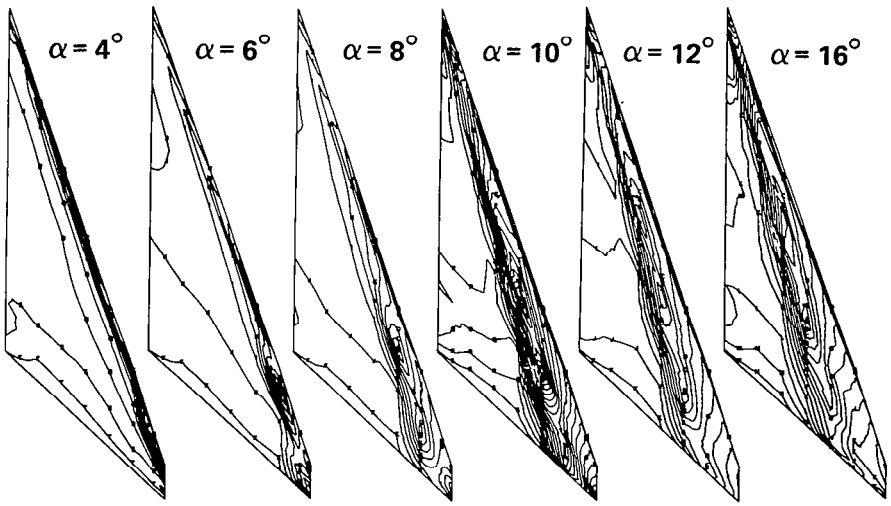

Figure 9.- Upper surface isobars, rounded-leading-edge flat wing, M = 0.40.

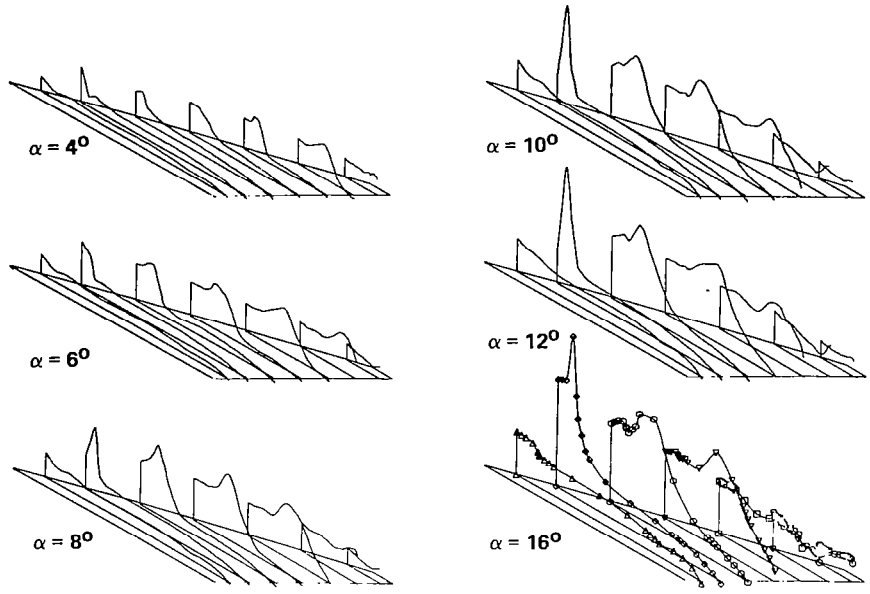

Figure 10.- Upper surface pressure distributions, sharp-leading-edge flat wing, M = 0.40.

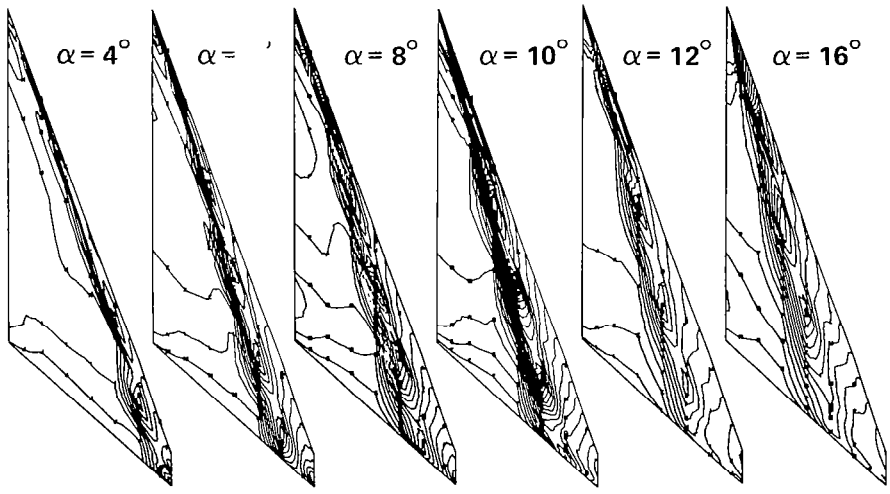

Figure 11.- Upper surface isobars, sharp-leading-edge flat wing, M = 0.40.

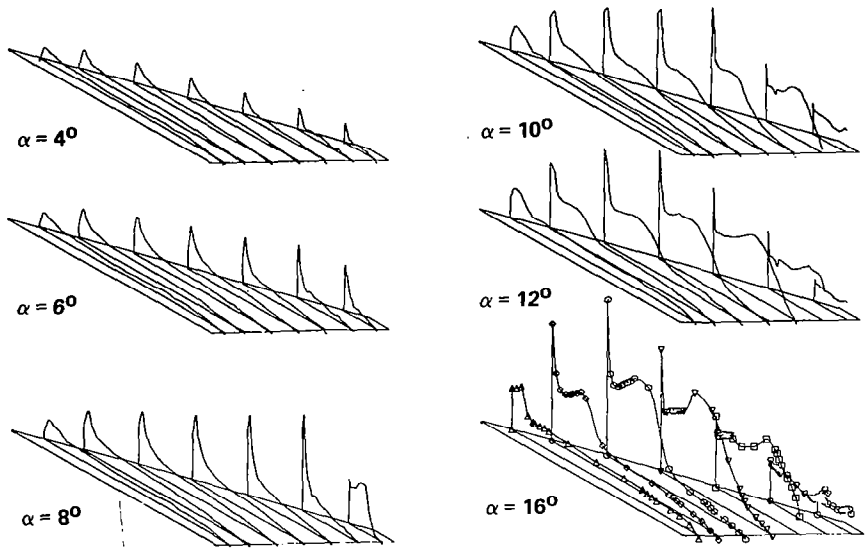

Figure 12.- Upper surface pressure distributions, rounded-leading-edge twisted wing, M = 0.40.

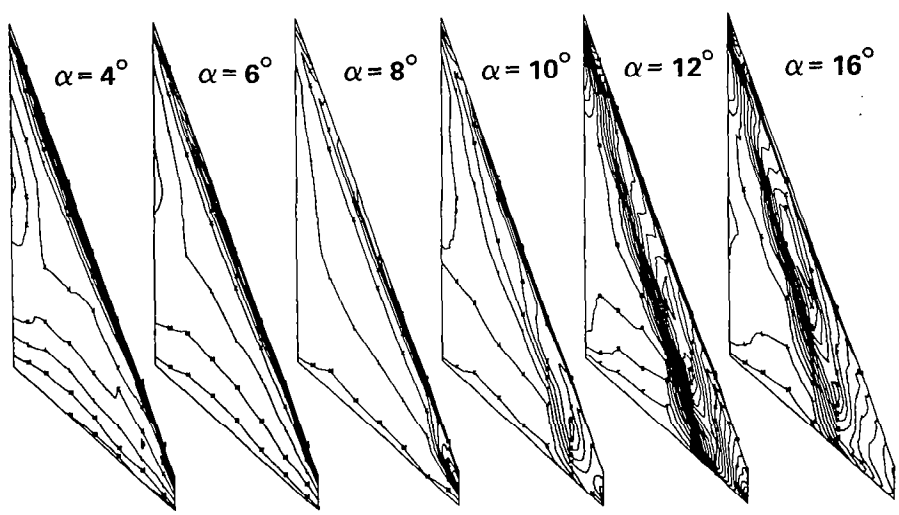

Figure 13.- Upper surface isobars, rounded-leading-edge twisted wing, M = 0.40.

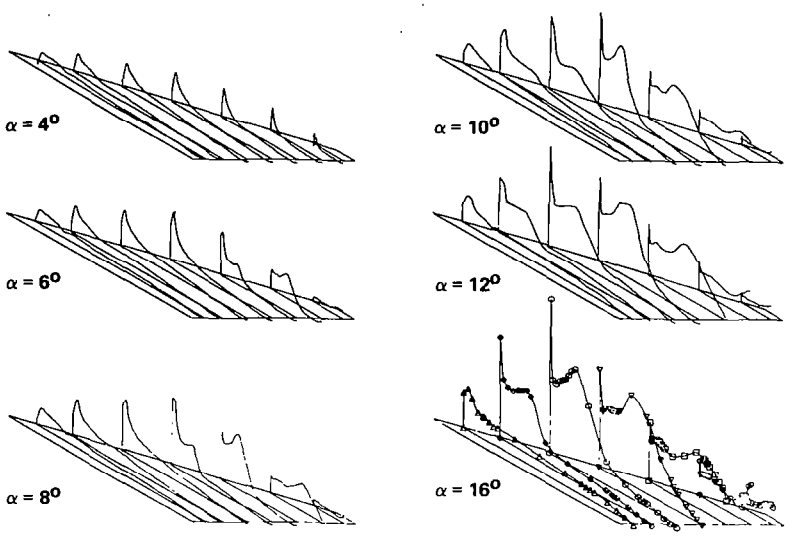

Figure 14.- Upper surface pressure distributions, rounded-leading-edge cambered-twisted wing, fin off, M = 0.40.

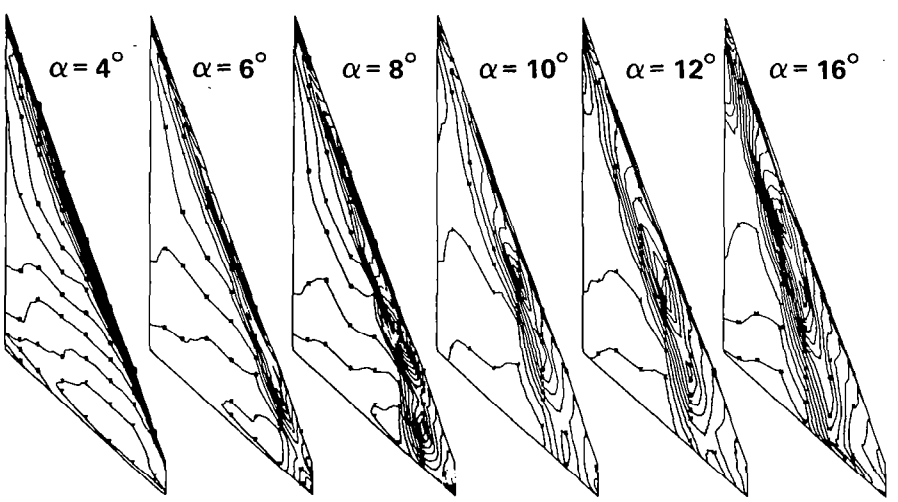

Figure 15.- Upper surface isobars, rounded-leading-edge cambered-twisted wing, fin off, M = 0.40.

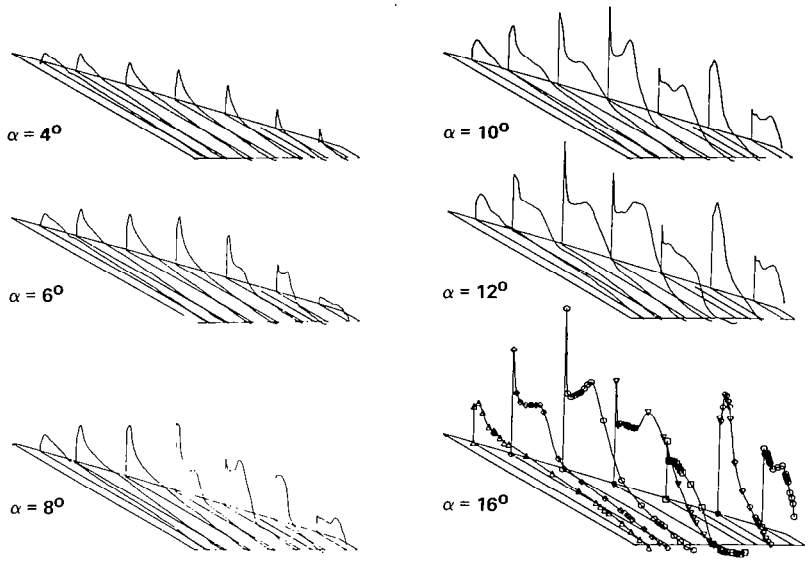

Figure 16.- Upper surface pressure distributions, rounded-leading-edge cambered-twisted wing, fin on, M = 0.40.

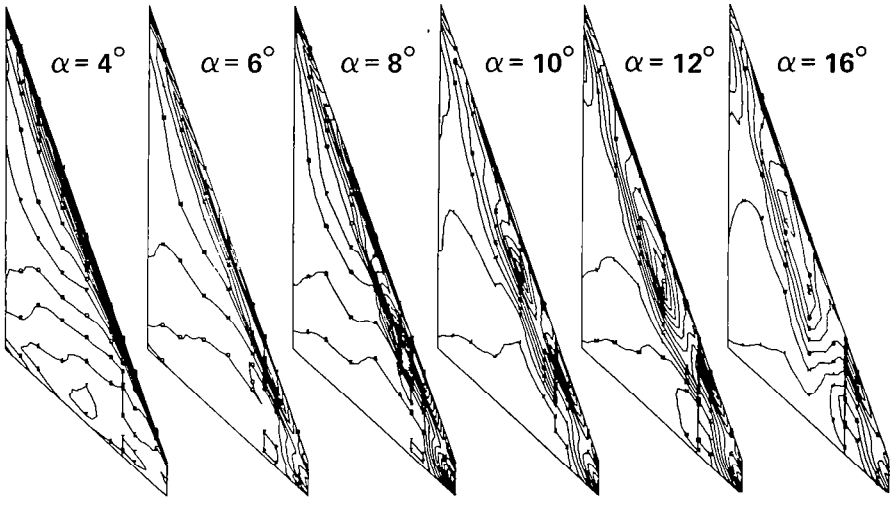

Figure 17.- Upper surface isobars, rounded-leading-edge cambered-twisted wing, fin on, M = 0.40.

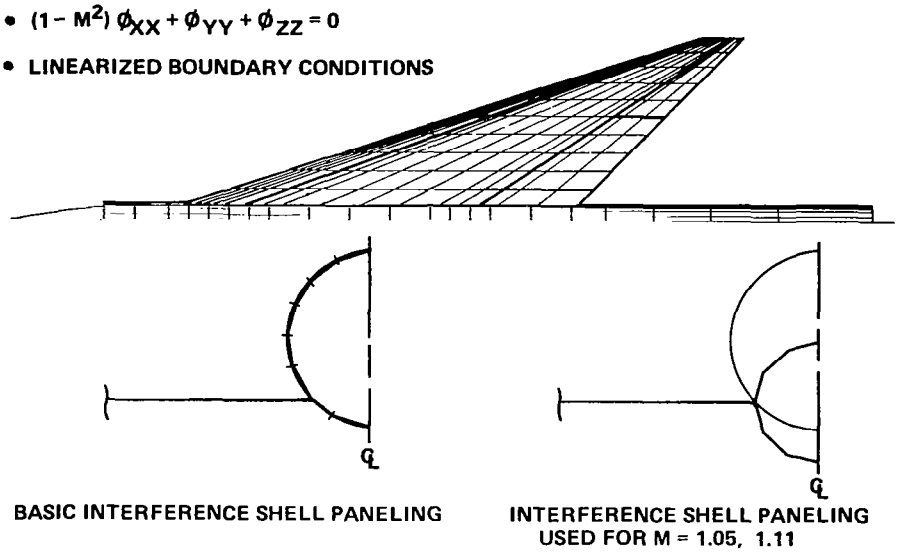

Figure 18.- FLEXSTAB paneling scheme.

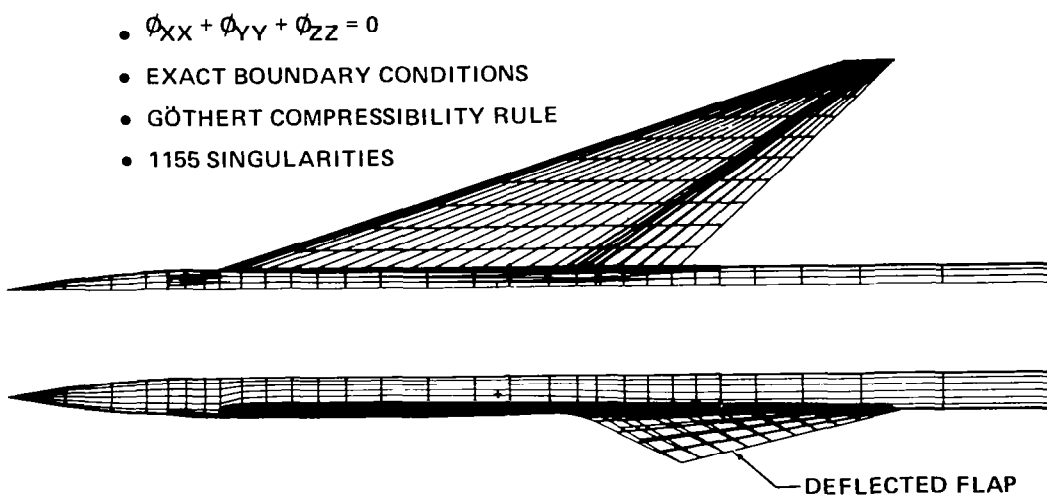

Figure 19.- TEA-230 paneling scheme.

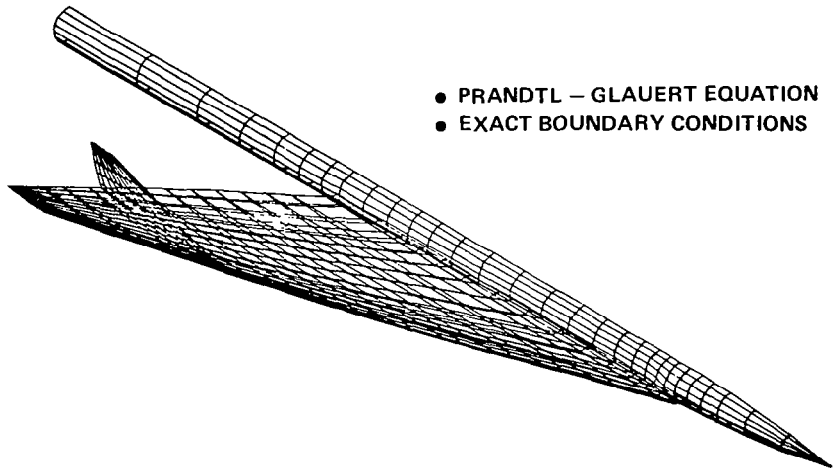

Figure 20.- PANAIR paneling scheme.

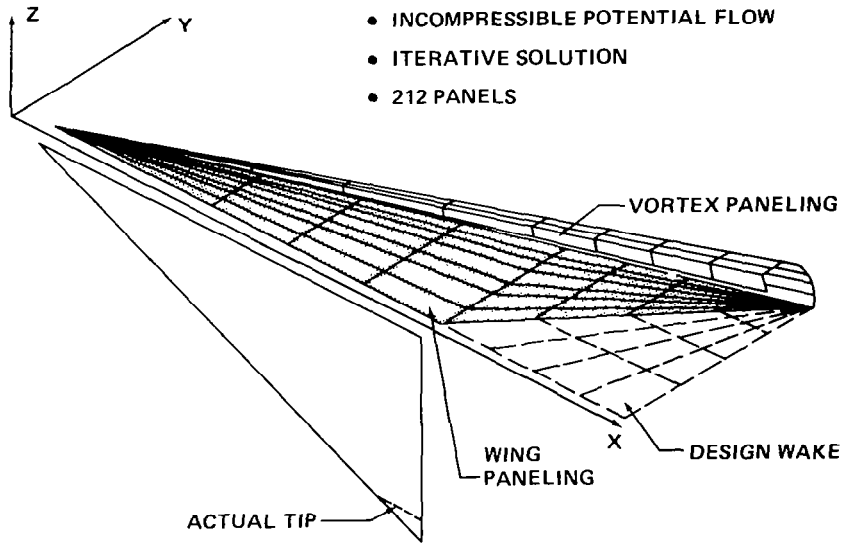

Figure 21.- Leading edge vortex (LEV) program paneling scheme.

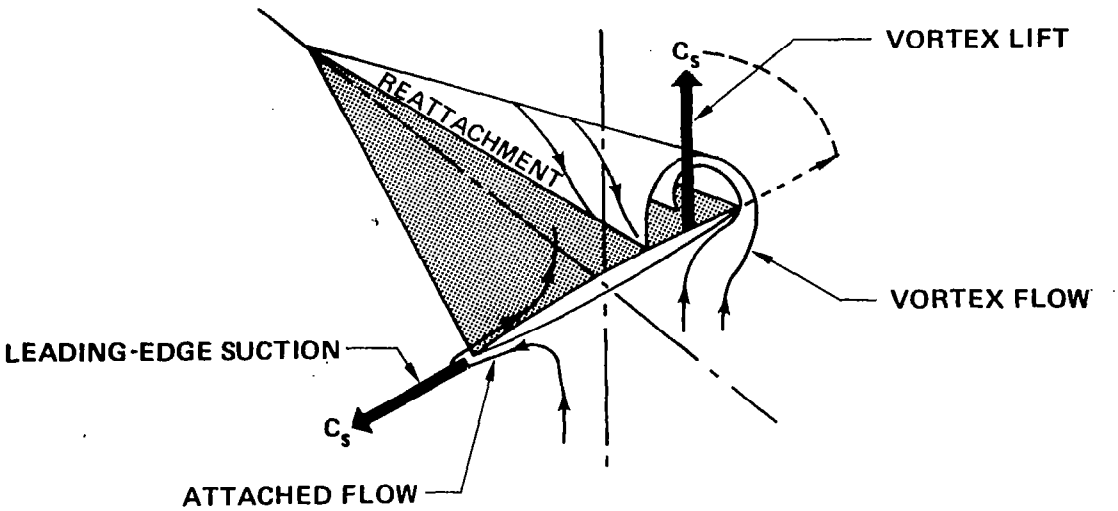

Figure 22.- Leading edge suction analogy — thin, sharp-leading-edge wings.

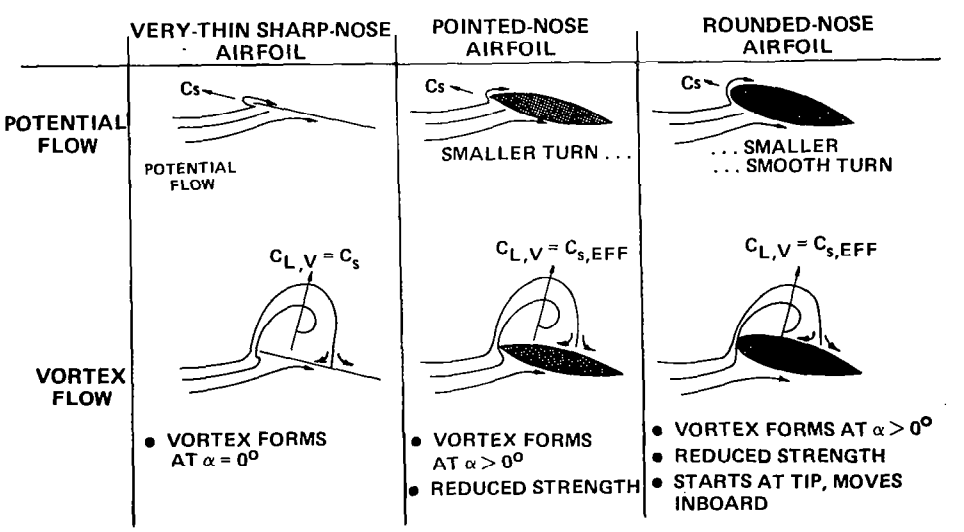

Figure 23.- Effect of airfoil shape on the vortex lift of a highly-swept wing.

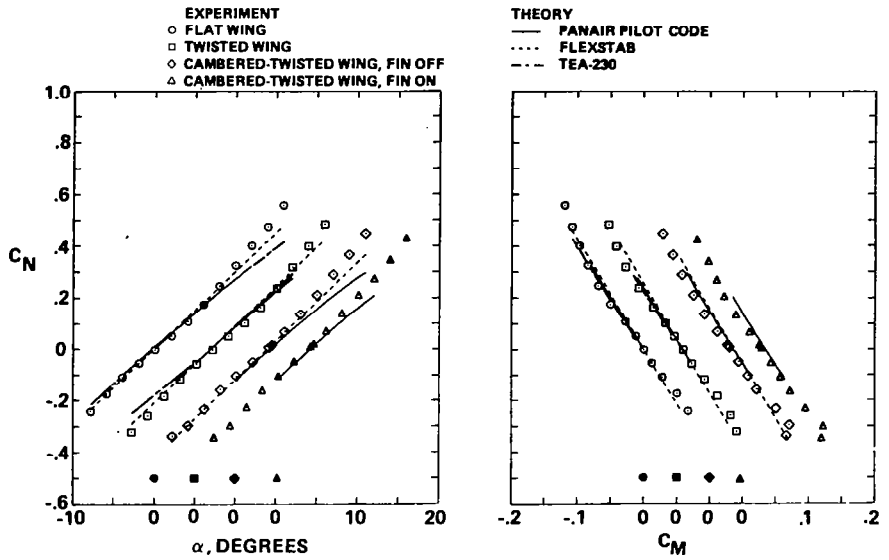

Figure 24.- Wing normal force and pitching moment coefficients, M = 0.40.

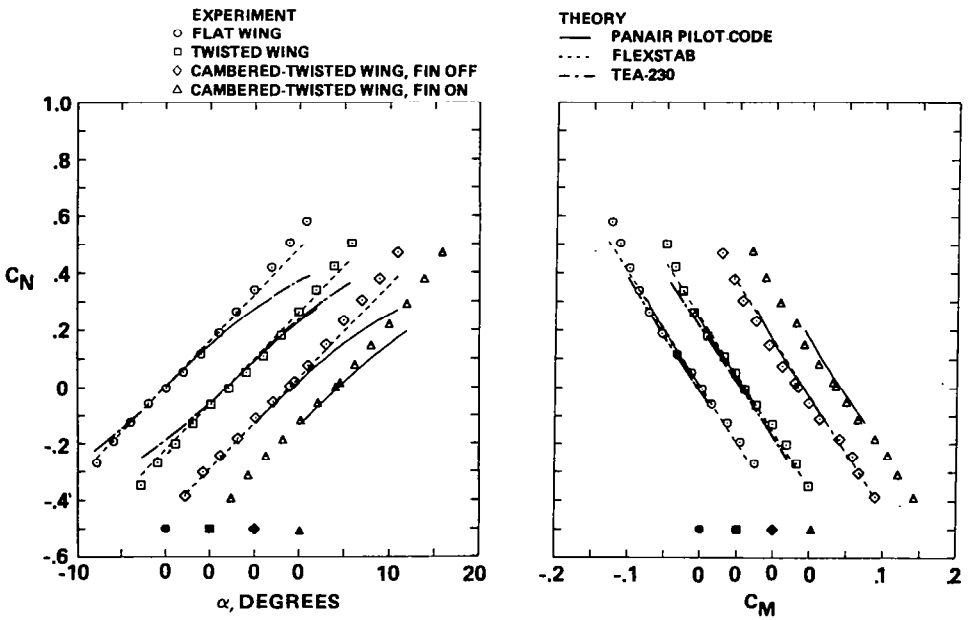

Figure 25.- Wing normal force and pitching moment coefficients, M = 0.85.

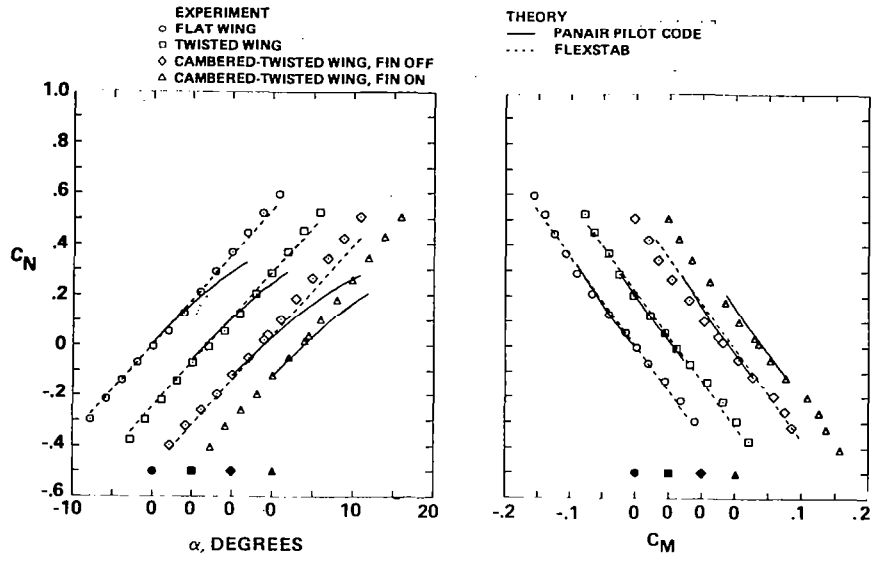

Figure 26.- Wing normal force and pitching moment coefficients, M = 1.05.

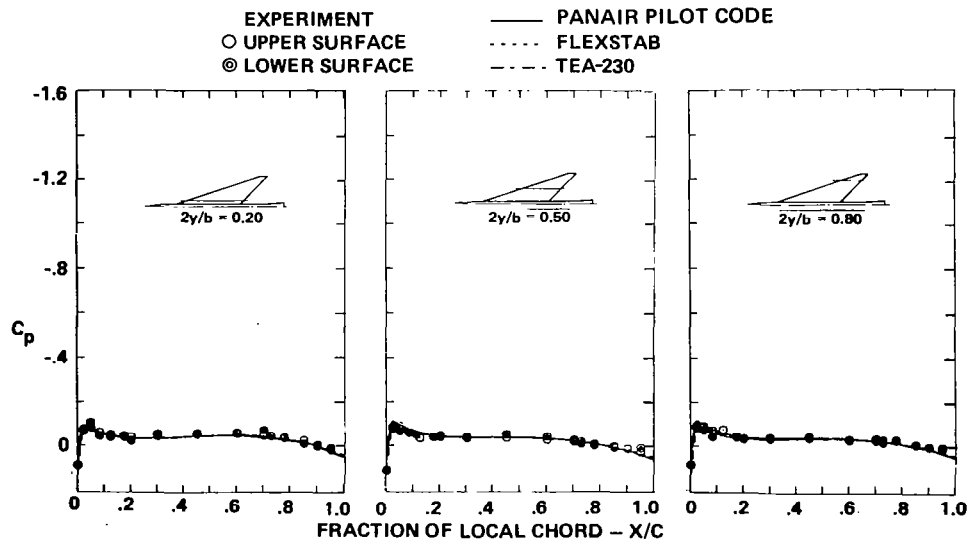

Figure 27.- Surface pressure distributions, flat wing, M = 0.40, $\alpha = 0^{\circ}$.

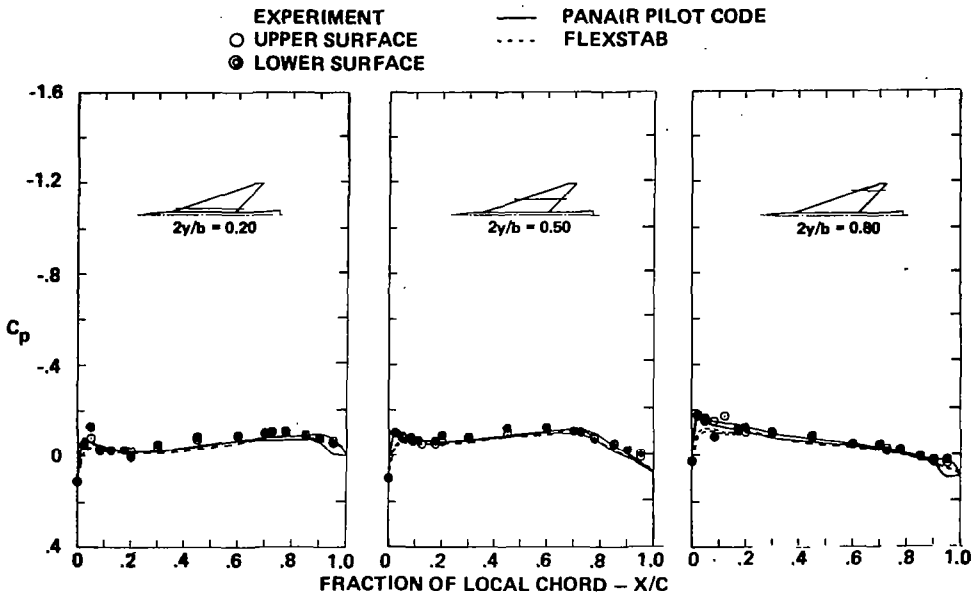

Figure 28.- Surface pressure distributions, flat wing, $M = 1.05$, $\alpha = 0^{\circ}$.

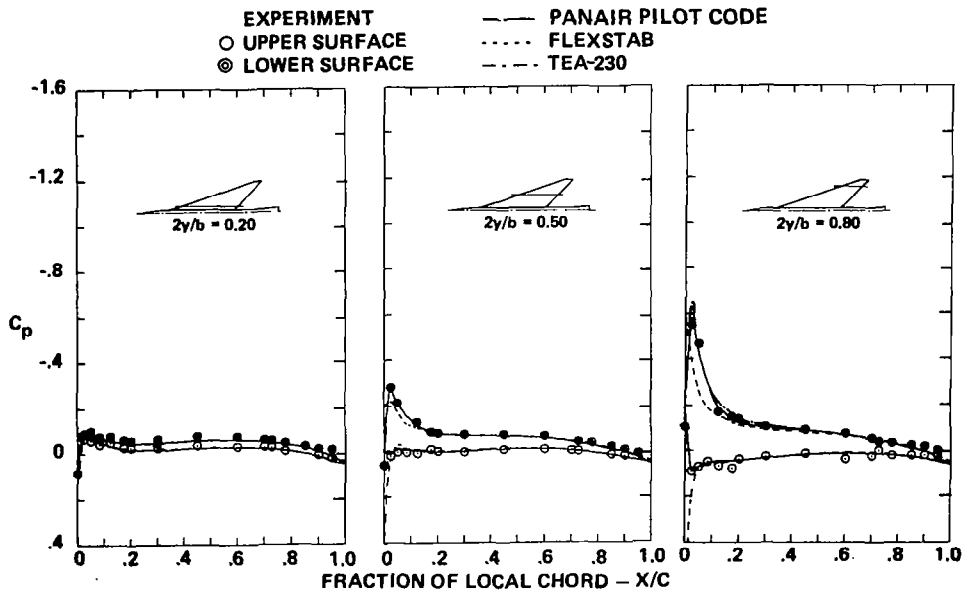

Figure 29.- Surface pressure distributions, twisted wing, $M = 0.40$, $\alpha = 0^{\circ}$.

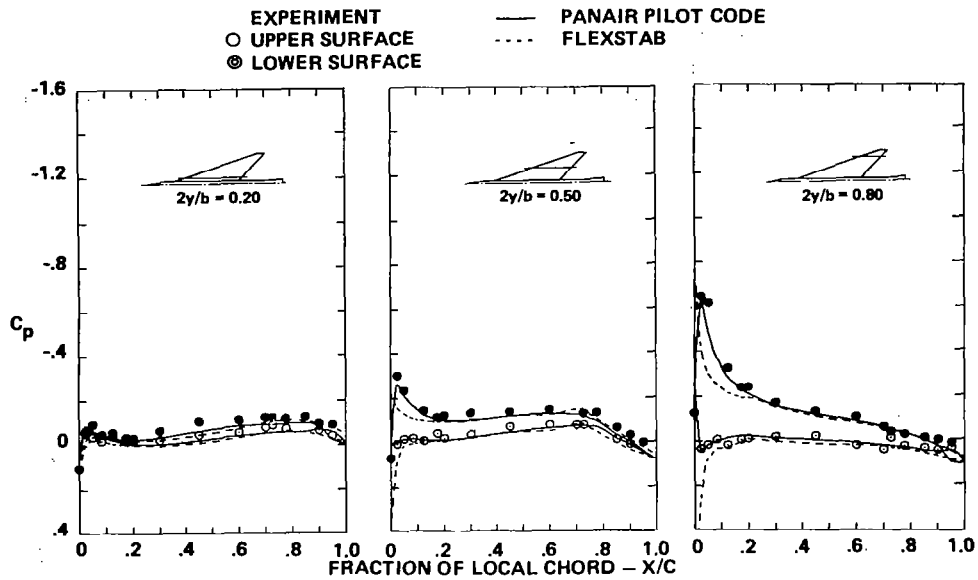

Figure 30.- Surface pressure distributions, twisted wing, $M = 1.05$, $\alpha = 0^{\circ}$.

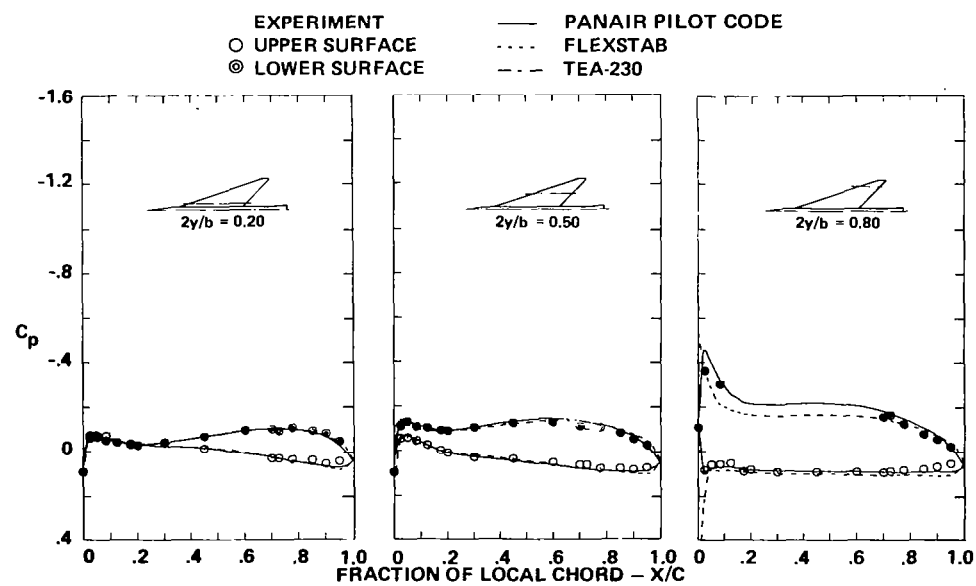

Figure 31.- Surface pressure distributions, cambered-twisted wing, fin off, $M = 0.40$, $\alpha = 0^{\circ}$.

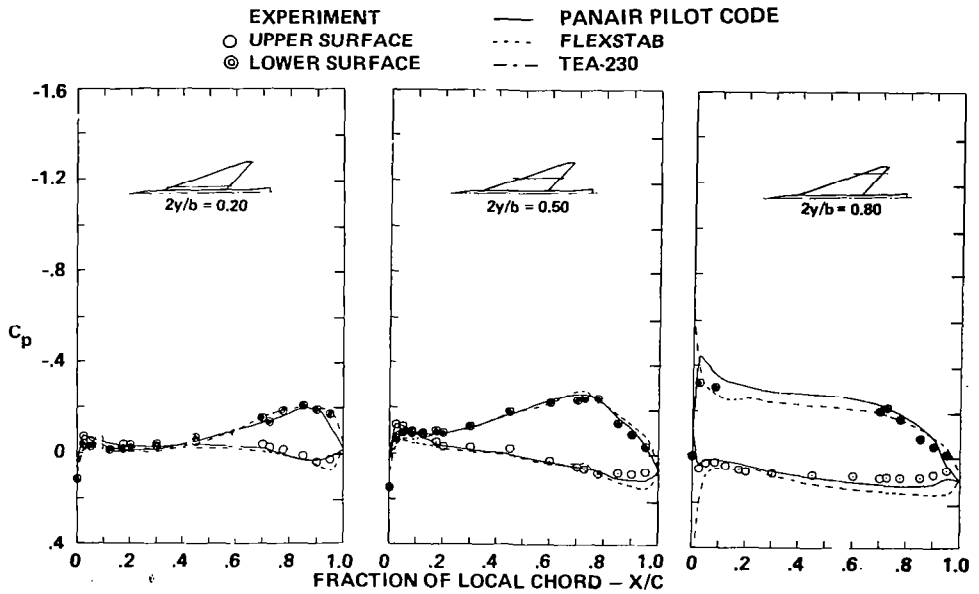

Figure 32.- Surface pressure distributions, cambered-twisted wing, fin off, $M = 1.05$, $\alpha = 0^{\circ}$.

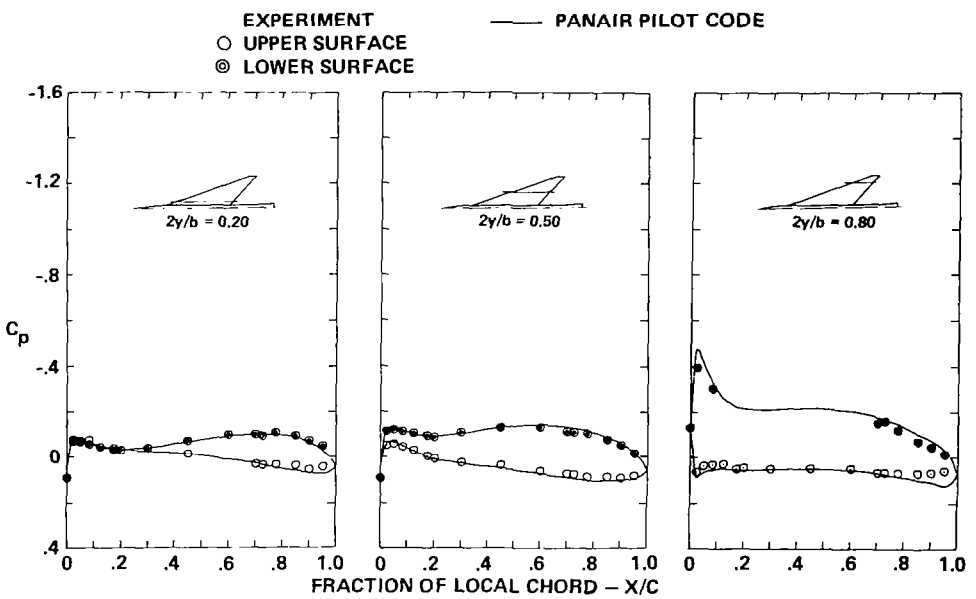

Figure 33.- Surface pressure distributions, cambered-twisted wing, fin on, $M = 0.40$, $\alpha = 0^{\circ}$.

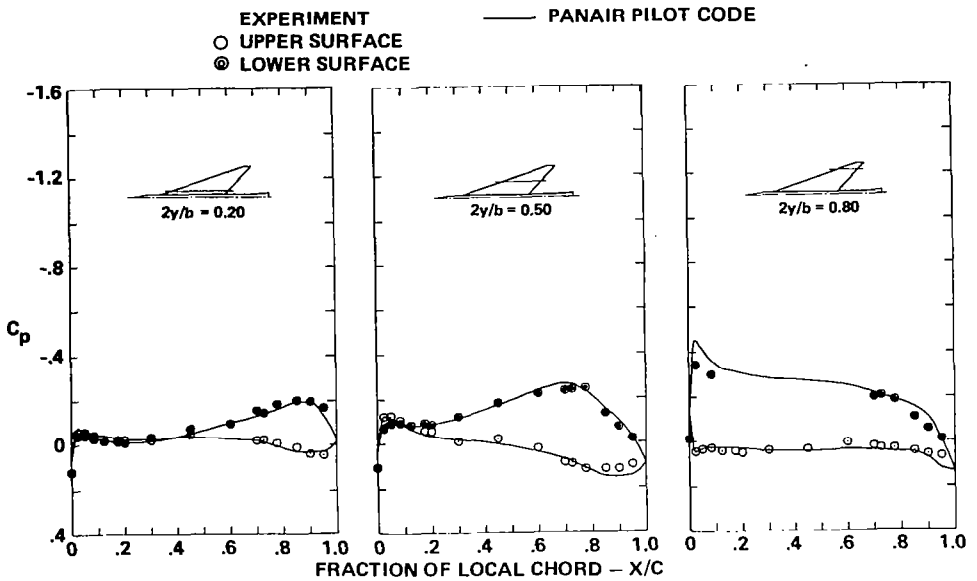

Figure 34.- Surface pressure distributions, cambered-twisted wing, fin on, $M = 1.05$, $\alpha = 0^{\circ}$.

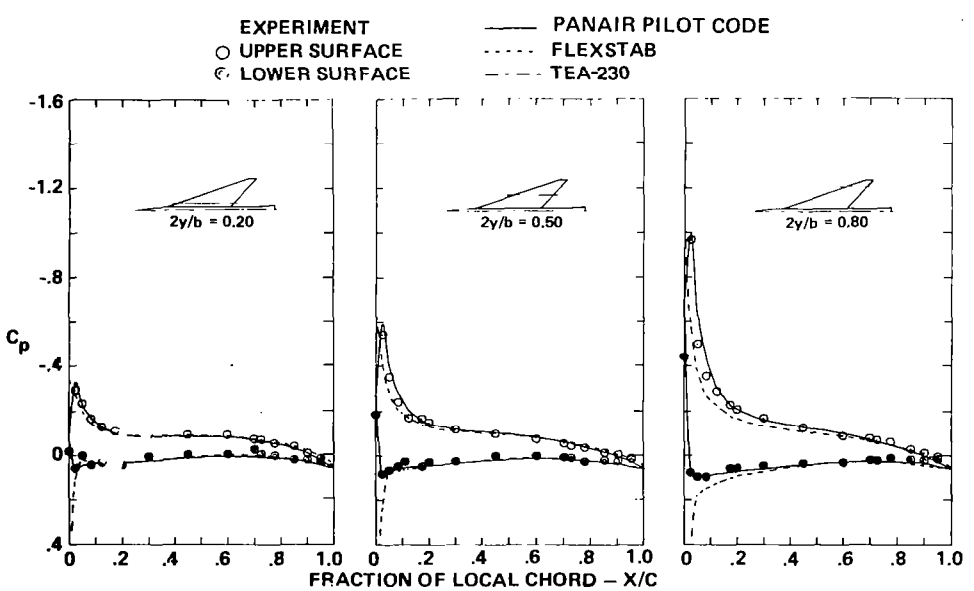

Figure 35.- Surface pressure distributions, flat wing, $M = 0.40$, $\alpha = 4^{\circ}$.

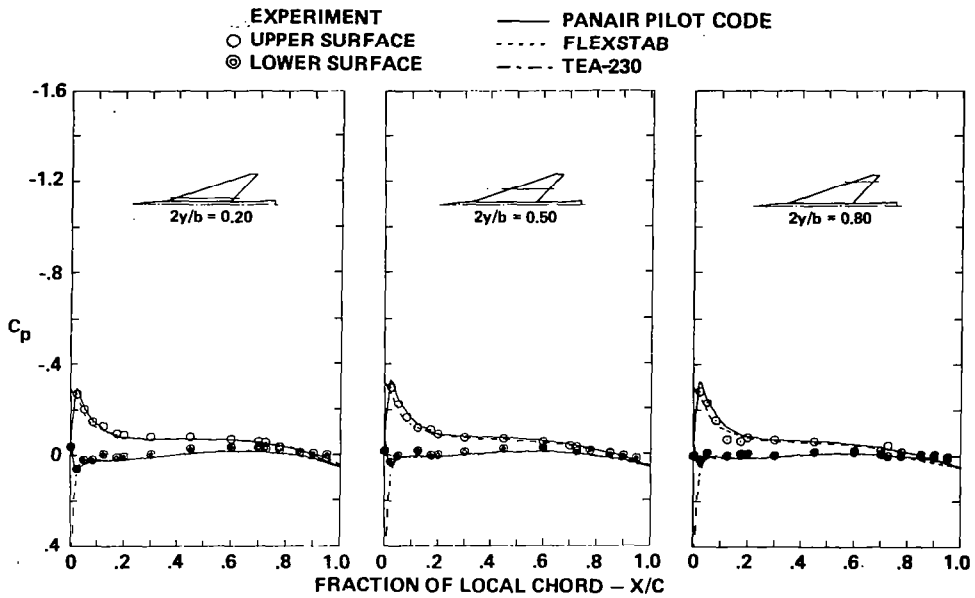

Figure 36.- Surface pressure distributions, twisted wing, M = 0.40, $\alpha = 4^{\circ}$.

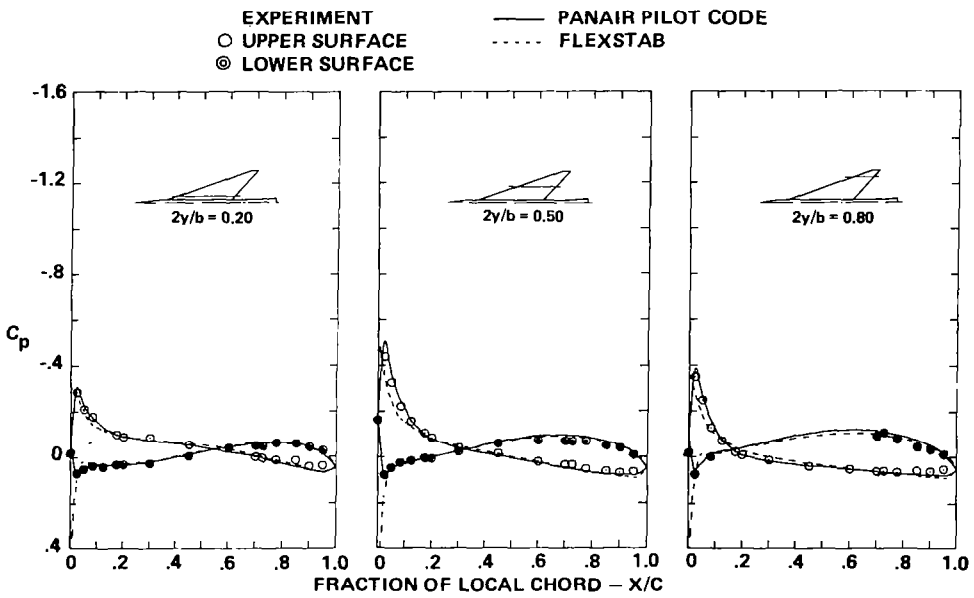

Figure 37.- Surface pressure distributions, cambered-twisted wing, fin off, M = 0.40, $\alpha = 4^{\circ}$.

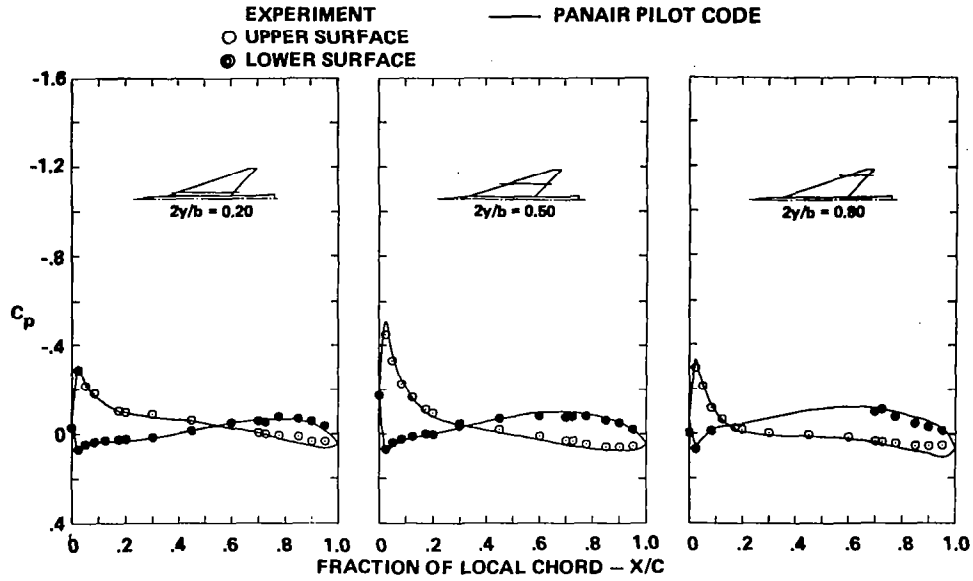

Figure 38.- Surface pressure distributions, cambered-twisted wing, fin on, $M = 0.40$, $\alpha = 4^{\circ}$.

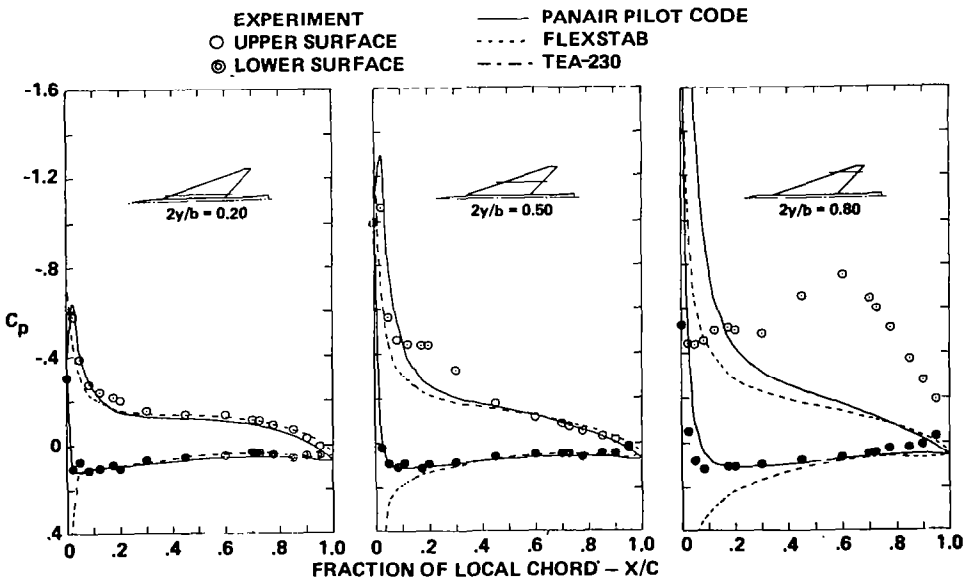

Figure 39.- Surface pressure distributions, flat wing, $M = 0.40$, $\alpha = 8^{\circ}$.

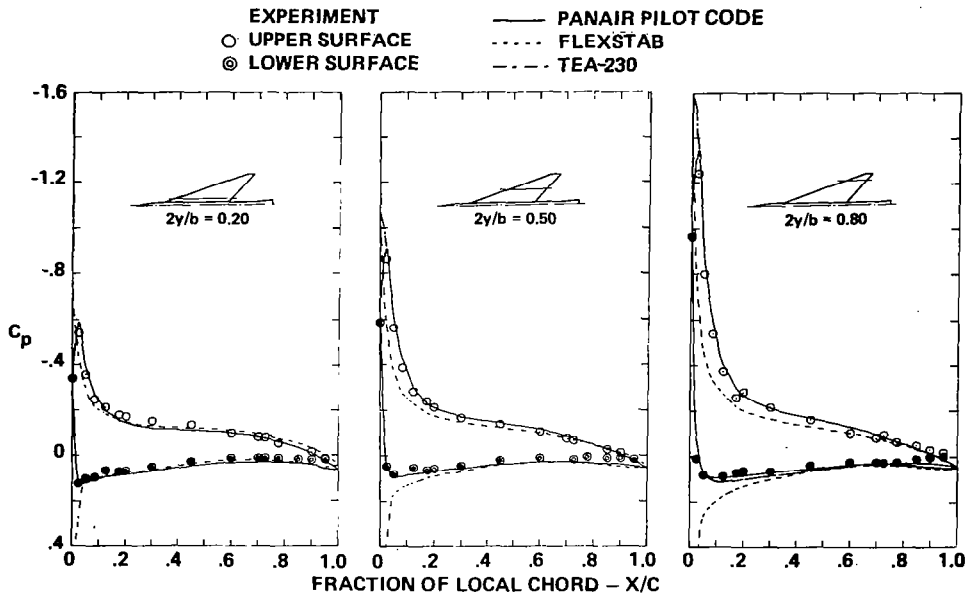

Figure 40.- Surface pressure distributions, twisted wing, $M = 0.40$, $\alpha = 8^{\circ}$.

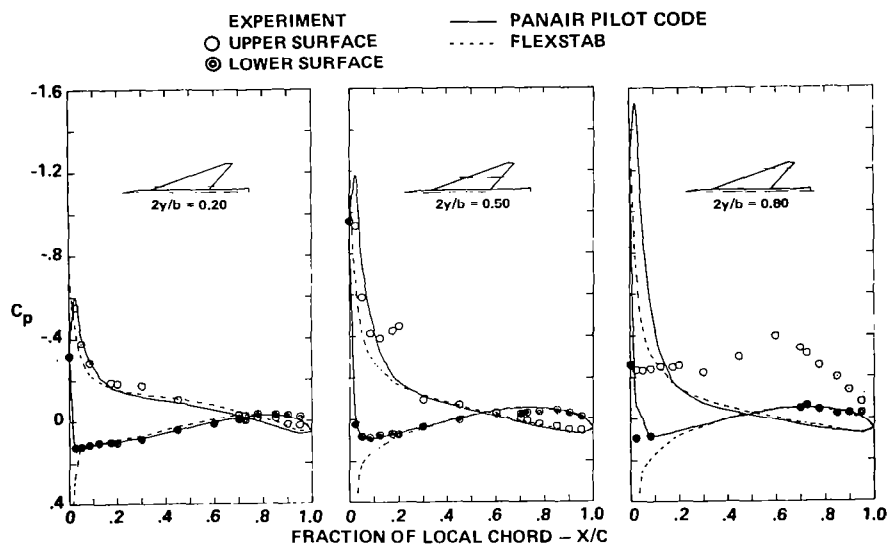

Figure 41.- Surface pressure distributions, cambered-twisted wing, fin off, $M = 0.40$, $\alpha = 8^{\circ}$.

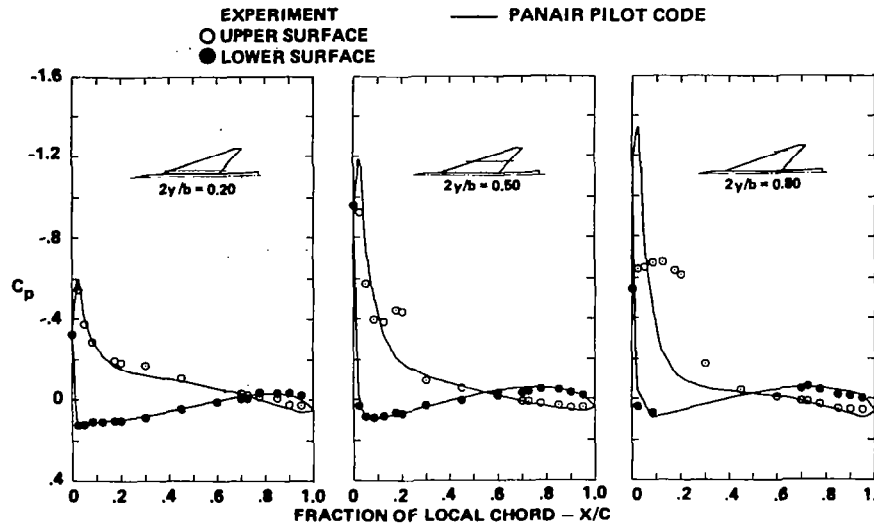

Figure 42.- Surface pressure distributions, cambered-twisted wing, fin on, $M = 0.40$, $\alpha = 8^{\circ}$.

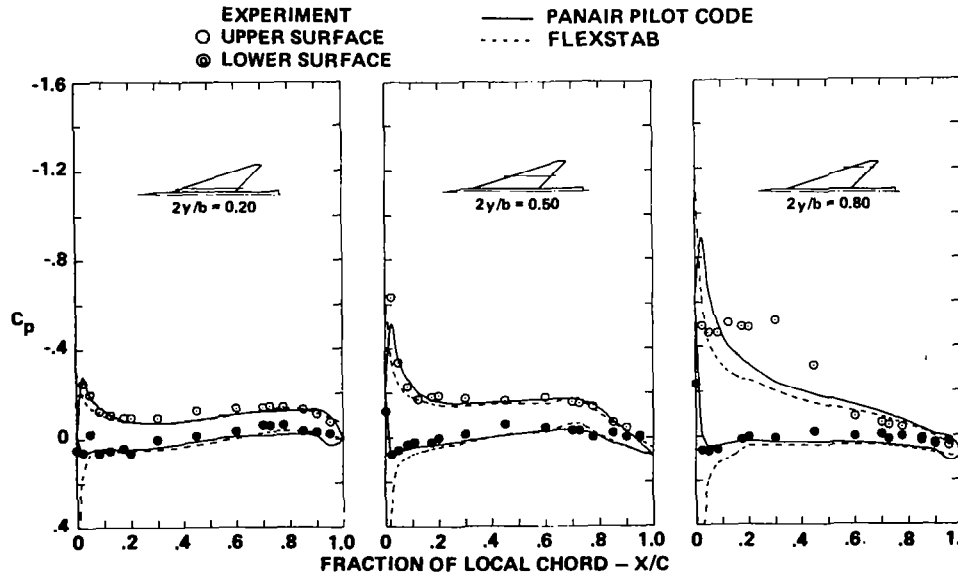

Figure 43.- Surface pressure distributions, flat wing, $M = 1.05$, $\alpha = 4^{\circ}$.

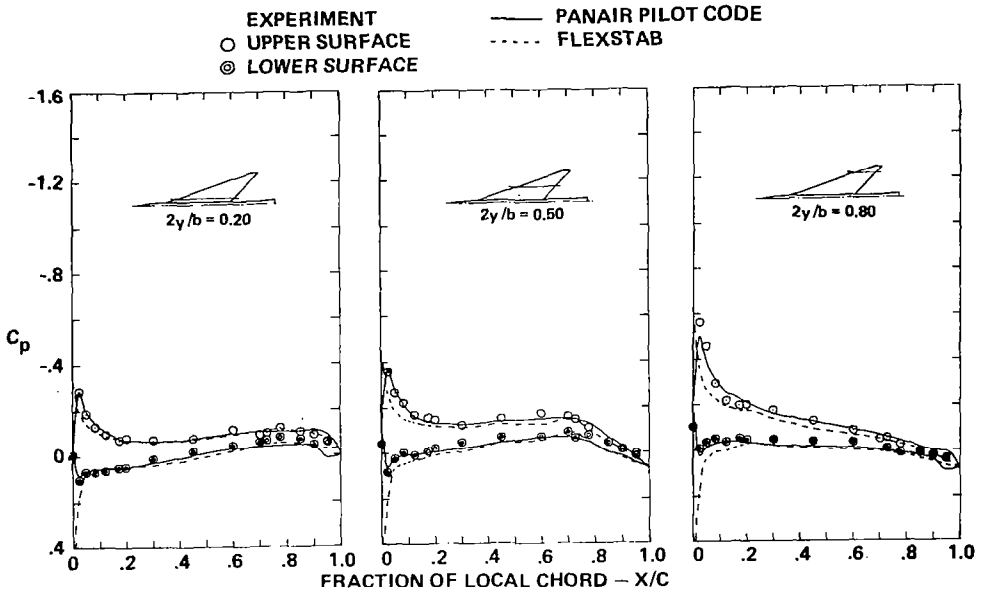

Figure 44.- Surface pressure distributions, twisted wing, M = 1.05, $\alpha = 4.5^{\circ}$.

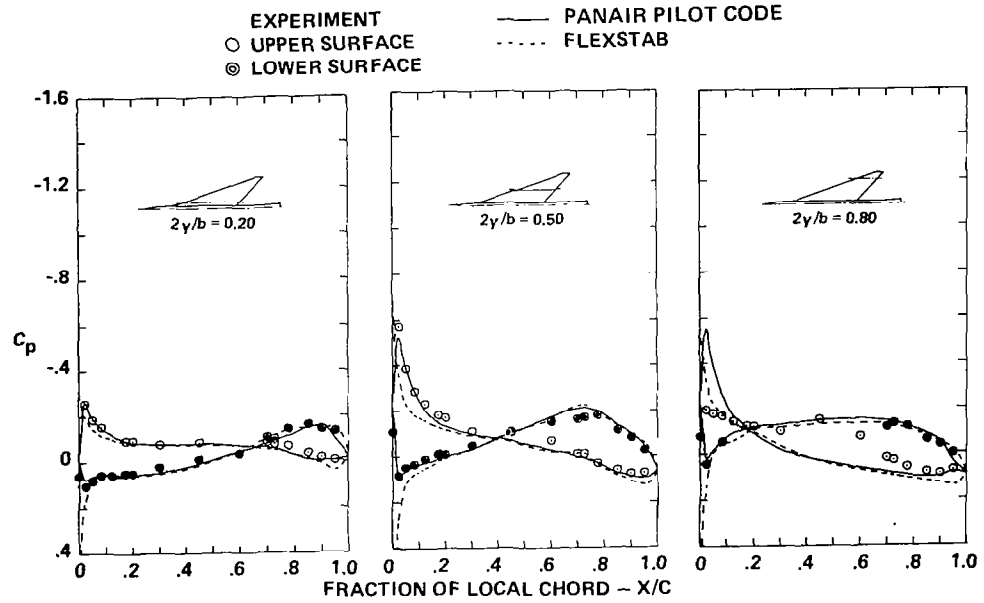

Figure 45.- Surface pressure distributions, cambered-twisted wing, fin off, M = 1.05, $\alpha = 4^{\circ}$.

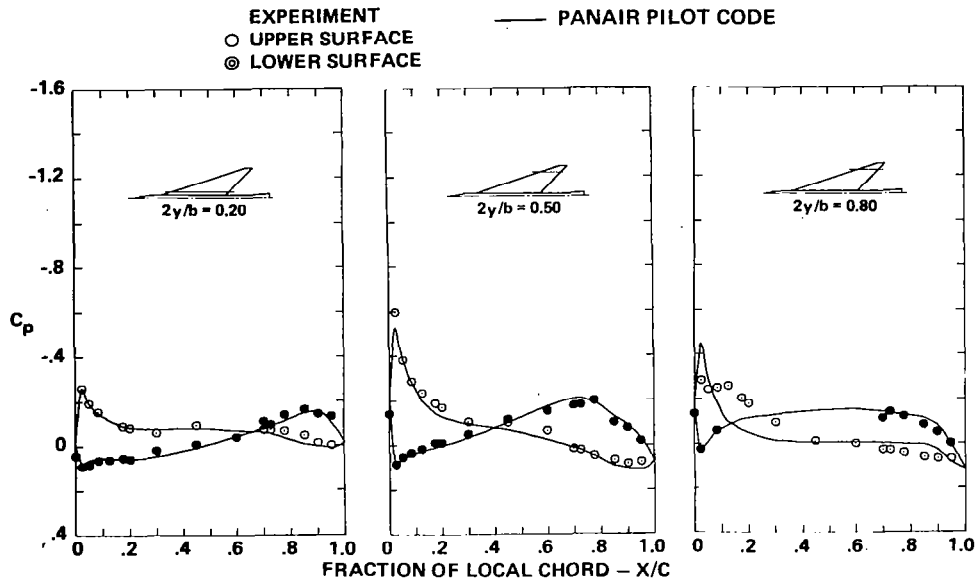

Figure 46.- Surface pressure distributions, cambered-twisted wing, fin on, $M = 1.05$, $\alpha = 4^{\circ}$.

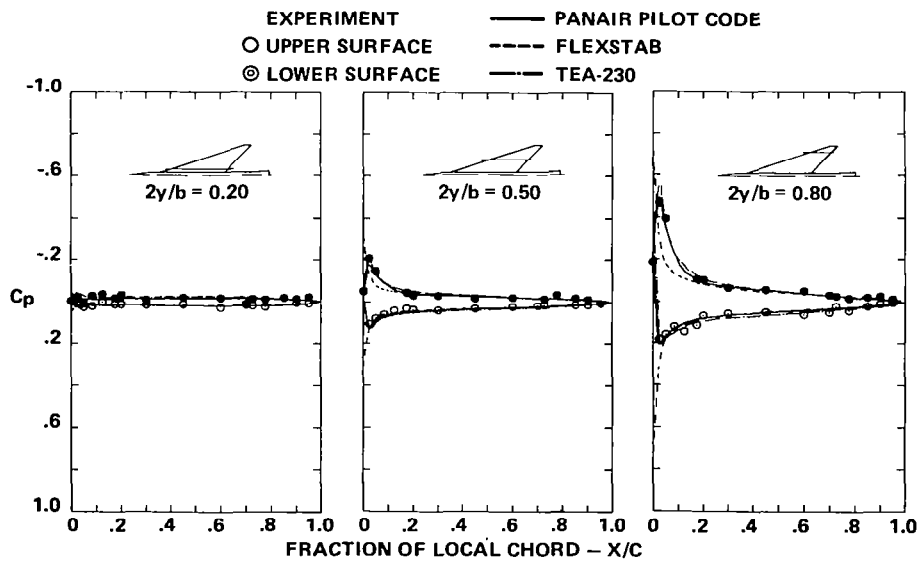

Figure 47.- Incremental surface pressure distributions due to twist, $M = 0.40$, $\alpha = 0^{\circ}$.

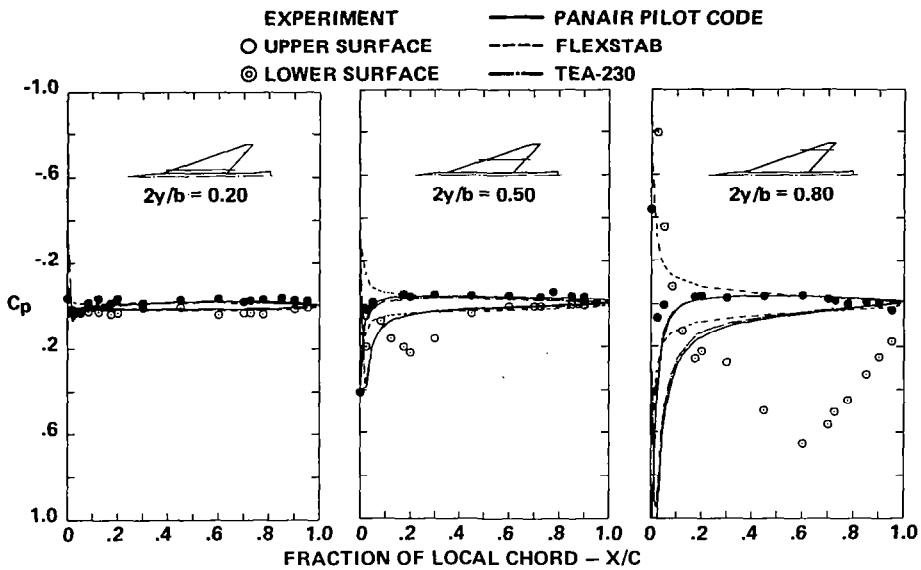

Figure 48.- Incremental surface pressure distributions due to twist, $M = 0.40$, $\alpha = 8^{\circ}$.

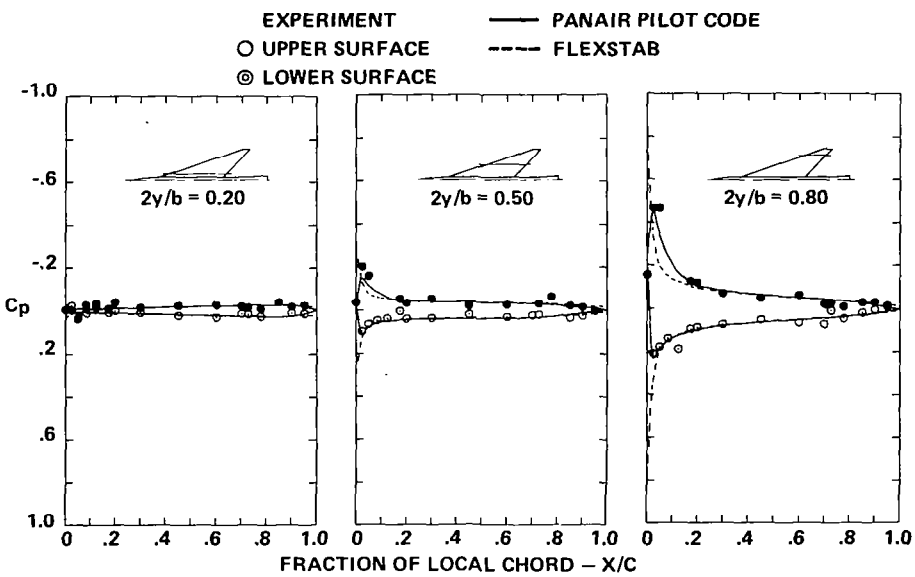

Figure 49.- Incremental surface pressure distributions due to twist, $M = 1.05$, $\alpha = 0^{\circ}$.

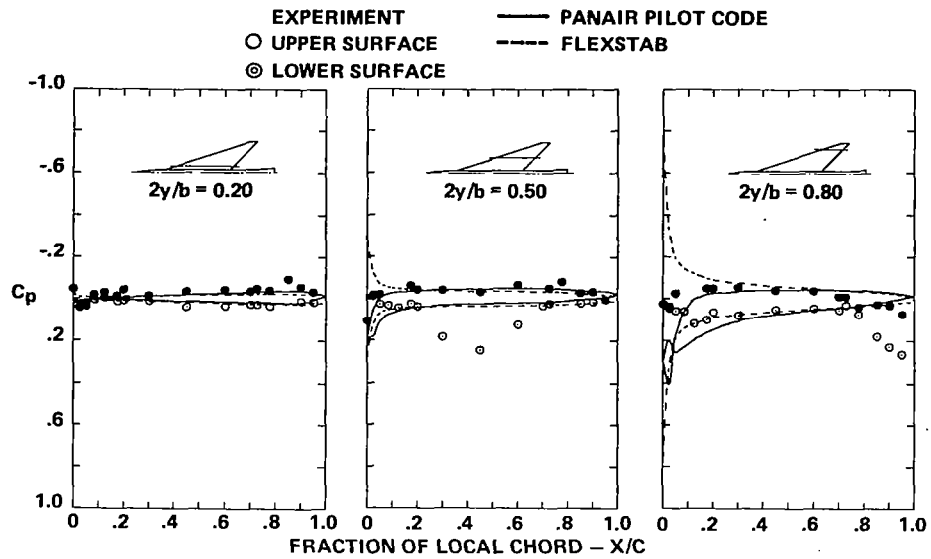

Figure 50 - Incremental surface pressure distributions due to twist, $M = 1.05$, $\alpha = 8^{\circ}$.

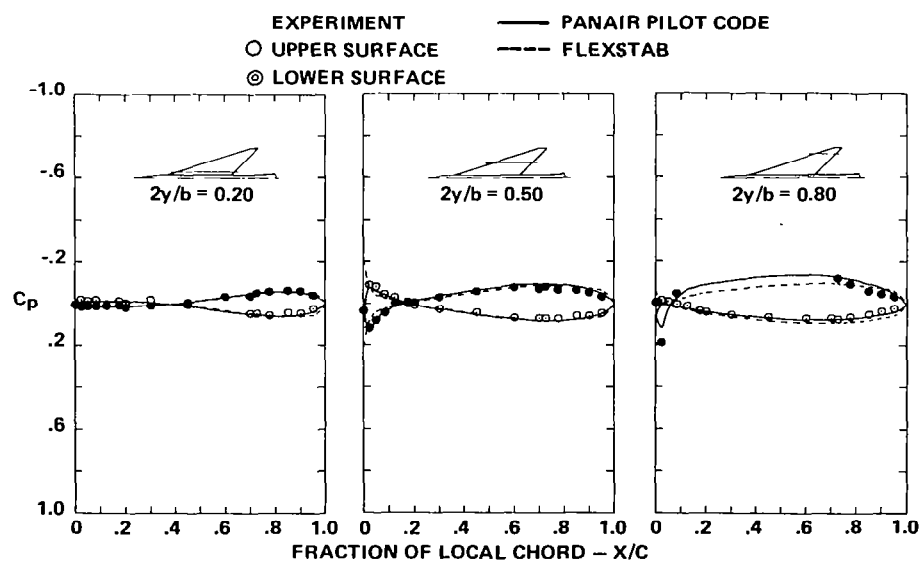

Figure 51.- Incremental surface pressure distributions due to camber, $M = 0.40$, $\alpha = 0^{\circ}$.

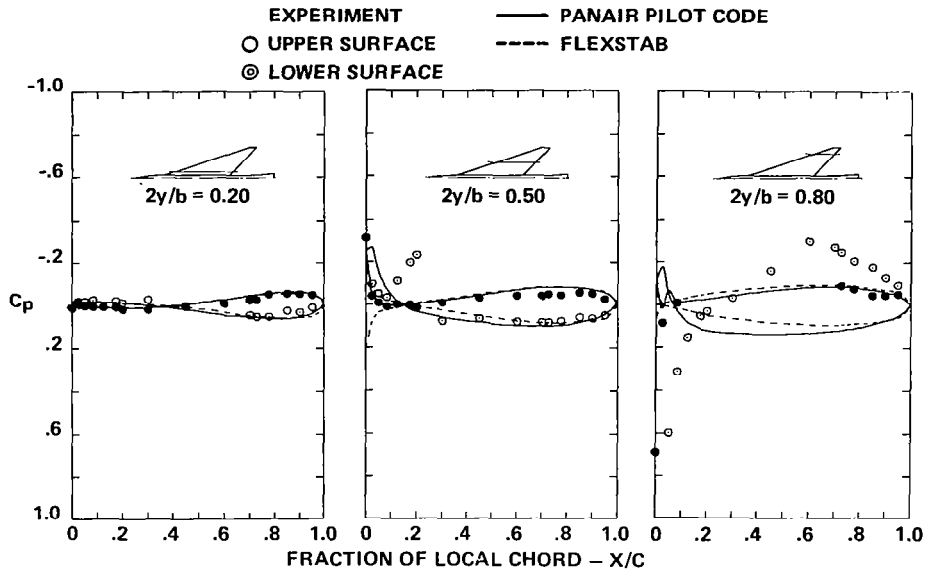

Figure 52.- Incremental surface pressure distributions due to camber, $M = 0.40$, $\alpha = 8^{\circ}$.

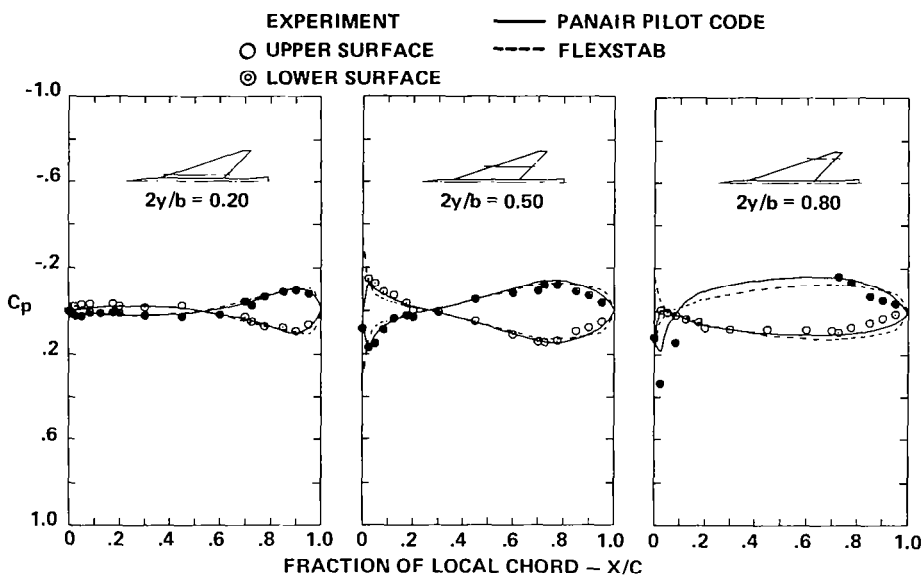

Figure 53.- Incremental surface pressure distributions due to camber, $M = 1.05$, $\alpha = 0^{\circ}$.

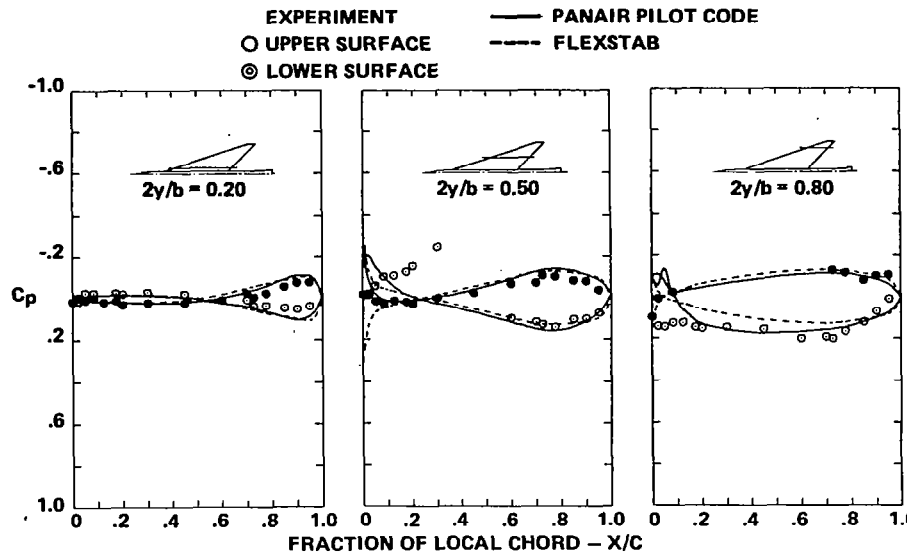

Figure 54.- Incremental surface pressure distributions due to camber, $M = 1.05$, $\alpha = 8^{\circ}$.

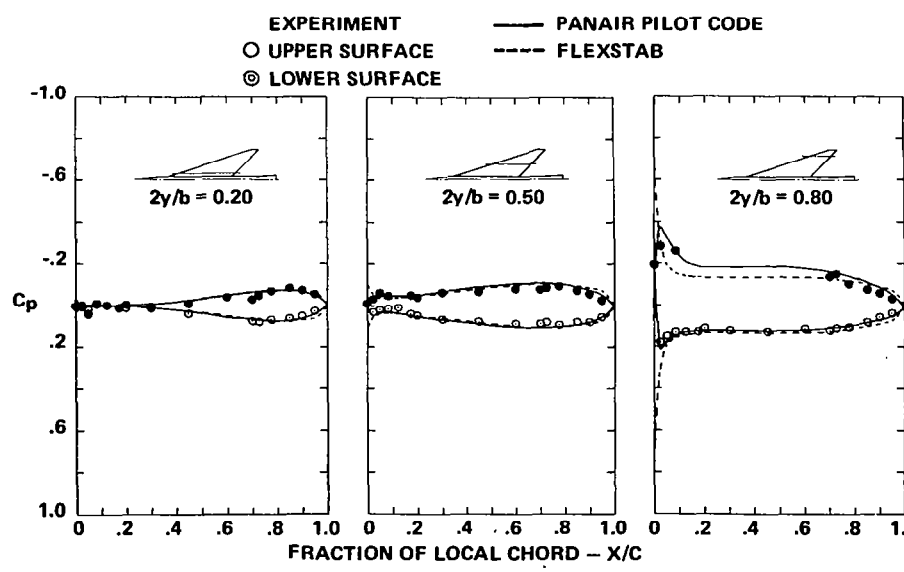

Figure 55.- Incremental surface pressure distributions due to camber and twist, $M = 0.40$, $\alpha = 0^{\circ}$.

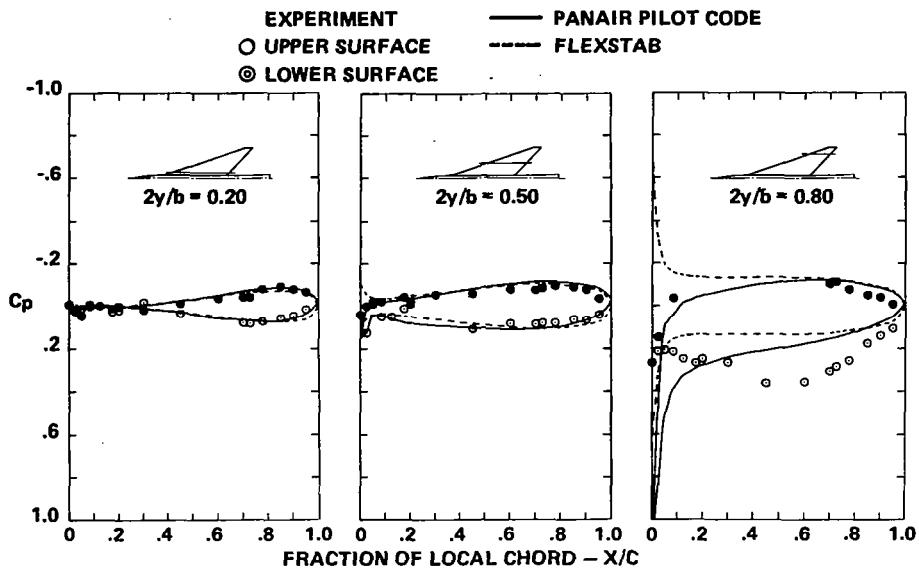

Figure 56.- Incremental surface pressure distributions due to camber and twist, $M = 0.40$, $\alpha = 8^{\circ}$

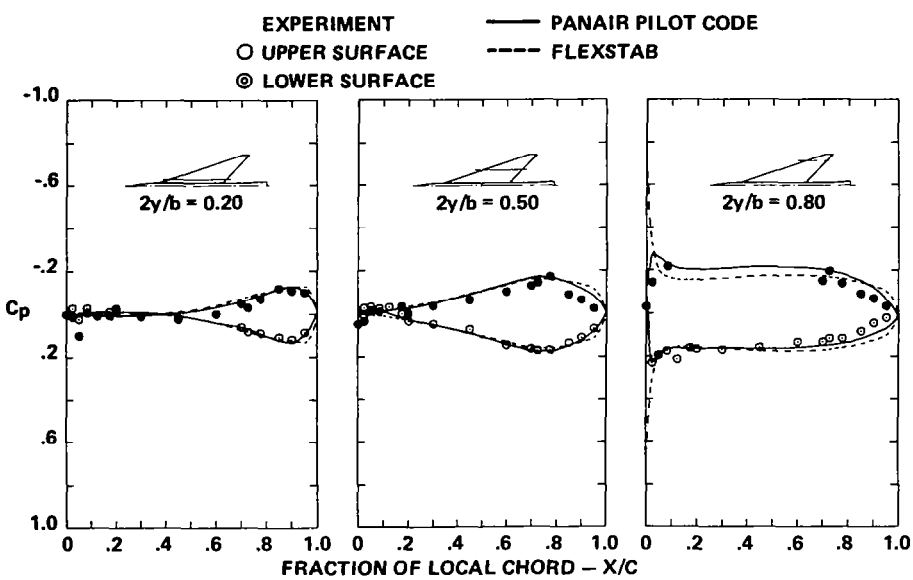

Figure 57.- Incremental surface pressure distributions due to camber and twist, $M = 1.05$, $\alpha = 0^{\circ}$.

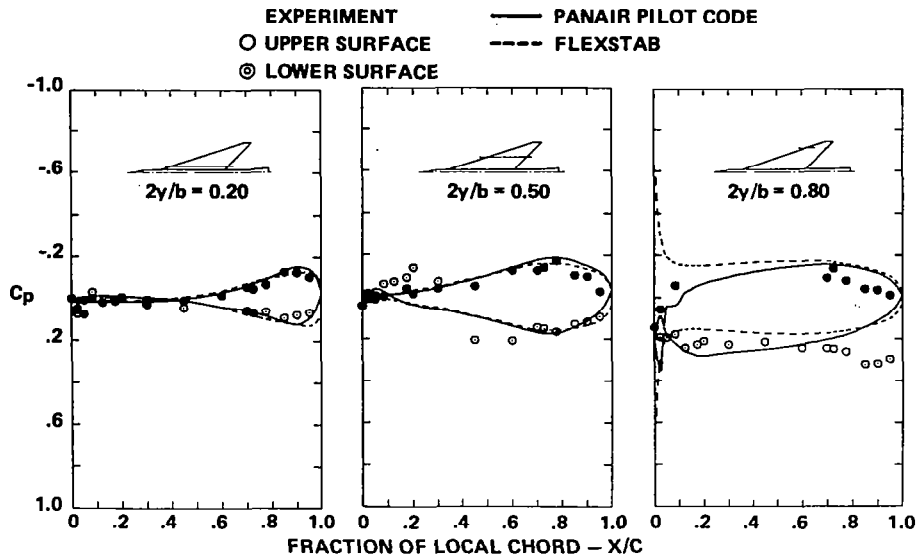

Figure 58.- Incremental surface pressure distributions due to camber and twist, M = 1.05, $\alpha = 8^{\circ}$.

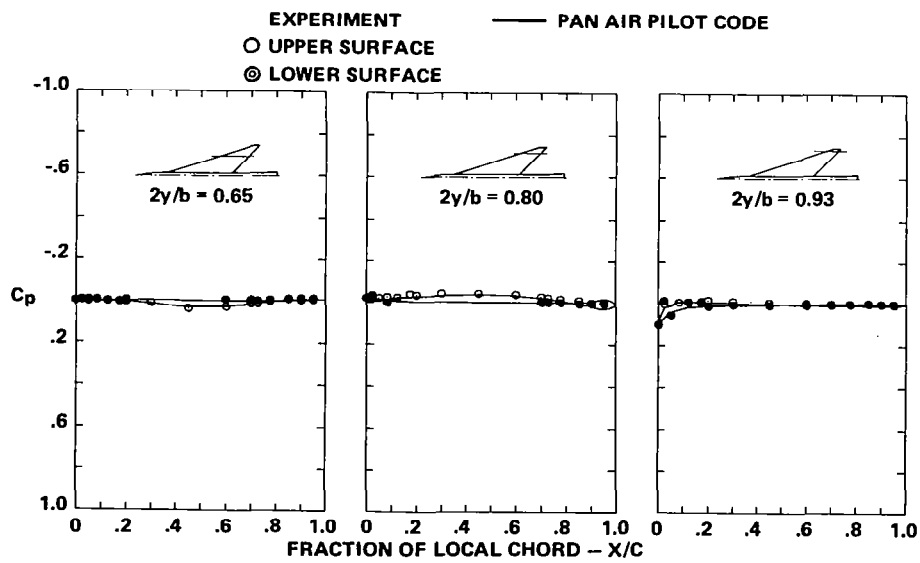

Figure 59.- Incremental surface pressure distributions due to a wing fin on the cambered-twisted wing, M = 0.40, $\alpha = 0^{\circ}$.

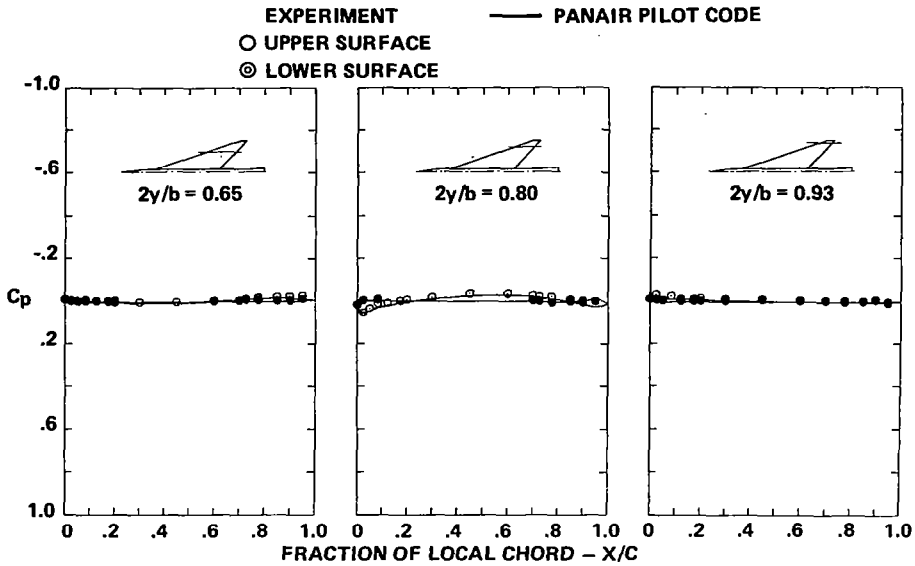

Figure 60.- Incremental surface pressure distributions due to a wing fin on the cambered-twisted wing, $M = 0.40$, $\alpha = 4^{\circ}$.

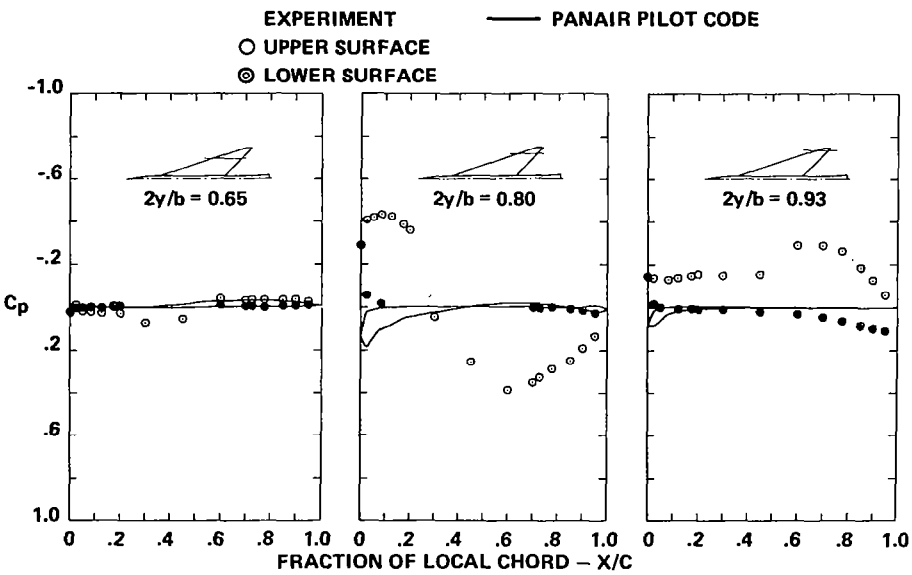

Figure 61.- Incremental surface pressure distributions due to a wing fin on the cambered-twisted wing, $M = 0.40$, $\alpha = 8^{\circ}$.

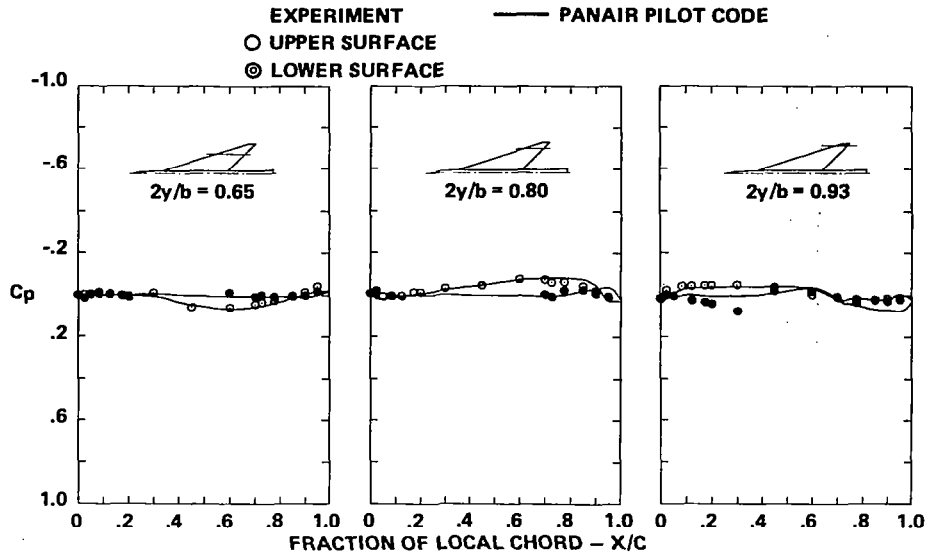

Figure 62.- Incremental surface pressure distributions due to a wing fin on the cambered-twisted wing, $M = 1.05$, $\alpha = 0^{\circ}$.

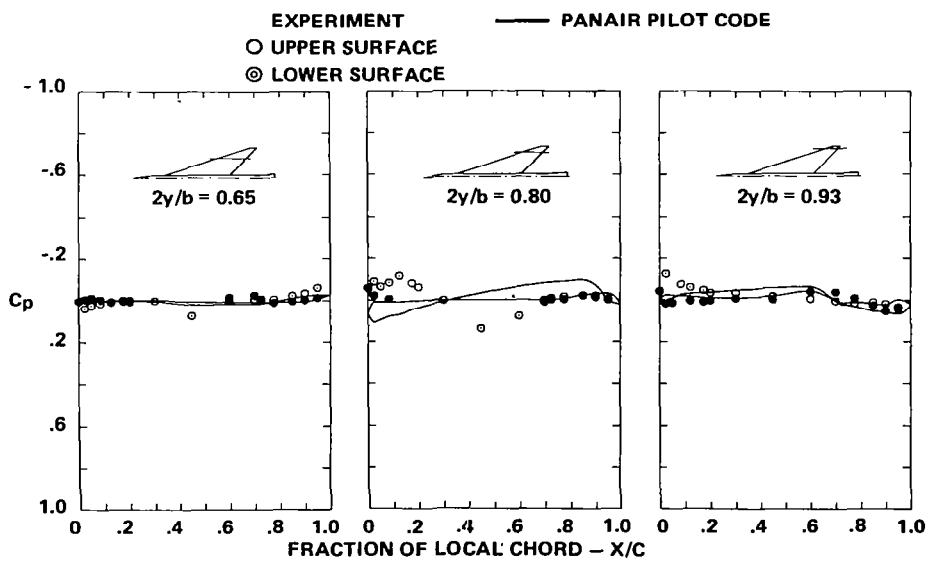

Figure 63.- Incremental surface pressure distributions due to a wing fin on the cambered-twisted wing, $M = 1.05$, $\alpha = 4^{\circ}$.

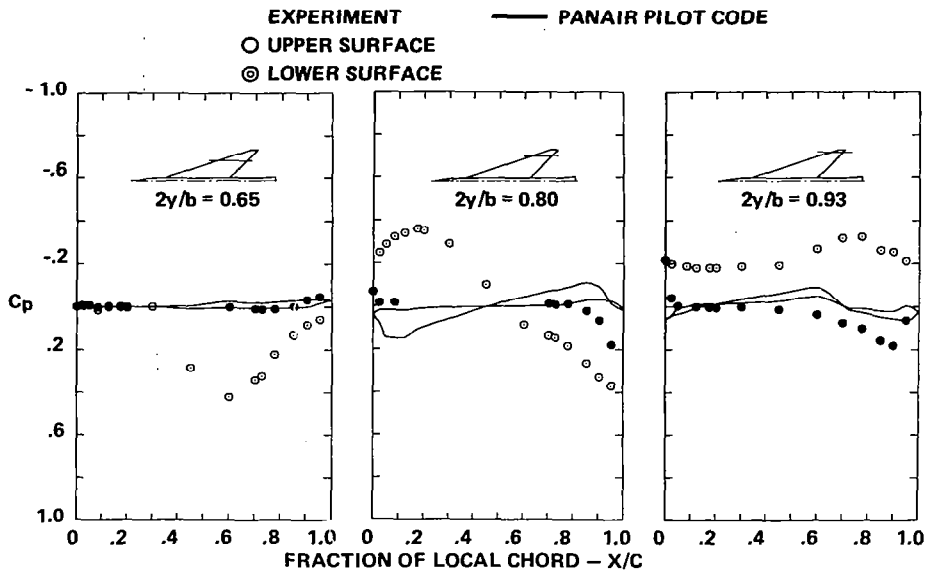

Figure 64.- Incremental surface pressure distributions due to a wing fin on the cambered-twisted wing, M = 1.05, $\alpha = 8^{\circ}$.

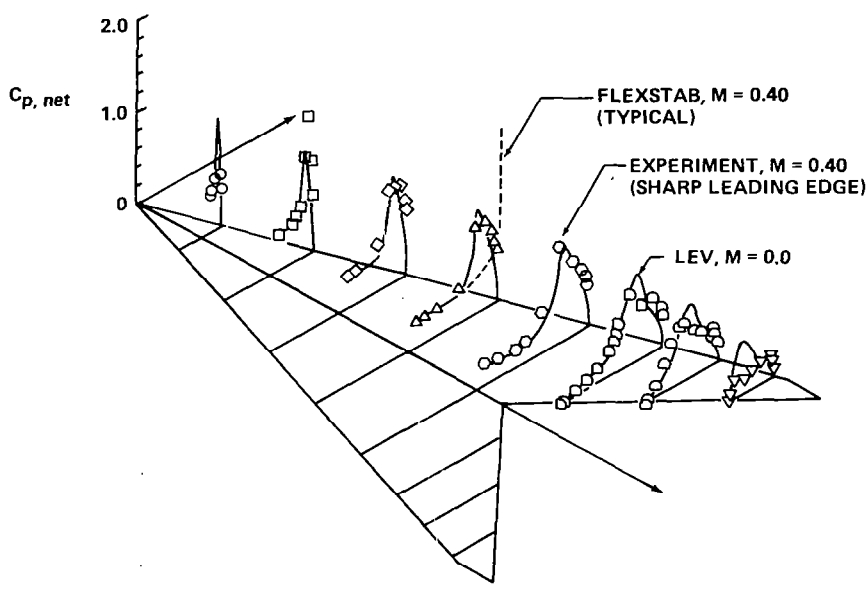

Figure 65.- Net pressure distributions, leading edge vortex (LEV) program, flat wing, $\alpha = 12^{\circ}$.

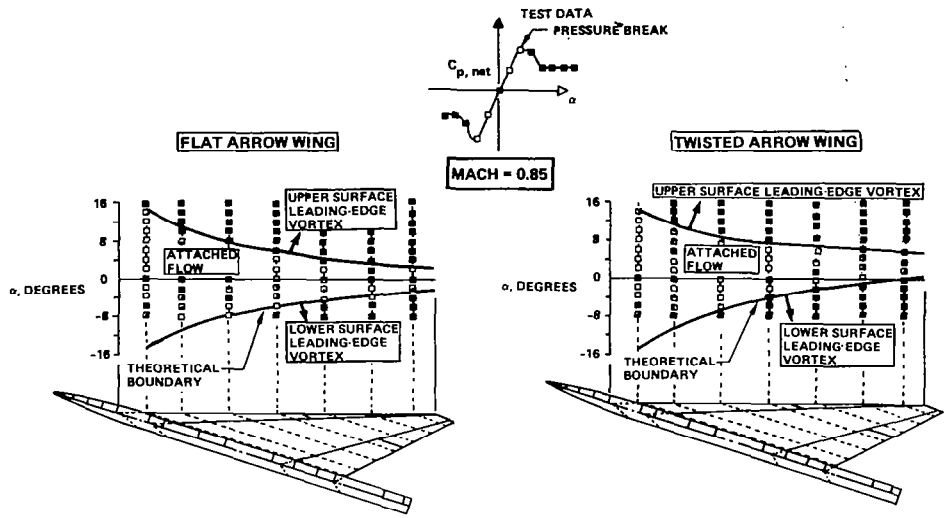

Figure 66.- Comparisons of predicted vortex development with experimental leading-edge pressures.

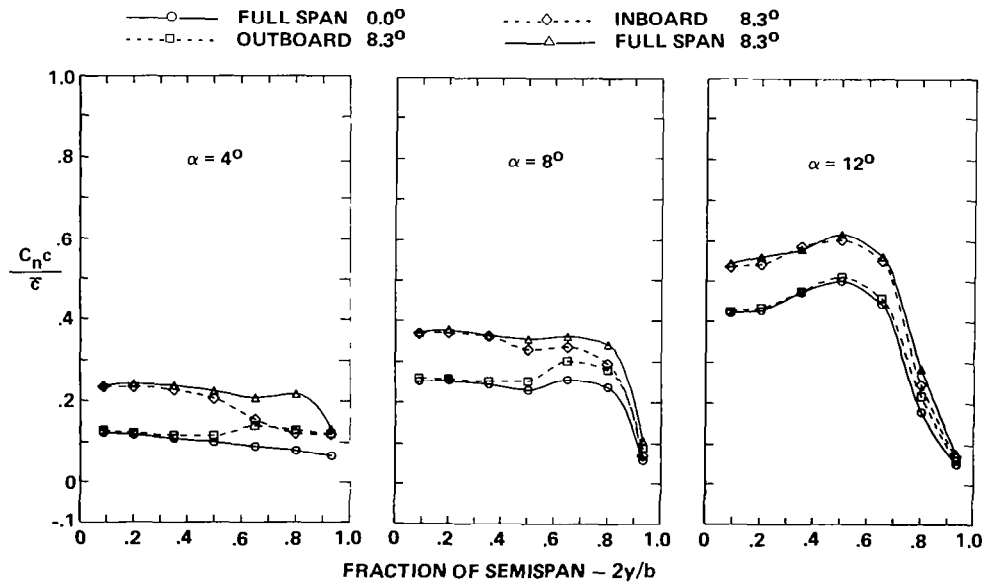

Figure 67.- Spanload distributions, effect of trailing-edge control surface deflection, flat wing, M = 0.40.

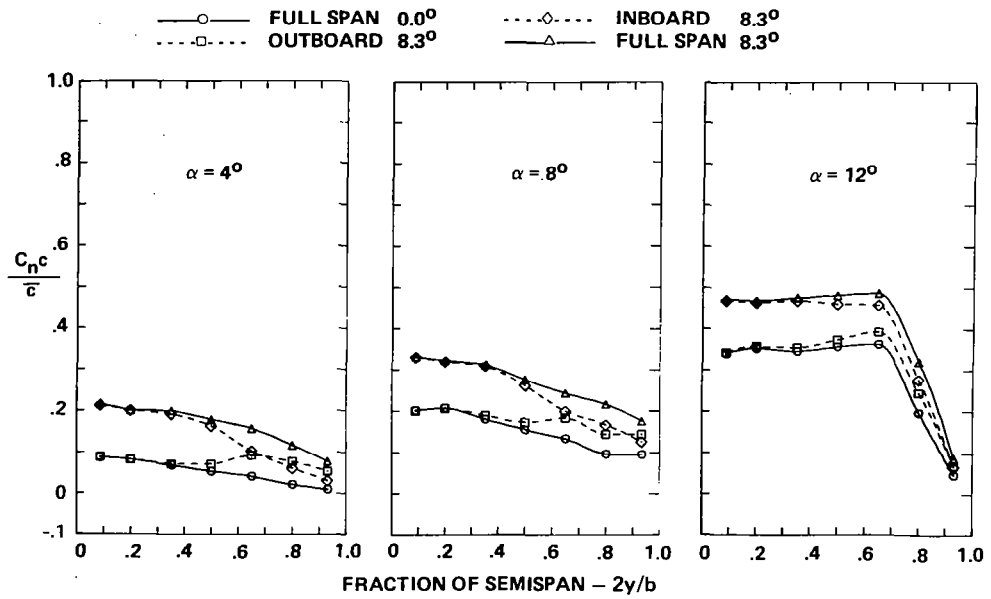

Figure 68.- Spanload distributions, effect of trailing-edge control surface deflection, twisted wing, M = 0.40.

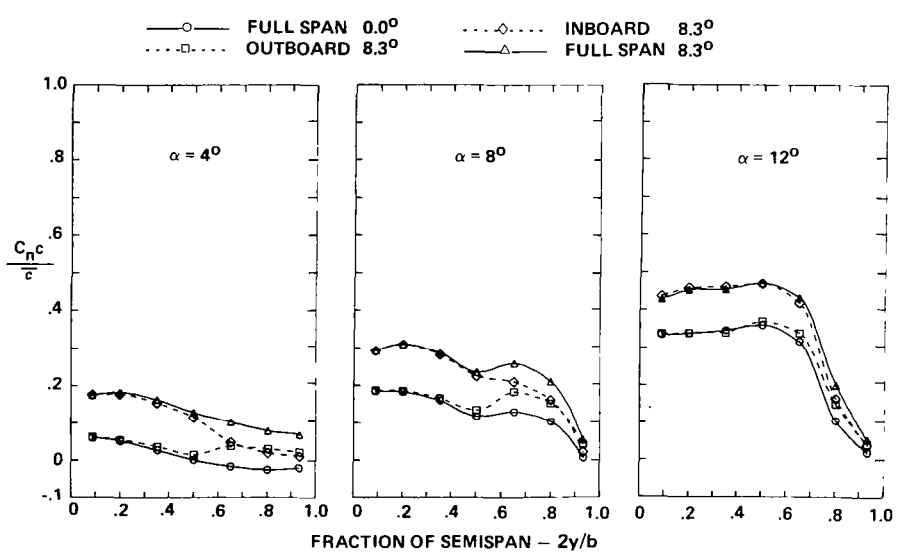

Figure 69.- Spanload distributions, effect of trailing-edge control surface deflection, cambered-twisted wing, fin off, M = 0.40.

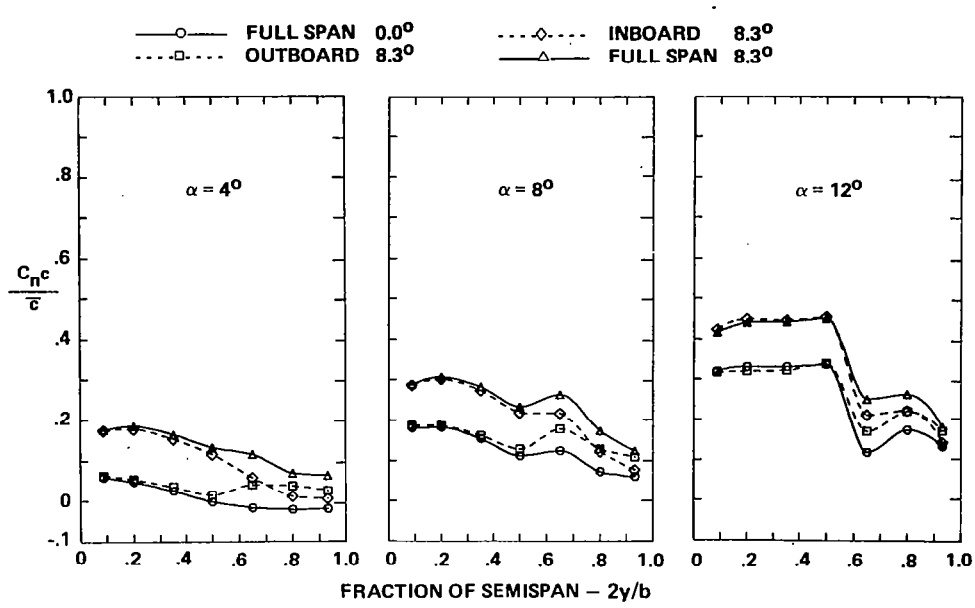

Figure 70.- Spanload distributions, effect of trailing-edge control surface deflection, cambered-twisted wing, fin on, M = 0.40.

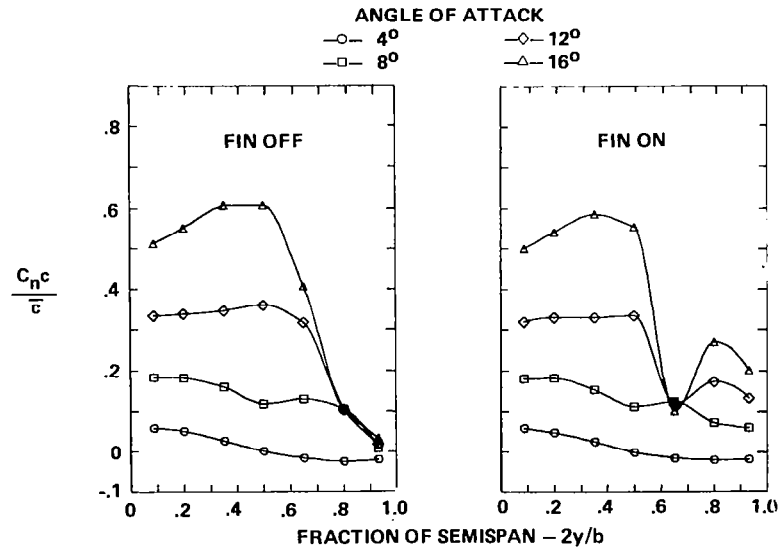

Figure 71.- Spanload distributions, effect of fin, cambered-twisted wing; T. E. deflection, full span = 0.0°; M = 0.40.

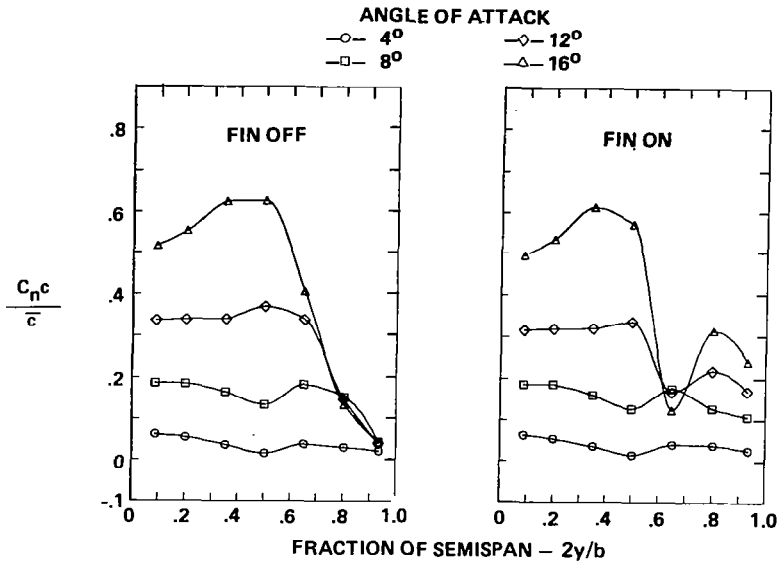

Figure 72.- Spanload distributions, effect of fin, cambered-twisted wing; T. E. deflection, inboard = 0.0°, outboard = 8.3°; M = 0.40.

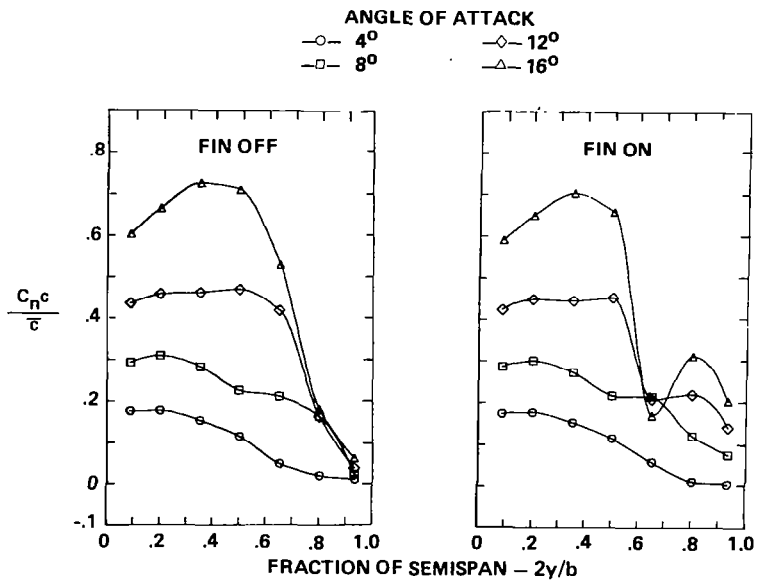

Figure 73.- Spanload distributions, effect of fin, cambered-twisted wing; T. E. deflection, inboard = 8.3°, outboard = 0.0°; M = 0.40.

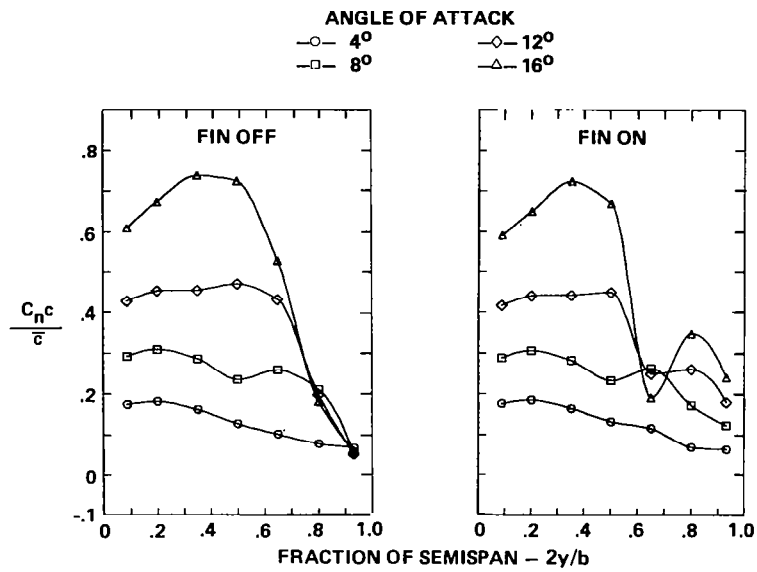

Figure 74.- Spanload distributions, effect of fin, cambered-twisted wing; T. E. deflection, full span = 8.3°; M = 0.40.

EXPLORATORY SUBSONIC INVESTIGATION OF VORTEX-FLAP CONCEPT ON ARROW WING CONFIGURATION*

Dhanvada M. Rao
Old Dominion University Research Foundation

SUMMARY

The drag-reduction potential of a vortex-flap concept, utilizing the thrust contribution of separation vortices maintained over leading-edge flap surfaces, has been explored in subsonic wind tunnel tests on a highly swept arrow wing configuration. Several flap geometries were tested in comparison with a previous study on the same model with leading edges drooped for attached flow. The most promising vortex-flap arrangements produced drag reductions comparable with leading-edge droop over a range of lift coefficients from 0.3 to 0.6 (untrimmed), and also indicated beneficial effects in the longitudinal and lateral static stability characteristics.

INTRODUCTION

The low-speed aerodynamics of highly swept, slender wings favored for supersonic cruise aircraft continues to receive attention on account of its serious performance, stability and control deficiencies. Leading-edge flow separation and resulting vortices are known to be the primary cause of drag and longitudinal instability problems encountered on such configurations at angles of attack. Control of separation at highly swept leading edges therefore has attracted much interest and remains a research and engineering problem with high pay-off potential.

An obvious approach to the problem is the use of leading-edge droop, which past experience has shown to be an effective means to raise the angle of attack limit for attached flow and thus delay the drag increase to a higher lift coefficient. It has limitations however on highly swept wings (leading-edge sweep of 70° or greater) where the circulation-induced upwash normal to the leading edges grows rapidly not only with angle of attack but also in a spanwise direction. A highly warped leading edge with pronounced droop angles will therefore be needed for fully attached flow subsonically. Since the drag penalty of such a leading edge could not be tolerated in supersonic cruise, an articulated and

* Research Supported by NASA Grant no. NSG-1315

mechanically complex leading-edge design with associated weight penalties appears inevitable. Also, the possibility of separation inboard along the highly curved knee-line (fig. 1, C) may limit the advantage of attached leading-edge flow. While the aerodynamic potential of optimally tailored droop on highly swept wings has been demonstrated (ref. 1), the question remains as to the feasibility of its realization in practice.

The vortex-flap concept is an alternative approach to swept leading-edge flow management with a view to retain effective leading-edge suction beyond the normal attached-flow angle of attack regime. It is based on controlled separation to produce coiled vortices whose suction effect over inclined leading-edge surfaces is utilized to generate a thrust component. Although unconventional, this approach is based on flow mechanisms that are physically well understood viz. streamwise vortices arising from swept-edge separations and their powerful interaction with the inviscid flow field.

The vortex-flap device is conceived here as a surface hinged just under the leading edge and retracted flush with the wing undersurface when inoperative (fig. 1, D). To deploy the flap, it is rotated forward and set at an angle less than the local upwash, forcing separation and a resultant coiled vortex close to its upper surface. The high degree of leading-edge sweep promotes stability and persistence of the vortex down the length of the flap. For most efficient utilization of the flap surface under the vortex suction and also for smooth entry to the wing, the vortex-induced reattachment should occur just at the wing leading edge as indicated in figure 1, D.

Proof-of concept tests were conducted at NASA Langley on a 74° delta wing research model for an initial assessment of the vortex-flap potential and to obtain a general understanding of the flap geometry variables of importance (ref. 2). The results of these trials were sufficiently encouraging to prompt further studies using a supersonic cruise configuration on which an extensive data base already existed, particularly with regard to leading-edge droop effects. Selected results of these exploratory investigations are presented in this paper to provide an indication of the drag-reduction potential of the vortex-flap concept relative to drooped leading edges and its impact on other low-speed aerodynamic characteristics of a realistic airplane configuration.

SYMBOLS

C_L	lift coefficient
C_D	drag coefficient
C_m	pitching moment coefficient
L/D	lift-to-drag ratio
α	angle of attack (deg.)

β angle of sideslip (deg.)

C_{n_β} body-axis directional static stability derivative (per deg.)

C_{l_β} body-axis lateral static stability derivative (per deg.)

PRELIMINARY VORTEX-FLAP EXPERIMENTS ON A DELTA WING

The initial trials of the leading edge vortex-flap (LEVF) concept were conducted on a flat-plate type 74° delta wing model with leading edges modified to a constant radius semi-circular section, in the NASA Langley 7x10 ft. high speed tunnel at a nominal Mach number of 0.2 (Reynolds number = 2.7×10^6 based on mean aerodynamic chord). The details of this test program and the results are reported in reference 2. A series of systematically-varied LEVF geometries were investigated, including constant chord full-length and part-length flaps and inverse-taper flaps, at two deflection angles (30° and 45° normal to the leading edge). The flap area was progressively reduced from over 25% to about 15% of the basic wing area through successive geometric refinements for improving the drag-reduction effectiveness.

A typical set of data pertaining to the final LEVF configuration of this test series is presented in figure 2. Also shown for comparison are the sharp leading edge data previously obtained on the same wing (see NASA TN D-6344) which correspond to zero leading-edge suction, as well as a calculated 100% suction curve for the blunt leading edge. These comparisons serve to indicate the lift/drag ratio benefits obtained largely as a result of lift-dependent drag reductions relative to the basic wing. A small part of the indicated improvement is due to the extra lift from the planform area addition of the flaps, which of course is integral to the present LEVF concept. It is noteworthy that the beneficial effect of LEVF is sustained to the highest lift coefficient (1.0) of the test range. The pitching moment characteristics with LEVF also shown in figure 2 remain linear in the C_L range of interest with only a small reduction in pitch stability.

VORTEX-FLAP STUDIES ON SWAT CONFIGURATION

As part of a research program aimed at advancing the subsonic limitations in swept wing aerodynamic technology (SWAT), the potential of leading-edge droop has been the subject of recent wind tunnel investigations at Langley on an arrow wing supersonic cruise aircraft configuration. The SWAT model details and analysis of data are presented in reference 1. These data were used to provide a reference for assessing LEVF arrangements studied in follow-on tests with the

same model in the Langley 7x10 ft. high speed tunnel. Selected results from these tests are presented and discussed below (test conditions: Mach no. = 0.14, Reynolds no. = 2.8×10^6 based on mean aerodynamic chord).

Vortex-Flap Details

The two final LEVF geometries of the present test series are shown in figure 3. The segmented arrangement of these LEVF designs distinguishes them from the one-piece flaps earlier tested on the 74° delta wing research model. At least two flap-segments (LEVF #9) were necessitated because of a break in the leading-edge sweep angle at about 50% semi-span location on the present configuration. A four-segment variation (LEVF #8) was also tested for a first look at multi-segment LEVF arrangements which permit spanwise tailoring of deflection angle to maximize drag-reduction and possibly for some pitching-moment control for trim; they may also be considered more practical than one-piece flaps on large vehicles. The limited scope of this study however covered only one deflection schedule for each LEVF arrangement as indicated in figure 3 (note that the tip panel leading-edge flap was always deflected down 50° unless otherwise stated, as this was found beneficial for drag at the higher angles of attack).

The total area of the four-segment flap arrangement was about two-thirds the two-segment LEVF and amounted to 10.5% of the wing reference area. The maximum flap chord (normal to hinge line) was 7.5% of the mean aerodynamic chord in both the LEVF configurations. The flap elements were cut from 1.6 mm thick aluminum sheet, bent as required and secured with screws under the leading edges which were in the undrooped position. No attempt was made to fair-in the steps and other protrusions resulting from this somewhat crude attachment method, and it is probably fair to assume that the LEVF installation drag was relatively much more on the wind tunnel model than will be incurred on a flight vehicle.

Lift and Drag Characteristics

The lift and drag measurements with LEVF (symbols) are compared with the data of reference 1 (curves) in figure 4. In addition to undrooped leading edge, data for two leading-edge droop configurations are available, one with constant 30° droop and the other with droop angle increasing continuously from 16° at the fuselage junction to 50° at the tip. The effectiveness of droop may be judged by the elimination of a distinctive upward break in the lift-curve slope found on the undrooped wing. However, elimination of vortices results in a lift loss of as much as 17% at 8° angle of attack. The lift data with LEVF arrangements are practically linear in the angle of attack range and indicate a much smaller lift loss.

The drag data (plotted versus C_L^2) in figure 4 show that LEVF #9 equals the drag-reduction capability of the 16°-50° droop configuration which probably represents the best attached-flow performance. The four-segment flap (LEVF #8) with 30% less flap area comes quite close to the performance of LEVF #9. These trends are further illustrated in terms of lift-to-drag ratio in figure 5.

The above LEVF data correspond to the tip panel leading-edge flap at 50°. Comparison with data for undeflected leading edges in figure 6 shows that a significant L/D gain results from this relatively simple tip-panel leading edge device. Although they have only 7.5% of the total wing area, the tip panels comprise 30% of the exposed span and therefore the effect of loss of leading-edge suction at the tip panels is substantial. The wing tips evidently operate in a region of high induced upwash even at moderate lift coefficients and so are prone to early stall. The data of figure 6 are indicative of the importance of flow management in this area not only for drag minimization, but also with regard to longitudinal stability as will be found in the following section.

Longitudinal Stability

The pitching moment characteristics with LEVF are compared with the results from reference 1 in figure 7 (note that these data pertain to 'tail off' condition since the aft fuselage and the empennage were not represented on the SWAT model). The undrooped leading edge data indicate a pitch-up at about $C_L = 0.35$, which could be caused by wing leading-edge separation or tip-panel stall, or both. With droop, this adverse feature is moderated. The pitching moment measurements with LEVF (taken about the same center-of-gravity position and therefore showing a positive slope) are linear up to $C_L = 0.45$ before a pitch-up appears; however the relative change of the moment-curve slope at pitch-up is only 20% of that on the undrooped wing, representing a considerable alleviation of the pitch-up intensity.

Additional tests with the tip panels removed were carried out in an attempt to separate out the tip-panel stall and leading-edge separation effects on the pitch-up behavior. With undrooped leading edge the data show that removing the tip panels does not essentially alter the pitch-up angle of attack, but the pitch-up intensity is much reduced (fig. 8). This result would indicate that leading-edge separation and tip stall both take place at the same time producing the strong pitch-up found with undrooped leading edges. With 30° droop and tip panels off the pitch-up is eliminated.

The LEVF effect on pitching moment without the tip panels is shown in figure 9. Not only is the pitch-up delayed to about 8° angle of attack but also the pitch-up intensity is much softened. It would appear that the vortex-flaps act partly as droop in alleviating the vortex strength over the wing.

Lateral/Directional Stability

The tail-off directional and lateral static stability derivatives for LEVF #8 obtained from tests at $\pm 5^{\circ}$ sideslip angle are compared with the undrooped and 30° droop data in figure 10. A rapid rise in directional stability of the undrooped wing starting at a lift coefficient corresponding to vortex onset suggests that it is related to the favorable asymmetry in the vortex pair found on slender lifting bodies of oblate cross-sections at sideslip, which generate upwind suction and corresponding restoring yawing moments (ref. 3). This feature is notably absent in the directional data for 30° droop where the vortices have been suppressed, and also with LEVF. This loss of vortex-related directional stability is not necessarily a bad feature since restoring side-forces that originate forward of the center-of-gravity also reduce yaw damping; it is therefore preferable to seek directional stability by the use of conventional aft vertical surfaces.

The combined effect of high sweep angle and low aspect ratio is to produce a high level of lateral static stability on the present arrow-wing configuration, as indicated by the data for undrooped leading edges in figure 10. Leading-edge droop does little to change this feature in the C_L range of interest. Because of limited roll control capability typical of such configurations, the high lateral stability compromises cross-wind approach and landing operations. In this context, the lateral derivative data with LEVF shown in figure 10 are of particular interest. They indicate a 20% lower dC_{l_β}/dC_L compared to the undrooped wing, resulting in a 25% reduction in C_{l_β} at a lift coefficient of 0.4. If this were a straight-forward anhedral effect, a change in the gradient dC_{l_β}/dC_L would not be expected. The ΔC_{l_β} due to vortex-flap in this instance is of the same order as demonstrated in reference 1 by the use of geometric anhedral on the same model; however the degree of anhedral needed may exceed the tip clearance constraints with a normal landing gear length. This favorable LEVF effect on lateral stability indicated by the present limited data appears sufficiently promising to merit further investigation.

Flow Visualization

Smoke visualization experiments were conducted at a very low speed (about 3 m/sec.) in an attempt to observe the qualitative nature of the flow over leading edge vortex-flaps. A thin plane of light illuminated a chosen cross-flow section of the model. A smoke-generating wand was held upstream of the model while photographs of the smoke pattern were taken from a downstream position at various angles of attack. The light plane was moved to different areas of the flaps to observe the origin and development of the vortices. At angles of attack of about 10° and greater, well-defined vortex cores could be seen over the flap segments. A typical visualization photograph is presented in figure 11.

CONCLUSIONS

The potential of leading edge vortex-flaps (LEVF) in reducing the subsonic lift-dependent drag of a representative supersonic cruise aircraft configuration was explored through wind tunnel tests. Two different LEVF arrrangements (a two-segment and a four-segment) were assessed by comparison with results from a previous test on the same model with the leading edges drooped for attached flow. The main results of this study may be summarized as follows:

1. The two-segment vortex-flaps (14.8% of the wing area) produced drag reductions equal to that obtained by optimally drooped leading edges at lift coefficients greater than 0.4.

2. The four-segment vortex-flaps (10.5% of wing area) performed as well as the constant 30° droop configuration.

3. The vortex-flaps raised the pitch-up angle of attack from 5° to 8° and also allayed its severity.

4. The vortex-flaps had the same effect as leading-edge droop in eliminating the vortex-related directional stability at higher angles of attack.

5. A 20% reduction in lateral stability was achieved at lift coefficients up to 0.5, indicating that vortex-flaps can contribute significantly towards improving cross-wind landing performance in addition to reducing drag.

REFERENCES

1. Coe, Paul L., Jr. and Huffman, Jarrett K.: Influence of Optimized Leading-Edge Deflection and Geometric Anhedral on the Low-Speed Aerodynamic Characteristics of a Low-Aspect-Ratio Highly Swept Arrow-Wing Configuration. NASA TM 80083, 1979.

2. Rao, Dhanvada M.: Leading Edge Vortex-Flap Experiments on a 74° Delta Wing. NASA CR-159161, 1979.

3. Chambers, Joseph R.; Gilbert, William P. and Grafton, Sue B.: Results of Recent NASA Studies on Spin Resistance. Paper no. 6, AGARD CP-199, 1975.

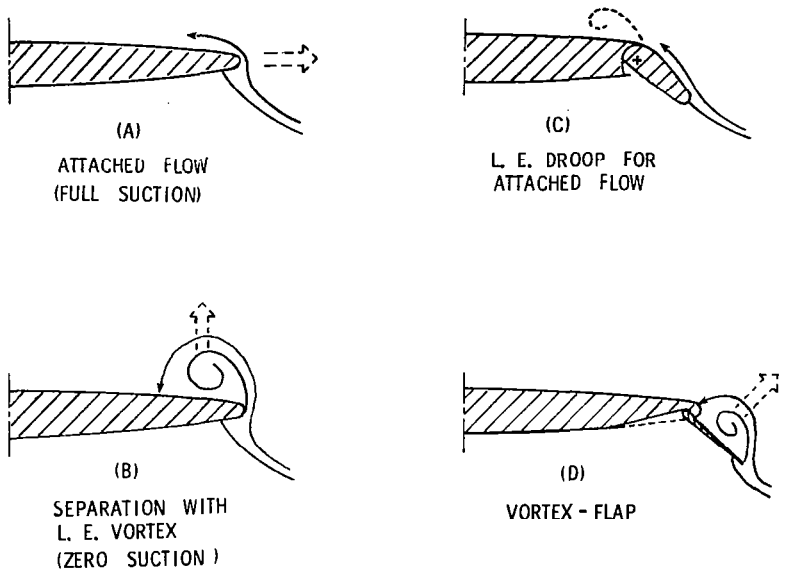

Figure 1.- Leading-edge flows over highly swept wing (viewed in cross-flow plane).

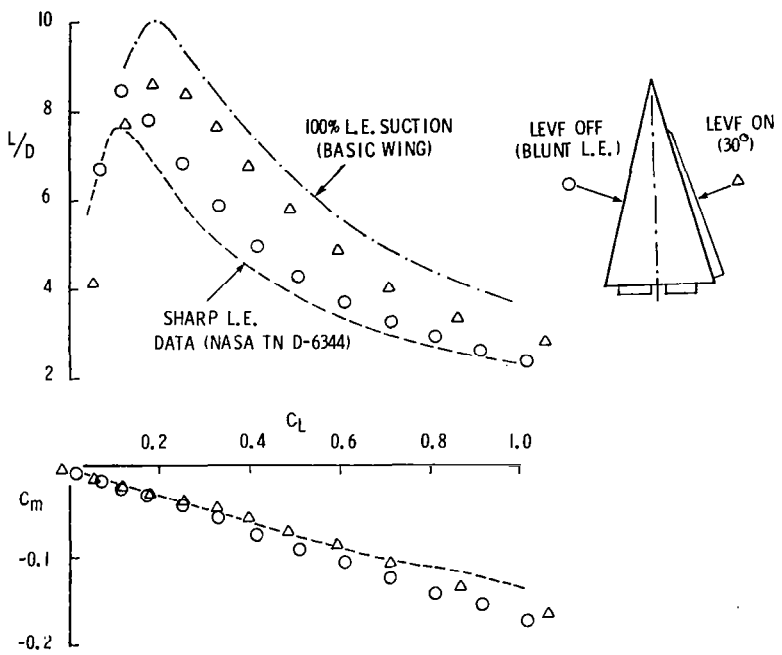

Figure 2.- Vortex-flap test results on 74° delta wing.

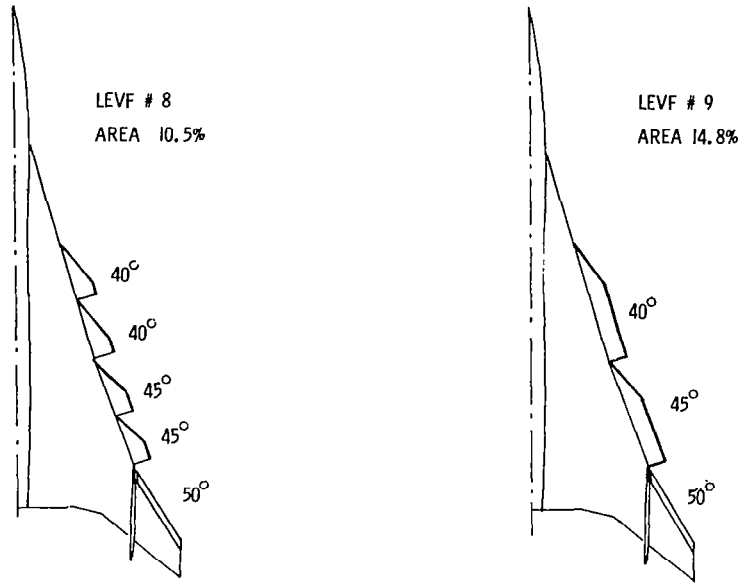

Figure 3.- Vortex-flap configurations on SWAT model.

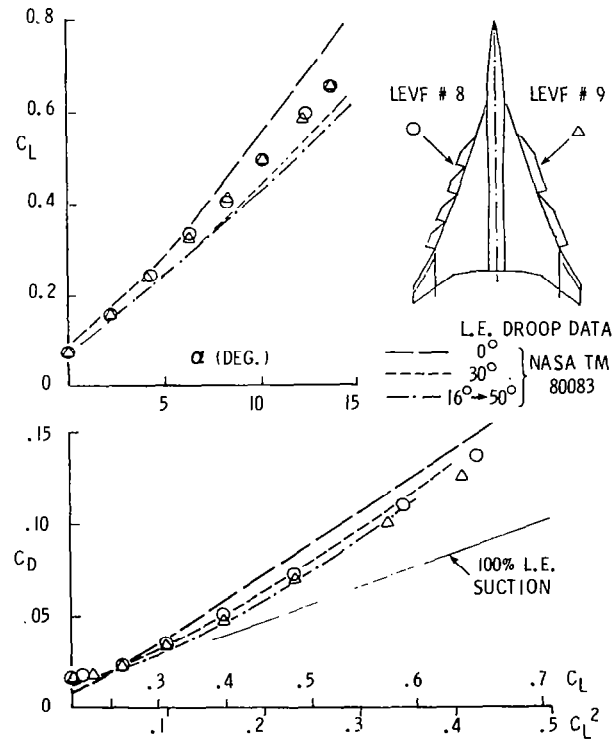

Figure 4.- Lift and drag comparison of vortex-flaps with leading-edge droop.

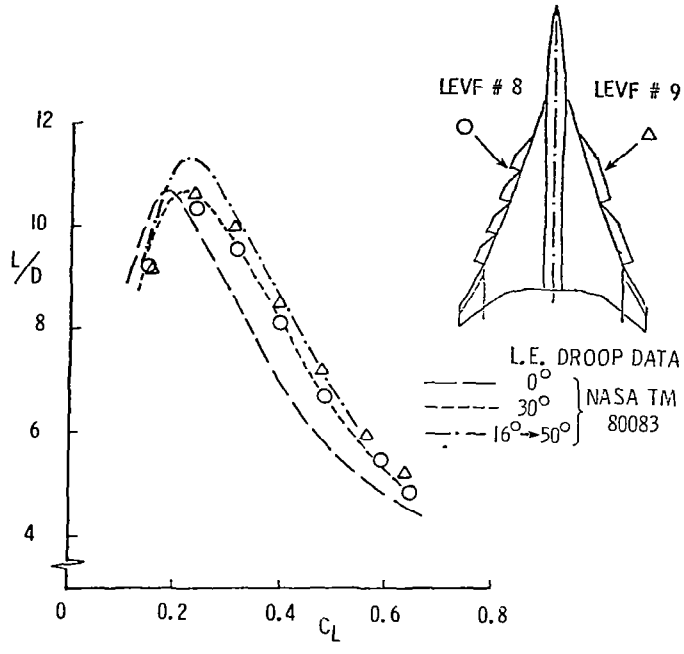

Figure 5.- Lift/drag ratio comparison of vortex-flaps with leading-edge droop.

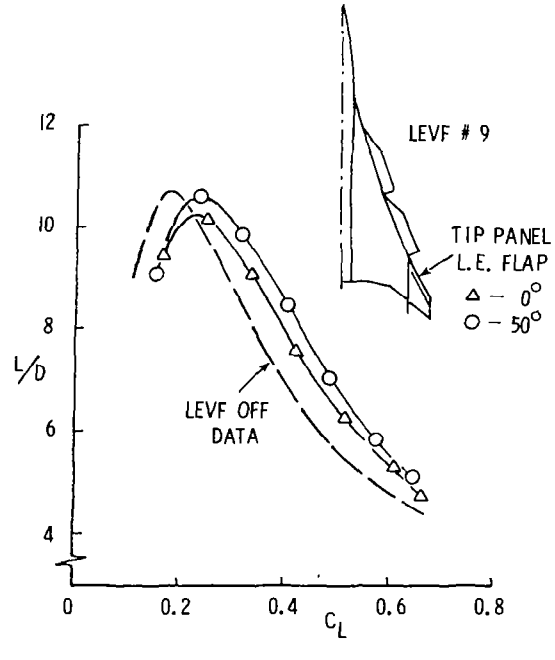

Figure 6.- Effect of tip-panel leading-edge flap deflection on lift/drag ratio.

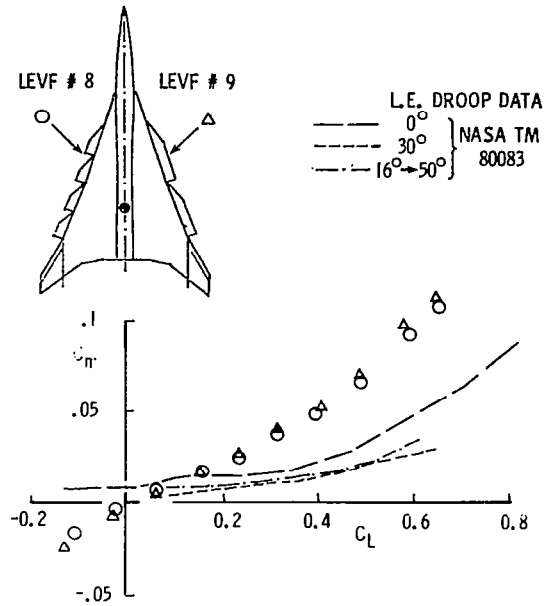

Figure 7.- Pitching moment comparison of vortex-flaps with leading edge droop.

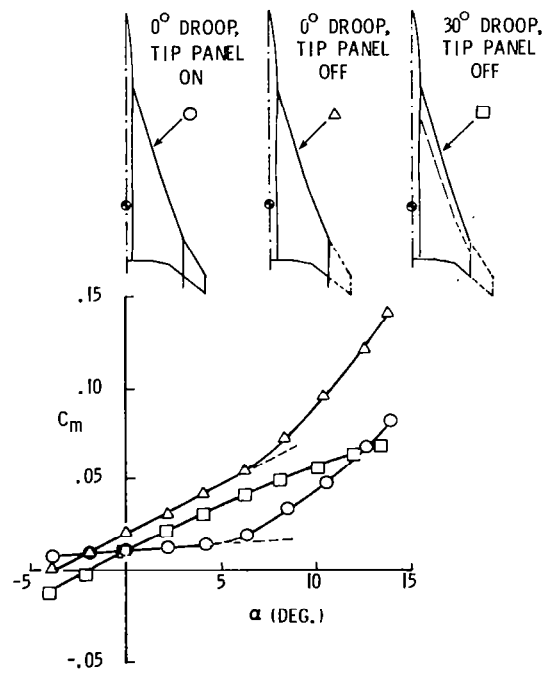

Figure 8.- Effects of leading-edge droop and tip panel on pitch-up.

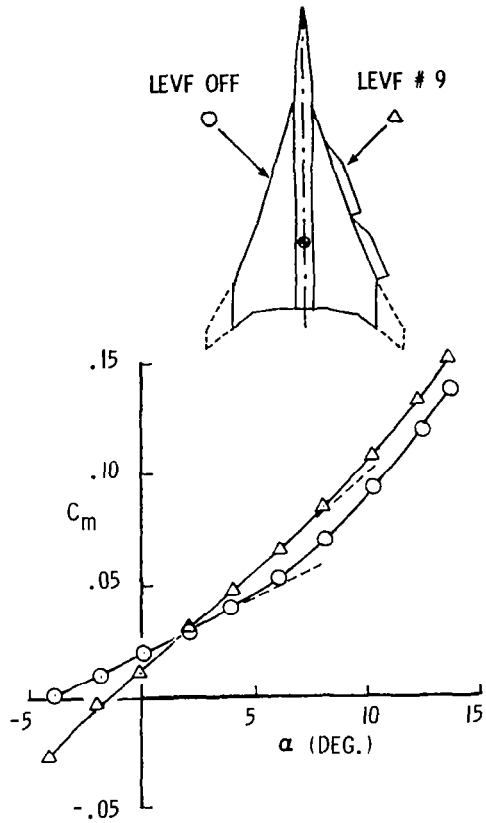

Figure 9.- Vortex-flap effect on longitudinal stability (tip-panels off).

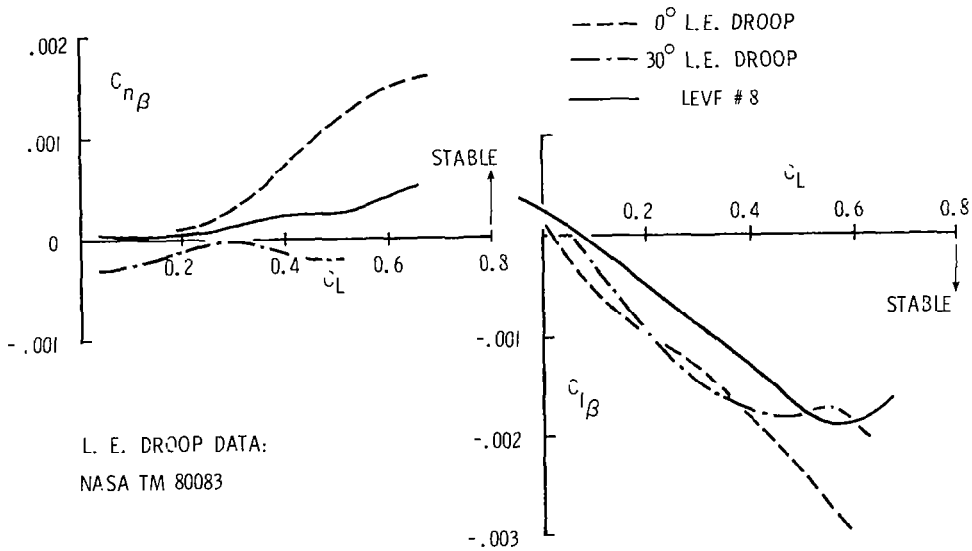

Figure 10.- Vortex-flap effects on directional and lateral stability.

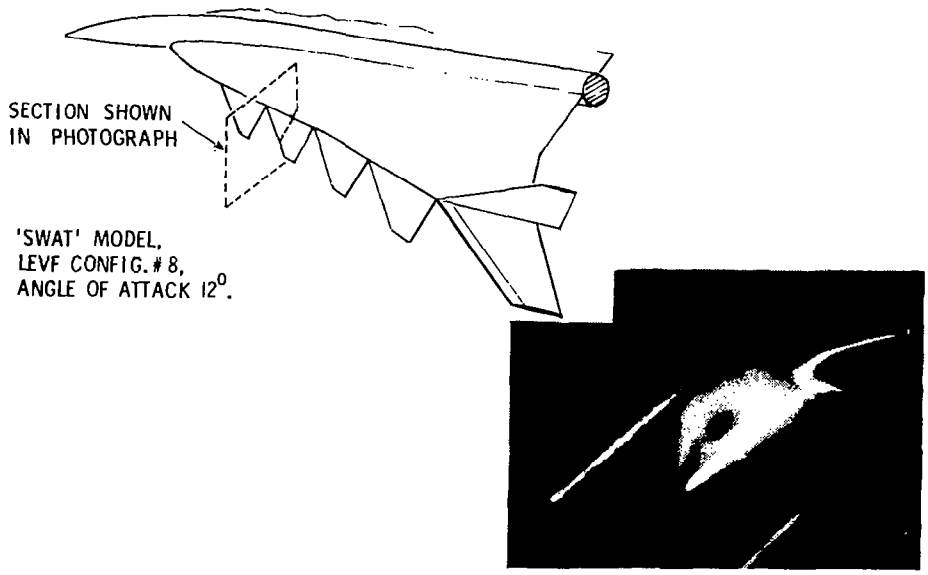

Figure 11.- Smoke flow visualization on vortex-flap.

WIND TUNNEL TEST RESULTS OF A NEW LEADING EDGE FLAP DESIGN FOR HIGHLY SWEPT WINGS - A VORTEX FLAP

L. James Runyan, Wilbur D. Middleton, and John A. Paulson,
Boeing Commercial Airplane Company

SUMMARY

A new leading edge flap design for highly swept wings, called a vortex flap, has been tested on an arrow wing model in a low speed wind tunnel. A vortex flap differs from a conventional plain flap in that it has a leading edge tab which is counterdeflected from the main portion of the flap. This results in intentional separation at the flap leading edge, causing a vortex to form and lie on the flap. By "trapping" this vortex, the vortex flap can result in significantly improved wing flow characteristics relative to conventional flaps at moderate to high angles of attack, as demonstrated by the flow visualization results of this test.

INTRODUCTION

At high angles of attack, highly swept, low aspect ratio wings develop a strong leading edge separation vortex (refs. 1-3). At a given angle of attack, this vortex results in an increase in lift, but an even larger increase in drag, thereby reducing L/D. Pitchup results due to the shift of lift inboard and toward the leading edge (ref. 4).

The usual method of preventing or delaying leading edge separation is to employ leading edge flaps, hinged panels deflected downward (refs. 5 and 6). A proposed alternate solution (see figure 1) is to induce and control separation on the deflected leading edge flap by use of a counterdeflected vortex flap extending from the leading edge of the main flap. The result is a "dog-leg" type flap on which a vortex is trapped. The low pressures associated with this trapped vortex act on the forward facing surface of the main flap, resulting in a thrust and, thereby, reducing drag. In addition, the trapped vortex gives the appearance of a large-radius leading edge to the outer flow. This makes it easier for the outer flow to attach at the knee of the flap and over the remainder of the wing, helping to reduce drag and control pitchup.

In this paper the results of a flow visualization test of the vortex flap on an arrow wing model are presented. Several different vortex flap configurations were tested at angles of attack ranging from 0° to 20°. The flow visualization techniques included fluorescent oil, tufts, and a photographic wake pressure survey. The vortex flap results are compared to those of the basic arrow wing without flaps and to those with plain flaps.

SYMBOLS

b	wing span
C_p	pressure coefficient
L	length
MS	model station
P	pressure
q	dynamic velocity
WBL	wing buttock line
V	velocity
y	distance along the span
α	angle of attack
δ	deflection angle
η	normalized distance along span (y/b/2)

Subscripts:

F	flap
LE	leading edge
T	tab
o	total
∞	remote, undisturbed conditions
$\perp$	normal to wing leading edge

WIND TUNNEL DESCRIPTION AND MODEL GEOMETRY

Wind Tunnel

This test was performed in a Boeing low speed closed-circuit wind tunnel having a test section size of 36.6 cm by 45.7 cm. The Reynolds number for this test was about 2×10^5 based on the average model chord of 15.2 cm. The low Reynolds number should not have a significant effect on the vortex

flap results, because in all cases the leading edge of the flap is sharp, causing flow separation at that point. Also, based on results for similar flaps at higher Reynolds numbers (ref. 5), the plain flap results would not be expected to change significantly at higher Reynolds numbers.

Model and Flaps

The arrow wing half model tested is shown in figure 2. It has a leading edge sweep of 67.2° and consists of a flat plate with sharpened leading and trailing edges. A fence on the inboard portion of the model near the wall prevented wind tunnel boundary layer air from being drawn onto the wing. Angle of attack was varied from 0° to 20°.

Figure 3 shows the leading edge flap configurations tested. One plain flap, two vortex flaps, a hybrid flap (plain flap inboard, vortex flap outboard), and a leading edge split flap were tested.

Flow Visualization Techniques

The visual flow techniques used in this test were: fluorescent oil and mini-tufts to define the surface flow characteristics, streamers and smoke to reveal the flow field around the wing, and a wake survey technique which photographically maps the wake pressure just downstream of the wing.

Surface flow characteristics were made evident using fluorescent oil and tufts on separate runs. The tufts were very fine (0.0018 cm monofilament nylon), trimmed to a length of about 0.64 cm. Streamers 10 to 25 cm in length, of the same thread used for tufts, were also fixed in the incoming flow near the leading edge. Since the aerodynamic forces on these streamers are very low, streamlines can be approximated where the flow is steady. Smoke generated by heating kerosene was introduced in the wind tunnel inlet and illuminated as it passed over the model using a slit of light. With separated flow, the separation boundaries can be defined with this technique. Streamers caught in a vortex will also follow the separation boundary if properly positioned.

The wake pressures downstream of the model were mapped photographically, using the test apparatus illustrated in figure 4. A total pressure tube is mounted on the end of an arm which allows both vertical and radial motion in a plane approximately 1 cm downstream of the most aft point of the wing trailing edge. The pitot tube is traversed through the wing flow field in a series of radial arcs, each having a small vertical displacement from the preceding one. Pressure measured by the pitot tube, which is referenced to freestream static pressure, is sensed by a transducer, and the output from the transducer is fed through a voltage amplifier and filter into a signal splitter, which has several output circuits. Only one output circuit is activated at any given instant, corresponding to a specific voltage range on the incoming signal. The limits of each range can be adjusted, with no overlap. Two diodes, red and green, mounted on the traversing arm, each respond to one of these circuits. In the present test, the circuit to which the green diode was

connected was set to activate over the pressure range ($P_0 - P_\infty$) from 50% to 90% of freestream q. A camera placed in front of the diodes with the lens in the open position recorded an inverted picture of the wing wake, as shown in the left hand side of figure 5. A typical vortex has a green outer band, a red inner band, and a "black hole" in the center of the red band. Yellow bands occur in regions of high turbulence near the cross-over pressure level which result in rapid flickering of the red and green diodes, which the camera superimposes and sees as yellow. The amount of yellow in the pictures can be controlled, to a large extent, by filtering out the high frequency components of the signal.

LEADING EDGE VORTEX CHARACTERISTICS

To assist in the interpretation of the oil flow photographs, the following description of leading edge vortex characteristics is given.

At angle of attack the flow separates from the leading edge of slender wings, creating vortex sheets which roll up to form a primary vortex on the suction side of the wing, as shown in figure 6a. The primary vortex rolls up above the wing and entrains additional airflow over the leading edge ahead of the aft attachment line. Inboard of this attachment line the upper surface flow is principally streamwise, as shown in figure 6b.

Under the primary vortex, the flow is accelerated strongly toward the leading edge until it passes under the vortex core, after which it recompresses and separates (along the secondary separation line). In the oil flow photographs, this area is seen as a series of scrubbed lines on the wing surface, which turn spanwise along the secondary separation line.

Forward of the secondary separation line, in the case of fully developed vortex flow, a secondary vortex is formed, rotating counter to the primary vortex. The secondary vortex, which is approximately 20 percent as strong as the primary vortex, looks like a zone of thick boundary layer in the photographs because it accumulates oil. Flow passing over the secondary vortex reattaches forward of the secondary vortex and continues to the leading edge where it separates again to join the primary vortex.

When the primary vortex moves off the wing trailing edge, the secondary vortex collapses to the trailing edge at the line of secondary separation. The wing tip flow outboard then consists of inboard reattached flow expanding to fill in under a "roof" formed by the lower layer of outboard wing leading edge separation. Depending upon the degree of expansion required and resultant recompression, the wing tip flow may remain attached or it may separate.

Figure 6c shows typical total pressure isobar patterns in the wake downstream of a highly swept wing with leading edge vortices. The vortices result in roughly circular low pressure isobar patterns above the outboard regions of the wing.

RESULTS AND DISCUSSION

Basic Arrow Wing

The flow characteristics of the basic arrow wing with no flaps are shown in figure 7. Oil flow and wake survey photographs at angles of attack of 5°, 10°, and 15° are shown. At $\alpha = 5^{\circ}$, there is a small vortex that can be seen in the oil flow to originate at about 70 percent span. In the wake pressure survey this shows up as a small red area at the tip.

The oil flow photograph at $\alpha = 10^{\circ}$ shows that the primary vortex has increased in size and moved inboard. A secondary vortex can also be seen just outboard of the primary vortex. The wake pressure survey at $\alpha = 10^{\circ}$ shows the primary vortex as the large red area near the tip surrounded by the green and yellow band. The secondary vortex is the smaller red circular region just outboard of the primary vortex. The third (and smallest) red area nearest the wing tip is the tip vortex.

At $\alpha = 15^{\circ}$ the oil flow photo shows that the primary and secondary vortices now dominate the outboard half of the wing. The wake pressure survey shows that, downstream of the wing trailing edge, the primary and secondary vortices have begun to merge.

Plain 50° Flap

Oil flow results on the upper surface of the arrow wing with a 50° leading edge plain flap are shown in figure 8. A vortex begins to develop at $\alpha = 5^{\circ}$, becoming larger and moving inboard as angle of attack is increased. The separation evident at the flap shoulder at this low Reynolds number would probably not change by a significant amount at higher Reynolds numbers.

Smoke flow was used to illuminate the dividing streamline characteristics of the plain flap, using the wind tunnel instrumentation illustrated in figure 9. A slit of light from a source mounted outside a window in the side of the test section impinges on smoke flowing over the wing leading edge, which is then photographed to produce a cross-sectional view of the flow.

The dividing streamline characteristics of the plain flap at $\alpha = 10^{\circ}$, as shown by smoke flow photographs, are shown in figure 10. Smoke introduced ahead of the wing reveals the exterior flow. If the smoke plume is moved inboard, the smoke is entrained inside the separation vortex. In both cases, the boundary between exterior flow and the interior (separated vortex) flow is defined. At $\eta = .80$ the flow can be seen to separate at the knee of the flap and reattach a short distance downsteam. At $\eta = .98$ the chordwise extent of separation is larger than at $\eta = .80$.

50° Vortex Flap

Figure 11 shows the results for the 50° vortex flap. At $\alpha = 10^o$ the oil flow photograph shows the flow to be attached over most of the wing upper surface, although the flow in the boundary layer is largely spanwise. A weak primary vortex subtends the flap from leading edge to the flap/wing corner, becoming stronger near the wing tip. The wake survey photos show both this primary vortex and a smaller vortex outboard resulting from the merging of the secondary and tip vortices. The improved flow over the surface and the reduced vortex size indicate a lower drag for this configuration than for the basic arrow wing with no flaps. Thus, it appears that the 50° vortex flap is performing well at $\alpha = 10^o$.

At $\alpha = 15^o$, the 50° vortex flap results in a small reduction in the size of the primary vortex (compared to the basic wing). The secondary separation line inboard lies near the leading edge wing/flap break, trailing back behind the flap at about 40 percent span. Outboard, the secondary vortex (which is separate from the primary in the wake photograph) moves from the flap onto the wing surface and the flow separates from the flap at about 90% span. The vortex flap may still be somewhat effective at reducing drag at this condition.

The upper surface flow characteristics at 10° angle of attack of the basic wing, the 50° plain flap, and the 50° vortex flap are compared in figure 12. It can be seen that only the 50° vortex flap shows no sign of a vortex on the wing.

Smoke patterns for the 50° vortex flap, shown in figure 13, show that the trapped vortex on the vortex flap gives the wing the appearance of having a large leading-edge radius with attached upper surface flow, except for the tip region. At $\eta = .80$, it can be seen that the vortex flap is successful in preventing separation at the wing-flap junction. A relatively thick boundary layer appears to remain, however. This is further illustrated by the streamer shown in two views in figure 14. The streamer was located as close to the wing surface as possible for stability. Note the strong shear indicated by direction of the tufts compared to the streamer. The streamer could not be located this close to the wing with plain flaps.

Variable Deflection Vortex Flap

A variable deflection vortex flap was designed so that the local deflection angle of the main flap would nominally match the local angle of attack for a wing angle of attack of 8°. The resulting deflection angle varied from 16° at the root to 76° at the tip, with the tab bent back parallel to the wing plane.

Results for the variable deflection vortex flap are shown in figure 15. At $\alpha = 5^o$, a primary vortex appears to subtend the flap out to approximately 60 percent span, with the aft attachment line near the flap/wing corner. The flap appears ineffective at $\alpha = 10^o$ and greater. The flow at $\alpha = 10^o$ looks much like the 50° vortex flap at $\alpha = 15^o$. At $\alpha = 15^o$, the flow

outboard of approximately 40 percent span is separated and eddying with a secondary vortex near the secondary separation line on the main wing surface. The vortex size in the wake photographs is approximately the same as for the basic wing. (The extensive regions of yellow coloration in figure 15 resulted from the use of a different transducer signal filter setting than was used for figures 7 and 11. The overall size of the vortex as seen by the camera is not appreciably affected by the filter setting, however.)

Hybrid Flap

Another alternative to the 50° vortex flap was a hybrid arrangment, consisting of a 30° plain flap on the inboard 25% of the wing span, a vortex flap having a deflection angle varying from 30° inboard to 50° outboard extending from 25% span to 50% span, and a 50° vortex flap on the outboard 50% of the wing. The philosophy of the plain flap inboard was to postpone intentional tripping of the vortex to a more outboard location, thereby resulting in a weaker primary vortex at the tip. The oil flow photo at $\alpha = 10^{\circ}$ in figure 16 shows a small separation bubble at the hinge of the 30° plain flap, with subsequent flow reattachment. The size of the vortex near the wing tip at $\alpha = 10^{\circ}$ is about the same as that of the 50° vortex flap. There are also two small vortices near the mid-span location which trail back from the junctions of the flap segments. At $\alpha = 15^{\circ}$, the flow characteristics for the hybrid flap are very similar to the 50° vortex flap.

Leading Edge Split Flap

The leading edge split flap had a constant deflection of 45° along the entire span and an increased flap chord (1.8 cm). The junction of the wing and flap was 0.5 cm behind the rounded leading edge. The flow characteristics resulting from this flap configuration, as shown in figure 17, exhibit strong secondary vortex flow. At $\alpha = 15^{\circ}$, it has a significantly smaller primary vortex than all others tested. Since it is a design goal to have a flap design which works well on the arrow wing at $\alpha = 15^{\circ}$, further investigation of the leading edge split flap concept is planned.

CONCLUDING REMARKS

Flow visualization tests of an arrow wing model in a Boeing low speed wind tunnel have shown promising results for vortex flaps. These results indicate that the vortex flap is able to "trap" the leading edge separation vortex on its surface at angles of attack up to 10°. The "trapped" vortex gives the appearance of a large radius leading edge to the outer flow. As a result, no flow separation at the wing-flap junction was observed for angles of attack up to 10°. A hybrid flap configuration consisting of a plain flap inboard and a vortex flap outboard was also successful in improving the upper surface flow characteristics at $\alpha = 10^{\circ}$. Optimization of the vortex flap geometry parameters should result in additional improvements in the performance of the vortex flap.

REFERENCES

1. Stanbrook, A., and Squire, L. C.: Possible Types of Flow at Swept Leading Edges, The Aeronautical Quarterly, pp 77-82, February 1967

2. Kulfan, R. M.: Wing Airfoil Shape Effects on the Development of Leading Edge Vortices, AIAA Paper No. 79-1675, Presented at the AIAA Atmospheric Flight Mechanics Conference, Boulder, Colorado, August 7, 1979

3. Kulfan, R. M.: Wing Geometry Effects on Leading Edge Vortices, AIAA Paper No. 79-1872,, Presented at the AIAA Aircraft Systems and Technology Meeting, New York, New York, August 20-22, 1979

4. Chambers, Joseph R.: Aerodynamic Characteristics at High Angles of Attack, Paper Presented at the AGARD/VKI Lecture Series on "Aerodynamic Inputs for Problems in Aircraft Dynamics", Rhode-St-Genese, Belgium, April 25-29, 1977

5. Coe, Paul L. and Weston, Robert P.: Effects of Wing Leading-Edge Deflection on the Low-Speed Aerodynamic Characteristics of a Low-Aspect-Ratio Highly Swept Arrow-Wing Configuration. NASA Technical Memorandum 78787, September 1978

6. Coe, Paul L. and Huffman, Jarrett K.: Influence of Optimized Leading-Edge Deflection and Geometric Anhedral on the Low-Speed Aerodynamic Characteristics of a Low-Aspect-Ratio Highly Swept Arrow-Wing Configuration, NASA TM-80083, June 1979

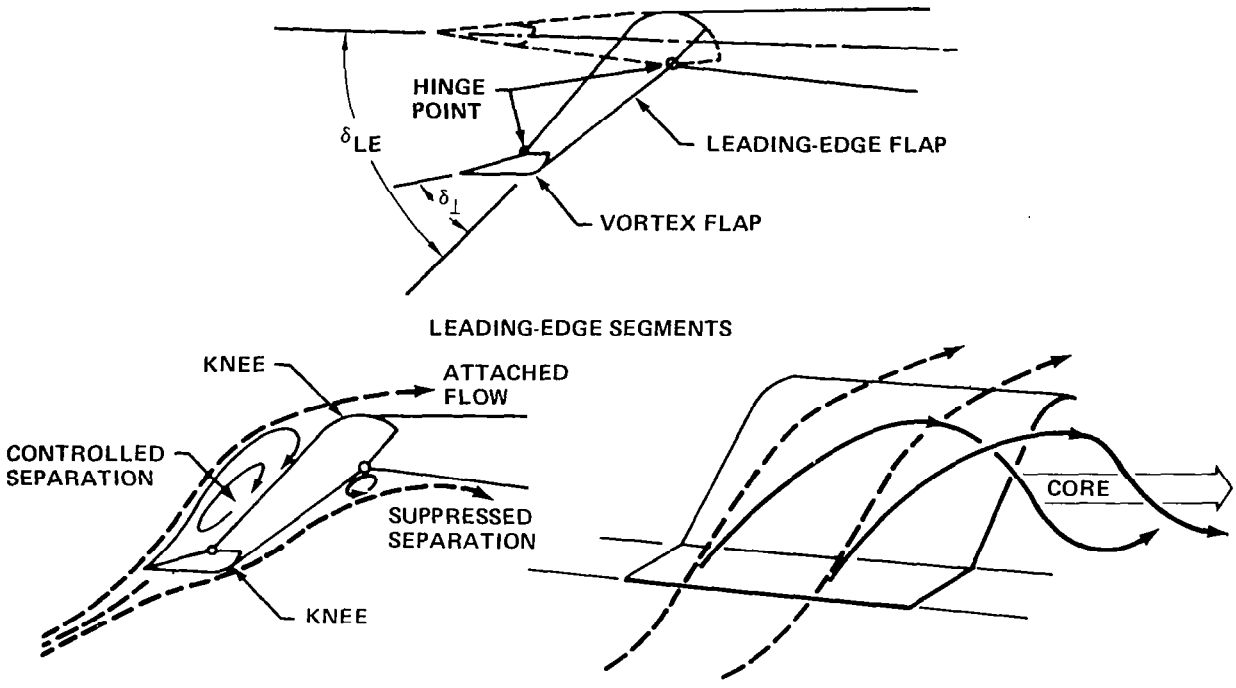

Figure 1.- Vortex control flaps.

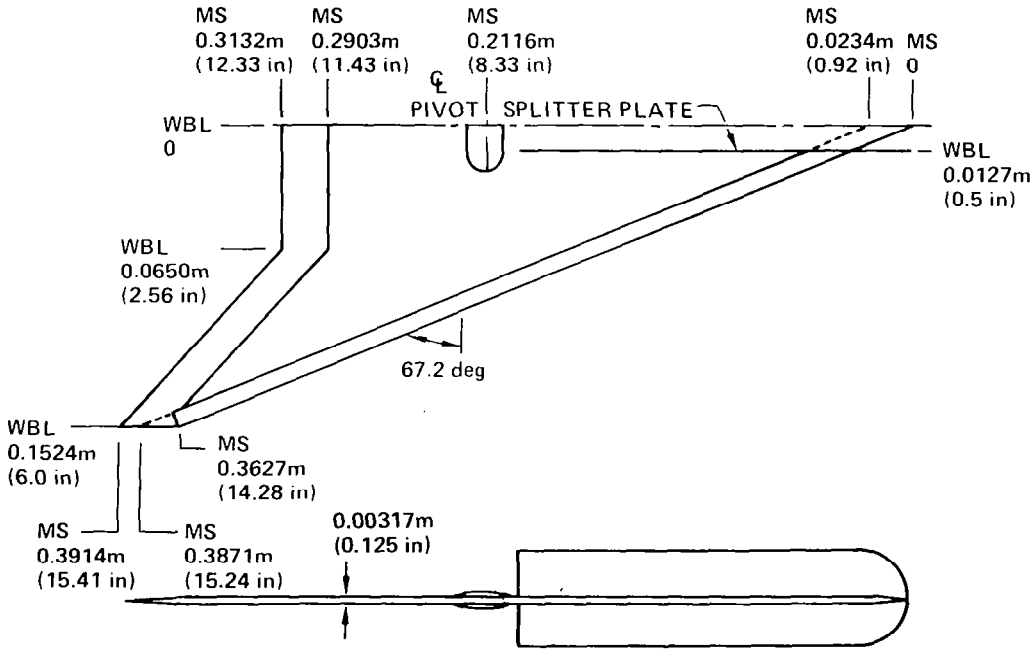

Figure 2.- Arrow wing model geometry.

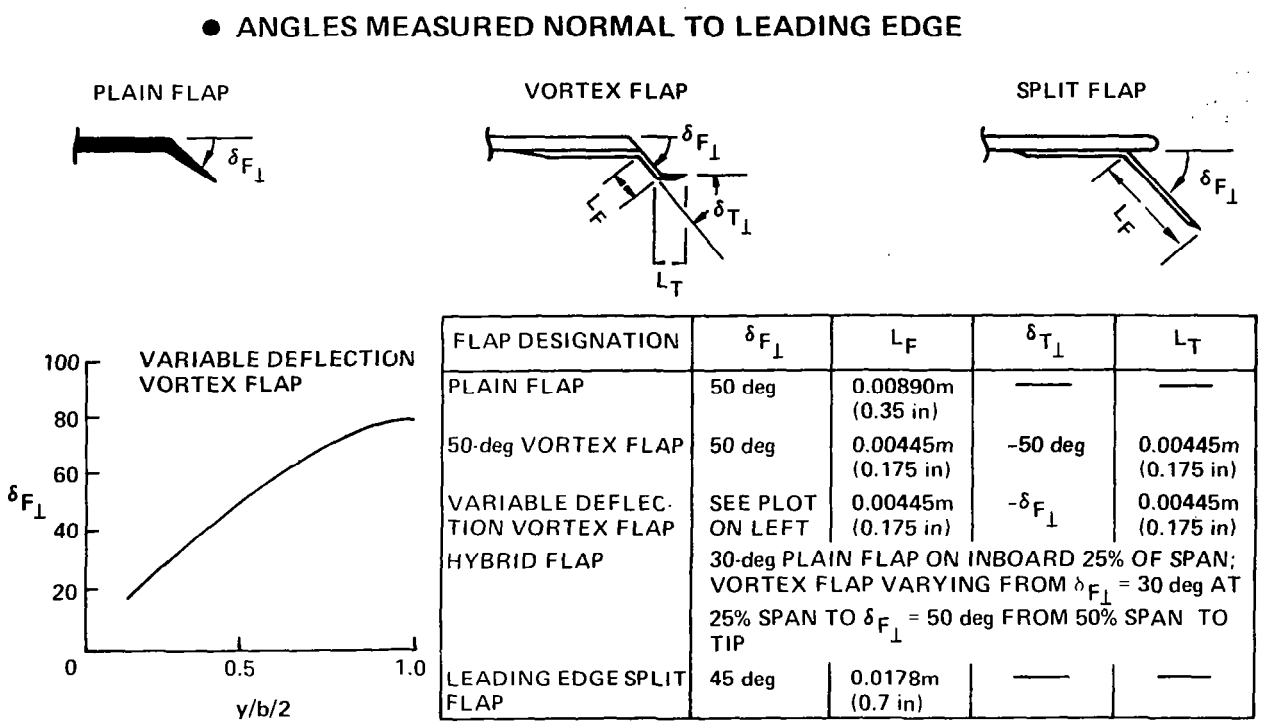

FLAP DESIGNATION	$\delta_{F_\perp}$	L_F	$\delta_{T_\perp}$	L_T
PLAIN FLAP	50 deg	0.00890m (0.35 in)	—	—
50-deg VORTEX FLAP	50 deg	0.00445m (0.175 in)	-50 deg	0.00445m (0.175 in)
VARIABLE DEFLECTION VORTEX FLAP	SEE PLOT ON LEFT	0.00445m (0.175 in)	$-\delta_{F_\perp}$	0.00445m (0.175 in)
HYBRID FLAP	30-deg PLAIN FLAP ON INBOARD 25% OF SPAN; VORTEX FLAP VARYING FROM $\delta_{F_\perp}$ = 30 deg AT 25% SPAN TO $\delta_{F_\perp}$ = 50 deg FROM 50% SPAN TO TIP			
LEADING EDGE SPLIT FLAP	45 deg	0.0178m (0.7 in)	—	—

Figure 3.- Flap geometry.

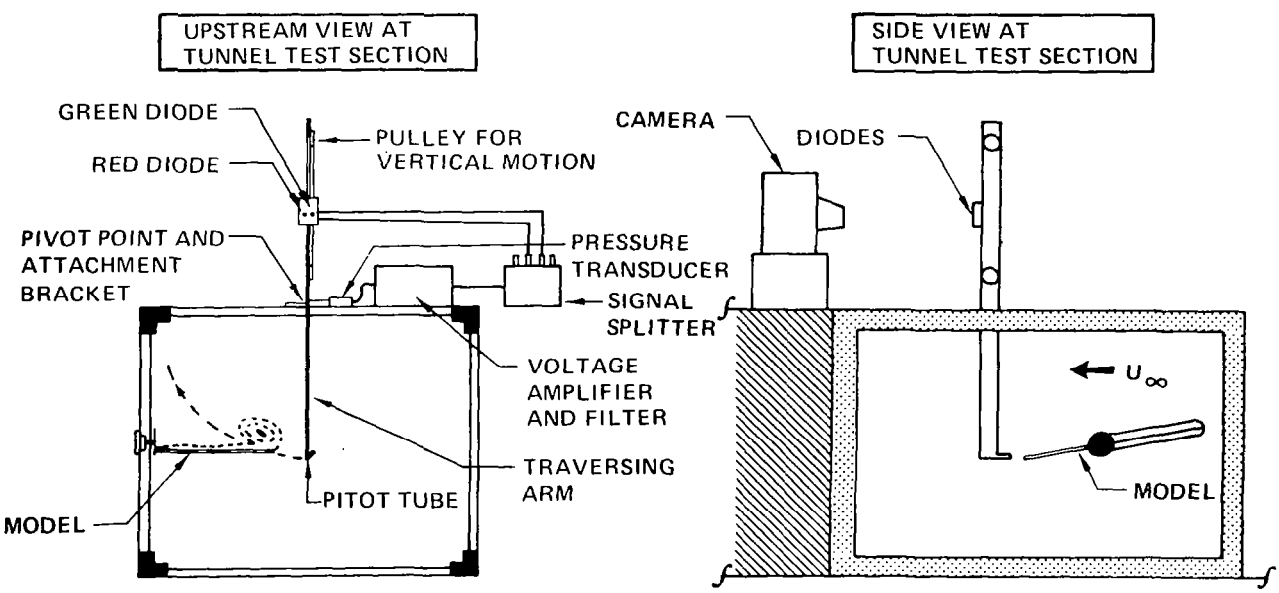

Figure 4.- Wake pressure survey apparatus.

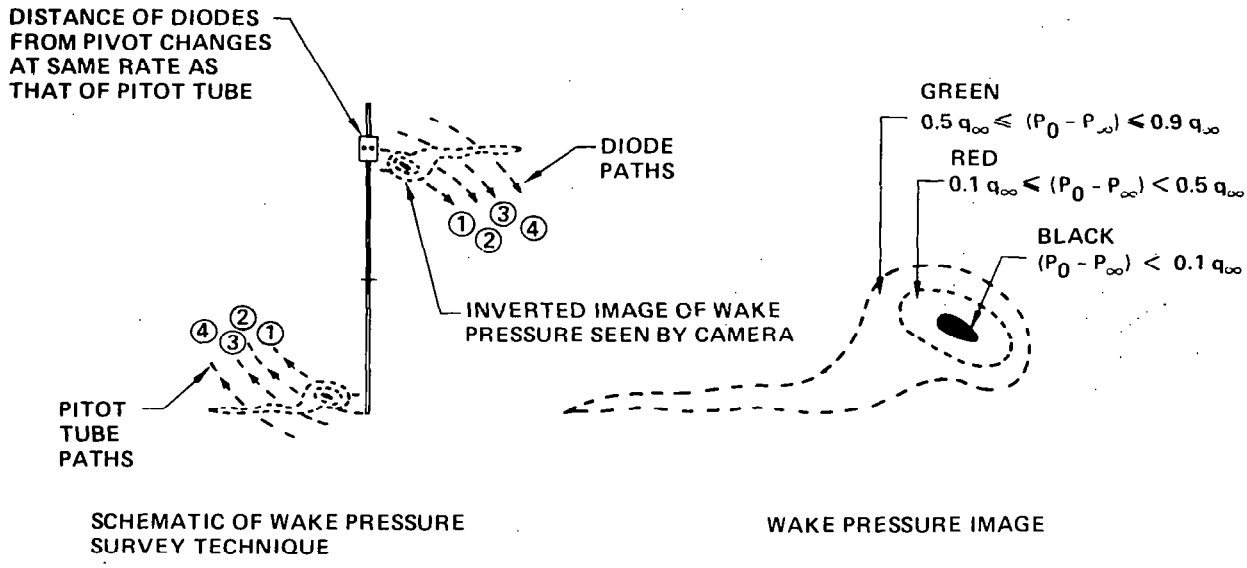

Figure 5.- Wake pressure survey technique.

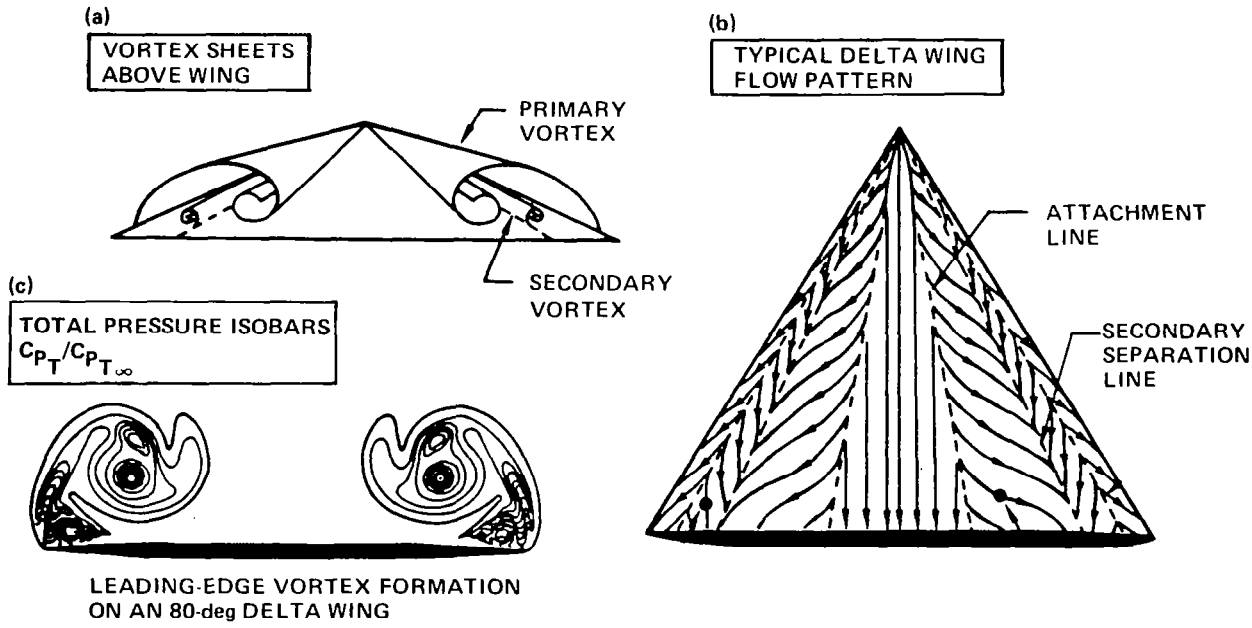

Figure 6.- Vortex flow characteristics.

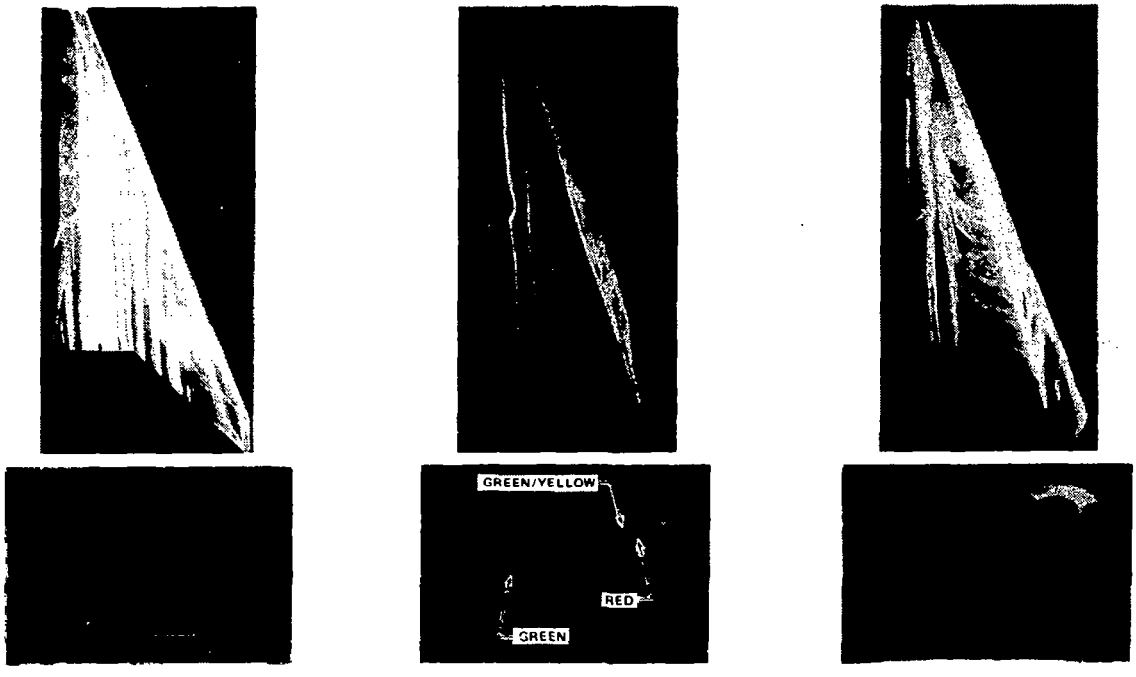

α = 5 deg α = 10 deg α = 15 deg

Figure 7.- Oil flow and wake survey of basic arrow wing.

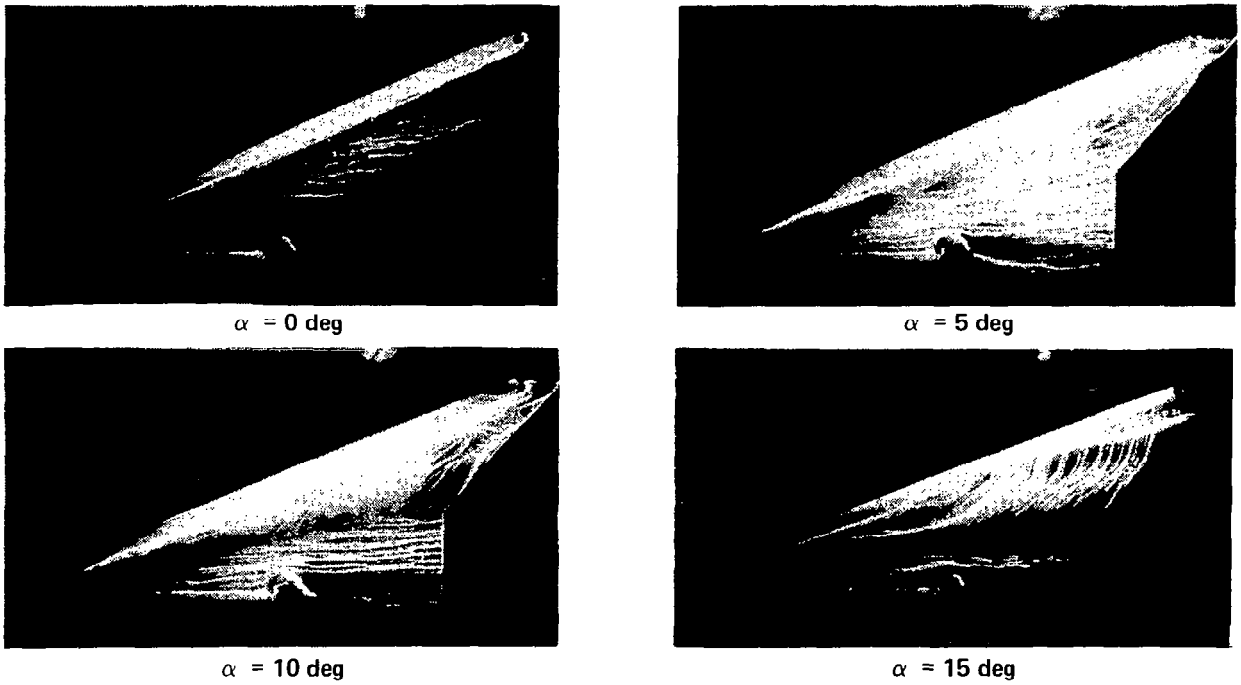

α = 0 deg α = 5 deg

α = 10 deg α = 15 deg

Figure 8.- Oil flow for 50° plain flap.

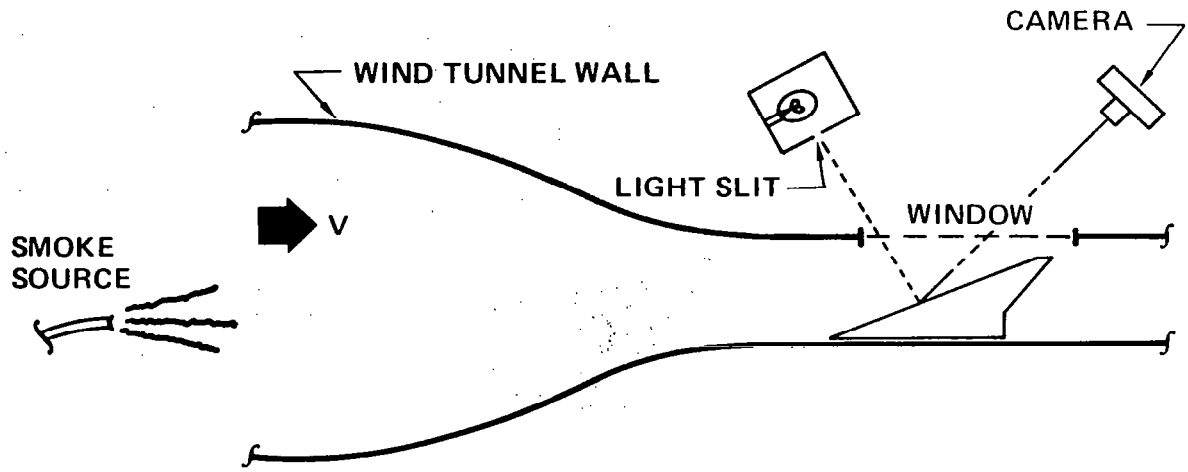

Figure 9.- Wind tunnel instrumentation for dividing streamline photographs.

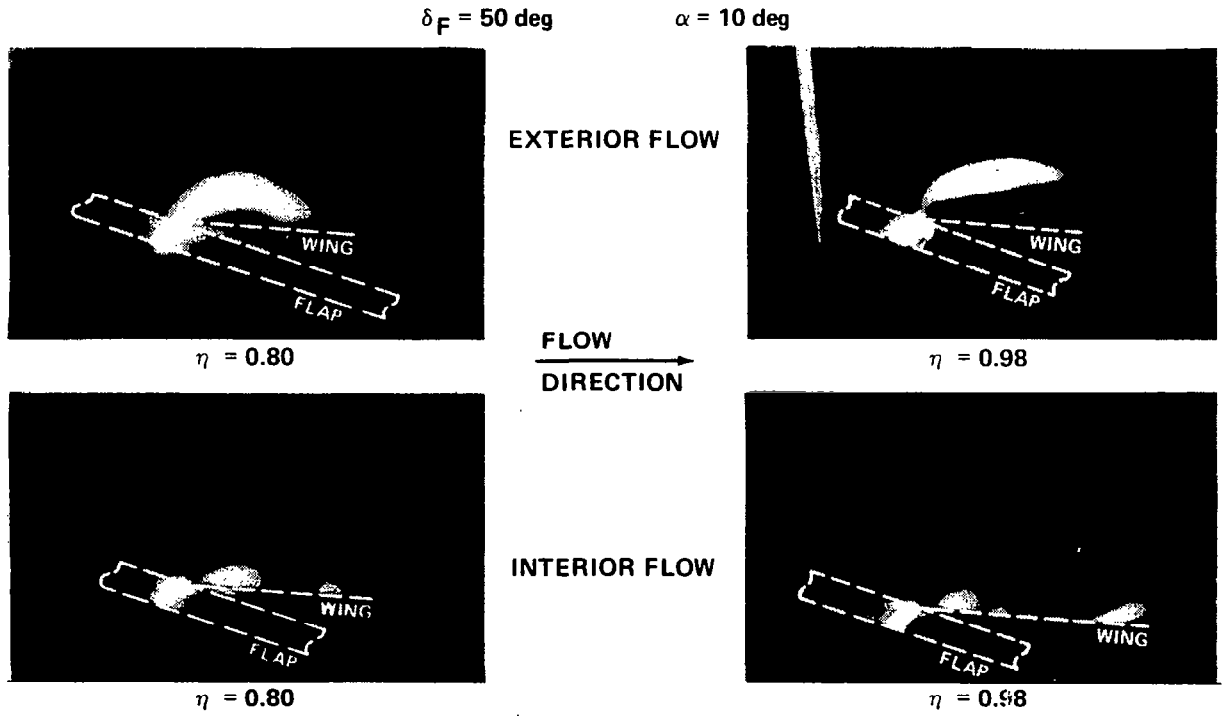

Figure 10.- Dividing streamline characteristics for 50° plain flap.

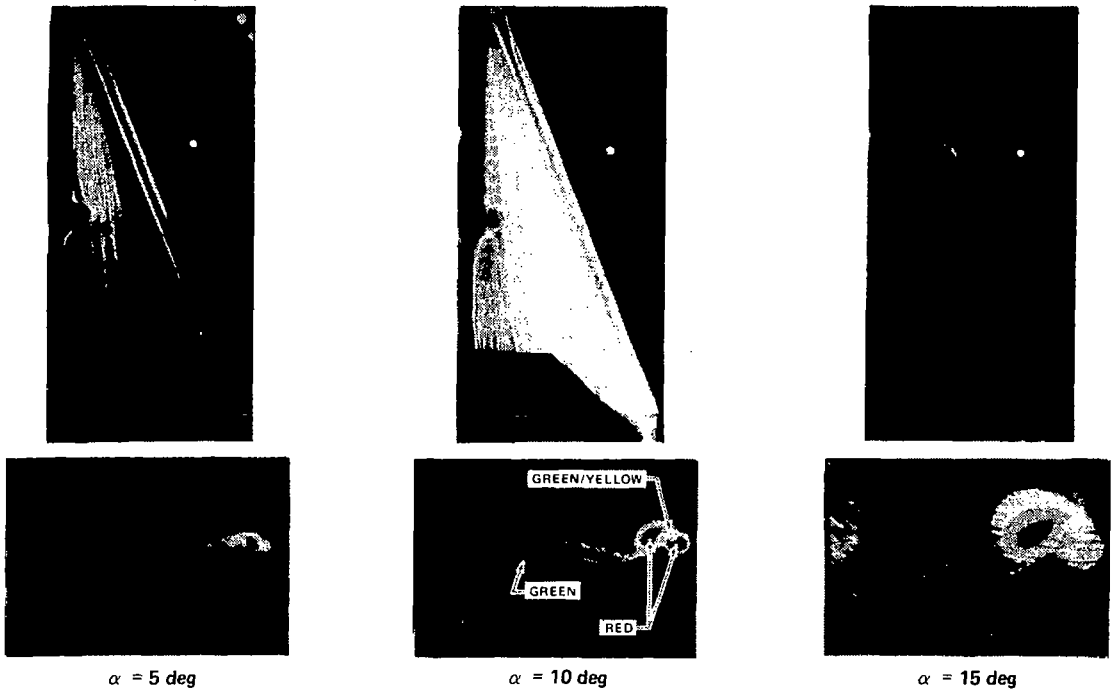

Figure 11.- Oil flow and wake survey for 50° vortex flap.

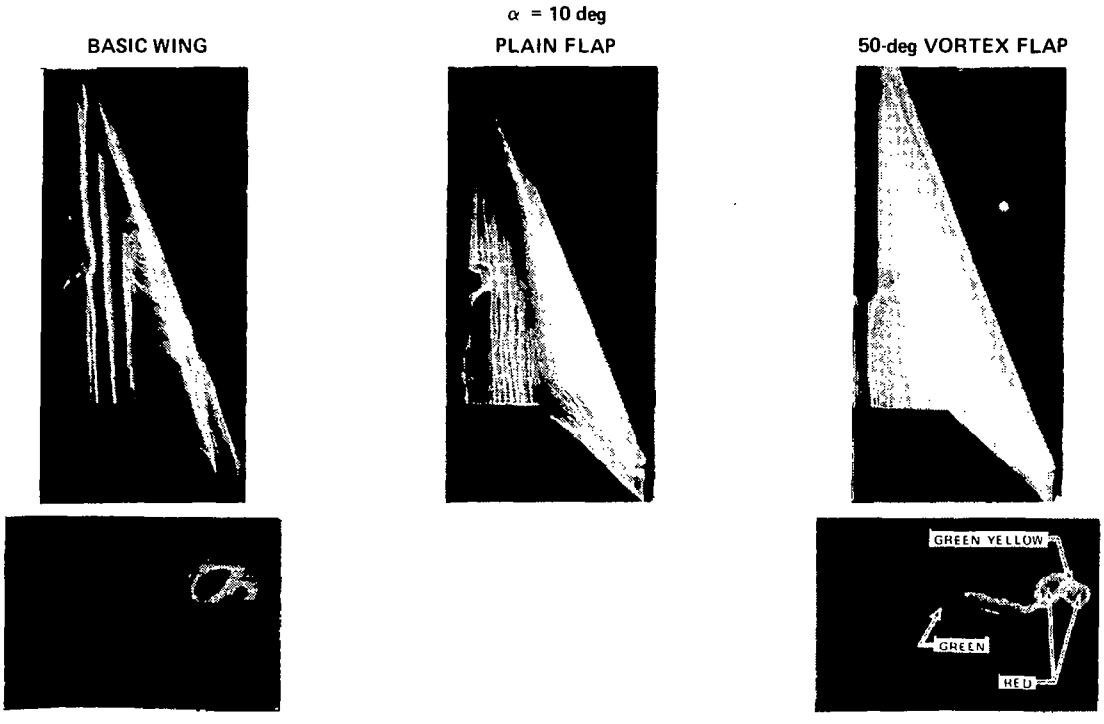

Figure 12.- Comparison of basic wing, plain flap, and 50° vortex flap.

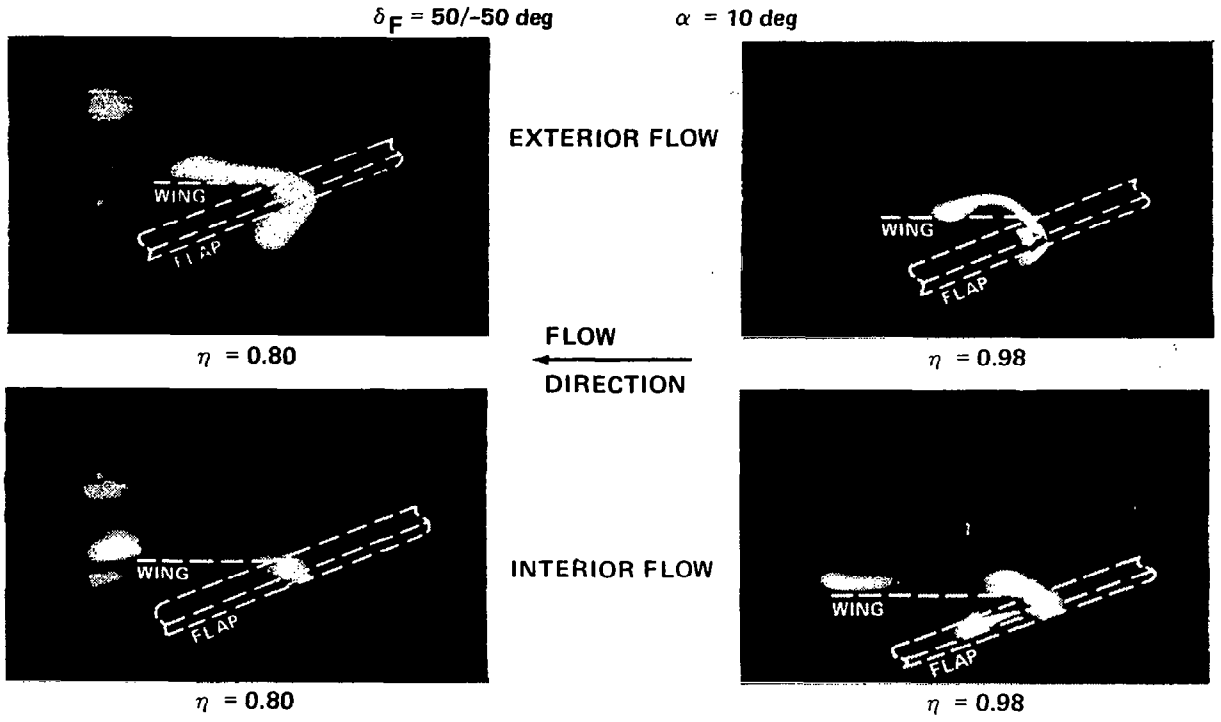

Figure 13.- Dividing streamline characteristics for 50° vortex flap.

α = 10 deg η = 0.80

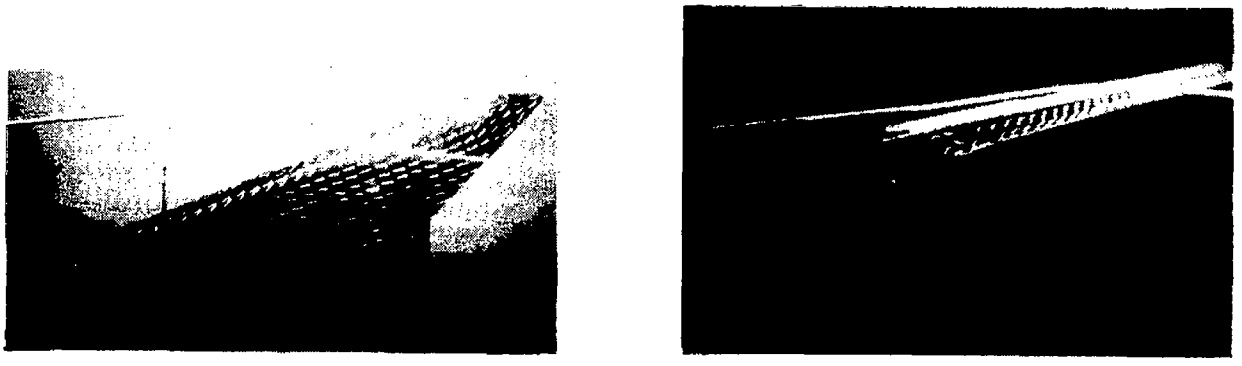

Figure 14.- Streamer above arrow wing with 50° vortex flap.

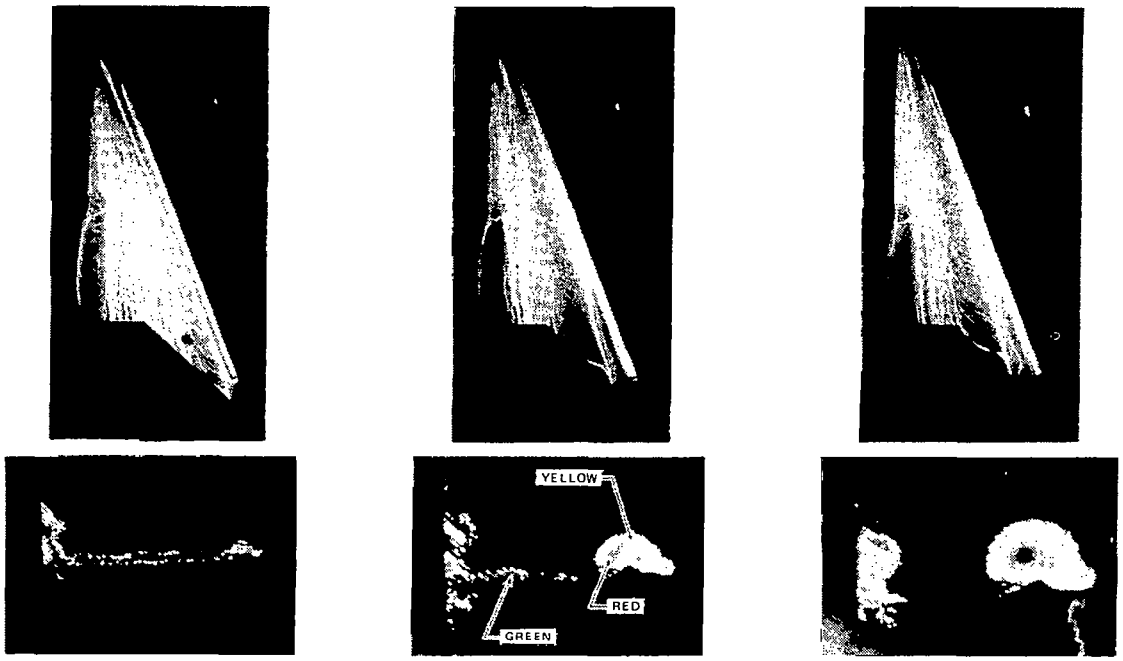

α = 5 deg α = 10 deg α = 15 deg

Figure 15.- Oil flow and wake survey for varying deflection vortex flap.

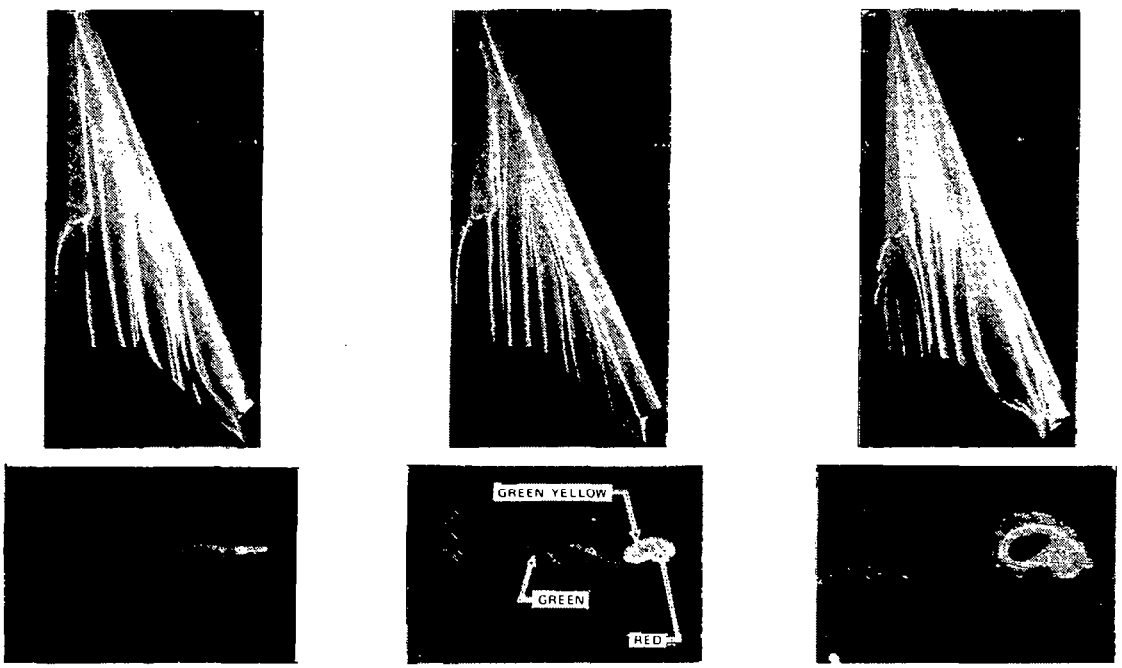

α = 5 deg α = 10 deg α = 15 deg

Figure 16.- Oil flow and wake survey for hybrid flap.

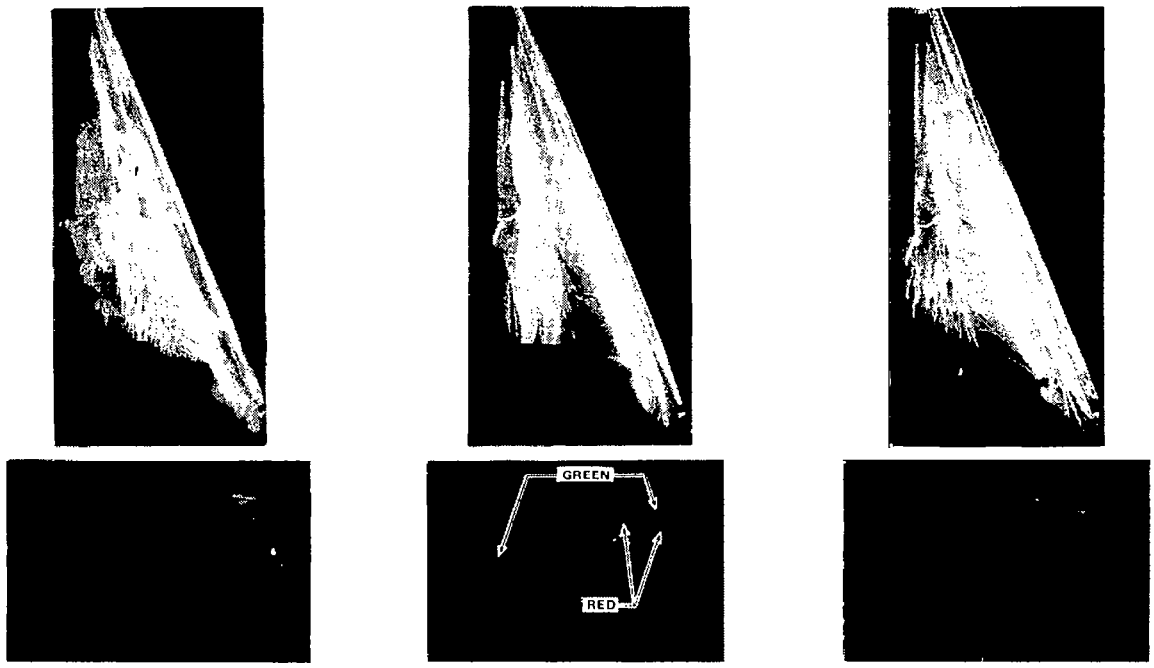

α = 5 deg α = 10 deg α = 15 deg

Figure 17.- Oil flow and wake survey for 45° leading-edge split flap.

A STUDY OF WING BODY BLENDING FOR AN ADVANCED SUPERSONIC TRANSPORT*

T.P. Goebel, E. Bonner, and D.A. Robinson
North American Aircraft Division
Rockwell International

SUMMARY

Increases in supersonic cruise lift-drag ratio were sought at Mach numbers 2.2 and 2.7 using wing-body planform and thickness blending. Constrained twist and camber optimization was performed in the presence of nacelles. Wing and fuselage thickness distributions were optimized for either minimum volume wave drag or minimum total pressure wave drag. The zero leading edge suction lift drag ratios were determined for three wing planforms. The magnitude of the effect of leading edge suction on attainable lift drag ratio was defined on one planform and an estimation of available leading edge suction was made.

INTRODUCTION

A variety of configuration arrangements have been considered for large supersonic cruising aircraft in past NASA and industry studies. Many early arrangements are described in a 1967 NASA summary and index of experimental characteristics (ref. 1). One promising configuration has been used as a focus for recent AST-100, 105-1, and 200 studies (refs. 2-4). This arrangement employs a highly swept wing of moderate taper ratio, underslung nacelles, an aft-fuselage-mounted horizontal tail surface and fuselage-and-wing-mounted vertical surfaces. The present study uses this arrangement as a starting point and defines improvements due to wing-body blending. A resized AST-100, designated the AST-102, was selected as the Mach 2.7 baseline configuration. The objective of the present study is to evaluate the effect of wing-body blending on the performance of a supersonic cruising aircraft. The approach, as shown on figure 1, emphasizes the aerodynamic design tools available at Rockwell and which differ from those available elsewhere in the industry.

*Work performed under Contract NAS1-15720

SYMBOLS

C	chord, m
C_D	drag coefficient
C_L	lift coefficient
D	drag, N
L	lift, N
q	dynamic pressure, N/m^2
S	leading edge suction parameter
S_W or S_{REF}	reference wing area, m^2
t	thickness, m
x,y,z	cartesian coordinates, m
β	$\sqrt{M^2-1}$
η	nondimensional spanwise coordinate
Λ	sweepback angle, deg
θ	roll angle, deg

Subscripts:

c.g.	center of gravity
C.P.	center of pressure
F	friction
L	lifting
LE	leading edge
TE	trailing edge
W	wave drag

PLANFORM SELECTION

The AST-102 leading edge has three straight line segments with sweepback angles of 74, 71 and 60 degrees. The Rockwell blended RB-1 leading edge has, except for an inboard modification, two straight line segments with sweepback angles of 74 and 68.5 degrees, figure 2. The inboard leading-edge modification was made to facilitate blending. Increased outboard leading-edge sweep was used to achieve a higher supersonic cruise lift-to-drag (L/D) ratio and is consistent with an earlier design integration study (ref. 5). An outboard leading edge sweep of 68.5 degrees was selected as the highest for which acceptable low speed characteristics could be expected at landing angles up to 8 to 10 degrees. A leading edge sweep increase to 72.3 degrees would be required at M = 2.7 to satisfy the recently developed Carlson suction criteria $\beta \cot \Lambda_{LE} \leq 0.8$. The inboard trailing edge was kept identical to the AST-102 because good low speed flap effectiveness requires low trailing edge sweep. The outboard trailing edge sweep was increased, however, from 41.5 degrees on the AST-102 to 45.4 degrees on the RB-1 to allow sufficient outboard chord for leading and trailing edge devices. With these planform modifications and after application of the aerodynamic design codes, the blended configuration indicated on figure 3 evolved.

TWIST AND CAMBER OPTIMIZATION

Two linear optimizers are available for use with a swept panel analysis program (ref. 6). All three solvers can treat the wing, fuselage, and horizontal and vertical surfaces as twisted and cambered surfaces within the framework of linearized flow theory. The analysis program can represent several fuselage and nacelle shaped bodies as slender bodies.

12 spanwise and 10 chordwise wing panels and 1 spanwise and 20 chordwise fuselage panels were used in all three programs. In the analysis program, rectangular shells were placed around circular slender-body nacelles, figure 4. 10 chordwise and 4 wrap-around panels were used on the rectangular shells. The function of the shells is to provide surfaces for matching boundary conditions between the slender body nacelle solutions and cambered and twisted surface solutions.

Due to differing capabilities of the available computer programs, the twist and camber design cycle required several steps, figure 5. In step A the wing is represented as a thin cambered and twisted surface and the fuselage as a cambered plate. The basic design program produces the optimum twist and camber of the wing and fuselage for a specific lift and moment constraint.

In step B this twist and camber are evaluated in the analysis program with nacelles present. In step C the design is refined with the nacelle upwash from step B added at the control points of those wing panels influenced by the nacelles. In step D the analysis program was used to evaluate the revised optimum twist and camber with nacelles on. In step E the auxiliary design program was used to establish the changes in twist and camber to cancel the wing pressure differences between steps C and D. The blended wing-body-nacelle design achieved a lifting efficiency level within 2% of the wing alone case and is equivalent to an arrow wing of the same sweep and aspect ratio with a notch ratio of 0.4 (see figure 14 of reference 5). The final twist and camber distribution was evaluated in the analysis program across the Mach number range to obtain trimmed drag due to lift for 0% and 100% leading edge suction (L.E.S.) condition. The M = 2.7 design twist and camber for the blended planform at $C_L = 0.1$ is presented on figures 6 through 9.

WING-FUSELAGE VOLUME OPTIMIZATION

An analysis program is available to calculate supersonic volume and lift-volume wave drag. The spatial singularities which are solutions to the linearized equations of motion are reduced to a series of equivalent lineal distributions by application of the cutting (oblique) plane concept. The drag is calculated using slender body theory (refs. 7 and 8). The total wave drag includes volume, angle of attack, twist and camber, and lift-volume interference effects. In the analysis mode, the wave drag is evaluated using 13 roll angles and 50 longitudinal cuts.

For wing and fuselage thickness optimization, a design solver is used to minimize either volume wave drag or total wave drag subject to specific volume and local thickness constraints. The physical geometry is perturbed by a set of harmonic functions. Lagrange's method for extremal problems with constraints is applied to the expression for wave drag. A set of linear equations is solved for the perturbation coefficients that minimize the drag. In the design mode, the wave drag is evaluated using 5 roll angles and 50 longitudinal cuts.

In an application of the volume wave drag option with a fixed wing-body volume of 1139.5 m^3, the volume wave drag (5 roll angles) was reduced from $D/q = 1.501$ to 1.370 m^2, figure 10. In this case, 13 thickness constraints were used. The resulting fuselage and wing sections are shown on figure 11 and the volume wave drag versus Mach number on figure 12. The wing and fuselage were treated as a single wing-like component. When the components were treated separately, the lowest C_{D_W} value obtained by successive optimizations of the fuselage and wing was 0.002044 compared to the 0.001765 value of figure 10.

In an application of the total wave drag option with a fixed wing body volume of 1009.9 m^3, the total pressure wave drag (5 θ) was reduced at C_L = 0.1 from D/q = 2.652 to 2.521 m^2, figure 13. Fourteen (14) thickness constraints were used for this case. The resulting fuselage and wing sections are shown on figure 14. With either option, the optimizer reduced the thickness ratio of wing sections to the minimum allowed (0.025) just outboard of the wing fuselage juncture at η = 0.0835.

LOWER BOUND DRAG

The 100% leading edge suction airplane drag is obtained from predictions of wave drag due to volume and lift, and vortex drag. The 100% suction drag due to lift is evaluated from this information as follows

$$C_{D_L}(100\%\ \text{LES}) = C_{D_{\text{WAVE LIFT+VOL}}} - C_{D_{\text{WAVE VOL}}} + C_{D_{\text{VORTEX}}}$$

An alternative estimation procedure is to evaluate the strength of the leading edge singularity from calculated chordwise net pressure distributions. These independent predictions of drag-due-to-lift are compared on figure 15. The analysis program calculation of the 0% LES drag due to lift is considered more accurate due to inclusion of nacelle effects. The far field evaluation of the 100% suction drag due to lift is regarded as more accurate based on comparison with exact conical solution for delta wings.

LEADING EDGE SUCTION ESTIMATION

A correlation was made of available low speed supersonic transport data on leading edge suction. The framework for the correlation used 0% and 100% LES curves for a cambered and twisted plate calculated by a variant of the analysis program discussed earlier (ref. 6). The leading edge suction parameter S has the value 0.0 at 0% LES and 1.0 at 100% LES. With leading and trailing edge flaps undeflected and based on wind tunnel data in the freestream Reynolds number ($R_{e\bar{c}}$) range 2.5 x 10^6 to 13.6 x 10^6, correlated S values of 0.3 to 0.4 were obtained. With leading edge flaps deflected and based on data in the freestream Reynolds number range 2.5 x 10^6 to 6.0 x 10^6, correlated S values approaching 0.9 were obtained. The low speed S value variation with C_L is indicated by the symbols at Mach number 0.2 on figure 16. Full scale freestream Reynolds number based on $\bar{c}$ is 1.3 x 10^8 at Mach number 0.2.

Exploratory calculations were made at higher speeds using the Carlson-Mack LES correlation (ref. 9) and leading edge radii at span stations $\eta = 0.15$ and 0.70 on the RB-1 wing for lift coefficients of 0.1 and 0.25. This correlation uses chords and leading edge radii on sections normal to the leading edge. Correlated data shown (ref. 9) are in the normal Reynolds number (Re_{cn}) range 0.4×10^6 to 6.0×10^6. With leading and trailing edge flaps undeflected, S values are shown on figure 16 for $C_L = 0.25$ at Mach number 0.9 and 2.7 and for $C_L = 0.1$ at Mach number 2.7. These point values fall above and below the integrated correlated curves. Full scale normal Reynolds numbers are in the range 0.6 to 2.6×10^8.

In either of these correlations, the extrapolation with Reynolds numbers from the wind tunnel data base to full scale is from 10^6 to 10^8 or two orders of magnitude.

Estimated S values based on these correlations are shown as solid lines on figure 16 and were used to obtain the estimated drag due to lift curves shown as dashed curves on figures 17, 18, and 19 and versus Mach number on figure 20.

DESIGN STATUS

Nacelles were integrated into the RB-1 configuration with a drag penalty of roughly 77% of the nacelle skin friction drag, figure 21.

Several different 0% LES comparisons have been made with the AST-102 baseline, figure 22. In the first, the geometry was provided by NASA and the AST-102 was analyzed by Rockwell analysis codes. Results are the first line of numbers shown on figure 22. The drag due to lift value C_{D_L} is suspect since the analysis program does not reproduce design results when geometry is transferred as ordinates rather than slopes. The twist constrained basic design program was run on the AST-102 planform to obtain $C_{D_L} = 0.004202$, step A on figure 5. The difference between steps A and F was added to give an approximate nacelle integration penalty. Results are the second line of numbers on figure 22. An NASA/Langley AST-102 analysis was obtained at $M = 2.62$ and was adjusted to $M = 2.7$. Results are the third line of numbers on figure 22. The fairest comparison to show the effect of blending is considered to be between 0% LES L/D values of 9.614 and 9.234 or a benefit of 0.380 over the AST-102 baseline.

The 0% and 100% LES design status is summarized on figure 23. The 0% LES wing body was optimized for minimum volume wave drag. The 100% LES wing body was optimized for minimum lift-volume wave drag. Based on an estimated LES

attainable of 66%, an L/D of 10.20 is indicated at the design point. The corresponding complete trimmed drag polar is presented on figure 24.

Part of the study was a task to design a Mach number 2.2 configuration. Related to this task 0% LES analyses were carried through at Mach number 2.2 on three planforms, figure 25. 0% LES comparisons are summarized on figure 26. Geometry and data to obtain C_{D_L} for the D-77 baseline were taken from a wind tunnel data report (ref. 10). Rockwell analysis codes gave the results shown on the first line of numbers on figure 26. The twist constrained basic design program was run on the D-77 planform to obtain C_{D_L} = 0.003943 at M = 2.2, step A on figure 5. The difference between step A and F for a M = 2.2 analysis on the RB-1 was added to give an approximate nacelle integration penalty on the D-77. The wing body volume was redistributed subject to thickness constraints to minimize volume wave drag. Results are the second line of numbers on figure 26. The twist constrained basic design program was, again, rerun on the AST-102 planform to obtain C_{D_L} = 0.003276 at M = 2.2. Again the difference between steps A and F for an M = 2.2 RB-1 was added to give an approximate nacelle integration increment. The effects of blending at M = 2.2 were an 0.326 increase in 0% LES L/D over the AST-102 baseline and a 1.186 increase over the D-77 baseline.

CONCLUSIONS

1) Although planform compromises to insure good low speed characteristics tend to make achievement of high supersonic efficiency difficult, cruise L/D ratios of approximately 10.0 appear possible at a Mach number of 2.7 for a blended configuration. Careful attention must be given to wing twist and camber, wing fuselage thickness distributions, nacelle integrations, and wing leading edge suction attainment.

2) Improved determination of leading edge suction attainable at Reynolds numbers two orders of magnitude higher than covered in available published data would reduce the uncertainty of supersonic L/D estimates.

REFERENCES

1. Ray, E. J.: NASA Supersonic Commercial Air Transport (SCAT) Configuration: A Summary and Index of Experimental Characteristics. NASA TM X-1329, Jan. 1967.

2. Baber, H. T., Jr. and Swanson, E. E.: Advanced Supersonic Technology Concept AST-100 Characteristics Developed in a Baseline-Update Study. NASA TM X-72815, Jan. 1976.

3. Baber, H. T., Jr.: Characteristics of the Advanced Supersonic Technology AST-105-1 Configured for Transpacific Range with Pratt and Whitney Aircraft Variable Stream Control Engines. NASA TM-78818, March 1979.

4. Walkley, K. B. and Martin, G. L.: Aerodynamic Design and Analysis of the AST-200 Supersonic Transport Configuration Concept. NASA CR-159051, April 1979.

5. Baals, D. D., Robins, A. W. and Harris, R. V., Jr.: Aerodynamic Design Integration of Supersonic Aircraft. AIAA Paper 68-1018, 1968.

6. Bonner, E., Clever, W. and Dunn, K.: Aerodynamic Preliminary Analysis System Part I - Theory. NASA CR-145284, April 1978.

7. Bonner, E.: The Expanding Role of Potential Theory in the Design of Supersonic Aircraft. Jour. of Aircraft, vol. 8, no. 5, May 1971, pp. 347-353.

8. Lomax, H.: The Wave Drag of Arbitrary Configurations in Linearized Flow as Determined by Areas and Forces in Oblique Planes. NACA RM A55A18, 1955.

9. Carlson, H. W., Mack, R. J. and Barger, R. L.: Estimation of Attainable Leading-Edge Thrust. NASA TP 1500, 1979.

10. Radkey, R. L., Welge, H. R. and Felix, J. E.: Aerodynamic Characteristics of a Mach 2.2 Advanced Supersonic Cruise Aircraft Configuration at Mach Numbers from 0.5 to 2.4. NASA CR-145094, Feb. 1977.

- OBJECTIVE
  - IMPROVE SUPERSONIC CRUISE PERFORMANCE
- APPROACH
  - LINEAR AERODYNAMIC OPTIMIZATIONS AT M = 2.7 AND C_L = 0.10

    DRAG DUE TO LIFT AND CAMBER

    ROCKWELL DESIGN CODE BASED ON WOODWARD FINITE ELEMENT

    VOLUME WAVE DRAG AND TOTAL PRESSURE DRAG

    ROCKWELL MODAL DESIGN CODES

Figure 1.- Blended wing body study.

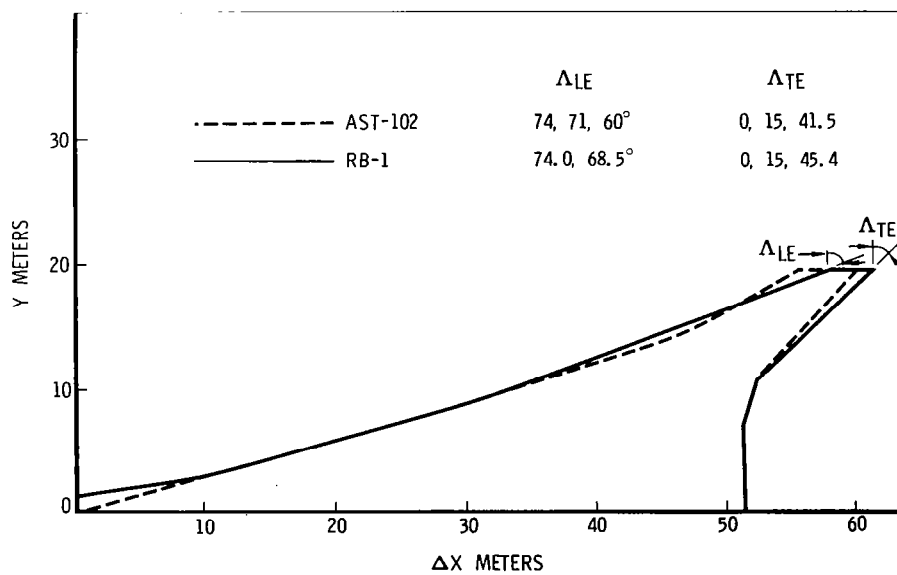

Figure 2.- Planform comparison.

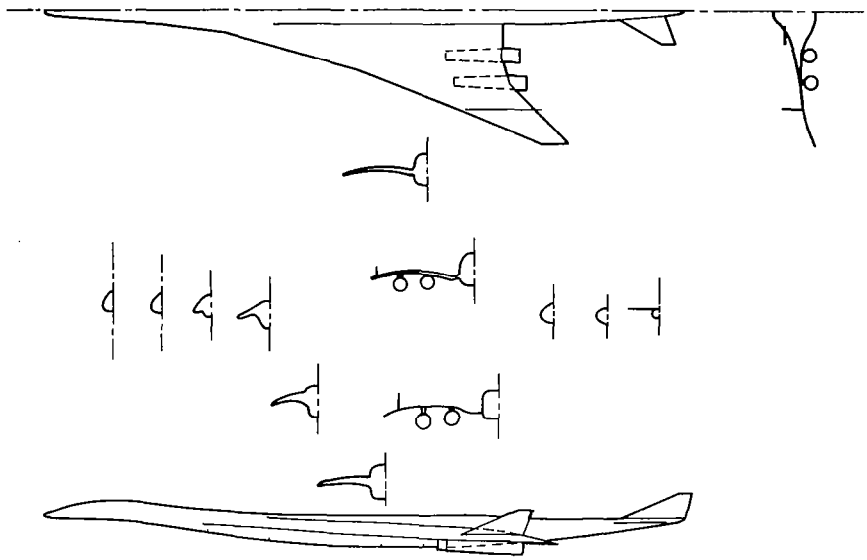

Figure 3.- Blended configuration - RB-1.

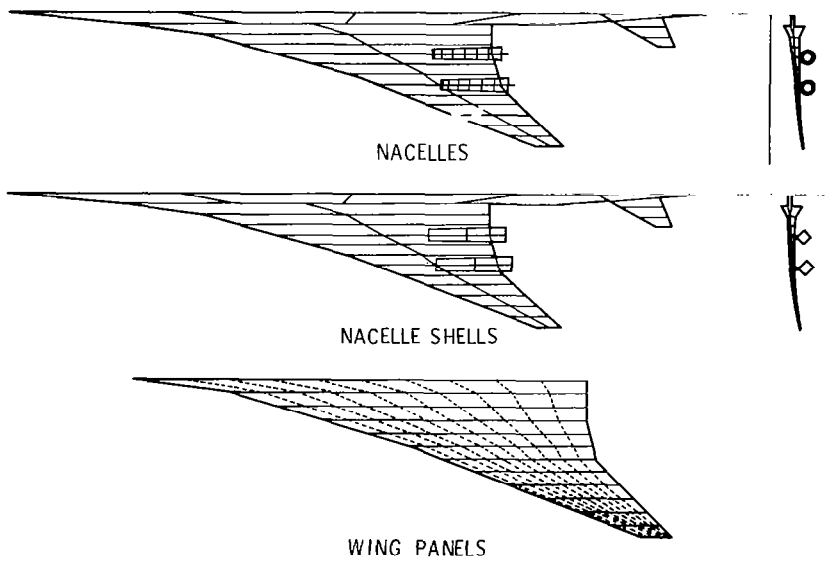

Figure 4.- Twist and camber theoretical models.

		ΔC_{D_L}*
A	BASIC DESIGN PROGRAM (NACELLES OFF)	
	TWIST CONSTRAINED NEAR PLANFORM DISCONTINUITY	0.004066
B	ANALYSIS PROGRAM (NACELLES ON)	0.004276
C	AUXILIARY DESIGN PROGRAM (NACELLES OFF)	
	NACELLE UPWASH FROM B	0.004080
D	ANALYSIS PROGRAM (NACELLES ON)	0.004300
E	INCREMENT IN TWIST AND CAMBER TO CANCEL PRESSURE DIFFERENCE BETWEEN C AND D	
F	ANALYSIS PROGRAM (NACELLES ON)	0.004146

*ZERO SUCTION, S_{REF} = 784.8 m^2

Figure 5.- Twist and camber design cycle steps — M = 2.7, C_L = 0.1.

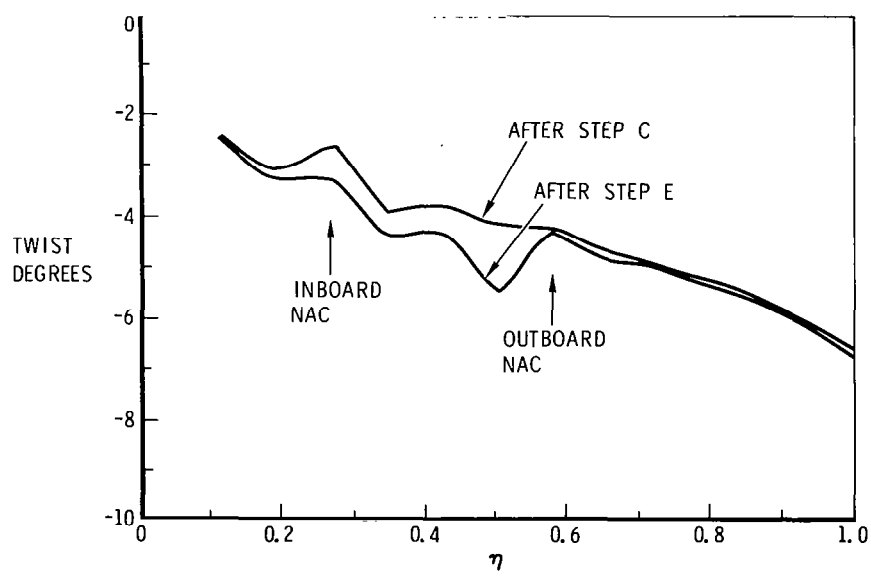

Figure 6.- Design twist — M = 2.7, C_L = 0.1.

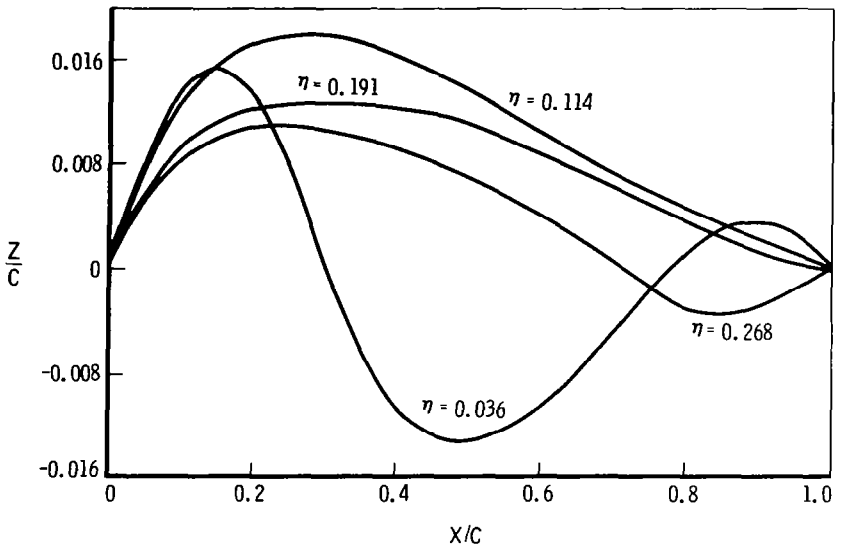

Figure 7.- Design camber — M = 2.7, C_L = 0.1.

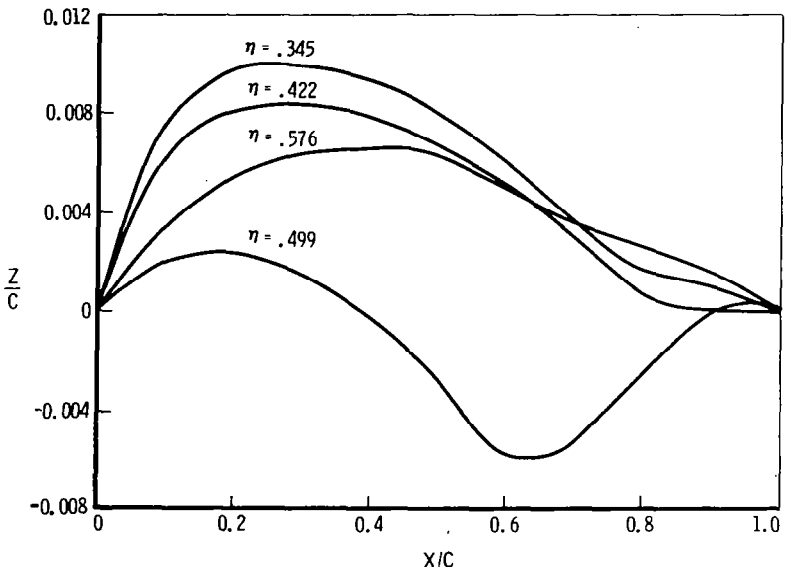

Figure 8.- Design camber — M = 2.7, C_L = 0.1.

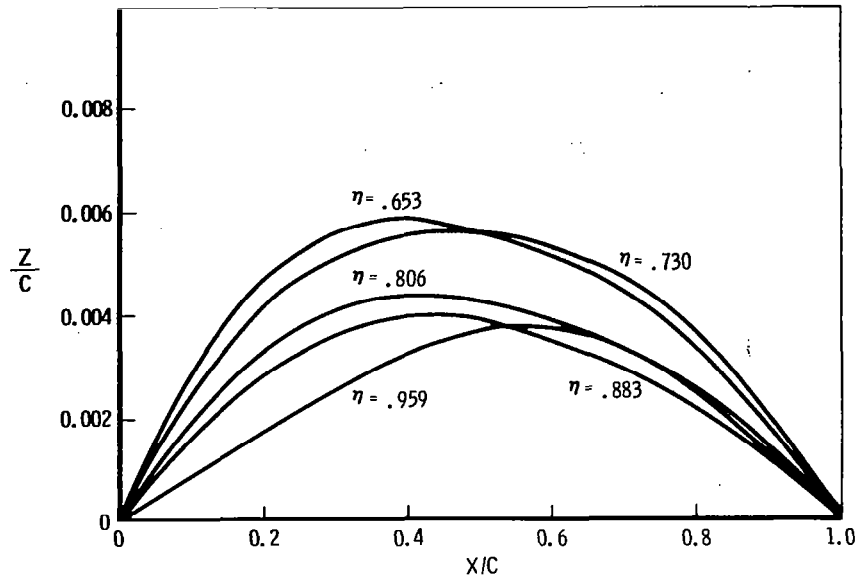

Figure 9.- Design camber — M = 2.7, C_L = 0.1.

CONSTRAINTS

η	X/C
0.0000	0.2, 0.8
0.0405	
0.0788	0.4
0.0835	0.4, 0.8
0.1538	0.4
0.2308	0.4
0.3077	0.4
0.4615	0.4
0.5385	0.4
0.6154	
0.6923	0.4
0.8462	0.4
1.0000	0.4

D/Q M²	OPT D/Q M²		ΔC_{D_W}
1.501	1.370	(5 Θ)	0.001745
	1.385	(13 Θ)	0.001765

Figure 10.- Wave drag optimization — M = 2.7, VOL_{WB} = 1139.5 m^3.

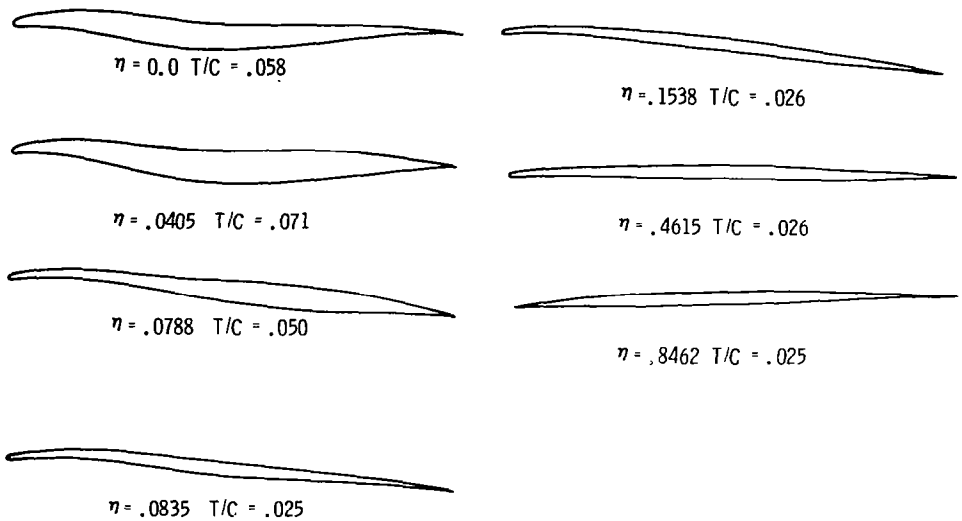

Figure 11.- Sections for minimum wave drag.

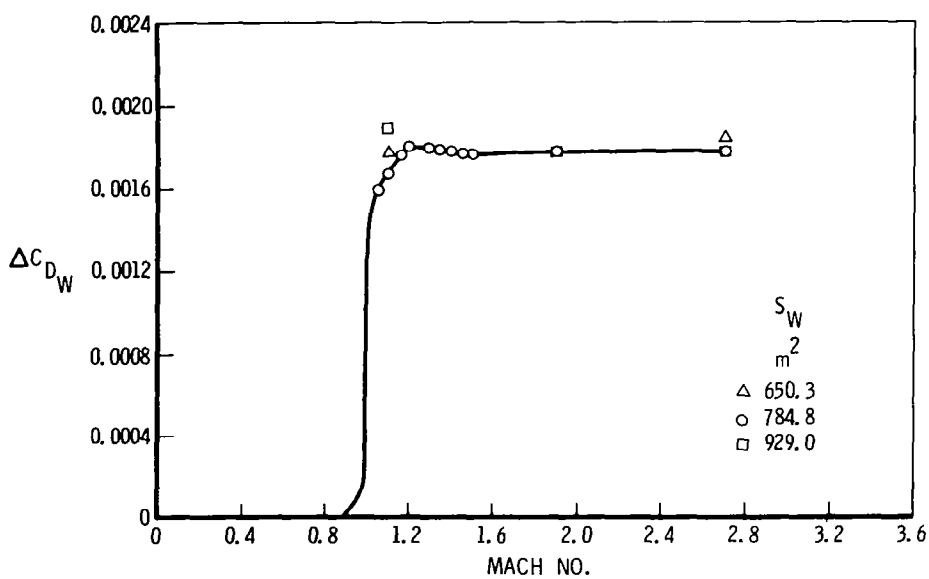

Figure 12.- Blended wing body wave drag.

CONSTRAINTS

η	X/C
0.0000	0.4
0.0405	
0.0788	0.4
0.0835	0.4, 0.8
0.1538	0.4
0.2308	0.4
0.3077	0.4
0.4615	0.4
0.5385	0.4
0.6154	0.4
0.6923	0.4
0.8462	0.4
1.0000	0.4, 0.8

D/Q M^2	OPT D/Q M^2		ΔC_{D_W}
2.652	2.521	(5 Θ)	0.003212
	2.409	(13 Θ)	0.003070

Figure 13.- Wave drag optimization — M = 2.7, C_L = 0.1, VOL_{WB} = 1009.9 m^3.

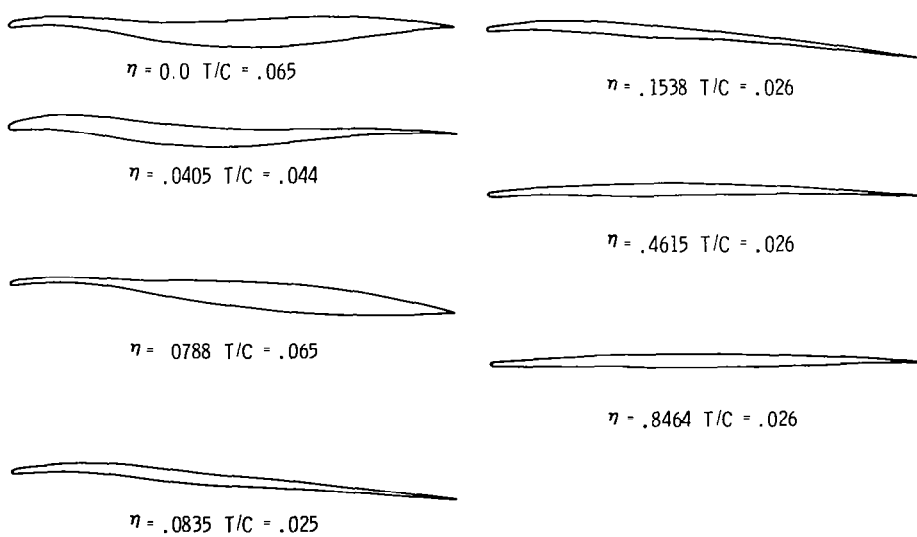

Figure 14.- Sections for minimum wave drag — C_L = 0.1.

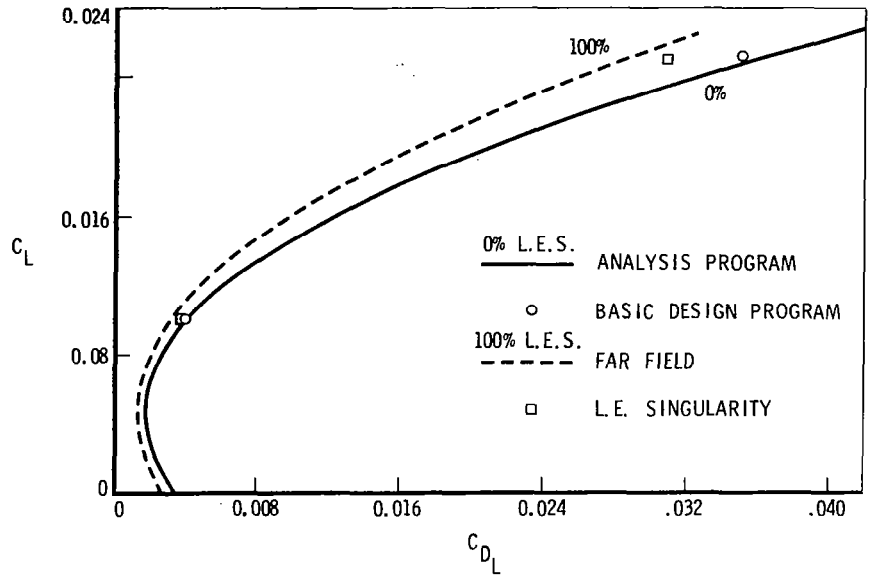

Figure 15.- Trimmed drag due to lift — M = 2.7.

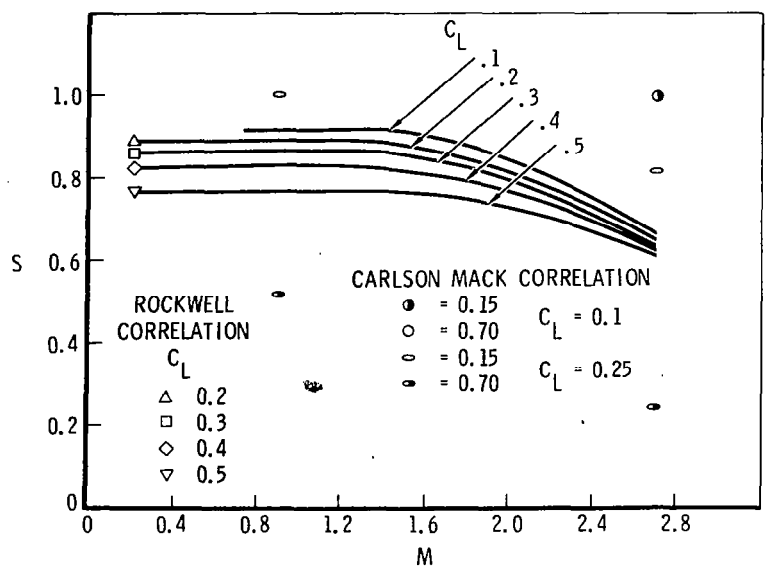

Figure 16.- Leading edge suction parameter.

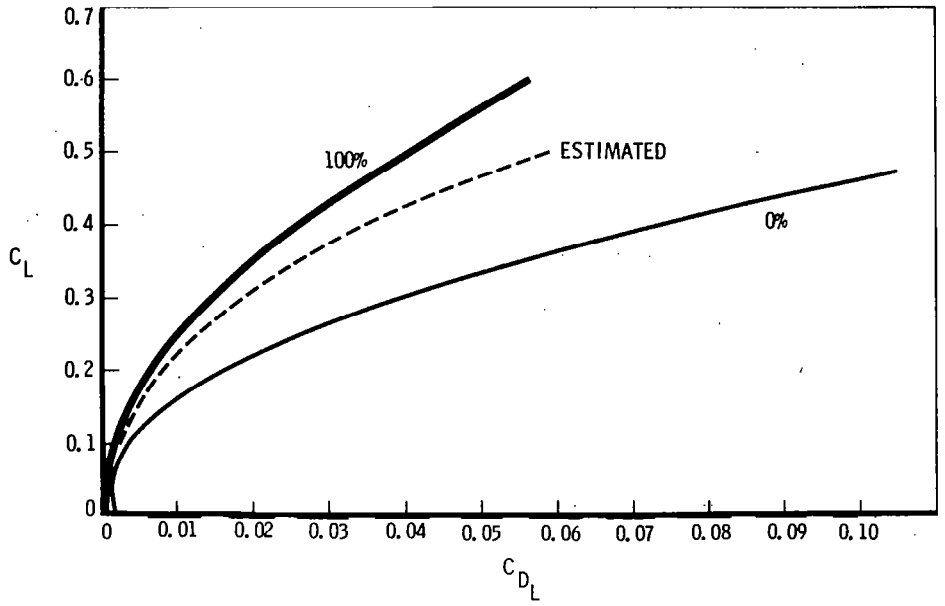

Figure 17.- Trimmed drag due to lift — M = 0.2.

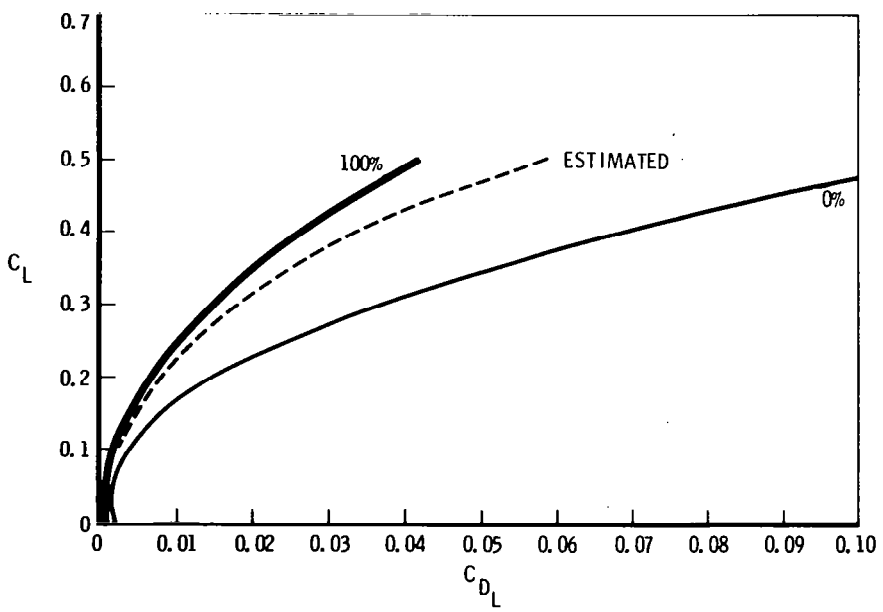

Figure 18.- Trimmed drag due to lift — M = 0.9.

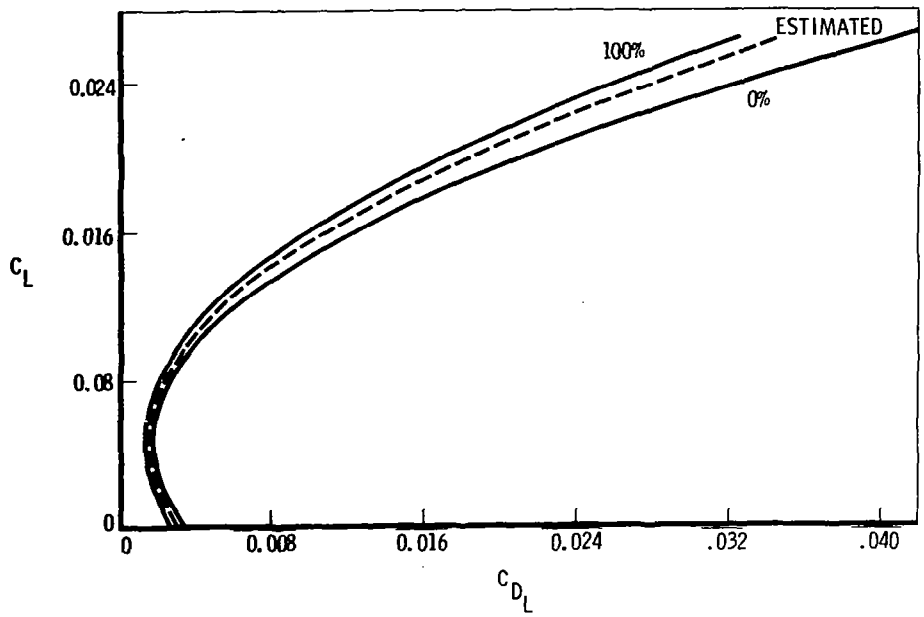

Figure 19.- Trimmed drag due to lift — M = 2.7.

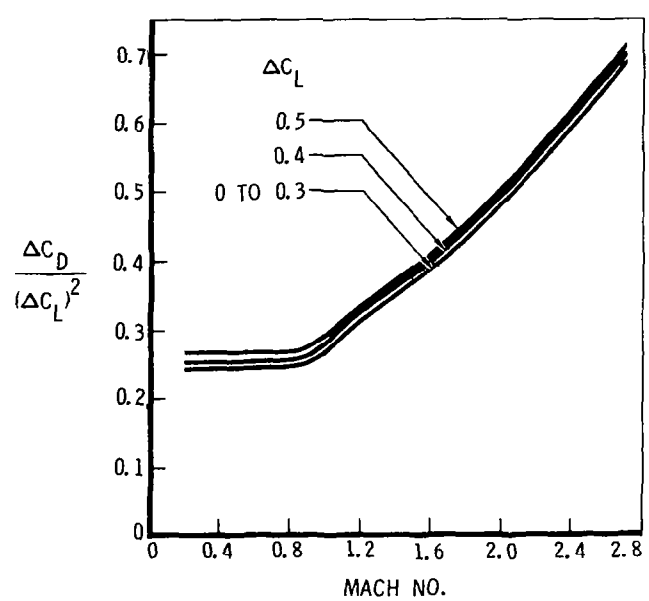

Figure 20.- Trimmed $\Delta C_D/(\Delta C_L)^2$ vs. Mach number.

ΔC_{D_F}	+0.000460
ΔC_{D_W}	-0.000186
ΔC_{D_L}	+0.000080
$\Delta C_{D_{NAC}}$	0.000354

Figure 21.- Nacelle drag increments — $C_L = 0.1$.

	C_{D_F}	C_{D_W}	C_{D_L}	C_D ROUGH MISC	L/D
AST 102	.004440(1)	.002108(1)	.004968(1)	.000	8.684
	.004440(1)	.002108(1)	.004282(2)	.000	9.234
	.004358(3)	.002038(3)	.004138(3)	.000261(3)	9.263
RB-1 BLENDED WING BODY	.004490	.001765	.004146	.000	9.614

(1) ROCKWELL ANALYSIS
(2) ROCKWELL TWIST AND CAMBER DESIGN
(3) LTV ANALYSIS ADJUSTED TO M = 2.7

Figure 22.- Zero suction blended wing body design status — $M = 2.7$, $C_L = 0.1$, $VOL_{WB} = 1139.5\ m^3$.

C_{D_F}	$C_{D_{WAVE}}$	$C_{D_{VORTEX}}$	LEADING EDGE SUCTION %	(L/D)
.004490	.003070[1] .003101[2]	.001934	100	10.533
			66	10.20
C_{D_F}	$C_{D_{VOLUME\ WAVE}}$	C_{D_L}		
.004490	.001773[1] .001760[2]	.004146	0	9.607

[1] LIFTING WAVE DRAG OPTIMIZATION

[2] VOLUME WAVE DRAG OPTIMIZATION

Figure 23.- Blended wing body design status — M = 2.7, C_L = 0.1, VOL_{WB} = 1009.1 m^3.

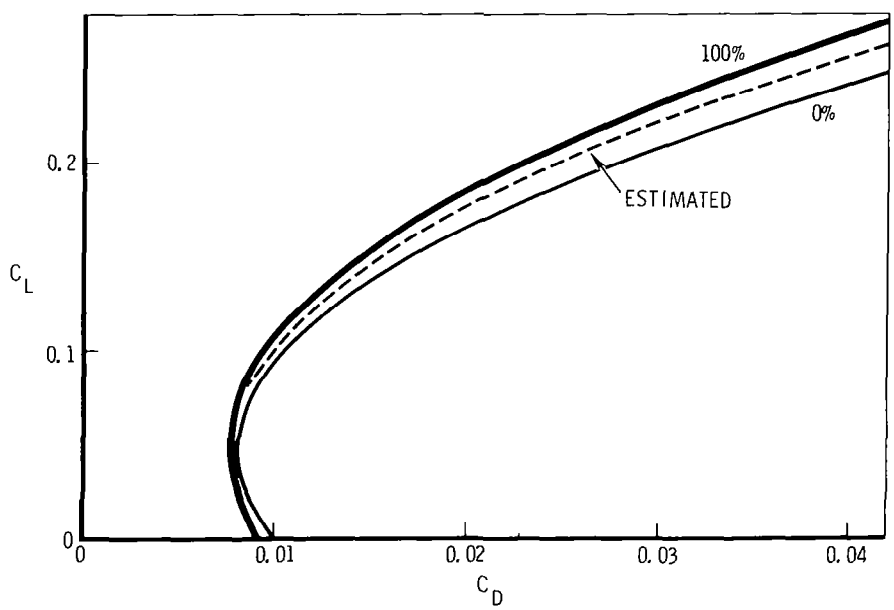

Figure 24.- Trimmed drag polars — M = 2.7.

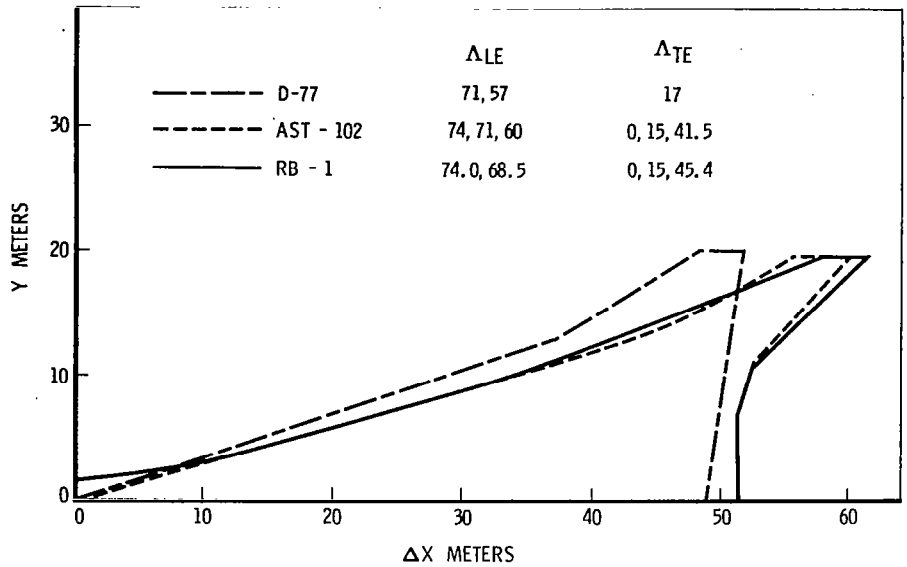

Figure 25.- Planform comparison — M = 2.2.

	VOL_{WB} M^3	S_{REF} M^2	C_{D_F}	C_{D_W}	C_{D_L}	L/D
D-77 BASELINE	1103.3	873.3	0.004710 0.004710	0.003032 0.002627**	0.004600* 0.004108**	8.102 8.737
AST–102 BASELINE	1139.5	784.8	0.004810	0.002190	0.003410**	9.597
RB–1 BLENDED WING BODY	1139.5	784.8	0.004970	0.001780	0.003328	9.923

* WIND TUNNEL MEASUREMENT

** D-77 PLANFORM ROCKWELL DESIGN CODES

Figure 26.- Zero suction blended wing body status — M = 2.2, C_L = 0.1.

PREDICTION OF NACELLE AERODYNAMIC INTERFERENCE EFFECTS AT LOW SUPERSONIC MACH NUMBERS

Robert M. Kulfan
Boeing Commercial Airplane Company

SUMMARY

A limited study is currently underway to assess the accuracy of analytical predictions of nacelle aerodynamic interference effects at low supersonic speeds by means of test versus theory comparisons. This paper presents a status report of the study.

Comparisons shown include:

- Isolated wing-body lift, drag, and pitching moments
- Isolated nacelle drag and pressure distributions
- Nacelle interference shock-wave patterns and pressure distributions on the wing lower surface
- Nacelle interference effects on wing-body lift, drag, and pitching moments
- Total installed nacelle interference effects on lift, drag and pitching moment.

The comparisons also illustrate effects of nacelle location, nacelle spillage, angle of attack and Mach number on the aerodynamic interference.

The initial results seem to indicate that the methods can satisfactorily predict lift, drag, pitching moment and pressure distributions of installed engine nacelles at low supersonic Mach numbers with mass flow ratios from 0.7 to 1.0 for configurations typical of efficient supersonic cruise airplanes.

1.0 INTRODUCTION

Mutual interference between engine nacelles and the airframe can have an important effect on the aerodynamic efficiency of a supersonic aircraft. Analytical methods exist that allow predicton of these mutual interference effects. A number of systematic analytic studies have been made to obtain an understanding of the design considerations necessary to optimize the favorable aerodynamic interference effects, (refs. 1, 2, 3, 4, 5).

The validation of the necessary design "tools" by means of test-theory comparisons is rather limited (e.g. refs. 3, 4). This is particularly true for the low supersonic speed regime. Additionally, engine spillage effects on aerodynamic interference are relatively unknown.

The National Aeronautics and Space Administration conducted an extensive wind tunnel test program to evaluate aerodynamic performance penalties associated with the propulsion system installation and operation at subsonic through low supersonic speeds. A parallel objective of this test program was to provide an experimental data base of detailed force and pressure measurements for use in systematic evaluations of analytical prediction methods. The results of the NASA experimental test program are reported in references 6 through 8.

A limited study is currently underway to assess the accuracy of the theoretical predictions of supersonic engine-airframe interference effects. The objective of this paper is to present the initial results of this study.

The NASA wind tunnel model geometry and test conditions are summarized in Section 2.0. The prediction methods being evaluated in this study are discussed in Section 3.0. A brief description of wing-nacelle aerodynamic interactions is given in Section 4.0.

Isolated wing plus body comparisons and isolated nacelle test versus theory comparisons are presented in Sections 5.0 and 6.0, respectively.

Nacelle interference pressures acting on the wing lower surface are shown in Section 7.0. Section 8.0 contains interference lift, drag and pitching moment comparisons.

The procedure that was used to calculate spillage effects on nacelle interference is described in Section 9.0. Comparisons of predicted spillage aerodynamic effects are presented in Section 10.0.

2.0 MODEL GEOMETRY AND TEST CONDITIONS

The NASA experimental program was conducted in the Ames 11- by 11-foot wind tunnel. The basic features of the nacelle-airframe interference model are shown in figure 1. The wing-body configuration is a .024 scale model of the 1971 SST. The wing-body was sting mounted with a six-component internal strain-gage balance. The left-hand wing had 126 static pressure orifices - 95 on the lower surface and 31 on the upper surface. The orifice locations are shown in figure 2. Two different nacelle geometries were tested. One set of nacelles had sharp inlets. The second set of nacelles had a slightly blunt inlet lip shape. The investigations reported in this paper concern only the sharp lip nacelles.

The tested nacelle shape is a simplified and slightly oversize representation of a typical supersonic nacelle installation, as shown in

figure 3. The nacelles were located approximately 1.2 inlet diameters below the wing chord plane. This resulted in a gap between the nacelles and the wing lower surface that does not exist in an actual nacelle/airframe installation.

The four individual nacelles were supported below the wing-body model on individual flow-through-stings. The two left-hand side nacelles (looking upstream) were pressure instrumented. The two right-hand side nacelles were mounted individually on separate six-component internal strain-gage balances. The pressure instrumented nacelles had 40 static-pressure orifices as shown in figure 2.

The six-component force balances used to support the right-hand nacelles were housed in the thickness of each nacelle. A two-shell flow-through balance located in each nacelle used four instrumented flexures located 90 deg. apart at two axial locations. The nacelle balances measured the aerodynamic forces on the external surface of the nacelle, plus the forces on a small portion of the internal duct near the inlet. The wind tunnel data corrections included removal of the estimated skin friction drag on this internal duct area.

The nacelle support system provided the flexibility of positioning the nacelles vertical, streamwise, and spanwise, relative to the wing-body combination and to each other. The range of achievable nacelle locations is indicated in figure 1. The support system also provided for independent control and measurement of mass flow through each nacelle by means of a mass-flow control plug and appropriate pressure instrumentation.

The test configurations included:

- Isolated wing-body
- Isolated nacelle
- Four nacelles in various relative positions
- Wing-body plus nacelles in various locations

The test data included:

- Wing-body lift (C_L), drag (C_D) and pitching moment (C_M) data
- Wing pressure measurements
- Lift, drag and pitching moment measurements of the individual inboard and outboard nacelles
- Nacelle surface pressures

These tested configurations provided the following measurements of isolated and interference data:

Isolated wing-body data -- measurements on wing-body without the nacelles present.

- Isolated nacelle data -- measurements on a singly tested nacelle.
- Mutual nacelle interference -- difference in nacelle measurements with and without the other nacelles present.
- Nacelle interference on wing-body -- difference in wing-body measurements with and without the other nacelles present.
- Wing-body interference on the nacelles -- difference in nacelle measurements with and without the wing-body present.
- Total wing-body plus nacelle data -- sum of wing-body data plus nacelle data.
- Spillage interference -- difference in measurements on identical configurations with the nacelles spilling according to a specific controlled mass flow ratio (MFR), and the corresponding data obtained without spillage.

The test conditions included:

Mach Number: 0.90, 0.98, 1.1, 1.15, 1.2, 1.3, 1.4

Angle of Attack: α = 0 to 6 deg.

Mass flow ratio: MFR = 0.6 to 1.0

All configurations were tested at the primary Mach numbers of 0.9, 1.15, 1.4. Some selected configurations were also tested at the remaining Mach numbers. Only a few configurations were tested at angles of attack different than zero. Configurations with spillage were tested only at zero angle of attack.

The model angle of attack was measured relative to a wing reference plane. At zero angle of attack, the model actually experiences significant negative lift.

Staggered and non-staggered arrangements were tested at six different nacelle stations and three different spanwise locations as shown in figure 4. In this paper only the "no-stagger" configuration results are presented as the staggered nacelle analyses are only currently underway.

Complete descriptions of the wind tunnel model, test conditions and available test data are given in reference 8.

3.0 PREDICTION METHODS

The aerodynamic force and moment predictions for the study reported herein have been made using the system of aerodynamic design and analysis programs described in reference 9. The aerodynamic force coefficients for a specified configuration are built up through superposition.

The drag prediction, as summarized in figure 5, includes:

- Skin friction drag, C_{D_F}, calculated using flat plate turbulent flow theory.

- Volume wave drag, C_{D_W}, -- calculated either by a far-field wave drag program (supersonic area rule) or by a near-field (surface pressure integration method) program.

- Drag-due-to-lift, C_{D_L}, which includes induced drag as well as wave-drag-due-to-lift -- calculated by a near-field analysis program.

The near-field force calculations are obtained by integration of the surface pressures (volume or lifting pressures) over each component of the configuration being analyzed. The surface pressures include the isolated component pressures plus the interference pressures acting on each component due to the other components of the configuration.

The nacelle pressure fields imposed on the surface of the wing can be calculated by either the "wrap" method or the "glance" method summarized in figure 6.

In the "wrap" method, the nacelle pressure fields and accompanying shock waves "wrap" around adjacent nacelles. In application, the pressure field generated by one nacelle is allowed to pass through another nacelle as if it were transparent. This is also the approach inherent in the far-field wave drag calculations.

In the "glance" method the pressure fields generated by one nacelle "glance" away from the wing when encountering adjacent nacelles. In application, the nacelle generated flow field is terminated on encountering another nacelle.

One of the objectives of the current study is to determine which of these methods is more nearly correct.

4.0 WING-BODY AND NACELLE INTERACTIONS

At supersonic speeds, the mutual interactions of the wing-body and the nacelles can produce significant interference effects. The nacelle installed drag is usually defined to include the drag of the isolated nacelles plus net effects of the nacelle pressure field acting on the wing-body as well as the effect of the wing-body pressure field acting on the nacelles.

Typically, the nacelle installed drag, as shown in figure 7, is calculated as the sum of the friction drag of the nacelles, the net wave drag, and the lift interference effects.

The net nacelle wave drag includes:

- Nacelle pressure drag
- Nacelle pressures acting on the wing-body volume or thickness
- The wing-body thickness pressures acting on the nacelles
- Mutual nacelle interference

The mutual nacelle interference consists of the effect of the pressure field of a nacelle acting directly on the other nacelles plus the effect of the pressure field reflecting off the wing surface back onto the nacelles.

The lift interference consists of three items:

- The nacelle pressures reflecting off the wing produce an interference lift, ΔC_L. Because of the interference lift, the wing-body incidence required to produce a specified total lift is reduced. This results in a reduction in the wing-body drag due to lift.

- The nacelle pressures acting on mean lifting surface produce a drag or thrust force.

- The wing lifting pressures produce a buoyancy force on the nacelles.

The net nacelle drag is therefore dependent not only on flight conditions and the shape of the nacelles but also on the shape and location of adjacent components of the airplane.

The near field methods described in the previous section calculate each of these contributions to the total nacelle installed drag. The NASA nacelle/airframe interference test described in Section 2 provides an extensive data base of experimentally determined measurements of these contributions to the total nacelle installed drag.

In the sections that follow, test versus theory comparisons provide an indication of the accuracy of the theoretical predictions of the various lift, drag, and pitching moment components with and without spillage.

5.0 ISOLATED WING-BODY COMPARISONS

Figures 8 through 14 contain comparisons of the predicted aerodynamic characteristics of the isolated wing-body configuration.

Drag predictions at zero-lift were made using both the far-field (area-rule) and near-field methods. The drag predictions for this wing-body configuration using the far-field theory wave drag estimates agree very well

with the test data. The near-field theory appears to slightly overestimate the wing-body zero-lift wave drag.

The predicted drag polars are shown in figures 9 and 10 for Mach 1.4 and 1.15, respectively. The near-field zero-lift wave drag estimates were used in these predictions. The main difference between the theoretical and experimental drag polars is the overestimated drag at zero lift. The predicted and experimental polar shapes are nearly the same.

The theoretical lift and pitching moment curves are compared with test data in figures 11 and 12. The theoretical lift curves agree very well with the test data.

The zero-lift pitching moment predictions agree fairly well with the test data. The differences in the slopes of the pitching moment curves indicate that theory predicts the aerodynamic center too far aft.

Figures 13 and 14 summarize the wing-body lift and pitching moment characteristics from subsonic through low supersonic Mach numbers. These figures also contain test data obtained by Boeing on the same model prior to the NASA nacelle-airframe interference test program. The subsonic predictions shown in the figures were obtained by a Boeing in-house aerodynamic influence coefficient method.

The good agreement between the theoretical and experimental drag polars and lift curves indicates that the theory should predict the reductions in wing-body drag-due-to-lift associated with the nacelle interference lift (described in section 4.0).

6.0 ISOLATED NACELLE COMPARISONS

Theoretical predictions of the surface pressure distributions and zero-lift drag of the isolated nacelle are compared with the test data shown in figure 15.

Nacelle wave drag estimates were made using both the far-field and near-field methods. The theoretical predictions agree with the test results at Mach 1.3 and 1.4. The near-field estimates are slightly better than the far-field estimates. Theory overestimates the nacelle drag at Mach 1.2 and below.

The nacelle pressure distribution shown in figure 15 at Mach 1.4 closely matches the test data. At Mach 1.15, theory overestimates the expansion (i.e., negative) pressures on the nacelle boattail. This leads to the overestimation of drag at the lower supersonic Mach numbers. The pressure at the first station at both Mach numbers is less than theory. This is probably due to nacelles actually spilling a small amount of flow at the test conditions.

The near-field method has been used for wave drag predictions in the remainder of the analyses presented in this paper.

7.0 NACELLE INTERFERENCE PRESSURES ON THE WING

Theoretical nacelle shock wave patterns and interference pressures on the wing are compared with test data for one of the aft nacelle locations in Figures 16 and 17.

The experimental interference pressures were obtained as the difference in the wing lower surface pressures with and without the nacelles present.

The interference pressures were calculated by both the "wrap" method and "glance" method described in section 3.0.

The predicted nacelle bow shock locations agree well with the experimental shock locations as indicated by a sudden "jump" in interference pressures, C_{P_I}, from zero to some large positive value.

The interference pressures predicted by the "glance" method agree reasonably well with the experimental data. The theoretical bow shock strength is larger than indicated by the test data. This may be the result of a shock-boundary layer interaction softening this initial sudden pressure rise.

The additional pressure peaks predicted by the "wrap" method are not evident in the test data in either figures 16 or 17. These and similar results obtained, with the nacelles located in different streamwise locations below the wing, indicate that the "glance" method of nacelle pressure field superposition is more realistic than the "wrap" method. Consequently, all of the remaining results to be shown in this paper were obtained by the "glance" method.

Figures 18 and 19 contain comparisons of predicted shock wave patterns and interference pressure fields with test data for a forward nacelle location in which the outboard nacelle is near the wing leading edge. In this nacelle arrangement, the wing experiences not only the bow shocks from the nacelles, but also aft shocks. The aft shocks arise from the flow compression at the aft end of the nacelle where the flow-through-sting enters the nacelle shell.

The predicted and measured interference pressures for this wing-body-nacelle arrangement agree quite well except in local areas near the aft shock and also at the most outboard station.

In Reference 10 it is shown that flow across a glancing shock wave, in which the flow is deflected in the plane of the wing, will separate if the pressure rise across the shock wave exceeds 50%. Furthermore, it is shown that a local negative pressure field on the wing can amplify the pressure rise across a shock wave.

The calculated pressure rises across the nacelle bow shocks shown in Figures 18 and 19 are in the order of 25 to 30 percent. This should not cause separation. Indeed, the experimental bow shock data give no indication of separation.

The aft shock waves from the nacelle are much stronger because of the large boattail angle at the aft end of the nacelle. Furthermore, the nacelle area reduction along the boattail produces theoretically large negative expansion pressure just upstream of the aft shock waves. This local negative pressure field further amplifies the strength of the already strong aft shocks. Consequently, the pressure rise across the aft shocks varies from 60 percent to 100 percent across the wing. Thus, boundary layer separation is most certain to occur in the area of the aft shocks. The differences in the experimental and theoretical pressures near the aft shocks is probably due to shock induced boundary layer separation.

These results demonstrate the importance of limiting the strength of nacelle-created shock waves likely to interact with a wing, particularly in areas of local negative pressures.

8.0 INTERFERENCE LIFT, DRAG, AND PITCHING MOMENT

Comparisons are made in Figures 20 and 21 between calculated nacelle contributions to lift, drag, and pitching moment with the corresponding test data.

The drag comparisons include the nacelle interference on the wing-body as well as the total nacelle installed drag. The theoretical drag predictions agree well with the test data. The nacelle interference on the wing-body is favorable and increases with lift coefficient. This is primarily due to the reduction in wing-body drag-due-to-lift associated with the nacelle interference lift.

Theoretical interference lift and pitching moment increments are calculated from the nacelle interference pressure fields (discussed in the previous section) acting on the wing lower surface. The experimental lift and pitching moment data indicate that the nacelles also experience a change in lift and hence pitching moment when located in the wing lower surface pressure field. The effect of wing-body pressures on nacelle lift is not considered in the theoretical calculations.

The measured interference lift increment increases with angle of attack. The theoretical interference lift calculations shown in Figures 20 and 21 were made at a constant local Mach number equal to the free-stream Mach number. Slender body theory estimates were subsequently made to explore the effect of local Mach number on interference lift. The results of these slender body theory estimates are shown in Figure 22.

A negative pressure field in the area of the nacelles, corresponding to a local Mach number greater than free stream, reduces the interference lift. Conversely, a positive pressure field, or lower local Mach number, enhances the interference lift. The effect of the local pressure field on the interference lift is seen to be greatest at the very low supersonic Mach numbers. The calculated effects of local pressure field on interference lift are consistent with the experimental results shown in Figures 20 and 21.

As a result of the favorable interference effects, the total nacelle drag is less than friction drag at the higher lift coefficients for the analyzed configuration arrangement.

The effect of nacelle location on aerodynamic interference is shown in Figures 23 and 24. Nacelle location is seen to have a powerful effect on the nacelle interference. At the aft nacelle locations, both the interference of the nacelles on the wing-body and the wing-body on the nacelles are favorable. The nacelles in the aft locations produce a substantial level of favorable interference. As the nacelles are moved forward, both of these interference components become unfavorable. This results in considerable net unfavorable interference. The predicted interference effects agree reasonably well with the test data, but become less accurate at the most forward location, where the outboard nacelle moves in front of the wing leading edge.

9.0 SPILLAGE INTERFERENCE CALCULATION PROCEDURE

The results that have been presented in the sections thus far correspond to engine operation without spillage (i.e., mass flow = 1.0). The effects of nacelle spillage (mass flow ratios as low as 0.7) on the interference forces were also investigated in the NASA nacelle-airframe interference test program. Experimental measurements, however, were only obtained at zero angle of attack. As previously mentioned, the wing-body produces considerable negative lift at this attitude.

The mass flow through each nacelle was varied by a control plug in the corresponding flow-through-sting. At supersonic speeds a normal shock forms in front of the nacelle and moves progressively upstream as the mass-flow ratio through the nacelle is reduced.

To calculate spillage effects on the nacelle pressure distribution, the capture streamtube that separates the flow into the inlet from the flow that spills around the inlet is replaced by a solid surface in the mathematical analyses. A simple approach was used in this study to calculate the inlet streamtube shape for spillage behind a normal shock. The method developed by Moeckel (Ref. 11) was used to calculate both the distance of the normal shock forward of the spilling nacelle and the capture streamtube radius at the normal shock. The shape of the capture streamtube was then represented as shown in Figure 25 by a simple polynomial equation. The calculated streamtube shape grows with zero initial slope ($dr/dx = 0$) at the normal shock to match the inlet radius at the nose of the nacelle.

The presence of the capture streamtube changes the pressure distribution over the nacelle. Relative to a non-spilling nacelle, a large expansion occurs at the lip of the nacelle due to the capture streamtube shape at the inlet. This decreases the pressure near the front of the nacelle, thereby reducing the isolated nacelle drag. The isolated nacelle drag reduction is typically called "lip suction".

The presence of the capture streamtube changes the interference effects associated with the nacelle pressures acting on the wing-body, as well as on the isolated nacelle and the adjacent nacelles. The capture streamtube does not support a force across its surface. Consequently, in the analyses, only the pressures acting on the nacelle surface contribute directly to drag on the nacelle. Hence, the wing-body interference acting on the nacelles is unchanged by spillage.

10 SPILLAGE EFFECTS ON AERODYNAMIC INTERFERENCE

Streamtube shapes calculated by the method described in the previous section are shown in figures 26 and 27 for a range of mass flow ratios at Mach 1.4 and 1.15, respectively. The calculated shapes indicate rather large changes in the streamtube area occur over short distances relative to the smooth shape of the nacelle.

Figures 28 and 29 contain comparisons of predicted and measured isolated nacelle pressure distributions for different amounts of spillage. Reductions in mass flow ratio cause a decrease in local pressures on the forward section of the nacelle. The experimental pressure reduction is greater than predicted by the theory particularly at the lowest mass flow ratio (i.e., greatest spillage). This is probably because the theoretical analysis treats the capture streamtube as a solid shape in a supersonic flow field, whereas the actual nacelle experiences a complicated mixed subsonic-supersonic flow field.

The experimental data in Figure 30 show large reductions in isolated nacelle drag associated with the reduced nose pressures.

Slender body theory estimates of the effect of spillage on interference lift are shown in Figure 31. The slender body theory calculations of interference lift depend only on the net area change of the capture streamtube and not the shape. The trends predicted by the slender body theory estimates agree well with the test data.

Calculated shock wave patterns and nacelle pressure distributions on the wing are compared with test data for the nacelles with and without spillage at Mach 1.4 and 1.15 in Figures 32 and 33, respectively. These calculations were made with the streamtube geometries shown in Figure 26.

The predicted effect of spillage on nacelle bow-shock locations agrees with the test data. The predicted effects of spillage on the interference pressures on the wing are in fair agreement with the test results. The corresponding interference lift and pitching moment data are shown in Figure 34. Spillage is seen to have a rather large effect on the interference lift.

Figure 35 contains comparisons of calculated nacelle interference drag with test data for different mass flow ratios (i.e., amounts of spillage). The drag of the isolated nacelle, measured at the average mass flow for the

nacelles at each nominal test condition, was removed from the corresponding measured total wing-body-nacelle drag. Similarly the theoretical interference drag predictions do not include the calculated isolated nacelle drag.

The interference of the nacelle pressure field acting on the wing-body produces nearly all of the large favorable interference for this configuration arrangement. Increased nacelle spillage, which corresponds to reduced engine mass flow, has only a small effect on the net interference drag at a fixed angle of attack. For example, a more favorable interference drag increment of 2 counts (ΔC_D = -.0002) is indicated relative to the no-spilling condition for a mass flow ratio of 0.6. The test data, which includes only the nacelle interference on the wing-body, agree quite well with the predictions.

As previously mentioned, nacelle spillage has a rather large effect on the interference lift. Hence, the effects of spillage on net wing-body plus nacelle interference should become more significant when comparisons are made at constant total lift. Figure 35 contains predictions of the net wing-body plus nacelle interference variations with lift coefficient for different amounts of spillage. The favorable interference indeed becomes greater as lift is increased. For example, the nacelles with a mass flow ratio of 0.6 are predicted to produce a favorable interference drag increment of approximately 7 counts (ΔC_D = -.0007) relative to the nacelles without spillage at a lift coefficient of 0.2.

The combined effects of the increased favorable interference at lifting conditions (Fig. 35) plus reduced isolated nacelle drag (Fig. 30) can result in a total nacelle installed drag less than zero. This occurs, for example, for lift coefficients greater than 0.12 for an engine mass flow ratio of 0.6 (i.e., 40% spillage) at Mach 1.4. This is the approximate mass flow ratio of a supersonic inlet (Mach 2.4 to 2.7) operating at transonic speeds.

11.0 CONCLUDING REMARKS

"No-Spillage" Conclusions:

- Far-field and near-field methods adequately predict wing plus body aerodynamic characteristics.
- Far-field and near-field predictions of the isolated nacelle drag are good at Mach 1.4. The drag predictions at Mach 1.15 are higher than the test results because of an overestimate of the nacelle boattail pressures.
- The "glance" method of nacelle pressure field superposition is more accurate than the "wrap" method.
- The locations of nacelle shocks are predicted accurately by the theory.

- Predictions of nacelle interference pressures on the wing are good except in local areas near strong shocks where separation occurs.

- Predictions of Mach number, nacelle location and angle of attack on nacelle aerodynamic interference are good, but become less accurate as the nacelles are moved forward of the wing leading edge.

- With the nacelles located aft near the wing trailing edge, the favorable interference effects of the nacelle on the wing-body become increasingly large as C_L increases. The net installed drag, both measured and calculated, was less than skin friction drag.

"With Spillage" - Conclusions

- The analysis method developed in the study does not properly account for spillage effects on the isolated nacelle pressure distribution near the lip. Consequently, the method overpredicts the drag of the isolated nacelle with spillage.

- The method predicts the forward movement of the nacelle bow shocks on the wing due to spillage.

- The method adequately predicted spillage interference effects on lift, drag and pitching moment at zero angle of attack and Mach = 1.4.

- The predicted spillage interference effects are favorable and improve with lift coefficient. With spillage, the nacelle installed drag can be less than zero due to the reduction in isolated nacelle drag, plus the increased favorable lift interference.

These initial results seem to indicate that satisfactory methods are available to predict interference lift, drag, pitching moment and pressure distributions of intalled engine nacelles at Mach 1.15 and 1.4 with mass flow ratios from 0.7 to 1.0 for configurations typical of efficient supersonic cruise airplanes.

REFERENCES

(1) Swan, W. C.: Aerodynamics of Powerplant Installation, Part II, AGARDograph 103, October 1965

(2) Nichols, M. R.: Aerodynamics of Airframe-Engine Integration of Supersonic Aircraft, NASA TND-3390, 1966

(3) Sigalla, A; Hallstaff, T. H.: Aerodynamics of Powerplant Installation on Supersonic Aircraft, Journal of Aircraft, July-August 1967, pp 273-277

(4) Kane, E. J.; and Middleton, W. D.: Considerations of Aerodynamic Interference in Supersonic Airplane Design, AGARD Conference on Aerodynamic Interference, Proceedings No. 71, paper 3, September 1970

(5) Bencze, D. P.: Nacelle-Airframe Interference at Low Supersonic Mach Numbers, AIAA Paper No. 72-1113, November 1972

(6) Bencze, D. P.: Wind Tunnel Investigation of Nacelle-Airframe Interference at Mach Numbers of 0.90 to 1.4 - Data Report - Force Data, NASA TM X-62, 489, 1976

(7) Bencze, D. P.: Wind Tunnel Investigation of Nacelle - Airframe Interference at Mach Numbers of 0.9 to 1.4 - Data Report - Pressure Data, Volume I - NASA TM X-73, 149, Volume II - NASA TM X-73, 088, 1976

(8) Bencze, D. P.: Experimental Evaluation of Nacelle-Airframe Interference Forces and Pressures at Mach Numbers of 0.9 to 1.4, NASA TM X-3321, March 1977

(9) Middleton, W. D.; Lundry, J. L.; and Coleman, R. G.: A Computational System for Aerodynamic Design and Analysis of Supersonic Aircraft, Part 2 - User's Manual, NASA CR-2716, August 1976

(10) Kulfan, R. M.; Sigalla, A.: Real Flow Limitations in Supersonic Airplane Design, Journal of Aircraft, Vol 16, No. 10, pp 645-658, October 1979

(11) Moeckel, W. E.: Approximate Method for Predicting Form and Location of Detached Shock Waves Ahead of Plane or Axially Symmetric Bodies, NACA TN 1921, June 1949

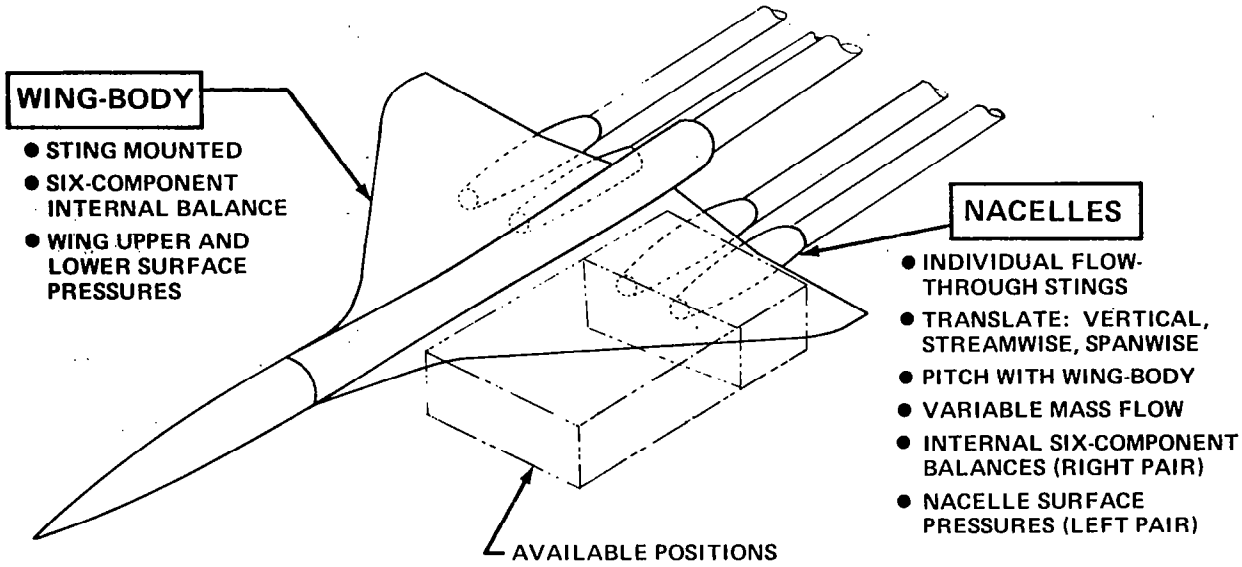

Figure 1.- NASA-Ames nacelle/airframe interference model features.

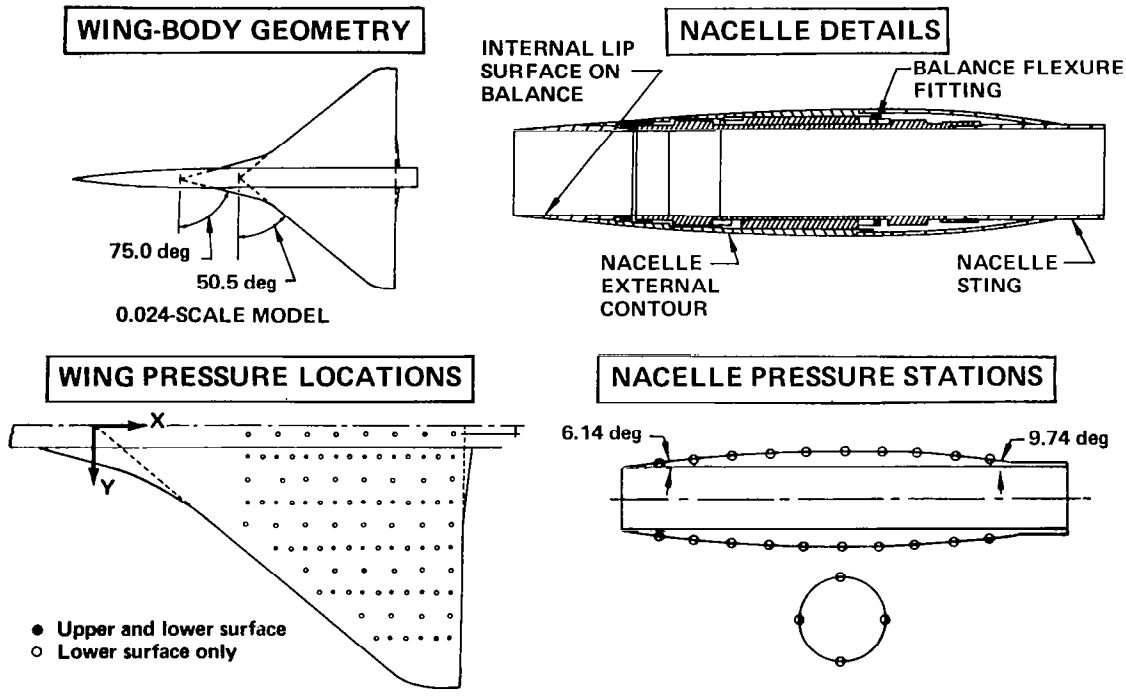

Figure 2.- Wind tunnel model details.

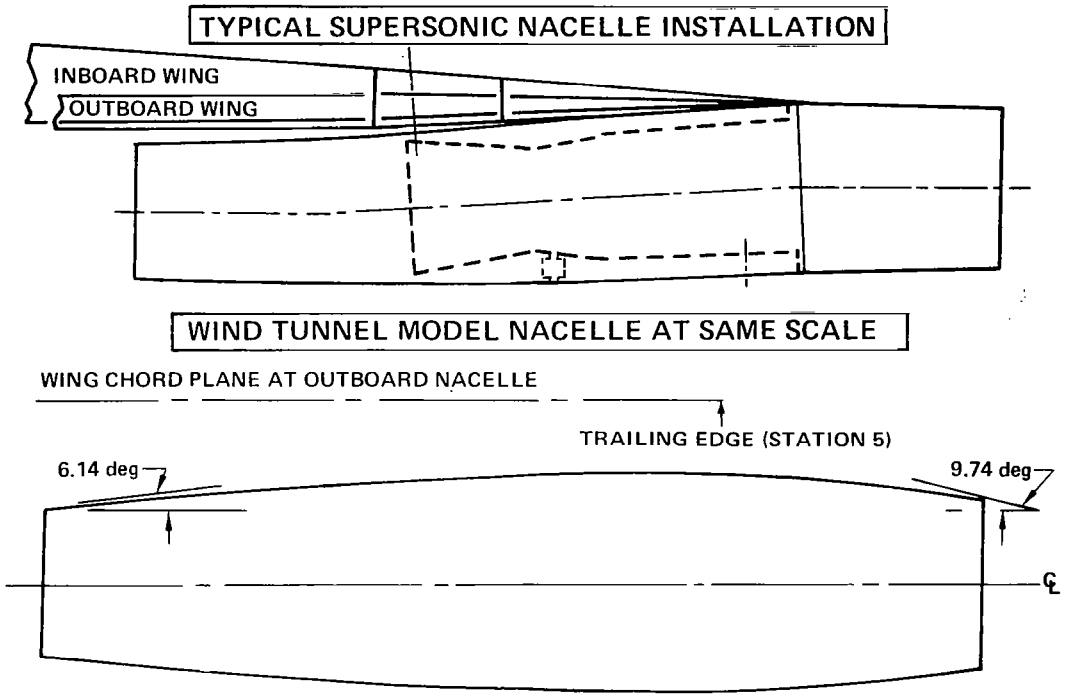

Figure 3.- Nacelle geometry comparison.

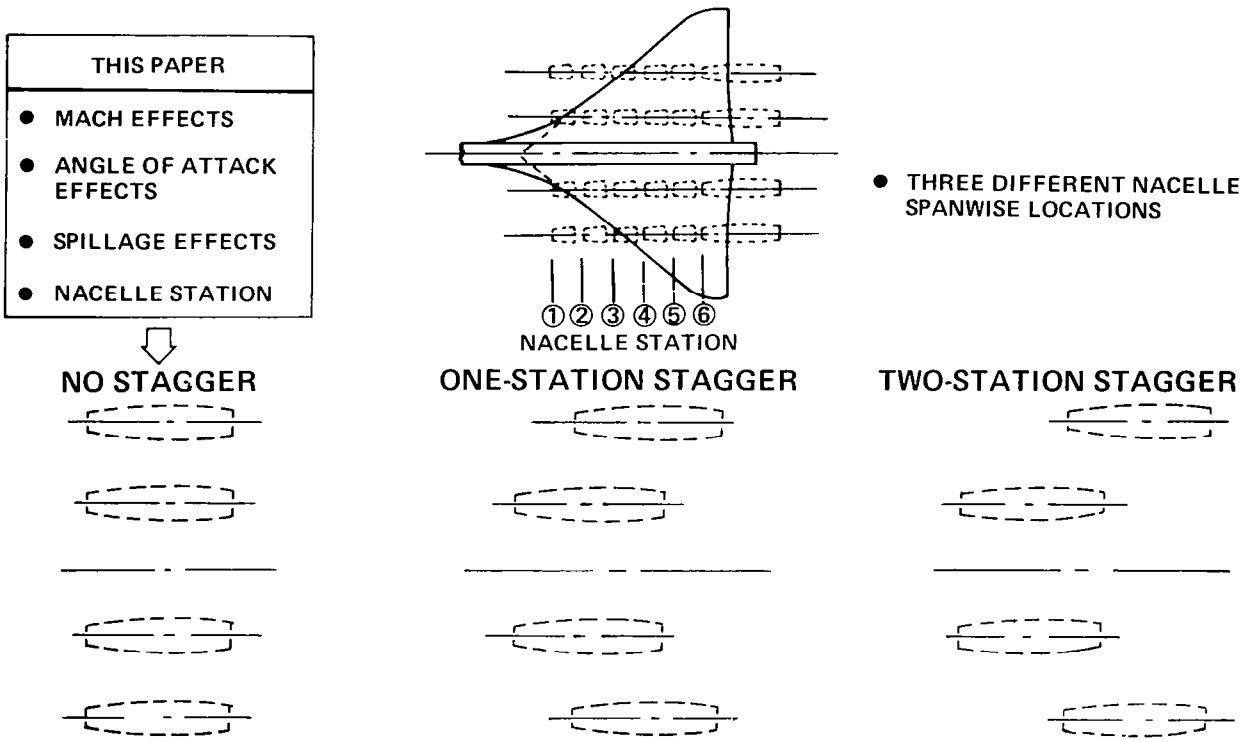

Figure 4.- Tested nacelle locations.

DRAG COMPONENT	METHOD [a]	NACELLE PRESSURE FIELD REPRESENTATION				
		INLET MACH NUMBER		THEORY	PRESSURE FIELD SUPERPOSITION	
		M_∞	M_{LOC}		"WRAP"	"GLANCE"
C_{D_F}–FRICTION DRAG	●SOMMER AND SHORT T* METHOD	●	X	———	——	——
C_{D_W}–VOLUME WAVE DRAG	●FAR-FIELD THEORY (AREA RULE) PROGRAM	●		LINEAR	●	
	●NEAR-FIELD THEORY PROGRAM	●		"WHITHAM"	●	●
C_{D_L}–DRAG DUE TO LIFT	●LIFT ANALYSIS PROGRAM	●	X	"WHITHAM"	●	●

X–CAPABILITY
●–USED IN THIS STUDY

[a] MIDDLETON/CARLSON–SUPERSONIC AERODYNAMIC DESIGN AND ANALYSIS SYSTEM

Figure 5.- Drag prediction methods.

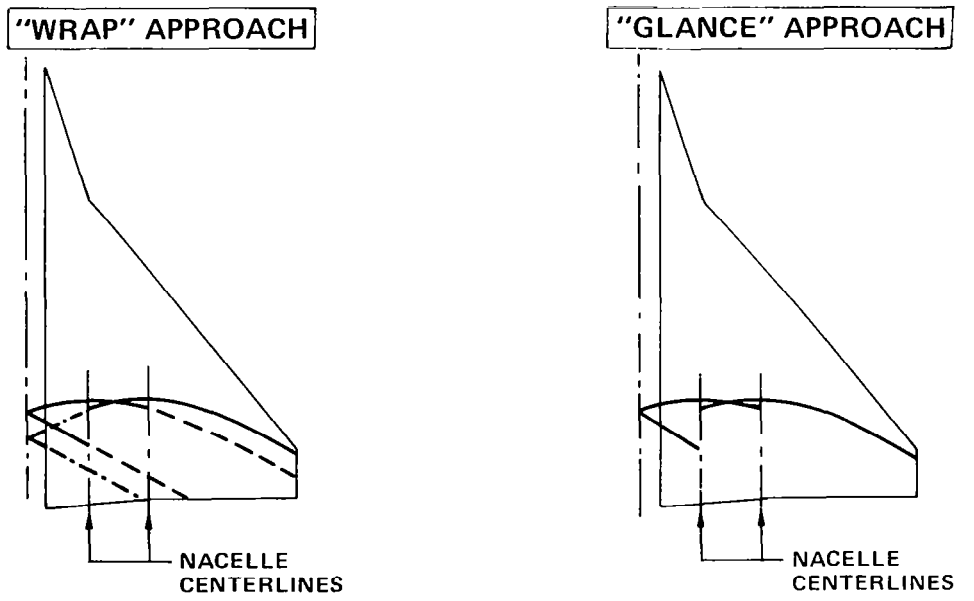

- SHOCKS AND PRESSURE "WRAP" AROUND NACELLES ADJACENT TO OUTER WING
- FAR-FIELD APPROACH

- SHOCKS AND PRESSURES "GLANCE" AWAY FROM WING AT ADJACENT NACELLES

Figure 6.- "Glance" and "wrap" pressure fields superposition.

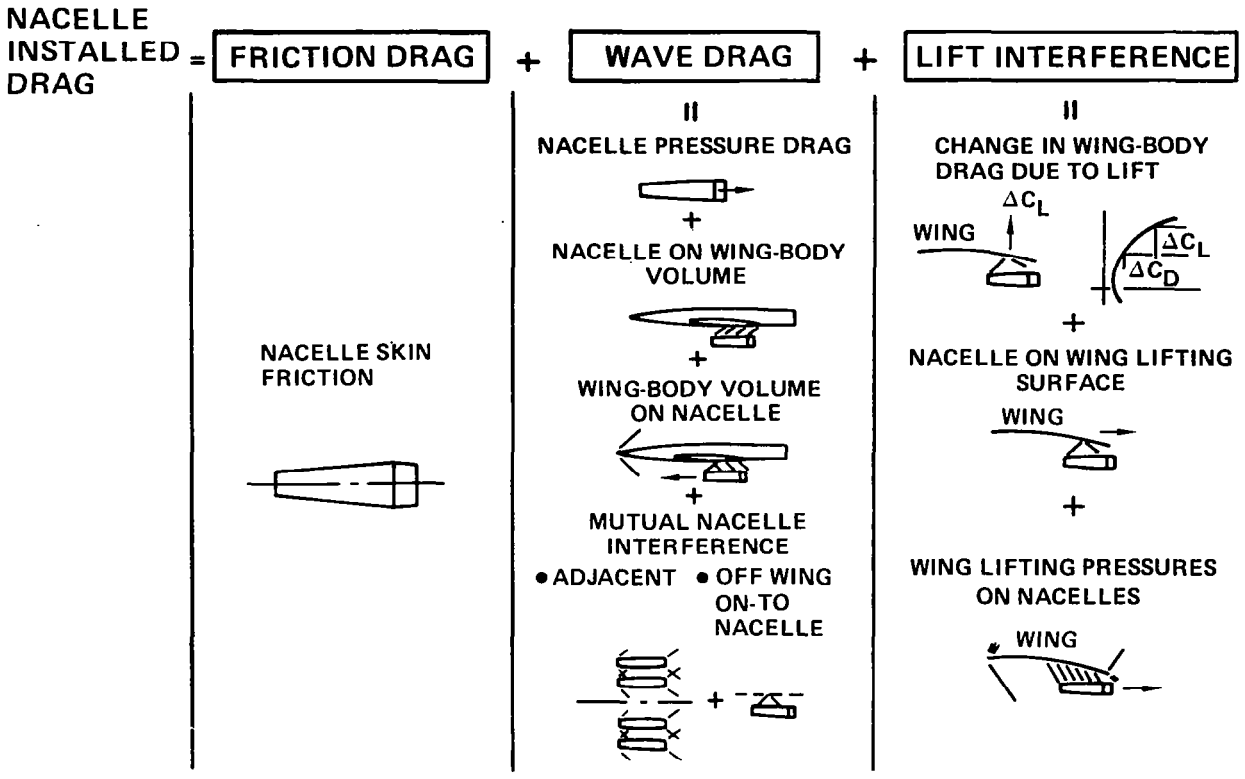

Figure 7.- Nacelle installed drag components — no spillage.

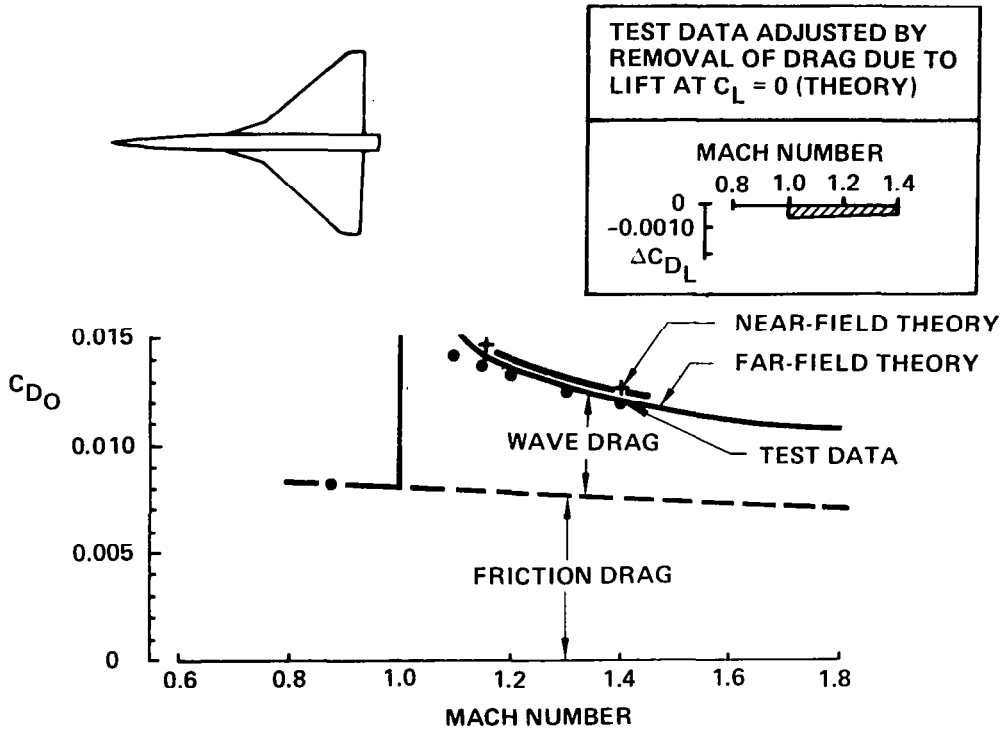

Figure 8.- Wing + body drag comparisons at zero lift.

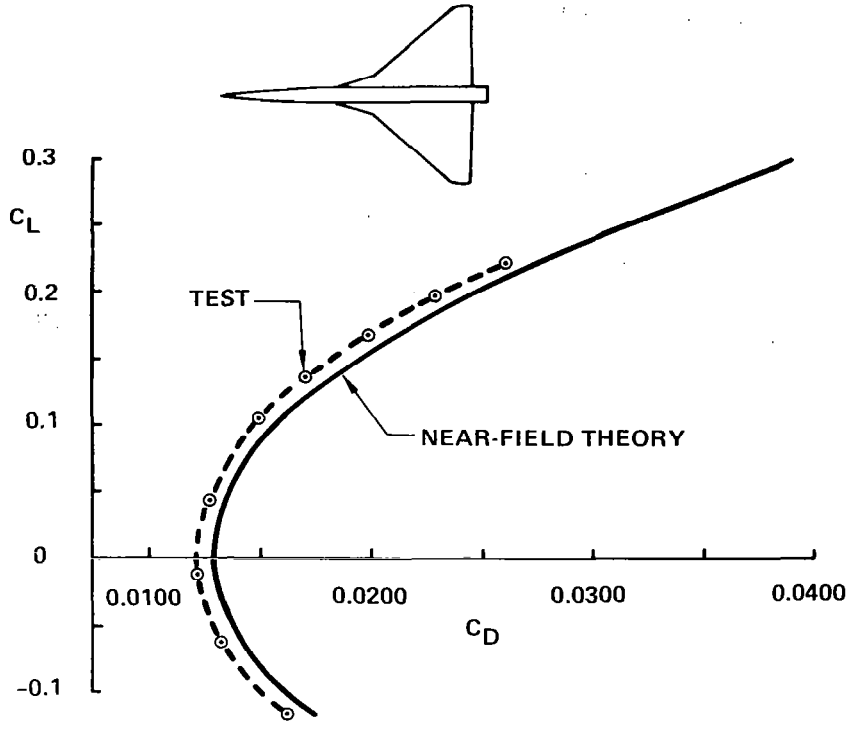

Figure 9.- Wing + body drag polar — mach 1.4.

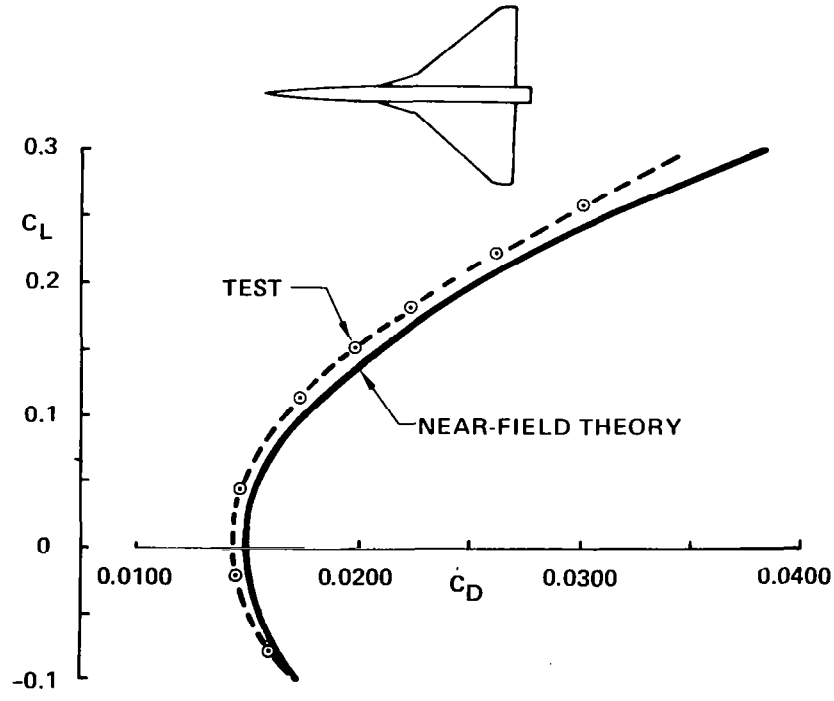

Figure 10.- Wing + body drag polar — mach 1.15.

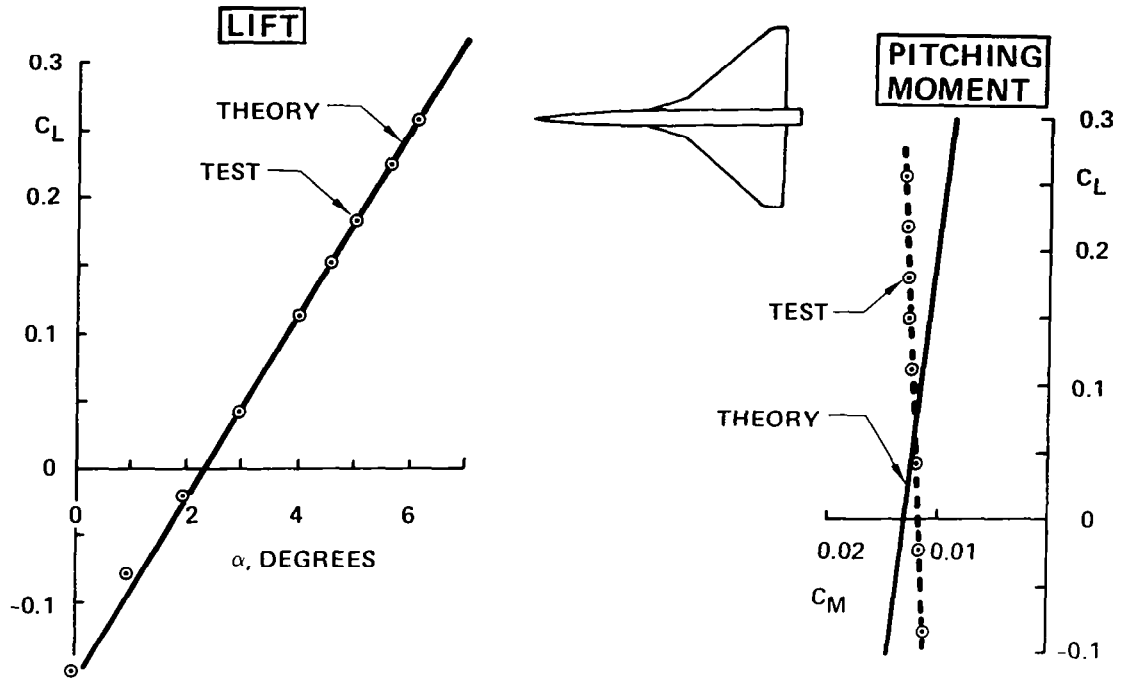

Figure 11.- Wing + body lift and pitching moment curves — M = 1.4.

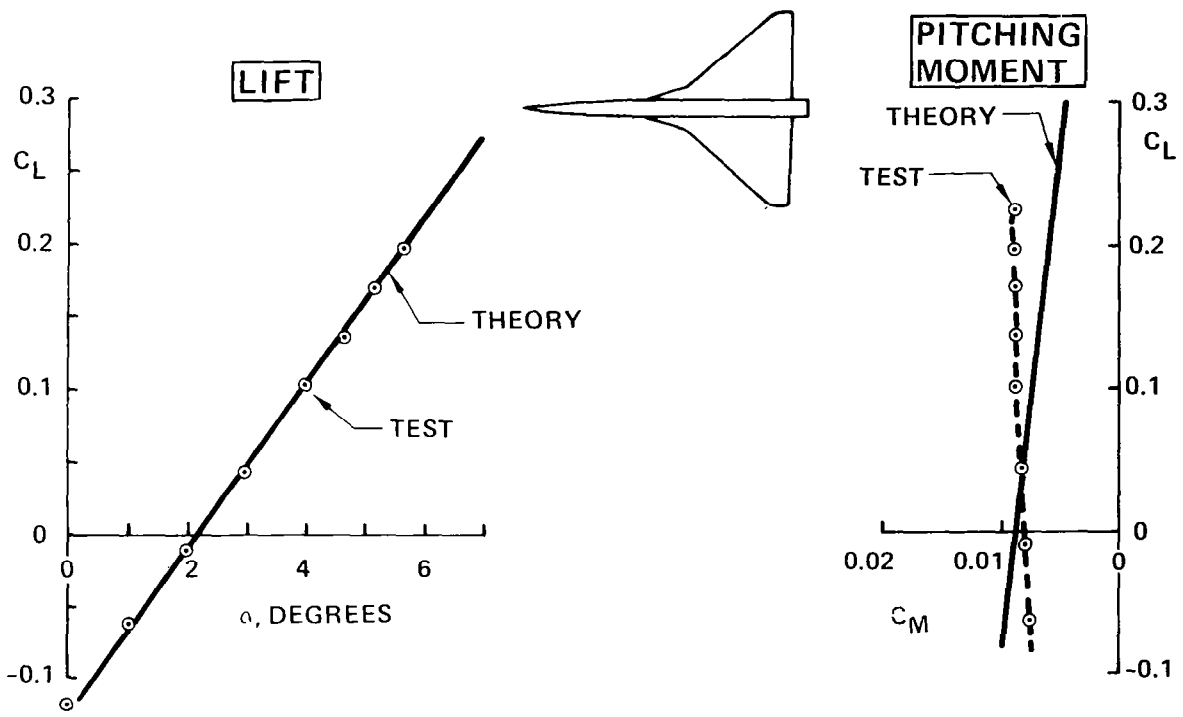

Figure 12.- Wing + body lift and pitching moment curves — M = 1.15.

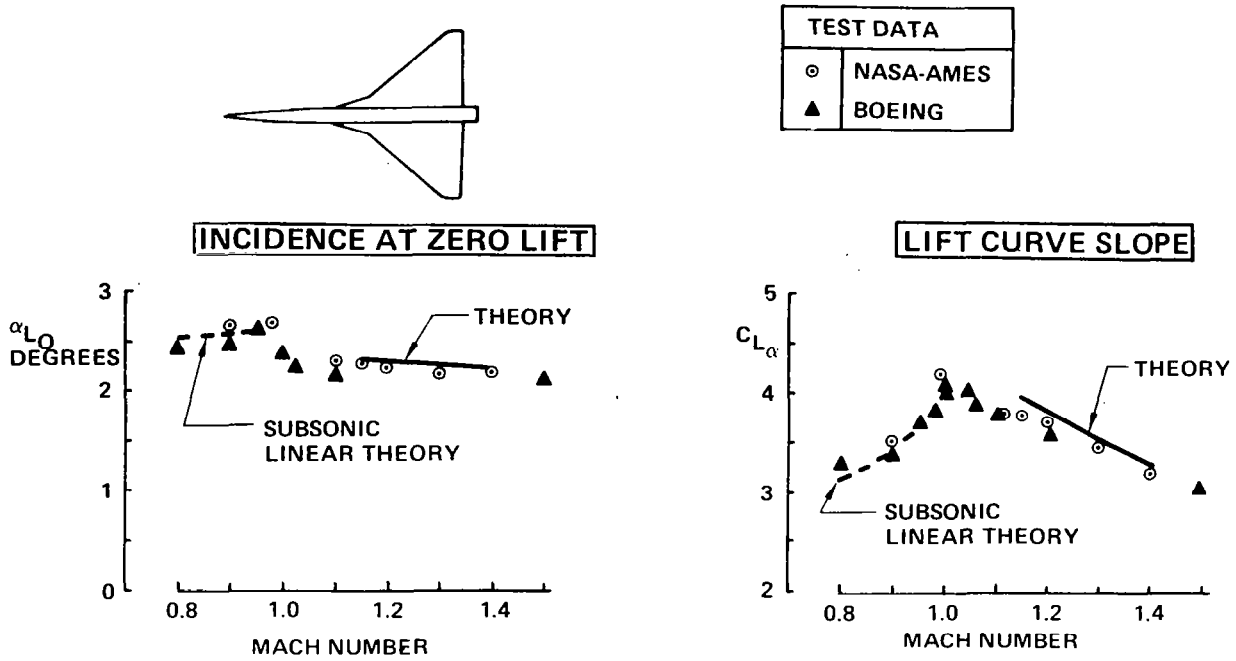

Figure 13.- Wing + body lift characteristics.

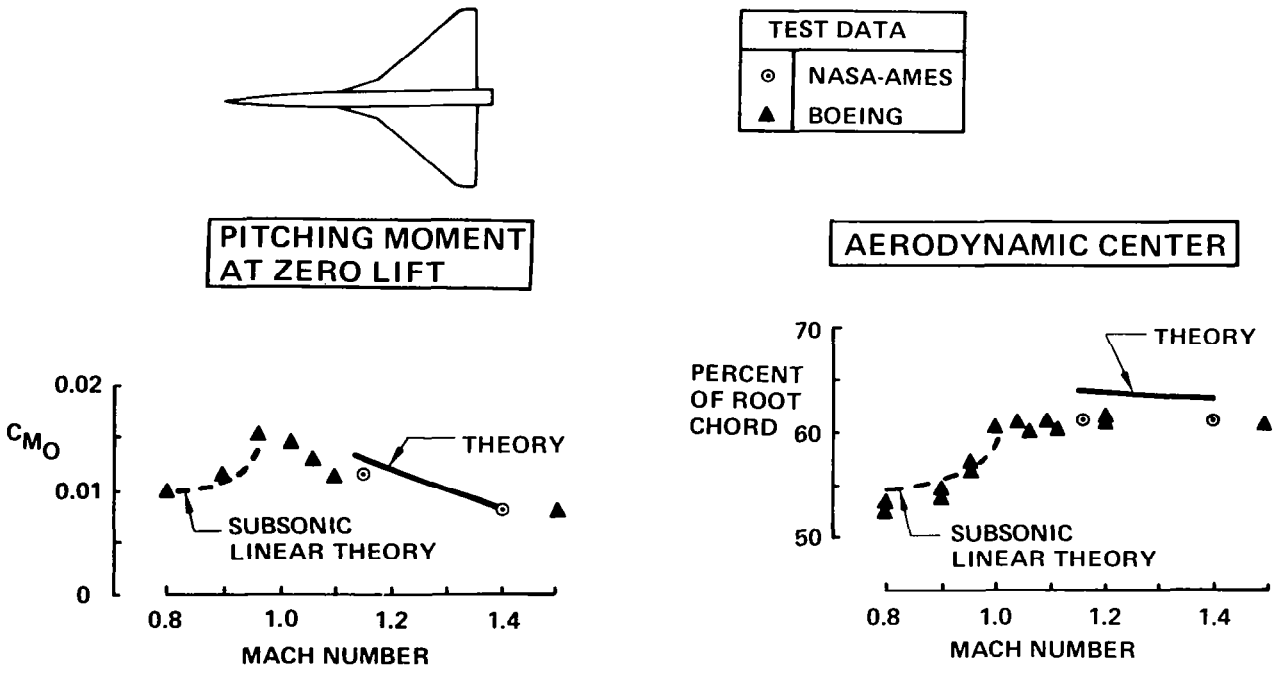

Figure 14.- Wing + body pitching moment characteristics.

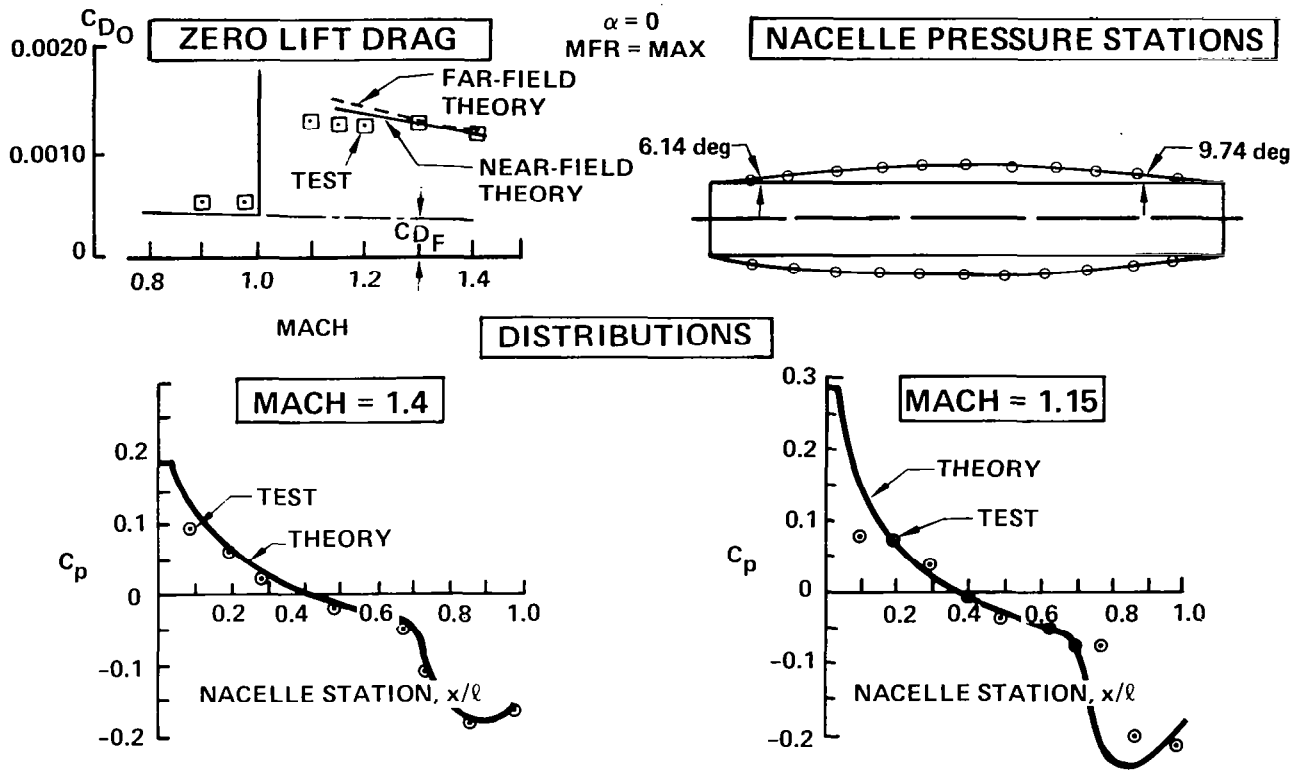

Figure 15.- Isolated nacelle zero-lift comparisons.

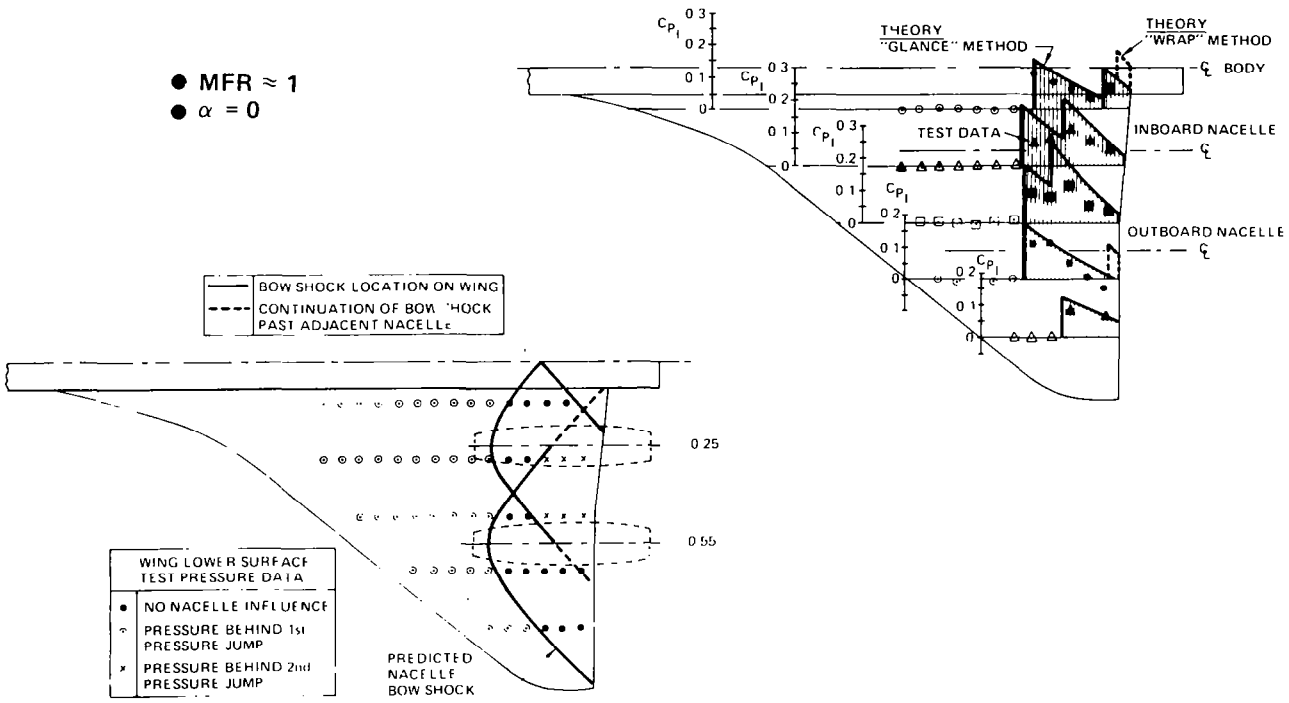

Figure 16.- Nacelle interference pressure fields, M = 1.4; aft nacelle location — station 5.

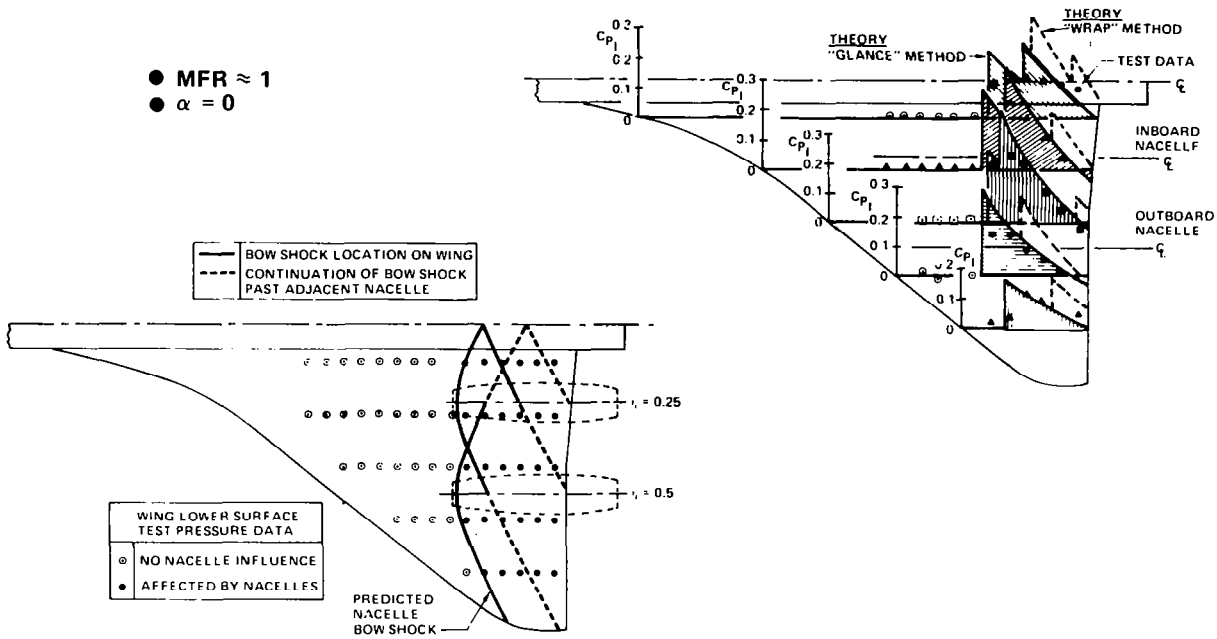

Figure 17.- Nacelle interference pressure fields, M = 1.15; aft nacelle location — station 5.

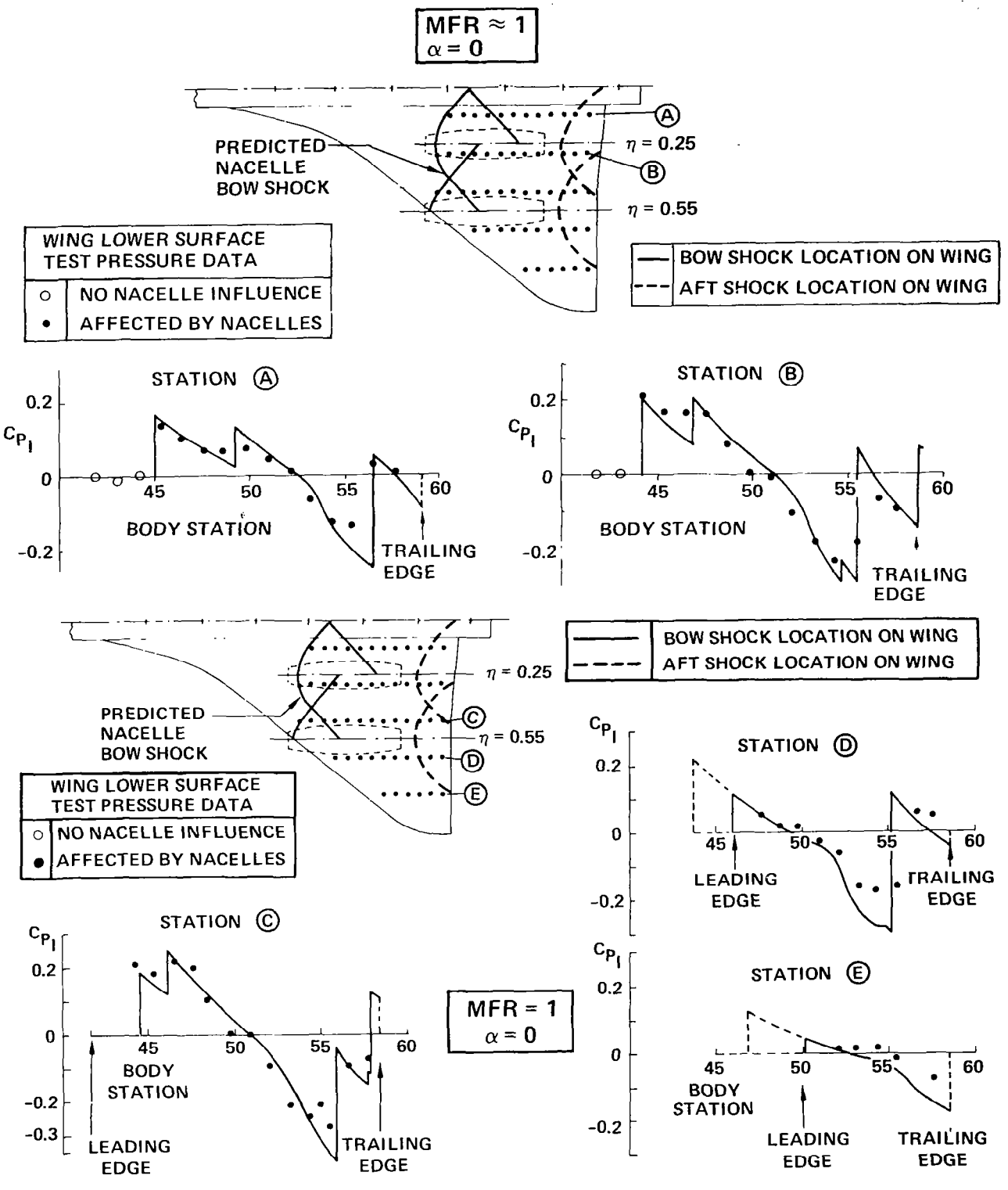

Figure 18.- Nacelle interference pressure fields — M = 1.4; forward location — station 3.

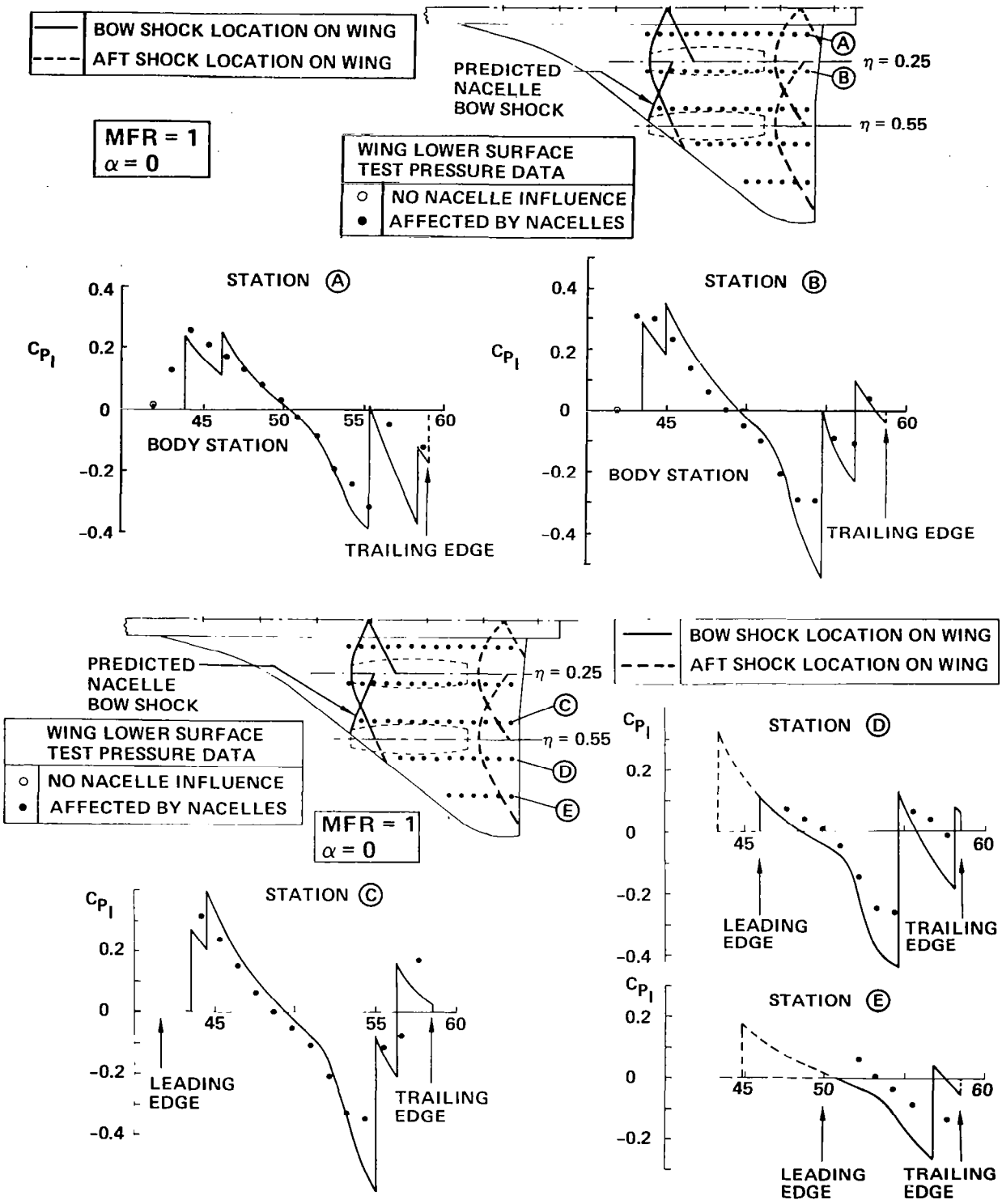

Figure 19.- Nacelle interference pressure fields — M = 1.15; forward nacelle location — station 3.

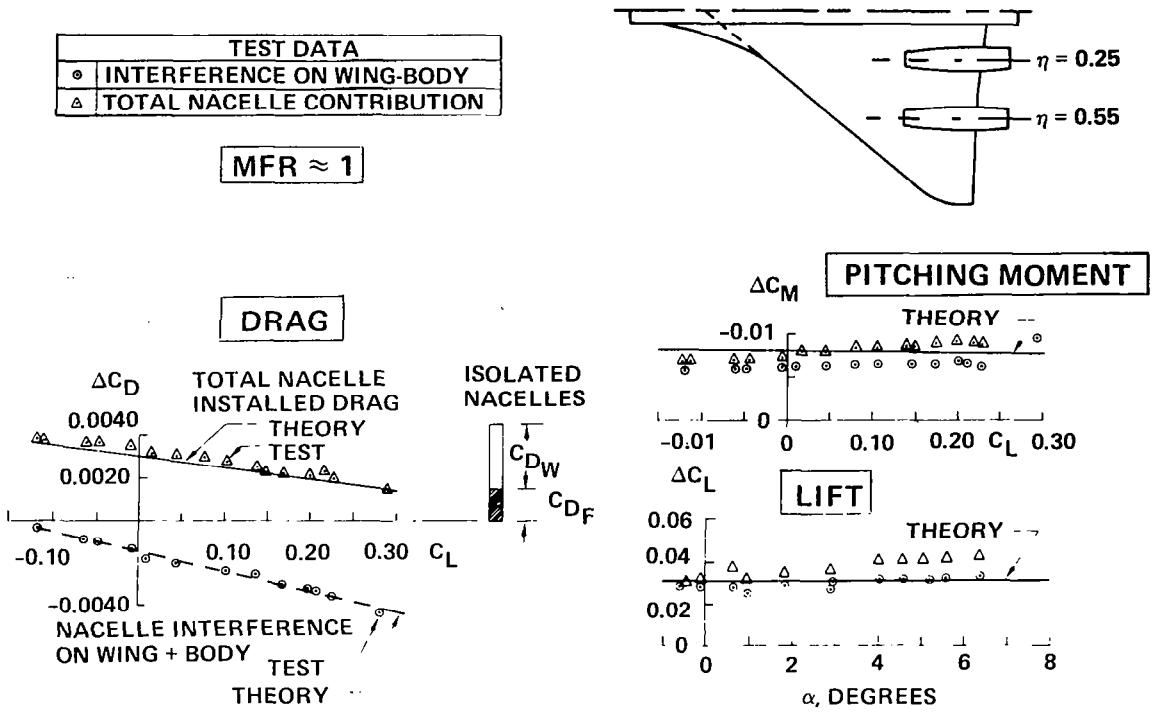

Figure 20.- Nacelle contribution to lift, drag, and pitching moment — M = 1.4.

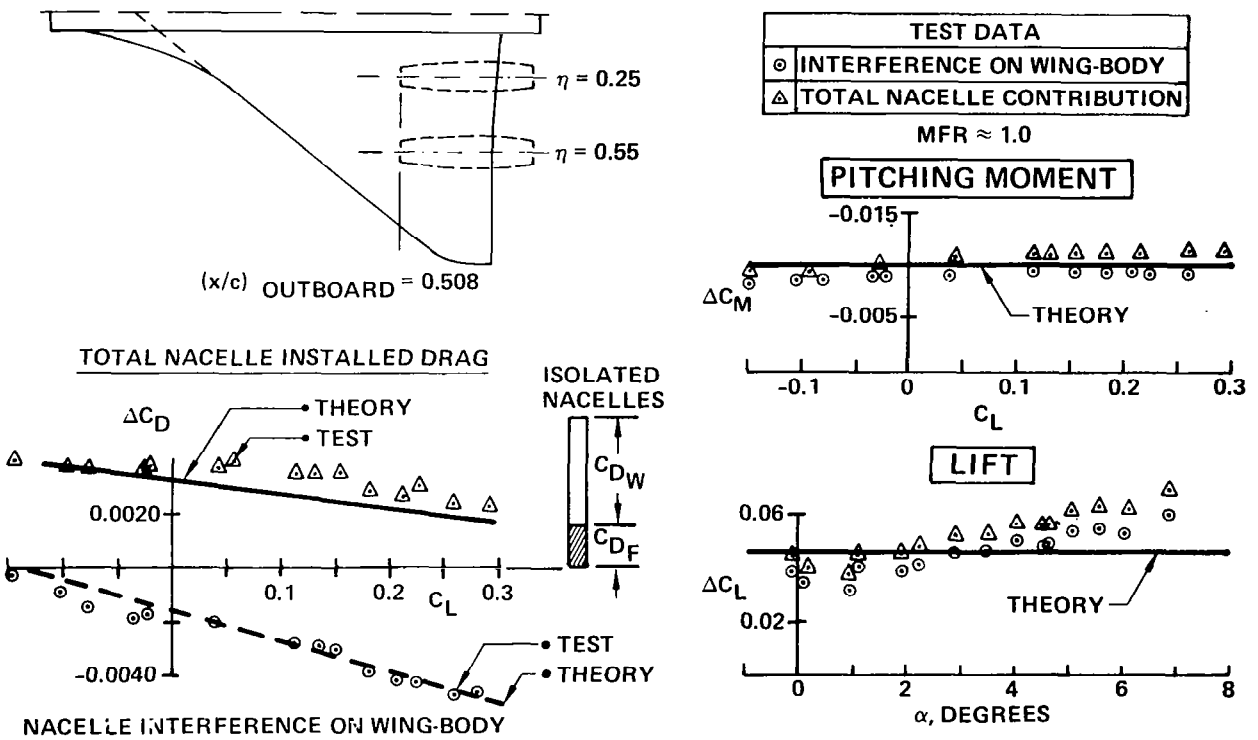

Figure 21.- Nacelle contribution to lift, drag, and pitching moment — M = 1.15.

$$\Delta C_L = \frac{L}{q S_R} = \frac{2\,\Delta S}{\beta S_R}$$

$$\frac{(\Delta C_L)_{CP}}{(\Delta C_L)_{C_P = 0}} = \frac{\beta_\infty q_\ell}{\beta_\ell q_\infty} = \left[0.7\, C_P\, M_\infty^2 + 1\right]\left(\frac{M_\ell}{M_\infty}\right)^2\left(\frac{\beta_\infty}{\beta_\ell}\right)$$

$$M_\ell = \sqrt{5\left[\frac{1 + 0.2\, M_\infty^2}{\left\{0.7\, C_P\, M_\infty^2 + 1\right\}^{1/3.5}} - 1\right]}$$

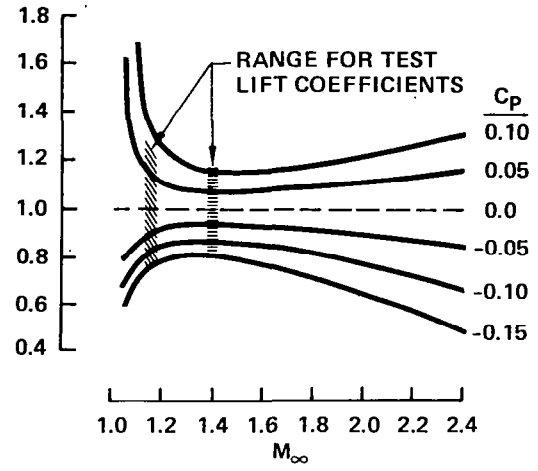

Figure 22.- Effect of local pressure field on interference lift.

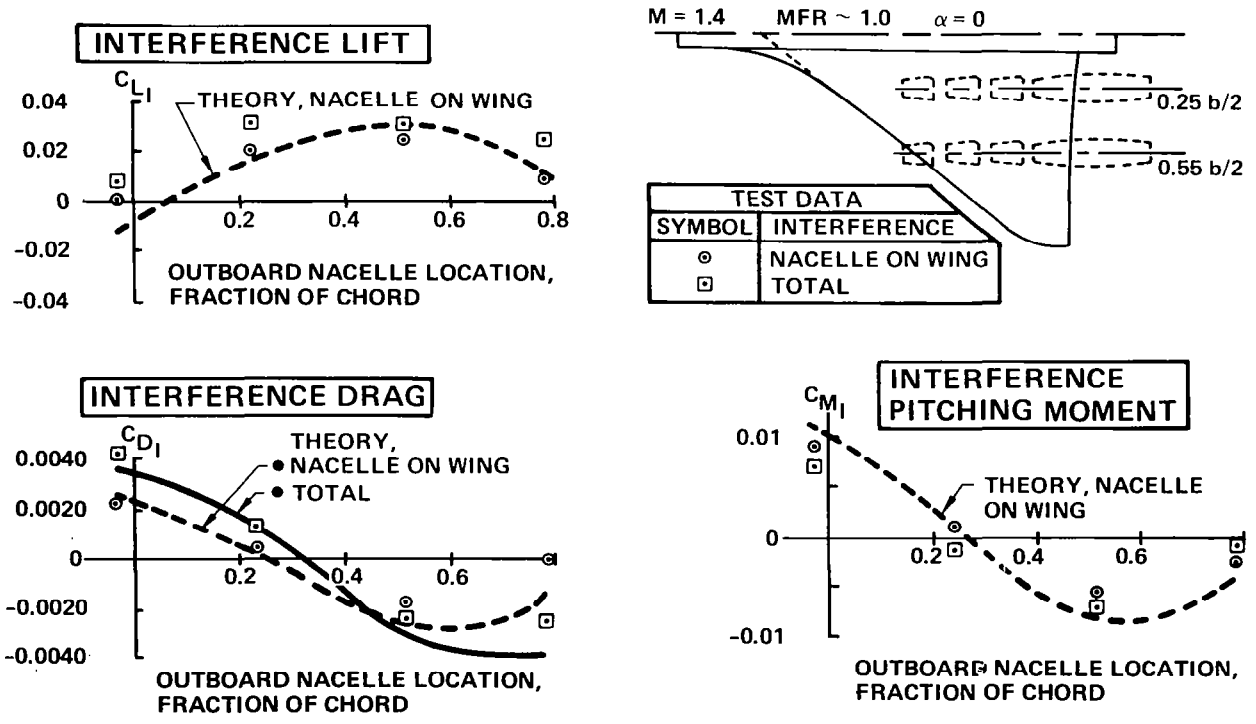

Figure 23.- Effect of nacelle locations on aerodynamic interference — M = 1.4.

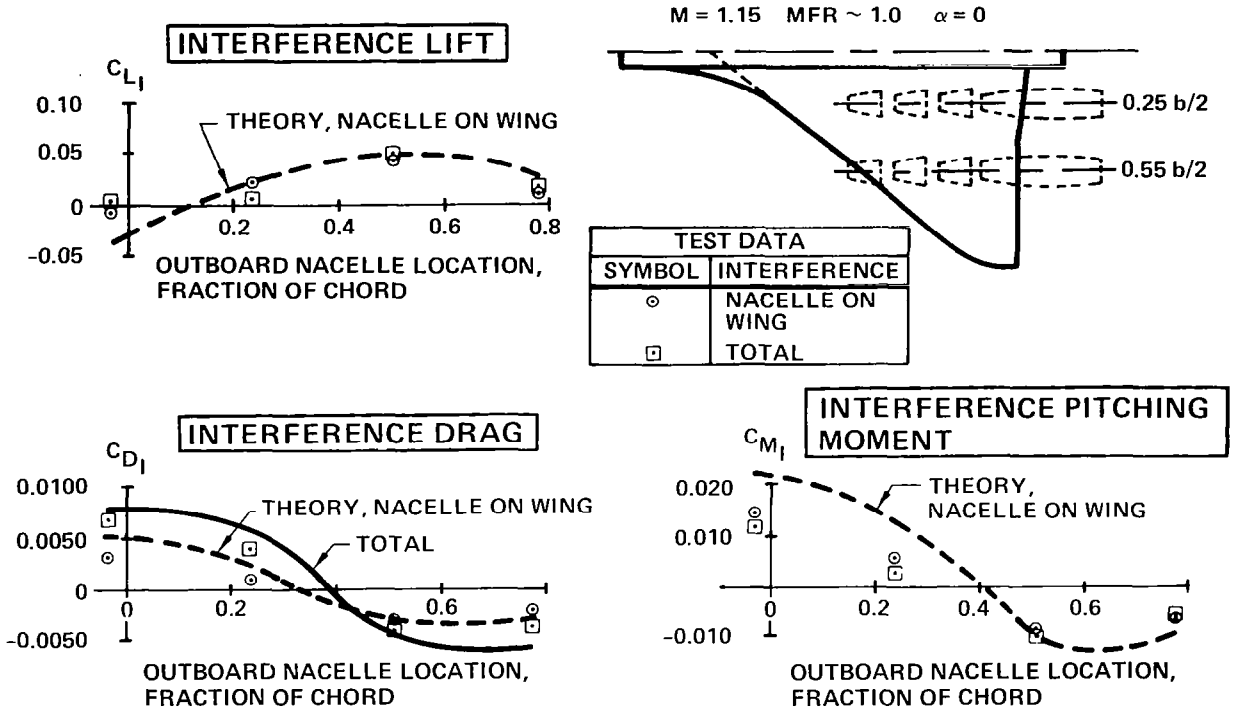

Figure 24.- Effect of nacelle location on aerodynamic interference — M = 1.15.

APPROACH:

- USE MOECKEL'S METHOD TO PREDICT NORMAL SHOCK LOCATION
- USE SIMPLE POLYNOMIAL REPRESENTATION OF STREAMTUBE SHAPE
- CHECK STREAMTUBE REPRESENTATION
  - NACELLE PRESSURES
  - NACELLE FORCES

CAPTURE STREAMTUBE EQUATION

$$\frac{r_S}{R_I} = \sqrt{MFR} + \left(1 - \sqrt{MFR}\right)\left(1 - \left|\frac{X}{L_S}\right|^N\right)$$

QUADRATIC REPRESENTATION: N = 2

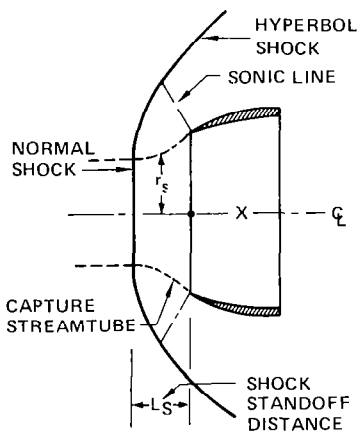

$$MFR = \frac{\text{CAPTURE AREA}}{\text{INLET AREA}}$$

Figure 25.- Spillage streamtube representation.

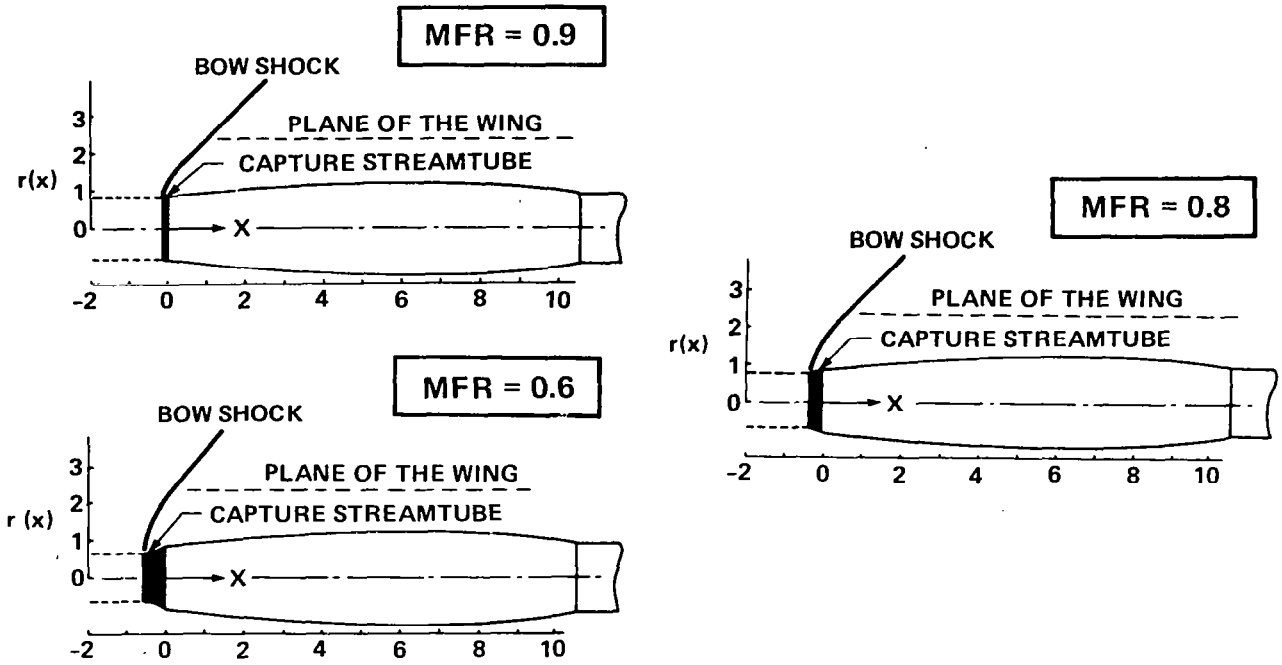

Figure 26.- Calculated streamtube shapes — M = 1.4.

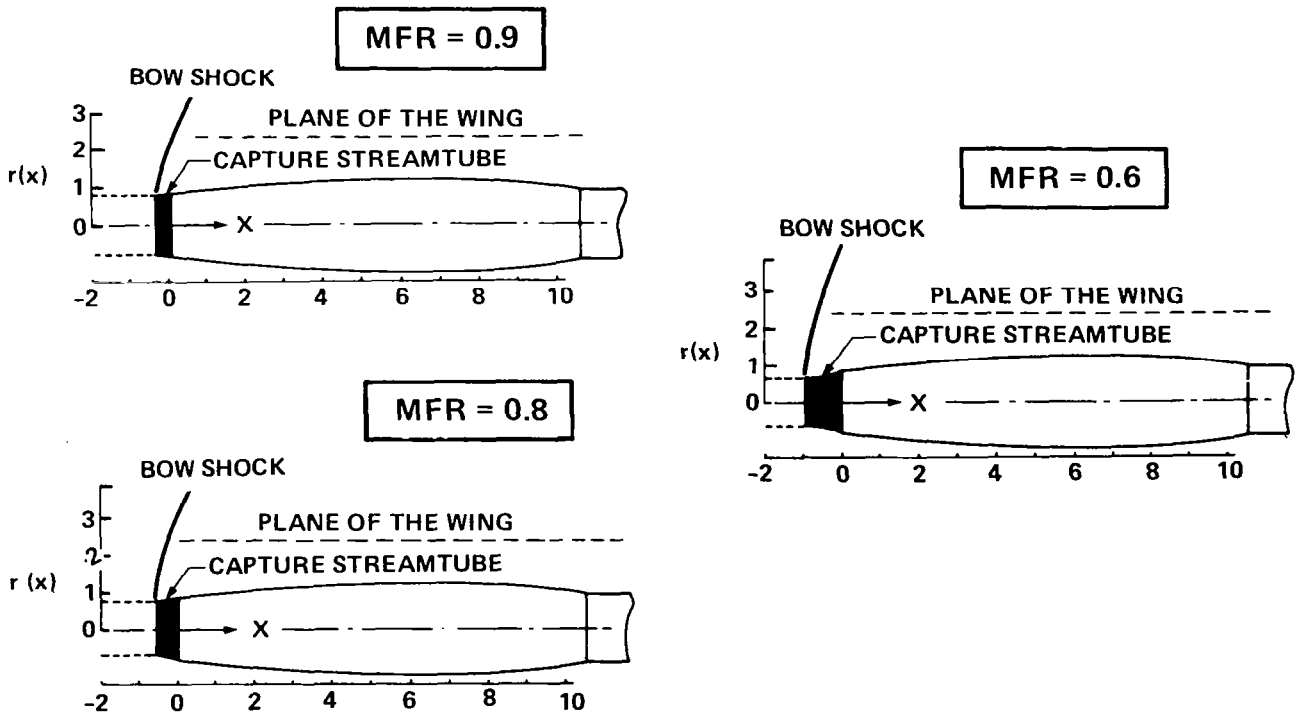

Figure 27.- Calculated streamtube shapes — M = 1.15.

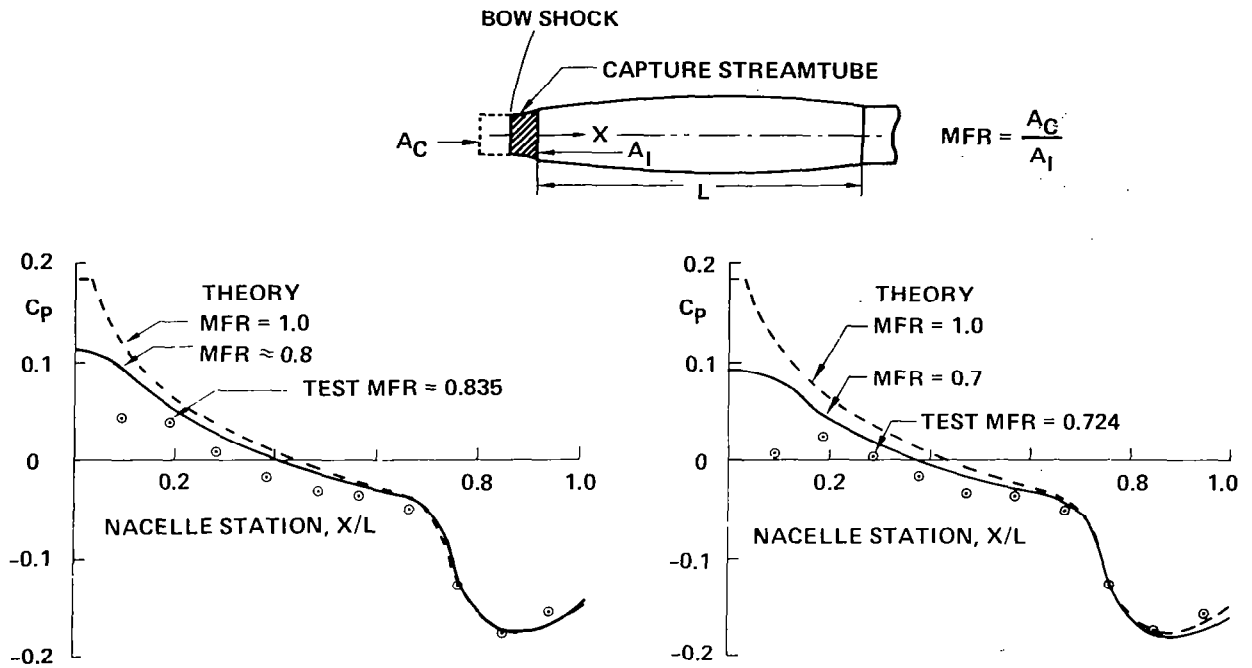

Figure 28.- Effect of spillage on isolated nacelle pressures — M = 1.4.

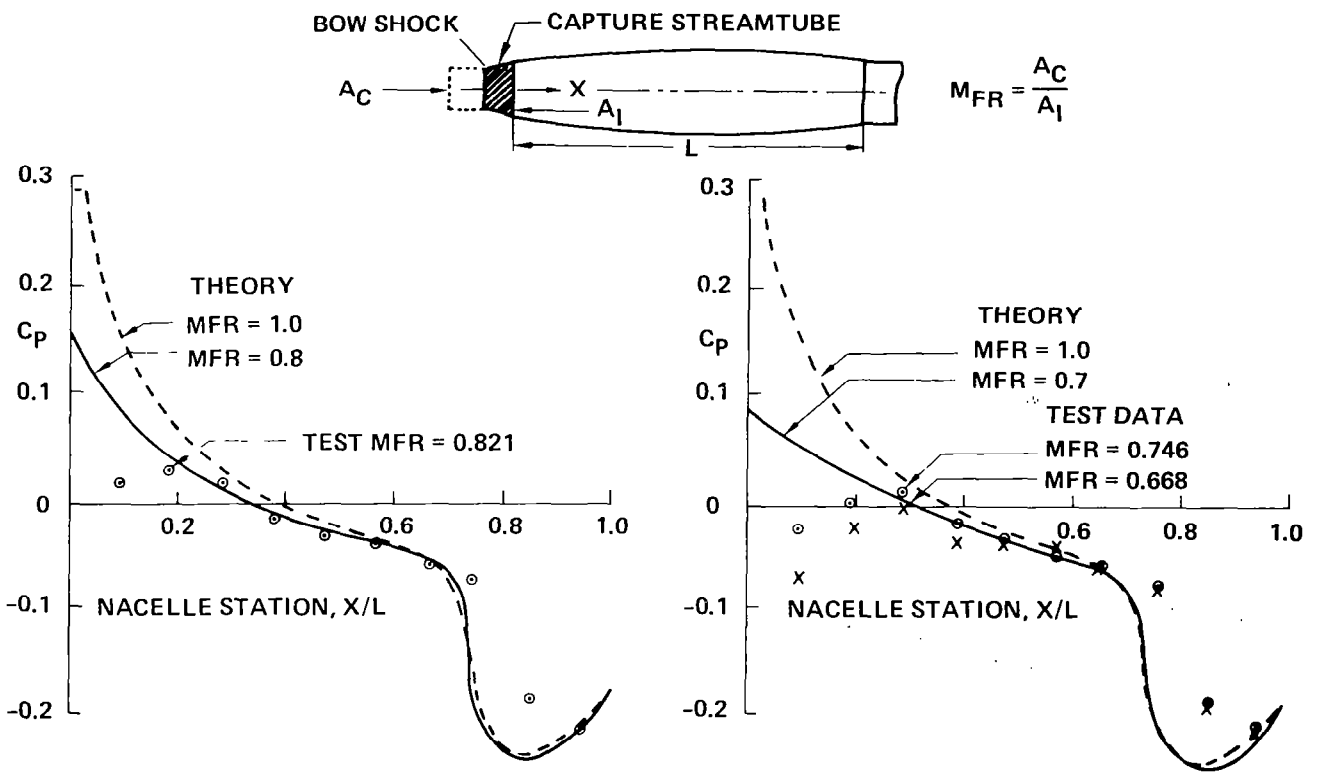

Figure 29.- Effect of spillage on isolated nacelle pressures — M = 1.15.

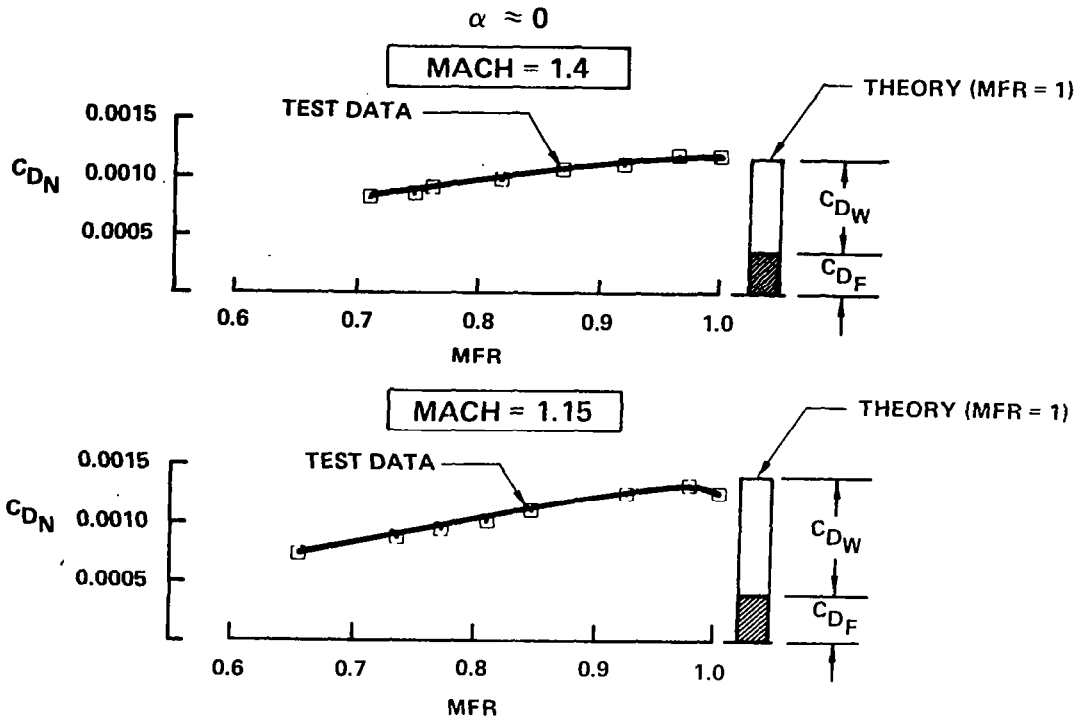

Figure 30.- Effect of spillage on isolated nacelle drag.

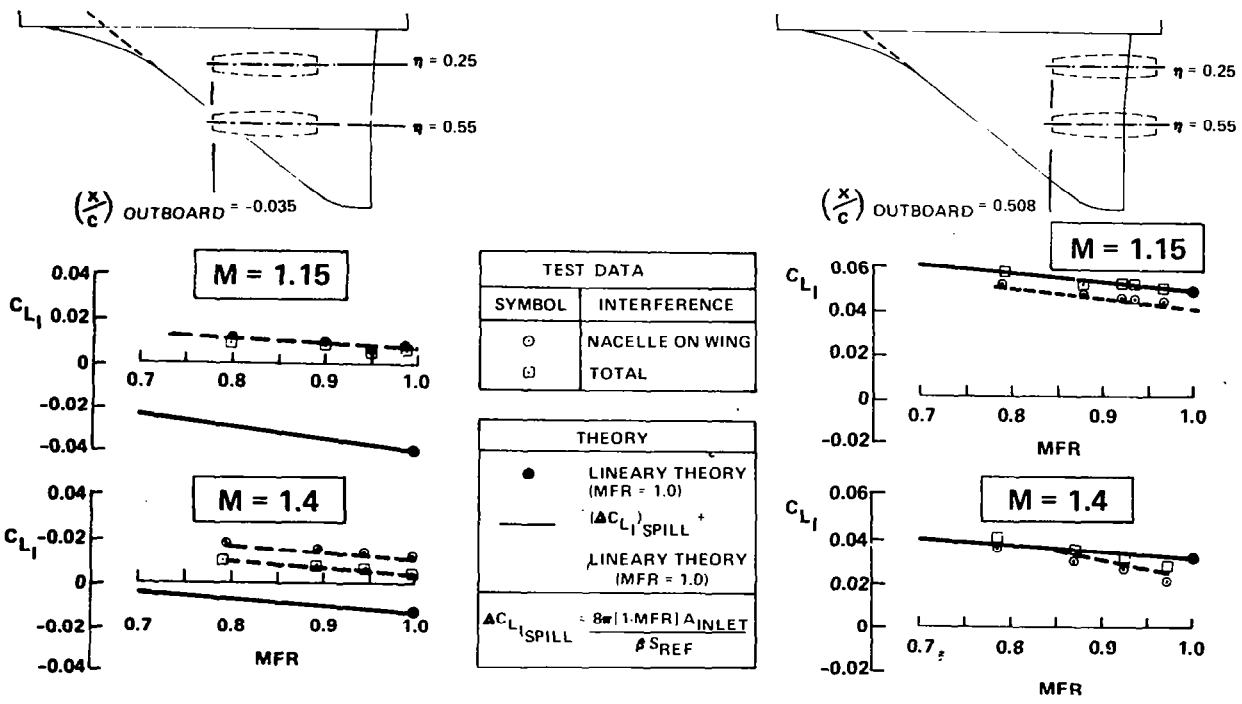

Figure 31.- Slender body theory estimates spillage interference lift.

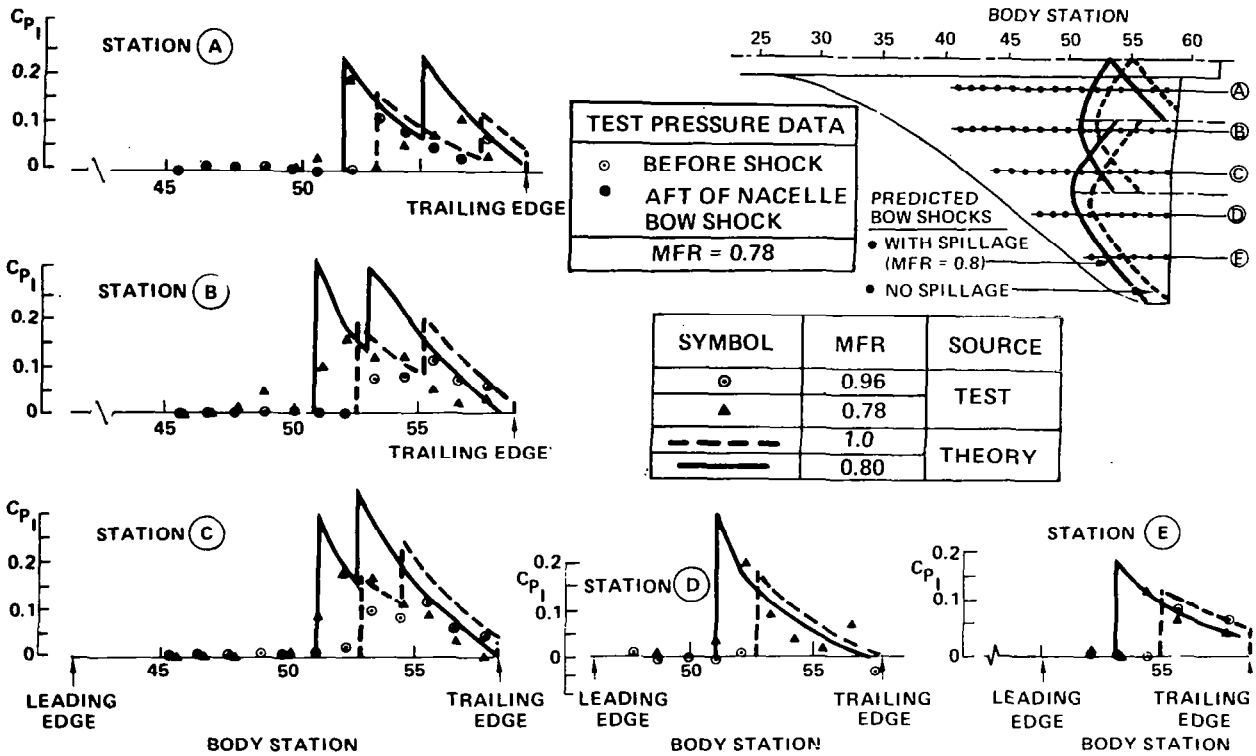

Figure 32.- Effect of nacelle spillage on interference pressures — M = 1.4.

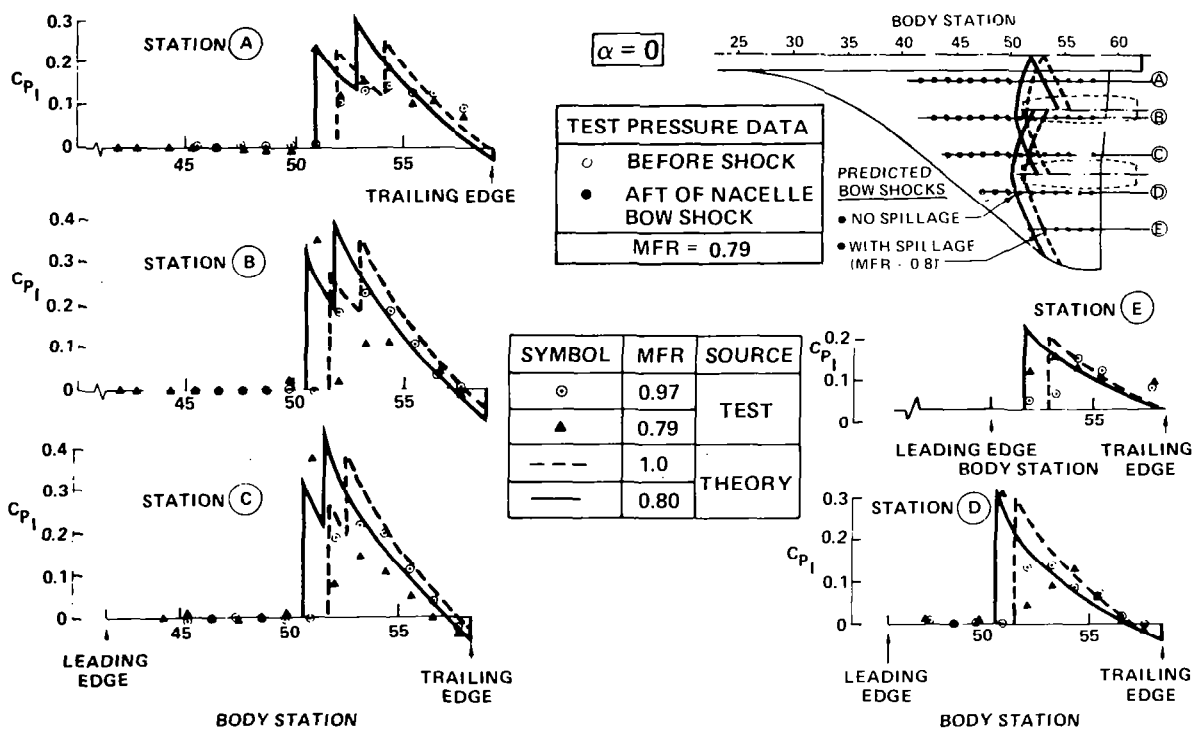

Figure 33.- Effect of nacelle spillage on interference pressures — M = 1.15.

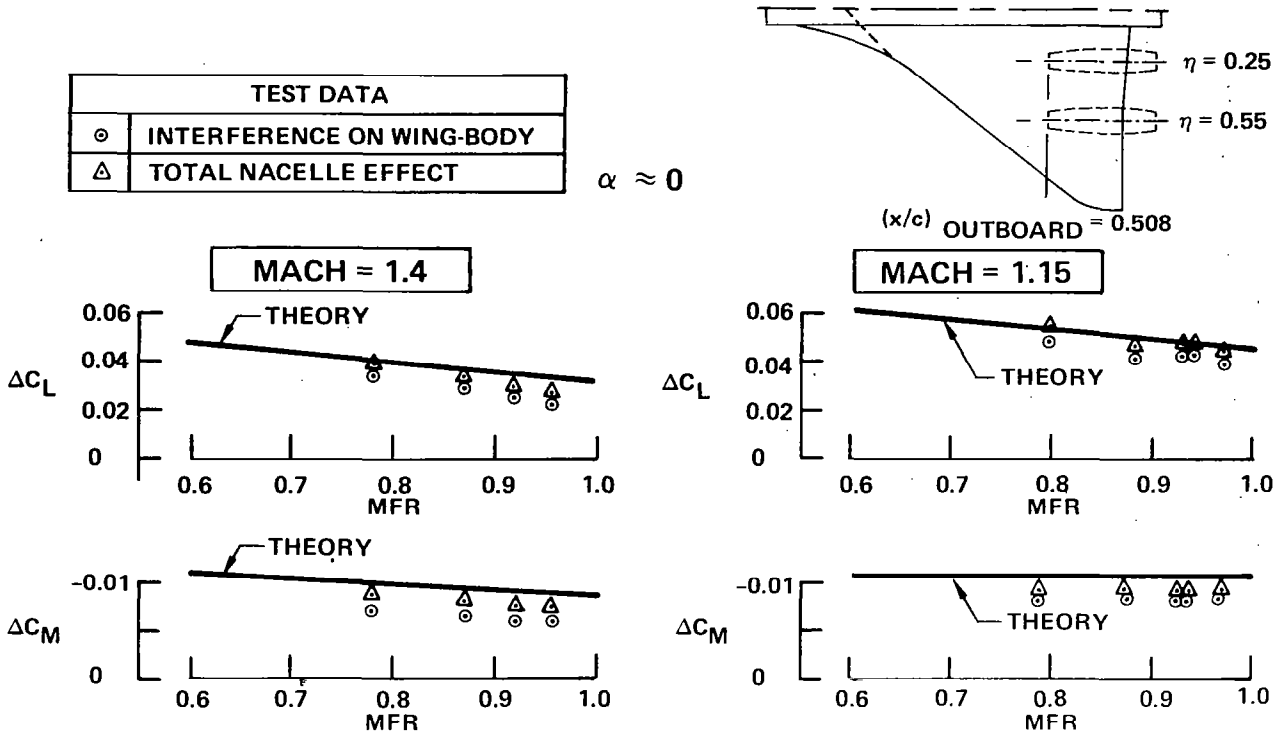

Figure 34.- Effect of spillage on lift and pitching moment.

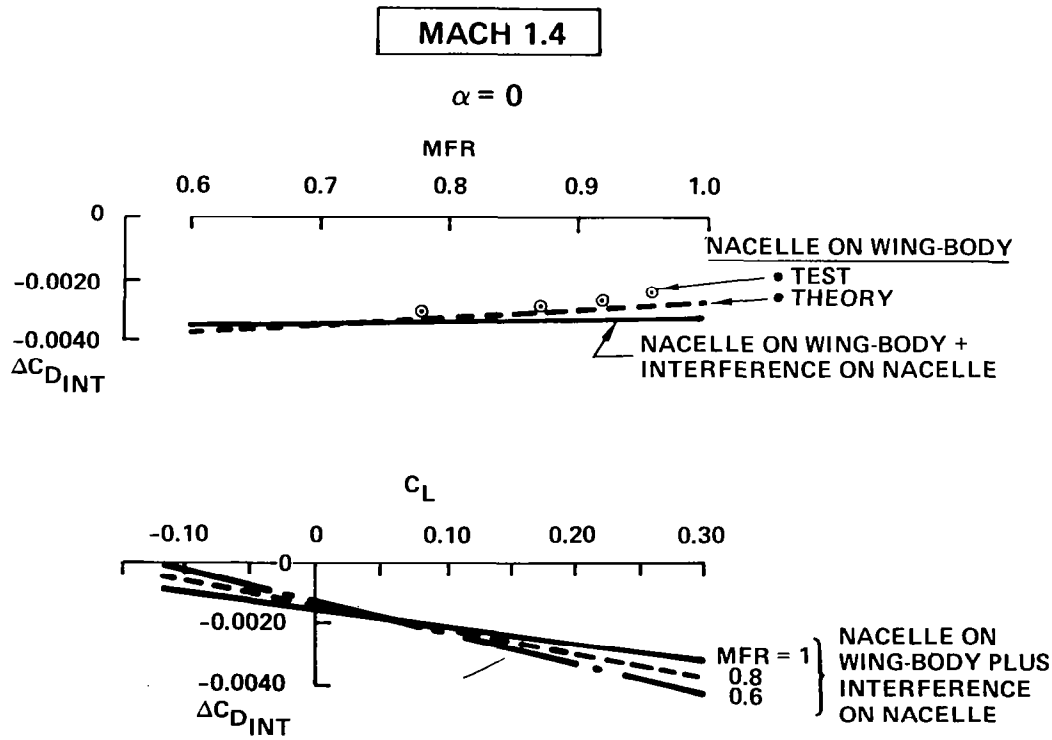

Figure 35.- Spillage effects on nacelle interference.

ANALYTIC DEVELOPMENT OF AN IMPROVED SUPERSONIC CRUISE AIRCRAFT BASED ON WIND TUNNEL DATA*

R. L. Roensch and G. S. Page
Douglas Aircraft Company
McDonnell Douglas Corporation

SUMMARY

Data obtained from the MDC/NASA cooperative wind tunnel program were used to develop empirical corrections to theory. These methods were then used to develop a 2.2M Supersonic Cruise Aircraft Configuration with a cruise trimmed maximum L/D of 10.2. The empirical corrections to the theory are reviewed, and the configuration alternatives examined in the development of the configuration are presented. The benefits of designing for optimum trimmed performance, including the effects of the nacelles, are discussed.

INTRODUCTION

A cooperative MDC/NASA wind tunnel test program for an MDC designed supersonic cruise aircraft configuration was conducted in 1975. Testing was conducted in the NASA Ames Research Center 9- by 7-foot supersonic wind tunnel at Mach numbers from 1.6 to 2.4, and in the Ames 11- by 11-foot transonic wind tunnel at Mach numbers from 0.5 to 1.3. A complete description of the test is presented in reference 1.

The configuration for the MDC/NASA tests was the McDonnell Douglas D3230-2.2-5E advanced supersonic transport configuration shown in figures 1(a) and 1(b). The configuration employs a modified arrow wing with 71-degrees leading-edge sweep inboard and 57 degrees leading-edge sweep outboard. The design cruise point is 2.2M.

SUMMARY OF PREVIOUS WIND TUNNEL TEST

The data from the 9- by 7-foot tunnel, shown in figures 2, 3, and 4, were presented at the 1976 SCAR Conference (reference 2). The estimates shown were based on Woodward lifting surface theory (reference 3), combined with wave drag from a supersonic area rule theory (reference 4), and skin friction drag estimates. Excellent agreement is shown between the estimated and experimental minimum drag in figure 2 for all Mach numbers. The estimated and experimental drag polar shapes differ, causing the wing body drag-due-to-lift to be overpredicted below 2.0M, underpredicted above 2.0M and to agree at 2.0M. Agreement in lift curve slopes, as shown in figure 3, is

---

*This work was performed under NASA Contract NAS1-14621

excellent at the lower Mach numbers, but the agreement decreases at the higher Mach numbers. The estimated and experimental pitching moments shown in figure 4 agree well considering the difficulty of predicting pitching moments for cambered, three-dimensional configurations. This characteristic of Woodward-calculated pitching moments is observed for other slender configurations.

The results of the MDC/NASA test justified the basic design and analysis of the MDC supersonic transport configuration. Although some discrepancy exists in the drag-due-to-lift, the overall data agreement was excellent and the test served as a good base for the methods and configuration development detailed in this paper.

DEVELOPMENT OF IMPROVED ANALYSIS METHODS

DRAG-DUE-TO-LIFT

When compared to the wind tunnel data, the basic Woodward theory underpredicts the drag-due-to-lift at Mach numbers greater than 2.0 as seen in figure 2. The comparison of data to theory also shows that the theory does not accurately predict the lift-curve slope at Mach numbers greater than 2.0 as seen in figure 3. The discrepancy in lift curve slope is also seen to increase with increasing Mach number. A correction to the Woodward-theory drag was developed based on the error in predicted lift curve slope and assuming no leading-edge suction. From the discrepancy in estimated and experimental lift curve slopes, a difference in angle-of-attack at constant C_L can be calculated. The change in angle-of-attack, $\Delta\alpha$, is calculated by equation 1.

$$\Delta\alpha = C_L\left(\frac{1}{C_{L_\alpha}}_{\text{EXP.}} - \frac{1}{C_{L_\alpha}}_{\text{THEORY}}\right) \tag{1}$$

The supersonic flat plate (no leading-edge suction) drag term based on the angle shift, from equation 2, is then applied to the Woodward drag estimates as shown in figure 5.

$$\Delta C_D = C_L{}^2\left(\frac{\Delta\alpha}{C_L}\right) \tag{2}$$

Analysis of three additional wing planforms for which experimental data were available (references 5 and 6) showed similar trends in lift-curve-slope and drag estimates. A generalized correction factor, $\Delta\alpha/C_L$ (equation (1)), was determined and the results are shown in figure 6. The correction term is a function of the Mach number normal to a nominal leading-edge sweep, Λ_{ED}, which was chosen to represent a multi-segment leading edge by a single leading-edge sweep value. This correction to the Woodward drag estimates, the transonic leading edge (TLE) correction, shows excellent agreement with the experimental data as shown in figure 7.

NACELLE-WING INTEGRATION

The Woodward program did not accurately predict the changes in drag-due-to-lift and pitching moment due to nacelle addition. The problem was in the inability of the Woodward program to model the flow diverter (pylon) and the interaction between the nacelle-shock and the wing-boundary-layer. As a result, the Woodward program did not accurately predict the nacelle-on-wing interference pressures. The measured nacelle-on-wing interference pressures are illustrated in figure 8. To correct the Woodward analysis, the program was modified to allow the inclusion of the experimental interference pressures on the wing. The ability of the program to predict pitching moments and induced drag was significantly improved, as seen in figures 9 and 10.

DEVELOPMENT OF AN IMPROVED PERFORMANCE WING

WING PLANFORM STUDY

A wing planform study was conducted using the improved methods developed above. The analysis of candidate planforms was conducted under the following constraints:

(1) Constant Wing Area
(2) Constant Aspect Ratio
(3) Constant Tip Chord
(4) Constant t/c Distribution
(5) Constant Design C_L
(6) Nacelle Induced Drag Not Included
(7) 0 degree trailing-edge sweep inboard of 31% semi-span

The wing camber surface was designed using the Woodward program optimization of an isolated wing. The wing was then integrated to the fuselage by modifying the root airfoil incidence. A four degree root incidence was used for all cases. The wing-body combination was analyzed for lifting effects using the Woodward program and incorporating the TLE correction derived above. Each configuration was optimized for minimum zero-lift-wave-drag using the Arbitrary Body program (reference 4). The configurations were trimmed at the c.g. location for maximum trimmed L/D.

The planform study included variations in geometric planform and wing camber. The geometry of the planforms is shown in table 1. Although wings W38 and W40 had good L/D's, as seen in table 2, they were dropped from the analysis because of excessive wing length which resulted in the wing overlapping the horizontal tail. Wings W36 and W37 were not retained for the full analysis due to their low L/D values. The data in table 2 presents the L/D values for several steps in the analysis process to show the trades for various wings. The gross wing L/D value is obtained from the wing-alone induced drag data, as produced by the optimized wing camber. A representative lift-independent drag, as previously estimated for the baseline aircraft, is added to adjust the data to the proper L/D range for correlation with the complete aircraft performance data. The wing-body induced drag data include the effects of rotating the wing-root incidence to four degrees and adding the fuselage. The representative lift-independent drag used above is retained. The wing-

body, trimmed L/D incorporates the effect of trim drag on the wing-body data with the c.g. located to achieve the maximum L/D, while maintaining the reference lift-independent drag. At the optimum c.g. location, the tail load is up, so the trimmed L/D is greater than the wing-body L/D (C_{D_0} of the tail is included in the reference lift-independent drag). The complete aircraft L/D corrects the wing-body trimmed L/D for the differences in the skin friction and zero lift wave drag of the actual aircraft configuration.

The planform study, using the complete configuration, showed a relation of both drag-due-to-lift and configuration wave-drag-due-to-volume to the wing trailing-edge-sweep (notch ratio), with the wave drag bounding the optimization process. When the trailing edge sweep angle approaches the Mach angle, the wing area distribution, calculated by the Mach cutting planes, experiences rapid changes in cross-sectional area. As a result, the configuration wave drag-due-to-volume increases at high trailing-edge sweep angles, canceling the drag-due-to-lift benefits associated with high trailing-edge sweeps (or large notch ratios). This produces an "optimum" trailing-edge sweep at approximately one-half of the Mach cone angle as seen in figure 11. This effect made the high trailing edge sweep of wing W33 and W39 less beneficial than the gross wing data of table 2 indicated, showing the importance of analyzing the complete aircraft when selecting the optimum wing planform.

The four most promising wings from the planform study are shown in figure 12. Based on the cruise L/D and consideration of structural weight, trailing edge flaps, and aileron effectiveness, wing W35 was chosen for further analysis.

WING ASPECT RATIO STUDY

An aspect ratio study was conducted based on the wing W35 planform. Three alternate methods for varying the aspect ratio were investigated. They were: (1) constant trailing-edge sweep or notch ratio (inboard panel L.E. sweep is allowed to vary); (2) constant leading-edge sweep (T.E. sweep is allowed to vary); (3) constant leading- and trailing-edge sweeps (tip chord is allowed to vary). The geometry of the study wings is given in table 3. The resultant L/D's for each approach, summarized in figure 13, are presented below for each type of planform constraint.

(1) Trailing-Edge Sweep Constant: As trailing-edge sweep was the key parameter for drag as shown in figure 11, an aspect ratio study was conducted at constant trailing-edge sweep.

AR	$L/D_{TRIMMED}$	COMMENTS
1.70	9.25	increased induced drag
1.84	9.60	base case
2.08	9.05	wave drag and induced drag penalty due to decreased L.E. sweep.

(2) Leading-Edge Sweep Constant: To evaluate the penalty shown for the high aspect ratio wing with fixed trailing-edge sweep, the analysis was repeated for constant leading-edge sweep:

AR	$L/D_{TRIMMED}$	COMMENTS
1.84	9.60	base case
2.08	9.66	40 degrees trailing edge sweep may cause degraded flap and aileron authority, additional low speed analysis required

(3) Leading-Edge Sweep Constant and Trailing-Edge Sweep Constant: Due to the strong impact of both leading- and trailing-edge sweeps in the previous analysis, a case was run holding all sweeps constant:

AR	$L/D_{TRIMMED}$	COMMENTS
1.61	9.27	increased induced drag
1.84	9.60	base case
2.09	9.47	wave drag penalty due to wing volume and induced drag penalty due to short tip chords.

The base case aspect ratio was near the optimum in all three studies, so the base aspect ratio of 1.84 was retained for the subsequent analyses.

WING-NACELLE INTEGRATION STUDY

The classical approach to nacelle integration (reference 7) for supersonic aircraft is to reflex the wing trailing edge in the region of influence of the nacelle interference pressures as shown in figure 14. The reflex is designed to cancel the change in wing loading generated by the nacelle-on-wing interference pressure. This approach attempted to eliminate the change in drag-due-to-lift produced by the nacelle interference, but did not fully consider that there may be a benefit in the trimmed configuration performance due to the change in pitching moment produced by the nacelle installation. Results of the 1975 MDC/NASA wind tunnel test (ref. 1) showed the reflex tested did not produce a favorable nacelle interference for the trimmed aircraft configuration. The loss in pitching moment with the nacelles installed created a signficicant loss in trimmed L/D for the design c.g. location. An improved wing-nacelle integration procedure was developed which includes the effect of the nacelle installation on the configuration pitching moment in addition to the effect on drag-due-to-lift.

The current procedure for wing-nacelle integration is based on the selection of the wing camber which will produce the maximum trimmed L/D for a specified c.g. location. The relation of maximum trimmed L/D to wing camber (referenced by the zero-lift pitching moment coefficient) and c.g. location is shown in figure 15. In figure 15, the maximum trimmed L/D attainable for a given c.g. location is shown by the envelope curve created from the plots of trimmed L/D as a function of c.g. location for the individual pitch-constrained wings. Each point on the envelope is a specific pitch-constrained wing. Therefore,

for any design c.g. location a wing can be defined which produces the maximum trimmed L/D.

The effect of nacelle addition on a fixed geometry wing is shown in figure 16. It is seen that if the design c.g. location is near the c.g. location for maximum trimmed L/D for a specified wing geometry, a favorable nacelle interference is obtained. If the design c.g. is sufficiently forward of the optimum c.g. location, a nacelle installation penalty may occur.

For cases where the design c.g. is forward of the optimum c.g. for the L/D envelope, shown in figure 15, a local wing reflex can be added which will result in a trimmed L/D greater than that for the non-reflexed wing. As seen in figure 17, a greater amount of reflex is desired as the c.g. location is moved farther forward. The reflexes shown on figure 17 are simple geometric reflexes (see inset, figure 14) that cancel approximately 50 percent and 100 percent of the nacelle induced wing loading.

The combination of re-camber and/or reflex results in the maximum L/D envelopes shown in figure 18. The amount of reflex used for the reflexed wing envelope increases as the c.g. moves forward until 100 percent alleviation of the nacelle induced load is achieved. Note that if the design c.g. location is not constrained to be forward of the c.g. location for maximum L/D of the re-cambered wing envelope, then there is no increase in L/D available for a reflexed and re-cambered wing. Since fuel pumping can be used for c.g. control, the re-cambered wing without reflex was selected for the aircraft. The resultant c.g. location at 37 percent MAC is equivalent to zero static margin for the rigid wing.

HORIZONTAL TAIL OPTIMIZATION

Since the MDC AST configuration uses a tail upload for trim to obtain a favorable trim drag, it is appropriate to consider optimizing the horizontal tail for its trim loading. The horizontal tail used in the 1975 MDC/NASA test was flat (no camber or twist) with a biconvex airfoil section and, as such, was not optimized for minimum drag-due-to-lift at its trim C_L. The experimental tail-on data are shown in figure 19. The experimental tail drag polars (with coefficients based on wing area) for three airplane angles of attack are shown in figure 20. (The estimated polar was calculated for the uncambered tail without the wing induced flowfield.) As shown, the estimated and experimental polar shapes are in good agreement. The C_L for minimum drag, C_{L_o}, shows a shift in the experimental polar relative to the estimate. The shift in C_{L_o} is due to the presence of a wing-induced flowfield which created an adverse, non-uniform onset flow at the tail. The resulting negative C_{L_o} of the experimental data has an adverse effect on trimmed L/D.

The L/D potential for an optimum tail was assessed by analysis of a series of tails with varied C_{L_o} values in a linear trim drag program. An approximation of the camber drag expected for the tail was included. The analysis showed a 0.2 improvement in trimmed L/D for the optimum tail, as shown in figure 21. An optimum tail has not been designed due to the inability of the Woodward program to adequately analyze a tail in the presence of the wing flowfield.

CONCLUSION

Results of the design studies described above, summarized in figure 22, have been used to develop a refined AST configuration with an estimated L/D of 10.18. The changes incorporated in the refined configuration are illustrated in figure 23, along with the 1975 MDC/NASA test configuration. The refined configuration is designated as the model D3232-2.2-3 and is shown in figure 24.

A cooperative MDC/NASA wind tunnel test is currently being planned to verify the performance estimated for the refined configuration described above. The existing model fuselage and tails will be retained, so the effects of fuselage shaping and the optimum tail design will not be verified. The primary objectives of the test are:

- Verify TLE correction
- Confirm performance improvements for W35
- Validate new nacelle installation procedure
- Obtain expanded nacelle-on-wing interference pressure data base for use in developing analytical prediction methods
- Obtain expanded horizontal tail drag data base to validate future wing-body-tail analysis and design methods

The test is expected to be conducted in a NASA facility in 1980.

SYMBOLS AND ABBREVIATIONS

α	angle of attack
$\frac{\Delta\alpha}{C_L}$	correlation factor for the TLE correction
η	span fraction
Λ	sweep angle
Λ_{ED}	equivalent derived sweep angle
Λ_{LE}	leading edge sweep angle
Λ_{TE}	trailing edge sweep angle
ϕ	angular change in slope of the wing camber surface
AR	wing aspect ratio
AST	Advanced Supersonic Transport
C_D	drag coefficient
C_{D_o}	lift independent drag coefficient
C_L	lift coefficient
C_{L_α}	lift curve slope
C_{L_o}	lift coefficient for minimum drag
C_m	pitching moment coefficient

C_{m_o}	zero lift pitching moment coefficient
c.g.	center of gravity
$\frac{dz}{dx}$	wing camber surface slope in the freestream direction
i_H	horizontal tail incidence
L.E.	leading-edge
L/D	lift to drag ratio
M	Mach number
M_o	freestream Mach number
MAC	mean aerodynamic chord
MDC	McDonnell Douglas Corporation
t/c	thickness to chord ratio
T.E.	trailing-edge
TLE	transonic leading edge

REFERENCES

1. R. L. Radkey, H. R. Welge, and J. E. Felix: Aerodynamic Characteristics of a Mach 2.2 Advanced Supersonic Cruise Aircraft Configuration at Mach Numbers From 0.5 to 2.4. NASA CR-145094, 1977.

2. R. L. Roensch: Aerodynamic Validation of a SCAR Design. Proceedings of the SCAR Conference - Part 2, NASA CP-001, [1977], pp. 155-168.

3. F. A. Woodward, E. N. Tinoco, and J. W. Larsen: Analysis and Design of Supersonic Wing-Body Combinations, Including Flow Properties in the Near Field. Part I - Theory and Application. NASA CR-73106, 1967.

4. A. E. Gentry, D. N. Smyth, and W. R. Oliver: The Mark IV Supersonic-Hypersonic Arbitrary Body Program. AFFDL-TR-73-159, 1973.

5. O. A. Morris, D. E. Fuller, and C. B. Watson: Aerodynamic Characteristics of a Fixed Arrow-Wing Supersonic Cruise Aircraft at Mach Numbers of 2.30, 2.70, and 2.95. NASA TM-78706, 1978.

6. R. B. Savelle III, and E. J. Landrum: Theoretical and Experimental Study of Twisted and Cambered Delta Wings Designed for a Mach Number of 3.5. NASA TN D-8247, 1976.

7. R. J. Mack: A Numerical Method for Evaluation and Utilization of Supersonic Nacelle-Wing Interference. NASA TN D-5057, 1969.

8. E. Bonner, M. H. Roe, R. M. Tyson, and R. Y. Mairs: Influence of Propulsion System Size, Shape, and Location on Supersonic Aircraft Design. NASA CR-132544, 1974.

TABLE 1.- WING PLANFORM GEOMETRY SUMMARY

PLANFORM REFERENCE NUMBER	LEADING EDGE			TRAILING EDGE	
	Λ INBOARD (DEGREES)	y BREAK (% SEMISPAN)	Λ OUTBOARD (DEGREES)	y BREAK (% SEMISPAN)	Λ OUTBOARD (DEGREES)
W33	71	NONE	N/A	30	46
W34*	71	63.6	57	30	17
W35	71	70	61.5	30	31
W36	61	NONE	N/A	NONE	0
W37	65	NONE	N/A	30	18
W38	74	NONE	N/A	30	62
W39	74	70	62	30	43
W40	74	55	62	30	25

*BASELINE

TABLE 2.- WING PLANFORM PERFORMANCE SUMMARY

PLANFORM REFERENCE NUMBER	DATA USING BASELINE* AIRCRAFT SKIN FRICTION AND WAVE DRAG			COMPLETE AIRCRAFT L/D
	GROSS WING L/D	WING/BODY L/D	WING BODY, TRIMMED L/D	
W33	9.75	9.91	10.10	9.75
W34*	8.69	8.76	9.10	9.10
W35	9.09	9.25	9.64	9.60
W36	8.32	8.39	8.66	
W37	8.61			
W38	10.50**			
W39	9.64	9.60	9.80	9.75
W40	9.18**			

*BASELINE

**DROPPED DUE TO STRUCTURAL LIMITATIONS

TABLE 3.- WING PLANFORMS FOR ASPECT RATIO STUDY

PLANFORM REFERENCE NUMBER	ASPECT RATIO	LEADING EDGE			TRAILING EDGE
		Λ INBOARD (DEGREES)	LEADING EDGE BREAK (%SEMISPAN)	Λ OUTBOARD (DEGREES)	Λ OUTBOARD (DEGREES)
W35	1.84	71	70	61.5	31
W41	2.08	71	70	62	40
W42	2.08	67	70	62	30
W44	1.70	72	70	62	30
W45	2.09	71	65	61.5	31
W47	1.61	71	75	61.5	31

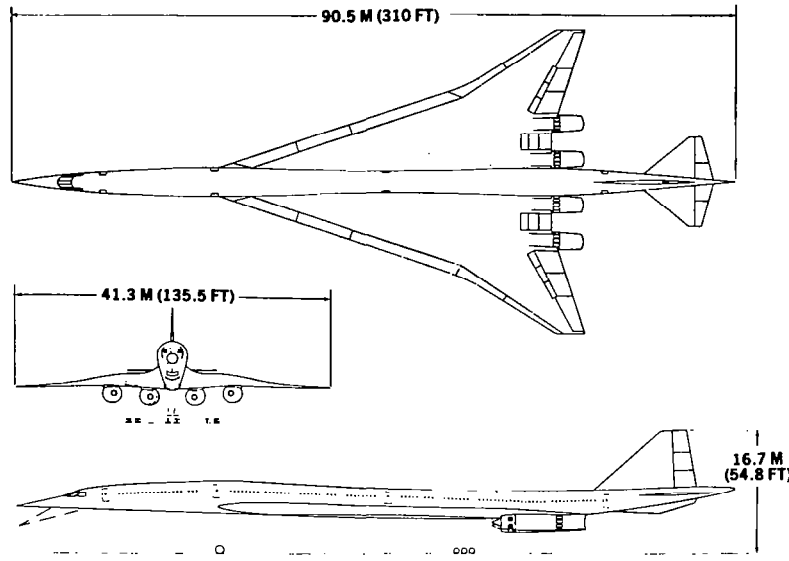

(a) Configuration details.

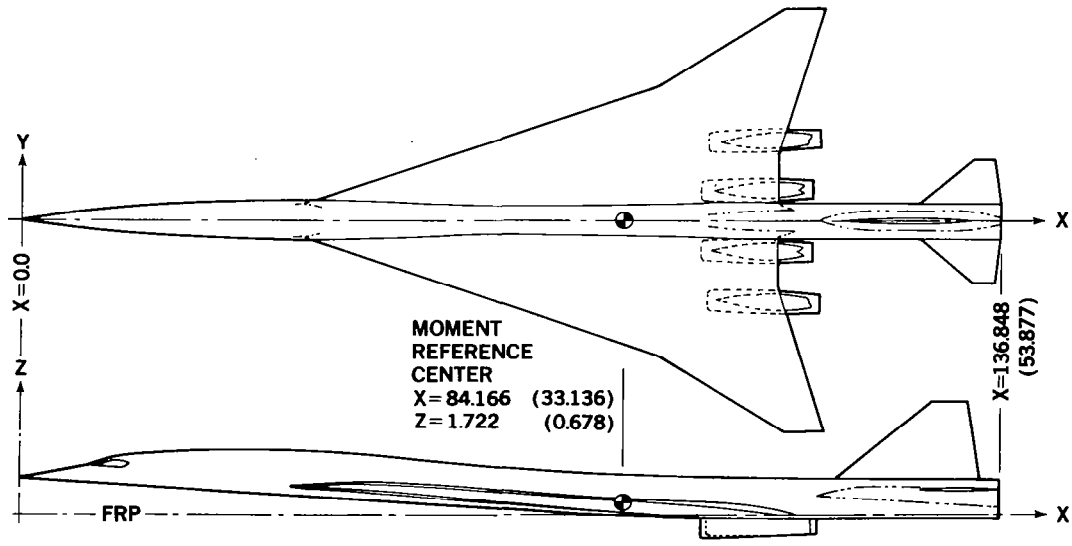

(b) High-speed wind tunnel model details.

Figure 1.- McDonnell Douglas D3230-2.2-5 configuration and model details.

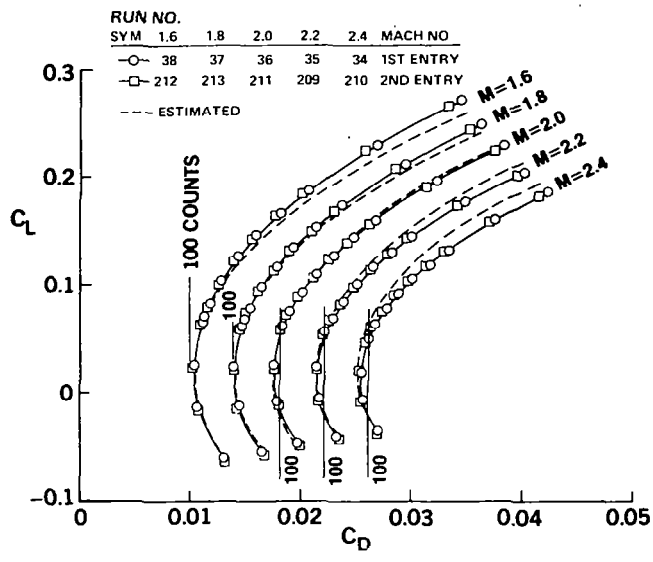

Figure 2.- Comparison of estimated and experimental drag polars for B_1W_2, Mach 1.6 to 2.4.

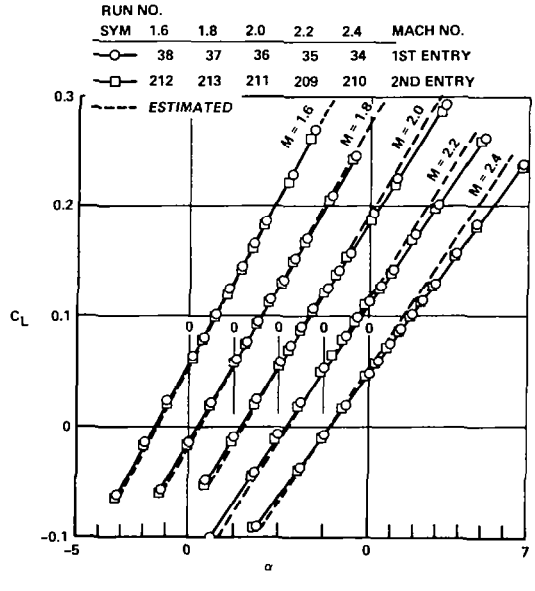

Figure 3.- Comparison of estimated and experimental lift curves for B_1W_2, Mach 1.6 to 2.4.

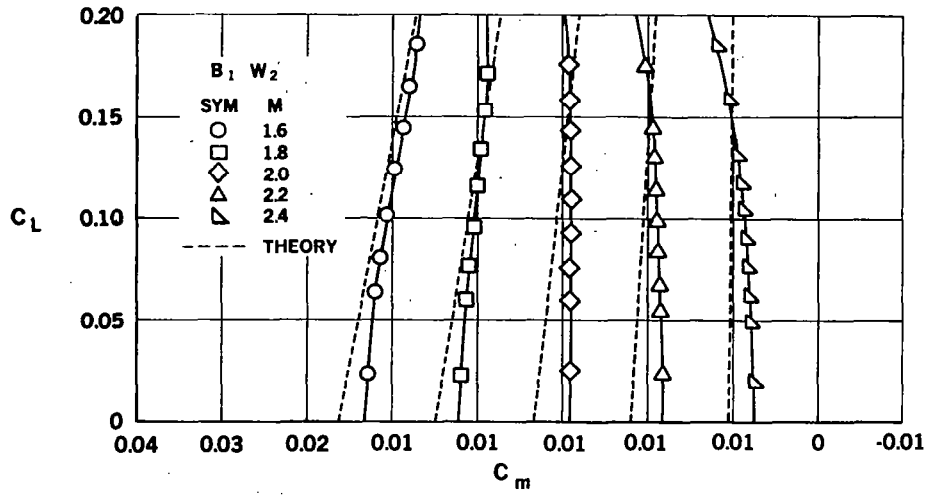

Figure 4.- Experimental and estimated supersonic pitching moments for B_1W_2.

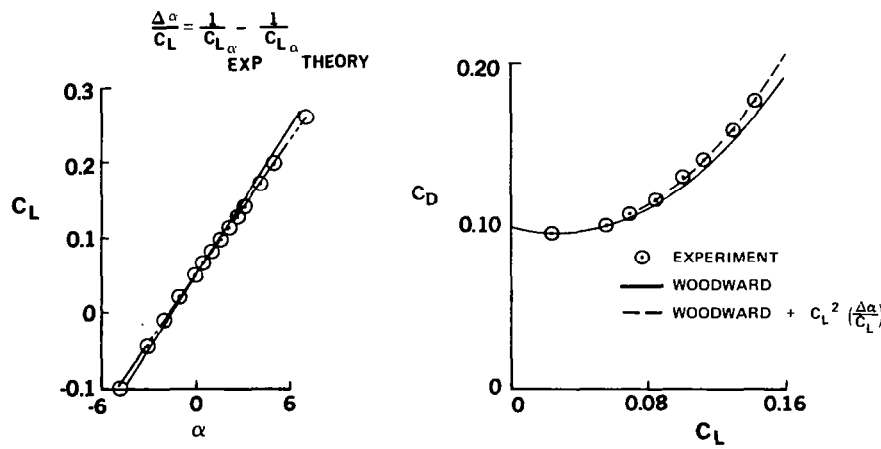

Figure 5.- Derivation of the transonic leading edge correction; 2.2 M.

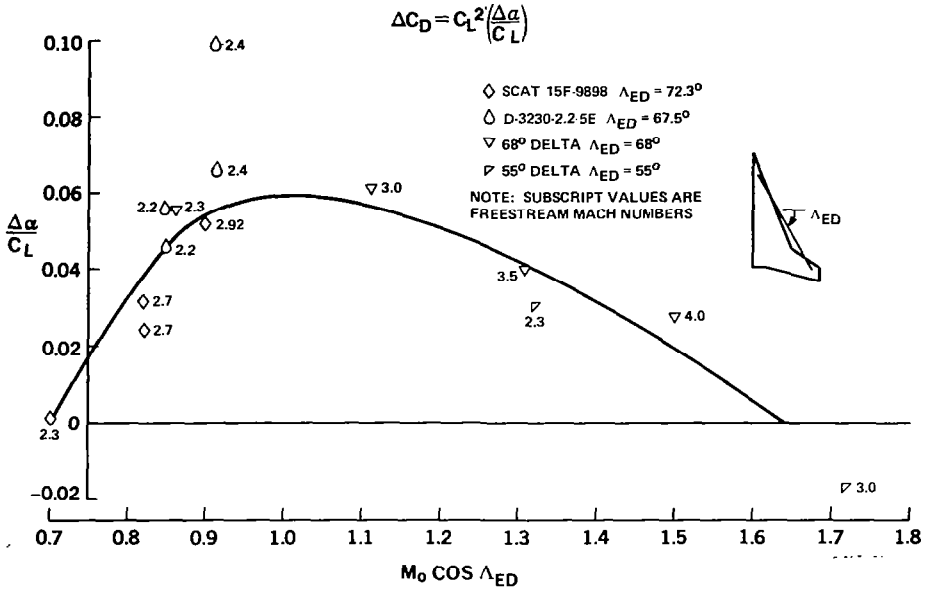

Figure 6.- Transonic leading edge (TLE) correction. (Semi-empirical correction of Woodward for improved drag prediction.)

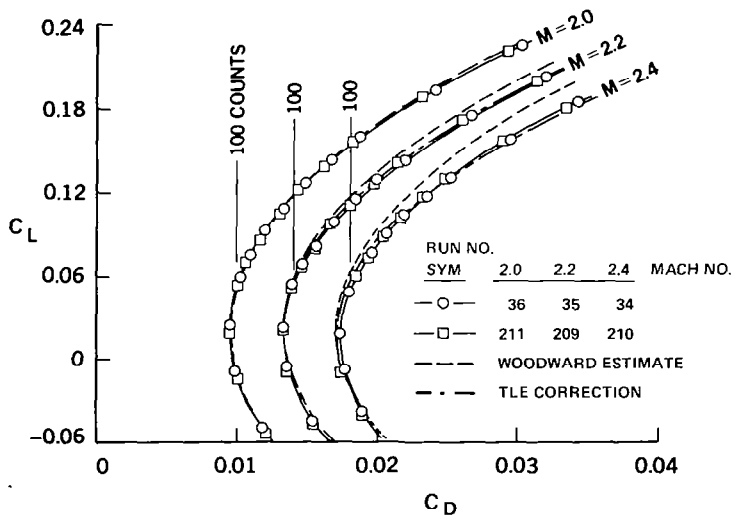

Figure 7.- Effect of TLE correction on estimated drag polars for B_1W_2, Mach 2.0 to 2.4.

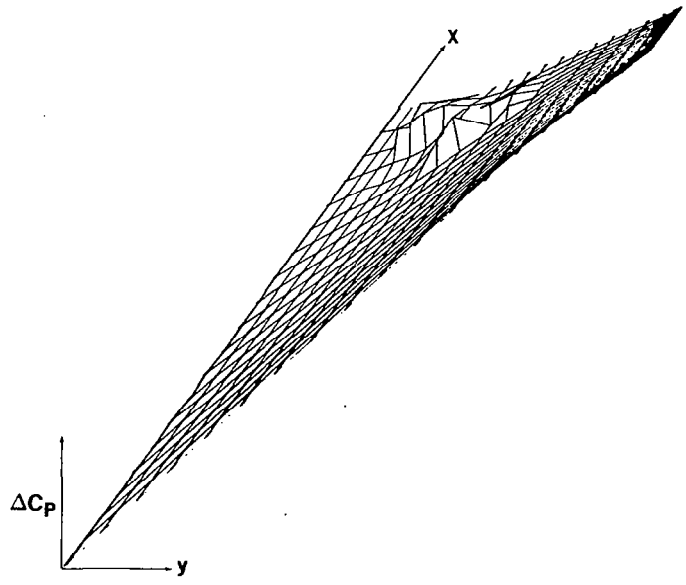

Figure 8.- Pictorial representation of nacelle-on-wing interference pressures.

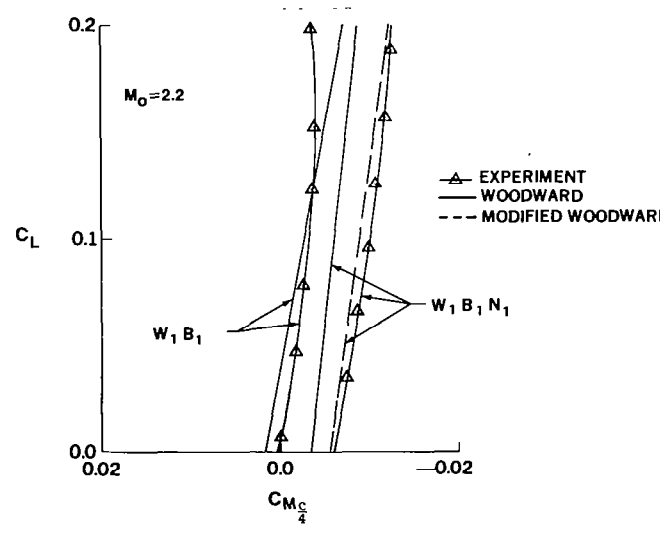

Figure 9.- Comparison of Woodward with nacelle interference modifications and experimental pitching moments; tail off, 2.2 M.

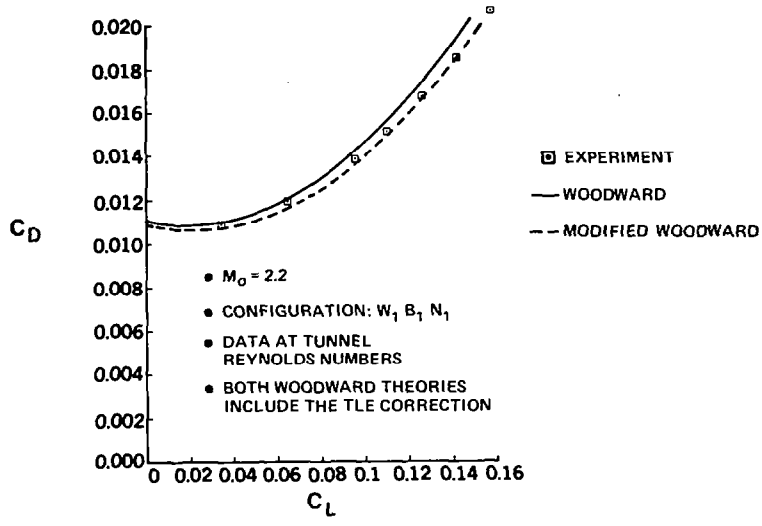

Figure 10.- Comparison of Woodward with nacelle interference modifications and experimental drag polars; 2.2 M.

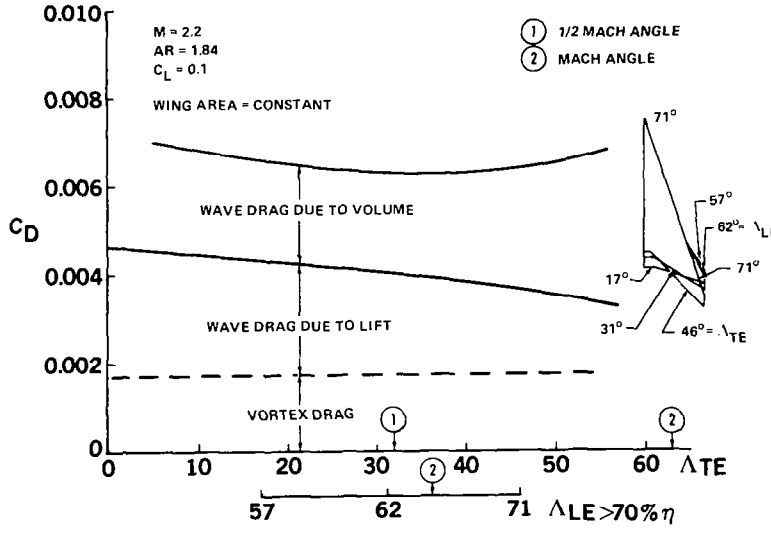

Figure 11.- Effect of trailing-edge sweep on induced drag and wave drag.

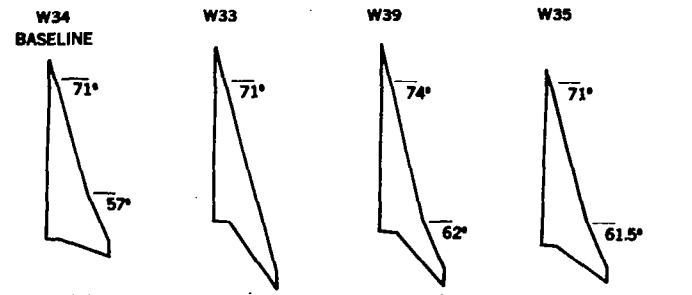

MAX TRIMMED L/D				
BASIC ANALYSIS (NO TLE CORRECTION)	9.45	9.80	9.75	9.70
REFINED ANALYSIS (WITH TLE CORRRECTION)	9.10	9.75	9.75	9.60

Figure 12.- Wing planform study, summary of selected wings; 2.2 M.

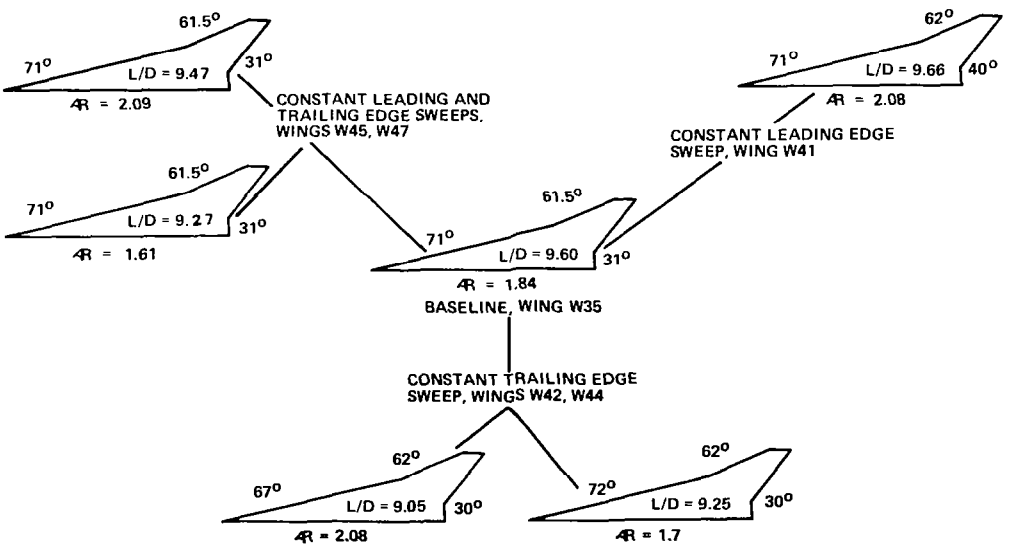

Figure 13.- L/D variations with aspect ratio; 2.2 M.

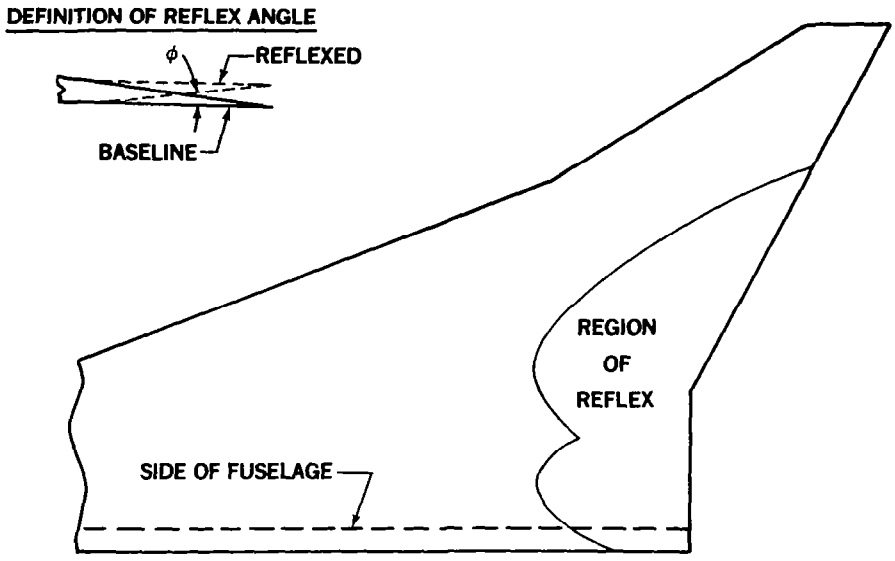

Figure 14.- Reflex in region of nacelle interference.

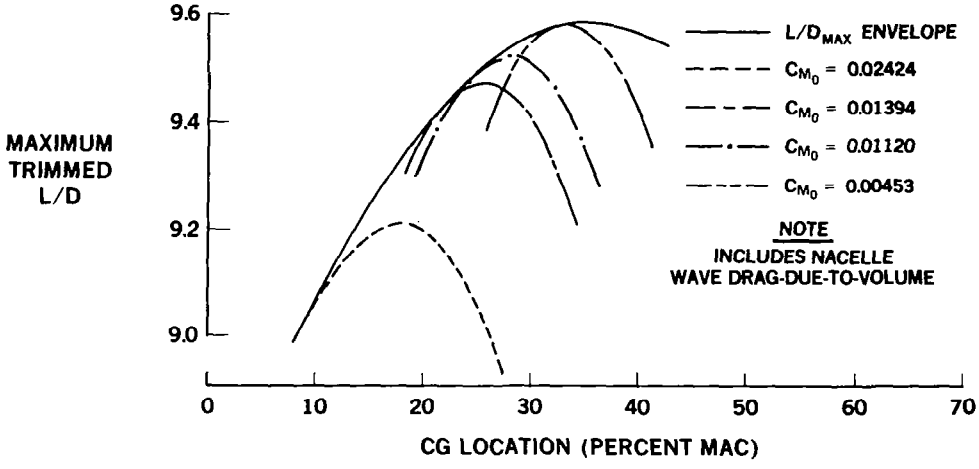

Figure 15.- Selection of wing pitching moment for optimum trimmed L/D; 2.2 M, nacelles off.

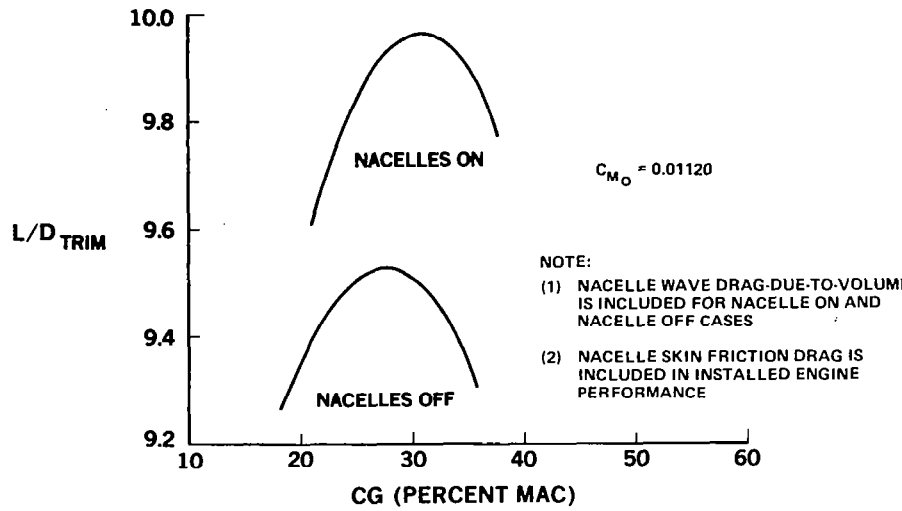

Figure 16.- Effect of nacelle addition on a pitch constrained wing; 2.2 M.

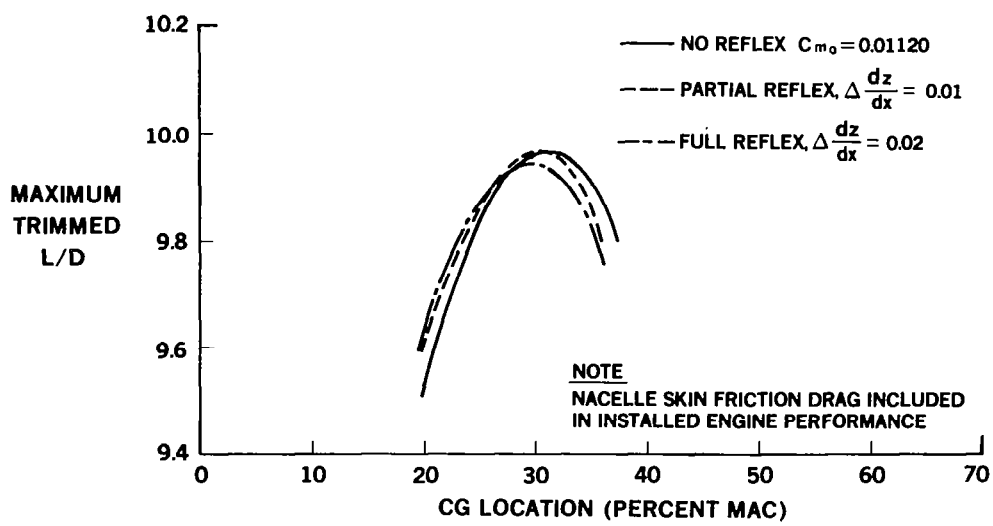

Figure 17.- Effect of reflex for nacelles on a pitch constrained wing; 2.2 M, nacelles on.

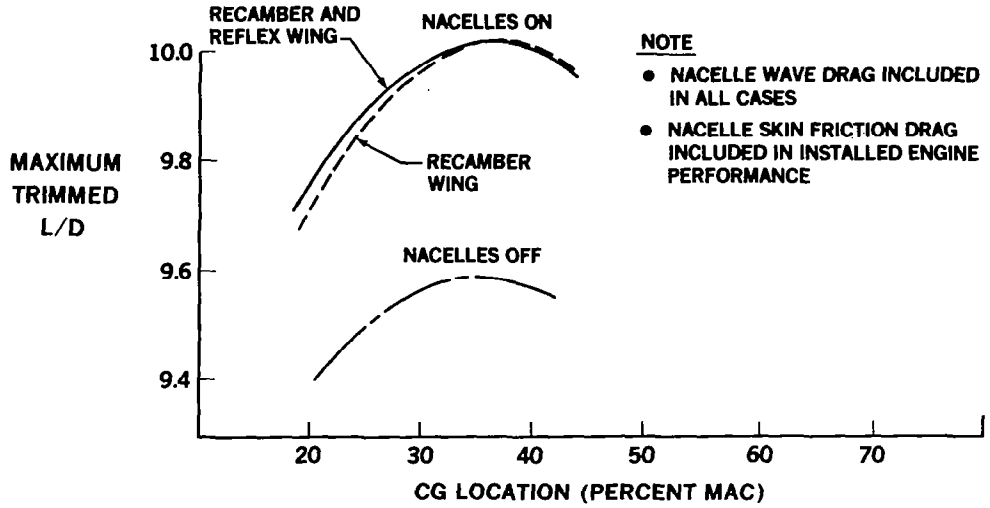

Figure 18.- Design L/D envelopes for nacelle addition with wing reflex and recamber; 2.2 M.

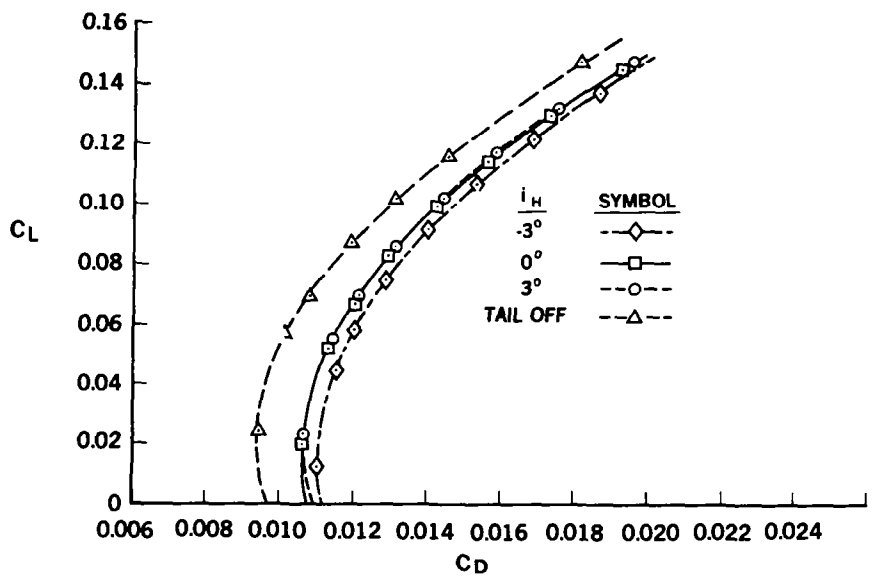

Figure 19.- Experimental tail on and off drag polars; 2.2 M.

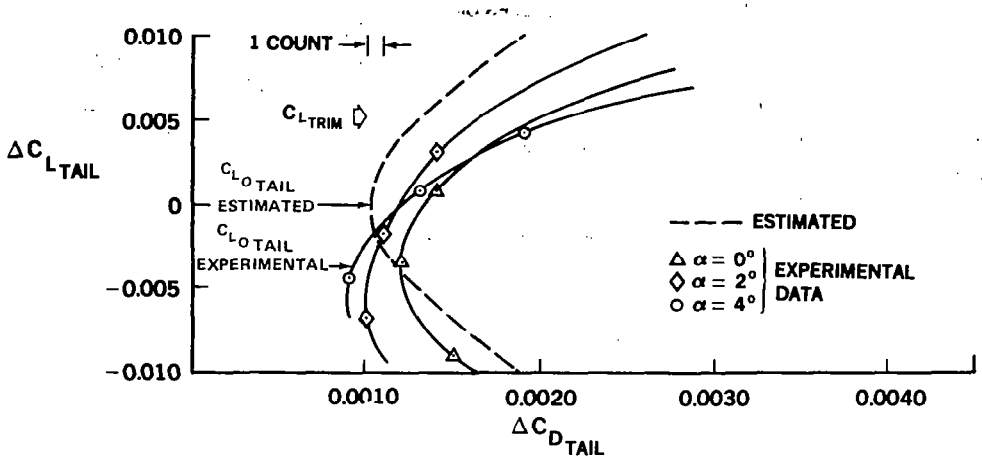

Figure 20.- Horizontal tail drag polars; 2.2 M, coefficients based on wing area.

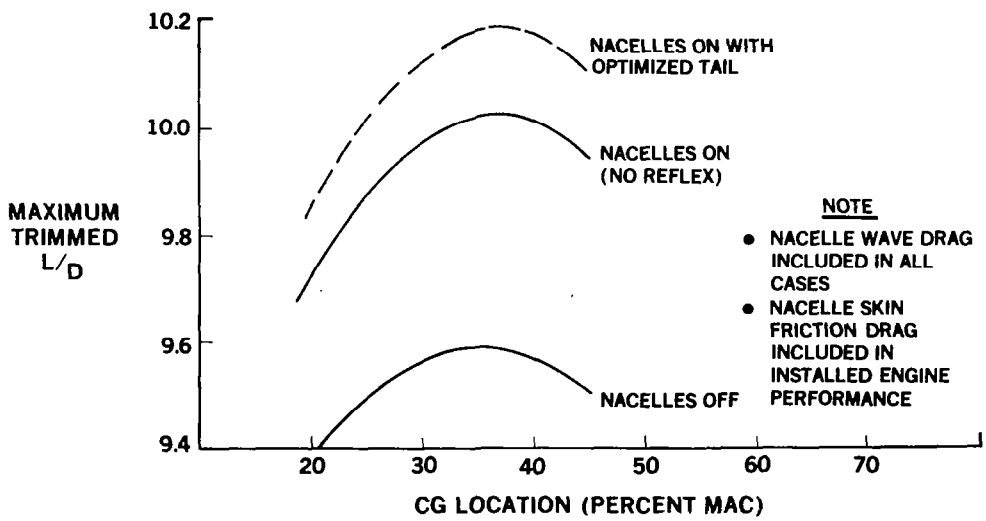

Figure 21.- Effect of optimized tail on design L/D envelopes; 2.2 M.

- TLE CORRECTION USED TO IMPROVE WOODWARD ESTIMATES
- WING W35 SELECTED AS NEW PLANFORM
- MODIFIED WOODWARD PROGRAM ACCURATELY PREDICTS EFFECT OF NACELLES
- WING RECAMBER PRODUCES FAVORABLE NACELLE INTERFERENCE
- WING REFLEX NOT NEEDED IF CG CAN BE ALLOWED TO VARY
- HORIZONTAL TAIL SHOULD BE OPTIMIZED FOR ITS TRIM LIFT
- IMPROVED METHODS ARE REQUIRED TO PROPERLY DESIGN AN OPTIMIZED TAIL

Figure 22.- Conclusions.

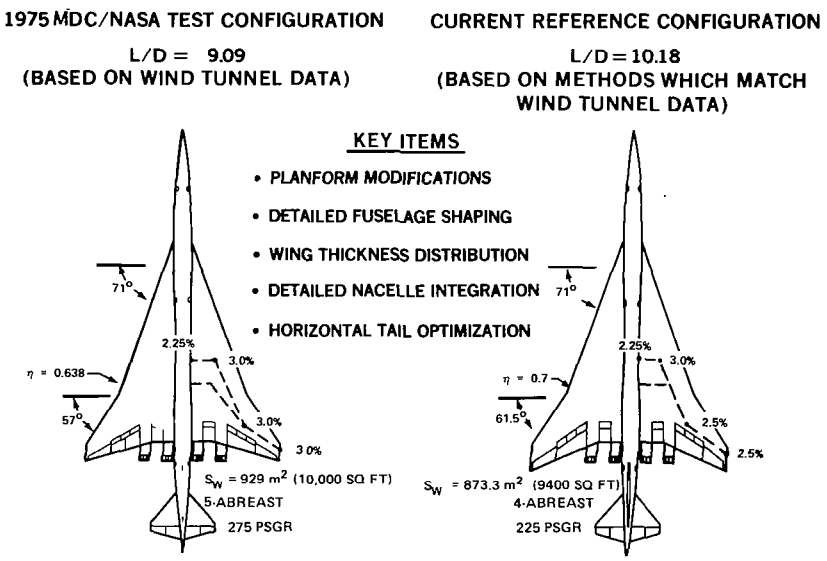

Figure 23.- Refined aerodynamic configuration; MDC/NASA test configuration compared with current reference configuration.

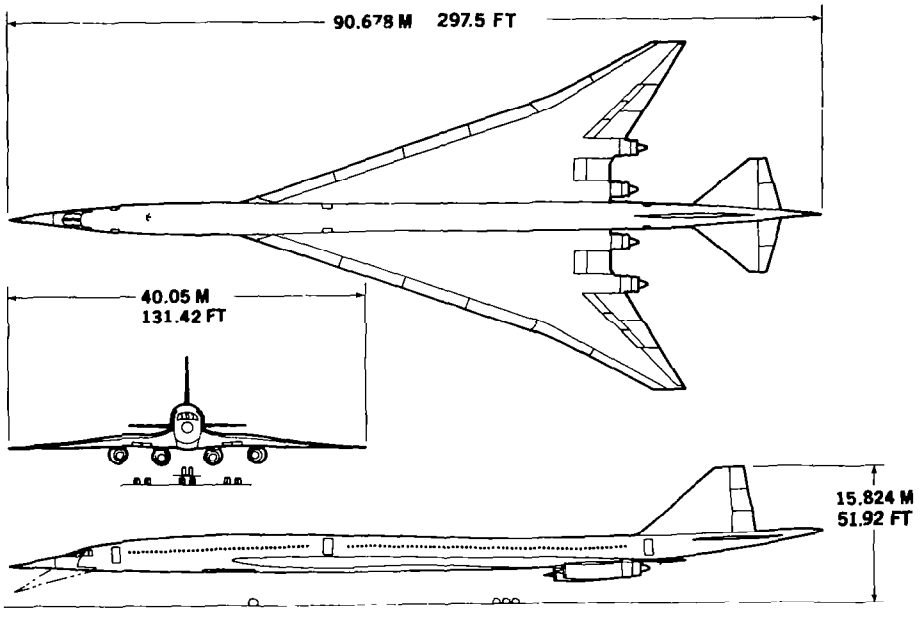

Figure 24.- Details of McDonnell Douglas D3232-2.2-3 configuration.

SUPERSONIC WINGS WITH SIGNIFICANT LEADING-EDGE THRUST AT CRUISE

A. Warner Robins, Harry W. Carlson, and Robert J. Mack
Langley Research Center

SUMMARY

Experimental/theoretical correlations are presented which show that significant levels of leading-edge thrust are possible at supersonic speeds for certain planforms which match the theoretical thrust-distribution potential with the supporting airfoil geometry. The new analytical process employed provides not only the level of leading-edge thrust attainable but also the spanwise distribution of both it and/or that component of full theoretical thrust which acts as vortex lift. Significantly improved aerodynamic performance in the moderate supersonic speed regime is indicated.

INTRODUCTION

Aerodynamicists have long known of the importance of leading-edge thrust to the performance of subsonic aircraft. These forces, which arise from the very low pressures induced by the high velocities of the flow around the leading edge from a stagnation point beneath the wing, largely counteract the drag from the remainder of the airfoil in high-aspect-ratio wings at low speeds. Very high aerodynamic efficiency for such wings is the result. The efforts to extend these benefits to the higher speeds have led to the swept wings commonly seen in present-day, long-range aircraft. Indeed, according to theory, should wing leading edges be swept sufficiently behind the Mach angle, there is potential for leading-edge thrust at supersonic speeds. Until very recently (refs. 1 and 2), however, the potential for leading-edge thrust at cruise in configurations suitable for extended supersonic cruising was generally thought to be negligible. It is the purpose of this paper to show that such is not the case, that certain planforms favor supersonic leading-edge thrust, and that with a new method for predicting the degree to which it exists as well as predicting its spanwise distribution, there exists some rationale for the exploitation thereof.

SYMBOLS

b wing span

c wing chord length

$\bar{c}$ mean aerodynamic chord

C_D drag coefficient

C_L	lift coefficient
$C_{L,opt}$	lift coefficient at maximum lift-drag ratio
C_m	pitching moment coefficient
C_A	axial or chord force coefficient
C_p	pressure coefficient
C_t	local thrust coefficient
C_T	total thrust coefficient, $2\int_0^{b/2} C_t d_y$
L/D	lift-to-drag ratio, C_L/C_D
M	free-stream Mach number
RN	free-stream Reynolds number
sfc	specific fuel consumption
t	maximum thickness of local wing chord
x	longitudinal distance to local wing leading edge
y	spanwise distance from reference axis
α	angle of attack, deg
β	$= \sqrt{M^2 - 1}$
Λ	leading-edge sweep angle

Subscript:

$\bar{c}$	referenced to mean aerodynamic chord
l	denotes limiting condition
n	quantities pertaining to a wing section normal to leading edge
max	denotes maximum value

DISCUSSION

Experimental/Theoretical Considerations

An experimental/theoretical comparison of the drag polars of three slender supersonic-cruise configurations is shown in figure 1. The two on the left which were tested at Mach number 2.7 were the last competing pair in the national SST program. The configuration on the right, which is an NASA concept (ref. 3) of essentially the same vintage, was tested at Mach number 2.6. All were tested in the NASA Langley Unitary Plan wind tunnel at a Reynolds number, based on mean aerodynamic chord, of approximately 5 million.

All three configurations have subsonic leading edges over much of the wing span (that is; local leading edge swept behind the Mach line), and the left-most concept has blunt airfoil sections; conditions conducive to leading-edge thrust. The generally good agreement between experiment and calculation (refs. 4, 5, 6) in which measured drag generally exceeds theory by small amounts, if any, would suggest some validity in the generally accepted assumption of no leading-edge thrust in the calculation methods. These data seem characteristic of supersonic drag polars at design speed, generally. Thus, supersonic design and evaluation methods have generally (and, perphaps, conveniently) neglected leading-edge thrust.

Some insight into the lack of evidence of supersonic leading-edge thrust may be gained from figure 2. Here theoretical maximum thrust and bluntness or thickness comparisons are shown (with thickness somewhat exaggerated for clarity) for two planforms having predominantly subsonic leading edges. In the case of the more conventional straight-leading-edge wing where there is potential for thrust, there is little thickness or bluntness for it to act upon. The complex-leading-edge wing, however, with its higher inboard sweep (reaching almost 80 degrees) and fuller inboard thickness shows a significant thrust potential where the geometry favors its attainment. Put another way, there is upwash where there is thickness. Experimental/theoretical comparisons of static longitudinal aerodynamic characteristics of a wing model having the planform of this complex wing will subsequently be shown. The model (ref. 1) had a design Mach number of 1.8, a design lift coefficient of 0.07, and NACA 65A004 airfoil sections and was essentially a wing alone, having a small balance housing mounted essentially symmetrically about the camber plane and faired smoothly into the forward surfaces of the wing. As shown in figure 3, tests were conducted at the design Mach number of 1.8 and at a Reynolds number, based on mean aerodynamic chord, of about 2 million. Compare first the experimental data with the no-leading-edge-thrust linear theory (refs. 7, 8, 9) without pressure-coefficient limiting or consideration of vortex lift (refs. 10 and 11). The experimental nonlinearities in the lift curve and in the pitching moment, in particular, are not represented by theory, nor is there adequate representation of lift-drag ratio at optimum lift (that is; lift coefficient for maximum lift-drag ratio). Arbitrarily limiting the linear-theory pressure coefficients (which might otherwise be below vacuum) to 3/4 vacuum results in the dashed curves. Breaks are now seen in the theory curves which would seem to result from significant and progressive lift losses from the tip region inboard, indicated by the severity of the pitching moment nonlinearity, Thus it would seem that

theory without pressure constraint calls for potential-flow pressures which physically cannot be achieved. Some other flow mechanism must therefore have existed. Assuming that, when potential flow cannot be fully maintained, the Polhamus vortex-lift analogy (ref. 10) applies, normal force increments representing the effects of separated vorticity were then applied to the limited linear theory values. These lift increments were obtained by a new method (ref. 12) which provides the necessary theoretical full leading-edge-thrust values for the arbitrary planform. The resulting theoretical values are seen (fig. 3) as the dot-dash curve. These curves of limited linear theory with vortex lift, all parameters considered, are certainly an improvement, but there remains a large discrepancy in maximum lift-drag ratio.

On the assumption that, prior to manifesting itself as vortex lift, some leading-edge thrust might, indeed, have occurred, the final curve showing the pressure-coefficient-limited linear theory without vortex lift but with full theoretical thrust is presented. Agreement at maximum lift-drag ratio is much improved. There remains, however, a problem beyond predicting leading-edge thrust or vortex lift at supersonic speeds, and that is the analytical representation of the transition from the thrusting mode to the vortex-lift mode.

New Analytical Method

A new method (ref. 13) for estimation of attainable thrust has been developed and the key features thereof are presented in figure 4. The method applies simple sweep theory to wings of arbitrary planform, permitting two-dimensional analysis. A comprehensive survey of two-dimensional data is correlated to provide limiting-pressure restraints as a function of these normal Mach and Reynolds numbers. Correlation equations derived from theoretical two-dimensional data then provide thrust-coefficient limitation as a function of theoretical thrust, limiting pressure, and airfoil section parameters. With these relationships programmed as a subroutine in existing lifting-surface programs, spanwise distribution of attainable thrust is directly available for use in lift and drag estimation. These lift and drag relationships are compatible with the Polhamus leading-edge-suction analogy for fully detached leading-edge flow when the analogy is taken to be the limiting case of a gradual rotation of the full suction vector as leading-edge thrust is lost. Thus the method does provide a rational analytical means for making the transition from the thrust mode to that of vortex lift.

In figure 5, experimental axial-force coefficient--a parameter sensitive to leading-edge thrust--is compared over the lift range to theoretical values for full leading-ledge thrust and for no leading-edge thrust, as well as for the attainable-thrust values from the new method. Not only is a significant amount of experimental leading-edge thrust indicated, but a reasonably good representation of experiment by the new attainable-thrust method is obtained in the positive-lift range up to lift coefficients of 0.3 or so.

Returning via figure 6 to the lift-drag ratio comparisons between theory and experiment, the attainable curve is seen to agree with the full-thrust values in a very limited low-lift range. From the low-lift-coefficient values of such

agreement to the highest values shown, the new method provides that less and less of the leading-edge force be manifested as thrust, and more and more be manifested as vortex lift. The inset flow-visualization photographs, taken at the conditions represented by the darkened symbols, are included to provide an understanding of the flow physics at those points. The upper pair of photographs are of the upper surfaces of the model with a fluorescent oil coating, which, under the action of the flow, has essentially stabilized at each of the two conditions. The picture at the right is taken from above the right rear quadrant of the model as it is immersed in humid, partially condensed flow and illuminated by a thin fan of intense light positioned normal to the flow. Strong vortices appear at this high-lift condition as the pair of dark circles located above the wing surface about midway between the wing leading edges and the model plane of symmetry. Thus the upper-surface flow appears to vary from the classic potential-flow condition at the lift coefficient for which the wing camber was designed, through a condition in which there is a mixed flow including some vorticity, to the condition at high lifts in which there is strong, fully separated vorticity located well inboard of the leading edge. In any event, the modified linear theory method, which attempts to account for these nonlinear types of flow, provides, in addition to an indication of significant amounts of leading-edge thrust, a substantially improved representation of the experimental results. Note for future reference that angles of attack of 2 and 4 degrees fall just below and above that for maximum lift-drag ratio.

Spanwise Distribution of Thrust

With supersonic thrust distribution being so critically dependent upon the degree to which the leading edge is swept behind the Mach line, consideration of the spanwise distribution of thrust in figure 7 begins with the spanwise distribution of a parameter, $1/(\beta \cot \Lambda)$, which is the ratio of the tangent of the leading-edge sweep to the tangent of the sweep of the Mach line. Thus, the higher the values of $1/(\beta \cot \Lambda)$, the more subsonic the leading edge, with the value of unity representing a sonic leading edge, and lesser values corresponding to a supersonic leading edge. The calculated values of local thrust coefficient for the experimental configuration at test Reynolds number (2.07×10^6) and at design Mach number (1.8) are shown divided by α^2. This is a convenient way to express local thrust, since theoretical maximum thrust coefficient is a direct function of α^2 and the aim here is to show that as angle of attack is increased the portion of maximum theoretical thrust which appears to be attainable becomes smaller. It should be recalled that the theory assumes that attainable thrust is that component of maximum theoretical thrust which manifests itself as thrust, while the normal component of that theoretical maximum manifests itself as vortex lift, with the difference between the $C_{t,max}$ and C_t curves defining the location and intensity of the latter. Thus, theoretically, the loss of thrust and the attendant development of vortex lift begins outboard and moves progressively inboard as angle of attack is increased. This analytical degradation in percent of maximum theoretical thrust and the corresponding increase in vortex lift, as angle of attack is increased from 2 to 4 degrees in this figure, correspond to the lift-drag-ratio decrements between full and attainable thrust at these two angles in

figure 6. The calculated values of both figures 6 and 7 indicate the effect of considerable vorticity at the higher angle (4°), with the former (figure 6) providing strong experimental evidence in the corresponding oil-flow photograph.

Lest it be assumed that attainable thrust decreases with increasing angle of attack, the remaining thrust-distribution figures, beginning with figure 8, will deal in absolute values of local thrust coefficient at the two angles of attack of 2 and 4 degrees. In fact, they will show that calculated attainable thrust at 4 degrees exceeds, in most cases, the theoretical maximum thrust at 2 degrees angle of attack.

The calculated values of absolute local thrust coefficients in figure 8 are for the same conditions as in the previous figure, except that values for a full-scale Reynolds number of 128 million (corresponding to $\bar{c}$ = 25.3 meters and an altitude of 17400 meters) have been added. For convenience, the value of total thrust coefficient C_T, which is twice the integral of the local coefficients, is shown for each Reynolds number. At an angle of attack of two degrees, thrust loss begins near midsemispan and there is a count (0.0001) or so difference in the total thrust coefficient between Reynolds numbers of 2.07 million and 128 million, with the value for 128 million being about two counts less than the theoretical maximum value (RN = ∞). At four degrees however, there is an appreciable difference in location of thrust loss and nearly five counts difference between tunnel and full-scale Reynolds number, with that for the latter being approximately half the 34-count theoretical maximum value. In this case, the effects of Reynolds number on thrust are seen to be important, but certainly not critical.

The local thrust coefficient values of figure 9 are for the same basic configuration at a Reynolds number of 128 million, but with another Mach number, 1.4, as well as the original 1.8. While the spanwise location of thrust loss here does not appear to be strongly Mach-number dependent, both the attainable and theoretical maximum values of total thrust appear to be very much so. At both angles of attack, attainable thrust at Mach number 1.4 is about double that at Mach number 1.8, with some 35-1/2 counts appearing to be attainable out of the 65 counts of theoretical maximum thrust at M = 1.4. The fact that, at both two and four degrees, the calculations show full thrust to extend somewhat further out on the wing semispan at Mach number 1.4 than at 1.8 is surprising, since the inboard leading edge contains a significant portion swept at 79-1/2 degrees--a very subsonic segment with a normal Mach number of 0.255. This suggests that design values of $1/(\beta \cot \Lambda)$ might be significantly increased over those of the present wing at Mach number 1.8.

In figure 10, calculated local thrust coefficients for a Mach number of 1.8 and a Reynolds number of 128 million are shown for the basic configuration with its 4-percent-thick wing, and for variations in wing thickness to 3 and 5 percent. Qualitatively, the inboard progression of thrust loss with decreasing thickness is as would be expected. As was the case for Reynolds-number variation in figure 8, the effect of the present variable (t/c) is seen, within the range shown (0.03 to 0.05), to be important to leading-ledge thrust, but certainly not critical.

Thrust-Dependent Lift-Drag Ratio

The previous thrust-distribution figures (8, 9, and 10) have shown, for the basic study configuration and variations thereof, the dependence of leading-edge thrust on Reynolds number, Mach number, and thickness ratio. Figure 11 addresses the effects of these same three variables (RN, M, and t/c) on maximum lift-drag ratio, including leading-edge thrust effects. In each case, the theoretical curves for full leading-edge thrust, no leading-edge thrust, and attainable thrust are shown. Where available, the appropriate experimental points are presented. Unless otherwise indicated on an abscissa, Mach number is 1.8 and thickness ratio is 0.04.

The large effect on maximum lift-drag ratio of the variation of Reynolds number is almost entirely that due to the change in viscous drag. Calculated attainable thrust is seen to vary from about half the increment between no thrust and full thrust at the lowest Reynolds number to about 60 percent at the highest--a small amount compared to that due to the viscous-drag change. The agreement between experiment and calculation seems reasonably good.

The effect on maximum lift-drag ratio of varying Mach number over the range shown is particularly large for the full-thrust case at both the test and full-scale Reynolds numbers, with the attainable-thrust curve showing a similarly large variation at the high Reynolds number. In contrast, the attainable-thrust variation at test Reynolds number (2.07 million) falls about midway between the full-thrust values and those for the relatively insensitive no-thrust curve. This greater thrust dependency on Mach number certainly suggests that the extrapolations of such wind-tunnel data to full-scale conditions take careful account of leading-edge thrust. Again, agreement between experiment and calculation is reasonably good, but particularly significant to the designer is that agreement at the $M = 1.5$ condition, for it suggests that very high values of $1/(\beta \cot \Lambda)$ (or very low Mach-number components normal to the wing leading edge) may be tolerated.

The sharp variations of maximum lift-drag ratio with thickness ratio is again seen to be an effect on mimimum drag. Here, it is a large variation of zero-lift wave drag with thickness. The steeper variation at the full-scale Reynolds number is due to the combining of the additional viscous-drag decrement with the sharply changing wave drag to produce, as thickness is reduced, very low values of minimum drag and consequently high lift-drag ratios. An interesting additional point is that, at full-scale Reynolds number, values of maximum lift-drag ratio corresponding to the attainable-thrust curve did not fall off toward the no-thrust curve as thickness decreased.

It is to be noted that supersonic-cruise designs have generally been based on analytical methods which excluded leading-edge thrust, corresponding to the dashed-curve values of figure 11. In the light of the experimentally and analytically indicated high tolerance to high values of $1/(\beta \cot \Lambda)$ (lower Mach numbers, here) and the calculatively indicated insensitivity of thrust to thickness (for moderate changes in thickness), very high levels of supersonic aerodynamic performance seem possible.

Returning via figure 12 to the spanwise variation of the design parameter, $1/(\beta \cot \Lambda)$, upon which leading-edge thrust is so dependent, an additional curve (beyond that shown in figure 7) corresponding to the basic configuration at a Mach number of 1.5 has been added as the dashed line. It is this much more subsonic leading edge which appears to have worked well at M = 1.5. The leading edge of a new wing with a design Mach number of 1.8, but with the same spanwise schedule of $1/(\beta \cot \Lambda)$ as the original wing (A) at Mach number 1.5, is defined by the indicated integration of the dashed curve. Requiring, in addition, the same tip chord, the same chord as at the trailing-edge break, and the same wing area as (A) results in the new wing (B) . Calculated maximum lift-drag ratio and the product of it and Mach number are shown for 4-percent-thick versions of both wings (A) and (B) at Mach numbers 1.5 and 1.8 and at test and full-scale Reynolds numbers in figure 13. The available corresponding experimental values are also shown as the circle symbols. An interesting result shown in this figure is that, at full-scale Reynolds number, both maximum L/D and M·L/D are higher for wing (B) at M = 1.8 than for wing (A) at either Mach number. From this point, a designer might profitably trade toward lower outboard panel sweep without significant performance loss and then trade toward a thickness substantially less than the present 4 percent so as to produce extraordinarily high levels of aerodynamic performance.

Additional Design Considerations

Taking a broader view of wings designed to operate at cruise with a significant amount of leading-edge thrust, several design-oriented observations can be made with the aid of figure 14. Here the planform of the present study is shown shaded and superimposed on the containing delta planform. Recognizing the seeming inevitable shrinkage in wing size (to reduce wetted area and weight) in the successive stages of design cycling from the initial concept, the lower half of the planform figure was prepared to show the containing delta and a shrunken version thereof having the same plan area as shaded above. Immediately apparent is its much-reduced effective lifting length and shorter span compared to the initial shaded planform. Considering that supersonic drag due to lift is an inverse function of the combination of the square of the lifting length and the square of the span, it is critically important to aerodynamic performance to be particularly selective in reducing wing area. The shaded planform reduces wing area but preserves the overall length and span, and thus should tend to retain the aerodynamic efficiency of the larger containing delta. Another point regarding the shaded planform is that structurally it should tend to resemble a wing having the planform represented by the shaded area rearward of the short-dash line, but to which has been added a forward strake.

A final point to be made through this figure is in regard to treatment of the planform at the wing tip. It is suggested that the wing tip be tailored to provide that the tip vortex initiate inboard along the leading edge so as to place not only its suction effect on the upper surface but its pumping or scavenging effect over the tip area which might otherwise experience flow separation as in the inset sketch below.

CONCLUDING REMARKS

There are several observations growing out of the present study which should be of interest to the designer of supersonic-cruise vehicles. Foremost is that experimental results indicate the presence of significant amounts of leading-edge thrust at supersonic speeds. Furthermore, there is a new methodology for the prediction of attainable leading-edge thrust and/or that component of thrust which acts as vortex lift. There is, as well, a new class of supersonic wings which matches the theoretical thrust-distribution potential with supporting airfoil geometry (that is, which places upwash where there is bluntness). These should lead to higher maximum lift-drag ratios at higher lift coefficients. Noting that with the attainment of substantial amounts of leading-edge thrust at supersonic speeds increasing with diminishing Mach numbers, efforts to significantly improve range factor ($M \cdot L/D \div sfc$) should give rise to serious consideration of lower supersonic-cruise speeds (of the order of Mach number 2 or less). These lower speeds will certainly offer more speed-compatible airframes and propulsion systems.

REFERENCES

1. Robins, A. Warner; Lamb, Milton; and Miller, David S.: Aerodynamic Characteristics at Mach Numbers of 1.5, 1.8, and 2.0 of a Blended Wing-Body Configuration With and Without Integral Canards. NASA TP-1427, 1979.

2. Robins, A. W.; and H. W. Carlson: High Performance Wings With Significant Leading-Edge Thrust at Supersonic Speeds. Presented at AIAA Aircraft Systems and Technology Meeting, August 20-22, 1979, New York, New York.

3. Morris, Odell A.; and Fournier, Roger H.: Aerodynamic Characteristics at Mach Numbers 2.30, 2.60, and 2.96 of a Supersonic Transport Model Having a Fixed, Warped Wing. NASA TM X-1115, 1965.

4. Harris, Roy V., Jr. An Analysis and Correlation of Aircraft Wave Drag. NASA TM X-947, 1964.

5. Middleton, Wilbur D.; and Carlson, Harry W.: Numerical Method of Estimating and Optimizing Supersonic Aerodynamic Characteristics of Arbitrary Planform Wings. J. Aircraft, vol. 2, no. 4, July-August, 1965, pp. 261-265.

6. Sommer, Simon C.; and Short, Barbara J.: Free-Flight Measurements of Turbulent-Boundary-Layer Skin Friction in the Presence of Severe Aerodynamic Heating at Mach Numbers From 2.8 to 7.0. NACA TN 3391, 1955.

7. Middleton, W. D.; and Lundry, J. L.: A Computational System for Aerodynamic Design and Analysis of Supersonic Aircraft. Part 1 - General Description and Theoretical Development. NASA CR-2715, 1976.

8. Middleton, W. D.; Lundry, J. L; and Coleman, R. G.: A Computational System for Aerodynamic Design and Analysis of Supersonic Aircraft. Part 2 - User's Manual. NASA CR-2716, 1976.

9. Middleton, W. D.; Lundry, J. L.; and Coleman, R. G.: A Computational System for Aerodynamic Design and Analysis of Supersonic Aircraft. Part 3 - Computer Program Description. NASA CR-2717, 1976.

10. Polhamus, Edward C.: Predictions of Vortex-Lift Characteristics by a Leading-Edge Suction Analogy. J. Aircraft, vol. 8, no. 4, April 1971, pp. 193-199.

11. Kulfan, R. M.: Wing Geometry Effects on Leading Edge Vortices. Presented at AIAA Aircraft Systems and Technology Meeting, August 20-22, 1979, New York, New York.

12. Carlson, Harry W.; and Mack, Robert J.: Estimation of Leading-Edge Thrust for Supersonic Wings of Arbitrary Planform. NASA TP-1270, 1978.

13. Carlson, Harry W.; Mack, Robert J.; and Barger, Raymond L.: Estimation of Attainable Leading-Edge Thrust for Wings at Subsonic and Supersonic Speeds. NASA TP-1500, 1979.

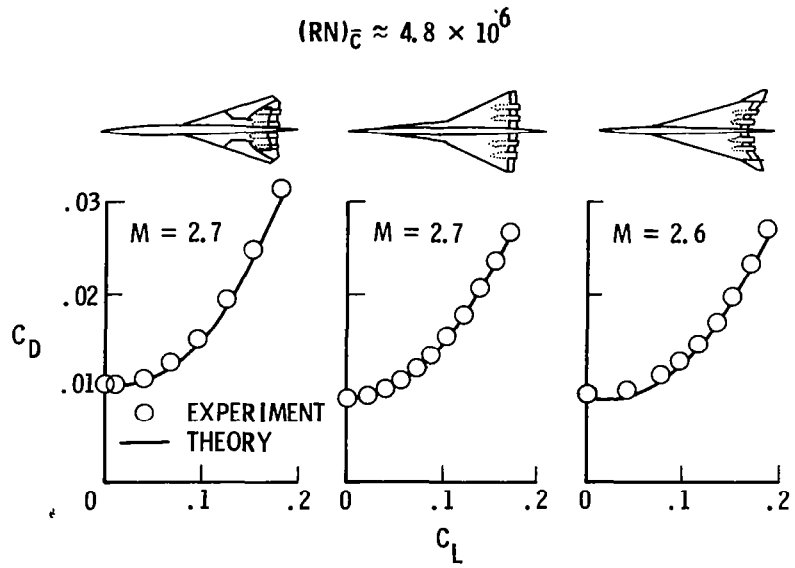

Figure 1.- Experimental/theoretical drag polars of models of supersonic-cruise aircraft.

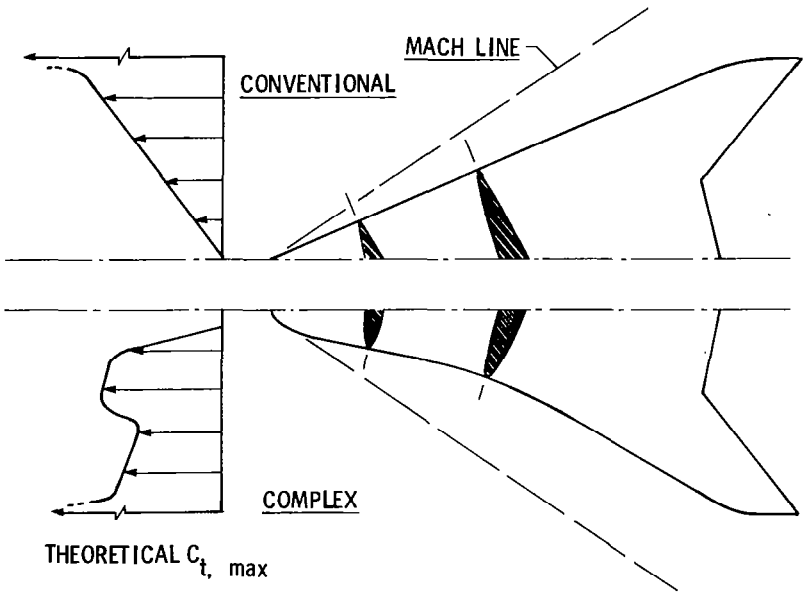

Figure 2.- Thurst and thickness comparisons near wing leading edge.

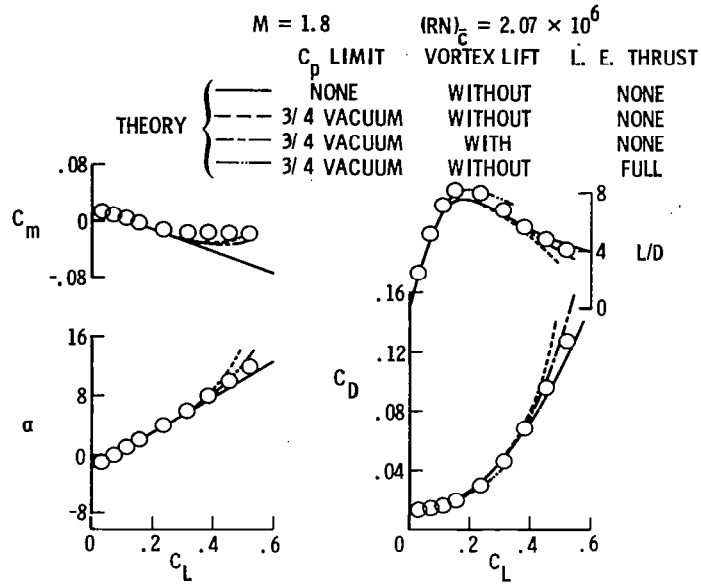

Figure 3.- Experimental/theoretical comparisons of longitudinal aerodynamic characteristics.

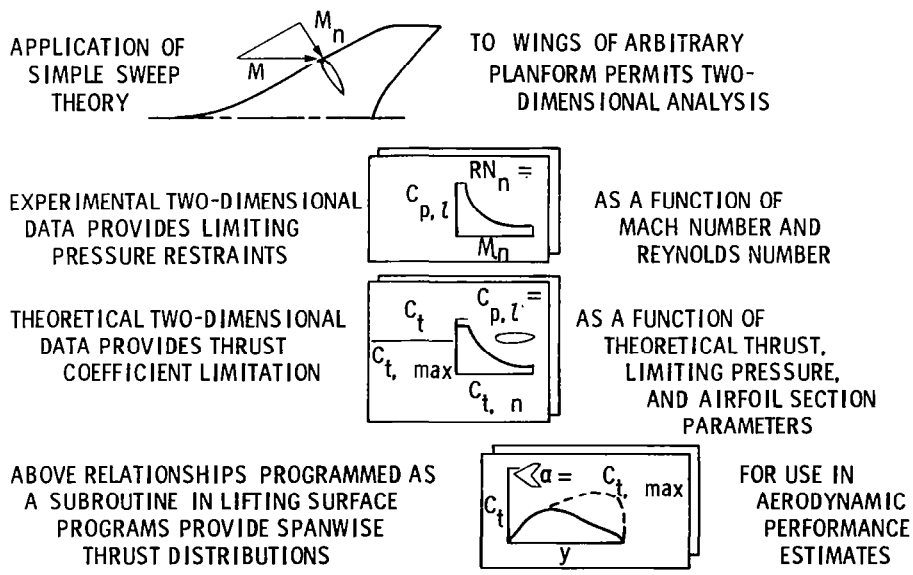

Figure 4.- Key features of attainable-thrust prediction method.

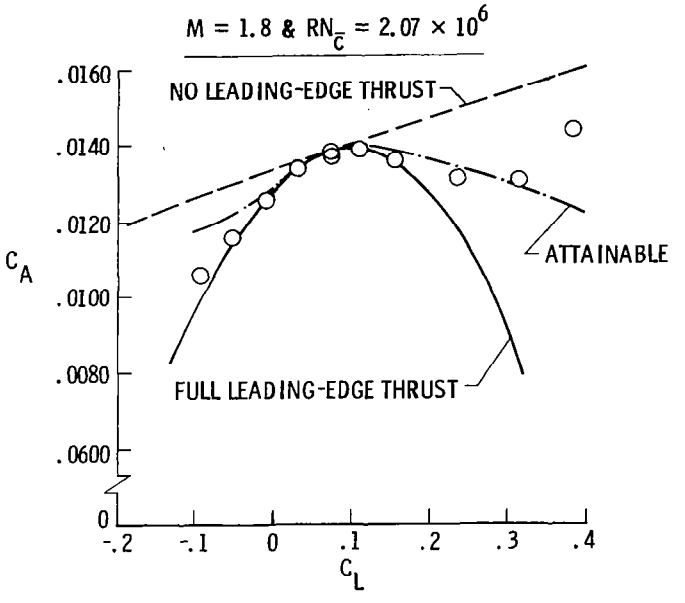

Figure 5.- Experimental/theoretical axial-force coefficients.

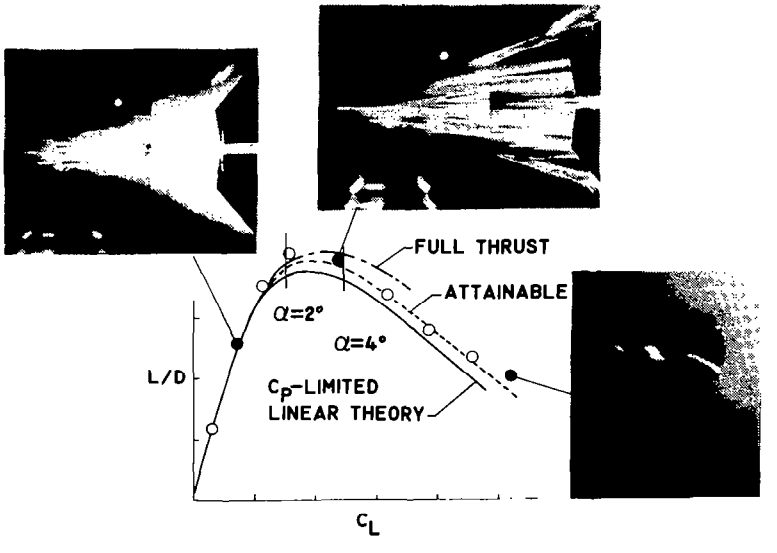

Figure 6.- Comparison of theories with both qualitative and quantitative experimental data.

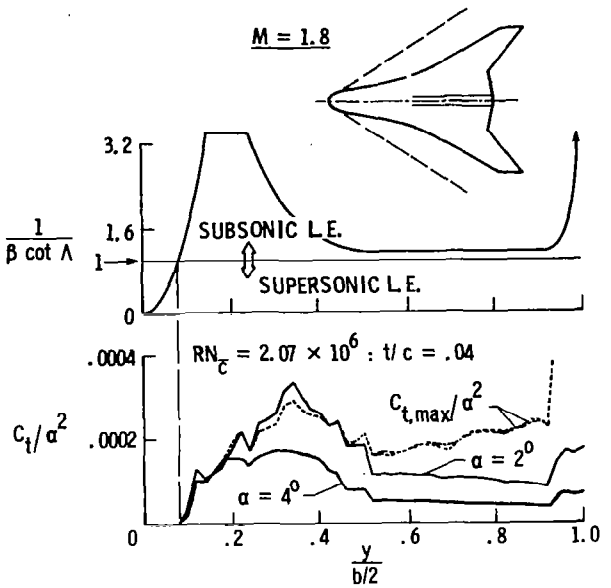

Figure 7.- Spanwise distribution of leading-edge thrust.

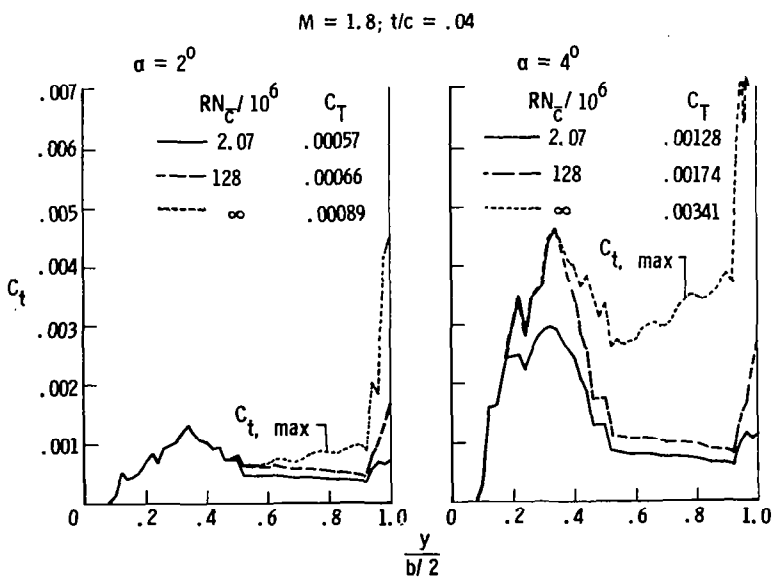

Figure 8.- L. E. thrust dependency on Reynolds number.

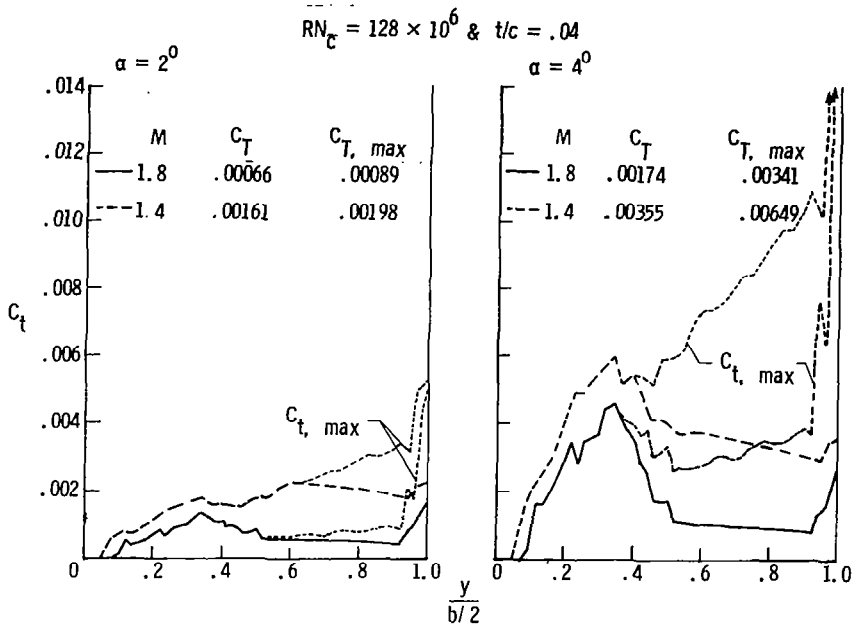

Figure 9.- L. E. thrust dependency on Mach number.

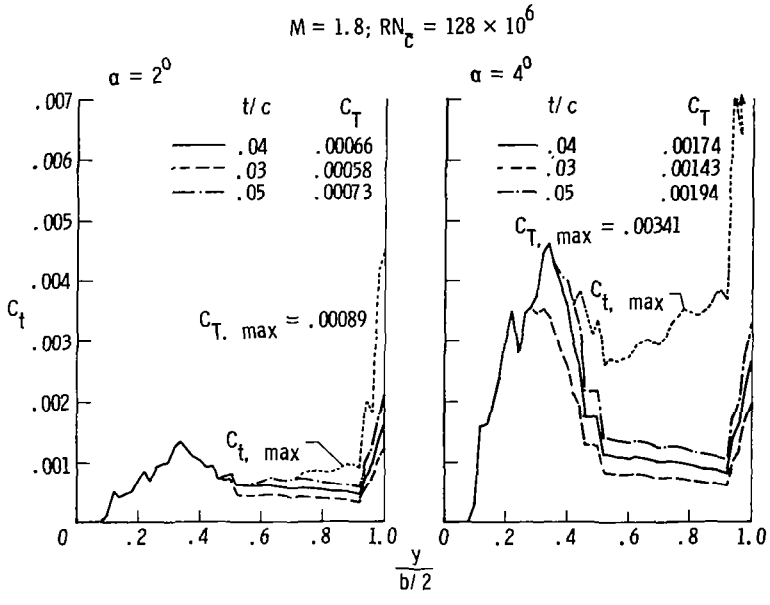

Figure 10.- L. E. thrust dependency on thickness ratio.

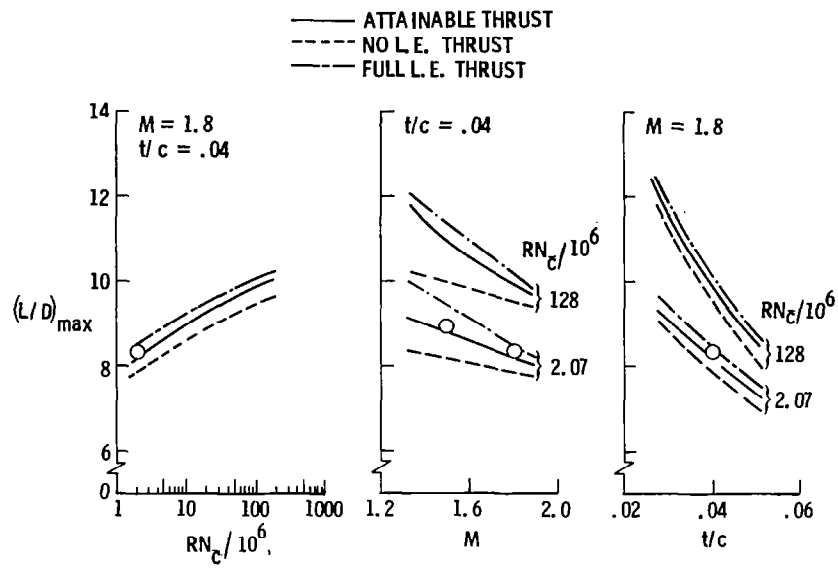

Figure 11.- Maximum lift/drag ratio as affected by Reynolds & Mach numbers & thickness.

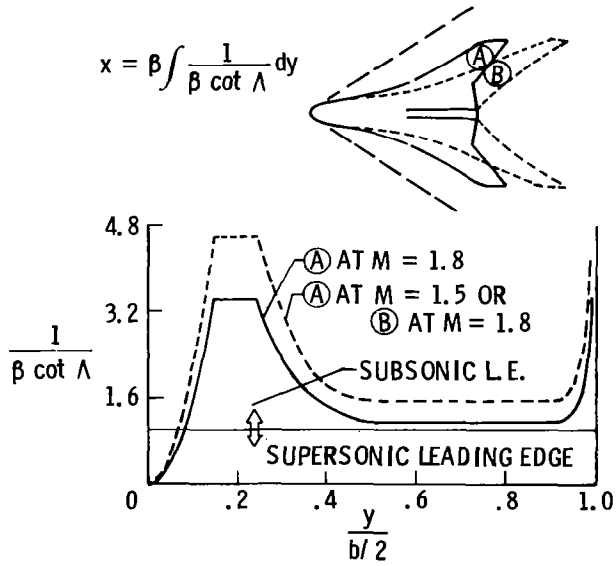

Figure 12.- Generation of alternate wing.

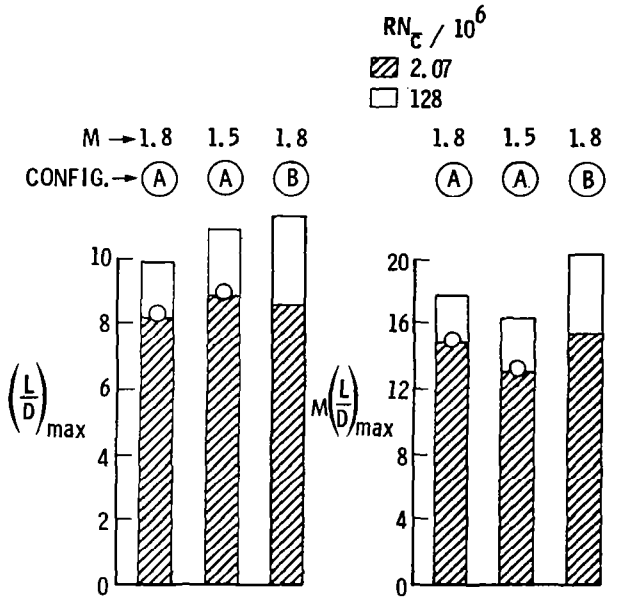

Figure 13.- Aerodynamic performance of original & alternate wings.

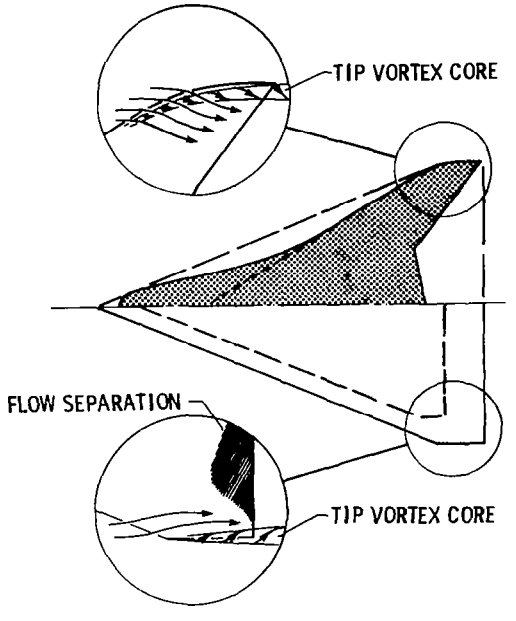

Figure 14.- Additional design considerations.

SESSION II - STABILITY AND CONTROL

INTRODUCTORY REMARKS

Seth B. Anderson
NASA Ames Research Center

The 1976 SCAR conference pointed out that the aerodynamic configuration required for performance considerations of supersonic cruise aircraft (SCA) adversely affected stability and control particularly at low speeds. More so than for conventional (subsonic) transport aircraft, there are more complex interdisciplinary relationships in the design of SCA configurations. In addition to the traditional disciplines such as aerodynamics, propulsion, and structure, increased demand for improved efficiency has made the obtainment of satisfactory stability and control characteristics even more of a challenge. In addition, only a relatively small data base on handling qualities criteria exists to aid the certification process for advanced SCA transports.

The purpose of the stability and control session is to review results of recent research related to stability and control problems peculiar to SCA configurations. For example, the long, slender fuselage required for low drag places the cockpit far ahead of the C. G. resulting in greater difficulty for the pilot to make precise flight path adjustments in landing approach. The first paper in this session describes the format used for the design criteria for handling qualities which address specific failures, approach to dangerous flight conditions, flight at high angles of attack, longitudinal and lateral directional stability and control requirements, and the primary and secondary flight control system failure states. The effect of the large forward placement of the crew is brought out by examples of the design criteria for lateral accelerations at the cockpit during rolling maneuvers, roll control effectiveness, and effective time delay in the pilot's command channel.

It is well known that more efficient flight can be achieved for SCA by flying with neutral or unstable longitudinal stability conditions. This requires, however, a stability augmentation control system to ease the pilot's workload. The second paper examines control system design features including the type of system used to handle non-linear conditions, the adequacy of the augmentation gains, and how the quantization levels and filter update rates affect control system performance. These studies were carried out for the landing approach task using a fixed base, real time simulator set-up.

The arrow wing SCA has long been considered a promising concept for achieving superior high Mach number cruise performance; however, some sacrifice in low speed, high angle of attack stability and control can occur. Typical problem areas include static and dynamic longitudinal instability, sluggish pitch response, excessive positive dihedral effect, low attainable roll control power, poor turn entry characteristics, low Dutch roll damping, and non-linear, reduced directional stability. The third paper gives an evaluation of an arrow wing design in landing approach using a piloted moving base simulator with particular

reference control system design concepts to improve the inherently poor stability and control features of this configuration.

Finally, airport and community noise enters into the stability and control requirements because of the influence of the propulsion system on flight path control. The last paper of this session examines the difficulty of flying "ideal" flight profiles for community noise abatement, the degree of stability augmentation required, and the need for pilot information displays to provide tracking guidance. These results were obtained in piloted simulation studies during take-off and landings.

FLYING QUALITIES DESIGN CRITERIA APPLICABLE TO SUPERSONIC CRUISE AIRCRAFT*

Charles R. Chalk
Calspan Advanced Technology Center

SUMMARY

A comprehensive set of flying qualities design criteria has been prepared for use in the NASA Supersonic Cruise Research Program. The framework for stating the design criteria is established and design criteria are included which address specific failures, approach to dangerous flight conditions, flight at high angle of attack, longitudinal and lateral-directional stability and control, the primary flight control system and secondary flight controls. In this paper, examples are given of lateral-directional design criteria limiting lateral accelerations at the cockpit, time to roll through 30° of bank and time delay in the pilot's command path. Flight test data from the Concorde certification program are used to substantiate a number of the proposed design criteria.

INTRODUCTION

NASA/Langley Research Center and the three system study contractors are beginning to perform analysis and simulation studies to define the flying qualities, ride qualities and flight control characteristics of the large flexible aircraft which are typical of supersonic cruise aircraft concepts. To facilitate comparison of the flying qualities characteristics of the aircraft concepts being studied by the system study contractors and to aid NASA/LRC in directing flying qualities research activities, a comprehensive set of flying qualities design criteria have been prepared by Calspan Corporation (Ref. 1) under NASA/LRC sponsorship. These design criteria are not intended to replace the Federal Aviation Regulations, FAR, in any formal or legal sense. The proposed design criteria are more quantitative than the FAR's and are more similar to the requirements of the military specification for flying qualities, MIL-F-8785B(ASG). The design criteria are intended to aid the system study contractors and to provide NASA with a common basis for comparison of design concepts for supersonic cruise aircraft.

---

*The research reported upon in this paper was performed under U.S. Air Force Contract F33615-78-C-3602 and funded by the Langley Research Center of the National Aeronautics and Space Administration.

FORMAT OF DESIGN CRITERIA DOCUMENT

The general format of the design criteria document is similar to MIL-F-8785B(ASG), however, the structure is simplified because only one class of aircraft is being addressed. The concepts of Flight Phases and Levels of flying qualities are employed to permit tailoring the design criteria to the task and to indicate how much degradation in the stability and control characteristics can be tolerated in particular circumstances. The designer is required to define airplane normal states (i.e., combinations of weight, center of gravity, moments and products of inertia, and configuration), failure states, operational flight envelopes and service flight envelopes for the aircraft and its operational role.

The possibility that the airplane may be required to operate under abnormal conditions is recognized and a degraded Level of flying qualities is permitted for flight outside the operational envelope, for failure of airplane components and for combinations of these circumstances. The design procedure for determining theoretical compliance with airplane failure state requirements is adopted from MIL-F-8785B(ASG). This procedure is illustrated in Figure 1. (This figure is taken from Ref. 2 which contains a comprehensive review of the methods used, in various civil and military flying qualities documents, to deal with system failures that degrade flying qualities.) The probabilistic approach to the treatment of failure effects illustrated in Figure 1 is supplemented in Ref. 1 by inclusion of design criteria for specific failure cases which must be considered regardless of the probability of occurrence.

The general content and organization of Ref. 1 is indicated by the outline of major sections illustrated in Figure 2. The number of design criteria paragraphs contained in Ref. 1 prohibits presenting a detail review of the criteria in this paper; however, three design criteria relating lateral-directional responses to pilot roll controller commands are presented and discussed in a following section. In preparing the design criteria, the author has drawn on previous work performed by Calspan during development of MIL-F-8785B(ASG), MIL-F-83300 and the study to revise MIL-F-8785B(ASG) reported in Ref. 3. In addition, flying qualities special conditions developed by the FAA for certification of the Concorde were reviewed as were the TSS standards developed by the French and British certification authorities for application to the Concorde. The results of flying qualities experiments such as those reported in Refs. 4 and 5 have also been used to formulate and to substantiate the design criteria.

With permission from British Aerospace, Inc. and Aerospatiale, the flight test data, Ref. 6, used for certification of the Concorde by the British, French and U.S. authorities was made available to Calspan and has been used where appropriate to substantiate the proposed design criteria. Additional Concorde flight test data taken by FAA test teams is contained in Ref. 7.

Since MIL-F-8785B(ASG) was adopted in 1969, the Air Force has sponsored a number of studies to compare the characteristics of existing aircraft with the flying qualities requirements of that specification. Ref. 8 documents the comparison of the C-5A aircraft with MIL-F-8785B(ASG) requirements. Flight test data in Ref. 8 were also used to substantiate the proposed design criteria.

EXAMPLES OF DESIGN CRITERIA

Lateral Acceleration at the Cockpit During Rolling Maneuvers

In 1977, Calspan performed in-flight simulation tests, Ref. 9, of a supersonic cruise aircraft equipped with a flight control system designed by NASA/LRC engineers. Although this configuration had been given satisfactory pilot ratings, Ref. 10, when evaluated on the NASA/LRC fixed base simulator, it was rated unacceptable when evaluated in the TIFS in-flight simulator. Figure 3. This configuration was rated unacceptable even though it satisfied the lateral-directional flying qualities requirements of MIL-F-8785B(ASG) and the revised versions of these requirements recommended in Ref. 3. The major reason for the unacceptable pilot ratings was the lateral acceleration response at the pilot's station during rolling and turning maneuvers. The configuration being evaluated had the pilot located 44.2 m ahead of the C.G. and 11 m above the x stability axis. Thus, angular accelerations in roll and yaw following an abrupt roll controller input caused lateral acceleration at the pilot's station. This problem was ameliorated by redesign of the flight control system to reduce proverse yaw due to aileron and by filtering the pilot's roll commands with a low-pass first-order filter to reduce the roll acceleration. This solution makes it more difficult to meet roll performance requirements and tends to introduce phase shift and effective time delay in the pilot's roll command channel.

In 1978 a second in-flight simulation program was performed in the TIFS airplane to obtain data which could be used to draft a design criterion to limit the magnitude of the lateral acceleration at the pilot's station, which occurs when the pilot performs rolling and turning maneuvers. Configurations evaluated in this experiment included a simulation of the lateral-directional dynamics and cockpit location of the Boeing 747, but mostly the configurations were based on a supersonic cruise aircraft defined by NASA/LRC and variations of the lateral-directional stability and control augmentation system. One version of the flight control system produced an airplane that could be maneuvered, in roll and turning maneuvers, with the roll controller without producing any sideslip. This configuration had the spiral root at the origin and quite high roll damping although the Dutch roll mode was low frequency and not very heavily damped. This configuration was used to explore the effects of locating the pilot's station at various positions in the rigid body. The

following coordinate locations in the stability axis system were simulated.

x_s	z_s	
44.2	-11	*Nominal pilot location*
44.2	0	*On x_s stability axis*
0	-11	*Above C.G.*
0	0	*At C.G.*

Thus, the airplane dynamics and conventional flying qualities parameters were identical for these four configurations, but the linear accelerations experienced by the pilot were different. The simulation concept is illustrated by the profile drawing of Figure 4. This type of simulation is possible in the TIFS airplane because it is equipped with six independent force and moment controls which permit forcing the evaluation cockpit to follow the motions of any designated point in the model axis system.

The lateral acceleration response to a step roll controller command, for each of the simulated cockpit locations, is illustrated in Figure 5. The roll rate response, which is common to all of the configurations, is also shown in Figure 5.

The two sets of roll rate and lateral acceleration time histories shown in Figure 6 illustrate the effect of adding a first-order low-pass filter in the pilot's roll command channel. The filter is effective in reducing the initial lateral acceleration transient, but it also slows the development of maximum roll rate which increases the time required to change bank angle by 30°. Also, the filter causes an effective time delay, which, depending on the magnitude of the total time delay in the roll channel, may cause degraded flying qualities.

The pilot ratings from this TIFS experiment were correlated with a parameter derived from the roll rate and the side acceleration (at the pilot) time histories resulting from a step roll controller input

$$\left.\frac{n_{y_{pilot_{max}}}}{p_{max}}\right|_{\substack{step\ input \\ t \leqslant 2\ sec}}$$

The intent is to limit the magnitude of the lateral acceleration at the pilot location resulting from pilot roll commands. The lateral acceleration measure is divided by the roll rate measure as a somewhat arbitrary technique for normalizing the parameter for various magnitude control commands. The pilot rating data are plotted in Figure 7 and lines are sketched on the figure to illustrate the interpretation of the data that were employed to establish the following design criteria:

Level	$\left.\frac{n_{y_{pilot_{max}}}}{p_{max}}\right\|$ step input $t \leq 2.5$ sec
1	.012 g/deg/sec
2	.035 g/deg/sec
3	.058 g/deg/sec

This design criteria should influence the aircraft and control system design as follows:

- Avoid excitation of Dutch roll by roll controller commands.
- Avoid proverse yaw due to roll controller commands.
- Limit the roll acceleration resulting from pilot commands.
- Locate the pilot near the C.G..
- Locate the pilot near the x stability axis, i.e., keep the fuselage at low angle of attack.

Roll Control Effectiveness

Included in the design criteria of Ref. 1 is one which limits the time required to change bank angle by 30°. This design criteria is analogous to the roll performance requirement of MIL-F-8785B(ASG) except the application to Flight Phases is different, i.e., takeoff is grouped with nonterminal Flight Phases and the values of the time permitted to change bank angle by 30° are larger. The justification for increasing the t_{30} values, i.e., reducing the required roll performance relative to that specified in MIL-F-8785B(ASG) is firstly, that the roll performance required by MIL-F-8785B(ASG) was not well substantiated by data specific to large aircraft; secondly, flight test data for the C-5A and the Concorde aircraft are now available, Figures 8, 9, 10 and 11, which do not substantiate the Class III roll performance requirements of MIL-F-8785B(ASG) and, thirdly, flight experiments have been performed in which the roll control power used by the pilot during landing was measured. The roll control power available to the pilot was then progressively limited to smaller values in subsequent evaluations until the pilot ratings were degraded beyond the 6.5 boundary, see Ref. 11. These tests included the effects of crosswinds in the range 20-30 kts. The data set from Ref. 11 that is most typical of supersonic cruise aircraft in the landing Flight Phase is presented in Figure 12. Translation of this data into t_{30} values gives the following

Pilot Rating	t_{30}
3.5	3.27
6.5	4.80
8.5	6.80

where an increment $\Delta t = 0.3$ *sec* has been included to account for the time required for the control input to reach 50% of final amplitude. These t_{30} values do not substantiate the roll performance values for Class III airplanes in the Landing Flight Phase required by MIL-F-8785B(ASG) which are: Level 1, $t_{30} = 2.5$; Level 2, $t_{30} = 3.2$; Level 3, $t_{30} = 4.0$.

Because the side acceleration problem described in the previous section may cause designers to limit the roll acceleration that the pilot can command, which may degrade the roll performance, it is considered necessary to define minimum roll performance design criteria. Therefore, the preliminary draft of Ref. 1 includes the following limits on t_{30}.

Level	*Landing*	*Takeoff and nonterminal*
1	$t_{30} \leq 3.2$ *sec*	$t_{30} \leq 4.0$ *sec*
2	$t_{30} \leq 4.0$	$t_{30} \leq 5.0$
3	$t_{30} \leq 5.0$	$t_{30} \leq 6.0$

These are preliminary values which may be changed after further review of substantiation data.

EFFECTIVE TIME DELAY IN COMMAND PATH

Flight experiments performed by Calspan in variable stability aircraft (NT-33, B-26 and C-131H) have shown that phase shift and transport time delay in the pilot's command channel has a very degrading effect on the closed-loop pilot-airplane dynamic system. See for example Refs. 12 and 13. Similar results have been reported in Ref. 14 from experiments performed in the Princeton University variable stability Navion. Examples of the degradation in pilot rating that resulted from introduction of transport time delay in the pilot's pitch and roll command paths are illustrated in Figures 13 and 14 which are taken from Ref. 13. The effect on pilot rating of a first-order filter in the roll command path was also evaluated in Ref. 13 and the results are shown in Figure 15. Ref. 14 contains data on the effects of varying the sample rate of a zero-order sample and hold device in the pilot's command channel. All of these experiments demonstrate that phase shift and transport time delay can cause degraded flying qualities.

Phase shift and transport time delay can result from cascading dynamic elements in the command path such as a feel system, linkage boost servos, surface actuators, and shaping networks or prefilters. Digital flight control hardware such as A/D and D/A converters, sample and hold, computer iteration cycle, etc. can also introduce phase shift and transport time delay in the command path. As was indicated in the discussion of lateral acceleration

at the pilot's station, limiting the pilot's ability to command roll acceleration by including a filter in his command path is effective in ameliorating the lateral acceleration but it tends to increase phase shift and time delay in the command path. Also, in large flexible aircraft, the designer may include a filter on the pilot's commands to prevent excitation of structural modes.

Thus, there are design pressures which may tend to cause higher than desired amounts of phase shift or transport time delay in the command paths and because the degrading effects of having too much are so severe, it is highly important that the flying qualities design guide include design criteria to address this potential problem.

The flight experiments of Refs. 12, 13, and 14 demonstrate that the amount of phase shift and time delay that can be tolerated is highly task dependent, i.e., tasks requiring tight closed-loop control are most sensitive. Also, the tests indicate that the effects of low sample rate, pure transport delay or cascaded dynamic elements may not be equivalent and, therefore, specific analysis and simulation may be necessary to evaluate a given case.

The design guidance contained in Ref. 1 is stated as follows: In general, the designer should make every effort to provide a linear or smoothly varying response to cockpit controller displacement and to control force for all amplitudes of control input, including values of stick force within the range of allowable breakout forces. In particular, the phase lag and transport time delay in the pilot's pitch, roll and yaw command channels shall be kept to a minimum to avoid pilot-induced oscillations and degradation of the dynamic control capability with the pilot in the loop.

It is desirable to include command channel dynamic effects in an overall design criteria, such as paragraph 3.5.6 "Pitch Dynamics with the Pilot in the Loop"; however, limit values of effective time delay in the pitch, roll and yaw command channels are separately stated as follows:

t_1 ~ Effective Time Delay in Command Path

Level	Pitch	Roll and Yaw
1	.14 sec	.20 sec
2	.19 sec	.28 sec
3	.22 sec	.33 sec

These time delay values are maximums found tolerable in combination with good airplane dynamics. Significantly smaller command path time delays may be required to realize acceptable flying qualities in specific cases.

CONCLUDING REMARKS

This paper has briefly described the work performed by Calspan during the first phase of a contracted effort with NASA/LRC which has dealt primarily with flying qualities of the rigid aircraft. The next phase of the effort will be concerned with mathematical models used for representation of airframe structural modes and the effects of airframe flexibility on flying qualities, ride qualities and flight control system design.

REFERENCES

1. Chalk, C. R.: "Calspan Recommendations for SCR Flying Qualities Design Criteria," TIFS Memo No. 906, Claspan Corporation, Oct. 1979.

2. Snyder, C. T.: "Advanced Control Technology and Airworthiness Flying Qualities Requirements," AIAA Conference Paper, NASA TM X-3409, pp. 707-733, August 1976.

3. Chalk, C. R.; DiFranco, D. A.; Lebacqz, J. V.; and Neal, T. P.: "Revisions to MIL-F-8785B(ASG) Proposed by Cornell Aeronautical Laboratory Under Contract F33615-71-C-1254," April 1973, AFFDL-TR-72-41.

4. Wasserman, R.; and Mitchell, J. F.: "In-Flight Simulation of Minimum Longitudinal Stability for Large Delta-Wing Transports in Landing Approach and Touchdown," February 1973, AFFDL-TR-72-143.

5. Weingarten, N. C.: "An Investigation of Low Speed Lateral Acceleration Characteristics of Supersonic Cruise Transports Utilizing the Total In-Fligth Simulator (TIFS)," July 1979, NASA CR 159059.

6. Aerospatiale: "T.S.S.Concorde, RAPPORT D'ESSAIS EN VOL DE CERTIFICATION - QUALITES DE VOL," 1976.

7. Abrams, R.; Benefield, T. D.; and Tuck, D. A.: "Concorde 001 Flying Qualities Tests," July 1973, Report No. FAA-FS-73-1.

8. Lockheed-Georgia Company: "Evaluation of the Flying Qualities Requirements of MIL-F-8785(ASG) Using the C-5A Airplane," March 1975, AFFDL-TR-75-3.

9. Reynolds, P. A.; and Weingarten, N. C.: "Calspan Data From the Advanced Supersonic Technology Flight Tests," Calspan/TIFS Memo No. 821, 24 June 1977.

10. Grantham, W. D.; et. al.: "Ground-Based and In-Flight Simulator Studies of Low-Speed Handling Characteristics of Two Supersonic Cruise Transport Concepts," NASA Technical Paper 1240, July 1978.

11. Hall, G. W.; and Boothe, E. M.: "An In-Flight Investigation of Lateral-Directional Dynamics for the Landing Approach," October 1970, AFFDL TR-70-145.

12. Smith, R. E.: "Effects of Control System Dynamics on Fighter Approach and Landing Longitudinal Flying Qualities," March 1978, Calspan Report No. AK-5280-F-12.

13. Smith, R. E.: "Equivalent System Verification and Evaluation of Augmentation System Effects on Fighter Approach and Landing Flying Qualities," August 1979, Calspan Report No. 6241-F-3.

14. Stengel, R. F.; and Miller, G. E.: "Flight Tests of a Microprocessor Control System," AIAA Computers in Aerospace II Conference, October 22-24, 1979, Los Angeles, California.

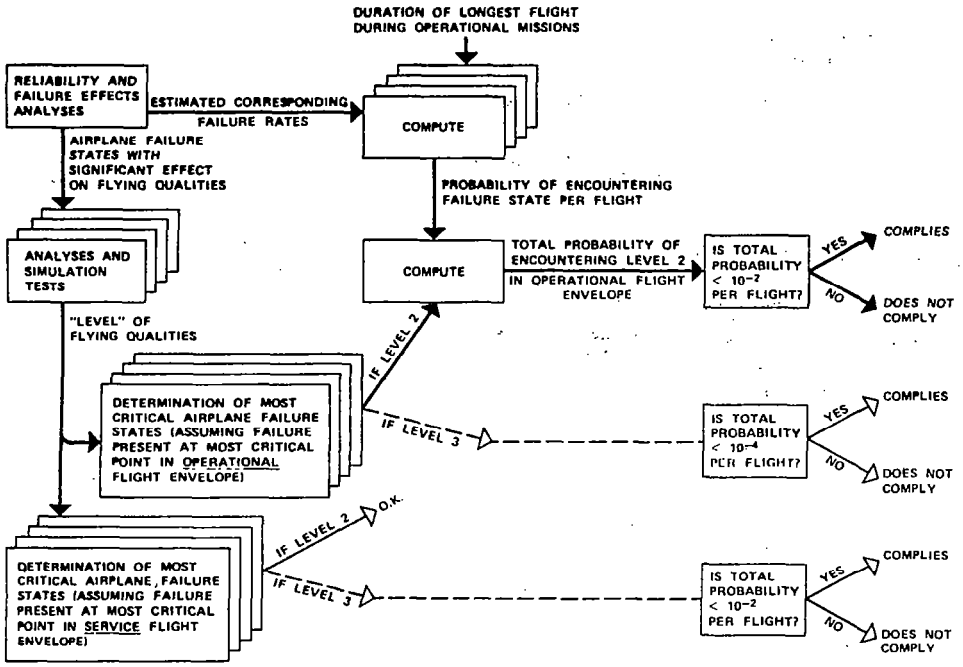

Figure 1.- MIL-F-8785B (ASG) procedure for determining theoretical compliance with airplane failure state requirements.

OUTLINE

1. SCOPE AND CLASSIFICATIONS
   - APPLICABILITY
   - FLIGHT PHASES
   - LEVELS OF FLYING QUALITIES

2. DEFINITIONS AND ASSOCIATIONS
   - AIRPLANE STATES
   - FLIGHT ENVELOPES
   - ASSOCIATION OF LEVELS - AIRPLANE STATE - FLIGHT ENVELOPES

3. FLYING QUALITIES DESIGN CRITERIA
   - SPECIFIC FAILURE STATES
   - APPROACH TO DANGEROUS FLIGHT CONDITIONS
   - FLIGHT AT HIGH ANGLE OF ATTACK
   - LONGITUDINAL DESIGN CRITERIA
   - LATERAL-DIRECTIONAL DESIGN CRITERIA
   - CHARACTERISTICS OF THE PRIMARY FLIGHT CONTROL SYSTEM
   - CHARACTERISTICS OF SECONDARY CONTROL SYSTEMS

4. SYMBOLS AND DEFINITIONS

Figure 2.- Outline of major sections of reference 1.

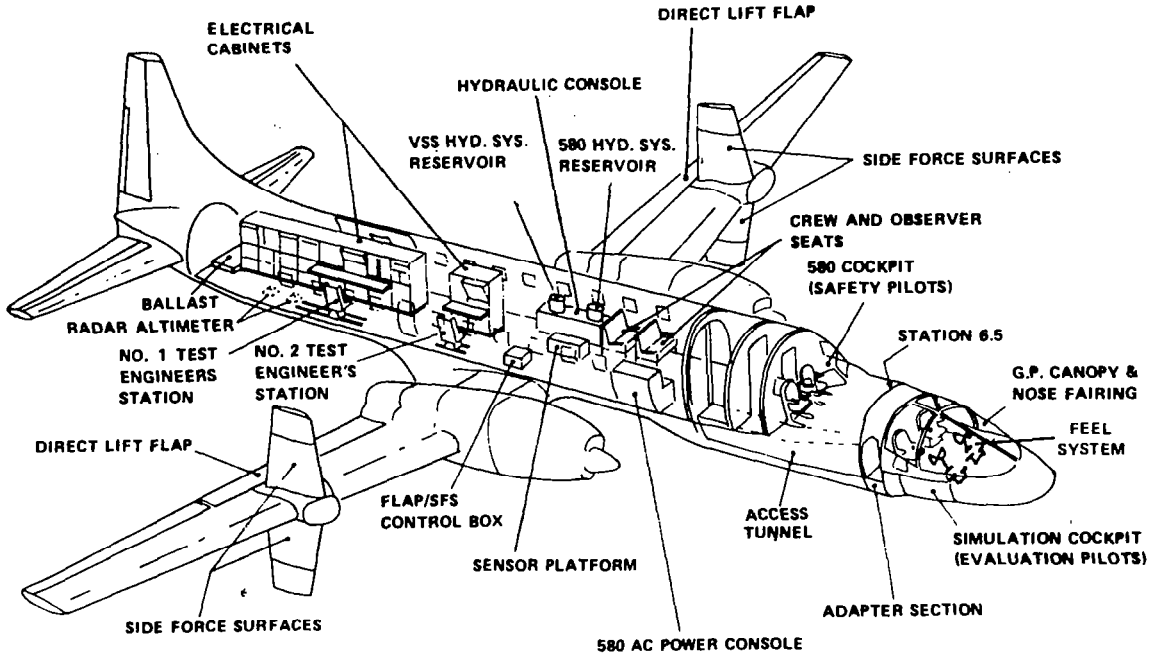

Figure 3.- USAF/Calspan TIFS airplane.

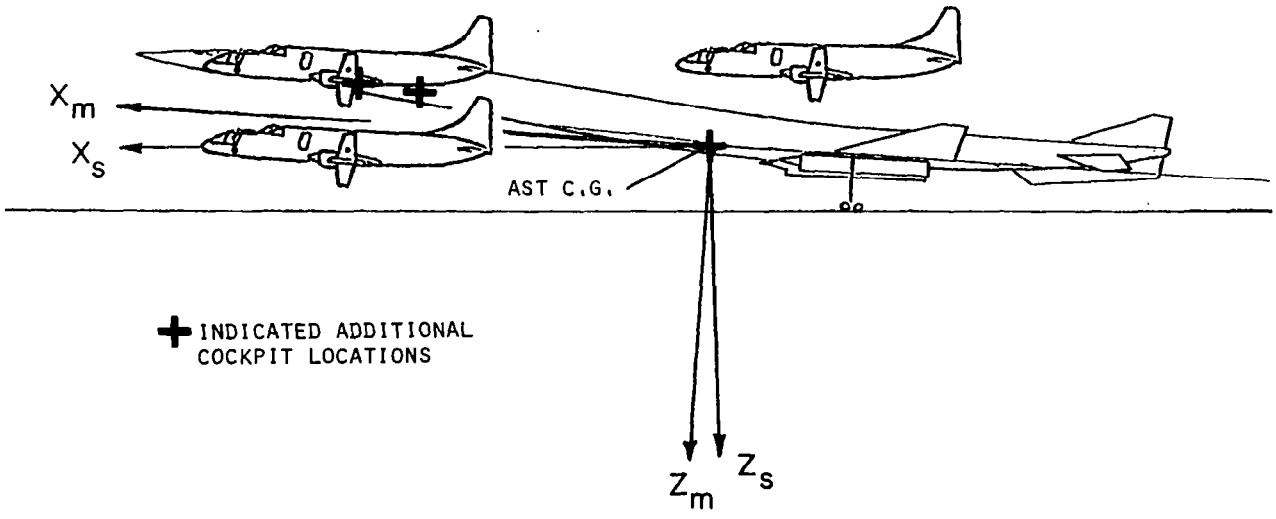

Figure 4.- Cockpit locations simulated in TIFS experiment.

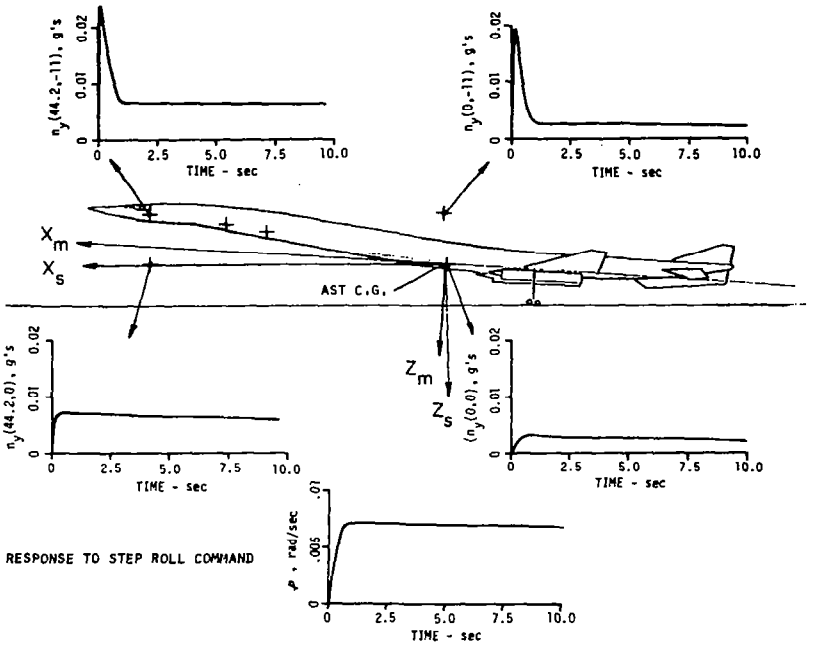

Figure 5.- Response to step roll command.

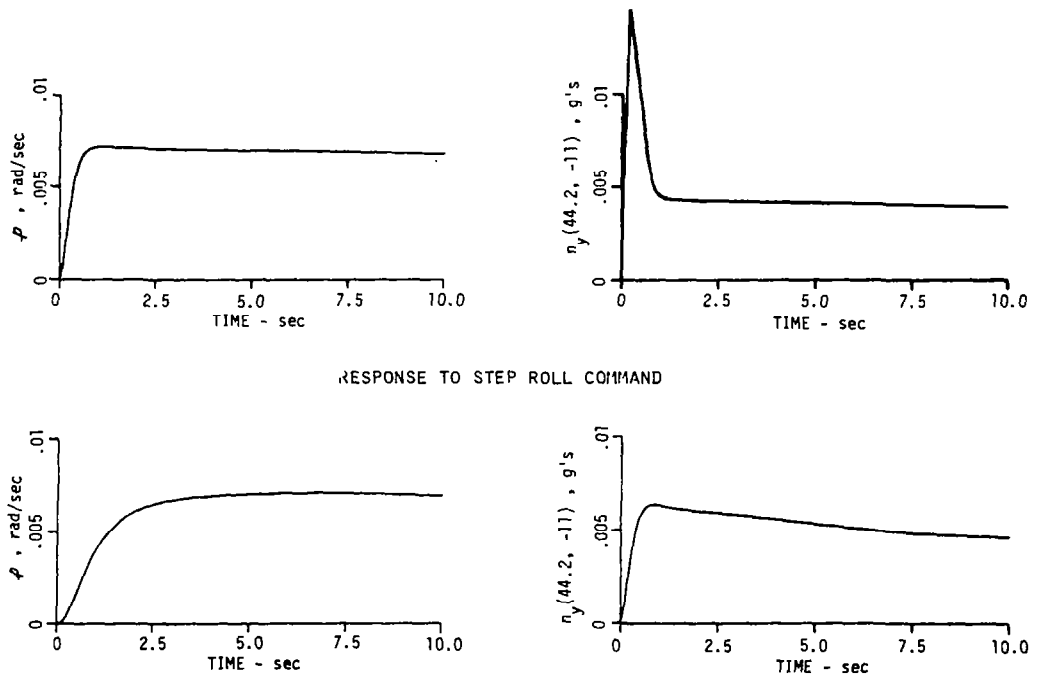

Figure 6.- Response to step roll command through first order filter with time constant, T = 0.91.

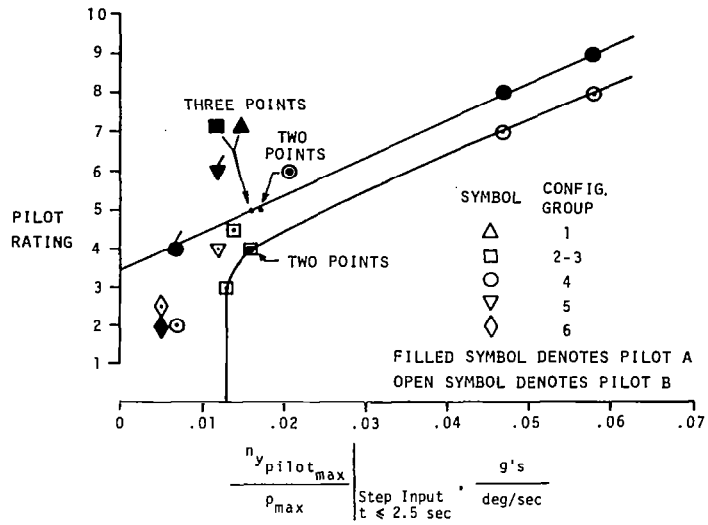

NOTES: 1. Flagged points are configurations specifically downgraded by Pilot A due to poor Dutch roll damping - not lateral acceleration.

2. The lines indicate degredation in pilot rating to be expected because of ride qualities for an airplane with otherwise satisfactory flying qualities parameters.

Figure 7.- Lateral acceleration criterion versus pilot rating.

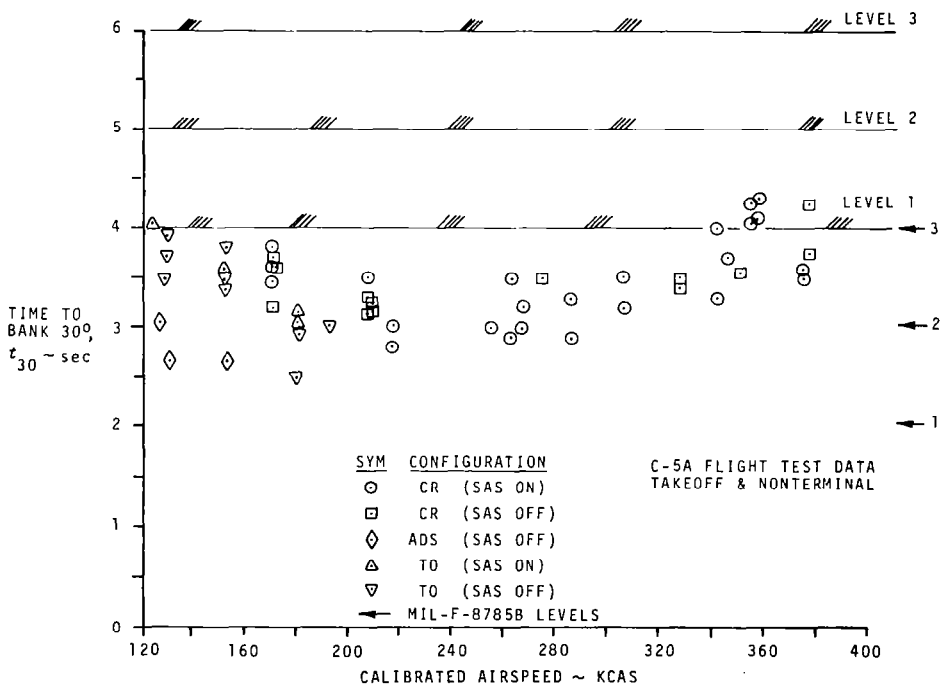

Figure 8.- C 5A flight test data - takeoff and nonterminal.

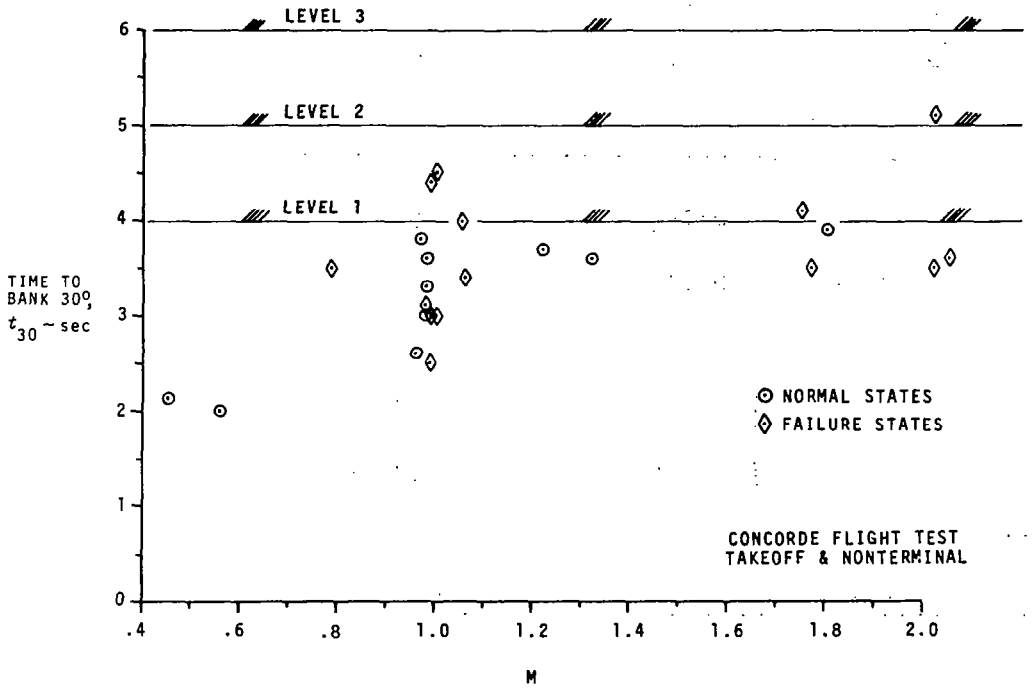

Figure 9.- Concorde flight test data - takeoff and nonterminal.

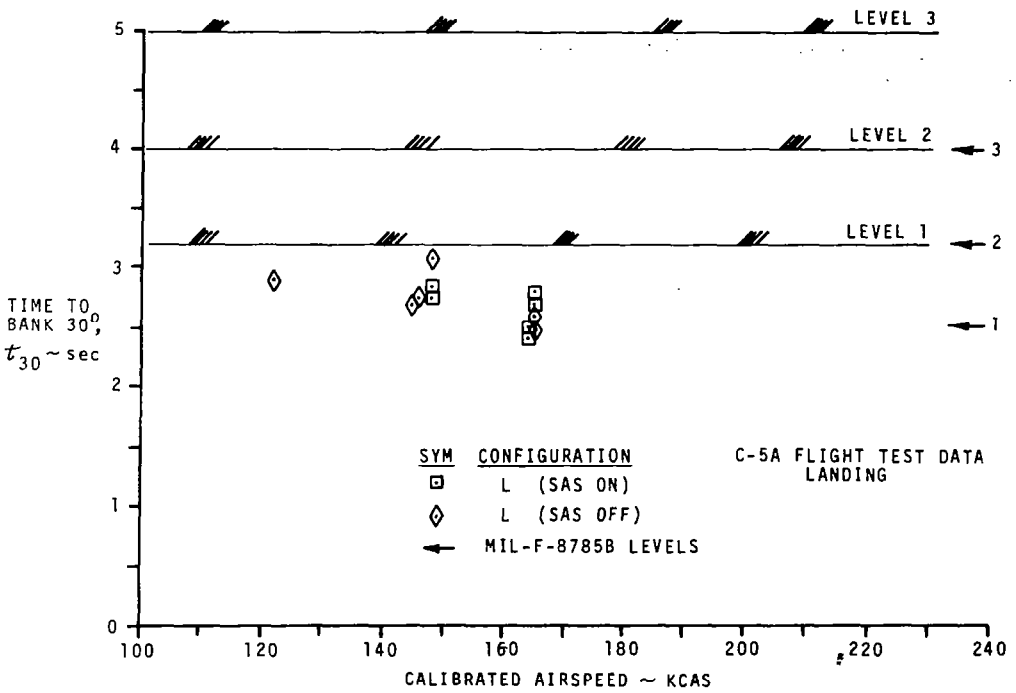

Figure 10.- C-5A flight test data - landing.

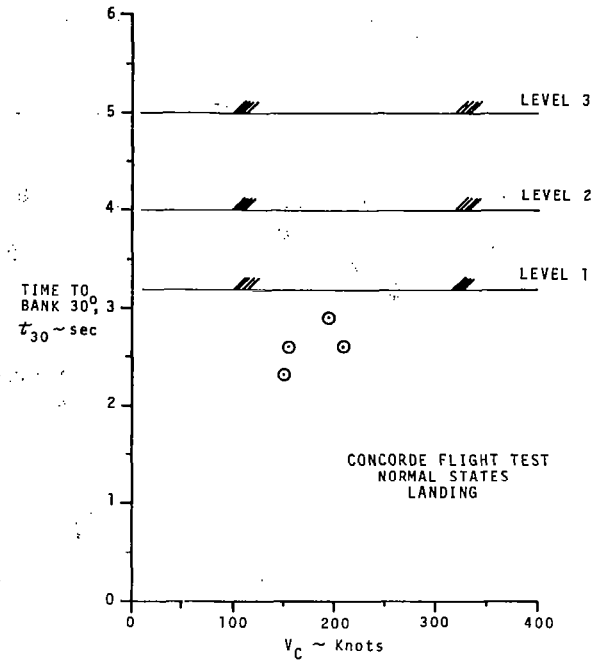

Figure 11.- Concorde flight test normal states landing.

CONF	PILOT/PR	$L'_{\delta_{AW}}$ (DEG/SEC² DEG)	ROLL CONTROL POWER USED (DEG/SEC²)	MAXIMUM $\delta_{AW_{EFF}}$ (DEG)	MAXIMUM δ_{AW} USED (DEG)	ϕ_1* (DEG)	$\phi_{1.8}$* (DEG)	P_{SS}* (DEG/SEC)
1	A/3	4.78**	47.8	±10	11	13.2	30.1	17.1
2	B/4	4.78	35.8	±7.5	8	8.9	19.8	12.6
3	B/1.5	4.78	31.8	±6.5	6.5	7.7	16.4	10.8
4	A/3	3.00	30.0	±10	12	7.6	18.5	10.7
5	B/6	4.78	23.9	±5	17	6.0	12.6	8.3
6	A/9	3.00	7.7	±2.5	25	1.8	4.1	2.7

**INCORRECTLY FLOWN WITH SENSITIVITY SELECTED BY PILOT B.

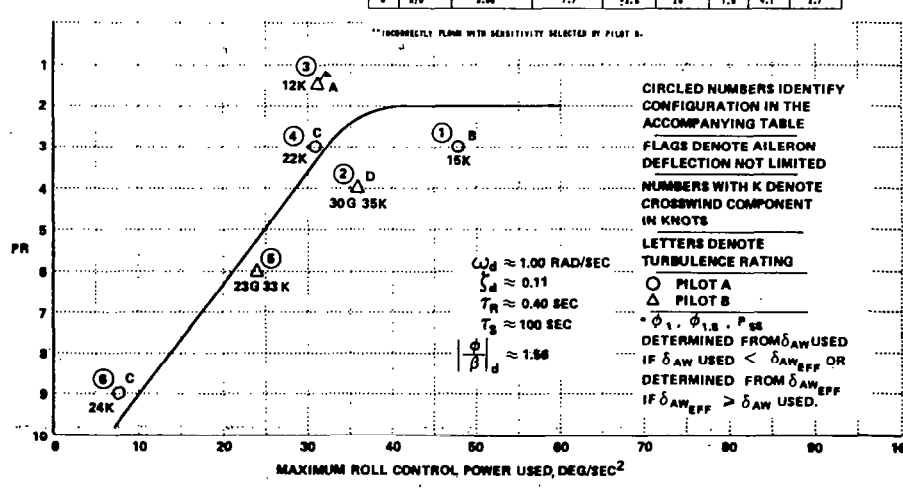

Figure 12.- Pilot rating versus maximum roll control power used - Group 6.

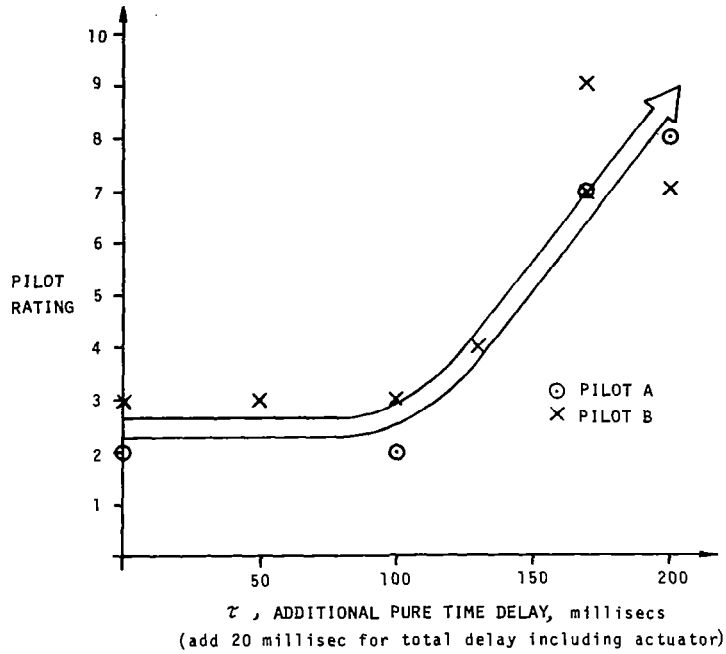

Figure 13.- Effect of pure time delay (pitch).

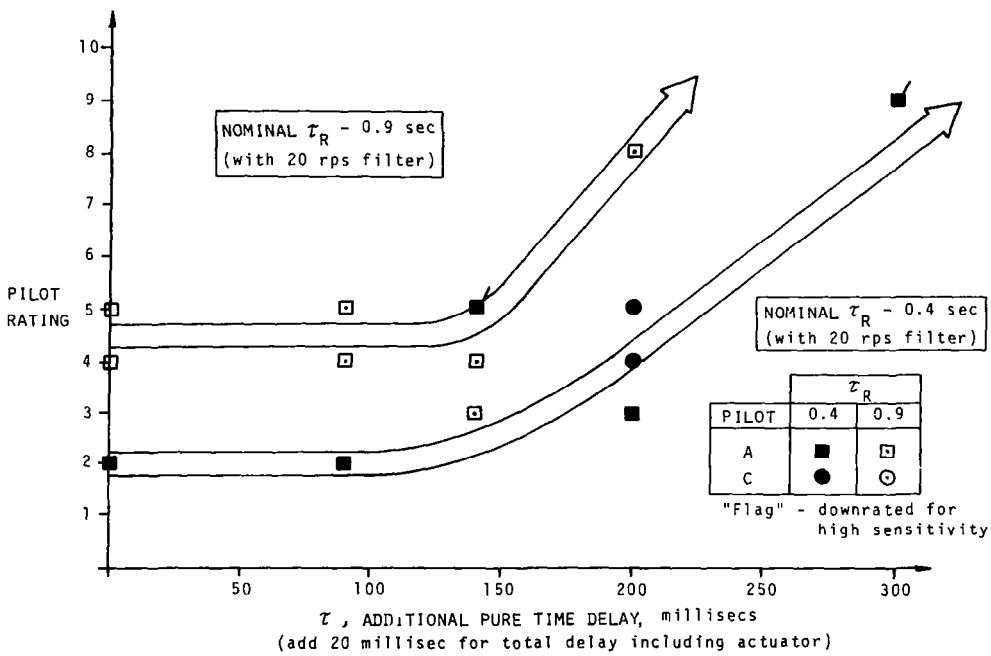

Figure 14.- Effect of pure time delay (roll).

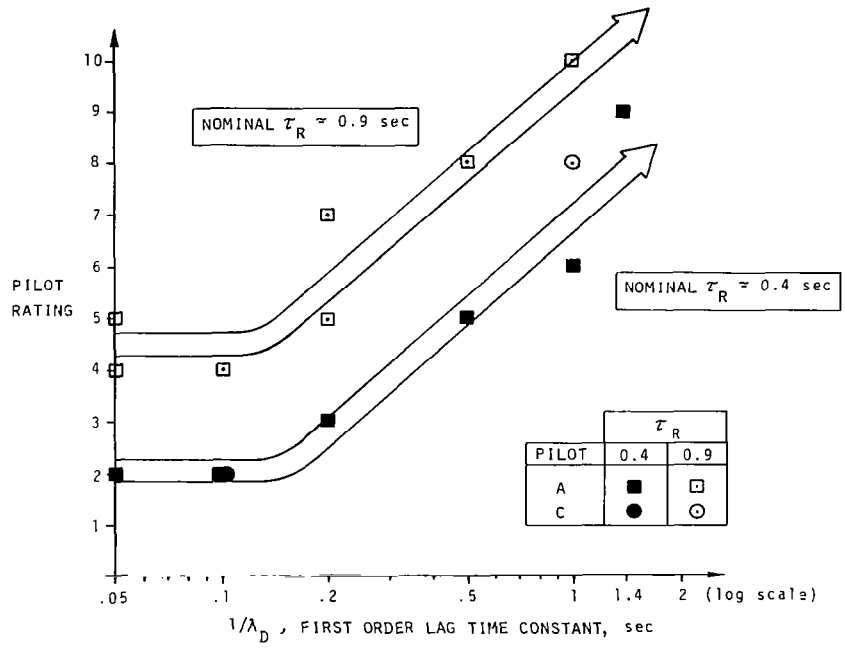

Figure 15.- Effect of lag (roll).

ADVANCED SUPERSONIC TRANSPORT FIXED-BASE SIMULATOR EVALUATIONS AT LANDING APPROACH

John B. Feather
Douglas Aircraft Company

SUMMARY

Equations of motion simulating the landing approach case for the supersonic cruise vehicle have been programmed and exercised using a fixed-base simulation facility. The objectives of the study are to provide unaugmented and augmented system comparisons using this facility, and to make refinements as necessary for system performance improvement.

The unaugmented longitudinal responses to elevator commands are slow and sluggish, requiring augmentation to increase the speed of the response. In the lateral-directional case, the Dutch roll is highly underdamped and requires an augmentation system to increase this damping and provide satisfactory flying qualities. The status of this fixed-base study is that the longitudinal equations, updated with recent wind tunnel data, have been evaluated on the simulator and the system found to be satisfactory. The lateral-axis equations are linearized and have not yet been updated to large excursion capability; consequently, only limited, preliminary findings on this system are available.

The basic results so far indicate augmentation systems are required to provide a satisfactory longitudinal system, and that additional study and evaluation of the lateral-directional case are necessary before a more complete assessment can be made.

INTRODUCTION

Development of augmentation systems for flying qualities improvement was begun under previous NASA contracts (references 1 and 2) using linear system theory and modern control techniques. The longitudinal and lateral control systems were analyzed separately and the results assessed using reference 3 criteria to provide Level 1 flying qualities (pilot ratings of 3.5 or less). Results from these tasks were then used to develop a full six degree of freedom, non-linear simulation for real-time pilot in the loop evaluation. The subject of this paper is a review of this augmentation system development, a discussion of recent results, and a brief description of the on-going and planned simulator studies.

The unaugmented responses of the airplane in landing approach are acceptable in the pitch axis and unacceptable in the lateral directional axis. The longitudinal short period responses are sluggish, whereas the lateral Dutch roll is highly underdamped. Consequently, the augmentation systems for these two axes have rather diverse jobs to perform. The task, then, is to reshape the airplane responses so they are satisfactory, i.e., that they exhibit Level 1 flying qualities.

Analytical results stemming from past mechanization efforts to fulfill this stated task have been successful in providing Level 1 systems. These results are based on linear system techniques and criteria taken from MIL-F-8785B (ref 3) specifications for transport aircraft. The main objectives of the simulator studies to be discussed are the augmentation system evaluation using a pilot in the loop, and refinements to these systems as a result of these evaluations.

SYMBOLS

a_n	normal acceleration, m/sec^2 (ft/sec^2)
a_y	lateral acceleration, m/sec^2 (ft/sec^2)
$f_{\delta_{ij}}$	feedforward gain values
$f_{x_{ij}}$	feedback gain values
K_{an}	HSAS acceleration gain, deg per m/sec^2 (deg per ft/sec^2)
$K_{\dot{\phi}}$	roll rate gain to aileron, deg per deg/sec
$K_{\dot{\phi}_r}$	roll rate gain to rudder, deg per deg/sec
K_β	sideslip gain, deg per deg
$K_{\dot{\psi}}$	yaw rate gain, deg per deg/sec
t_2	time to double amplitude, sec
u	forward velocity, m/sec (ft/sec)
β	sideslip angle, deg
δ_{ac}	commanded aileron angle, deg
δ_{af}	feedback aileron signal, deg
δ_{col}	column deflection, deg
δ_e	elevator deflection, deg

$\delta_{e_{FB}}$	elevator feedback signal, deg
$\delta_{e_{FF}}$	elevator feedforward signal, deg
δ_p	rudder pedal deflection, cm (in.)
δ_r	rudder deflection, deg
δ_{rc}	commanded rudder angle, deg
δ_{rf}	rudder feedback signal, deg
δ_T	throttle servo position, deg
δ_{TH}	throttle setting, deg
$\delta_{T_{FB}}$	throttle feedback signal, deg
$\delta_{T_{FF}}$	throttle feedforward signal, deg
δ_w	wheel position, deg
δ_1	output of yaw rate washout, deg
ζ_{D_R}	Dutch roll damping ratio
ζ_{PH}	phugoid damping ratio
ζ_{SP}	short period damping ratio
θ	pitch attitude angle, deg
τ_R	roll time constant, deg
ϕ	roll attitude angle, deg
ψ	yaw attitude angle, deg
ω_{DR}	Dutch roll natural frequency, rad/sec
ω_{PH}	phugoid natural frequency, rad/sec
ω_{SP}	short period natural frequency, rad/sec

ABBREVIATIONS AND SPECIAL SYMBOLS

A/D	Analog-to-Digital Converter
D/A	Digital-to-Analog Converter

DETAC	Digital Equipment Technology Analysis Center
MAC	Mean Aerodynamic Chord
HSAS	Hard Stability Augmentation System
ILS	Instrument Landing System
$(\dot{\ })$	Time Derivative
(k)	sampled signal at k^{th} iteration
$(\hat{\ })$	estimate or reconstructed signal

UNAUGMENTED AIRCRAFT DESCRIPTION

A three view of the MDC Supersonic Cruise Vehicle is shown in Figure 1. This 273 passenger aircraft is designed for ranges in excess of 8300 km (4500 n. mi.) at a takeoff gross weight of 340,194 kg (750,000 lb). It features a 929 m^2 (10,000 ft^2) arrow-type wing designed for a cruise Mach number of 2.2 with the planform based on the NASA SCAT-15F concept, a conventional horizontal tail, a single fuselage-mounted vertical tail, and four engines mounted in axisymmetric nacelles. The inboard leading edge of the wing has a sweep of 71 degrees, with the sweep reduced to 57 degrees outboard of the leading edge break. The average thickness ratio of the wing is slightly less than three percent. The thickness ratio is equal to 2.25 percent of the chord at the wing root and is constant at three percent of the chord from the trailing edge break to the wing tip.

Perturbation equations of motion for the landing approach flight condition have been developed for this configuration. These equations are documented for the longitudinal axis in Reference 1 and for the lateral axis in Reference 2. Instead of listing the detailed sets of equations for this aircraft here, only the important characteristics that have led to the decision that augmentation systems are required for flying qualities improvement will be given. Longitudinally, the pitch response to an elevator input is slow and does not exhibit Level 1 flying qualities. Decreased damping in pitch, therefore, is required of the longitudinal augmentation system. In the lateral directional case, the Dutch roll damping of the airplane is very low and an augmentation system to increase this damping is required. These two conditions are the reasons augmentation systems are necessary in both axes. In fact, in the lateral case, there is a tendency toward instability with a pilot in the loop for any inputs except those of very small magnitudes. This fact has led to development of a hard stability augmentation system (HSAS) in the lateral axis that provides Level 2 flying qualities. This HSAS contains fewer feedbacks and sensors than the full-up system and would operate in a back-up mode in case of primary augmentation system failure.

SIMULATION FACILITIES

The Digital Equipment Technology Analysis Center (DETAC) is a technology investigation facility at Douglas used for conducting studies and providing hands-on experience with digital equipment. This facility generally fulfills a requirement to upgrade the existing electronic system study capabilities, particularly in the area of aircraft digital systems, inclusive of flight control computers and advanced display systems. The DETAC has been used specifically to study the landing approach tasks of the supersonic cruise vehicle in real time with a pilot in the loop.

Figure 2 shows the general view of the facility, and Figure 3 is an interior view of the "soft cockpit." The controls available to the pilot here are side and center stick controllers, throttle, and flap setting controls. No rudder pedals are provided, but the software does have rudder pedal effectiveness coefficients included in it (which can be used by the augmentation systems as required). A CRT provides an Electronic Attitude Director Indicator (EADI) display that can be used in a heads-down configuration or projected on a TV screen. Figure 4 is a typical EADI format with the various display quantities as noted. The pilots' landing task using this type of EADI is to keep the aircraft symbol centered in the ILS box (marked with a + symbol).

Wind shear, gust inputs, and initial condition changes are options that can be input through the interactive CRT display. Several simulation outputs will be discussed later that have exercised these options.

AUGMENTATION SYSTEM DEVELOPMENT

Full Augmentation System

Both the longitudinal and lateral augmentation systems were developed using perturbation equations of motion and linear system theory. The main objective was to provide a control system configuration that could be incorporated into a six degree-of-freedom, non-linear simulation to verify the performance under real-time operating conditions.

Modern control theory was used in the longitudinal case to define the feedback and feedforward gains via implicit model following. The model used was selected to represent an airplane whose flying qualities were all Level 1. The resulting augmentation system approximates the model to the degree the two controls (elevator and throttle) permit. In the lateral case, it was found that classical root locus techniques could be used to determine the gains that produced a Level 1 augmented system. Yaw and roll rate gyro feedbacks were employed, plus a gain on sideslip angle β (reconstructed from measurable signals). The block diagrams in Figures 5 and 6 show the details of both augmentation systems. Digital implementation of the required calculations for augmentation purposes will be made for both of these systems.

Table 1 compares some of the basic parameters of the system with the criteria specified in MIL-F-8785B. Note that the unaugmented short period roots are both real in contrast to the usual complex conjugate pair. In the lateral axis, the Dutch roll roots have a damping ratio of only 0.074. This fact, coupled with the marginal roll time constant, produces a poorly responding system. The augmented system provides values for the indicated parameters that are within the Level 1 requirements, and it is this system that will be incorporated into the real-time simulation for evaluation.

Hard Stability Augmentation System

A much simplified augmentation system has been devised that would serve as a back-up system. This HSAS is depicted in Figures 7 and 8 for each axis. The longitudinal system is simply an accelerometer feeding back to the elevator actuator. The dynamic responses of this system are better than no augmentation but do not possess the Level 1 flying qualities of the fully augmented system. This accelerometer loop provides approximately a 0.7 damping ratio on the short period roots. The lateral system of Figure 8 is similar to the complete system except the sideslip feedback has been removed. This simplification allows only rate sensors to be used and eliminates the digital feedback filter for reconstructing β . The resulting system exhibits Level 2 flying qualities when assessed by reference 3 criteria.

Simulation Checkout

The simulation program containing linear aerodynamic data was checked against the perturbation results previously obtained for both axes. Nonlinear coefficients were then included in the longitudinal equations as obtained from recent wind tunnel data. (Time considerations prevented the lateral equations to reflect the tunnel data, and the results to be presented are based on simplified, linear lateral equations.)

STUDY RESULTS

The results to be presented are based on pilot-in-the-loop evaluations of the longitudinal and lateral systems. The evaluations to be discussed include pilot assessments obtained from the fixed-base simulator utilizing its capabilities and the various types of visual presentations available. Since these visual displays are limited in their data presentation and no motion is provided to the pilot, the results are used basically to compare the various augmentation systems.

Longitudinal Axis

Pilot evaluations have led to modifying the previously developed augmentation system gains for the longitudinal case. Two specific points were noted. First, the cross feed from throttle to elevator servo caused an unwanted pitch command when the throttle settings were changed. The gain $f_{\delta 12}$ of Figure 5 was reduced to zero and improved responses resulted. Second, the gain from accelerometer to elevator servo, f_{x12}, was increased by a factor of two in order to provide better handling as noted by pilot comments during the augmentation system evaluation.

A shift in center-of-gravity from the nominal 24% MAC was made and the pilot was given pitch tracking tasks under these conditions. Even though the augmentation system was developed for a 24% cg location, other aft cg locations (which would otherwise be unstable) were stabilized by the system. For a cg shift to 36% MAC, the pilot could still maintain control, but this was the limit for aft cg locations based on pilot comments. Figure 9 shows the response in pitch to a step elevator input with the augmentation on at a cg location of 36%. This response shows convergence of response for this condition.

Only preliminary simulator data on evaluating the HSAS system have been taken so far. It appears that the flying qualities can be made acceptable (Level 2) in the pitch axis. Additional evaluation of the HSAS system is planned on the simulator.

Lateral Axis

As noted previously, the Dutch roll damping is very low and leads to large oscillations in roll rate for aileron inputs. The linear system technique used to define the lateral augmentation system gains and compensation networks was successful in providing a Level 1 system. The linear system roots were shifted to the Level 1 region, and the response as assessed by the roll rate oscillation criterion was improved by the addition of the augmentation system. The system was determined to be satisfactory based on the criteria of reference 3; consequently, this augmentation system was included in the six degree-of-freedom equations programmed on the fixed base simulator. Pilot-in-the-loop evaluations of the unaugmented airplane confirmed its uncontrollability in the lateral case. The current simulation effort is a continuing evaluation of the augmented airplane with a pilot in the loop. The results are of a preliminary nature and are not complete, but the indication is that adjustment of the previously developed gains and/or addition of compensation networks will be necessary to provide a satisfactory system when the pilot is included in the loop.

Responses of the airplane degrees of freedom to gust inputs for the lateral axis with augmentation are lower than without augmentation because the natural frequency of the Dutch roll roots has been decreased. Figure 10 compares the system roll response, ϕ , with and without augmentation for a gust input level of 1 kt RMS. The pilot controls were fixed during this run. This result is consistent with the improvement in flying qualities as in Table 1, and follows from

the increase in Dutch roll damping.

Step response results also show improvement in the lateral case with the augmentation system engaged. Figure 11 is a comparison of roll rate transients to a step wheel command with and without augmentation. The decreased damping is evident in this comparison, and the system is augmented to Level 1 when assessed by the criterion of MIL-F-8785B.

CONCLUDING REMARKS

The simulator evaluations of the augmentation system in the longitudinal case have allowed improvements as a result of the real-time analyses. Specifically, gain redefinition has yielded a better responding system when evaluated by piloted simulation runs. More detailed studies involving the longitudinal axis (especially the HSAS system) need to be undertaken.

The lateral-directional case requires refinement in its augmentation system in order to improve the flying qualities. Addition of a pilot in the loop has changed the flying qualities rating as compared to the analytical results obtained via linear system theory. When a pilot was included in the loop, the lateral augmentation system was not determined to be Level 1 as it was using reference 3 criteria with no pilot. The reasons for this problem, and the corrections to it, will be the subject of future studies.

Generally, using the fixed-base simulator for augmentation system verification has proved very useful. It has identified several areas in which improvement was made to the longitudinal system and has shown the need for some type of compensation to the lateral case. Additional simulation activities will include implementation on a moving base simulator to fully assess the handling qualities of the airplane at landing approach in both axes.

REFERENCES

1. Technology Application Studies for Supersonic Cruise Aircraft. NASA CR-145130 (Douglas Aircraft Report MDC-J4550). November, 1976.

2. Technology Application Study of a Supersonic Cruise Vehicle. NASA CR-159034. March, 1979.

3. Flying Qualities of Piloted Airplanes. MIL Spec. MIL-F-8785B (ASG). August, 1969

TABLE 1

COMPARISON OF DYNAMIC CHARACTERISTICS WITH AND WITHOUT AUGMENTATION ENGAGED

PARAMETER		UNAUGMENTED	AUGMENTED	MIL-F-8785B (LEVEL 1 CRITERIA)
SHORT PERIOD:		Real Roots:		
ω_{SP}	(RAD/SEC)	-0.650	0.840	$\geq$ 0.8
ζ_{SP}		-0.258	0.688	$\geq$ 0.35
PHUGOID:				
ω_{PH}	(RAD/SEC)	0.119	0.209	--
ζ_{PH}		0.149	0.082	$\geq$ 0.04
ROLL:				
τ_R	(SEC)	1.35	0.495	$\leq$ 1.4
SPIRAL:				
t_2	(SEC)	∞	35.5	$\geq$ 20.0
DUTCH ROLL:				
ω_{DR}	(RAD/SEC)	0.797	0.583	$\geq$ 0.4
ζ_{DR}		0.074	0.307	$\geq$ 0.08*
$\omega_{DR}\zeta_{DR}$	(RAD/SEC)	0.059	0.179	$\geq$ 0.15

*For ω_{DR} > 1.88 RAD/SEC, this requirement supersedes the $\omega_{DR}\zeta_{DR}$ product requirement.

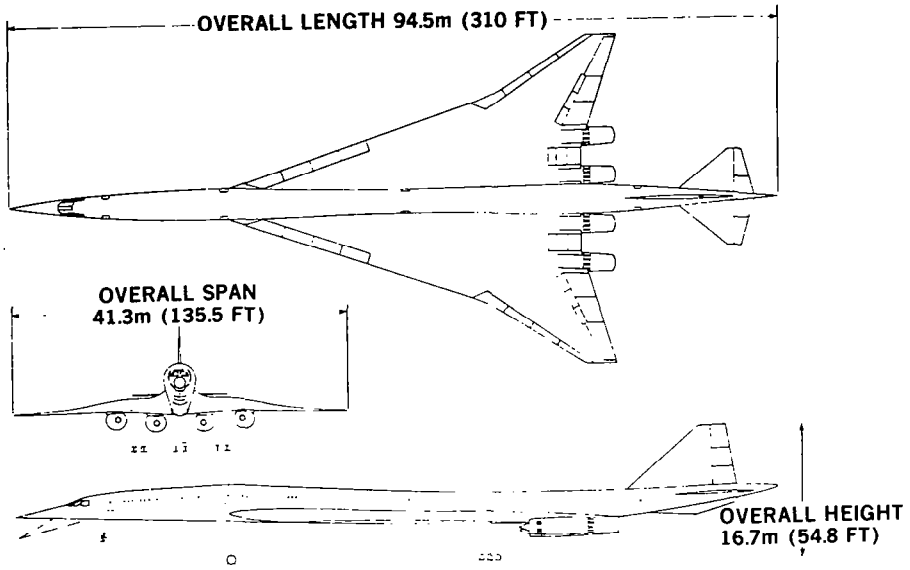

Figure 1.- MDC supersonic cruise vehicle used for active controls simulation purposes.

Figure 2.- DETAC simulation facility.

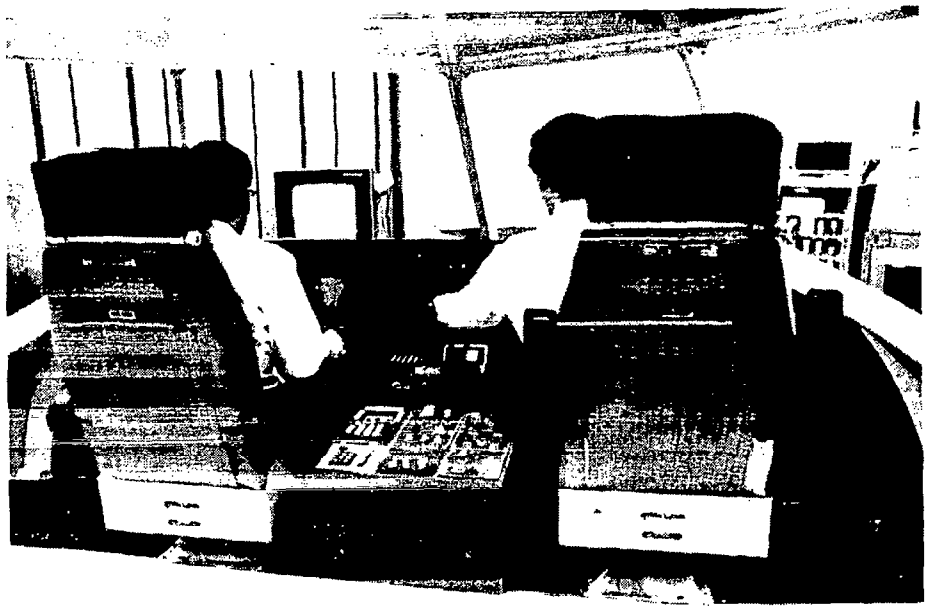

Figure 3.- Cockpit mockup.

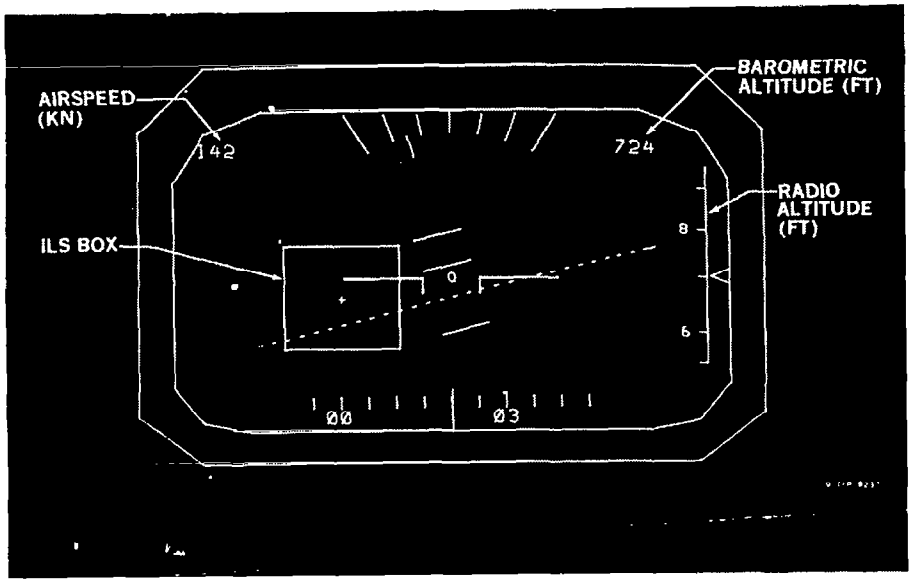

Figure 4.- EADI used for display to pilot.

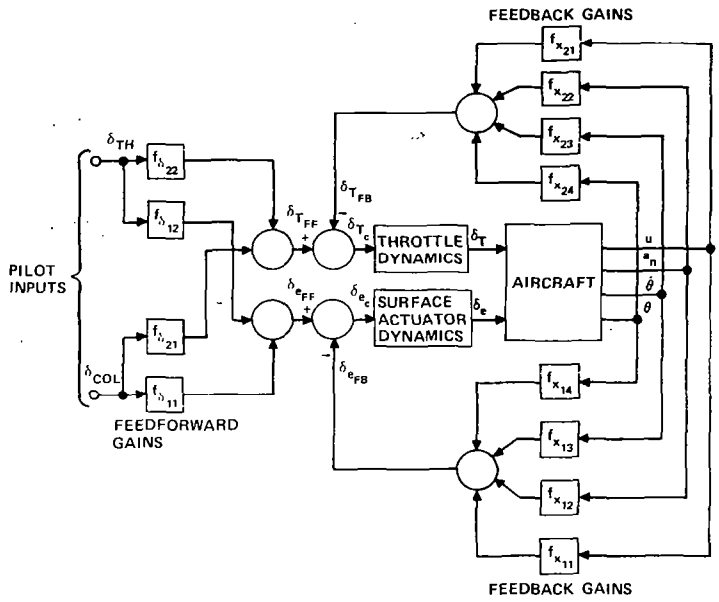

Figure 5.- Longitudinal augmentation system.

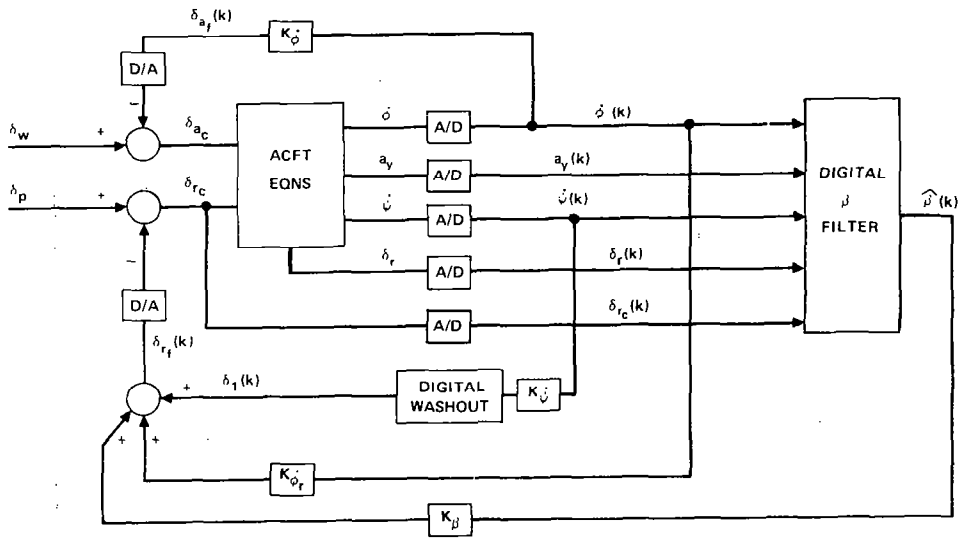

Figure 6.- Lateral augmentation system.

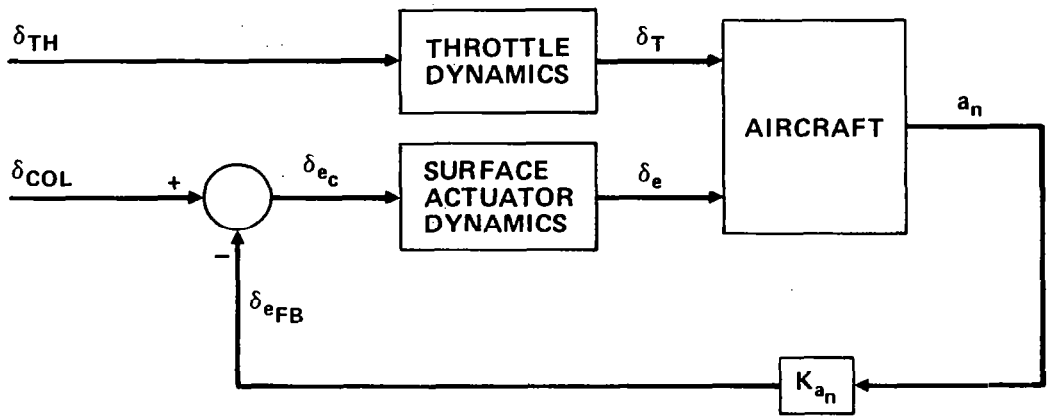

Figure 7.- Hard stability augmentation system for longitudinal axis.

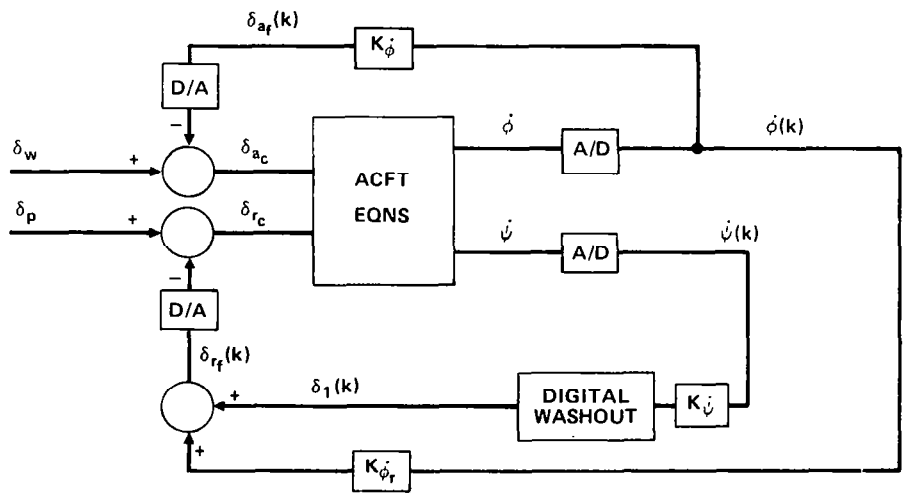

Figure 8.- Hard stability augmentation system for lateral axis.

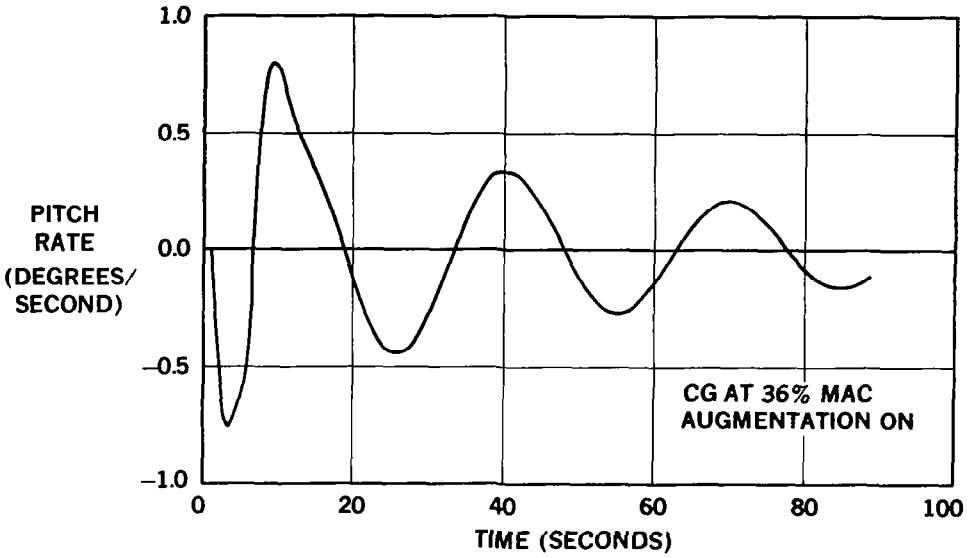

Figure 9.- Pitch rate response to a 1.0-degree step column command.

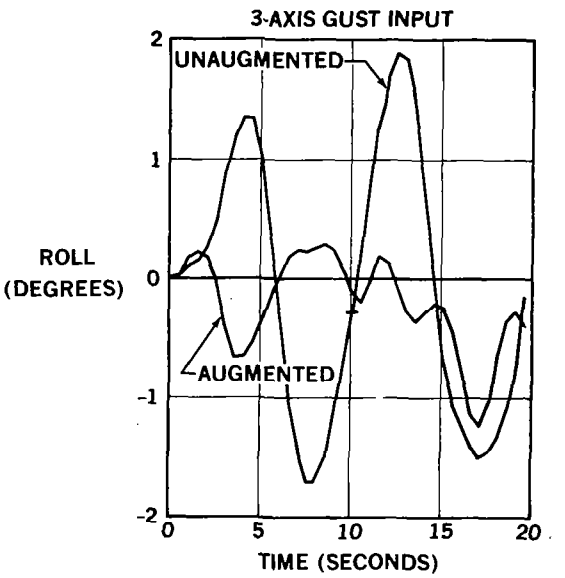

Figure 10.- Augmentation system reduction of wind gust inputs.

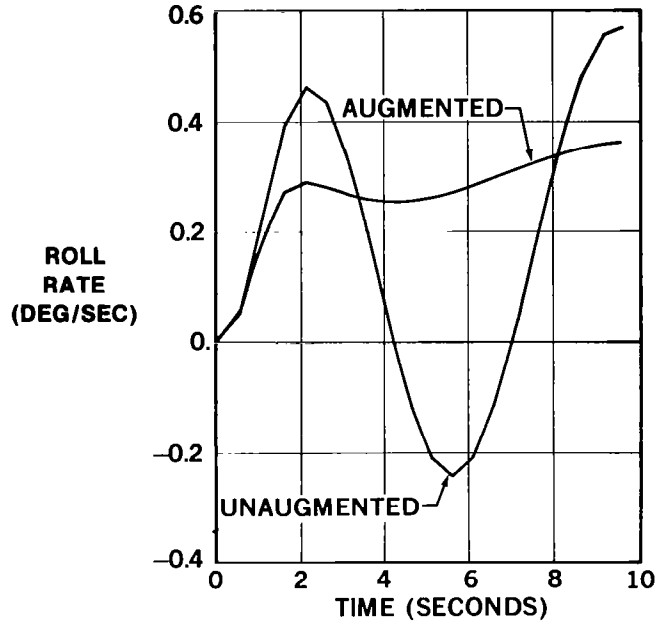

Figure 11.- Roll response to a 1.0-degree step wheel command.

SIMULATOR INVESTIGATION OF ARROW-WING LOW-SPEED HANDLING QUALITIES

Ben T. Averett

Lockheed Aircraft Corporation

SUMMARY

Low speed handling qualities of arrow wings were investigated with a piloted simulator. Existing aerodynamic data were used from NASA SCAT 15F tunnel tests augmented with new Lockheed low speed wind tunnel test data. Two arrow wing planforms were chosen for the simulation effort - a Mach 2.0 design and a Mach 2.7 design. These designs are in the SCAT 15F Mach 2.7 design family, having the same βAR and $\beta \cot \Lambda$.

Piloted simulation results indicate that both the Mach 2.0 and Mach 2.7 planforms have satisfactory longitudinal flying qualities. However, in the control of bank angle the Mach 2.0 planform demonstrates satisfactory handling qualities while the Mach 2.7 planform is unacceptable. This situation applies for crosswind landings at FAA limits and for lineup in heavy turbulence. The low-speed superiority of the Mach 2 planform with its lower sweep and higher aspect ratio is also shown by its ability to approach at least 8 m/s (15 knots) slower than the Mach 2.7 planform without degradation in handling qualities.

INTRODUCTION

Since the development of the SCAT-15F arrow-wing aircraft configuration by NASA in the mid 1960s, supersonic cruise aircraft research has centered around a design cruise Mach number of 2.7. Recent Lockheed studies on the influence of design cruise Mach number on airline utilization, passenger acceptance, aircraft complexity, and operating costs have revealed that cruise Mach numbers as low as M = 2.0 may be competitive. An additional factor, not included in these studies, is the influence of design Mach number on low-speed flying qualities and airport performance. The available low-speed flying qualities data point out two potential problem areas for aircraft designed for M = 2.7. The highly swept, low-aspect-ratio wing, which is cambered and twisted for best cruise performance, does not develop adequate lift even with flaps extended to permit use of approach speeds comparable to current subsonic jets. This problem is further aggravated by approach attitude restrictions imposed by visibility requirements and low tail-scrape angles resulting from the long fuselage inherent in this type of design. In addition, the high rolling moments generated by a highly swept wing in sideslip and the severely limited roll control available from this wing planform restrict the crosswind landing capability.

The primary effects of reduced design Mach number on the aircraft are to increase the wing aspect ratio and reduce the wing leading-edge sweep angle. These parameters improve the lift capability of the wing by increasing the lift-curve slope and flap effectiveness. Roll control is improved by reduced aileron sweep angle, higher wing aspect ratio, and the lower rolling moments induced by sideslip.

These effects may be computed adequately if good aerodynamic data are available for use in the analysis, but the significance of the flying qualities parameters to a pilot attempting to land the aircraft is difficult to evaluate using conventional analysis methods. The objectives of this flight simulation program were to obtain test data on the magnitude of the low-speed improvements offered by a reduction in design Mach number from 2.7 to 2.0, and to qualitatively evaluate the significance of these improvements to a pilot attempting to land a simulated aircraft in various levels of air turbulence and crosswind.

STUDY APPROACH

The approach taken during the flight simulation program was to collect all available data on low-speed flying qualities for arrow-wing planforms and to supplement these data where necessary with wind tunnel data and analysis. Previous wind tunnel testing of various SCR configurations by Lockheed, together with NASA tests of control system effectiveness and basic planform characteristics were accumulated and used as a data base for the M = 2.7 configuration. These data were primarily for the NASA SCAT-15F configuration or for slight variations of that planform. Because there were very little data available for planforms designed to cruise at lower speeds, low-speed tests were deemed necessary to define the characteristics of the M = 2.0 planform. Both planforms were tested to determine the detailed differences between them and to permit the application of an accurate correction to the data for twist and camber effects.

Because the SCR configuration must be balanced to minimize trim drag in cruise, static longitudinal stability in the approach must be negative, which requires a rather sophisticated control system to permit the pilot to use conventional flying techniques. For this study, stability and control augmentation systems were developed based on the results of NASA flight simulation tests from which the control laws required for acceptable approach control were determined. These data, together with configuration characteristics, such as weight and inertia, ground clearance, engine geometry and dynamics, and cockpit location derived from previous SCR configuration studies, constituted a flight simulator data package which was programmed on the Lockheed Developmental Flight Simulator.

A piloted flying qualities evaluation of approach and landing characteristics on the M = 2.0 SCR, the M = 2.7 SCR, and the L-1011 subsonic transport aircraft was conducted in various levels of air turbulence and crosswinds to assess the significance of differences in aerodynamic characteristics of the two study planforms.

STUDY SCOPE

- Testing was limited to general flying qualities in the approach configuration and to an evaluation of controllability and pilot workload during an instrument approach in crosswind and turbulence.

- An existing transport cockpit (L-1011) was used for all testing. No attempt was made to simulate the visibility restrictions that may be present in an SCR design.

- All approach testing was initiated in IFR conditions, and a flight-director similar to the L-1011 system was used for glideslope and localizer commands.

- The flight control system was a control-wheel steering (CWS) system utilizing attitude-hold and rate command logic in pitch and roll. Autopilot inputs were isolated from the control column and wheel to avoid disturbing control system motion that can result from CWS-type systems.

- All approach testing was terminated at main-wheel touchdown.

- Crosswinds up to 15.45 m/sec (30 knots) and air turbulence up to 2.7 m/sec (9 fps) rms were introduced into the aerodynamic equations.

- The L-1011 aircraft was simulated and compared to the two study configurations in all test conditions to provide a reference point for the pilot ratings.

DESCRIPTION OF SIMULATED AIRCRAFT

To evaluate flying quality variations with planform, two wings were designed: one to cruise at Mach 2.7 and the other at Mach 2.0. Wing area, notch ratio, taper ratio, βAR, and $\beta \cot \Lambda$ were held constant for the two designs by varying sweep angle and aspect ratio. A comparison of the Mach 2.7 and Mach 2.0 planforms is shown in Figure 1, where the differences in sweep angle, aspect ratio, and trailing-edge flap configuration can be seen. A tabular comparison of the planform properties is given in Table 1. Pertinent dimensions are listed in the table, showing that the planform parameters are consistent between the Mach 2.0 and 2.7 planforms. All other aircraft dimensions besides wing geometry and engine location were identical for the two test configurations. The engines were located at a constant percentage semi-span location, and thus were farther from the aircraft centerline on the Mach 2.0 configuration because of its larger span. Wing area and landing gross weight were maintained constant, but differences in mass moments-of-inertia between the two designs were accounted for.

Aerodynamic data were derived principally from a low-speed wind-tunnel test of the Mach 2.0 and Mach 2.7 designs in the Lockheed low-speed wind tunnel. These data, derived from flat-plate wing models, were corrected for twist

and camber effects using existing NASA wind tunnel data in which both twisted and flat-plate wing data were available. Basic aerodynamic force and moment data, as well as control surface and high lift system effectiveness were determined from the wind tunnel tests. Flexibility corrections in the roll control effectiveness and effective dihedral parameter are included in the data for the airspeeds evaluated in this study. Ground effects on lift and pitching moment were derived from previous wind tunnel tests of similar configurations. Dynamic stability derivatives were estimated using conventional estimation techniques.

The flight control systems used in this study were developed from the systems described in Reference 1, which reported the results of NASA ground-based and in-flight simulation of a similar configuration. The longitudinal and lateral control systems are attitude-hold autopilot-type systems with control-wheel-steering rate-command inputs for maneuvering. The gains and time-constants in the control systems were chosen to make the systems feel as much as possible like conventional control systems. For the same reason, the control-surface inputs generated by the automatic systems were isolated from the control column and wheel to avoid the disturbing motions that result from CWS-type control systems in current subsonic jets. Because supersonic cruise vehicles operate well on the backside of the thrust required curve at approach speeds, an autothrottle was developed to relieve the pilot of the high workload associated with airspeed control in these conditions.

DESCRIPTION OF FLIGHT SIMULATOR

The Lockheed Developmental Flight Simulator is a hybrid computer facility with peripheral hardware designed to create the illusion of flight. Computational hardware consists of general-purpose digital and analog computers, and special-purpose computers to simulate cockpit control forces and engine noise cues. Several peripheral pieces of equipment, such as a visual display system, a motion generation system, and a cockpit complete with operational flight instruments are available to enhance pilot flight impressions. The digital computer is programmed with the aircraft equations of motion, all aerodynamic and propulsion data, geometric and inertial data, and additional equations to control the peripheral equipment and data recording devices. The analog computer is used to simulate flight control systems, which require high-frequency computing to adequately represent the system dynamics.

The cockpit used for this simulation is a mock-up of the L-1011 cockpit with flight instruments and controls installed in the L-1011 configuration.

The visual system is a single-window television system with a 63.5-cm (25-in.) TV monitor mounted on the pilot's glare shield. The source of the displayed image is a three-dimensional 1500:1 scale model of the Palmdale, California airport and surrounding terrain mounted on a continuous moving belt. The monitor image is generated by a closed-circuit television channel, the camera of which is mounted on a servo-controlled carriage that moves across the width of the model belt and at right angles to its surface. These movements, along with model belt motion, present the true position of the aircraft,

relative to the airport runway. A servo-controlled prism-mirror system, attached to the camera, provides pitch, bank, and heading displacements.

The cockpit is mounted on a 4-degree-of-freedom motion system, providing pitch, roll, vertical, and lateral motions. The motion system provides completely independent motion in each degree of freedom, such that full excursion is available in any axis, independent of the excursions in the other axes. Because of the importance of air turbulence in this evaluation, motion system gains were optimized to present the most realistic turbulence simulation possible within the limits of the actuators.

Air turbulence was simulated by inserting random velocity inputs in the aerodynamic equations. Magnitudes and filtering of the input velocities were controlled according to the Dryden form of the random turbulence equations. In the basic Dryden model the characteristic lengths are reduced as a function of height near the ground. As a result, the peak velocity gusts simulate vertical and horizontal wind-shear bursts on landing approach. Flying qualities were evaluated in levels of turbulence from still air to heavy turbulence. Heavy turbulence is defined for this study as 2.7 m/s (9 ft/s).

Crosswinds were simulated by simply adding a constant value of lateral velocity to the earth-oriented velocity derived from the inertial aircraft equations. This accounted for the lateral movement of the air mass relative to the fixed airport coordinates.

TEST CONDITIONS

The approach speeds evaluated in the flight simulation program were selected from a static analysis of lift and roll control available from both the M = 2.0 and the M = 2.7 configurations at a typical landing weight. In Figure 2, the available approach speeds of the two designs are compared as a function of angle attack for δ_F = 0.35 rad (20 deg). At the maximum allowable angle of attack, the M = 2.0 design can approach 7.7 m/s (15 knots) slower than the M = 2.7 design. If approach attitude is more critical than approach speed, the M = 2.0 design can approach at an attitude of 0.044 rad (2.5 deg) lower than the M = 2.7 design.

Another consideration for approach speed is the control available for a crosswind landing, which usually is degraded as approach speed is reduced.

Figure 3 shows the variation with approach speed of sideslip angle required to land either aircraft in a 15.4 m/s(30-knot) crosswind, assuming the pilot decrabs the aircraft just prior to touchdown and lands with the longitudinal axis aligned with the runway centerline. This is the accepted crosswind landing technique for aircraft without special crosswind landing gear. Also shown in Figure 3 is the sideslip angle which can be controlled at full aileron for the two aircraft designs. At 87.4 m/s (170 knots), the M = 2.7 design requires a full roll control to counter the rolling moment produced by sideslip. For the M = 2.0 design, full roll control is reached at 72 m/s (140 knots), an improvement of 15.4 m/s (30 knots) over the M = 2.7 design.

Figure 4 summarizes the constraints on approach speed previously discussed. From these considerations, test conditions were selected to evaluate each of the aircraft configurations in the flight simulator. Since the roll control constraint is associated only with crosswind landing, approach speed was selected as 160 knots based on scrape angle considerations, and roll control was evaluated at that speed.

RESULTS OF PILOT EVALUATION

Four test pilots evaluated the simulated aircraft including three engineering test pilots from the Lockheed Commercial Flight Test organization and a NASA-Langley test pilot. A total of 50 test hours were completed.

General Flying Qualities In Approach Configuration

In order to evaluate the general flying qualities of each configuration in the approach flight condition, several flight test maneuvers were executed and pilot ratings were obtained. The evaluation maneuvers included level turns and step roll inputs to evaluate roll control, cockpit control doublets to evaluate aircraft dynamics, small heading changes and steady sideslips to evaluate directional control, and engine transients to evaluate asymmetric conditions and control for missed approach. The Cooper-Harper pilot rating scale was used to quantify the pilots' opinions of the test configurations. Figure 5 is a simplified version of the rating scale.

The evaluation pilots were asked to rate the workload and controllability for each of the test maneuvers and to comment on any other flying quality characteristics that became apparent during the simulated flight. The following comments are a summary of those received from all evaluation pilots.

For the Mach 2.7 design, roll control sensitivity and roll rate capability were judged to be lower than current subsonic jets and possibly inadequate, particularly in turbulence. Other lateral directional characteristics such as adverse yaw and dutch roll damping were excellent. Pitch dynamics and pitch response were rated good, with a slight tendency to overcontrol pitch inputs. Because of the low roll response, control force harmony was not optimum. In a steady heading sideslip, roll control was good up to 2/3 pedal travel, where lateral control limits were reached. Beyond this point bank angle control was unacceptable. Control for engine failure was excellent in all axes.

For the Mach 2.0 design, roll control sensitivity and rate capability were much improved over the Mach 2.7 design. Because of the improved roll characteristics, control force harmony was good. In a steady sideslip, roll control was good up to full pedal, where about 2/3 of the lateral control was used.

Figure 6 presents an average of the pilot ratings obtained for the test maneuvers previously listed. In most maneuvers, the M = 2.0 SCR was rated easiest to fly, and the L-1011 and M = 2.7 SCR were rated slightly more difficult. In level flight turns, both of the SCR designs were rated slightly

better than the L-1011 because of the attitude hold control system, which simplified the pilot's task of holding altitude. Pitch dynamics and workload during waveoff also were rated better for the SCR designs for the same reason. The roll sensitivity of the M = 2.0 SCR was rated better than either the L-1011 or the M = 2.7 SCR because of a nonlinearity in roll response in the L-1011 and because of inadequate roll control power in the M = 2.7 SCR. Similar ratings and comments were given for control in steady sideslip. The M = 2.0 SCR could be controlled in a full pedal sideslip with 0.43 rad (25 degrees) of wheel and the L-1011 with about 1.05 rad (60 degrees) of wheel. In the M = 2.7 SCR, full pedal sideslips could not be controlled with full wheel. The average rating of 4 given this condition is a compromise between the relative ease of controlling sideslips up to two-thirds pedal and the inability to control full pedal sideslips. Dutch roll dynamics were rated good for all configurations, and control for engine failure also was easy in all configurations, but slightly more difficult in the L-1011 because of the lack of attitude hold.

Control for Approach in Turbulence

The workload and controllability of the three aircraft during a landing approach in turbulent air were evaluated by each of the four pilots. Turbulence was introduced into all three aircraft axes at levels up to 2.7 m/s (9 ft/s) rms. The effect of increasing turbulence was evaluated by attempting to execute an instrument approach to a typical airport. The simulation was initiated with the aircraft located 9.66 km (6 miles) from the runway threshold on the extended runway centerline. The aircraft was trimmed in level flight at 305 m (1000 ft) AGL at the specified approach airspeed with landing gear extended and trailing edge flaps extended to the landing position. In the L-1011, flap changes were made during the approach in accordance with established airline procedures for that aircraft. The pilots flew the simulated aircraft at the initial altitude, following the localizer inbound until the glideslope was intercepted. The glideslope was then captured, and glideslope and localizer were tracked to touchdown. The pilots transitioned from instrument flight to visual references at about 60 m (200 ft) above the runway and made final adjustments in lineup and glidepath.

For the Mach 2.7 design, pitch control and pitch response were good. The attitude-hold function in the control system handled the turbulence quite well; however, at high turbulence levels, a higher gain in the attitude loop would make the aircraft feel more stable. Roll response was sluggish in all levels of turbulence, but was totally inadequate in high turbulence. Bank angle and line-up corrections close to touchdown could not be made in a timely manner. It was necessary to supplement roll control with rudder inputs to pickup a downgoing wing close to touchdown.

For the Mach 2.0 design, pitch control was more precise than the Mach 2.7 design, and pitch control and glideslope control were precise even in high turbulence levels. Roll control was much improved over the Mach 2.7 design. Late line-up and bank angle corrections were much easier to accomplish and roll sensitivity was much higher, making control harmony better. The improvement in roll control lowered the overall workload sufficiently to permit more precise control of pitch attitude and glideslope.

Figure 7 shows the average pilot ratings assigned to the task of landing approach in turbulent air. The pilots' preference for the attitude-hold system is apparent from the ratings of glideslope control, where both SCR configurations were rated better than the L-1011. The severely limited roll control capability of the Mach 2.7 configuration is reflected in the poor ratings assigned to the lineup control task. The good overall controllability and low workload for the Mach 2.0 SCR can be seen from the overall rating, where the Mach 2.0 SCR was rated as satisfactory even in heavy turbulence. The other configurations were rated more difficult to fly for reasons previously stated.

Control for Crosswind Landing

Evaluation of workload and controllability of the aircraft in a crosswind approach was accomplished using a test technique identical to that for approaches in turbulent air, except for a steady crosswind component 1.57 rad (90 deg) from the runway heading. Crosswinds of 10.3 and 15.45 m/s (20 and 30 knots) were evaluated first with no air turbulence and then with 1.82 m/s (6 ft/s) of turbulence. In this manner, the combined effects of the two tasks could be evaluated. The 15.45 m/s (30 knots) crosswind corresponds to the FAA requirement for commercial aircraft.

In the 10.3 m/s (20-knot) crosswind, the aircraft was crabbed about 0.12 rad (7 deg) into the wind direction and the new heading was maintained until an altitude of about 60 m (200 ft) was reached. At this point, the pilot visually aligned the aircraft with the runway and dropped the upwind wing slightly to avoid drifting downwind. In all the aircraft evaluated, this was a relatively easy task as shown by the ratings in Figure 8. When 1.82 m/s (6 ft/s) air turbulence was added, the ratings were degraded by about one pilot rating unit in the L-1011 and the Mach 2.0 SCR, and by about two units in the M = 2.7 SCR. The ratings assigned to this task are nearly identical to those assigned for this turbulence level with no crosswind, indicating little increase in workload due to the crosswind. When the crosswind was increased to 15.45 m/s (30 knots) with no air turbulence, the pilot ratings increased only slightly from the 10.3 m/s (20 knots) case for the L-1011 and Mach 2.0 SCR, but the rating for the Mach 2.7 SCR increased significantly, into the unacceptable range. The pilots reported that they were unable to align the aircraft with the runway from the 0.21 rad (12-deg) crab angle required in this level of crosswind without exceeding lateral control limits. The pilots quickly adopted a technique whereby they determined the maximum controllable rudder pedal input and landed the aircraft with about 0.90 rad (5 deg) remaining crab angle at touchdown. This situation was definitely unacceptable, because of the workload required to ascertain the control limit and the probable landing gear loads developed at the high crab angles. When 1.82 m/s (6 ft/s) of turbulence was added, the workload increased proportionately, producing pilot ratings of 4.0 and 4.5 for the L-1011 and Mach 2.0 SCR, and an average rating of 8 for the Mach 2.7 SCR, which is totally unacceptable.

Controllability at Reduced Approach Speeds

Because of the lateral control problems encountered by the Mach 2.7 configuration at 81.4 m/s (158 knots), no attempt was made to approach at lower air speeds. In the Mach 2.0 SCR design, approaches were flown at 73.6 m/s (143 knots) with no apparent degradation in either pitch or roll control.

CONCLUSIONS

Based on test results from this flight simulation program, the following conclusions have been reached concerning pilot acceptance of low-speed flying qualities and controllability in landing approach:

- Longitudinal flying qualities of both the Mach 2.0 and Mach 2.7 SCR configurations were satisfactory even in heavy turbulence.
- Pitch control and pitch response were slightly better in the Mach 2.0 SCR than in the Mach 2.7 configurations.
- Roll control and response were satisfactory in the Mach 2.0 SCR configuration in all levels of turbulence and crosswind.
- Roll control was not sufficient in the Mach 2.7 configuration for acceptable control of bank angle and line-up in heavy turbulence or for a crosswind landing at FAA limits.
- Crosswind landing gear could eliminate the requirement to decrab in a crosswind, but roll control would still be marginal in heavy turbulence for the Mach 2.7 SCR.
- The Mach 2.7 SCR approach speed is limited to at least 81.4 m/s (158 knots) by both attitude limits and roll control capability. The Mach 2.0 SCR has acceptable flying qualities down to 73.6 m/s (143 knots).

Throughout this study, the planforms have been identified by reference to design Mach numbers of 2.0 and 2.7. It should be emphasized that these results are applicable to the planforms, regardless of design Mach number. The wing sweep angles and aspect ratios of the study configurations were the significant variables in the study, and these results are applicable to any configuration with equivalent planform characteristics.

REFERENCE

1. NASA Technical Paper 1240 - "Ground-Based and In-Flight Simulator Studies of Low-Speed Handling Characteristics of Two Supersonic Cruise Transport Concepts", Grantham, William D., Nguyen, Luat T., Deal, Perry L., Neubauer, M.J., Smith, Paul M., and Gregory, Frederick D.; July, 1978.

TABLE 1. SIMULATION PROGRAM PLANFORM PARAMETERS

WING PARAMETER	DESIGN MACH NO. 2.7	DESIGN MACH NO. 2.0
Span ~ m(ft)	31.7 (103.9)	38.1 (125.1)
mac ~ m(ft)	26.2 (85.9)	22.6 (74.3)
Λ_1 ~ rad (deg)	1.29 (74.0)	1.19 (68.2)
Λ_2 ~ rad (deg)	1.24 (70.8)	1.11 (63.7)
Λ_3 ~ rad(deg)	1.05 (60.0)	0.84 (48.2)
AR	1.61	2.23
β AR	4.03	4.03
$\beta \cot \Lambda$	0.72	0.69

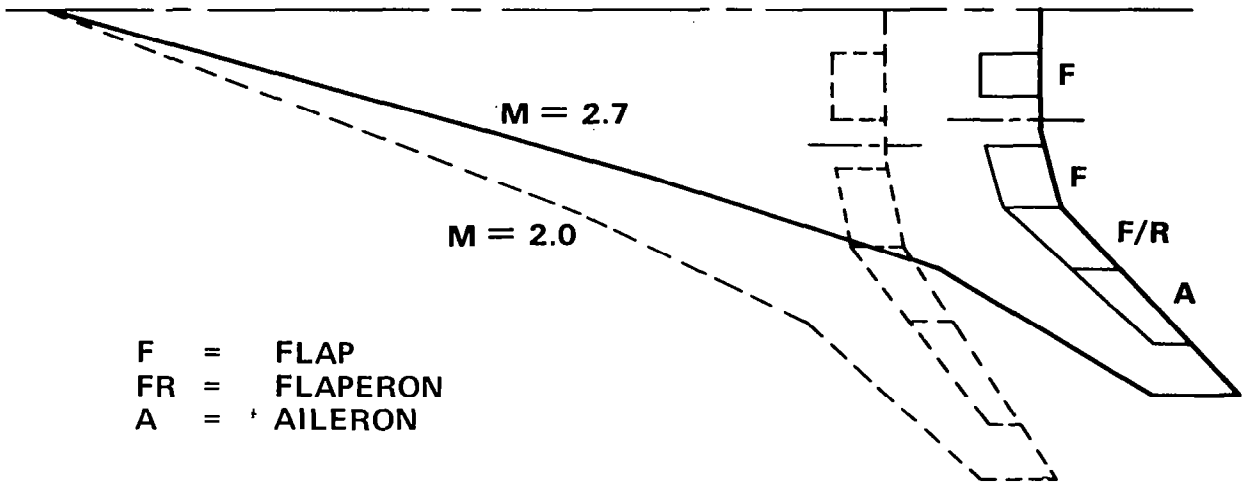

Figure 1.- Planform comparison.

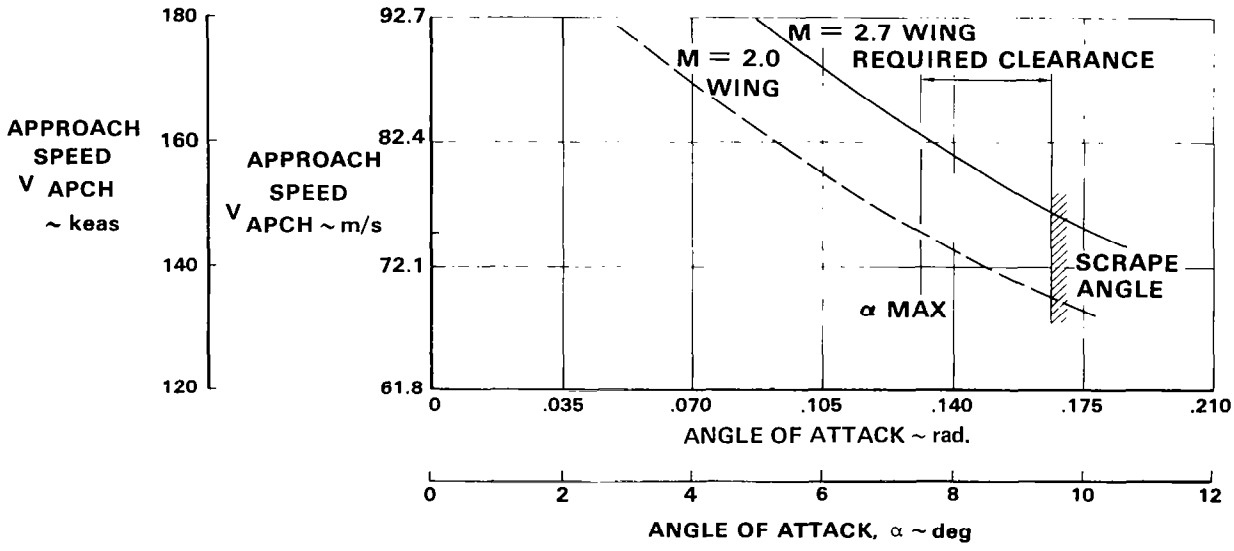

Figure 2.- Approach speed comparison, $\Delta_F = 20^{\circ}$.

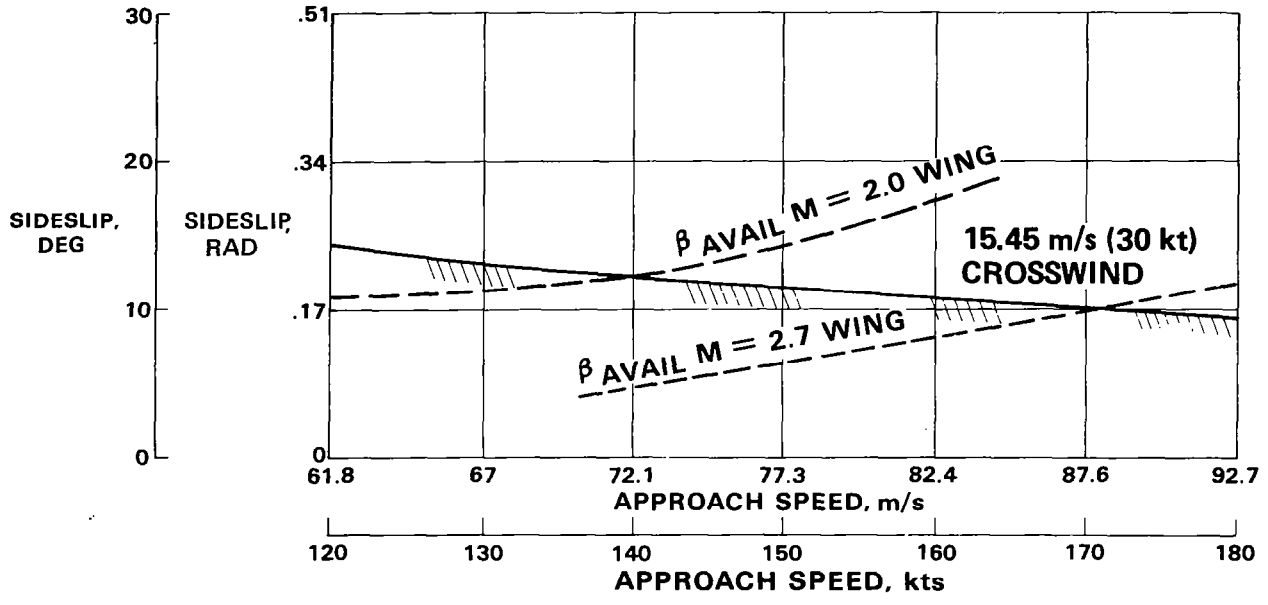

Figure 3.- Crosswind capability.

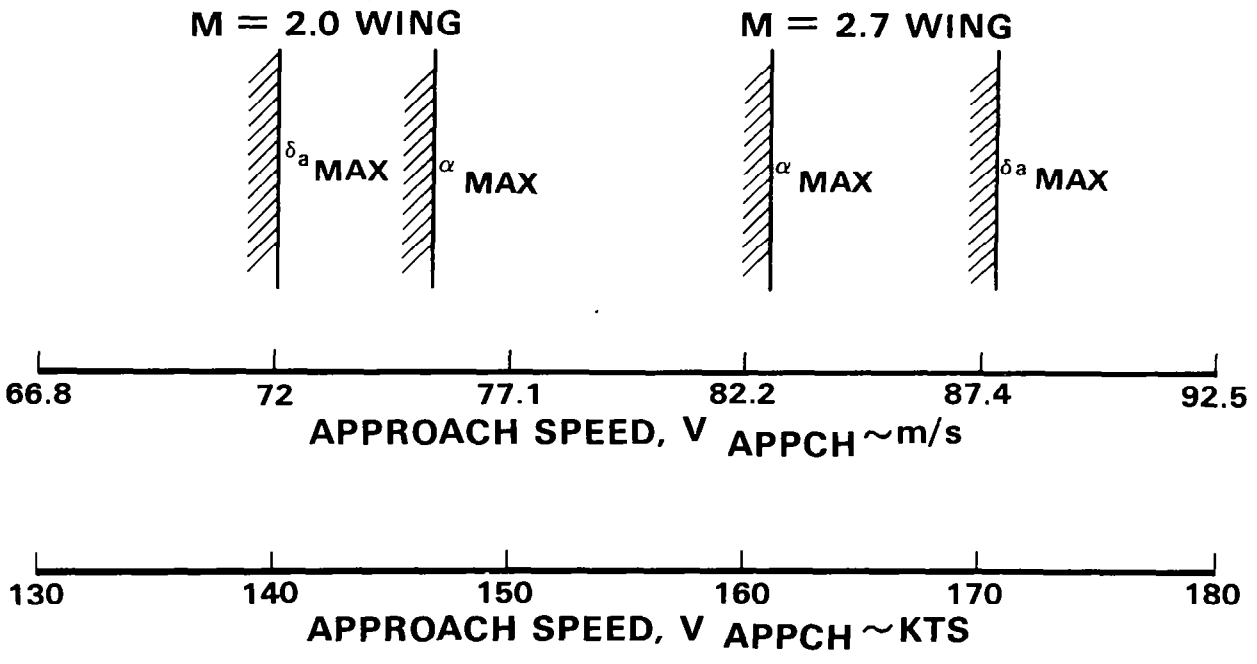

Figure 4.- Approach speed constraints.

1. EXCELLENT 2. GOOD 3. FAIR		SATISFACTORY
4. MINOR DEFICIENCIES 5. MODERATE DEFICIENCIES 6. VERY OBJECTIONABLE		ACCEPTABLE
7. 8. 9.	MAJOR DEFICIENCIES	UNACCEPTABLE
10.		UNCONTROLLABLE

Figure 5.- Pilot rating scale.

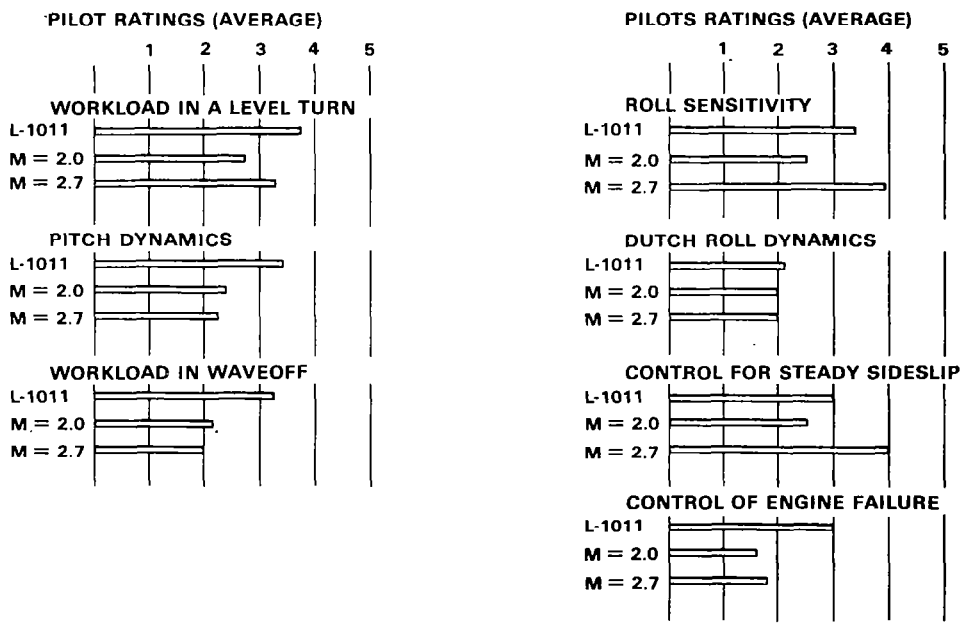

Figure 6.- General flying qualities ratings.

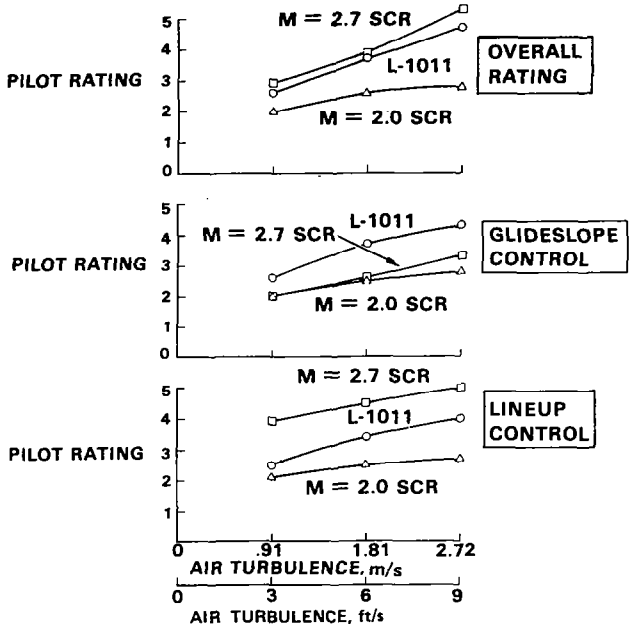

Figure 7.- Effect of air turbulence on approach.

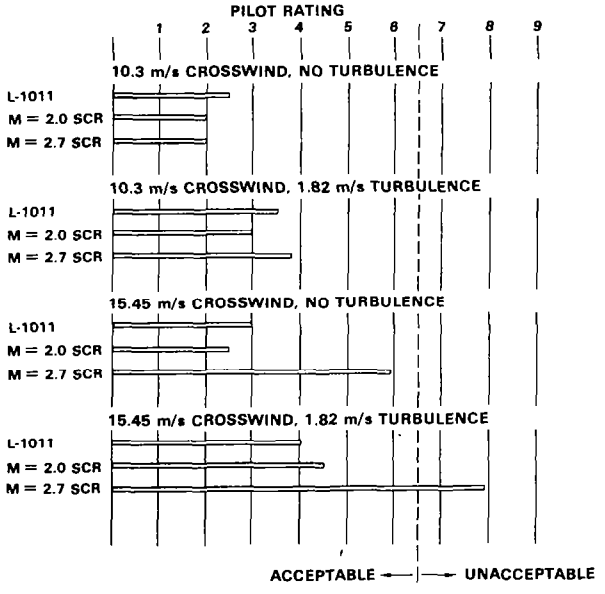

Figure 8.- Control for crosswind landing.

DEVELOPMENT OF SCR AIRCRAFT TAKEOFF AND LANDING PROCEDURES FOR COMMUNITY NOISE ABATEMENT AND THEIR IMPACT ON FLIGHT SAFETY

William D. Grantham
NASA Langley Research Center

Paul M. Smith
Kentron International Incorporated
Hampton Technical Center

SUMMARY

Piloted simulator studies have been conducted to determine takeoff and landing procedures for a supersonic cruise transport concept that result in predicted community noise levels which meet current Federal Aviation Administration (FAA) standards.

The results of the study indicate that with the use of advanced procedures, the subject simulated aircraft meets the FAA traded noise levels during takeoff and landing utilizing average flight crew skills. The advanced takeoff procedures developed involved violating three (3) of the current Federal Aviation Regulations (FAR) noise test conditions. These were: (a) thrust cutbacks at altitudes below 214 meters (700 ft); (b) thrust cutback level below those presently allowed; and (c) configuration change, other than raising the landing gear. It was not necessary to violate any FAR noise test conditions during landing approach.

It was determined that the advanced procedures developed in this study do not compromise flight safety.

Automation of some of the aircraft functions reduced pilot workload, and the development of a simple head-up display to assist in the takeoff flight mode proved to be adequate.

INTRODUCTION

Since 1972, the Langley Research Center of the NASA has been working in advanced supersonic technology for potential application to future U. S. transport aircraft. Among the significant advances which have been made during this period is the development of a new engine concept that is a duct burning turbofan variable stream control engine (VSCE) which has the potential to be operated in such a manner as to create less jet noise than conventional turbojets during takeoff and landing — the improvement being attributed to coannular nozzle jet noise relief.

Current Federal Aviation Regulations (FAR's) for subsonic transport aircraft specify takeoff and landing "piloting" procedures for noise measurement, requiring constant flight speed and no configuration changes (except the landing gear may be retracted after liftoff). It should be considered, however, that a supersonic transport with VSCE engines will have airframe-engine characteristics that are different from the present-day subsonic jet transports, and if utilized properly, could significantly reduce community noise during takeoff and landing. Under the NASA Supersonic Cruise Research program, advanced noise abatement procedures have been identified requiring modifications to the current FAR's for use with future supersonic transports.

Noise characteristics of a typical supersonic cruise research (SCR) concept, designated the AST-105-1, during takeoff and landing were calculated at the three measuring stations prescribed in Ref. 1, and the results are reported in Ref. 2. Although the results of Ref. 2 indicated that the use of advanced operating procedures could be an important additional method for noise reduction, the preliminary procedures reported therein were insufficient to meet the noise requirements of Ref. 1 for takeoff noise (both flyover and sideline), and it was therefore suggested that more detailed studies were required to identify the "optimum" procedures.

The preceived noise level limits dictated by Ref. 1 for an airplane of the class of the subject SCR concept is 108 EPNdB for flyover, sideline, and approach. Although the approach noise for the AST-105-1 was calculated to be 106.6 EPNdB using standard procedures and therefore met the 108 EPNdB requirement, Ref. 2 showed that by using advanced procedures for flying the landing approach, such as steep-decelerating approaches, the calculated approach noise could be reduced below 100 EPNdB. The advanced procedure used in Ref. 2 in an attempt to reduce the flyover and sideline noise during takeoff resulted in a decrease in flyover noise from 115.8 to 113.2 EPNdB, and resulted in an increase in the sideline noise from 113.8 to 115.3 EPNdB — both obviously still much too high to meet the 108 EPNdB requirements even if the noise level "tradeoffs" of Ref. 1 were exercised. [The noise standards, Ref. 1, allow tradeoffs between the measured approach, sideline, and flyover noise levels if: (1) the sum of exceedance is not greater than 3 EPNdB; (2) no exceedance is greater than

2 EPNdB; and (3) the exceedances are completely offset by reductions at other required measuring points.]

This piloted simulation study was therefore conducted using the AST-105-1 SCR concept in an attempt to determine:

1. Advanced takeoff and landing procedures for which the noise level requirements of Ref. 1 could be met.

2. If a pilot with average skills could perform the task of flying the suggested profiles without compromising flight safety.

3. The degree of automation required.

4. The pilot information displays required.

SYMBOLS AND DEFINITIONS

Values are given in both the International System of Units (SI) and U. S. Customary Units. The measurements and calculations were made in U. S. Customary Units. Dots over symbols denote differentiation with respect to time.

AK_V	gain on airspeed error
GK_I	integrator gain
$G_{(ENG)}$	acceleration and deceleration engine inverse time constants, per second
h	altitude, m (ft)
K	gain
M	Mach number
s	Laplace operator
t_1	deceleration time, sec
T	thrust, N (lbf)
T_G	gross thrust
V	airspeed, knots (ft/sec)
V_1	decision speed (engine failure speed + ΔV for a 2-sec reaction time), knots

V_2	airspeed of aircraft at obstacle, knots
V_c	climb speed, knots
V_R	rotate airspeed, knots
V'_R	reference airspeed, knots
V_{RI}	desired airspeed upon completion of deceleration, knots
W	airplane weight, N (lbf)
X	distance from brake release, m (ft)
α	angle of attack, deg
δ_f	trailing-edge flap deflection, deg
δ_{SB}	speed brake deflection, deg
ε	error
γ	flight-path angle, deg
ϕ	angle of roll, deg
ψ	heading angle, deg
τ	time constant, sec
τ_B	pitch attitude bias time constant, sec
Θ	pitch attitude, deg

Subscripts:

C	commanded
FI	flight idle
IAS	indicated airspeed
IC	initial condition
INT	initial
LG	landing gear
LO	lift off

max	maximum
min	minimum
N	net
PFD	pitch command sensitivity to flight director
PIL	pilot
sb	speed brake
VFD	velocity flight director

Abbreviations:

ADI	attitude director indicator
ADV	advanced
AST	advanced supersonic technology
dB	decibel
EF	engine failure
ENG	engine
EPNdB	effective perceived noise decibels
EPNL	effective perceived noise level
FAR	Federal Aviation Regulations
KIAS	knots of indicated airspeed
MOD	modified
PLA	power lever angle
PNL	perceived noise level
PNLT	tone-corrected perceived noise level
PROC	procedure
SCR	supersonic cruise research

STD	standard
TH	track/hold
VMS	visual motion simulator
VSCE	variable stream control engine

DESCRIPTION OF SIMULATED AIRPLANE

The supersonic cruise transport concept simulated in this study was a resized version of the configuration of Ref. 3 and is described in detail in Ref. 2. Reference 2 also presents the mass and dimensional characteristics, control-surface deflections and deflection rate limits, and most of the aerodynamic data used in this study. A three-view sketch of the simulated airplane is presented in Fig. 1.

To facilitate steep-decelerating approaches, a speed brake was designed which incorporated bifurcated "rudders" on the two wing fins. To minimize ground roll following touchdown, the speed brakes and wing spoilers were utilized. The aerodynamic effects of ground proximity were obtained from the test data of Ref. 4. The dynamic aerodynamic derivatives were estimated by using a combination of the forced oscillation test data of Ref. 5 and the estimation techniques of Ref. 6.

The variable stream control engine concept, designated VSCE-516, was selected for this study. The engine was scaled to meet the takeoff design thrust-to-weight ratio of 0.254 for the simulated SCR airplane. The engine performance data generated by the manufacturer was provided in the form of an unpublished data package which included the performance for a standard day plus 10°C. The engine performance for a standard day plus 10°C was used for the takeoff and landing analyses as well as the subsequent noise analyses made during this study.

DESCRIPTION OF SIMULATION EQUIPMENT

Studies of advanced takeoff and landing procedures for a typical SCR transport concept were made using the general-purpose cockpit of the Visual Motion Simulator (VMS) at the Langley Research Center. This ground-based six-degree-of-freedom motion simulator had a transport-type cockpit which was equipped with conventional flight and engine-thrust controls and with a flight-instrument display representative of those found in current transport airplanes (see Fig. 2). Instruments indicating angle of attack, sideslip, pitch rate, and flap angle were also provided. A conventional cross-pointer-type flight director instrument was used, and the command bars (cross pointers) were driven by the main computer program. The horizontal bar of the ADI was used for flight path control command during landing

approaches, and was also used as a simplified airspeed control command during takeoffs. This "takeoff" director was programmed with two options: (1) to command the pilot to climb at an airspeed of $(V_2 + \Delta V)$; or (2) to command the pilot to climb at an airspeed of 250 KIAS. See Fig. 3 for block diagram of takeoff director.

The control forces on wheel, column, and rudder pedals were provided by a hydraulic system coupled with an analog computer. The system allows for the usual variable feel characteristics of stiffness, damping, coulomb friction, breakout forces, detents, and inertia.

The visual display of an airport scene used was an "out-the-window" virtual image system of the beam splitter, reflective mirror type (see Fig. 4). In addition to the airport scene presented on the out-the-window virtual image system, a "head-up" display was superimposed on the same system. The head-up portion of the display consisted of angle of attack, pitch rate, and climb gradient presentations that were used only for the takeoff and climb maneuvers — the head-up display was not used for landing approaches (see Fig. 5).

The motion performance characteristics of the VMS system possess time lags of less than 50 milliseconds. The washout system used to present the motion-cue commands to the motion base was nonstandard (see Ref. 7).

A runway "model" was programmed that was considered to have certain roughness characteristics and a slope from the center to the edge representing a runway crown. Only a dry runway was considered in this study.

TESTS AND PROCEDURES

The tests consisted of both simulated takeoffs and landings using "advanced" procedures. A NASA test pilot participated in the simulation program, and his comments dictated the type of pilot information displays and the degree of automation that was developed for performing the task of "flying" the advanced takeoff and landing procedures used in this study.

The pilot information displays (in addition to the normal-type displays used in present day subsonic jet transports) consisted of a takeoff director and a head-up display — both previously described in this paper and used only during takeoff and climb. The automated features consisted of an autothrottle for controlling airspeed and an auto-decel control. The auto-decel control was programmed as a part of the autothrottle and was used only when the decel switch was activated by the pilot. The autothrottle portion of the system was sometimes used for both takeoffs and landings, whereas the auto-decel mode was only used during landing approaches (see Fig. 6 for block diagram of autothrottle).

By operating the VSCE engines used in this study at maximum allowable turbine inlet temperature, the maximum thrust is increased approximately

16 percent over that for the "normal" operation procedure (T_{max} = 100%). The higher values of thrust allow the achievement of higher speeds, increased lift-drag ratio, better climb performance, and permitted larger power cut-backs — resulting in lower community noise. Therefore, the initial thrust used for takeoffs in this study was 116.4 percent unless otherwise noted.

All computations were made for a standard day plus 10°C. Also, constant weights were used for takeoff, W = 3051.48 kilonewtons (686000 lbf), as well as approach and landing, W = 1744.81 kilonewtons (392250 lbf) — no weight changes due to fuel burn were considered. Current Federal Aviation Regulations (FAR's) were adhered to at all times throughout this simulation study, with the exception of some of those presented in FAR-36. Some of the procedures presented in FAR-36, Ref. 1, were not followed at all times in order to determine the benefits (noise savings) that may be realized should these "rules" be changed. Specifically, the rules listed in Ref. 1 that were not always followed during the present study were:

(1) A constant takeoff configuration must be maintained throughout the takeoff noise test, except that the landing gear may be retracted.

(2) Takeoff power or thrust must be used from the start of takeoff roll to at least an altitude above the runway of 214 meters (700 ft).

(3) Upon reaching an altitude of 214 meters (700 ft), or greater, the power or thrust may not be reduced below that needed to maintain level flight with one engine inoperative, or to maintain a four percent climb gradient, whichever power or thrust is greater.

(4) A steady approach speed must be established and maintained over the approach measuring point.

(5) The approaches must be conducted with a steady glide angle of 3° ±0.5°.

Noise characteristics of the simulated SCR concept at the three measuring stations prescribed in Ref. 1 and indicated in Fig. 7 were calculated for both takeoffs and landing approaches using the NASA Aircraft Noise Prediction Program (ANOPP) described in Ref. 8.

Takeoffs were performed using rotation speeds from 172 KIAS to 200 KIAS, and the climb speeds varied from 211 KIAS to 250 KIAS. During these takeoffs, thrust reductions (cut-backs) were made as a function of distance from brake release and/or altitude. Also, these thrust reductions were made manually as well as automatically. It should be mentioned that after the "final" thrust reduction was made (always made prior to reaching the flyover measuring point), the climb gradient was reduced to 0.04 ($\gamma \approx 2.3°$).

Landing approaches were made at: (1) constant speed for various constant glideslope angles; and (2) decelerating speeds for various constant glideslope angles. The glideslope angles varied from 3° to 5°, and the approach speeds varied from 250 KIAS to 158 KIAS.

The results of this study, using the aforementioned evaluation procedures, will primarily be presented in the form of effective perceived noise level (EPNL) savings as a function of piloting techniques used to perform takeoffs and landings on the subject SCR transport concept. The more significant results are reviewed in the following sections.

RESULTS AND DISCUSSION

The results of this study are discussed in terms of the previously stated objectives and primarily presented in the form of effective perceived noise level (EPNL) as the piloting technique varied while performing takeoffs and landings on the simulated SCR transport concept. The noise levels discussed pertain to jet noise only.

Takeoff

Takeoffs were performed using rotation speeds (V_R) from 172 KIAS to 200 KIAS, an angular rotation rate ($\dot{\Theta}$) of 3°/second, and "initial" rotation angles of attack (α_{int}) from 4° to 8° (depending on the desired climb speed (V_c)). The α_{int} as used here is the angle of attack to which the pilot rotates and maintains until V_2 is achieved.

Determination of rotation speed.- The procedures used to determine the minimum and maximum rotation speeds to be used in this simulation study were those prescribed in FAR-Part 25, (Ref. 9). In general, the range of V_R's used were selected from the V_1 information determined on the simulator and presented in Fig. 8. The V_1 concept was developed for civil air transport certification, and its intent is to provide the pilot sufficient information to decide whether to refuse or to continue the takeoff. If the pilot elects to refuse the takeoff, the total distance required for the maneuver (from brake release, to V_1, to full stop) is called the accelerate-stop distance. If the pilot elects to continue the takeoff, the total distance required from brake release, to V_1, to an altitude of 10.7 meters (35 ft) is called the takeoff distance. (As can be seen from Fig. 8, the intersection of the two curves (balanced field length) occurs at approximately 172 KIAS.) In addition, Ref. 9 states that the critical engine-inoperative takeoff distance, using a rotation speed of 5 knots less than V_R, must not exceed the corresponding critical engine-inoperative takeoff distance using the established V_R. Therefore, it can be seen from the "takeoff distance" curve of Fig. 8 that the minimum "established" V_R should be no less than approximately 185 KIAS. However, during the present simulation program, a minimum $V_R = V_1 = 172$ KIAS was chosen in order to get the maximum possible variable range for V_R and the corresponding V_c. From the "accelerate-stop-distance" curve, in combination with the

"takeoff distance" curve of Fig. 8, the maximum V_R chosen to be used in this simulation program was 200 KIAS, due to tire speed limitations. Thus, the range of rotation speeds used in this study was from 172 KIAS to 200 KIAS, resulting in lift-off speeds from 193 KIAS to 215 KIAS, respectively. It should also be mentioned that the range of V_R's used does not exceed the limits dictated by the Tentative Airworthiness Standards for Supersonic Transports (unpublished).

Angular rotation rate.- An angular rotation rate $(\dot{\Theta})$ of approximately 3°/sec was used for all takeoffs in the present study. This value was selected from considering tail-scrape as well as pilot-passenger comfort. It was also noted that the nominal angular rotation rate used by the pilots when flying the Concorde simulation, Ref. 10, was approximately 2.8°/second.

Initial rotation angle of attack.- The initial α selected for each takeoff varied depending upon the selected rotate speed and climb speed. For example, for a selected V_R of 172 KIAS and a climb speed of V_2 + 10 KIAS, the initial α used for the best performance was determined to be approximately 8°, whereas for a selected V_R of 200 KIAS and a V_C of 250 KIAS, the initial α used for the best performance was determined to be approximately 4°.

Minimum flyover noise during takeoff.- Using simulated takeoff procedures with no power cut-backs, the flyover noise was calculated to be approximately 118 EPNdB, regardless of the selected rotate speed or the selected climb speed, and the sideline noise was calculated to be greater than 116 EPNdB for all takeoffs.

The scheme used to determine a piloting technique that would result in acceptable noise levels for both flyover and sideline was to first define the minimum flyover noise procedure — with no consideration for the sideline noise generated.

Reference 1 states, in part, that: (1) takeoff power or thrust must be used from the start of takeoff roll to an altitude of at least 214 meters (700 ft) for airplanes with more than three engines; (2) upon reaching an altitude of 214 meters, the power or thrust may not be reduced below that needed to maintain level flight with one engine inoperative, or to maintain a four percent climb gradient, whichever power or thrust is greater; and (3) a speed of at least V_2 + 10 knots must be maintained throughout the takeoff noise test. Therefore, the first task was to determine the amount of allowable thrust cutback and this is indicated in Fig. 9. As can be seen, for airspeeds greater than approximately 240 KIAS the four-engine, four percent climb gradient criterion should be used, whereas the three-engine, zero climb gradient criterion should be used for airspeeds below 240 KIAS. For the present study, the four-engine, four percent climb gradient criterion was arbitrarily used for all climb speeds considered since it was more beneficial at the lower climb speeds (V_C < 240 KIAS) and was almost as beneficial at the higher climb speeds (V_C > 240 KIAS). Therefore, the net thrust was reduced to 71 percent, at the cutback point, when the slowest climb speed was flown (V_R = 172 KIAS and $V_C = V_2$ + 10 = 211 KIAS) and was

reduced to 58 percent, at the cutback point, when a climb speed of 250 KIAS was flown. (It should be noted that the maximum airspeed allowed below an altitude of 3048 meters (10000 ft) is 250 KIAS due to Air Traffic Control considerations.

The "ideal" cutback altitudes were then determined using the lowest V_R and V_c investigated (V_R = 172 KIAS and V_c = 211 KIAS), as well as the highest V_R and V_c investigated (V_R = 200 KIAS and V_c = 250 KIAS), and the results are presented in Fig. 10. Indications are that for V_R = 172 KIAS and V_c = 211 KIAS the ideal cutback altitude, from an effective perceived noise level standpoint, was approximately 400 meters (1312 ft), and for V_R = 200 KIAS and V_c = 250 KIAS, the ideal cutback altitude was approximately 290 meters (951 ft). Figure 10 also indicates that the faster climb speed, which allowed more thrust cutback, was approximately 2 EPNdB less noisy than the slower climb speed (107.7 EPNdB compared to 109.6 EPNdB) even though the cutback altitude was approximately 110 meters (361 ft) lower. It should also be noted that the minimum flyover EPNL for the V_R = 200 KIAS, V_c = 250 KIAS technique was slightly lower than the maximum level allowed (108 EPNdB; Ref. 1).

These two takeoff profiles are presented in Fig. 11. The piloting procedures used were to: (a) accelerate from brake release to V_R (172 KIAS and 200 KIAS); (b) at V_R, rotate the airplane at an angular rotation rate of 3°/sec to an angle of attack of 8° and 4°, respectively, and maintain those α's until V_2 was achieved; (c) after attaining V_2, the pilot merely "flew" the takeoff director commands, which in these cases commanded climb speeds of V_2 + 10 = 211 KIAS and 250 KIAS, respectively; and (c) upon attaining the designated "ideal" cutback altitudes (400 meters (1312 ft), and 290 meters (951 ft), respectively) the co-pilot reduced the net thrust to 71 percent and 58 percent, respectively, and the pilot simultaneously reduced the climb gradient to 0.04 in each instance. The results indicate that the airplane was at an altitude of 492 meters (1614 ft) when it flew over the noise measuring station (a distance of 6500 meters (21325 ft) from brake release) for the slower V_R and V_c compared to an altitude of 420 meters (1378 ft) for the faster V_R and V_c. The calculated flyover perceived noise levels (PNL) and effective perceived noise levels (EPNL) are also presented in Fig. 11, and indicate that the maximum calculated PNL's for the slower and faster takeoffs were 110.8 dB and 109.6 dB, respectively, resulting in EPNL's of 109.6 dB and 107.7 dB, respectively. Therefore, it was concluded that the faster climb speed was more beneficial from a noise standpoint, and thus the majority of the takeoffs made and discussed throughout the remainder of the present study pertain to rotate speeds of 200 KIAS and climb speeds of 250 KIAS.

Figure 12 indicates that for climb speeds greater than approximately 233 KIAS, less thrust is required to trim on a 0.04 climb gradient for δ_f = 10° than for δ_f = 20°. For example, at V_c = 250 KIAS, two percent less thrust is required to trim for the δ_f = 10° configuration (T_N = 56 percent compared to 58 percent). Figure 13 presents the flyover EPNL savings due to raising the flaps to 10° (after V_c > 233 KIAS) and indicates that since the ΔdB was less than one for any cutback altitude, the

configuration change would probably not be justified. (It should be noted that Ref. 1 requires a constant configuration throughout the takeoff noise test - with the exception of landing gear retraction.)

During the generation of the flight profiles necessary to calculate the corresponding EPNL's shown in Figs. 10 and 13, it was found that the rate of thrust cutback and the rate of climb gradient change were very important as to whether the climb speed was maintained. Therefore, instead of manually reducing the thrust to the specified level (depending upon the V_C and δ_f), the autothrottle was activated at various altitudes and, again, the climb gradient was reduced to 0.04. These results are presented in Fig. 14 and compared to the manual throttle cutbacks. The results indicate that the use of the autothrottle makes for approximately one EPNdB savings for the "ideal" cutback altitude. Figure 15 presents the flight profiles comparing the manual cutback and autothrottle activation at an altitude of approximately 290 meters (951 ft). Note that although the same approximate altitude (417 meters (1368 ft)) was achieved at the flyover measuring station (6500 meters from brake release), the calculated values for PNL and EPNL were somewhat different, even though both takeoffs were for the same configuration and the same takeoff procedures were used — with the exception of the method used to reduce the thrust at the designated altitude. The differences in the EPNL's were attributed to the differences in the thrust management. Note from the net thrust trace that for the manual cutback procedure, the co-pilot gradually reduced the thrust from T_{max} to 58 percent with no overshoot. However, when the thrust was reduced by the autothrottle, an overshoot in thrust resulted (T_N became as low as approximately 44 percent at one instance) and therefore the EPNL was lower at the measuring station due to the lower values of net thrust. It should be noted that the climb speed was maintained relatively constant at approximately 250 KIAS during both flights.

Obviously, it will be necessary to use the minimum amount of thrust during takeoff in order to keep the sideline noise at a minimum. However, sufficient thrust must be used to keep the takeoff flyover noise at 110 EPNdB or less in order to even consider the possibility of using the present FAR tradeoff capabilities. Therefore, takeoffs were performed for which only 100 percent of the maximum available thrust was used. Figure 16 presents the calculated flyover EPNL's against various cutback altitudes for initial values of thrust of 100 percent and 116.4 percent, and as can be seen, the minimum flyover effective perceived noise level that was experienced was greater than 111 dB when 100 percent thrust was used for takeoff, regardless of the cutback altitude, compared to a minimum EPNL of less than 108 dB when maximum available thrust (116.4 percent) was used for takeoff.

It was therefore concluded that an initial value of thrust greater than 100 percent must be used in order to achieve a flyover EPNL equal to or less than 110 dB. Furthermore, these results indicated that at some point during the early stages of the takeoff, the thrust must be reduced below 100 percent in order to reduce the sideline noise being generated -- the sideline noise was greater than 110 EPNdB even when only 100 percent thrust

was used for takeoff. (As mentioned previously, the sideline noise was greater than 116 EPNdB for the maximum thrust takeoff.)

Summary of results pertaining to minimum flyover noise during takeoff.- With no consideration given to the sideline noise being generated, various takeoff procedures were used in an attempt to define the "best" piloting procedure that could be used in order to create the minimum effective perceived noise level at the flyover noise measuring station (6500 meters from brake release). The more significant results were as follows:

•With no power cutbacks the flyover EPNL was approximately 118 dB, regardless of the rotate speed and/or climb speed.

•Using the noise abatement takeoff procedures presently allowed by the Federal Aviation Regulations of Ref. 1, the maximum allowed rotation speed and climb speed (V_R = 200 KIAS and V_c = 250 KIAS) were the most beneficial for creating the minimum noise at the designated flyover noise measuring station. This takeoff procedure resulted in a flyover EPNL of 107.7 dB, which met the 108 EPNdB requirement of Ref. 1.

•Minor additional noise benefits could be realized by reducing the flap deflections from 20° to 10° for airspeeds greater than approximately 233 KIAS.

•Additional noise benefits were gained by activating the autothrottle (as opposed to manual throttle manipulations) at the "ideal" cutback altitude.

The best advanced piloting procedure used during this study for minimum flyover noise, disregarding the sideline noise being generated, was as follows:

(a) with maximum available thrust (116.4 percent), accelerate the airplane from brake release to 200 KIAS;

(b) at V = 200 KIAS, rotate the airplane at an angular rotation rate of 3°/sec to an angle of attack of 4°. Retract the landing gear after liftoff;

(c) maintain $\alpha = 4°$ until V_2 is achieved; V_2 is defined as the aircraft velocity at the hypothetical obstacle ($h_{L.G.}$ = 10.67 m (35 ft));

(d) accelerate the airplane from V_2 to a climb speed of 250 KIAS (V_c = 250 KIAS is the maximum speed allowed below an altitude of 3048 m (10000 ft));

(e) prior to achieving V_c = 250 KIAS, reduce the flap deflections from 20° to 10°; and

(f) at an altitude of 290 m (951 ft), activate the autothrottle and reduce the climb gradient to 0.04.

This takeoff procedure resulted in a flyover noise level of 106.7 EPNdB, which is 1.3 dB less than the maximum allowed EPNdB of 108 (Ref. 1).

Sideline noise considerations during takeoffs.- In an attempt to determine a takeoff procedure that would allow the use of the aforementioned noise tradeoffs between the flyover noise, sideline noise, and approach noise and thus meet the 108 EPNdB requirements of Ref. 1, various piloting procedures were used during simulated takeoffs. Since it was determined earlier that the most advantageous procedure for flyover noise was to rotate as late as possible and climb as fast as possible, the majority of the "sideline noise" takeoffs were made for which V_R was 200 KIAS and V_C was 250 KIAS.

Figure 17 indicates the sideline effective perceived noise levels calculated for a standard procedure (no FAR rules were broken) takeoff. Note that the sideline EPNL approaches 108 dB approximately 1800 meters (5906 ft) after brake release and has exceeded 110 dB prior to liftoff (X = 2496 m (8189 ft)). Therefore, it was obvious that some degree of power cutback would be required prior to liftoff in order to keep the sideline noise equal to or less than 110 EPNdB, the maximum level that would allow the use of the previously discussed noise tradeoff criterion.

Various piloting techniques were then used in an attempt to determine the optimum takeoff procedure insofar as the minimum sideline and flyover jet noise were concerned. Power cutbacks were made at various distances from brake release as well as at various altitudes in an attempt to keep the sideline noise to a minimum. Then — a "final" power cutback was made (sometimes autothrottle was used) and the climb gradient reduced to 0.04, prior to reaching the flyover noise measuring station, in order to keep the flyover EPNL to a minimum. The objective was to keep the sideline EPNL equal to or less than 110 dB and at the same time keep the flyover EPNL equal to or less than 109 dB.

A typical takeoff using "advanced" procedures is presented in Fig. 18. The piloting procedures used were as follows:

(a) with the flaps set at 20°, and using maximum available thrust, accelerate the airplane from brake release to V = 200 KIAS;

(b) at V = 200 KIAS, rotate at a $\dot{\theta} \approx 3°/\text{sec}$ to an initial angle of attack of approximately 4°. At $X \approx 2225$ meters (7300 ft) and $V \approx 208$ KIAS, reduce the net thrust to 110 percent;

(c) after liftoff ($X \approx 2500$ meters (8202 ft) and $V \approx 217$ KIAS), raise the landing gear and accelerate to V_2 while maintaining $\alpha \approx 4°$;

(d) at V_2, which was approximately 235 KIAS, reduce the net thrust to 90 percent and, by following the commands of the takeoff director, accelerate to 250 KIAS. Prior to attaining V_C = 250 KIAS, raise the flaps from 20° to 10°; and

(e) continue the climb-out at V_C = 250 KIAS. At an altitude of approximately 185 meters (607 ft), activate the autothrottle and reduce the climb gradient to 0.04.

Figure 18 indicates that the sideline EPNL exceeds 108 dB at $X \approx 2700$ meters (8858 ft) from brake release and that the maximum sideline EPNL was 109.8 dB, occurring at $X \approx 3350$ meters (10991 ft). Note that an altitude of 254 meters (833 ft) was attained at the flyover noise measuring station and that the calculated flyover EPNL was 108.1 dB. It should also be mentioned that the autothrottle caused the net thrust to overshoot the allowed level of 56 percent. (T_N actually became as low as 38 percent at one point and was less than 56 percent for approximately 5 seconds, which corresponded to the time just prior to, and immediately after, flying over the flyover noise measuring station.) It is believed that although this large, temporary, thrust reduction exceeded the limit allowed (Fig. 12), flight safety would not be jeopardized in that, for example, should an engine fail during the time the autothrottle had driven the thrust to this "unacceptably" low value, the autothrottle would very quickly command sufficient thrust on the remaining three (3) engines to maintain an airspeed of 250 KIAS. It is therefore concluded that this piloting procedure is a realistic and safe takeoff procedure if autothrottle is used, and that by utilizing the aforementioned tradeoff criterion, the traded noise can be kept below 108 EPNdB at the designated measuring stations, again assuming that the approach noise is no more than 105 EPNdB.

Effects of modifying the VSCE engine for maximum coannular acoustic benefit.- As mentioned previously, the noise levels discussed in this paper are those due to jet noise only. For example, the effects of engine shielding on the sideline noise levels have not been included in the noise calculations, and, therefore, the sideline noise levels discussed previously for takeoffs would have been somewhat lower if the engine-shielding effects were included. It was also determined during the simulation program that very large cutbacks in thrust were possible in order to reduce the flyover noise during takeoff. It was realized at that time that the design of the simulated VSCE engine was such that the coannular nozzle acoustic benefit was lost for thrust settings below approximately 60 percent. Therefore, in general, the flyover jet-noise levels discussed previously would be somewhat lower if the coannular benefit could be maintained for thrust settings lower than 60 percent.

The engine designers were therefore asked to investigate the impact of retaining the coannular nozzle acoustic benefit at cutback thrust settings approaching 40 percent of maximum thrust. These data were supplied for use in the present simulation study with the warning that design changes to the "current" VSCE engine might be required, with potential impact on weight and performance. Nevertheless, these "modified" engine data were used to repeat some of the advanced procedure takeoffs, and the results indicated that although the engine modification did not improve the sideline EPNL, the flyover EPNL was reduced approximately 2 dB. (Repeating the takeoff procedure indicated in Fig. 18, but using the modified VSCE engine, reduced the flyover jet noise from 108.1 EPNdB to 106.0 EPNdB.)

Landing Approaches

Reference 1 states that a constant airspeed and configuration must be maintained on a constant glide angle of 3° ±0.5° throughout the landing approach noise test. However, for the purposes of this study, all of these were varied in an attempt to determine the noise benefits that could be realized should these "rules" be changed. During the present simulation study, landing approaches were made at constant speed for various constant glideslope angles, as well as for decelerating speeds for various constant glideslope angles. (Segmented approaches were not performed.) The glideslope angles varied from 3° to 5°, and the approach speeds varied from 250 KIAS to 158 KIAS during the decelerating approaches.

Reference 1 (FAR-36) landing approach test procedure.- The approach noise calculated using a constant airspeed of 158 KIAS, a constant configuration, and a constant glide angle of 3° was 101.5 EPNdB. Note that this approach noise was well below the allowed 108 EPNdB, and in fact was sufficiently low to allow the use of the tradeoff rules previously discussed.

Constant speed for various constant glide angles.- Landing approaches were made using a constant configuration and a constant airspeed of 158 KIAS for various constant glideslopes. In addition to the standard 3° glideslope discussed above, glide angles of 4° and 5° were used, and the resulting calculated effective perceived noise levels were 96.8 EPNdB and 92.3 EPNdB, respectively.

Decelerating speeds for various constant glide angles.- During the decelerating approaches, an initial airspeed of 250 KIAS was used and the final airspeed used was 158 KIAS. (It should be noted that speed brakes were sometimes used during the decelerating approaches.) The results indicated that only minor noise reduction benefits were gained by flying decelerating approaches. For example, the approach noise for a glideslope of 4° and a constant airspeed of 158 KIAS was 96.8 EPNdB; whereas for the same glideslope (4°) and decelerating from an initial airspeed of 250 KIAS to V = 158 KIAS, the calculated approach noise was 95.4 EPNdB, a reduction of only 1.4 EPNdB.

Summary of results pertaining to landing approach noise tests.- It was determined that the calculated landing approach effective perceived noise level for the simulated SCR transport concept, using present-day FAR-36 test procedures, was 101.5 EPNdB, which was well below the allowed 108 EPNdB. It was also found that substantial noise reduction benefits could be gained by increasing the glide angle and flying a constant airspeed, but that only minor additional noise reduction benefits were realized by flying decelerating approaches. It should be noted, however, that although the decelerating approach produced minor noise benefits insofar as the noise at the approach noise measuring station of Ref. 1 (2000 meters short of the runway threshold, Fig. 7), decelerating approaches should be very beneficial for reducing the approach noise contours (footprints). It is also concluded from these results that these "low" noise levels underscore the need for examining

other noise sources such as engine fan noise, turbomachinery noise, and airframe noise.

Noise Tradeoffs

The Federal Aviation Regulations Noise Standards, Ref. 1, dictate a maximum noise limit of 108 EPNdB at the approach, sideline, and flyover noise measuring stations. (See Fig. 7 for location of noise measuring stations.) However, Ref. 1 allows tradeoffs between the approach, sideline, and flyover noise levels if: (1) the sum of the exceedance is not greater than 3 EPNdB; (2) no exceedance is greater than 2 EPNdB; and (3) the exceedances are completely offset by reductions at other required measuring points. Therefore, these noise tradeoff rules were applied to the noise levels calculated during the previously discussed takeoffs and landings performed using various piloting procedures.

Takeoff and landing using standard procedures.- The term "standard procedure," as used in this paper, applies to the piloting procedure used that abides by all present-day Federal Air Regulations, and in particular, the noise standards certification regulations of Ref. 1. The minimum flyover noise obtained, using standard procedure, was 107.7 EPNdB (Fig. 11), and the sideline noise produced was 114.8 EPNdB (Fig. 17). Therefore, since the approach noise was 101.5 EPNdB, the traded noise was 112.8 EPNdB. It should be mentioned that this traded noise could be reduced by using less initial thrust for takeoff, thereby reducing the sideline noise to some extent and allowing the flyover noise to become greater. For example, if 100 percent of thrust (as opposed to 116.4 percent) was used for takeoff, the flyover noise would increase to 111.7 EPNdB, and the sideline noise would decrease to 112.3 EPNdB, producing a traded noise level of 110.5 EPNdB. However, the traded noise for either procedure was well above the allowed 108 EPNdB.

Advanced procedure used for takeoff.- The term "advanced procedure," as used within this paper, applies to the piloting procedure used that did not abide by the recommended FAR-36 noise test procedures for airplane certification (Ref. 1). Advanced piloting procedures were developed in an attempt to decrease the sideline noise generated during takeoff. These procedures were discussed previously and presented in Fig. 18. The takeoff noise levels, using these procedures, were calculated to be 108.1 EPNdB for flyover and 109.8 EPNdB for sideline, resulting in a traded noise level of 107.8 EPNdB. Therefore, by using these advanced procedures, the traded noise level was reduced by 5 EPNdB. It should also be noted that this traded noise level (107.8 EPNdB) meets the noise limit requirements of 108 EPNdB, Ref. 1.

Advanced procedure and modified VSCE engine used for takeoff.- As discussed previously, the simulated VSCE engine was modified in order to retain the coannular nozzle acoustic benefit at much lower thrust settings than the basic engine design. Also, the use of this modified engine reduced the flyover noise from 108.1 EPNdB to 106.0 EPNdB when the same procedures were used for takeoff. (The modified engine did not affect the sideline

noise generated.) Therefore, a new takeoff procedure was developed for use with the modified engine in an attempt to further reduce the sideline noise level (allowing the flyover noise to increase above 106.0 EPNdB) and thus reduce the traded noise level below 107.8 EPNdB. The piloting procedure used is presented in Fig. 19 and was as follows:

(a) with the flaps set at 20°, and using maximum available thrust, accelerate the airplane from brake release to $V = 200$ KIAS;

(b) at $V = 200$ KIAS, rotate at a $\dot{\Theta} \approx 3°/\text{sec}$ to an initial angle of attack of approximately 4°;

(c) after liftoff ($X \approx 2496$ meters (8188 ft) and $V \approx 218$ KIAS), raise the landing gear and accelerate to V_2 while maintaining $\alpha \approx 4°$;

(d) at V_2, which was approximately 235 KIAS, reduce the net thrust to 75 percent and, by following the commands of the takeoff director, accelerate to 250 KIAS. Prior to attaining V_c = 250 KIAS, raise the flaps from 20° to 10°; and

(e) continue the climb-out at V_c = 250 KIAS. At an altitude of approximately 152 meters (500 ft), activate the autothrottle and reduce the climb gradient to 0.04.

Figure 19 indicates that the flyover noise was 106.8 EPNdB and the maximum sideline noise was 108.2 EPNdB, occurring at $X \approx 2743$ meters (9000 ft); thus the traded noise would be 106.2 EPNdB. An interesting point to be noted here is that the maximum sideline noise occurred prior to reaching the end of the runway.

It is concluded from these results that by using advanced takeoff procedures, the simulated SCR transport concept, with the modified VSCE engines, readily meets the noise certification standards of Ref. 1.

The histogram presented in Fig. 20 summarizes the traded noise levels calculated for the various conditions and test procedures flown during the present study. It can be seen that by using "advanced" takeoff procedures, the traded noise level for the subject SCR transport concept can be reduced by approximately 4.5 EPNdB.

Impact of Advanced Procedures on Flight Safety As Determined by Recovery From Critical Engine Failure

The advanced takeoff procedures developed for the subject SCR transport involved violating some of the current FAA noise certification test conditions, Ref. 1, in order to meet the required noise levels. (No rule violations were required to meet the required noise levels during landing approach.) The three rule violations were as follows:

(1) Reference 1 required that takeoff power or thrust be used from the start of takeoff roll to at least an altitude of 214 meters (700 ft) for airplanes with more than three turbojet engines.

[During the present SCR simulation program, thrust reductions were required at altitudes below 214 meters in order to meet the takeoff sideline noise requirement.]

(2) Reference 1 states that upon reaching an altitude of 214 meters (700 ft), the power or thrust may not be reduced below that needed to maintain level flight with one engine inoperative, or to maintain a four percent climb gradient, whichever power or thrust is greater.

[During the SCR simulation program, it was determined that larger temporary thrust reductions reduced the flyover noise at the flyover noise measuring station — and the climb speed could still be maintained.]

(3) Reference 1 states that a constant takeoff configuration must be maintained throughout the takeoff noise test, except that the landing gear may be retracted.

[It was determined during the SCR simulation program that additional noise reduction could be achieved by raising the flaps from 20° to 10° for climb speeds greater than 233 KIAS.]

Of these three (3) rule violations, the number (1) rule listed above is of primary importance. That is, only minor noise reduction benefits were realized by violating the rules listed above as numbers (2) and (3).

Obviously, it must be shown that violating these current FAA rules does not jeopardize flight safety. To demonstrate this, the advanced-procedure takeoffs were repeatedly performed, and an outboard engine was failed at various locations during the takeoff. The test pilot felt that the most critical stage of the takeoff was immediately after liftoff. Therefore, one location included during the engine-failure takeoffs was the point immediately following the thrust cutback made upon attaining V_2 (altitude of 10.67 meters (35 ft)), and this time history is presented in Fig. 21. After the number 4 engine (outboard engine on right wing) was failed, the pilot advanced the thrust on the remaining three engines, attempted to maintain wings-level and heading, and continued to accelerate to a V_C of 250 KIAS. As indicated in Fig. 21, the wings were kept within ±1° of being level and the heading was maintained within approximately 2°.

The pilot commmented that the aforementioned advanced takeoff procedures posed no safety problems. He stated that, due to the excess thrust available on the simulated airplane, after attaining approximately 230 KIAS, instead of declaring an engine-failure an emergency situation, the pilot could safely choose to continue to follow the noise abatement procedure.

CONCLUDING REMARKS

The subject piloted simulation study was conducted using the AST-105-1 Supersonic Cruise Research (SCR) transport concept to determine: (a) advanced takeoff and landing procedures for which the Federal Aviation Regulations (FAR) noise level requirements could be met; (b) if a pilot with average skills could perform the task of flying the suggested profiles without compromising flight safety; (c) the degree of automation required; and (d) the pilot information displays required. This paper has attempted to summarize the results of this study which support the following major conclusions.

Utilizing the current Federal Aviation Regulations test procedures for aircraft noise certification produced the following results: (a) the landing approach effective perceived noise level (EPNL) was 101.5 dB; (b) the flyover EPNL was 107.7 dB; and (c) the sideline EPNL was 114.8 dB.

Advanced takeoff procedures were developed that involved violating three of the current FAR noise test conditions. These were: (a) thrust cutbacks at altitudes below 214 meters (700 ft); (b) thrust cutbacks below those presently allowed; and (c) configuration change, other than raising the landing gear. Utilizing the current FAR noise test conditions, with these three exceptions, the calculated effective perceived noise levels for flyover and sideline were 108.1 dB and 109.8 dB, respectively.

The basic variable stream control engine (VSCE) used in this study was modified in order to retain the coannular nozzle acoustic benefit at thrust levels below 50 percent. With this engine modification, the advanced takeoff procedure was also modified in an attempt to reduce the takeoff noise levels below the presently allowed 108 EPNdB. With this "up-dated" takeoff procedure and modified engine, the flyover noise was calculated to be 106.8 EPNdB and the sideline noise was 108.2 EPNdB.

Utilizing the current FAR noise tradeoff rules, it was determined that the traded noise level was 110.5 EPNdB, when using current FAR noise certification test conditions, compared to a traded noise level of 106.2 EPNdB when advanced takeoff procedures were used — a traded noise reduction of approximately 4.5 EPNdB.

It was determined that the advanced takeoff procedures developed and evaluated during this study did not compromise flight safety.

It is concluded that the subject SCR transport concept, with the augmented variable stream control engines modified to maintain its coannular nozzle acoustic benefit at thrust settings below 50 percent, can meet the current FAA noise standards if the current noise certification test conditions are modified in such a manner to allow maximum performance utilization of the aircraft — as long as it does not jeopardize flight safety.

It is further concluded that the automation of some of the aircraft functions reduced the pilot workload when performing the advanced procedure takeoffs, and that very simple piloting displays seemed to be adequate for the task.

REFERENCES

1. DOT/FAA Noise Standards: Aircraft Type and Airworthiness Certification, FAR Part 36, June 1974.

2. Baber, Hal T., Jr.: Characteristics of the Advanced Supersonic Technology AST-105-1 Configured for Transpacific Range with Pratt and Whitney Aircraft Variable Stream Control Engines. NASA TM 78818, March 1979.

3. Baber, Hal T., Jr.; and Swanson, E. E.: Advanced Supersonic Technology Concept AST-100 Characteristics Developed in a Baseline-Update Study. NASA TM X-72815, 1976.

4. Coe, Paul L., Jr.; and Thomas, James L.: Theoretical and Experimental Investigation of Ground Induced Effects for a Low-Aspect-Ratio Highly Swept Arrow-Wing Configuration. NASA TM 80041, 1979.

5. Freeman, Delma C., Jr.: Low Subsonic Flight and Force Investigation of a Supersonic Transport Model with a Highly Swept Arrow Wing. NASA TN D-3887, 1967.

6. USAF Stability and Control Datcom. Contracts AF 33(616)-6460 and F33615-75-C-3067, McDonnell Douglas Corporation, October 1960. (Revised April 1976).

7. Martin, D. J., Jr.: A Digital Program for Motion Washout on Langley's Six-Degree-of-Freedom Motion Simulator. NASA CR-145219, July 1977.

8. Raney, John P.: Noise Prediction Technology for CTOL Aircraft. NASA TM-78700, 1978.

9. DOT/FAA Airworthiness Standards: Transport Category Airplanes, FAR Part 25, June 1974.

10. Tomlinson, B. N.; and Wilcock, T.: A Piloted Simulation of the Takeoff of a Supersonic Transport Aircraft, With and Without a Takeoff Director. A.R.C.R. & M. 3594, 1969.

FOUR VSCE-516 ENGINES

4500 n. mi. RANGE

CRUISE AT M = 2.62

273 PASSENGERS

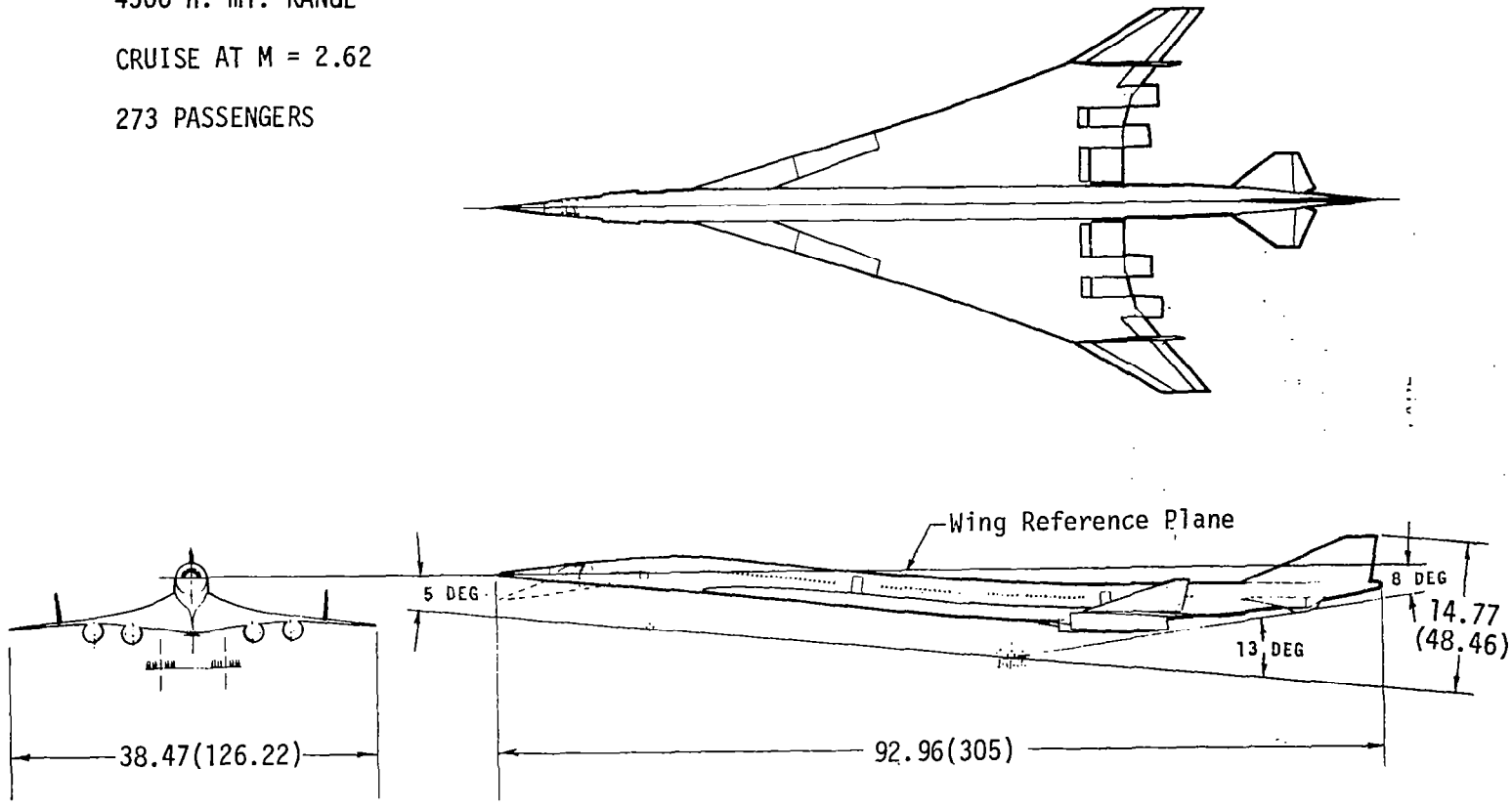

Figure 1.- Three-view sketch of simulated SCR concept (AST-105-1). All linear dimensions are in meters (feet).

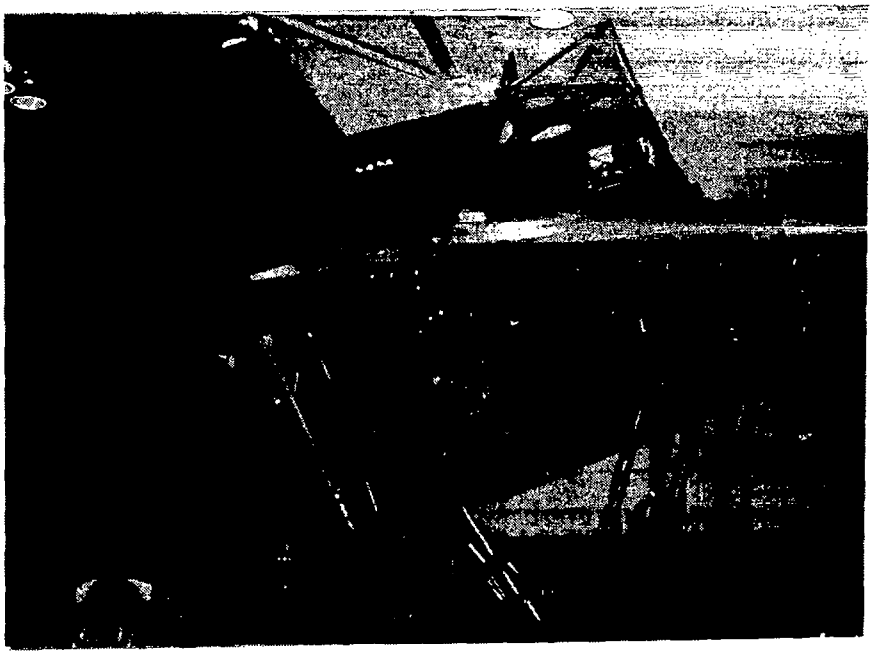

(a) Visual Motion Simulator (VMS).

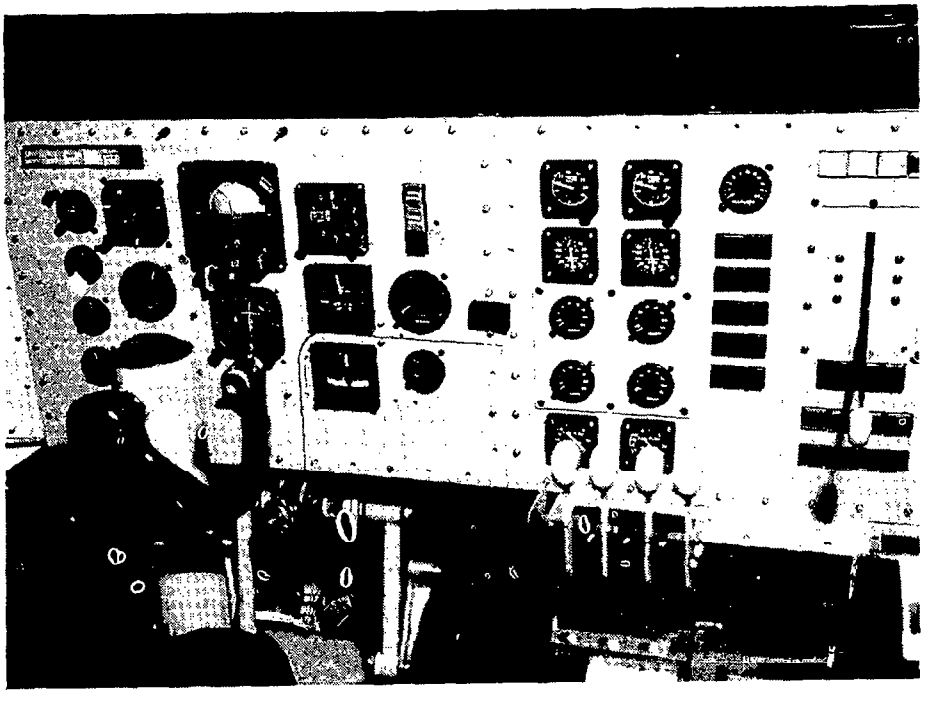

(b) Instrument panel.

Figure 2.- VMS and instrument display.

* SWITCHES ACTIVATED AT PREDETERMINED CAPTURE VELOCITY

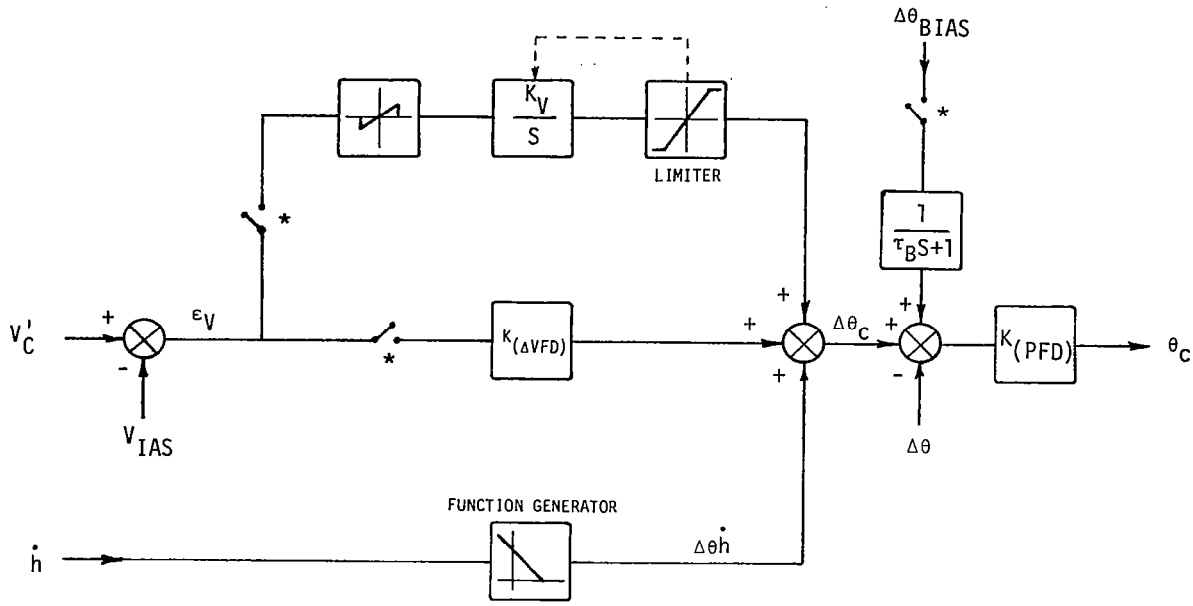

Figure 3.- Block diagram of takeoff director.

(a) Head-up display superimposed on airport scene.

Figure 4.- View of airport scene as seen by pilot.

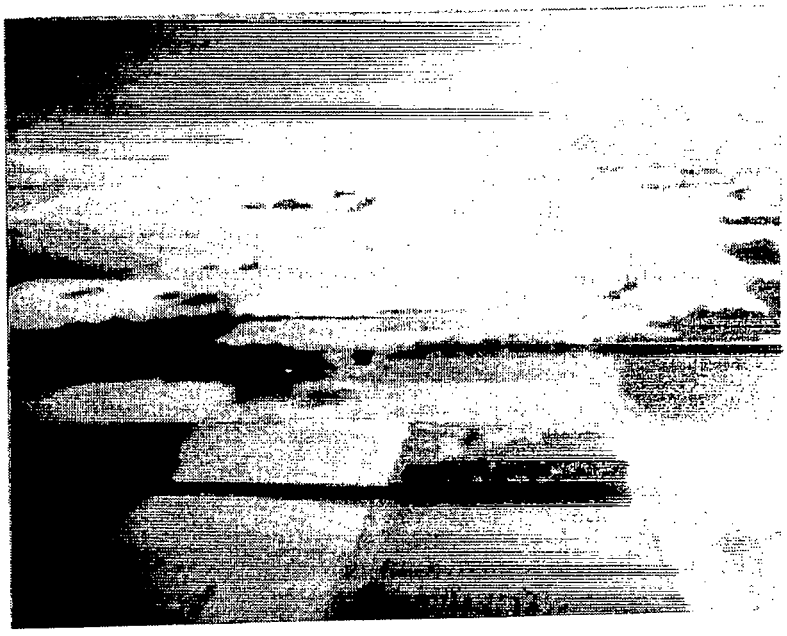

(b) Approach scene.

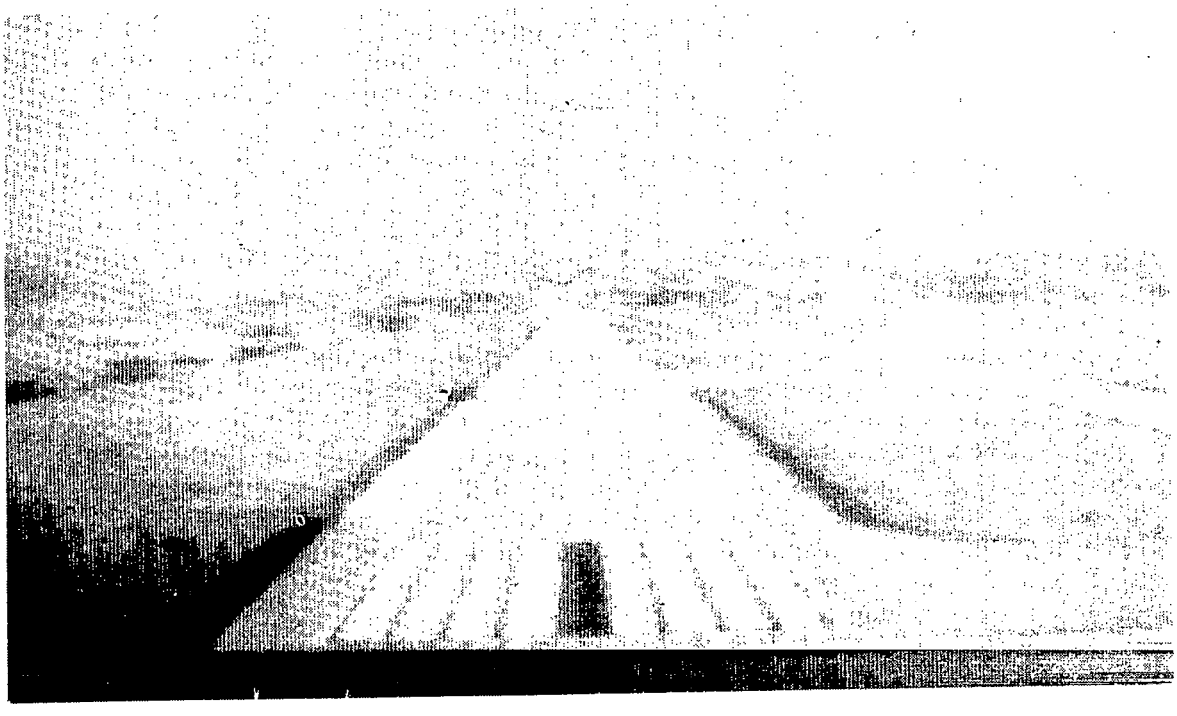

(c) Landing scene.

Figure 4.- Concluded.

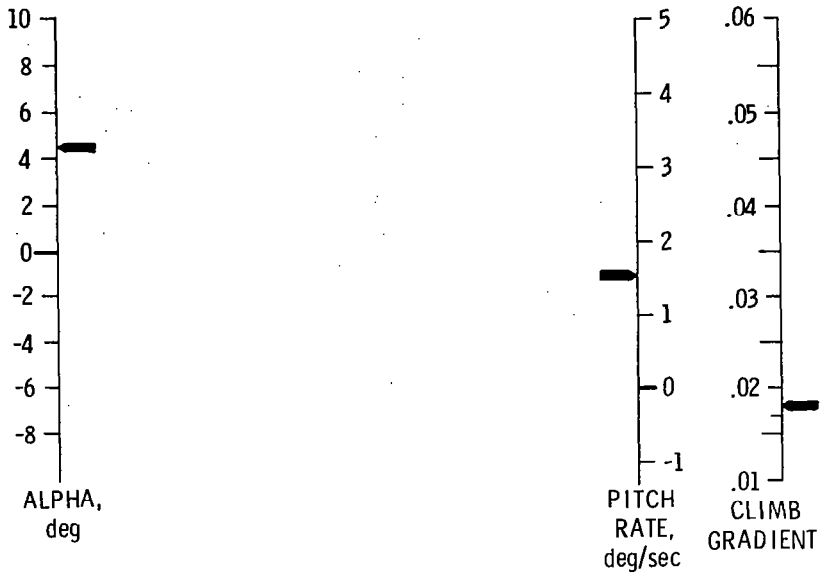

Figure 5.- Sketch of head-up display.

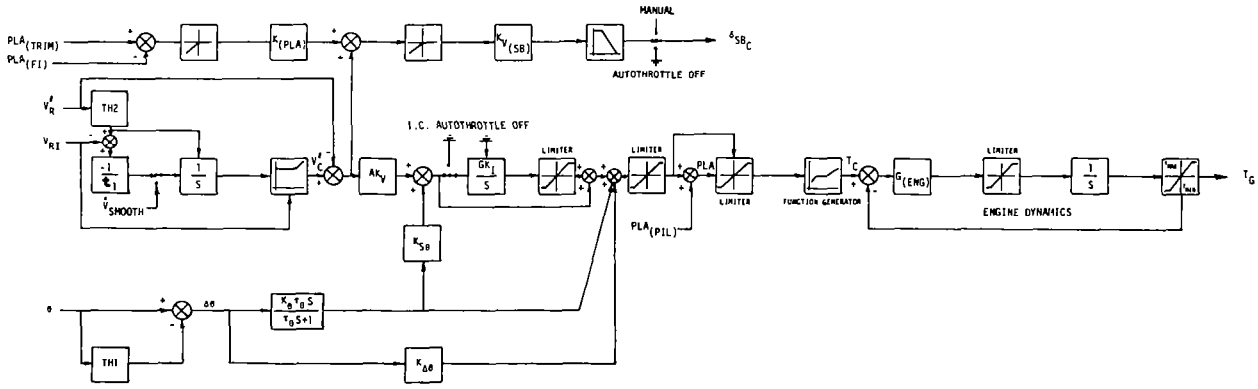

Figure 6.- Block diagram of autothrottle.

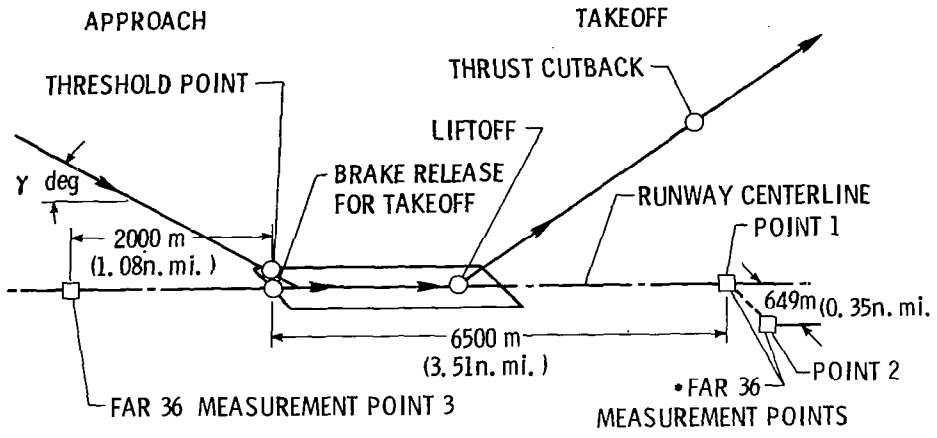

*NOTE: SIDELINE NOISE IS MEASURED WHERE NOISE LEVEL AFTER LIFTOFF IS GREATEST

Figure 7.- Noise measurement locations for takeoff and landing.

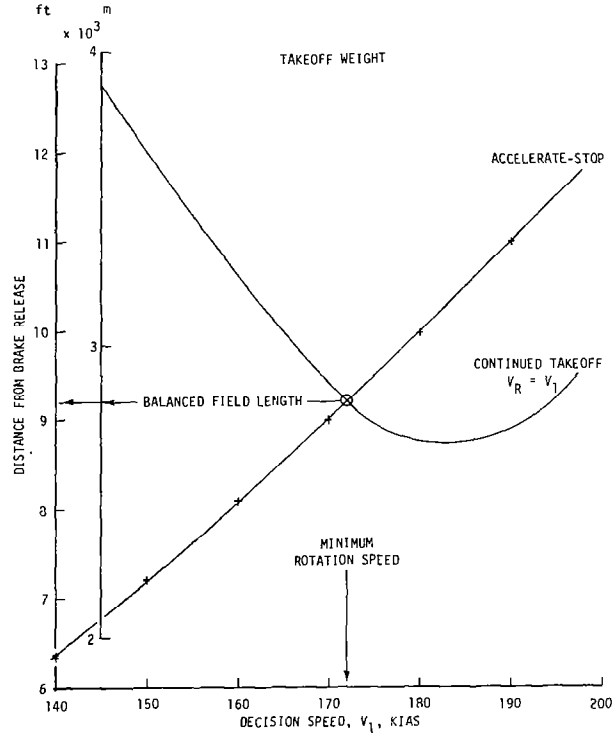

Figure 8.- Indication of three-engine balanced field length.

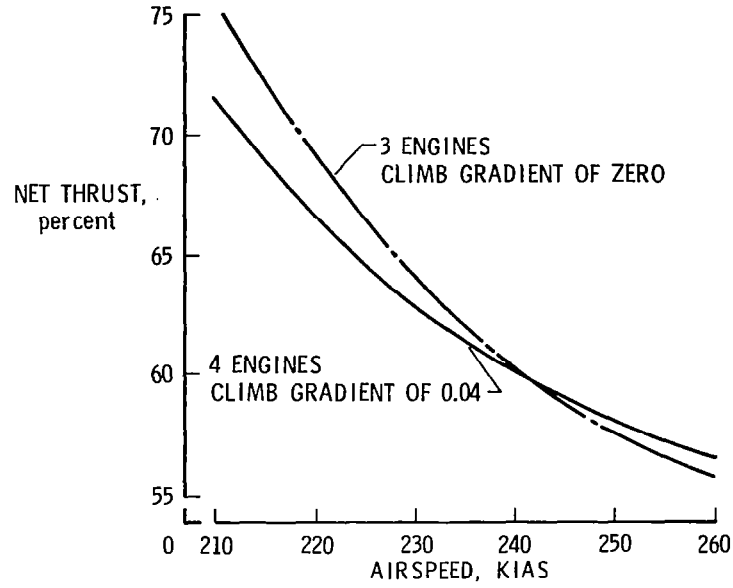

Figure 9.- Net thrust and airspeed used in establishment of allowable thrust cutback.

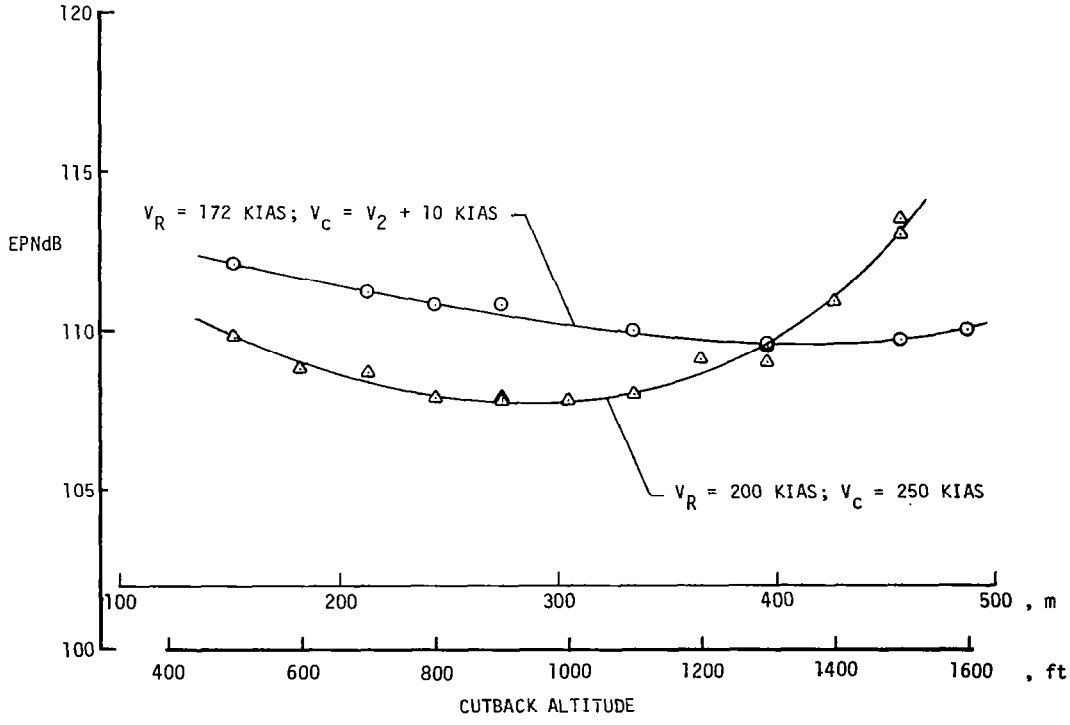

Figure 10.- Flyover effective perceived noise level as function of thrust cutback altitude for two takeoff conditions.

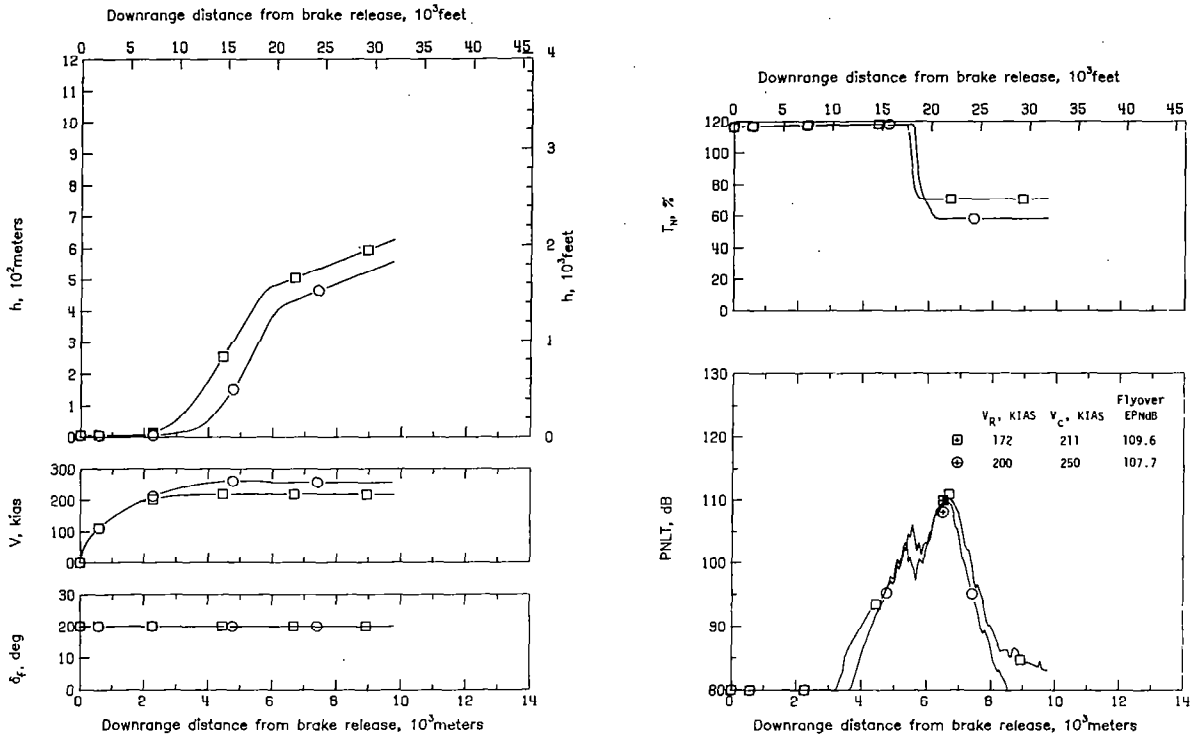

Figure 11.- Takeoff profiles and flyover noise generated for minimum and maximum simulated rotate and climb speeds.

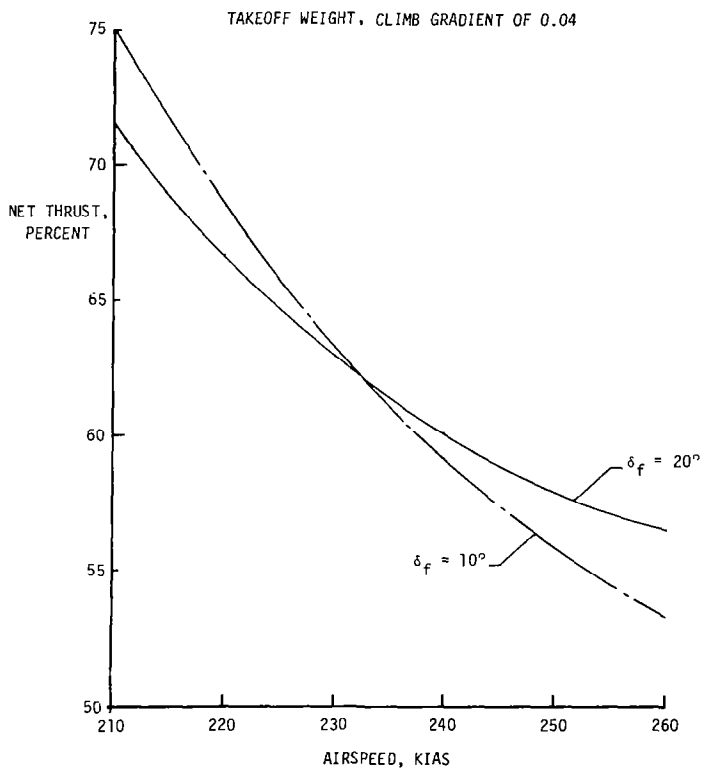

Figure 12.- Effect of airspeed on net thrust required for two trailing edge flap deflections.

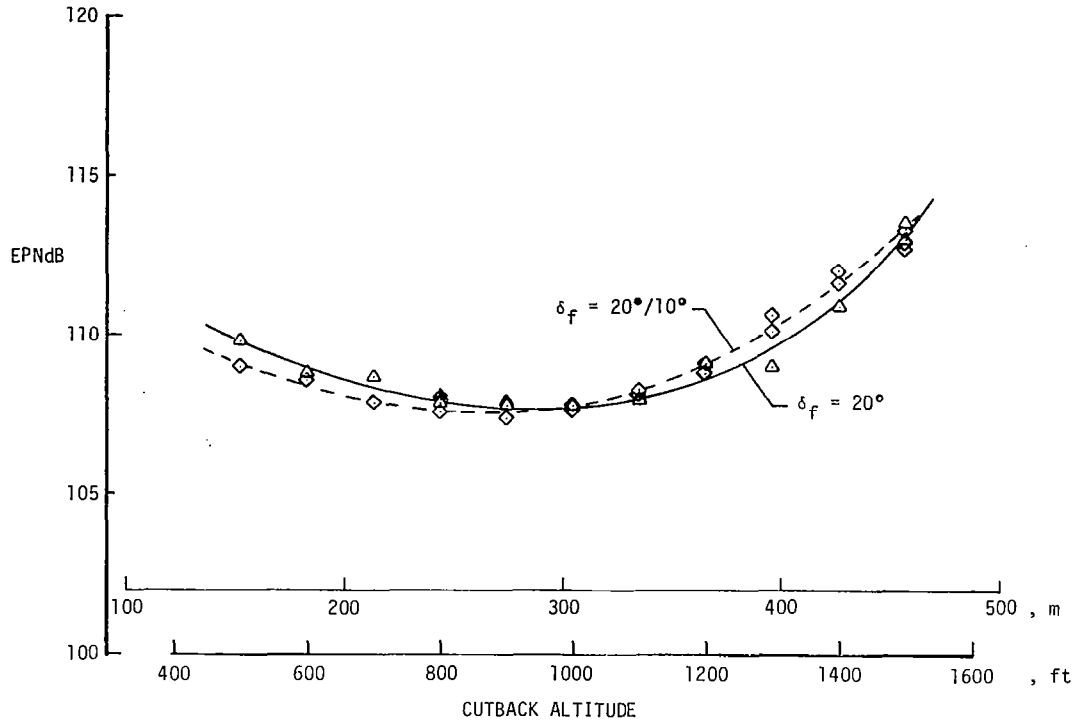

Figure 13.- Flyover effective perceived noise level as a function of cutback for two trailing edge flap schedules.

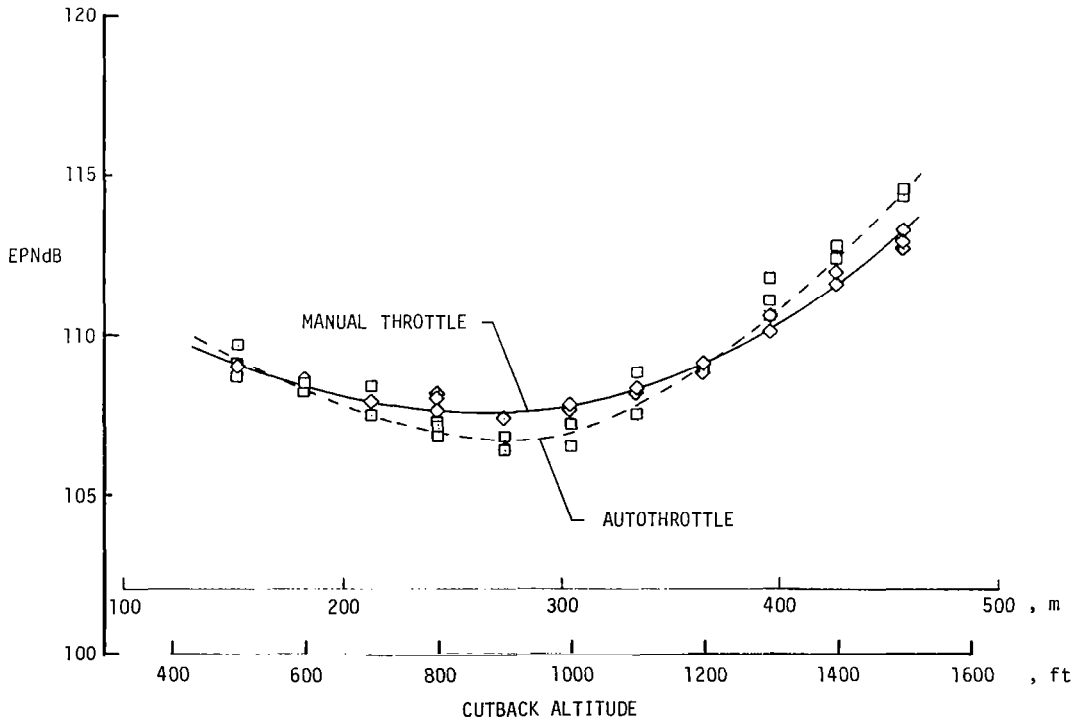

Figure 14.- Flyover effective perceived noise level as a function of cutback altitude for manual and automatic throttle operation.

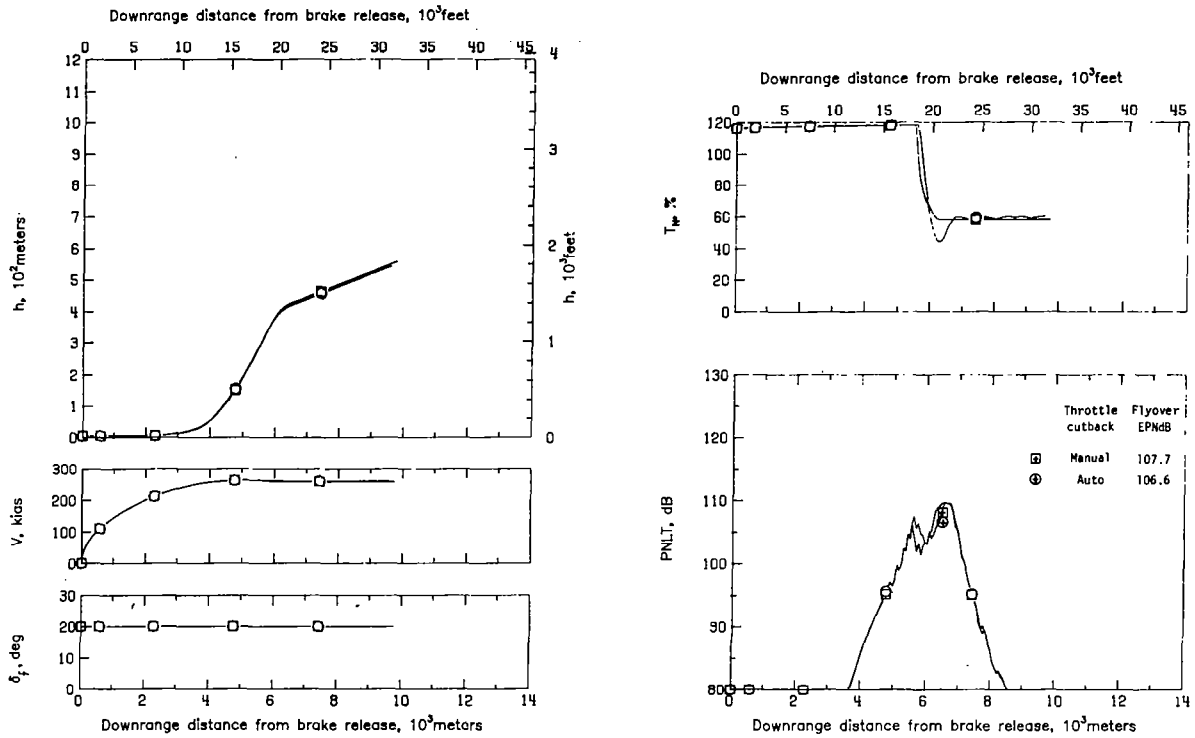

Figure 15.- Takeoff profiles and flyover noise for different cutback procedures.

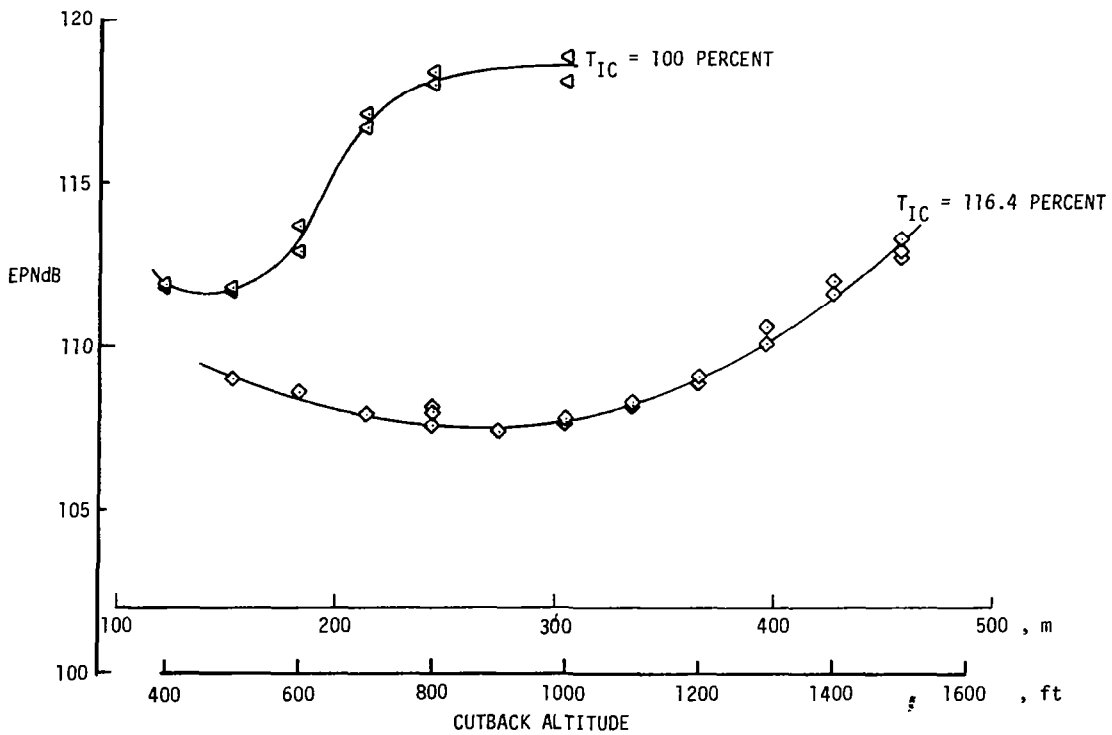

Figure 16.- Effect of cutback altitude on flyover effective perceived noise level for two initial thrust settings.

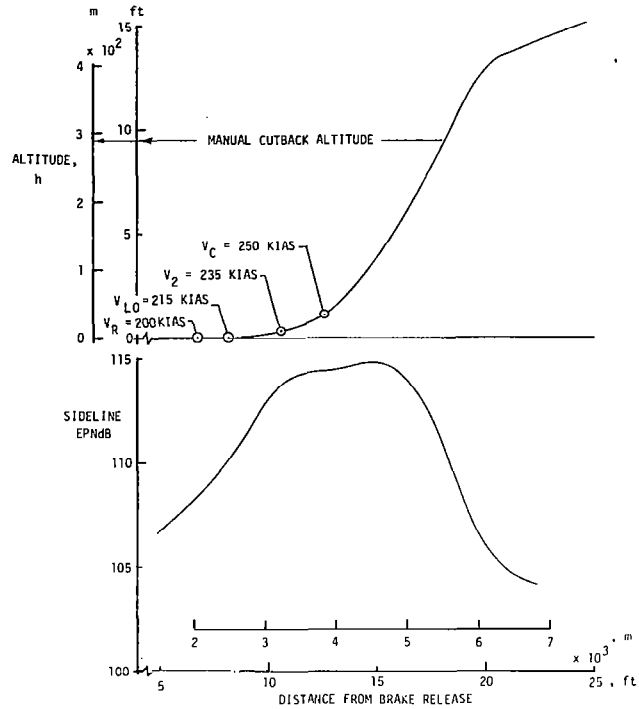

Figure 17.- Indication of altitude profile and sideline effective perceived noise level buildup during standard procedure takeoff (Flyover EPNL = 107.7 dB).

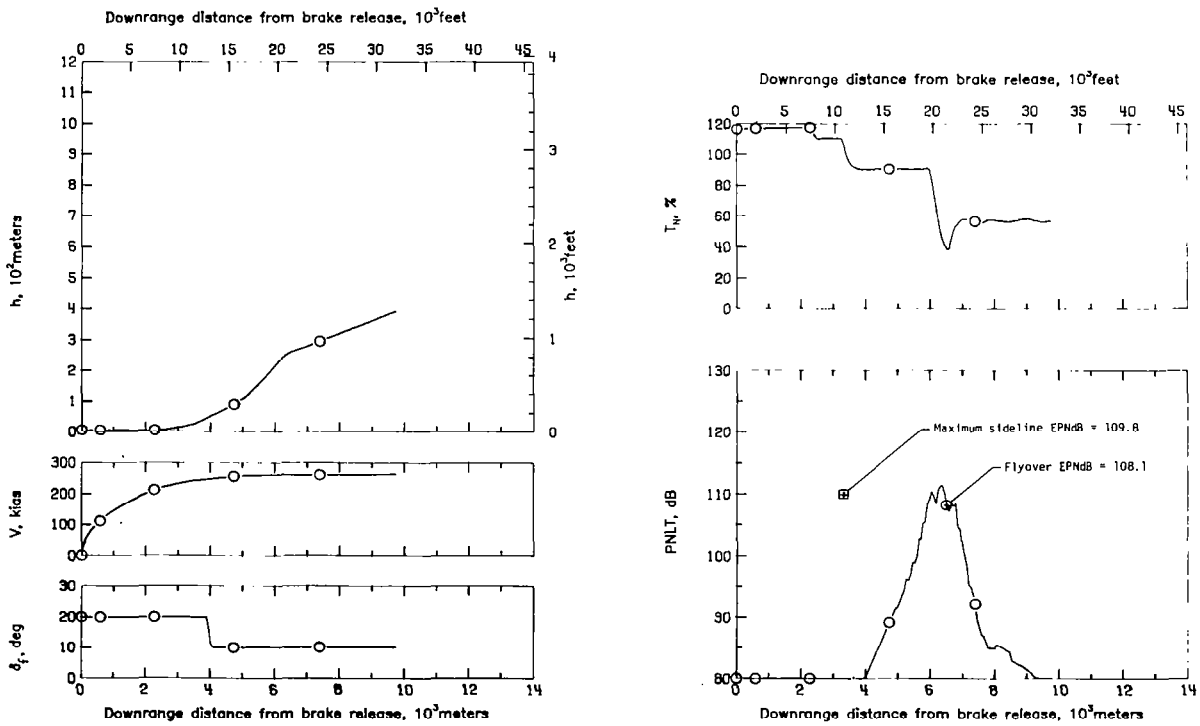

Figure 18.- Advanced procedure I takeoff and corresponding calculated sideline and flyover noise.

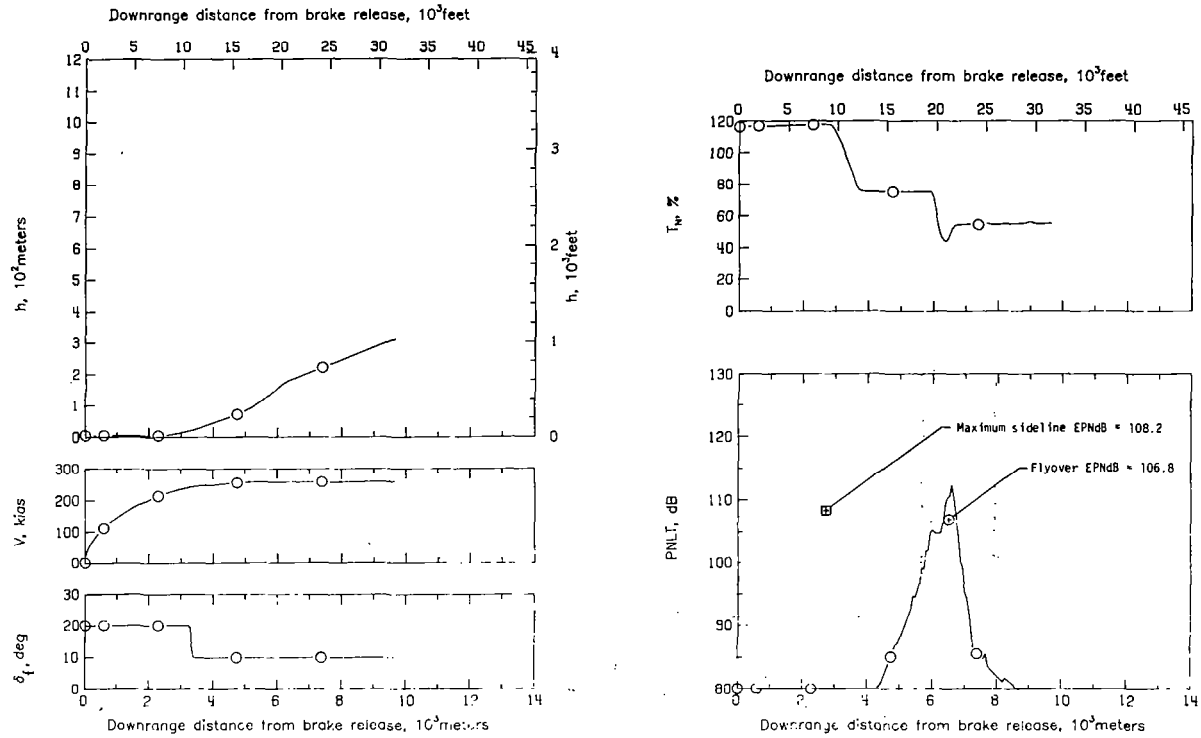

Figure 19.- Advanced procedure II takeoff and corresponding calculated sideline and flyover noise.

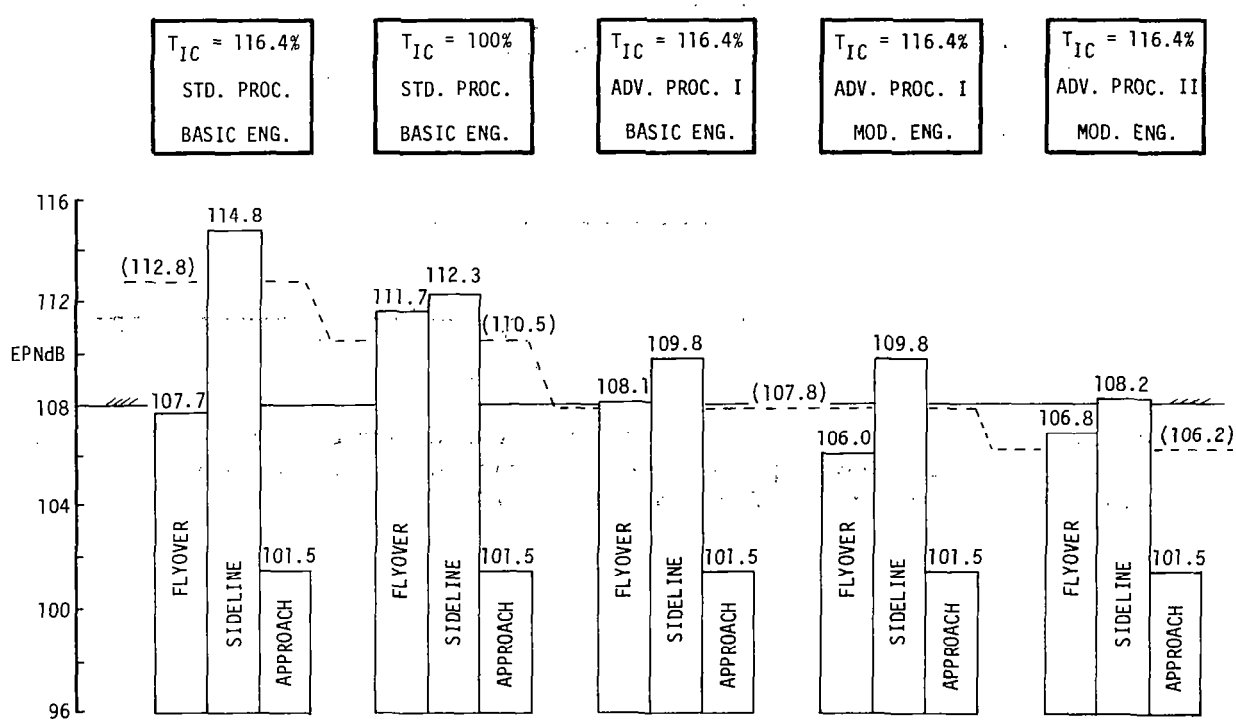

Figure 20.- Histogram of the traded noise levels calculated for the various conditions and test procedures flown. (Number in parentheses indicates traded noise levels.)

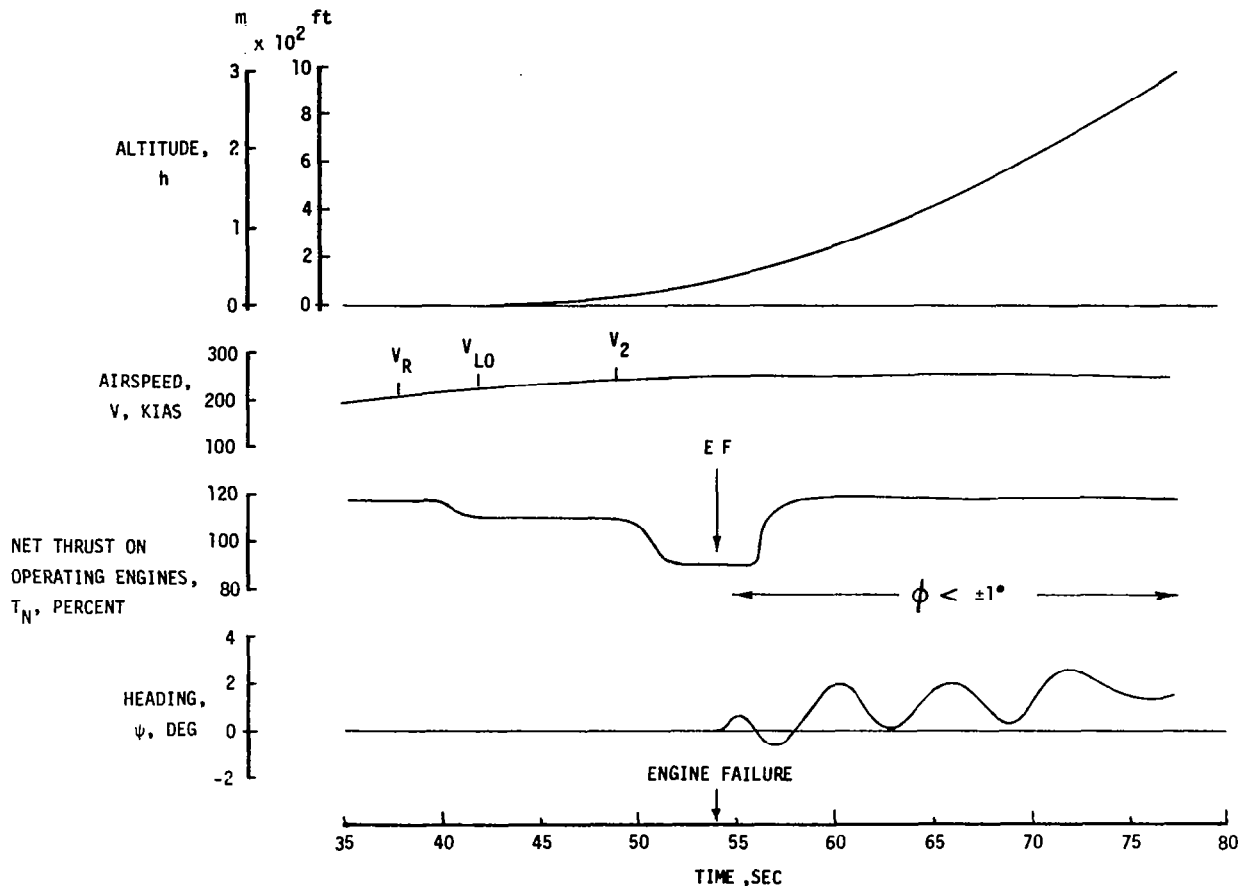

Figure 21.- Indication of bank angle and heading excursion following failure of number 4 engine while performing an advanced procedure takeoff. (Advanced procedure takeoff shown in fig. 18.)

SESSION III - PROPULSION

INTRODUCTORY REMARKS

Warner L. Stewart
NASA Lewis Research Center

Achievement of a viable, advanced supersonic transport will require solving many challenging technological problems in areas such as those shown in figure 1. Of these, propulsion - the subject of this session - is one of the most critical elements of this type aircraft. The fuel required to operate the engine is the heaviest single constituent of the airplane takeoff weight. In addition, the engine is the potential source of offensive pollution and noise.

The propulsion system design must thus respond to the often-conflicting requirements of good performance both subsonically and supersonically while satisfying the applicable environmental constraints. An extensive research program has been sponsored by NASA to advance the necessary propulsion technologies, as outlined in figure 2. A continuing series of propulsion system studies have been performed by the two principal engine company contractors, General Electric Co. and Pratt & Whitney Aircraft. In conjunction with overall airplane system studies by NASA-Langley and its contractors, candidate engine types have been analyzed in progressively more detail. The studies were supported by research in emissions and noise. Two promising variable-cycle concepts were identified by the studies, and large-scale experiments were initiated to explore their critical components. More recently, additional research has been started on the inlets and nozzles that are necessary for the complete propulsion system.

Figure 2 also serves as a roadmap for the organization of the session. Authors from each engine company will present a paper on the cycle studies, followed by a paper on the related engine testbed program. The fifth paper deals with the question of inlet design for these types of engine systems.

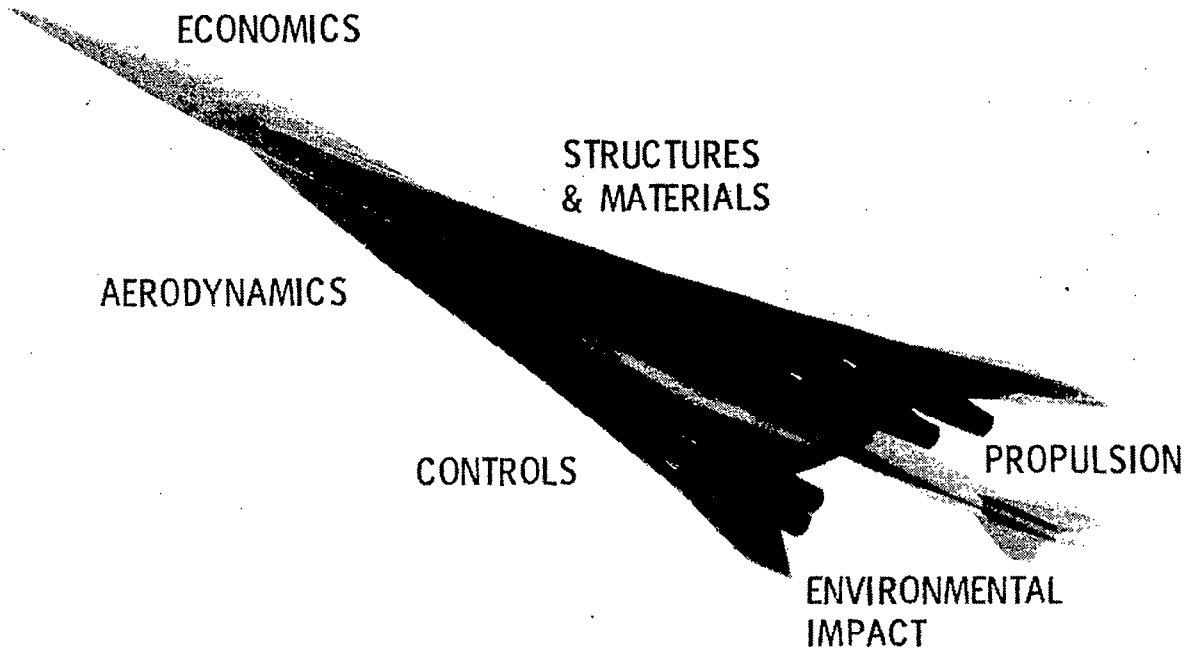

Figure 1.- Supersonic cruise research.

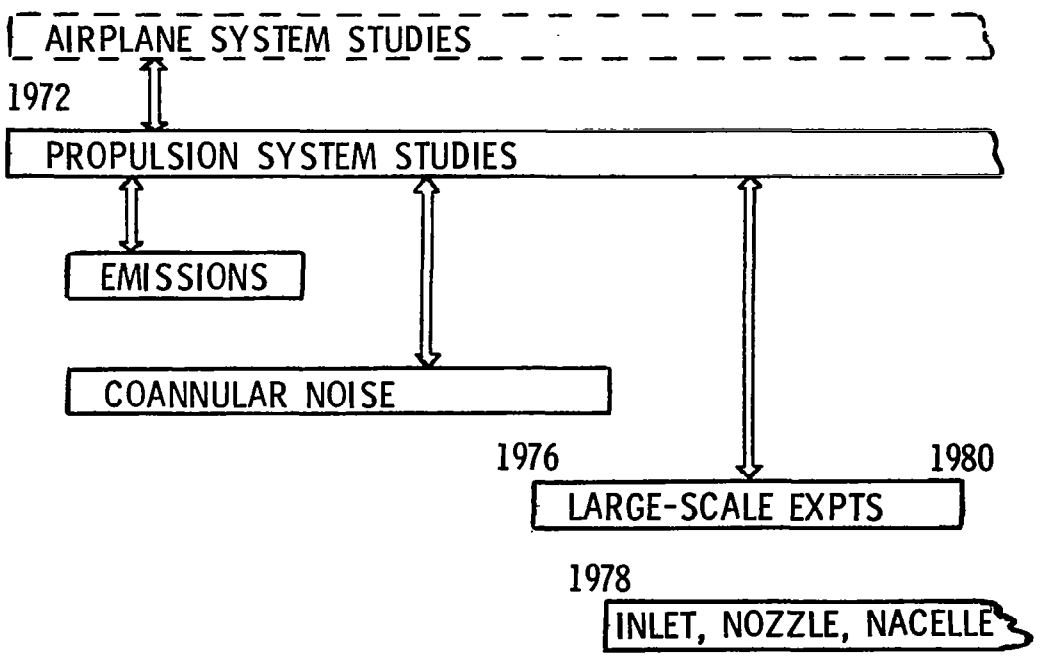

Figure 2.- Propulsion program.

SUPERSONIC CRUISE RESEARCH PROPULSION SYSTEM

STUDIES - SLIDE PRESENTATION

R. D. Allan and J. E. Johnson

General Electric

Variable Cycle Engines

Does the Flexibility of the VCE Pay Off?

For —

- **Performance**
- **Cost**
- **Reliability and Maintainability**
- **Low Noise**

Figure 1

NASA Lewis Sponsored Program

- Investigated Payoff of VCE Features
- Identified Potentials of
  - — Double Bypass VCE
  - — Single Bypass VCE
  - — Fixed Cycle Turbofan

Figure 2

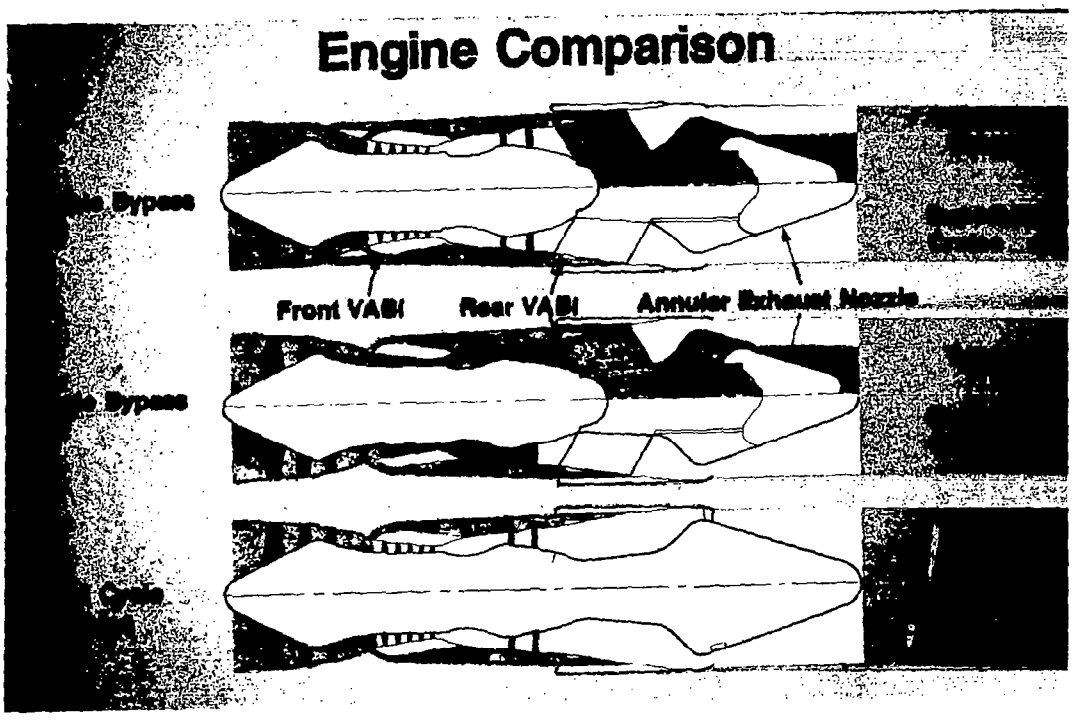

Figure 3

Mission Comparison

4000 N.M. Range with 600 N.M. Initial Subsonic Leg

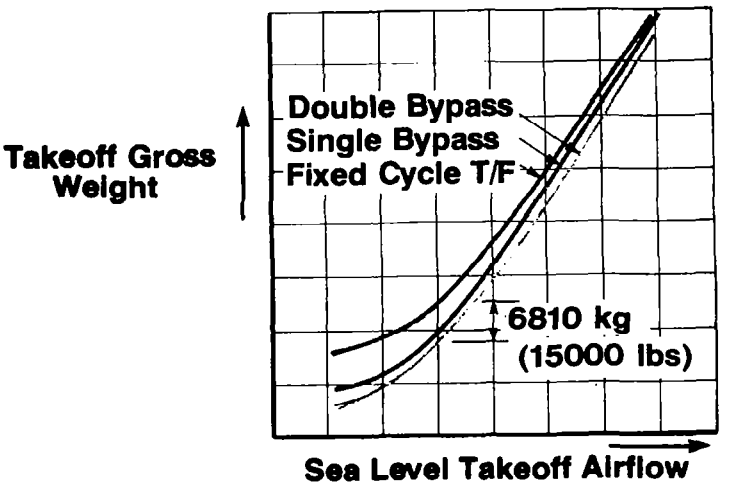

Figure 4

Summary of Reliability, Maintainability and Manufacturing Cost

	Ratios Shown as a Function of the Double Bypass VCE		
	Engine Removal Rate x 10^{-3}	$/Eng. Flt. Hr. (Excluding Fuel Costs)	Mfg. Cost @ 250th Eng.
Double Bypass VCE	1.0	1.0	1.0
Single Bypass VCE	.994	.99	0.974
Fixed Cycle Turbofan	.952	1.188	1.04

Figure 5

Reliability and Maintainability

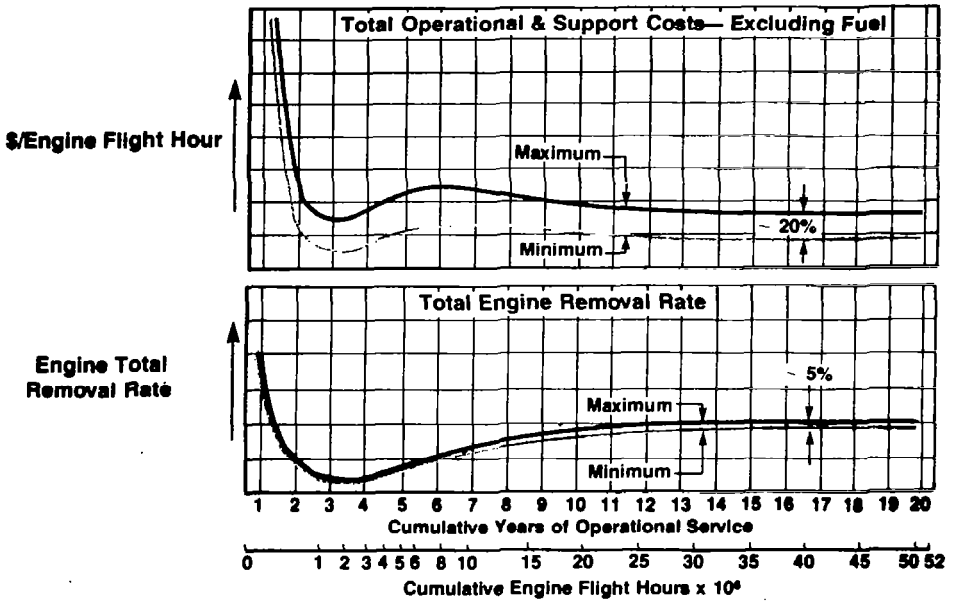

Figure 6

Noise Impact

Important Coannular Exhaust Stream Parameters

1. V_J Mass Average $\left(\frac{V_{J\,Hot} * W_{Hot} + V_{J\,Cold} * W_{Cold}}{W_{Hot} + W_{Cold}}\right)$
2. $V_{J\,Cold}/V_{J\,Hot}$ Ratio (Large Loss in Suppression for Levels > .6)
3. P_9/P_0 & P_{99}/P_0 (Shock Noise Problem)
4. A_{Cold}/A_{Hot} & W_{Cold}/W_{Hot}
5. Stream Densities

Figure 7

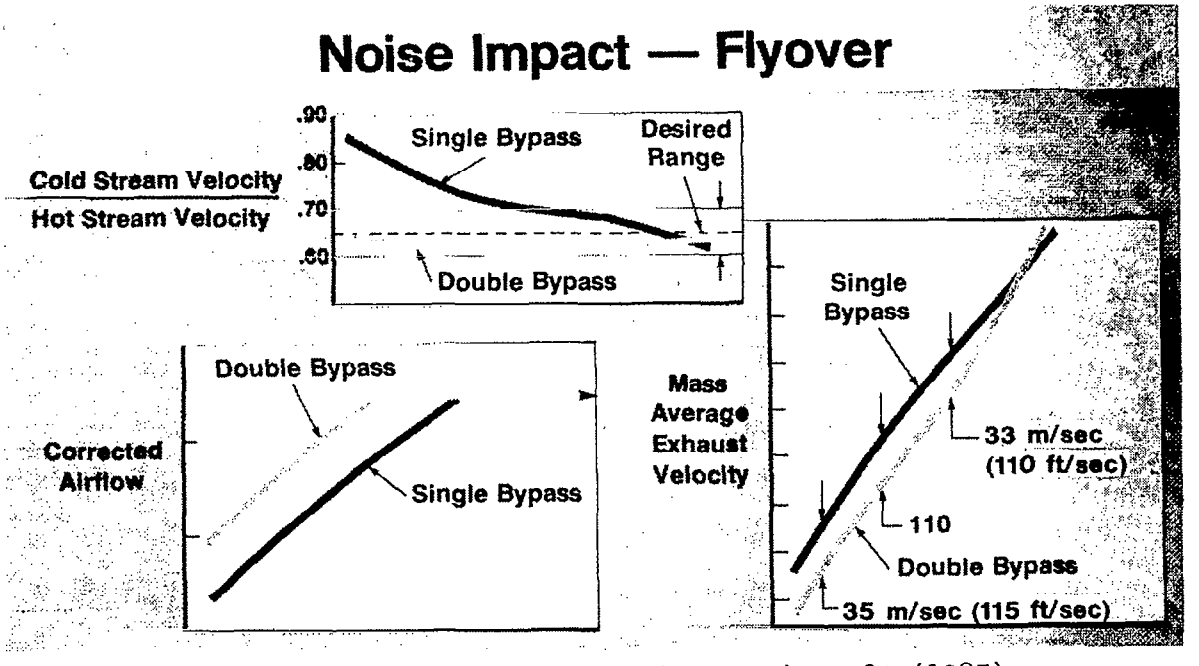

Net thrust at M = 0.327/366 m (1200 ft)/+10°C (18°F)

Figure 8

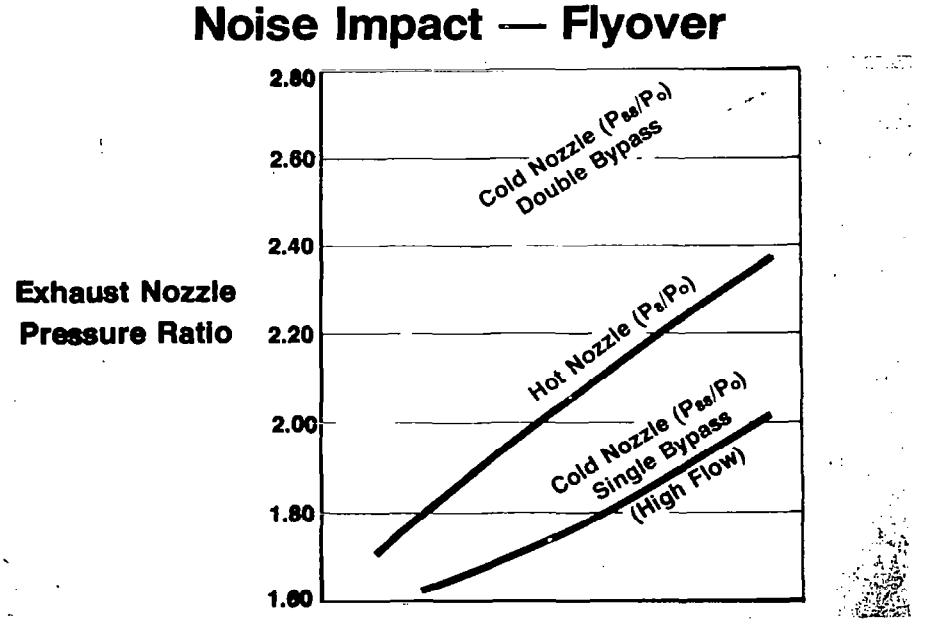

Net thrust at M = 0.327/366 m (1200 ft)/+10°C (18°F)

Figure 9

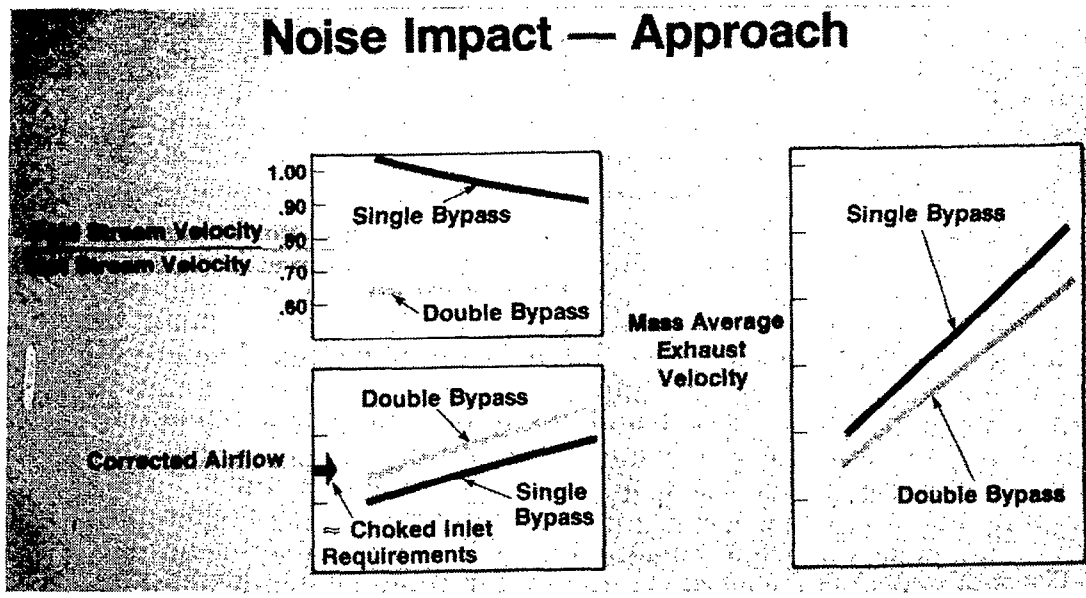

Net thrust at M = 0.253/113 m (360 ft)/+10°C (18°F)

Figure 10

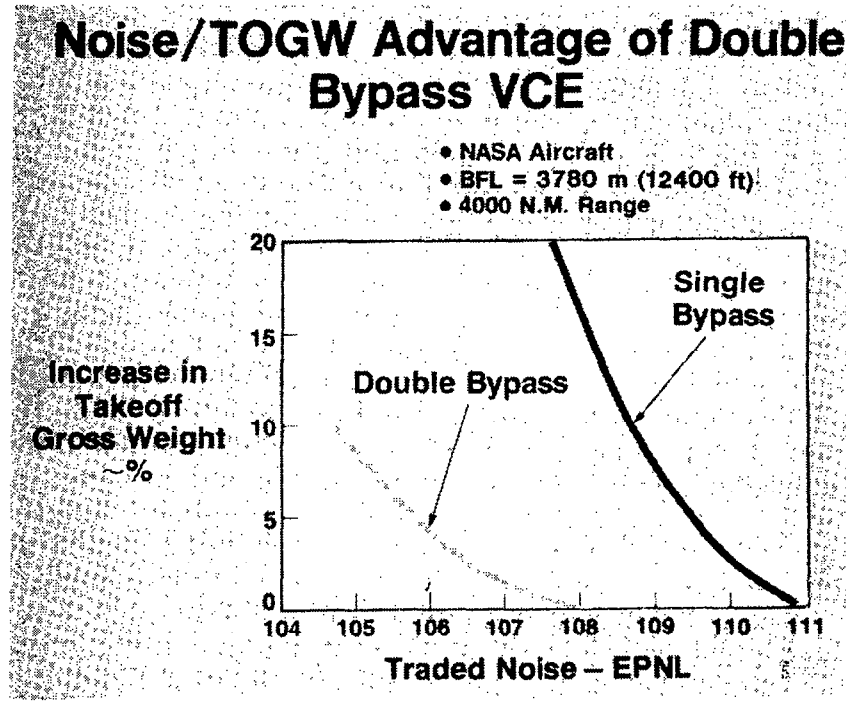

Figure 11

Summary

- The Additional Flexibility of the Single and Double Bypass Features Shows a Minor Degradation in Engine Removal Rate, But Improves
  - — Engine Operational Cost
  - — Manufacturing Cost

  Caused by Simple Exhaust Nozzle

- When Fuel Costs Are Added Additional Payoffs for Single and Double Bypass Occur.

- The Double Bypass Feature Has the Biggest Impact on Reducing Noise at Minimum Overall Cost. It Also Can Match Almost Any Acoustic Requirement.

- Testing of Double Bypass VCE Should Continue. Explore Possibility of Simplification.

Figure 12

VCE TEST BED ENGINE FOR SUPERSONIC CRUISE RESEARCH

J. W. Vdoviak and J. A. Ebacher
General Electric Company

General Electric initiated a broad investigative variable cycle demonstrator engine test program in 1976, utilizing the YJ101 engine as the basic vehicle. This program is aimed at evaluating variable cycle concepts applicable to a supersonic, mixed mission propulsion system which would combine the merits of a turbofan at subsonic operating conditions with those of a turbojet for supersonic operating conditions. Over the last four year period five sequential VCE demonstrator tests have been accomplished under combined U.S. Air Force, U.S. Navy, and NASA auspices in a uniquely cooperative and complementary test program. This test program is illustrated in the attached Figure 1. By way of background, the first USAF Single Bypass Test investigated the effects of a variable rear mixer. This was followed by the first split fan/double bypass VCE test which was the USAF 1 X 2. (1 X 2 refers to the number of fan stages in the forward and rear fan blocks respectively, i.e., 1 stage front fan block and 2 stage rear fan block.) A Navy sponsored 2 X 1 double bypass VCE demonstrator test was evaluated next. This combined double bypass with a variable area low pressure turbine nozzle (VATN), a product type rear VABI (Variable Area Bypass Injector) or mixer and an augmentor. All of these test vehicles employed separate bypass ducting for the front and rear fan block flow and considerable exhaust system complexity. The NASA Forward VABI VCE test combined the features of a split fan, variable area LP turbine nozzle, and rear variable area mixer with a concept to substantially simplify the bypass ducting and exhaust system of a double bypass VCE engine. This is referred to as a Front Variable Area Bypass Injector or Front VABI. The Front VABI allows both single and double bypass operation with a common bypass duct and single exit exhaust nozzle. Upon successful demonstration of this concept, a unique co-annular exhaust nozzle was tested with the same basic gas generator in a combined performance and acoustic test at an external test facility. The results of this co-annular nozzle acoustic testing is the subject of another presentation later in this conference. The NASA Acoustic Test VCE engine configuration incorporating all of these features, which was tested successfully in late '78, is illustrated in Figure 2. The top view shows a typical low noise take-off operating mode (double bypass), and the bottom view shows the high specific thrust (single bypass) operating mode. In excess of 300 test hours have been accumulated in this step-wise VCE Test Program to date. The basic YJ101 has proven to be a highly versatile and dependable test vehicle, adaptable to a broad range of test requirements.

Figure 3 summarizes the technical payoffs or advantages that have been demonstrated with the various variable cycle features. Double bypass allows bypass ratio increase for specific fuel consumption (SFC) improvement at part power subsonic cruise operating conditions. Beyond the SFC gain, there is the prospect of providing air flow modulation at constant thrust to potentially simplify and/or improve the performance of inlet and afterbody configurations. For a future supersonic transport application double bypass provides for low noise at take-off by virtue of lower specific thrust/lower exhaust velocity. The Rear VABI (variable mixer) allows fan operating line control for thrust

and SFC gain and bypass flow extension. The Rear VABI concept appears applicable to Military requirements such as Advanced F404 and F101 DFE, and is being further pursued under new, recently initiated USN and USAF auspices. The Variable Area Low Pressure Turbine Nozzle (VATN) provides for rotor speed ratio and core stall margin control. It can also provide reducd compressor exit temperature at constant T_4 - important to low level - high density - high flight speed requirements. As previously described, the benefits of the forward or Front VABI are mainly for engine simplification with single and double bypass capability with respect to the bypass ducting and the exhaust nozzle. The acoustic nozzle is a unique subcomponent applicable to low noise requirements. Early next year the same basic engine used in the recent NASA VCE tests will be tested with a Full Authority Digital Electronic Control (FADEC) under U.S. Navy auspices as part of the continued VCE test sequence. Such a control allows full utilization of variable cycle flexibility and operating benefits.

This summary provides a backdrop for the next NASA program referred to as the Test Bed Engine Program. A description of this program is the principal purpose for this presentation. The concept of the Core Driven (aft fan block) Fan Stage is a logical benefit for variable cycle propulsion engines, in fact, it has broad applicability to any low pressure ratio, mixed mission requirement including single bypass (only) engine arrangements. The Core Drive Concept is illustrated in Figure 4. In the simplest terms this puts the second block fan stage of a split fan, double bypass VCE engine on the high pressure core spool. The high pressure compressor is mechanically attached to the aft fan block through a rotor coupling. The prior VCE demonstrators described earlier evaluated several variations of split fans, but all were driven by the low pressure/LP turbine shaft. The core drive arrangement is integrated with a forward VABI to allow high flow/double bypass operation or high specific thrust/single bypass operation. This is accomplished by geometric variation of the Forward VABI valving in conjunction with the Variable Inlet Guide Vane of the core driven fan stage. The variable inlet guide vane modulates the second block fan air flow over a relatively broad range and is nominally open in the single (low bypass) flow condition and substantially closed for the double (high bypass) flow condition. Under double bypass operating conditions, a relatively small portion of the total (increased) bypass flow is handled by the inner rear bypass duct and most of the flow is discharged forward of the core driven fan stage into the outer bypass duct. In the single bypass operating mode the aft fan block flow is matched to the front block by rotor speed ratio and to the high pressure compressor by the inner bypass duct and high pressure inlet guide vane scheduling, respectively.

The unique technical benefits or payoffs of the core driven concept are summarized in Figure 5. It allows a redistribution of compression system work so that an oversized front block fan can be driven with a single stage low pressure turbine. This has been adopted for future SCR/VCE configurations for reduced take-off noise, but it also provides further reductions in subsonic SFC. A 20% increase in front block fan flow is planned for future NASA VCE test engines and has also been incorporated into the SCR product engine studies. The corresponding increase in compression work with the rear block fan stage on the high pressure spool provides a higher energy extraction in the high pressure turbine. This has two benefits: It reduces the high pressure turbine bucket

metal temperature, hence reduces chargeable cooling air requirements and it also reduces the inlet temperature to the low pressure turbine, thereby also reducing the LPT cooling requirements as well. In essence, this turbine work re-arrangement allows a better utilization of increased turbine temperature technology with reduced associated cooling penalties.

Additionally, the core driven principle allows split fan flow modulation using rotor speed variation in addition to variable stator manipulation. Higher rear block compression efficiencies are projected by using the speed ratio flexibility.

Typical part power (subsonic) SFC expected improvements are shown in Figure 6. This graph displays SFC as a function of air flow. Both benefits of double bypass operation are depicted, SFC reduction and air flow extension. With reference to the single bypass SFC characteristic, an improvement in air flow of 25% at the same SFC, or a reduction in SFC of 5.3% at a flow increase of 9.6% is expected. The core drive SFC characteristic is better than the LP turbine driven fan characteristic by virtue of the improved aft fan block aerodynamic performance and turbine loading characteristics.

The core driven fan aerodynamic characteristics are relatively conservative and are defined in Figure 7. The selected design has a stage pressure ratio of 1.37 at a tip speed of 381 m/s (1251 fps) at relatively modest levels of flow per unit of annulus area. The unique aspect of this compression stage lies in the broad swing in inlet guide vane variation for the rear block flow modulation which accompanies transition from single to double bypass operation. This is further illustrated in Figure 8 where several of the key and widely divergent operating modes are described. It is noted that the transition in operating mode essentially halves the inner bypass ratio. The inlet guide vane closure with double bypass operation brings about a very large swing in fan rotor outlet air angle; in excess of 40 degrees for that portion of the flow which exits through the inner bypass duct. The corresponding flow angle in the high pressure compressor inlet guide vane varies to a smaller degree because of the designed acceleration of the air flow in that path along with the high pressure matching. Furthermore, the high pressure compressor incorporates a variable inlet guide vane to handle the inlet swirl variation.

To accommodate this exit swirl problem, a unique configuration of blading has been devised. This is shown in Figure 9, which is a flow path illustration of the Core Driven Fan Stage.

The current two stage fan front block exit transitions through a structural frame into both the outer bypass and core driven stage inlet. A selector valve, made up of individual flaps positioned between the struts, is actuated closed as shown for single bypass operation and is opened for double bypass operation. The core driven stage has a flap type IGV with a fixed forward portion and movable aft portion for broad variation capability. Downstream of the low aspect ratio rotor a part span delta vane is positioned to straighten the flow into the inner bypass duct. A delta shaped part span airfoil has been selected based on relatively broad aircraft wing experience which shows that delta wings have higher angle of attack capability than conventional wings. The fixed exit guide vanes in the inner bypass duct complete the flow straightening upstream of the

VABI modulating valve. It is planned to test the beneficial effects of the delta exit guide vane in the initial core test on a comparative basis - i.e., with the vanes installed and removed.

The planned NASA Test Bed Engine Program will be conducted in two steps. First, the core driven stage will be coupled with the core engine to evaluate the aerodynamic performance of this stage and the matching with the high pressure compressor. Performance mapping including individual variability of the two inlet guide vane systems as well as the high pressure compressor stators is available to optimize the performance and compressor variable stator schedules. This initial test setup is shown in Figure 10. The core test vehicle will be tested in the Lynn engine ram test facility which allows simulation of the front block fan exit pressure and temperature. The front VABI selector and modulating valves are integrated with the core testing to provide initial evaluation of those Test Bed features as well. For this testing the modulating valve serves as the fan stage throttle valve. This testing is planned to be accomplished in the first half of 1980. In this phase the additive effects of the delta exit guide vanes will be tested. The core test phase will result in the selected compressor geometry for complete engine testing.

The addition of the low pressure rotor system, including the front block fan, and low pressure turbine with VATN (Variable Area Turbine Nozzle) to the afore-defined core vehicle will provide the complete Test Bed Engine shown in Figure 11. The co-annular nozzle exhaust system planned for the Test Bed Engine is a modification of the design tested earlier, with the addition of a radial chute type of noise suppressor to further reduce the take-off noise levels. A more detailed description of the suppressor is available by reference to Figure 12, which is a perspective drawing of the radial chute suppressor integrated with the co-annular nozzle. The suppressor will be tested in a fixed geometry arrangement, however, the chutes would be retractable into the plug in a product implementation.

In summary, the NASA Test Bed Engine Program is a logical extension of the VCE technology previously demonstrated on the YJ101 test vehicle. Some attractive test options beyond the described and currently planned Test Bed Engine tests are available as potential additive test phases and may be implemented later.

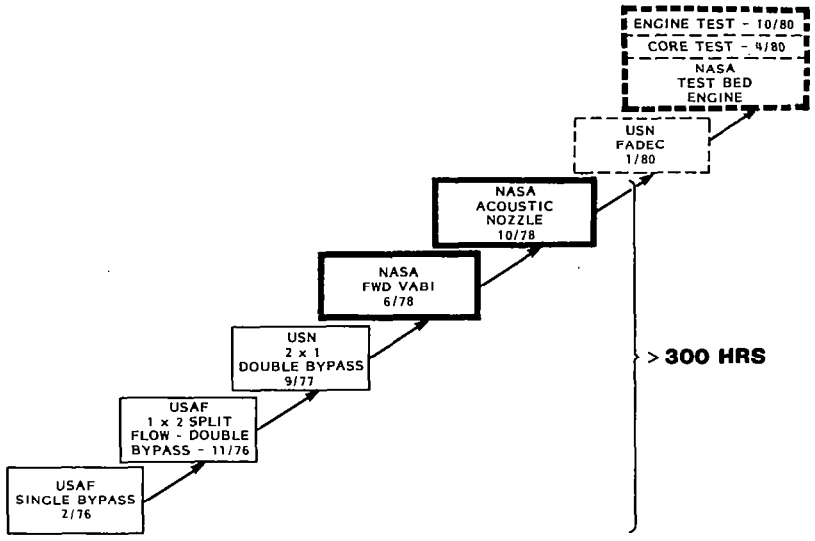

Figure 1.- YJ101 VCE concept demonstrators - test summary.

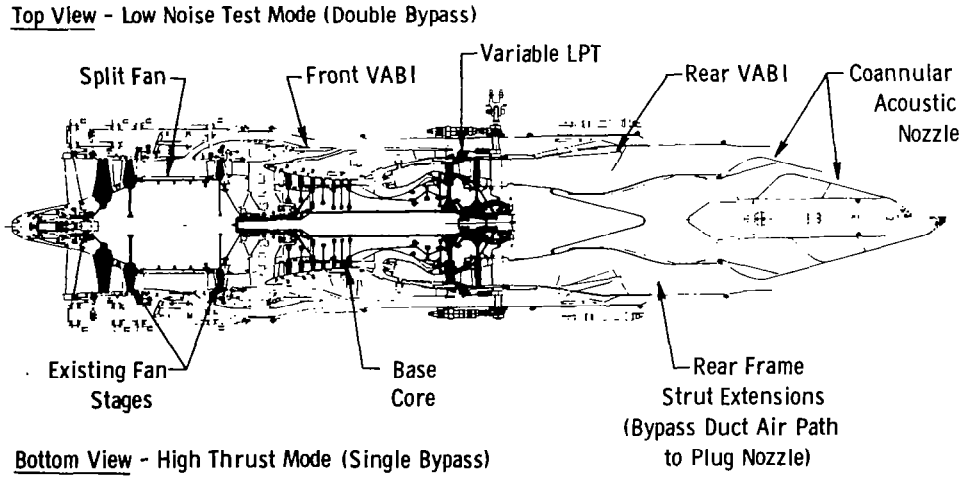

Figure 2.- NASA AST acoustic test VCE - initial double bypass VCE noise test configuration.

DOUBLE BYPASS	• PART POWER SFC GAIN (5%) • AIR FLOW EXTENSION AT CONSTANT F_N • LOW NOISE/AST
REAR VABI (VARIABLE MIXER)	• FAN OPERATING LINE CONTROL (THRUST AND SFC GAIN) • BYPASS FLOW EXTENSION
LPT VATN (VARIABLE AREA TURBINE NOZZLE)	• CONTROL OF ROTOR SPEED RATIOS • T_3 CONTROL AT CONSTANT T_4 • CORE STALL MARGIN
FORWARD VABI	• SINGLE EXIT EXHAUST NOZZLE FOR DOUBLE BYPASS • SIMPLIFIED BYPASS DUCTING
ACOUSTIC NOZZLE	• REDUCED SIDELINE NOISE ($\sim$5 PndB)

Figure 3.- Demonstrated VCE technical payoffs.

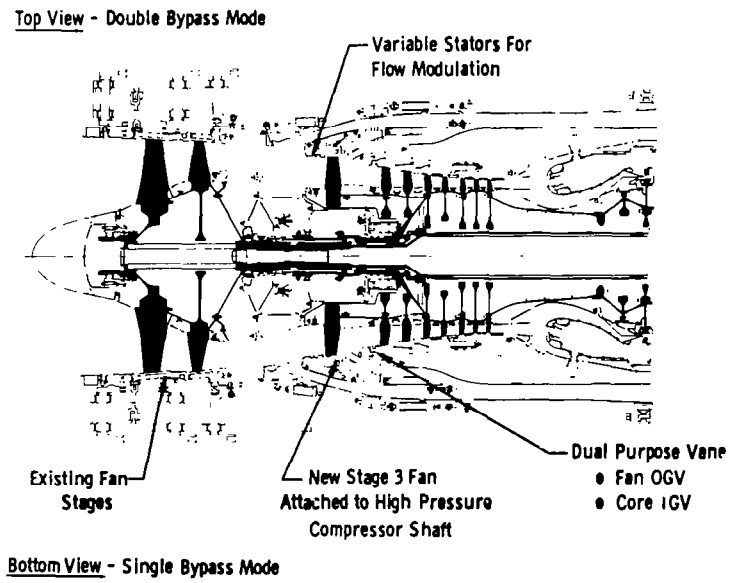

Figure 4.- NASA core driven fan stage.

- ALLOWS OVERSIZE FRONT BLOCK FAN WITH SINGLE STAGE LP TURBINE.
- HIGHER HPT ENERGY EXTRACTION.
  - LOWER BUCKET METAL TEMPERATURE WITH INCREASED T_4.
- LOWER LPT INLET TEMPERATURE.
  - REDUCED COOLING REQUIREMENTS.
- ROTOR SPEED FLEXIBILITY.
  - FLOW MODULATION

BROAD APPLICABILITY FOR MIXED MISSION/LOW CORE PRESSURE RATIO SYSTEMS.

Figure 5.- Core driven third stage technical payoffs.

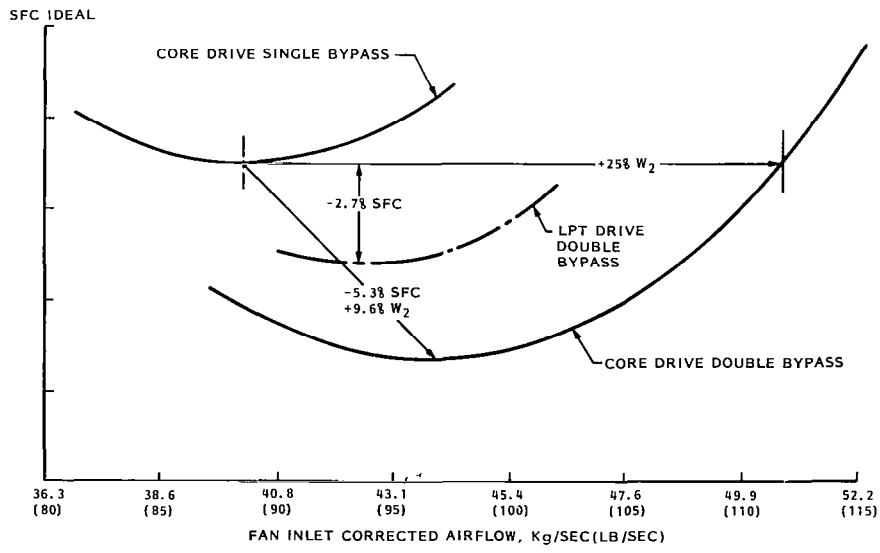

Figure 6.- Typical VCE SFC/airflow characteristics (Part Power ∿50% F_N).

STAGE PRESSURE RATIO -	1.37
CORRECTED TIP SPEED M/SEC (FT/SEC) -	381 (1251)
INLET RADIUS RATIO -	.69
CORRECTED FLOW/ANNULUS AREA -	36
ROTOR ASPECT RATIO -	1.4
IGV VARIATION -	SINGLE BYPASS - NOM./OPEN DOUBLE BYPASS - 40° CLOSED

Figure 7.- Core driven fan stage - aerodynamic description.

SIMULATED FLIGHT CONDITION	HIGH SPECIFIC THRUST	TAKEOFF/ LOW NOISE	SS CRUISE
OPERATING MODE (BYPASS)	SINGLE	DOUBLE	SINGLE
CDFS % $N/\sqrt{\Theta}$	100	96.8	94.3
INNER BYPASS RATIO	.45	.23	.66
FLOW ANGLE INTO BYPASS OGV	37	69	27
		(Δ42°)	
FLOW ANGLE INTO CORE IGV	41	50	46

Figure 8.- Core driven fan stage - operating conditions.

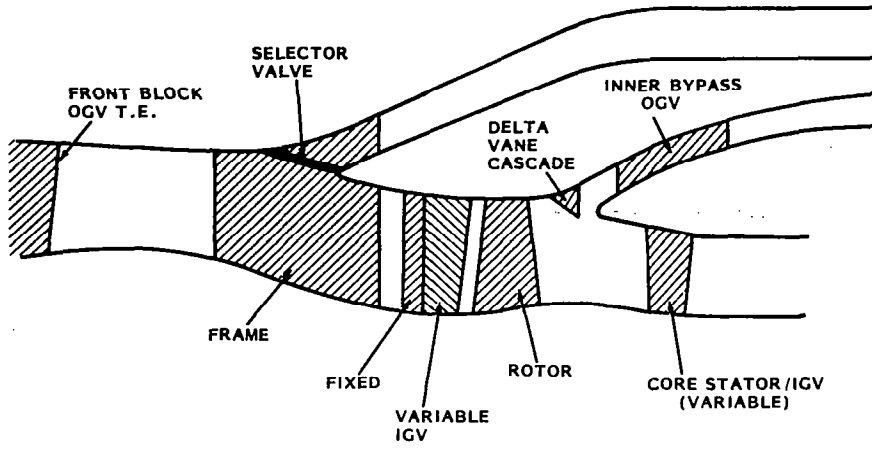

Figure 9.- Core driven fan stage flowpath - test bed engine.

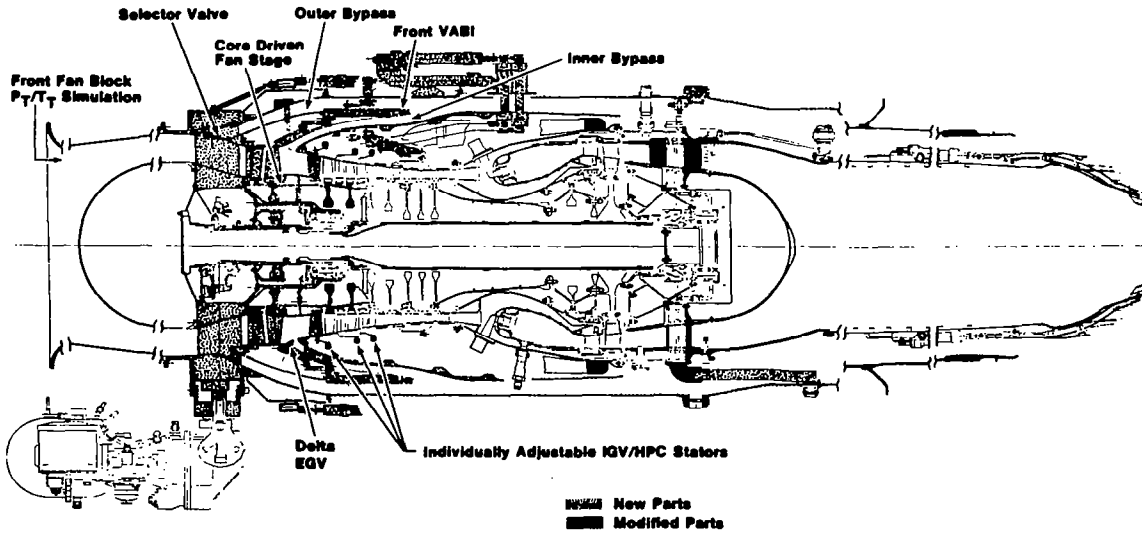

Figure 10.- Core test configuration - VCE test bed engine.

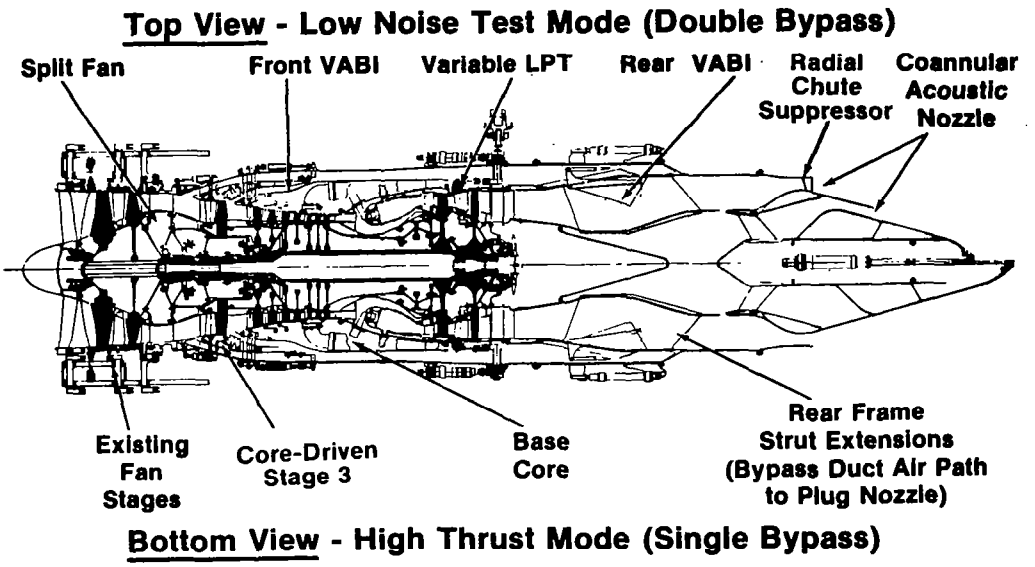

Figure 11.- NASA AST test bed VCE - core-driven 3rd stage configuration.

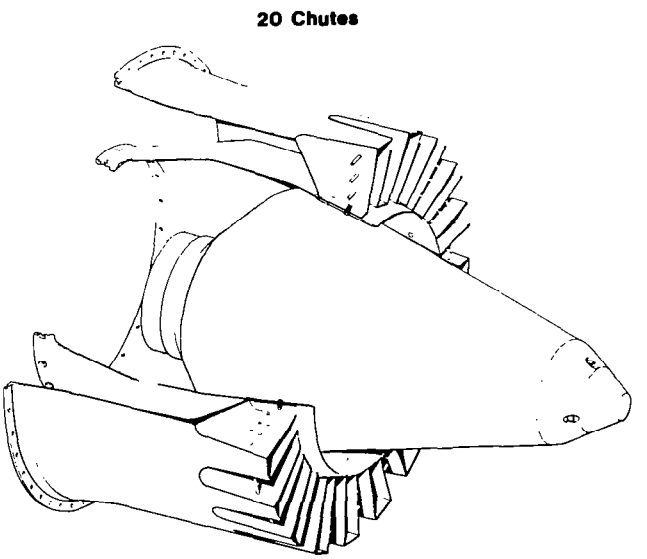

Figure 12.- Coannular nozzle suppressor - test bed engine.

VARIABLE STREAM CONTROL ENGINE FOR ADVANCED SUPERSONIC AIRCRAFT DESIGN UPDATE*

Richard B. Hunt and Robert A. Howlett
United Technologies Corporation, Pratt & Whitney Aircraft Group,
Commercial Products Division

SUMMARY

The Pratt & Whitney Aircraft study engine concept for a second-generation supersonic transport, the Variable Stream Control Engine (VSCE), has been updated in terms of mechanical design definition and estimated performance. The design definition reflects technology advancements projected for the late 1980 time period that improve system efficiency, durability and environmental performance. On the basis of the design update, technology requirements were established. The components unique to the VSCE concept, a high performance duct burner and a low noise coannular nozzle, and the high temperature components are identified as critical technologies. Technology advances for the high temperature components (main combustor and turbines) are not exclusive to the VSCE, but are equally applicable to any advanced supersonic propulsion system whether a low bypass engine, inverted flow engine or other variable cycle engine configuration. To address the requirements in this area, the technical approach for undertaking a High Temperature Validation Program has been defined. The multi-phased effort would include assorted rig and laboratory tests, then culminate with the demonstration of a flight-type main combustor and single-stage high-pressure turbine at operating conditions envisioned for a VSCE.

INTRODUCTION

For the past seven years, Pratt & Whitney Aircraft has been conducting analytical and experimental technology programs under NASA sponsorship in the area of advanced supersonic technology. A result of earlier parametric cycle studies (refs. 1-4) was identification of the Variable Stream Control Engine (VSCE) concept as having the greatest potential to meet performance, environmental and economic requirements for a second-generation supersonic cruise vehicle. The Variable Stream Control Engine is based on two unique components -- a high performance duct burner for thrust augmentation and a low noise coannular nozzle.

As this engine concept has evolved (refs. 5-7), substantial progress has been made in refining the basic mechanical configuration as well as system aerothermodynamic and environmental performance. The VSCE design history is illustrated in Figure 1 showing progress made since its inception to the most recent study configuration, the VSCE-515.

* Work performed under NASA Contract NAS3-21389

The VSCE-515 reflects the latest technology projections in the areas of advanced aerodynamics, materials and structure-mechanics. As defined, the technology in the VSCE-515 could be attainable to be commensurate with an engine development program in the late 1980 time period. This could lead to engine certification in the mid 1990's.

This paper describes the VSCE-515 and also outlines plans for a future technology program, the High Temperature Validation Program, which is a major step in realization of a mid 1990 certification date.

VARIABLE STREAM CONTROL ENGINE - AN OVERVIEW

The Variable Stream Control Engine is an advanced, moderate bypass ratio turbofan configuration that uses duct burner thrust augmentation, along with a coannular nozzle for jet noise reduction. A distinctive operating feature is the independent control of both core and fan stream temperature and velocity levels for in-flight cycle matching. Cycle matching is further enhanced by a technique referred to as the inverse throttle schedule. The inverse throttle schedule offers the following advantages:

- Meeting the unique thrust schedule of advanced supersonic cruise aircraft over the entire flight spectrum,
- Provides low core exhaust velocity at takeoff to obtain the inverted velocity profile and associated noise benefit, and
- Minimizing fuel consumption at supersonic cruise by high flowing the core engine to control the cycle bypass ratio.

Thus, the inverse throttle schedule is a feature that enables sizing the VSCE for optimum supersonic cruise performance, while also meeting FAR (Federal Aviation Regulation) Part 36 noise levels at the other end of the operating spectrum by means of the coannular noise benefit. Figure 2 illustrates the in flight flexibility of the VSCE with the inverse throttle schedule at three key flight conditions -- takeoff, subsonic cruise and supersonic cruise.

As indicated during takeoff, the main burner is throttled to an intermediate power setting so that jet noise from the core stream is low. However, the duct burner is operated at a moderate temperature level to provide both the required takeoff thrust and inverted velocity profile. For climb out over the community, both streams are throttled back, and the inverted velocity profile is retained. Relative to military afterburner systems, the peak duct burner temperatures are low for the VSCE.

At the takeoff power settings corresponding to FAR Part 36 sideline and community noise levels, the variable components (fan, high-pressure compressor, nozzle exhaust system) and throttle settings are matched to "high flow" the engine. High flowing is the capability to maintain maximum design flow during part power operation for low noise. This capability complements the coannular noise benefit to enhance overall noise characteristics of the VSCE.

The engine operates as a moderate bypass ratio turbofan during subsonic cruise. As a result, it has fuel consumption characteristics that are significantly improved relative to a turbojet cycle at this condition. Figure 2b shows the engine configuration that achieves a flat exit velocity profile for the attendant fuel economy benefits. The main burner operates at a low exit temperature and there is no duct augmentation. Again, the variable geometry components are matched to high flow the engine so that the engine airflow can be matched almost exactly with the inlet airflow. This greatly reduces inlet spillage and bypass losses and also improves nozzle performance by working with the ejector to fill the nozzle exhaust area. In turn, installation losses, including boattail drag, are reduced.

At supersonic cruise, fuel consumption characteristics approach those of a cycle designed exclusively for supersonic operation. The main burner temperature is increased (relative to takeoff), and the high spool speed is also increased. This is accomplished with the inverse throttle schedule by matching the variable engine components to a higher main burner temperature and high-pressure spool flow rate. The high flow condition reduces the cycle bypass ratio so the level of duct burner thrust augmentation required during supersonic operation can be decreased. As shown in Figure 2c, the exhaust temperatures from both coannular streams are almost equal, and the variable nozzle areas are set for a flat velocity profile to reach peak propulsive efficiency.

VARIABLE STREAM CONTROL ENGINE DESIGN UPDATE

Updating the Variable Stream Control Engine design definition involved surveying projected technology advancements that offer improvements in cycle efficiency, weight, durability and environmental performance. The technology projections were based on the following:

- Test results and experience acquired from the current NASA sponsored VCE Technology Programs -- the Duct Burner Segment Rig Program, the Coannular Nozzle Model Program and the VCE Testbed Program

- A technology forecast that extends component technology levels in the areas of aerodynamics, materials/cooling and structure mechanics five years beyond that in the NASA/Pratt & Whitney Aircraft Energy Efficient Engine Program.

- Technology readiness attainable by the late 1980 time period with engine certification to follow in the mid 1990's.

Engine General Description

The updated Variable Stream Control Engine, study designation VSCE-515, retains the same basic configuration as the preceding engine definition, the VSCE-502B. A cross-sectional view of the VSCE-515 is presented in Figure 3. The dual spool configuration is designed for an inlet mass flow of 340 kg/sec (750 lb/sec) at sea level static conditions. All components are arranged in a

close-coupled manner to provide an optimum flowpath by avoiding transition ducts in either the core or fan stream. Structurally, the low-pressure spool is supported by three main bearings and the high-pressure spool is supported by two. This five bearing arrangement povides a short, stiff rotor system for optimum blade tip clearance control.

In the mechanical design, the low-pressure spool contains a three-stage fan driven by a two-stage turbine. The high-pressure spool uses a single-stage turbine to drive a five-stage compressor. The main combustor is an annular, staged system similar in concept and operating principle to the duct burner. Both combustion systems are based on the Vorbix (vortex burning and mixing) technology demonstrated under the NASA/Pratt & Whitney Aircraft Experimental Clean Combustor Program. The exhaust nozzle system is a coannular configuration that includes an ejector with acoustic treatment and a thrust reverser. Management and control of integrated engine/aircraft operating functions is accomplished with a full-authority electronic control system. Components with variable geometry capability are the fan, the high-pressure compressor and the coannular nozzle. A more detailed description of the individual component designs is presented in a subsequent section of this paper.

VSCE-515 Performance Relative to First-Generation Supersonic Propulsion System

The performance improvements offered by the VSCE-515 relative to the first-generation supersonic transport engine are presented in Table I. The reduction in takeoff noise by 8 dB results from the jet noise suppression produced by the coannular exhaust nozzle. For a constant engine flow size, a 23 percent weight reduction results from the two-stream engine configuration where as much airflow bypasses the core as passes through it, thereby reducing core size and weight. Also, the advanced component designs and materials contribute substantially to this weight improvement.

The capability of a VSCE to operate as a conventional turbofan during subsonic cruise offers a significant 20 percent improvement in fuel efficiency compared to first-generation engines. These improvements in subsonic fuel consumption, noise, and engine weight are obtainable while still maintaining good supersonic fuel consumption characteristics. Improvements in subsonic fuel consumption are particularly important with respect to meeting environmental performance goals since VSCE-powered aircraft will be capable of cruising subsonically over land without a loss in range where supersonic cruising is prohibited by noise constraints.

The overall effect of VSCE characteristics, based on the level of technology in the updated engine, is very significant on advanced supersonic airplane performance, as shown in Figure 4. The VSCE-515 offers both a 25 percent improvement in airplane range and an 8 dB reduction in takeoff noise. Thus, this engine configuration provides the potential for practical airplane range while maintaining acceptable noise levels.

VSCE-515 Component Definition

Fan

The fan in the VSCE-515 is an advanced three-stage unit, and the design concept emphasizes high efficiency at supersonic cruise, compatibility with supersonic inlets and compatibility with the duct burner. Compatibility with the duct burner necessitates high diffusion capability. The aerodynamic design is based on a low elevation (low hub to tip ratio) to meet nacelle envelope dimensions established by the Supersonic Cruise Research (SCR) airplane contractors for good installed performance and provide space for packaging accessories around the case. A tip speed of approximately 487 m/sec (1600 ft/sec) has been established as optimum on the basis of low-pressure turbine blade stress considerations, in addition to the emphasis for high efficiency and low noise.

In the mechanical design, the first two rotating stages contain low aspect ratio blades made of an advanced composite material. The high strength properties of composite materials eliminate the requirement for part span shrouds. Conventional titanium material blades are required in the third stage because of the higher temperature environment. The trailing edge of the inlet guide vane and leading edge of the fan exit guide vane are variable. For noise suppression, axial spacing between the blades and vanes in each stage is increased in a graduated manner.

High-Pressure Compressor

The high-pressure compressor in the VSCE-515 is unique compared to other advanced subsonic commercial engines because it operates at a high exit temperature of 649°C (1200°F) during supersonic cruise as well as at a low pressure ratio and high rotational speed. As defined, the compressor is a five-stage, drum-type rotor with integral abradable trench tip rubstrips. The blades are multiple circular arc controlled-diffusion airfoils and the vanes in the first two stages have variable geometry capability. All airfoils are coated with an advanced erosion resistant coating. Interstage cavities are designed for low volume and multiple knife-edge seals provide effective interstage sealing to reduce recirculation losses.

Main Combustor

Because of environmental constraints, compounded by prolonged high temperature operation at supersonic cruise, design requirements for the main combustor in a VSCE reflect a substantial departure from requirements for current subsonic applications. A combustor configuration considered for the VSCE-515 is an annular two-stage design, based on the Vorbix operating principle. However, another design concept, derived from more conventional low emissions combustion systems, was also considered as part of this design update.

In the two-stage configuration, the first stage is a pilot premixing zone where combustion is initiated. Combustion is completed in the second

stage or main combustion zone. Each stage has a separate fuel supply system, and air for combustion is introduced into the main combustion zone through a series of swirler tubes.

The liners are a double wall structure with an efficient impingement transpiration cooling scheme. For additional thermal protection, the interior liner surfaces are coated with a thermal barrier ceramic coating.

High-Pressure Turbine

The high-pressure turbine, as in preceding generations of VSCEs, is an advanced single-stage system. This configuration is designed for sustained high temperature operation at high rotational speeds and high mechanical loadings.

The design concept specifically addresses effective coolant management and the use of advanced materials with high temperature capability. Airfoils, both rotating and stationary, are designed with internal cooling passages to promote a high heat transfer rate and cooled with advanced convective and film cooling techniques. One feature of the turbine cooling system is the use of a heat exchanger to reduce the coolant temperature so that a smaller percentage of cooling air is required. The heat exchanger uses fan air as the cooling medium of the turbine coolant.

The airfoils are made from materials that offer superior creep strength properties, along with a good resistance to thermal fatigue. Both the vanes and the blades are coated with a dual coating that consists of a high grade ceramic material for added thermal protection, plus a substrate oxidation coating.

Low-Pressure Turbine

Many of the design features used in the high-pressure turbine have been adapted for the low-pressure turbine. Basically, the low-pressure turbine is designed for efficient operation at a high rotational speed. The high speed capability allows a two-stage configuration and provides a low elevation flowpath for the three-stage fan. The flowpath also has a low profile to minimize the duct burner diameter. This is a key design consideration since the low-pressure turbine and duct burner together set the maximum nozzle diameter.

Both stages are air cooled. However, like in the high-pressure turbine design, cooling losses are minimized by the application of advanced materials, coatings and cooling air management techniques. Interstage sealing is accomplished with conventional platform single knife-edge seals. The blade tips, which incorporate mini shrouds, also have a knife-edge sealing arrangement.

Duct Burner

The duct burner, one of the unique components in the Variable Stream Control Engine concept, is a simplified two-stage version of the three-stage configuration currently undergoing experimental testing in the Duct Burner Rig

Technology Program and VCE Testbed Program. Results from these efforts will be instrumental in improving the design definition.

The aerothermal definition is based on the Vorbix technology, and the design employs many of the technology features in the main combustor. The first combustion zone, or pilot/low power stage, is a double wall geometry. This stage is enclosed by a hood to ensure positive air management for combustion and dilution. The second zone, the high power stage, resembles the primary combustion zone in the main burner. The liner is also a double wall construction, and a series of aerodynamically-designed swirler tubes introduces the combustion air. An insulating ceramic coating is used in this stage for additional temperature capability.

Exhaust Nozzle System

The exhaust nozzle is the other unique component in a VSCE. The nozzle is comprised of three main components: the nozzle proper, the ejector and the reverser. If a mechanical jet noise suppressor is required, it will be included only in the duct stream and the main engine stream will be designed with a low exit velocity which will not require suppression. Progress from the present analytical effort and from anticipated follow-on model tests will have a large influence in optimizing the aerodynamic and acoustic design of the exhaust nozzle system.

The nozzle is coannular in design with variable geometry capability in both fan and core streams. An iris system is employed for varying the fan stream exit area. In the core stream, area variations are achieved by a translating plug. The nozzle is constructed from a lightweight material, and a small percentage of cooling is used to maintain acceptable metal temperature levels. The ejector and reverser are also constructed from a lightweight material. For added noise suppression, the ejector is lined with an acoustic treatment.

Electronic Control System

All engine operating functions such as air and fuel flows are coordinated and controlled by a full-authority electronic control system. The use of electronics, in comparison to hydromechanical units, enables responsive and accurate management of the engine components to match the operating requirements of the flight condition. In addition, the physical size and weight of the unit are greatly reduced. Input for control is provided by advanced sensing devices which monitor key operating parameters. Sensing redundancy is provided to ensure failsafe operation.

TECHNOLOGY REQUIREMENTS AND FUTURE PROGRAM CONSIDERATIONS

VSCE Technology Requirements

Technology requirements for a VSCE propulsion system are identified in Figure 5. Of these requirements, the duct burner, coannular nozzle and high temperature components -- the turbines and combustor -- are the areas most

critical. At present, work under NASA sponsorship is proceeding with the components unique to the VSCE concept. Efforts have been successful in demonstrating the design feasibility and performance potential of both the duct burner and coannular nozzle. However, the demonstration of technology should be expanded to include the high temperature components.

To indicate the necessity for advancements in the area of main engine high temperature technology, Figure 6 presents a comparison of VSCE operating temperatures with another advanced engine design, the Energy Efficient Engine, which is representative of the next generation of subsonic engines. The temperature levels correspond to cruise operation which comprises at least 50 percent of the total engine operating time. As shown, VSCE hot section temperatures are elevated appreciably over the Energy Efficient Engine levels. For further comparison, Figure 7 shows the contrast among the VSCE, the Energy Efficient Engine and a current technology subsonic engine, the JT9D. In addition to elevated turbine and cooling air temperatures, the VSCE is matched to high-flow the core during supersonic cruise for low fuel consumption. However, this produces the maximum rotational speeds and attendant stress levels. Thus, the combination of operating at high temperatures, high stress levels and extended operating times makes high temperature technology a critical requirement.

Future Program Considerations

Continued work in the Duct Burner Technology Program, Coannular Nozzle Technology Program, and VCE Testbed Program is required. Because of the importance of high temperature technology, a High Temperature Validation Program has been defined as the next major technology program. The following paragraphs present an overview of the High Temperature Validation Program.

High Temperature Validation Program

The overall objective of the High Temperature Validation Program is to substantiate the critical technology for a main combustor and single-stage high pressure turbine that reflects the requirements for a second-generation, commercial supersonic propulsion system. This objective would be accomplished by first verifying individual concepts in the areas of materials/cooling, aerodynamics and structures through a series of component rig evaluations, followed by a collective demonstration of the different technologies in real engine environment using a high-pressure spool as the testbed. As planned, the program is organized into three phases, as indicated in Figure 8.

The initial phase of the program involves the concept selection and the preliminary design definition. As part of this effort, advanced component concepts for the combustor and turbine would be evaluated analytically in terms of design feasibility, performance potential, technical risk, fabricability, and overall cost.

Phase II starts the design verification and component refinement process. Technologies selected for High Temperature Validation Program would be combined and rig tested for overall compatibility and suitability. Material

characterization testing would be conducted first. This would be followed by a series of specialized cascade and rig tests to demonstrate specific aerodynamic and cooling technologies.

The third phase of the program focuses on a technology validation test. In this effort, the configuration of the main combustor and single-stage high-pressure turbine, as derived from the preceding work, would be tested in a high-pressure spool arrangement. Testing would be completed over a range of operating conditions, including simulated high altitude, envisioned for a VSCE. The test program would consist of a series of diagnostic evaluations to assess all aspects of performance as well as durability.

CONCLUDING REMARKS

The battery of studies completed during the past several years has corroborated the economic and environmental attractiveness of the Variable Stream Control Engine concept for a second-generation supersonic cruise vehicle. In addition the technology requirements have been established. This leads to the next logical step, technology demonstration as the prerequisite to achieving technology readiness.

In this respect, technology development has been limited to the unique components in the VSCE configuration, namely the duct burner and coannular nozzle system. Although continuing these efforts, particularly the work under the VCE Testbed Program, is essential, work should be expanded to other key areas if engine certification by the mid 1990's is a realistic goal.

On the basis of technology requirements, the main combustor and turbines should be the next area of concentration. High temperature technology, since it is noncommittal to any particular engine configuration, has a wide application and offers the greatest return in technology for a given program investment. For example, the High Temperature Validation Program, as outlined in this paper, would address VSCE requirements but also provide the technology base for other advanced supersonic engine concepts such as the low bypass engine and inverted flow engine. Also, the technical achievements would be applicable to advanced commercial transport and military engines.

REFERENCES

1. Sabatella, J. A.: Advanced Supersonic Propulsion Study Phase I Final Report. NASA CR-134633, Jan. 1974.

2. Howlett, R. A.; Sabatella, J. A.; Johnson, J. A.; Aronstramm, G.: Advanced Supersonic Propulsion Study Phase II Final Report. NASA CR-134904, Sept. 1975.

3. Howlett, R. A.; Sabatella, J. A.; Johnson, J. A.; Sewall, T.: Advanced Supersonic Propulsion Study Phase III Final Report. NASA CR-135148, Dec. 1974.

4. Howlett, R. A.; Streicher, F. D.: Advanced Supersonic Propulsion Study Phase IV Final Report. NASA CR-135273, Dec. 1974.

5. Lohmann, R. P; Mador R.: Experimental Evaluation of a Low Emissions High Performance Duct Burner for Variable Cycle Engines (VCE). NASA CR-159694, Sept. 1979.

6. Larson, R. S.; Nelson, D. P.; Stevens, B. S.: Aerodynamic and Acoustic Investigation of Inverted Velocity Profile Coannular Exhaust Nozzle Models and Development of Aerodynamic and Acoustic Prediction Procedures. NASA CR-3168, May 1979.

7. Westmoreland, J. S.; Godston, J.:VCE Testbed Program - Planning and Definition Study Final Report. NASA CR-135362, Jan. 1978.

TABLE I - IMMPROVEMENTS PROVIDED BY VSCE
RELATIVE TO FIRST-GENERATION SUPERSONIC TURBOJET ENGINES

Takeoff Noise	8 EPNdB Reduction
Specific Fuel Consumption	
Subsonic Cruise	20 Percent Reduction
Supersonic Cruise	1 Percent Increase
Engine Weight	23 Percent Reduction

Note: Comparisons made by scaling first generation turbojet engine to flow size of VSCE

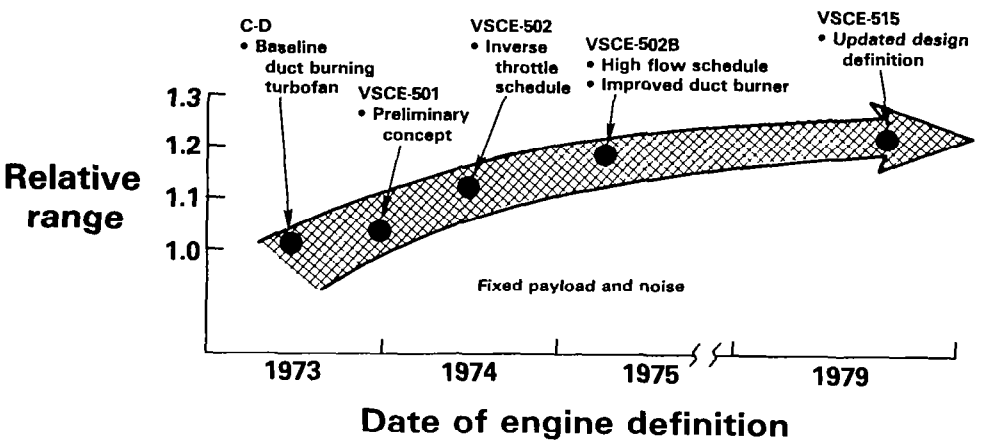

Figure 1.- Variable stream control engine evolution.

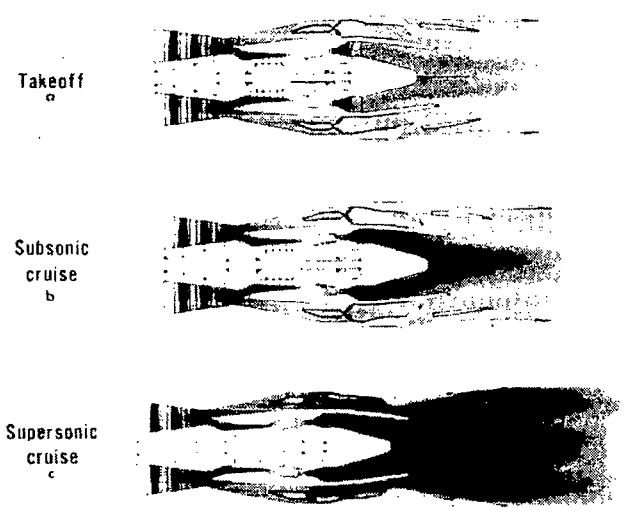

Figure 2.- VSCE with inverse velocity profile at critical flight conditions.

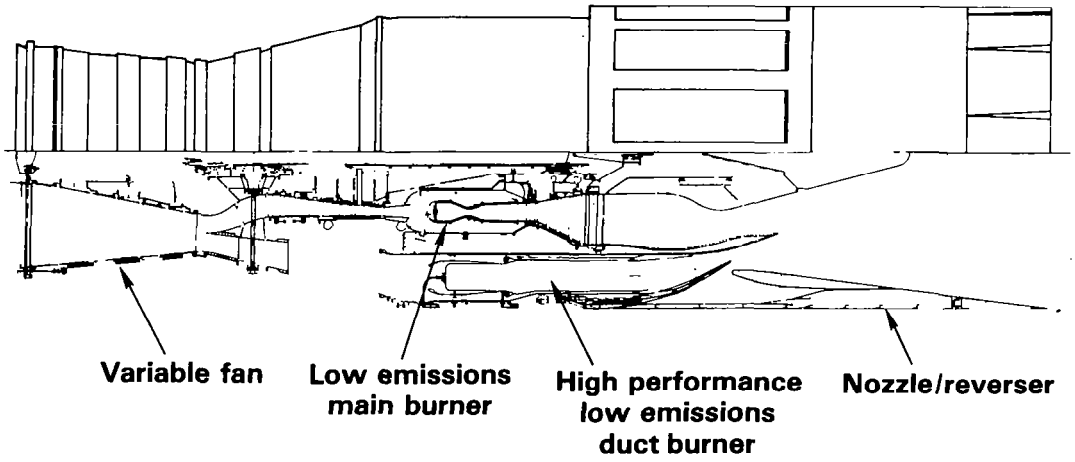

Figure 3.- Cross sectional view of the VSCE-515.

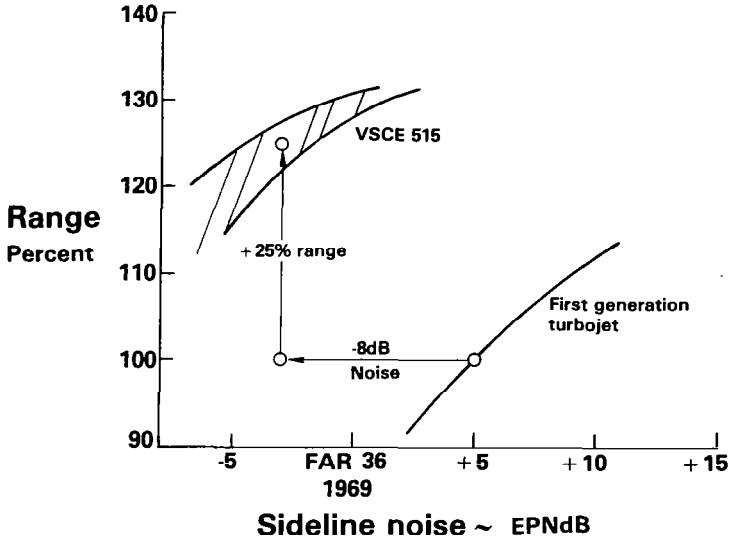

Figure 4.- VSCE performance improvement relative to first-generation turbojet.

- **Duct burner**
- **Coannular nozzle**
- **High temperature components**
  - Main combustor
  - Turbines
- **Stowable jet noise suppressor**
- **Variable geometry components**
  - Fan
  - Compressor
- **Integrated electronic control system**

Figure 5.- VSCE critical technology requirements.

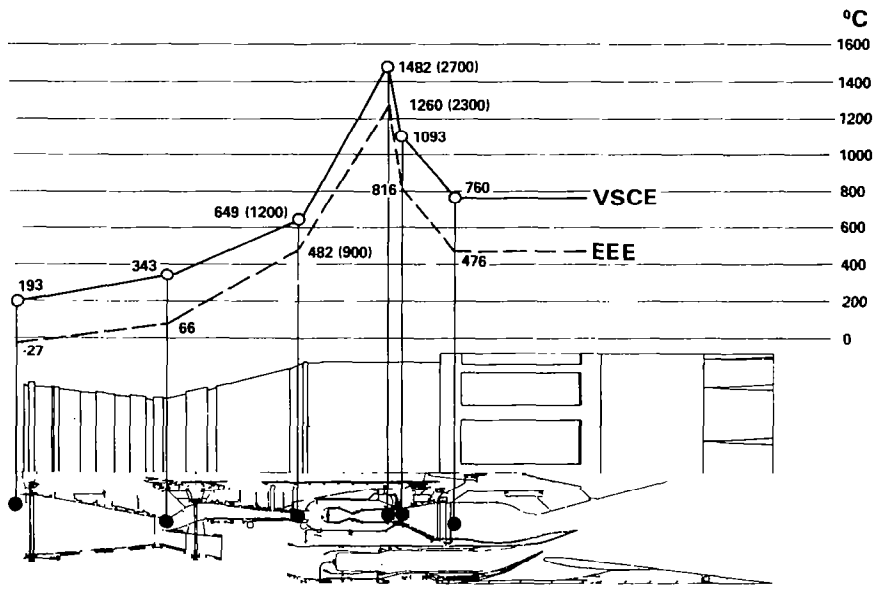

Figure 6.- VSCE operating temperature levels compared to the advanced technology energy efficient engine.

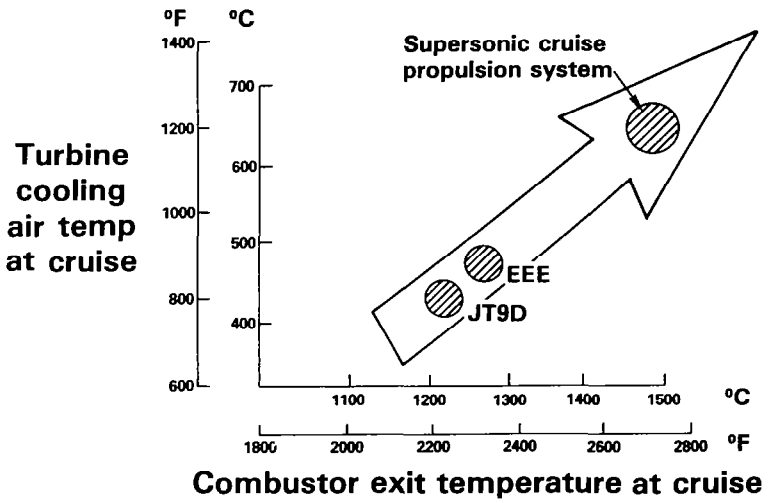

Figure 7.- Temperature levels at cruise.

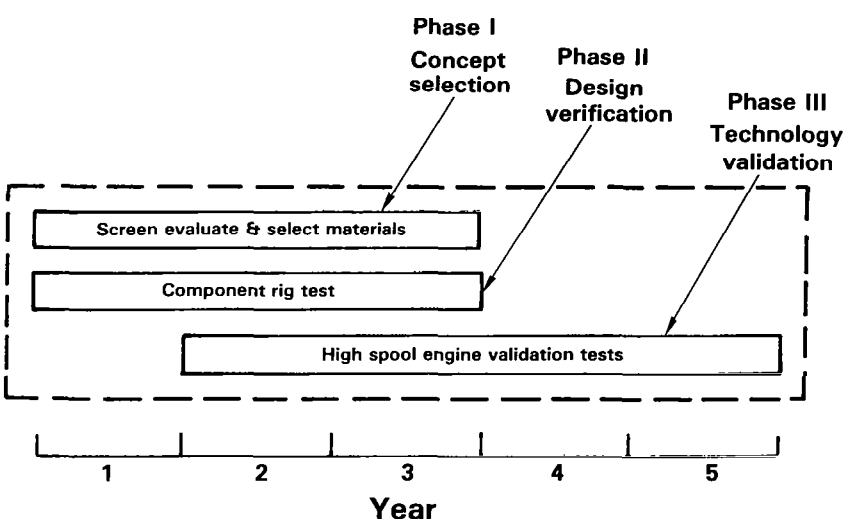

Figure 8.- High temperature validation program schedule.

PROGRESS WITH VARIABLE CYCLE ENGINES*

John S. Westmoreland
United Technologies Corporation, Pratt & Whitney Aircraft Group,
Commercial Products Division

SUMMARY

Under NASA sponsorship, Pratt & Whitney Aircraft has been evaluating and substantiating two of the most critical and unique components of an advanced propulsion system for a future supersonic cruise vehicle. These components, a high performance duct burner for thrust augmentation and a low jet noise coannular exhaust nozzle, are part of the Variable Stream Control Engine (VSCE). Studies have identified this engine as having the greatest potential for an advanced supersonic commercial cruise vehicle, when considering the overall environmental and economic requirements. An experimental test program involving both isolated component and complete engine tests has been conducted for the high performance, low emissions duct burner with excellent results. Nozzle model tests have also been completed which substantiate the inherent jet noise benefit associated with the unique velocity profile possible of a coannular exhuast nozzle system on a Variable Stream Control Engine. Additional nozzle model performance tests have established high thrust efficiency levels at takeoff and supersonic cruise for this nozzle system. Large scale testing of these two critical components is being conducted using an F100 engine as the testbed for simulating the Variable Stream Control Engine.

INTRODUCTION

For the past six years, Pratt & Whitney Aircraft has participated in a series of NASA-sponsored programs aimed at establishing the technology base for a future supersonic cruise transport, with special emphasis on improving environmental and economic characteristics. During this period, over 100 different engine concepts and cycle configurations were studied, including Variable Cycle Engines (refs. 1-4). The most attractive engine configuration identified from this matrix was the Variable Stream Control Engine (VSCE). This concept shows the potential for very significant improvements in range, noise and emissions relative to the first-generation supersonic transport (SST) engines. Figure 1 shows the basic mechanical arrangement of this engine. The latest update of this engine concept, including its mode of operation, is contained in reference 5.

* Work performed under NASA Contracts NAS3-20048, NAS3-20061 and NAS3-20602

Attaining the potential benefits of the Variable Stream Control Engine is contingent on extensive research and evaluation in many areas of advanced technology. The most critical of these technology requirements are the following: (1) low noise/high performance coannular nozzle, (2) low emissions/high performance burner systems, (3) high temperature component technology, (4) variable-geometry components (nozzle/ejector/reverser, inlet, fan, compressor), (5) electronic control system, and (6) an integrated propulsion system.

Concentrating on the two most unique components in the VSCE -- a low noise, variable geometry coannular nozzle and a low-emissions, high performance duct burner -- experimental component technology programs are being conducted by Pratt & Whitney Aircraft under NASA direction. The programs include a Coannular Nozzle Model Technology Program and a Duct Burner Rig Technology Program. Results from this work have provided the basis for the VCE Testbed Program, which involves large scale testing of these components at realistic VSCE conditions. This paper reviews the technical accomplishments and progress made in these programs.

COANNULAR NOZZLE MODEL TECHNOLOGY PROGRAM

Overview

The purpose of the Coannular Nozzle Model Technology Program is to identify and investigate aerodynamic and acoustic nozzle technology for an advanced powerplant in a second-generation supersonic cruise vehicle. More specifically, the major areas of the overall program, which have been completed or are in progress, include:

- Establishing aerodynamic and acoustic performance characteristics of both unsuppressed and suppressed coannular nozzle models over a large range of operating conditions.
- Determining the effect of flight velocity on coannular jets.
- Developing an aerodynamic/acoustic prediction procedure for refining coannular jet nozzles with inverted velocity profiles.
- Calibrating model data with acoustic data to be obtained from the VCE Testbed Program, and evaluating the performance of two supersonic coannular nozzle systems that combine low noise and high aerodynamic performance.

Effort in the first three areas of the program (refs. 6-8) was completed during or prior to 1977, and the significant results of this work will be discussed briefly. Experimental model testing on the fourth area has just been completed, and work for a follow-on effort has started.

Early Efforts

During the first phase of the program, scale models representing unsuppressed and suppressed coannular exhaust systems were evaluated statically under varying exhaust conditions. Ejectors with both hardwall and acoustically-treated inserts were also evaluated. The unsuppressed coannular configurations were found to be as much as 11 PNdB quieter than predictions of that time when scaled to a 2.62 m (50 in) equivalent diameter size. At typical VSCE operating conditions, noise reductions of approximately 8 PNdB were demonstrated.

In Phase II, wind tunnel tests showed that jet noise levels of the coannular nozzles were reduced, due to the simulated flight speed, by approximately the same amount as found for single stream nozzles. Thus, the coannular noise benefits identified during the preceding Phase I static test were essentially retained in the simulated flight environment. The noise reduction resulting from flight effects was a function of nozzle stream velocities and simulated flight speed.

The third part continued the experimental and analytical work mentioned above and was directed towards identifying and investigating aerodynamic/acoustic technology relating to the coannular nozzle design. This effort was directed toward the acquisition of static acoustic and aerodynamic performance data which were combined with existing data to support an aerodynamic/acoustic prediction procedure for inverted velocity profile coannular jet nozzles. A procedure was developed to predict jet noise sound pressure level spectra for coannular nozzles with inverted velocity profiles at all angles as a function of nozzle geometry, operating condition and flight velocity.

Recent Work

The recently completed effort involved two programs. In one program, a scale model of the VCE testbed nozzle system was fabricated and tested for acoustic performance. In the other, two potential supersonic nozzle systems for the VSCE study engine were evaluated over a wide range of operating conditions in the NASA-Lewis 8 x 6 foot supersonic wind tunnel.

The purpose of testing the VCE testbed nozzle model was to obtain model acoustic data that can be scaled directly to large scale engine data at the same aerothermodynamic conditions and so permit definition of scaling effects while at the same time provide test data for evaluation of the current acoustic prediction procedure. A one-sixth scale model of the testbed exhaust nozzle system with a fan to primary jet area ratio of 0.65 and 0.82 fan radius ratio was fabricated and tested in the Pratt & Whitney Aircraft Anechoic Jet Noise Test Chamber. This test facility, as shown in Fig. 2, is lined with acoustic absorbent wedges to provide an anechoic environment at frequencies above 150 Hz. The model was designed for testing both with or without an ejector. Acoustic data were obtained at operating conditions that bracket the testbed engine operating points.

The testbed model acoustic test results are consistent with the existing prediction procedure, as shown in Fig. 3, indicating that the results are similar to data obtained with models tested previously. With the inverted velocity profile, characteristic double hump spectra are present. The high frequency region is controlled largely by the fan stream, while the low frequency region is controlled by the merged fan and primary jet stream.

The second aspect of the program involved an evaluation of the two potential VSCE nozzle systems shown in Fig. 4. The main difference between the two configurations is that one uses a short flap nozzle for the fan stream with an isotropic splitter, while the other employs an iris fan nozzle with a conical splitter. Both configurations have plugs in the primary stream.

Six one-tenth scale models of the two exhaust systems were fabricated and tested in the NASA-Lewis 8 x 6 foot wind tunnel. In Fig. 5, one of the models is shown installed in the wind tunnel. The models simulated actual flight designs at takeoff, subsonic cruise and Mach 2.0 supersonic cruise. Over 200 data points were acquired at wind tunnel Mach numbers of 0.36, 0.9 and 2.0 for a wide range of nozzle operating conditions. Fan and primary nozzle areas were varied to match desired operating conditions, while fan to primary pressure levels were varied along with the ejector inlet area and clamshell reverser position. In addition, the supersonic configuration was tested with 0, 2 and 4 percent corrected secondary flow, which was released behind the duct throat in the gap formed by the reverser buckets.

Both nozzle configurations produced similar results at the same operating conditions. At takeoff and supersonic cruise, nozzle performance approached or met the desired performance goals (Fig. 6). However, subsonic cruise performance fell short of the target. Diagnostic tests of the subsonic cruise configurations showed that lower performance was a result of ejector inlet flow separation. The follow-on work is addressing this effort.

In evaluating the nozzles, the addition of secondary flow in the amount of 2 and 4 percent improved nozzle performance by approximately 2.5 and 3.8 percent. The effect of varying the fan to primary pressure ratio was negligible.

Future Program Plans

In future work, the nozzle designs will be refined by applying knowledge gained from the preceding phases. Work is also planned to improve analytical techniques. This involves modifying existing computer programs for supersonic flow fields so they can be applied to coannular nozzle geometries. Ultimately, integrated airframe nozzle configurations will have to be studied, designed and tested.

DUCT BURNER RIG TECHNOLOGY PROGRAM

Overview

The objective of the Duct Burner Rig Technology Program is to identify and substantiate the required technology to evolve a duct burner configuration with the necessary high performance and low emissions for second-generation supersonic propulsion systems. The efforts conducted under this program are directed at the duct burner application in the VSCE study engine. Three augmented operating conditions were established as being most critical to the duct burner design: (1) supersonic cruise at which the duct burner fuel/air ratio is low, but pressure loss and thrust efficiency are most critical to fuel consumption; (2) a climb condition at which a modest level of augmentation would be required to accelerate through the transonic flight regime; and (3) the takeoff condition at which the aircraft would be subject to airport vicinity noise and emissions regulations.

Critical performance goals established for this program include thrust efficiency at supersonic cruise equal to 94.5 percent, fan duct total pressure loss at supersonic cruise equal to 4.5 percent and a maximum ignition fuel/air ratio of 0.002.

The low ignition fuel/air ratio is dictated by operational constraints. Experience with conventional thrust augmentors indicates that if ignition occurs at a fuel/air ratio of 0.002 or lower, the pressure pulse is sufficiently low to avoid pressure pulsing the engine.

Exhaust emissions goals established for this program by NASA are listed in Table I. The goals for carbon monoxide (CO) and unburned hydrocarbons (THC) emissions indices are representative in that they are typical of those necessary to achieve the more general combustion efficiency goal. These goals are intended only as a standard for comparison and are not related to any proposed or established regulations for advanced supersonic aircraft.

Under the first phase of the Duct Burner Rig Technology Program, an analtyical screening and definition study was completed. At present, experimental rig development testing is continuing under the second and third phases of the program.

Early Effort

The first phase of the program was conducted under NASA Lewis Research Center Contract NAS3-19781 (ref. 9). The objective of this study was, through systematic analytical screening of combustor concepts, to identify duct burner concepts with the potential for high performance and low emissions. Combustion concepts were considered that ranged from improved versions of current state-of-the-art duct burners through the technology levels demonstrated in the NASA-sponsored Experimental Clean Combustor (ref. 10) and Pollution Reduction Technology Programs, to such advanced concepts as variable geometry premixed-prevaporized combustors. The concepts were used to define a number of duct burner configurations.

As the study progressed, it became evident that technology derived from advanced, low-emissions main combustor programs such as the NASA/P&WA Experimental Clean Combustor Program would be required to achieve the desired high performance and low emissions levels over the entire operating range. Analyses indicated that a three-stage Vorbix (vortex mixing and burning) duct burner concept has the potential to meet the overall engine requirements, including pressure loss, thrust efficiency and ignition margin and is compatible with the geometry of the VSCE. A schematic of the three-stage configuration in the fan duct of a VSCE is presented in Fig. 7.

In the basic mechanical configuration the pilot secondary stages are enclosed by a hood to ensure a positive air management for combustion. Air enters the pilot secondary stage through a row of swirler tubes that promotes rapid mixing of air with combustion gases exiting the prechamber stage. The rapid turbulent mixing produced by the swirling jets enhances complete combustion to reduce exhaust pollutants. A similar arrangement is used in the third combustion zone or high power stage. The fuel injectors for the secondary high power stages are located at the exit of the previous stage so that fuel may be rapidly vaporized in these hot combustion products. Combustor liners in both low and high power stages are a conventional louvered design.

Recent Effort

In the current rig test effort under NASA Lewis Research Center Contract NAS3-20602, tests are being conducted to substantiate and refine emissions and performance characteristics of the three-stage Vorbix duct burner as well as resolve any potential operational problems in the VCE Testbed Program. For this work, the test rig was sized to duplicate a 60-degree sector of the annular burner configuration required for the VCE Testbed Program. An exploded view of the duct burner rig is shown in Fig. 8.

A total of thirteen duct burner configurations have been tested. Data were obtained for emissions, smoke, and total pressure loss at both simulated sea level takeoff and supersonic cruise. Also, measurements were made to evaluate lighting and blowout characteristics and determine emissions characteristics at other operating conditions. This work has successfully substantiated the three-stage configuration. Some of the more important results and observations from recent testing are presented in the following paragraphs.

Historically, acoustic instability -- primarily high frequency screech associated with radial oscillatory modes -- has been a concern in the design of augmentors. No such instability was encountered during rig testing.

The ability to ignite the duct burner at low fuel/air ratios is necessary to avoid pressure pulses that might adversely affect operating stability. A very low ignition fuel/air ratio of 0.002 was established as a light off goal based on experience from other augmentor programs. This goal was surpassed during ignition tests with fuel/air ratios of 0.0014 to 0.0018.

As a tool strictly for technology evaluation, the duct burner rig does not incorporate commercial life-related design features and materials. Thus, minor cooling and buckling problems with liner high temperatures encountered during initial tests were eliminated in subsequent stages of testing. Inadequate liner cooling occurred in limited areas immediately downstream of the swirler tubes in the pilot secondary and high power stages. This was attributed to marginal film integrity on the louver caused by high turbulence generated by the swirling flow. A double louver scheme was incorporated in these areas to improve film integrity. Typical louver temperatures such as those indicated in Fig. 9 are used to help evaluate characteristics of the duct burner. In this case, a comparison is shown which illustrates the influence of swirler orientation on liner temperature.

Table II presents the duct burner emissions characteristics. These results indicate that the combustion efficiency exceeds both the NASA contract goals and predicted levels at all operating conditions. While NO_x emissions are above the goal and predicted levels, they are consistent with the projected emissions characteristics. It should be noted that the potential exists for tradeoffs between combustion efficiency and NO_x emissions by reducing residence time, i.e., the length, of the duct burner.

The SAE smoke number was well below the goal, on the order of 2, during high fuel/air ratio operation with all configurations evaluated.

Despite the external pressure distribution around the duct burner and the airflow distribution being close to the design intent, the overall total pressure loss across the duct burner was initially higher than projected. Analyses and flow visualization studies identified the mechanism causing the higher losses, and subsequent tests with a revised swirler geometry demonstrated a substantial reduction in pressure loss without significantly altering emissions or other performance characteristics.

Thrust efficiency is related to the uniformity of the gas temperature distribution at the duct nozzle exit plane. Test results have demonstrated minimal circumferential variation of the gas temperature at the duct burner exit. Typical radial temperature profiles are shown in Fig. 10. The profile at supersonic cruise is extremely uniform, thereby conducive to a high thrust efficiency required at this condition. Analysis of these profiles, including the effect of assumed nozzle cooling air and the existing circumferential variations, indicates that in a flight engine the thrust efficiency at supersonic cruise would be in the 96-98 percent range -- well above the 94.5 percent goal. At the higher fuel/air ratios of takeoff and transonic climb, the thrust efficiency is computed to be 92 to 94 percent, which also exceeds the projected levels.

Future Program Plans

Further experimental testing is scheduled with the duct burner rig. Future tests would be conducted in an effort to reduce the total pressure loss to the design level, optimize the emissions characteristics, investigate reductions in stage length, and reduce burner sensitivity to the fuel

spray characteristics of the high power stage fuel injectors. Additional efforts are planned to assess a simplified version of the three-stage design.

VCE TESTBED PROGRAM

Overview

The VCE Testbed Program, being conducted under NASA Lewis Research Center Contract NAS3-20048, provides an effective method to evaluate and verify the VSCE unique duct burner and coannular nozzle technologies. By testing a large scale duct burner and coannular nozzle in a realistic operating environment, the program will demonstrate:

- The coannular noise benefit with inverted velocity profile
- A high performance and low emissions duct burner
- Effectiveness of acoustic treatment on the ejector
- VSCE characteristics (inverted throttle schedule)

In addition, the testbed provides the opportunity to evaluate:

- Duct burner combustion noise
- Fan/duct burner noise interactions
- Fan/duct burner/nozzle stability
- Fan and core noise sources
- Validity of noise prediction based on model test data
- Improvements to advanced supersonic vehicle jet noise prediction

The VCE testbed configuration is shown in Fig. 11. A Pratt & Whitney Aircraft F100 engine was selected as the gas generator for the testbed since it has the potential to simulate the desired exhaust conditions of the VSCE study engine. Furthermore, it did not require extensive modification to incorporate the duct burner, a variable exhaust nozzle and an ejector that can accommodate both a hard wall surface and acoustic treatment.

The program plan includes two major series of tests: a duct burner emissions and performance evaluation, and a comprehensive aero/acoustic evaluation. Three different test sites are being employed for conducting these and other associated tests. Calibration of the F100 engine was performed at the Pratt & Whitney Aircraft Government Products Division in Florida. A checkout of the F100/testbed system and emissions evaluation is being performed at the Pratt & Whitney Aircraft Commercial Products Division in Connecticut. The Boeing Boardman facility in Oregon was selected as the site for completing the aero/acoustic test.

Design Philosophy

Since the intent of this program is to evaluate critical concepts and demonstrate VSCE operational characteristics, the testbed does not represent flight type hardware nor is it designed for long life. Standard cooling techniques and available materials we e employed in the duct burner and nozzle systems, realizing that future p ograms would be required to develop long term cooling methods and struc ural approaches.

Duct Burner

The duct burner for the testbed is based on the aerothermal and mechanical concepts described in the previous discussion of the Duct Burner Rig Technology Program. In the design process, particular emphasis was placed to ensure a similarity as close as possible between the testbed and the design concept for the flight engine. Design parameters that are identical to the VSCE study engine include:

- Local velocities and Mach numbers
- Stage lengths
- Mixing zone parameters such as the ratios of swirler diameter to radial height and fuel injector spacing to radial height
- Percent airflow and fuel/air ratios at end of stages.

The major variations between the testbed and a possible flight engine duct burner are the reduction in duct height and mean diameter by approximately 50 percent to match the F100 engine size.

Coannular Nozzle

The exhaust nozzle system used in the VCE testbed to evaluate the coannular noise effect is similar to the nozzle considered for the VSCE study concept. The axial orientation of the duct burner and primary nozzles in the testbed is nearly identical to that in the flight concept. Also, the ejector system is nearly the same.

One dissimilarity, however, is in the primary nozzle configuration. The study engine shows the potential for a variable throat, convergent divergent nozzle system, while the testbed utilizes a fixed convergent primary nozzle. This difference, however, will not produce any significant effects on the experimental data desired in the program. Several different sizes of fixed primary nozzles are used during testing to permit attainment of a variety of primary stream exit velocities.

Testbed Control System

The control system in the VCE testbed was designed to maintain control of all F100, duct burner and nozzle control variables in order to obtain the desired operating points for acquisition of aero/acoustic and emissions data. For repeatability of operating points, it was desirable that the system regulate the engine and testbed components such that actual duct airflow variations were accurate to 1 percent of the set point.

In addition, the control is capable of independently metering the duct burner fuel flow to the three combustion stages as well as sequencing the stage operation. Finally, the control system protects the test vehicle from control system failures such as sensor malfunction and permits ease of operation to establish operating points for data acquisition.

Recent Effort

Testing accomplished to date includes a checkout of the integrated F100/testbed system and a series of evaluations to demonstrate duct burner aerothermal/mechanical performance and acquire emissions data. Aero/acoustic testing is planned in 1980.

The testbed demonstrator vehicle became operational during mid 1978. The test configuration is shown in Fig. 12 installed in a test stand at the Commercial Products Division prior to emissions testing. The high performance/low emissions duct burner, initially demonstrated in the companion rig program, has been substantiated through testbed operation. Also, the VSCE concept, in which the exit velocity profiles are varied and controlled, has been demonstrated while maintaining good engine/duct burner/nozzle stability characteristics.

Approximately 100 hours of testing has been completed, and no major problems have been encountered with respect to duct burner operation. A photograph of the testbed exhaust plume with the duct burner operative is presented in Fig. 13. Velocity ratios (fan velocity/primary velocity) between 1.0 and 1.9 have been obtained at steady-state conditions. The development breadboard control system, which is computer controlled, has successfully maintained safe and stable operation of the test vehicle throughout the operating range.

An element related to VSCE operation is fan/duct burner/nozzle stability. At duct burner light off, upstream pressure pulses were expected to be on the order of 1 to 3 percent, but, in fact, instabilities have not been observed during testing. Moreover, intentional variation of the fan nozzle area did not produce any instabilities in the system. Also, a variation in fuel flow to any of the duct burner stages has been limited by wall temperatures and not stability problems. The transition from one to two to three combustion zones over a variety of fuel flow splits has proven the stability of the integrated engine, duct burner, and nozzle system.

For an accurate characterization of duct burner exhaust emissions, gas sampling instrumentation is especially critical. The emissions sampling system designed for this program is comprised of four probes located at the duct burner exit plane. Three of the probes are fixed and each of these contains nine sampling elements. The fourth probe is a traversing unit with a single sensing element capable of both radial and circumferential movement.

All probes in the system are steam cooled. As emissions samples are extracted by the probe sensing elements, the samples are passed through heated tubes to a collection chamber that is external to the test vehicle. From this point, the sample is transferred to the Pratt & Whitney Aircraft mobile emissions laboratory for analysis. The gas sampling system design addressed the mounting and positioning of sensors, in addition to quenching the sample without condensation through the switching and mixing prior to analysis in the mobile laboratory. Sampling probes and emissions sampling equipment were designed to conform with the specifications described in Federal Register Vol. 38, No. 136, Part II, July 17, 1973, "Control of Air Pollution from Aircraft and Aircraft Engines".

For emissions assessment, the testbed has been operated over a wide range of overall fuel/air (f/a) ratios from 0.005 to 0.030*. Various operating conditions were evaluated as the operating range and limits of the duct burner were investigated. Also, different pressure levels were run at various representative points in order to duplicate the nozzle model acoustic data that were discussed previously.

Typical emissions results for CO, THC and NO_x are shown in Fig. 14. Also shown are results from the companion rig program and the predicted data scatter band that is based on Pratt & Whitney Aircraft's burner experience. The testbed results tend to duplicate rig data, thereby corroborating the high overall performance of the basic duct burner design. As demonstrated during rig testing, the higher than expected combustion efficiency due to the excellent mixing characteristics yielded low CO and THC levels. A comparison of the testbed duct burner combustion and thrust efficiency at the three fuel/air ratios versus the predicted efficiency is presented in Table III. The results are based on data available at the time of this writing. Further work is expected to improve these initial emissions and performance characteristics.

Future Program Plans

Acquisition of acoustic data and the evaluation of the coannular effect are planned. Also the testbed demonstrator will be used to test and evaluate design refinements from the companion rig program. Follow-on plans may include testing the VCE testbed in a wind tunnel to evaluate flight effects on the coannular nozzle acoustic results and testing a simplified duct burner configuration.

---

* Fuel/air ratio refers to the fuel passing through eitner all or a particular set of nozzles ratioed to the total airflow passing through the burner, including air that actually bypasses the burner and is used to cool the nozzle.

REFERENCES

1. Sabatella, J. A.: Advanced Supersonic Propulsion Study - Phase I Final Report. NASA CR-134633, Jan. 1974.

2. Howlett, R. A.; Sabatella, J. A.; Johnson, J. A.; Aronstramm, G.: Advanced Supersonic Propulsion Study - Phase II Final Report. NASA CR-134904, Sept. 1975.

3. Howlett, R. A.; Sabatella, J. A.; Johnson, J. A.; Sewall, T.: Advanced Supersonic Propulsion Study - Phase III Final Report. NASA CR-135148, Dec. 1974.

4. Howlett, R. A.; Streicher, F. D.: Advanced Supersonic Propulsion Study - Phase IV Final Report. NASA CR-135273, Dec. 1974.

5. Hunt, R. B.; Howlett, R. A.: Variable Stream Control Engine for Advanced Supersonic Aircraft Design Update. Supersonic Cruise Research '79, NASA CP-2108, 1980. (Paper no. 16 of this compilation.)

6. Kozlowski, H.; Packman, A. B.: Aero/Acoustic Tests of Duct Burning Turbofan Exhaust Nozzles. NASA CR-2628, Jul. 1976.

7. Kozlowski, H.; Packman, A. B.: Flight Effects on the Aero/Acoustic Characteristics of Inverted Velocity Profiles Coannular Nozzles - Comprehensive Data Report. NASA CR-135236, 1976.

8. Larson, R. S.; Nelson, D. P.; Stevens, B. S.: Aerodynamic and Acoustic Investigation of Inverted Velocity Profile Coannular Exhaust Nozzle Models and Development of Aerodynamic and Acoustic Prediction Procedures. NASA CR-3168, May 1979.

9. Lohmann, R. P.; Riecke, G. T.: Analytical Screening of Low Emissions, High Performance Duct Burners for Supersonic Cruise Aircraft Engines. NASA CR-135157, Mar. 1977.

10. Roberts, R.; Fiorentino, A.: Experimental Clean Combustor Program - Phase I Final Report. NASA CR-135253, Oct. 1977.

TABLE I - DUCT BURNER EMISSIONS GOALS

Pollutant	Emissions Index (g pollutant/kg fuel)
NO_x	1.0
CO	30.0
THC	2.5
Smoke (SAE No.)	15.0

Note: Combustion efficiency at all operating conditions = 99 percent

TABLE II - DUCT BURNER RIG EMISSIONS CHARACTERISTICS

	CO (EI) gm/kg	THC (EI) gm/kg	COMB. EFFIC.	NOx (EI) gm/kg
Supersonic Cruise				
Meas.	1.6	0.03	99.9	5.7
Anal.	30	3	99.0	2.8
Goal	30	3	99.0	1.0
Transonic Climb				
Meas.	7.4	0.04	99.8	4.0
Anal.	225	22.5	92.5	1.2
Goal	30	3.0	99.0	—
Takeoff				
Meas. (f/a = 0.035)	13.7	0.001	99.7	2.7
Pred. (f/a = 0.0385)	30	3	99.0	1.8
Goal	30	3	99.0	1.0

TABLE III - VCE TESTBED DUCT BURNER COMBUSTION AND THRUST EFFICIENCY

	Combustion efficiency		Thrust Efficiency	
	Meas.	Pred.	Meas.	Pred.
Fuel/Air Ratio .013	99.6	99.0	97.3	94.5
Fuel/Air Ratio .019	98.5	--	96.0	--
Fuel/Air Ratio .030	99.3	99.9	96.8	86.0

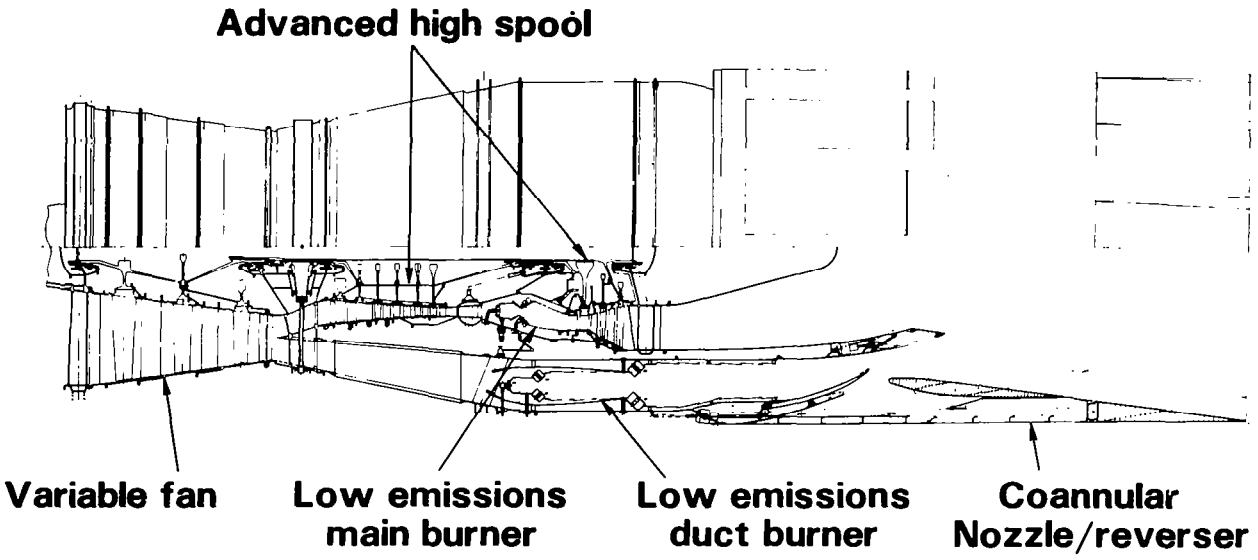

Figure 1.- Conceptual configuration of Variable Stream Control Engine (VSCE).

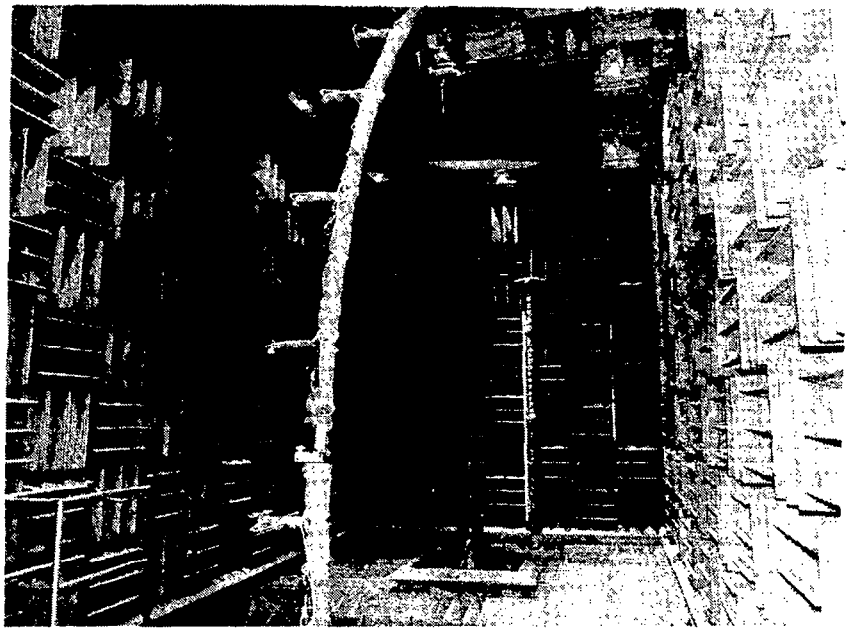

Figure 2.- Test nozzle model installed in Anechoic Jet Noise Facility.

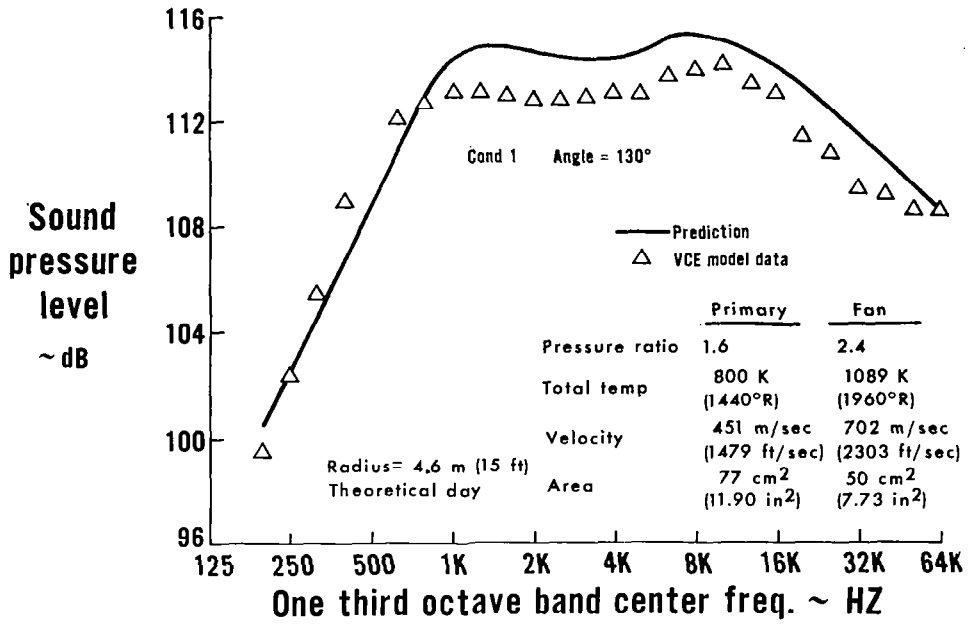

Figure 3.- Comparison of VCE coannular nozzle model test prediction and test data.

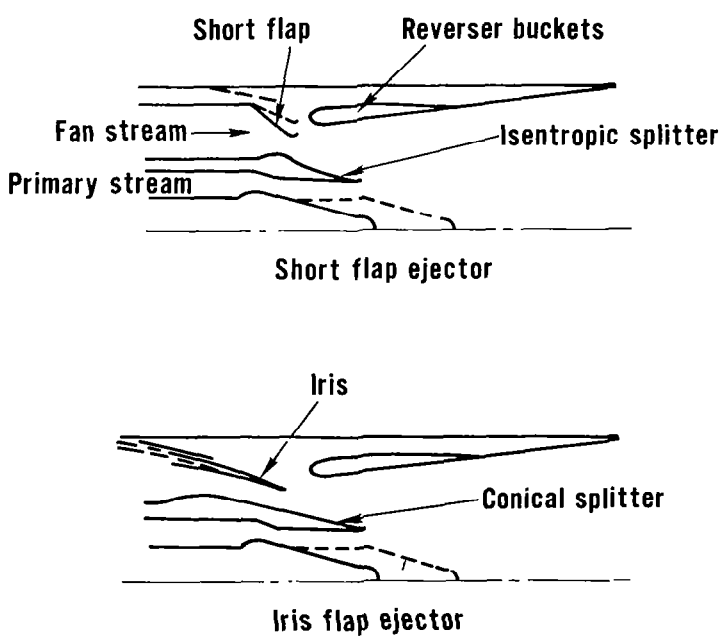

Figure 4.- Cross sections of potential VSCE nozzle configurations evaluated for aero/acoustic performance during Phase IV Program.

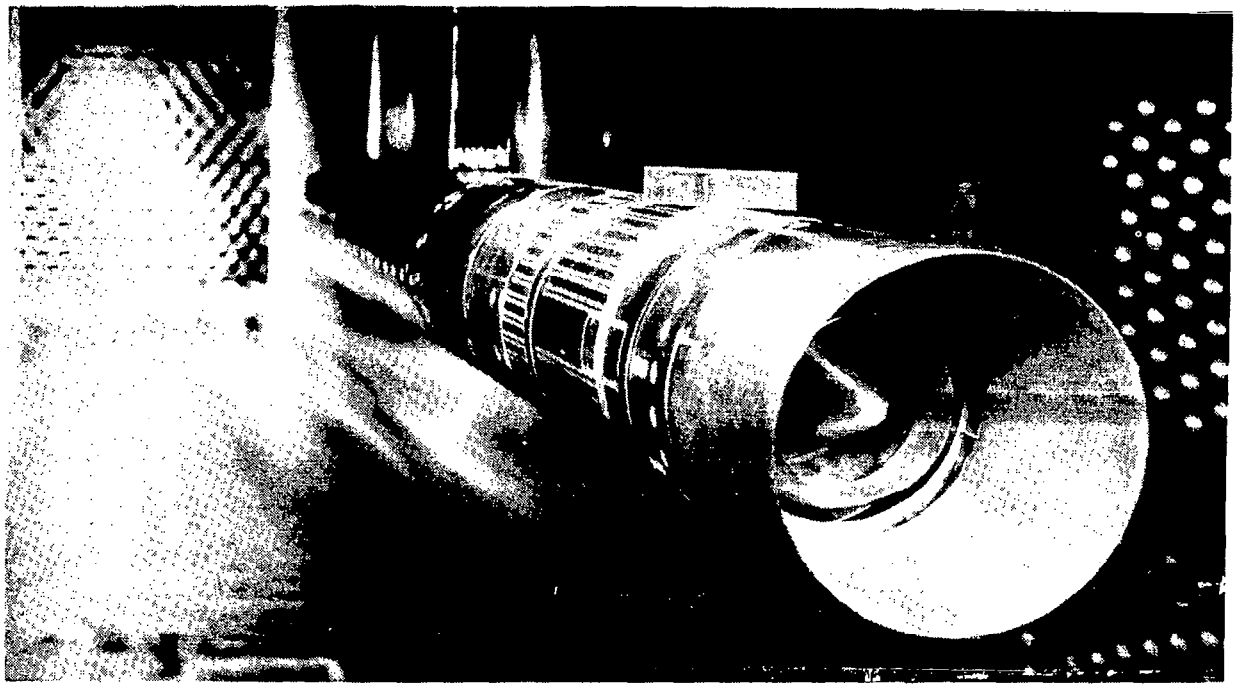

Figure 5.- Test nozzle installed in NASA-Lewis wind tunnel.

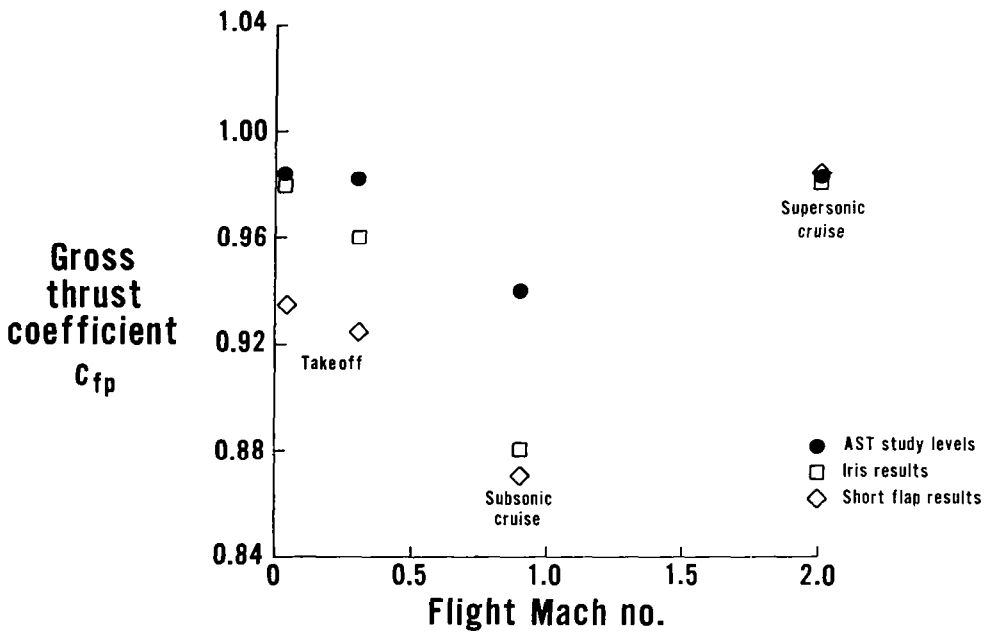

Figure 6.- Comparison of test results with advanced supersonic propulsion study nozzle performance.

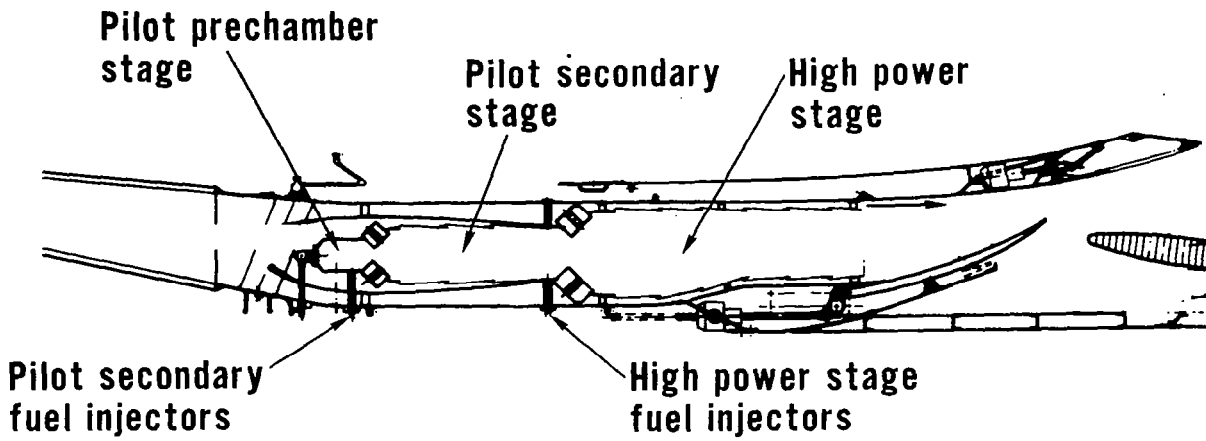

Figure 7.- Three-stage Vorbix duct burner configuration shown with fan exhaust nozzle.

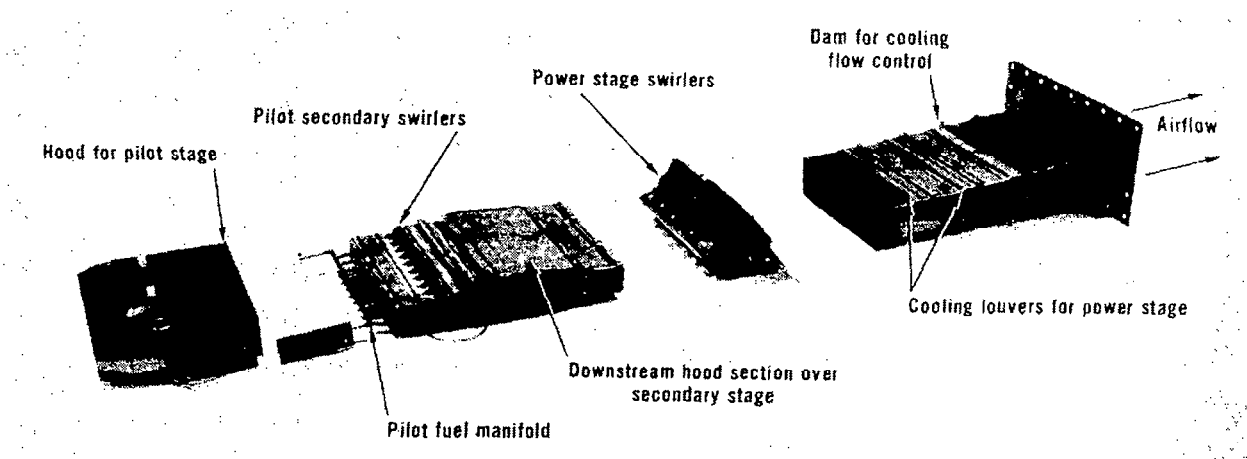

Figure 8.- Exploded view of duct burner rig.

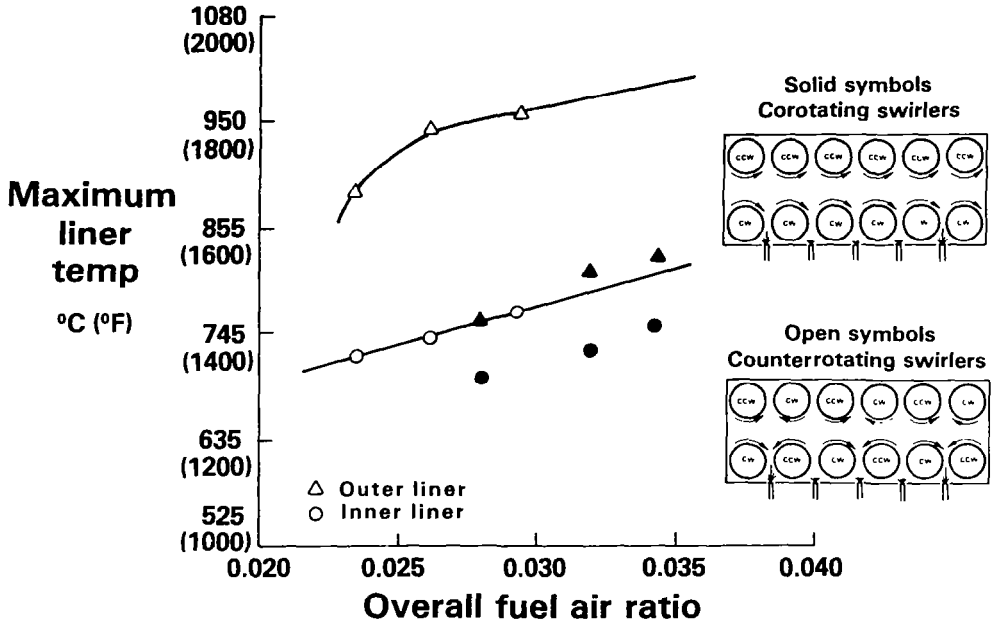

Figure 9.- Influence of swirler orientation on liner temperature.

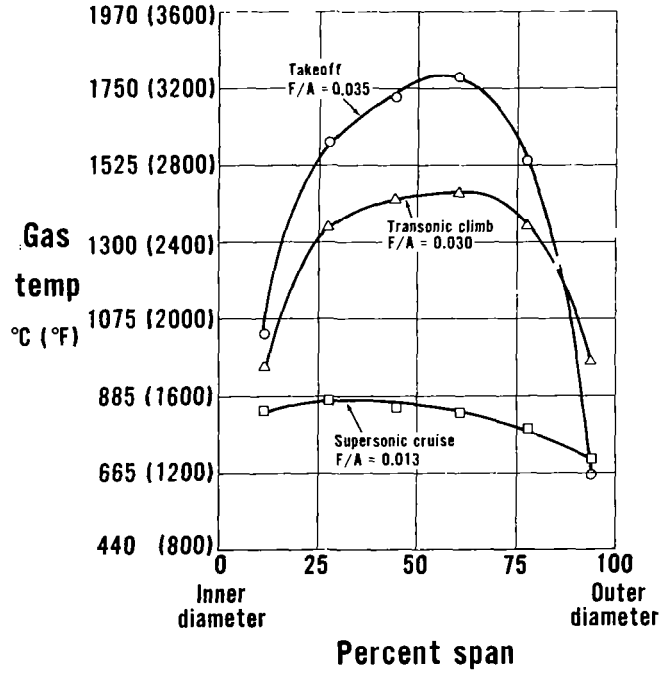

Figure 10.- Typical radial temperature profiles at duct burner exit plane for selected operating conditions.

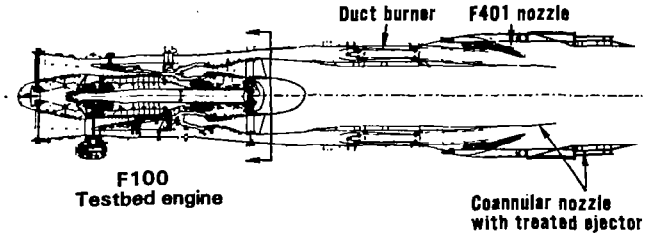

Figure 11.- VCE testbed demonstrator configuration using a Pratt & Whitney Aircraft F100 engine as gas generator to develop proper environment of testbed components - the duct burner and coannular nozzle.

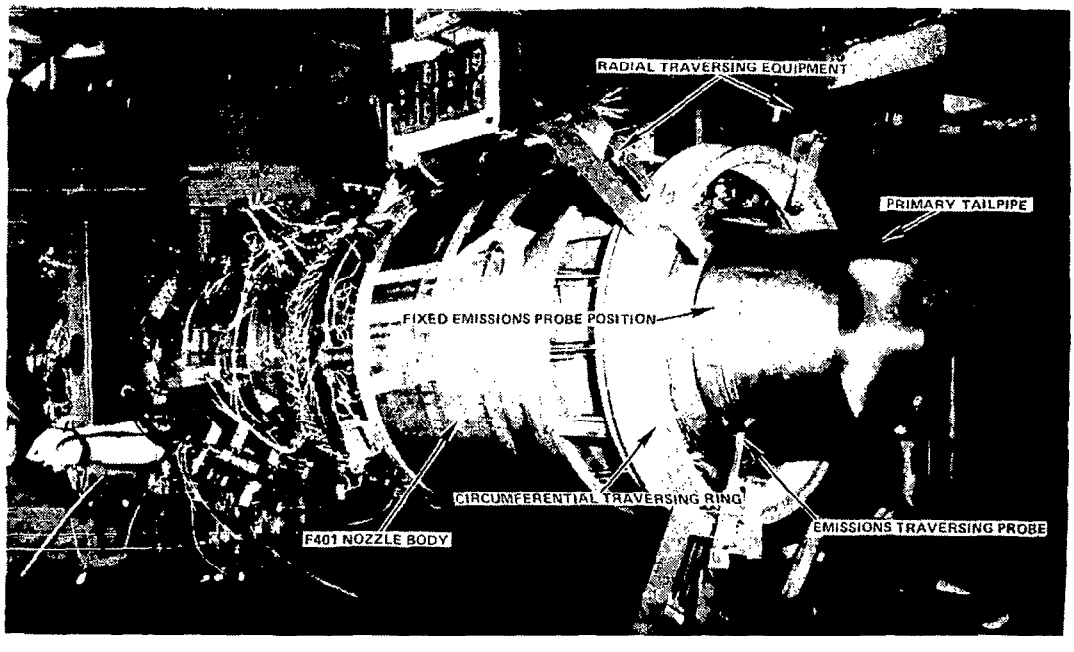

Figure 12.- VCE testbed demonstrator installed in test stand at Pratt & Whitney Aircraft Commercial Products Division in East Hartford, Connecticut.

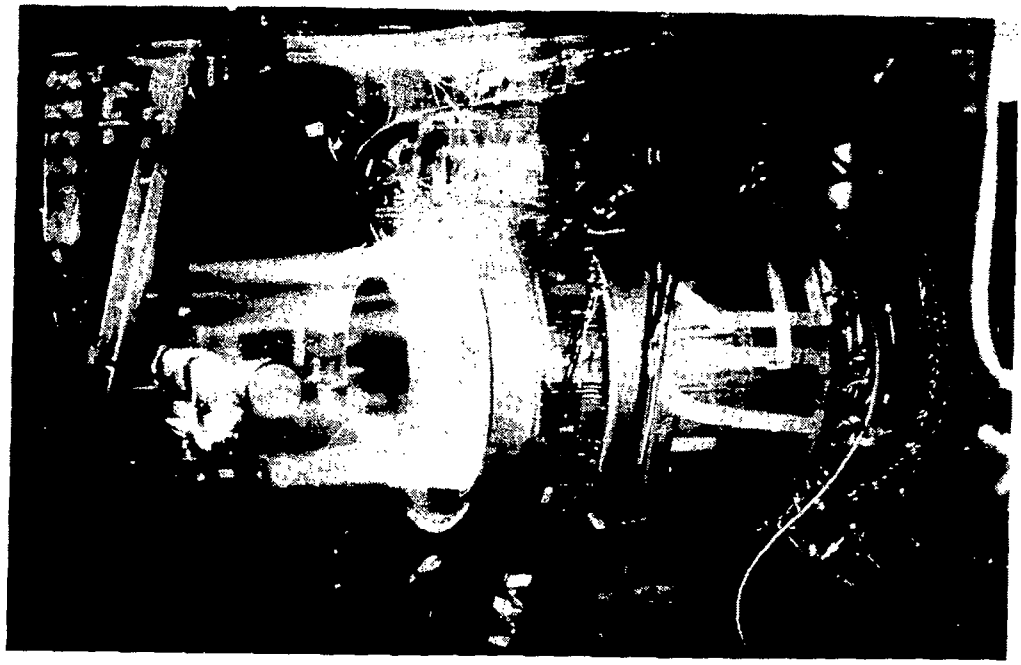

Figure 13.- VCE testbed demonstrator exhaust plume at duct burner augmentation.

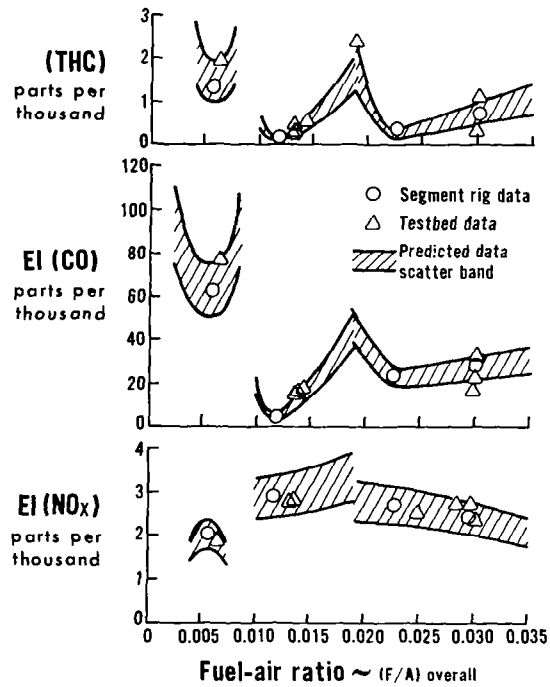

Figure 14.- Typical emissions results acquired from VCE testbed emissions testing.

EFFECTS OF INLET TECHNOLOGY ON CRUISE SPEED SELECTION

L. H. Bangert, D. M. Santman, G. Horie, and L. D. Miller

Lockheed-California Company

SUMMARY

Recent Lockheed studies of supersonic cruise research (SCR) aircraft have studied the impact of cruise speed on technology level for certain aircraft components. In the present study, external-compression inlets were compared with mixed-compression, self-starting inlets at cruise Mach numbers of 2.0 and 2.3. Inlet-engine combinations that provided the greatest aircraft range were identified. Results showed that increased transonic-to-cruise corrected air flow ratio gave decreased range for missions dominated by supersonic cruise. It was also found important that inlets be designed to minimize spillage drag at subsonic cruise, because of the need for efficient performance for overland operations. The external-compression inlet emerged as the probable first choice at Mach 2.0, while the self-starting inlet was the probable first choice at Mach 2.3. Airframe-propulsion system interference effects were significant, and further study is needed to assess the existing design methods and to develop improvements.

INTRODUCTION

Supersonic cruise research (SCR) studies at the Lockheed-California Company have recently been directed toward aircraft designed for different supersonic cruise Mach numbers. The general purpose of this effort was to assess where a change in supersonic cruise speed imposed a change in technology level for certain components of the aircraft. Through 1978, Lockheed studies concentrated on aircraft with a supersonic cruise speed of Mach 2.55. During 1979, these studies were expanded to include Mach 2.0 and Mach 2.3 cruise aircraft.

Mach 2.0 was approximately the lowest speed of interest in the Lockheed studies. At this speed, external-compression inlets were expected to be competitive with mixed-compression types. By contrast, cruise at Mach 2.55 clearly required mixed-compression inlets. Studies at Mach 2.3 were undertaken to define more clearly a crossover Mach number at which the advantage would swing to a higher-technology, mixed-compression inlet.

The main objectives of the present study are:

- Identify inlet-engine combinations that provide maximum range at Mach 2.0 and 2.3
- Evaluate effect of transonic-to-cruise corrected air flow ratio on aircraft range
- Obtain quantitative performance comparisons on the effect of internal contraction at Mach 2.0 and 2.3

Inlet performance cannot be optimized in isolation from engine performance. Thus, it was desired to identify those inlet-engine combinations that provided the greatest aircraft range. This in turn allowed those inlets which were leading candidates for further development to be identified.

An issue that arose from past studies was the desirability of engines with relatively large transonic air flow capacity. Because of the importance of transonic-to-cruise corrected air flow ratio on inlet design, it was desired to evaluate the influence of this parameter on aircraft range.

The completed study configurations are indicated by checks in figure 1. The mixed-compression inlets studied at Mach 2.0 and 2.3 were limited to self-starting types. Such inlets can be restarted without any change in inlet geometry, and so have potentially fewer unstart problems than inlets requiring variable geometry for restart. They also have potentially higher total pressure recovery and lower cowl drag than external-compression inlets. The present paper concentrates on using results for two-dimensional inlets to demonstrate effects of internal contraction and of corrected air-flow ratio on aircraft performance. A parallel effort is underway for the axisymmetric inlet types indicated in figure 1. These axisymmetric inlets have potentially lower drag and lower weight than the two-dimensional inlets in the podded nacelle configuration of the Lockheed SCR aircraft. The results of the axisymmetric inlet studies will be reported at a later date.

At Mach 2.55, both translating centerbody (TCB) and collapsing centerbody (CCB) inlets were analyzed, and the results were reported in reference 1. Both of these inlets were axisymmetric, with mixed compression and variable geometry for restart. Advantages of the CCB inlet were low bleed and low internal contraction, plus greater possible throat area variation. Its disadvantages were higher weight and greater complexity. The CCB inlet was preferred, but with reservations about its complexity.

The two-dimensional, self-starting inlet design at Mach 2.55 is described in reference 2. This design was based on that of the Lockheed supersonic transport of 1966.

Figure 2 summarizes the principal factors that influence the choice of transonic-to-cruise corrected air flow ratio. These factors point toward lower corrected air flow ratios for missions dominated by supersonic cruise.

Takeoff noise requirements may limit reductions in corrected air flow ratio, however. To obtain quantitative results, inlets at Mach 2.0 and 2.55 were combined with engines having different transonic-to-cruise air flow ratios. It was not considered necessary to repeat this study at Mach 2.3. Thus, the Mach 2.3 studies were mainly concerned with comparing inlet types for a given engine.

STUDY CONFIGURATIONS

The Mach 2.0 and Mach 2.3 aircraft used in this study are shown in figures 3 and 4, respectively. These aircraft are derivatives of the Lockheed baseline Mach 2.55 aircraft, which has takeoff gross weight of 268,527 kg (592,000 lb), 290 passengers, wing loading of 4213 N/m^2 (88 psf), leading-edge sweep angles 73/70/58 degrees, and aspect ratio 1.72 (ref. 1). The Mach 2.0 and 2.3 aircraft have the same takeoff gross weight and number of passengers as the Mach 2.55 aircraft. For the Mach 2.0 aircraft, the wing loading is 4357 N/m^2 (91 psf), the leading-edge sweep angles are 68/66/53 degrees, and the aspect ratio is 2.1. The Mach 2.3 aircraft has wing loading 4070 N/m^2 (85 psf), leading-edge sweep angles 71/67/55 degrees, and aspect ratio 1.95. The optimum wing loading and takeoff thrust-to-weight ratio for each aircraft were determined from the Lockheed ASSET (Advanced Systems Synthesis and Evaluation Technique) code results.

Figure 5 shows an isometric view of the Mach 2.0, two-dimensional, external-compression inlet (2.0/2D/EX) in the overwing/underwing configuration. (The wing is not shown.) The installation shown in the figure is on the left-hand side of the aircraft. The overwing inlet has part of the cowl cut away. The centerbody is in the cruise (expanded) position. Other features shown are the centerbody bleed slot and the bypass (nearer engine face) and auxiliary inlet doors. The underwing inlet has a toe-in, and the overwing inlet a toe-out, to align the inlets with the wing-induced flow direction. A similar isometric view of the Mach 2.0, two-dimensional, self-starting inlet is shown in figure 6. The shallower ramp and cowl angles are evident, compared with the 2.0/2D/EX inlet.

Each of the Mach 2.0 inlet types was matched with two or more engines, to assess the influence of transonic-to-cruise corrected air flow ratio on aircraft range. Certain modifications to each inlet type were required to match engine air flow requirements, while simultaneously maximizing total pressure recovery and minimizing drag. This is illustrated in figure 7, which shows the 2.0/2D/EX inlet contours when matched to the GE21/J11 B21 and the GE21/J11 B13 engines. The 2.0/2D/EX inlets have external compression provided by an initial wedge shock, followed by isentropic compression to a maximum ramp angle, and terminated by a strong-solution oblique shock from the cowl lip. The cowl-lip shock intersects the forward edge of the bleed slot. The most obvious differences between the inlets were in the length and the engine face diameter. These were both due to the larger front fan diameter of the -B13 engine, which has a larger transonic-to-cruise corrected air

flow ratio (table 1 summarizes some of the principal characteristics of the Mach 2.0 and 2.3 study engines). The larger engine diameter generally required greater inlet length, because of limitations on subsonic diffuser divergence angle.

There are significant differences in inlet local Mach number overwing and underwing. At a freestream Mach number of 2.0, the overwing local Mach number is 2.16, while the underwing value is 1.97. The design procedure followed here was to design the inlet for the overwing local Mach number. The underwing inlet was then operated off-design at cruise, but with only a small critical spillage drag penalty. The inlets were sized to provide the same corrected air flow rate at cruise; thus, the underwing capture area was smaller than the overwing value. For inlet started (self-starting type) or cowl-lip shock attached (external-compression type), ramp position depended only on local Mach number. At lower Mach numbers, the overwing and underwing ramp angles were scheduled separately with local Mach number and required engine air flow, to minimize spillage drag.

Figure 8 shows the contours of the 2.0/2D/SS inlets matched to the GE21/J11 B21 and the GE21/J11 B13 engines. For the 2.0/2D/SS inlets, external compression was provided by an initial wedge shock, followed by isentropic compression and a second ramp oblique shock. Internal compression was achieved by the cowl-lip shock, followed by isentropic cowl compression between the cowl lip and the throat, and terminated by a normal shock. The amount of internal contraction was limited by the requirement for self-starting. The allowable internal contraction was determined from existing experimental data, and was 42 percent for these designs. As in figure 7, the main differences between the two self-starting inlets were in length and in engine face diameter. These led to differences in weight and wave drag, as will be shown later.

Figure 9 illustrates the contours of the 2.3/2D/EX and the 2.3/2D/SS inlets that were matched to the GE21/J11 B19 engine. These inlets were designed according to the same criteria as their Mach 2.0 counterparts. At a freestream Mach number of 2.3, the overwing local Mach number is 2.48, and the underwing local Mach number is 2.26. The characteristic differences between these two inlet types are evident. The external-compression inlet was shorter by 24 cm, and thus had lower weight and lower bleed drag. The self-starting inlet had more gradual compression, hence higher total pressure recovery; and had a smaller cowl angle, giving lower wave drag. Its internal contraction was 35 percent. Each of the designs shown in figures 7 through 9 resulted from trade studies at supersonic cruise speed. Sensitivity factors for the effect of total pressure recovery, drag, and weight on aircraft range were used to select the inlet contours.

RESULTS

Inlet weight is affected by inlet type and by transonic-to-cruise corrected air flow ratio. Figure 10 shows results from some recent Lockheed studies. Here the average inlet weight was nondimensionalized by the ambient pressure at cruise altitude and by the average capture area. These altitudes were about 16 km at Mach 2.0, 17 km at Mach 2.3, and 18 km at Mach 2.55.

The weights of the 2.0/2D/EX and the 2.0/2D/SS inlets are nearly the same for the GE21/J11B21 engine. The 2.0/2D/EX inlet could have been shorter based on aerodynamic criteria, but had to be lengthened to accommodate auxiliary inlet doors. The inlets matched to the GE21/J11B13 are heavier mainly because of their longer subsonic diffusers (figures 7 and 8). At Mach 2.3, the self-starting inlets were heavier by about 360 kg (800 lb) overall because of the difference in length (figure 9).

The details of the Mach 2.55 studies were reported in reference 1. The collapsing centerbody inlets (CCB) for the GE21/J11B11 were about 1100 kg (2400 lb) heavier overall than the translating centerbody inlets, because of the added mechanism required for the CCB inlet. The CCB inlets with the GE21/J11B20 engine were longer than their counterparts for the -B11 engine, because of the increased engine face diameter. This resulted in an overall weight difference of about 800 kg (1800 lb) between these CCB inlets.

Table 2 presents total pressure recovery and bleed drag at supersonic cruise conditions for the Mach 2.0 and Mach 2.3 inlets. The self-starting inlets showed higher total pressure recovery, as expected, because some internal compression allows lower shock losses for a given cowl angle than does all-external compression. The 2.0/2D/SS inlet with the GE21/J11B13 engine showed higher pressure recovery than with the GE21/J11B21 engine for two reasons: (1) a higher cowl angle, required to match the maximum engine air flow rate, allowed more efficient supersonic compression with a weaker cowl lip shock; (2) the longer subsonic diffuser was more efficient. It may be noted that the self-starting inlet with the GE21/J11B21 engine was optimized at lower pressure recovery by a trade with cowl drag.

Figure 11 shows the bleed flow correlation presented by Bowditch in reference 3. Some data points have been added for Mach 2.2, two-dimensional inlets, plus other labeled points. The NASA-Lewis bicone-type inlets (ref. 4; circles, lower line) do not correlate well with the other data. These bicone-type inlets would probably have to be operated with a stability bleed system, however.

In the present studies the performance of a number of inlets was being compared. It was therefore necessary to account for differences in wetted area and local Mach number in a consistent manner. The upper line was used to estimate bleed flow requirements, although it may be conservative.

Bleed drag coefficient, referenced to wing area, is given in table 2. The principal differences were between the external-compression and the self-starting inlets. These resulted from the differences in wetted area in the supersonic diffusers of these inlets.

The differences in spillage drag at off-design conditions for the various inlet-engine combinations emerged as one of the more significant factors affecting aircraft range. These differences are illustrated in figure 12 for the Mach 2.0 study cases. The conditions correspond to the local Mach number and engine air flow along the SCR climb profile. Results are shown for the overwing inlets only, which had greater spillage and bypass drag than the underwing inlets. This is because the underwing inlet was able to supply the maximum engine air flow, and had a smaller capture area.

For the external-compression inlets, excess inlet air flow was bypassed if the strong-oblique, cowl-lip shock was attached, and was spilled if this shock was detached. The local Mach number at which detachment occurs is about 1.65. For the mixed-compression inlets, excess inlet air flow was bypassed if the inlet was started, and spilled if it was unstarted. The local Mach number for unstart is also about 1.65.

The study revealed that these external-compression inlets could be operated with no subcritical spillage, and the bypass amounts were very small. Thus, nearly all of the drag was due to critical spillage. As expected, the spillage drag correlated inversely with $(W\sqrt{\theta}/\delta)_{M1}/(W\sqrt{\theta}/\delta)_{CRUISE}$. The engine with the higher relative transonic air flow, the GE21/J11B13, led to the lower spillage drag.

At local Mach numbers below 1.65, the self-starting inlets had some subcritical spillage because they still had some internal contraction. This caused the high spillage drag relative to the 2.0/2D/EX inlets, as shown in figure 12. Again, the relative spillage drag of the 2.0/2D/SS inlets correlated inversely with $(W\sqrt{\theta}/\delta)_{M1}/(W\sqrt{\theta}/\delta)_{CRUISE}$.

The remaining internal contraction in the self-starting inlets, when below the unstart Mach number, could be removed by a design modification. For example, another hinge could be provided on the forward ramp, plus suitable actuation. This would involve some weight penalty, but would probably be desirable if the spillage drag could be reduced to the level of the external-compression inlets. This will be further illustrated later by the results of the aircraft mission analyses.

The Mach 2.3 studies showed the same trends of spillage and bypass drag as for Mach 2.0. Again, the self-starting inlet had high subcritical spillage drag because of internal contraction at unstarted conditions.

Wave drag comparisons for the Mach 2.0 study cases are shown in figure 13. The figure shows wave drag coefficient for all four nacelles, referenced to wing area. For a given engine, the external-compression inlets have higher

wave drag, as expected, because of their larger external flow turning. For a given inlet type, the wave drag increases as $(W\sqrt{\theta}/\delta)_{M1}/(W\sqrt{\theta}/\delta)_{CRUISE}$ increases. This follows from the general need for higher cowl angles to match the larger engine diameter.

The results in figure 13 are for the isolated nacelles, as computed by the near-field wave drag method of reference 5. The far-field wave drag method of reference 5 was used to obtain complete aircraft wave drag for the 2.0/2D/EX - GE21/J11B13 installation. The near-field method was used to compute wave and interference drag for each nacelle configuration. The increments in these near-field values from the 2.0/2D/EX - GE21/J11B13 case were used to arrive at complete aircraft wave drag for the remaining cases. Friction drag was also computed by the methods of reference 5.

The same procedure was followed to establish wave drag for the Mach 2.3 study cases. The isolated nacelle results, comparing the 2.3/2D/EX and 2.3/2D/SS inlets with the GE21/J11B19 engine were similar to those shown in figure 13.

There is some uncertainty about the accuracy of the wave drag results, because the design methods are based on modifications to linearized theory and on superposition of solutions. The greater the shock strengths and turning angles for a nacelle installation, the greater the expected error. A related example was reported in reference 6, in which the cowl drag of an external-compression inlet was underestimated by using linearized theories. By contrast, the same linearized theories agreed with the method of characteristics in predicting the wave drag of a mixed-compression inlet, which had a smaller external cowl angle. This example suggests that the wave drag of the external-compression inlets studied here may also have been underestimated, relative to the self-starting inlets.

Aircraft performance was evaluated for each of the study cases. The mission profile is illustrated in figure 14. Subsonic cruise segments considered were zero (all-supersonic cruise), 1111 km (600 n. mi.), and 2778 km (1500 n. mi.). These subsonic cruise segments were divided into two equal parts, occurring before and after the supersonic cruise segment.

In figure 15, results of mission analyses are used to illustrate the effect of transonic-to-cruise corrected air flow ratio on aircraft range. The 2.0/2D/EX inlets had nearly the same installed SFC at supersonic cruise (table 3). The case with the GE21/J11B21 engine had lower wave drag and lower weight, however, leading to greater range. The same circumstances applied for the 2.0/2D/SS inlets, and the bicone-type, CCB inlets at Mach 2.55. Thus, for engines of the same family, increased $(W\sqrt{\theta}/\delta)_{M1}/(W\sqrt{\theta}/\delta)_{CRUISE}$ yields reduced range. The responsible factors seem to be the higher wave drag, and higher weight that accompany higher transonic-to-cruise corrected air flow ratios.

Further reductions in corrected air flow ratio are now being explored. This will indicate whether range goes through a maximum with respect to corrected air flow ratio, and the nature of the controlling factors. Takeoff noise requirements may also limit reductions in corrected air flow ratio.

The effects of subsonic cruise distance on aircraft range were also explored. It is desirable for a supersonic transport aircraft to have efficient subsonic cruise capability, to enhance its usefulness for both overwater and overland operations. Any effects of inlet type on aircraft range for mixed supersonic and subsonic cruise are then potentially important.

Figure 16 shows total range as a function of subsonic cruise distance for the Mach 2.0 aircraft study cases. The aircraft with 2.0/2D/EX inlets showed small increases in range as subsonic cruise distance increased. This trend was a result of the relative values of $(M_o/SFC)(L/D)$ for supersonic and subsonic cruise. Average values of SFC and L/D are given in table 3. In contrast, the aircraft with the 2.0/2D/SS inlets showed a small decrease in range as subsonic cruise distance increased. From table 3 it is apparent that $(M_o/SFC)(L/D)$ for the 2.0/2D/SS inlets is slightly higher at supersonic cruise, and substantially lower at subsonic cruise, compared with the 2.0/2D/EX inlet cases. The subcritical spillage of the 2.0/2D/SS inlets, which was responsible for the higher subsonic SFCs, explains this behavior. As suggested earlier, this subcritical spillage could be eliminated by modifying the self-starting inlet to have no internal contraction at subsonic cruise. This would add weight, but would produce a more favorable variation of total range with subsonic cruise distance.

Mission results for the Mach 2.3 aircraft cases are shown in figure 17. Again, the behavior is due to the relative values of M_o/SFC at supersonic and subsonic cruise. For the aircraft with the 2.3/2D/EX inlet, the large relative improvement in M_o/SFC at subsonic cruise produced increases in range as subsonic cruise distance increased. For the aircraft with the 2.3/2D/SS inlets, the subcritical spillage greatly increased subsonic cruise SFC. The resulting unfavorable effect on subsonic M_o/SFC yielded a significant decrease in range as subsonic cruise distance increased. As for the Mach 2.0 cases, modification of the 2.3/2D/SS inlet to eliminate subcritical spillage at Mach 0.9 would greatly improve this situation.

These considerations of subsonic cruise distance indicate the importance of inlet performance at subsonic cruise conditions. In particular, it is important that inlets be designed to minimize spillage drag at subsonic cruise. In this connection, figure 16 also reveals that differences due to $(W\sqrt{\theta}/\delta)_{M1}/(W\sqrt{\theta}/\delta)_{CRUISE}$ became smaller as subsonic cruise distance increased. This resulted from the lower spillage drag associated with higher $(W\sqrt{\theta}/\delta)_{M1}/(W\sqrt{\theta}/\delta)_{CRUISE}$. Again, the importance of accurate estimation of spillage effects on nacelle-airframe interference should be noted.

The factors influencing the choice of 2.0/2D/EX inlets or 2.0/2D/SS inlets can now be summarized. The external-compression and self-starting inlets had nearly the same supersonic cruise SFC. The self-starting inlets were heavier because of their greater length. The small range advantage of the self-starting inlets at supersonic cruise was then a result of their lower wave drag. As noted before, however, the wave drag difference between the 2.0/2D/EX and the 2.0/2D/SS inlets may have been too low, thus possibly narrowing the range increment for all-supersonic cruise.

The external-compression inlets showed an advantage at subsonic cruise because of their capacity to operate at critical conditions, and so minimize spillage drag. For the 2.0/2D/SS inlets, their subcritical spillage drag could be eliminated at the cost of some added mechanical complexity.

In addition to performance factors, it is necessary to consider relative mechanical complexity and flow stability. Here the advantage goes to the external-compression inlets. More effort could be expected to develop a self-starting design than an external-compression design.

On balance, the external-compression inlets are the probable first choice for the Mach 2.0 aircraft. Their small supersonic cruise range deficit is offset by their simplicity and their relatively high performance at subsonic cruise. Thus, a lower technology approach seems adequate for the Mach 2.0 aircraft. For now, however, this conclusion must be qualified by the uncertainty in installed wave drag and spillage effects. Also, the results of the axisymmetric inlet studies may alter this conclusion.

For the Mach 2.3 aircraft, the 2.3/2D/SS inlet had a more distinct advantage at supersonic cruise. This was partly due to its lower wave drag, but mainly due to its lower SFC. Remaining trade-offs were similar to those of the Mach 2.0 aircraft. Thus, the external-compression inlet had somewhat lower weight, had greater flow stability, and had lower spillage drag at subsonic cruise. The 2.3/2D/SS inlet also had the capacity to eliminate subcritical spillage at subsonic cruise conditions at the cost of extra complexity. Finally, the wave drag difference between the 2.3/2D/EX and the 2.3/2D/SS inlets may have been underestimated.

On balance, the higher technology self-starting inlets are the probable first choice for the Mach 2.3 aircraft, if they are modified to minimize subcritical spillage. This is based on their superiority at supersonic cruise, and their potential for relatively high performance at subsonic cruise. The requirement for low spillage drag at subsonic cruise does impose additional complexity on the self-starting inlets, however.

Airframe-propulsion system interference effects are significant for aircraft performance and for design of components such as the inlet. This is apparent from the importance of wave drag and inlet spillage in the present results, and from many other studies. Further study is needed to assess and improve existing design methods for airframe-propulsion system interference, as these methods are largely based on linearized theory and modifications thereof. Examples of possible areas of improvement are in location of interference shocks and description of wave reflections, inlet spillage streamline shapes, and effects of inlet bypass and bleed flows.

CONCLUSIONS

- For the configurations studied, increased $(W\sqrt{\theta}/\delta)_{M1}/(W\sqrt{\theta}/\delta)_{CRUISE}$ gave decreased range for missions dominated by supersonic cruise. Reductions in corrected air flow ratio may be limited by takeoff noise requirements and by the need to minimize spillage at subsonic cruise, however.

- It is important that inlets be designed to minimize spillage drag at subsonic cruise, because of the need for relatively efficient subsonic cruise performance for overland operations. External-compression inlets seem to have an advantage in this respect.

- The external-compression inlet emerged as the probable first choice for the Mach 2.0 aircraft, while the self-starting inlet was the probable first choice at Mach 2.3. This indicated a change in inlet technology level between these Mach numbers.

- Airframe propulsion system interference effects (e.g., installed wave drag and inlet spillage flow) are significant for aircraft performance and for design of components such as the inlet. Further study is needed to assess existing design methods and to develop improvements.

REFERENCES

1. Wright, B. R., et al, "Supersonic Cruise Vehicle Technology Assessment Study of an Over/Under Engine Concept," NASA-CR-159003, Lockheed-California Company, December 1978.

2. Miller, L. D., "Supersonic Cruise Vehicle Inlet Design for Variable Cycle Engines," Lockheed-California Company, LR 27854, November 1976.

3. Bowditch, D. N., "Some Design Considerations for Supersonic Cruise Mixed-Compression Inlets," AIAA Paper No. 73-1269, November 1973.

4. Wasserbauer, J. F., Shaw, R. J., and Neumann, H. E., "Design of a Very-Low-Bleed Mach 2.5 Mixed-Compression Inlet with 45 Percent Internal Contraction," NASA-TM-X-3135, March 1975.

5. Middleton, W. D., Lundry, J. L., and Coleman, R. G., "Aerodynamic Design and Analysis System for Supersonic Aircraft," NASA CR-2520, 2521, 2522 March 1975.

6. Welge, H. R., Radkey, R. L., and Henne, P. A., "Nacelle Aerodynamic Design and Integration Study on a Mach 2.2 Supersonic Cruise Aircraft," AIAA Paper 76-757, AIAA/SAE 12th Propulsion Conference, July 1976.

TABLE 1. - ENGINE CYCLE CHARACTERISTICS

Engine	GE 21/J11B13	GE 21/J11B21	GE 21/J11B19
Cruise Mach No.	2.0	2.0	2.3
Oversize front fan (percent)	20	10	10
Augmentor	Afterburner	Afterburner	Afterburner
$(W\sqrt{\theta}/\delta)_{M1}/(W\sqrt{\theta}/\delta)_{CRUISE}$	1.32	1.23	1.45
$(W\sqrt{\theta}/\delta)_{CRUISE}$ (KG/SEC)	224	225	186
$(T/W)_{T/O}$	0.265	0.265	0.265
Bypass ratio	0.35	0.35	0.25
Overall cycle pressure ratio	18.8	18.1	16.0
Fan pressure ratio	3.7	3.5	3.7
Front fan diameter (M)	1.56	1.45	1.50

TABLE 2. - INLET PRESSURE RECOVERY AND BLEED DRAG AT SUPERSONIC CRUISE CONDITIONS

Configuration	1614 – 10A	1614 – 10C	1614 – 11A	1614 – 11C	1631 – 1A	1631 – 1C
Inlet	2.0/2D/EX	2.0/2D/SS	2.0/2D/EX	2.0/2D/SS	2.3/2D/EX	2.3/2D/SS
Engine	GE 21/J11B21	GE 21/J11B21	GE 21/J11B13	GE 21/J11B13	GE 21/J11B19	GE 21/J11B19
P_{T2}/P_{TO} (OW/UW)	0.916/0.940	0.932/0.943	0.916/0.940	0.946/0.953	0.867/0.894	0.913/0.933
C_D, bleed (4 inlets)	0.000292	0.000402	0.000291	0.000419	0.000306	0.000452
Internal compression, percent	0	42	0	42	0	35

TABLE 3. - INSTALLED SPECIFIC FUEL CONSUMPTION AND LIFT-DRAG RATIO

Configuration	1614 – 10A	1614 – 10C	1614 – 11A	1614 – 11C	1631 – 1A	1631 – 1C
Inlet	2.0/2D/EX	2.0/2D/SS	2.0/2D/EX	2.0/2D/SS	2.3/2D/EX	2.3/2D/SS
Engine	GE 21/J11B21	GE 21/J11B21	GE 21/J11B13	GE 21/J11B13	GE 21/J11B19	GE 21/J11B19
Supersonic cruise:						
Avg. SFC						
~KG/HR/daN (LBM/HR/LB)	1.273 (1.248)	1.266 (1.241)	1.276 (1.251)	1.265 (1.240)	1.450 (1.422)	1.373 (1.346)
Avg. L/D	8.2	8.3	8.0	8.1	7.8	7.8
Subsonic cruise:						
Avg. SFC						
~KG/HR/daN (LBM/HR/LB)	1.048 (1.027)	1.122 (1.100)	1.054 (1.033)	1.115 (1.093)	1.087 (1.066)	1.177 (1.154)
Avg. L/D	14.1	14.1	14.1	14.1	13.9	13.9

INTERNAL CONTRACTION	M2.0 2D	M2.0 AXI	M2.3 2D	M2.3 AXI	M2.55 2D	M2.55 AXI
NONE	✓	*	✓			
SMALL (SELF-STARTING)	✓	*	✓	*	✓	
LARGE (VARIABLE GEOMETRY FOR RESTART)						✓

✓ STUDY COMPLETED
* STUDY IN PROGRESS

Figure 1.- Study configurations.

- HIGHER $(W\sqrt{\theta}/\delta)_{M1}/(W\sqrt{\theta}/\delta)_{CRUISE}$ IMPLIES:

(+)	(−)
LOWER JET NOISE	HIGHER ENGINE WEIGHT
HIGHER TRANSONIC THRUST	HIGHER INLET WEIGHT
LOWER SPILLAGE/BYPASS DRAG	HIGHER WAVE DRAG

- POSITIVE FACTORS APPLY MAINLY AT OFF-DESIGN MACH NUMBERS
- NEGATIVE FACTORS APPLY AT ALL MACH NUMBERS

Figure 2.- Effects of transonic-to-cruise corrected air flow ratio.

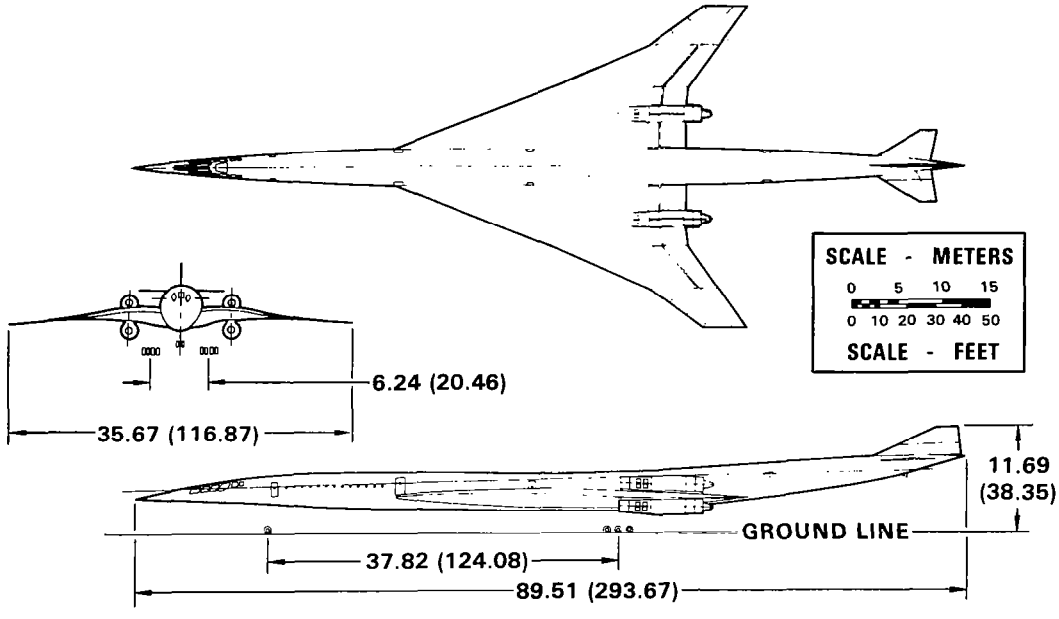

Figure 3.- General arrangement Mach 2.0 SCR vehicle.

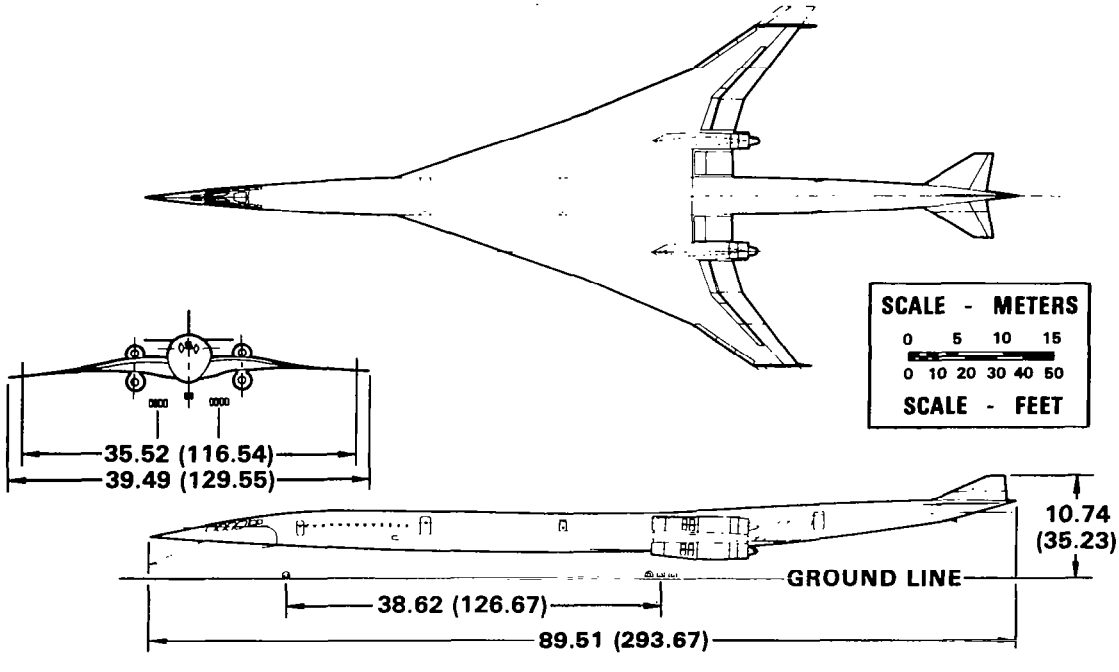

Figure 4.- General arrangement Mach 2.3 SCR vehicle.

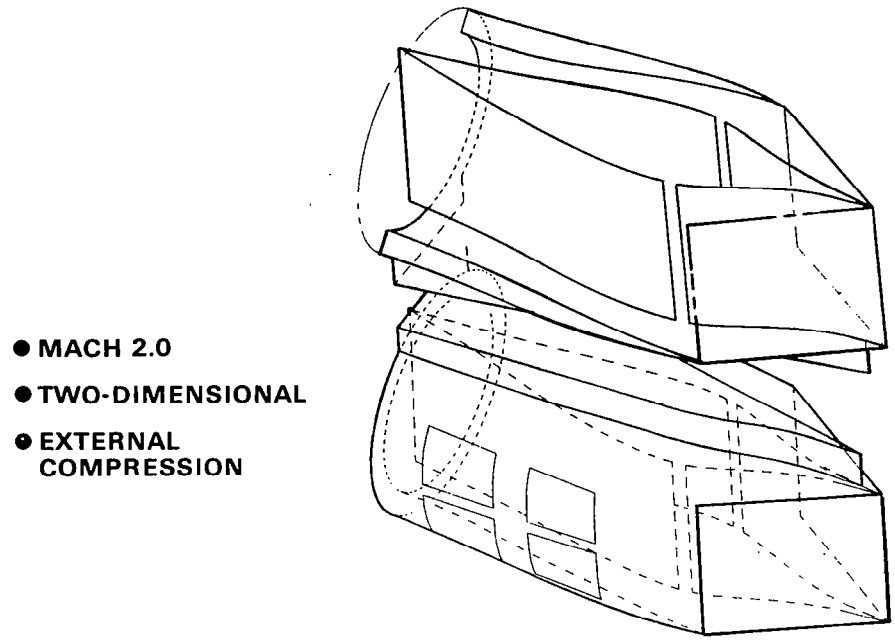

Figure 5.- 2.0/2D/EX inlet.

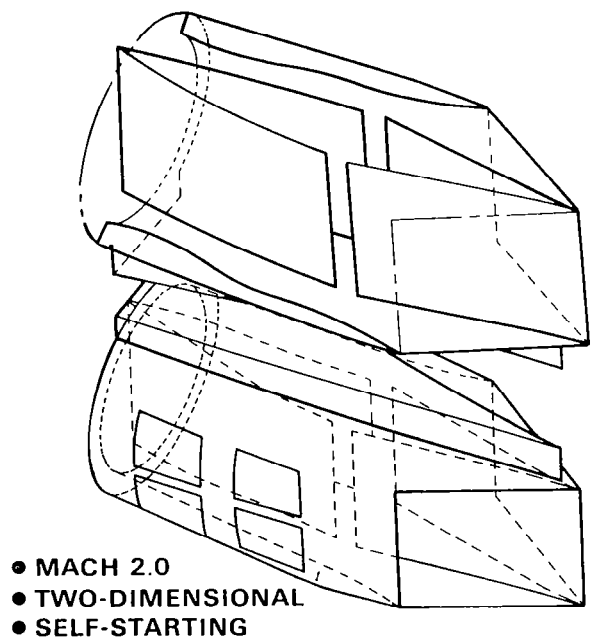

Figure 6.- 2.0/2D/SS inlet.

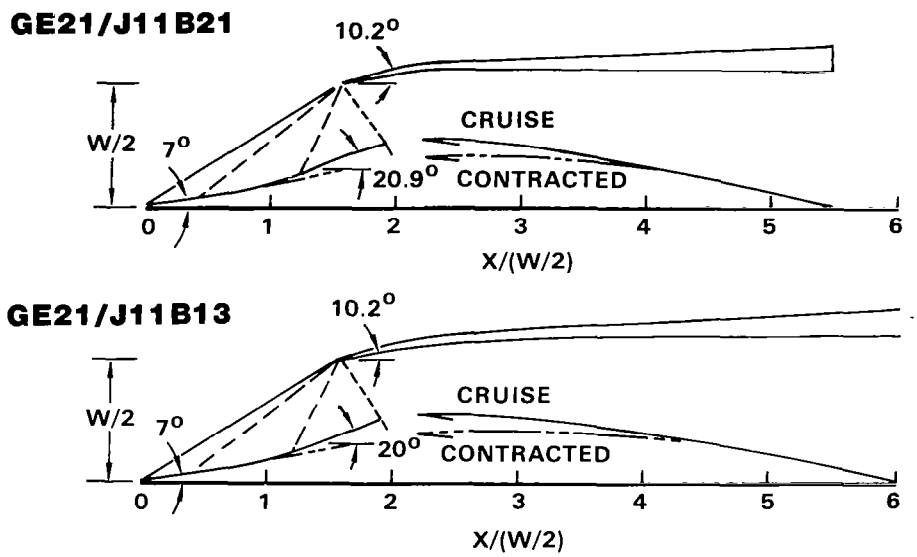

Figure 7.- 2.0/2D/EX inlet contours.

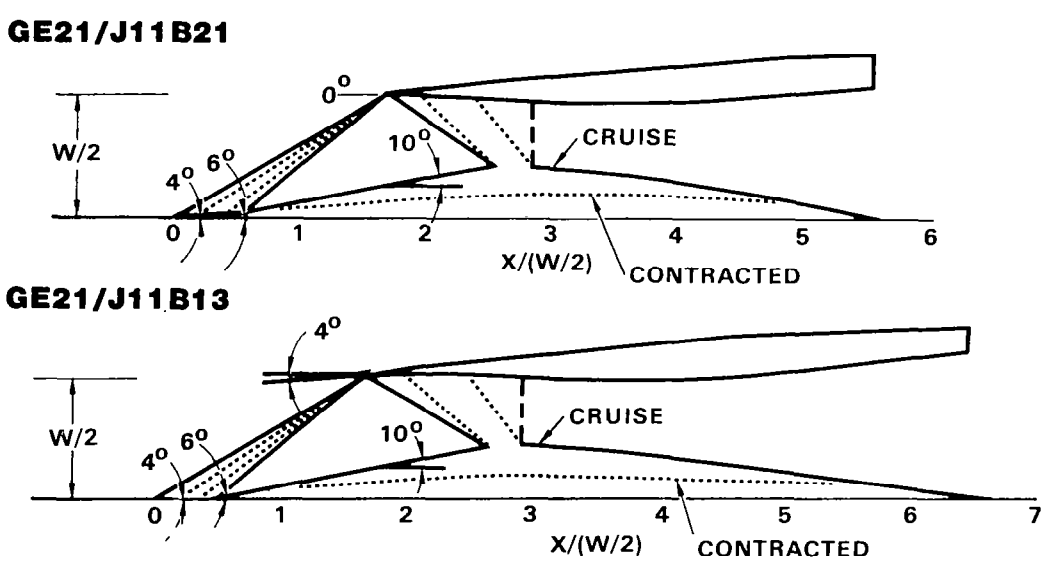

Figure 8.- 2.0/2D/SS inlet contours.

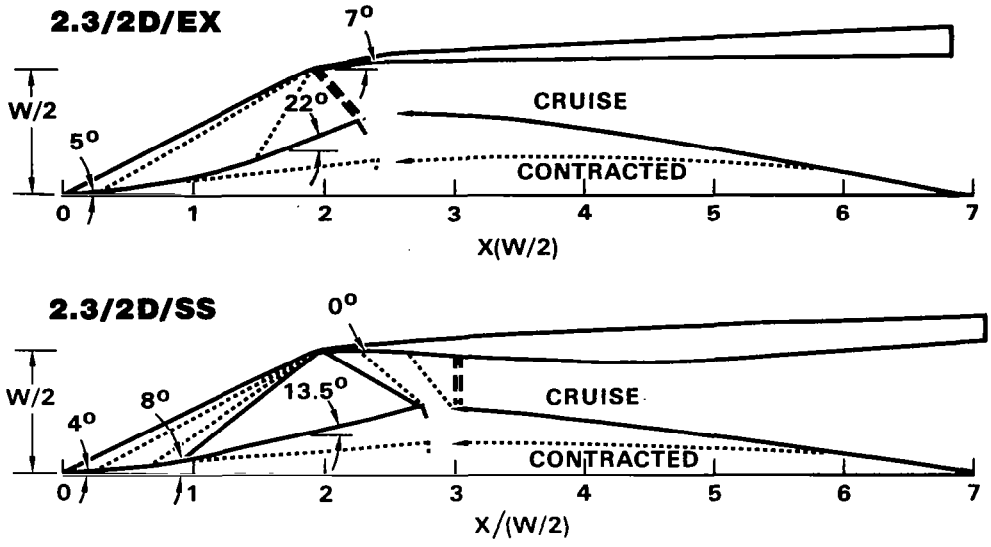

Figure 9.- Mach 2.3 inlet contours.

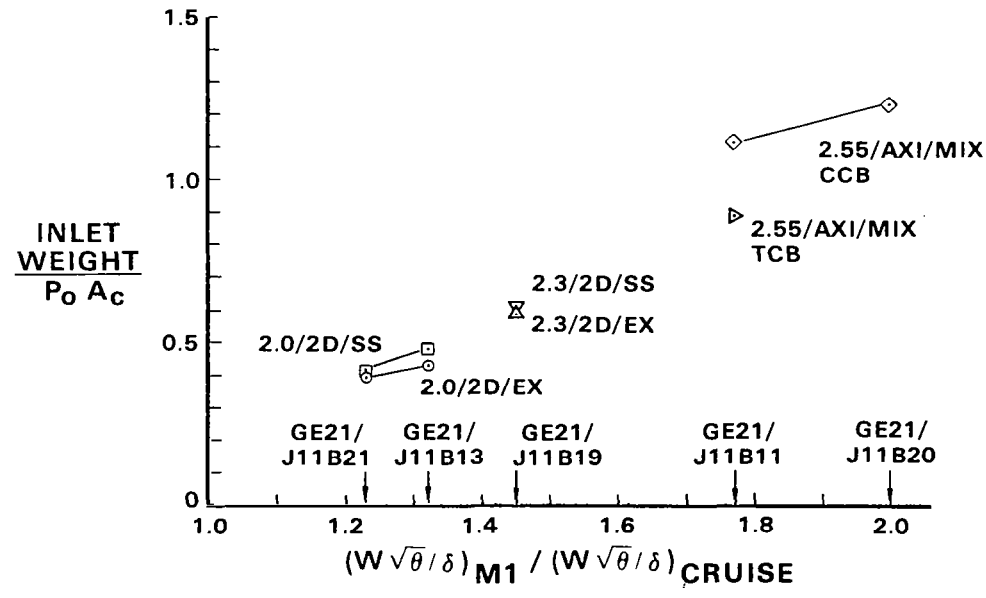

Figure 10.- Inlet weight.

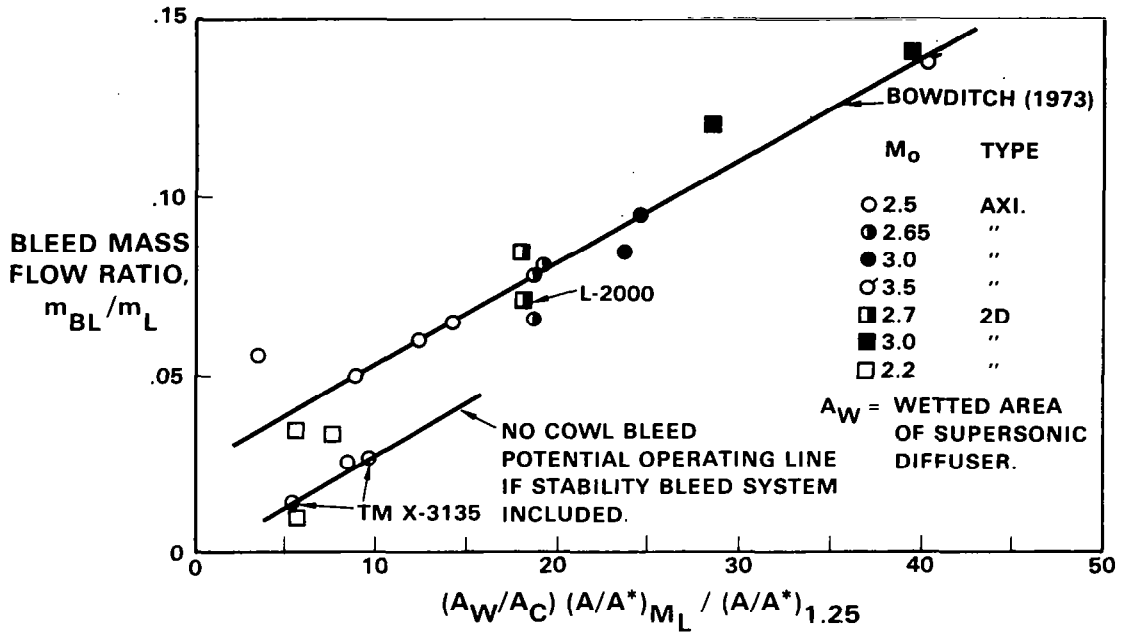

Figure 11.- Inlet bleed flow correlation.

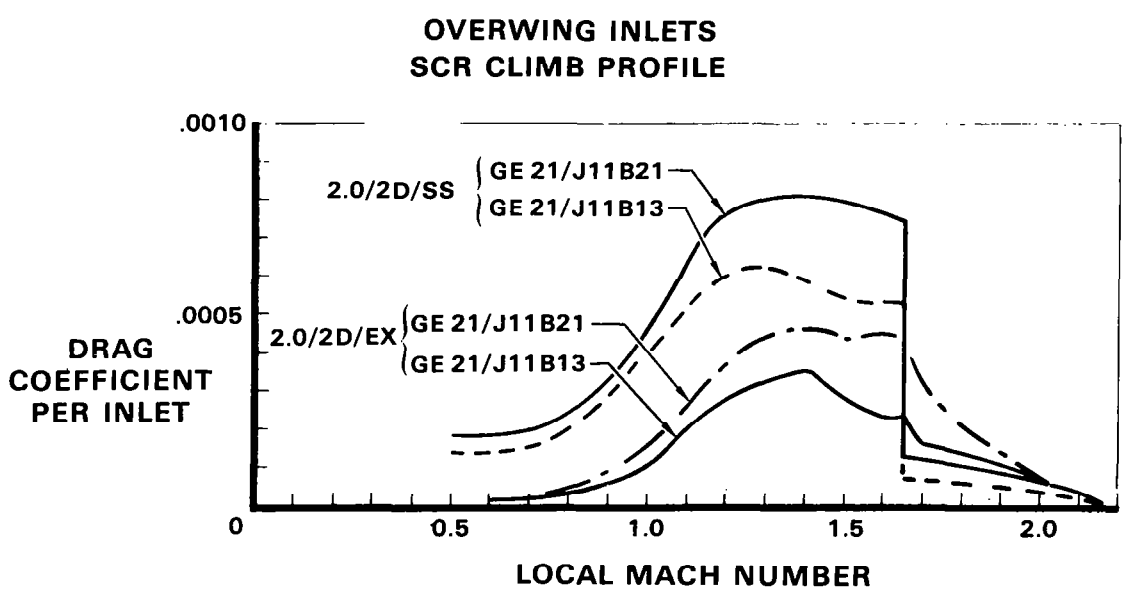

Figure 12.- Inlet spillage and bypass drag.

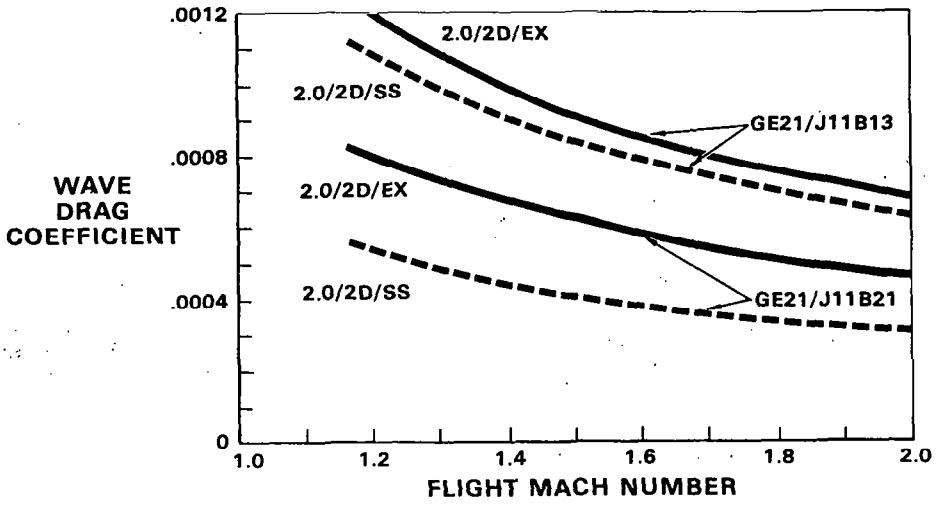

Figure 13.- Nacelle external pressure drag.

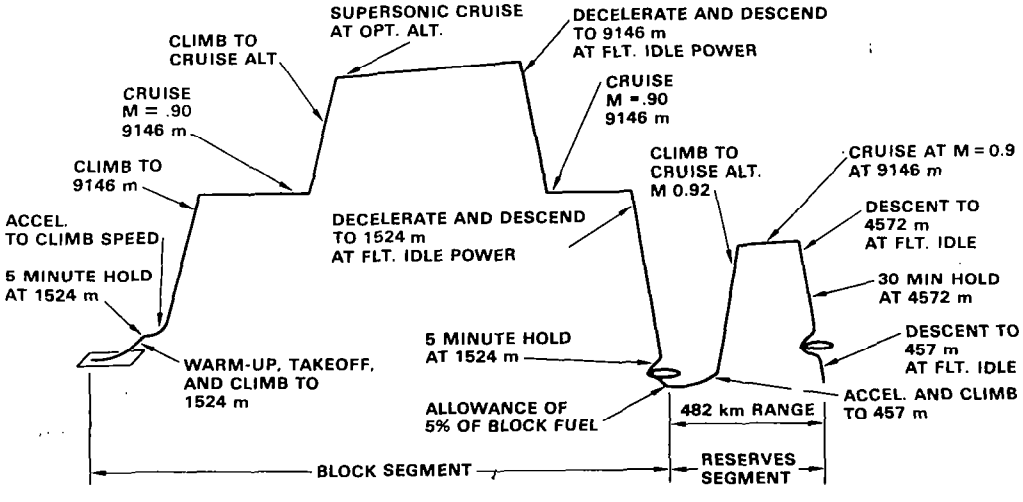

Figure 14.- SCR mission profile.

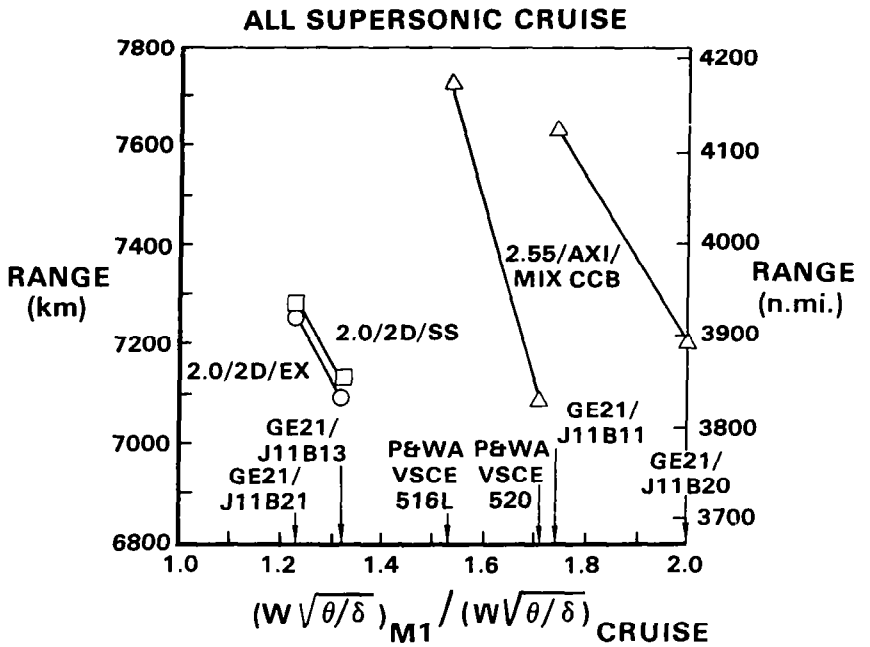

Figure 15.- Effect of corrected air flow ratio on range.

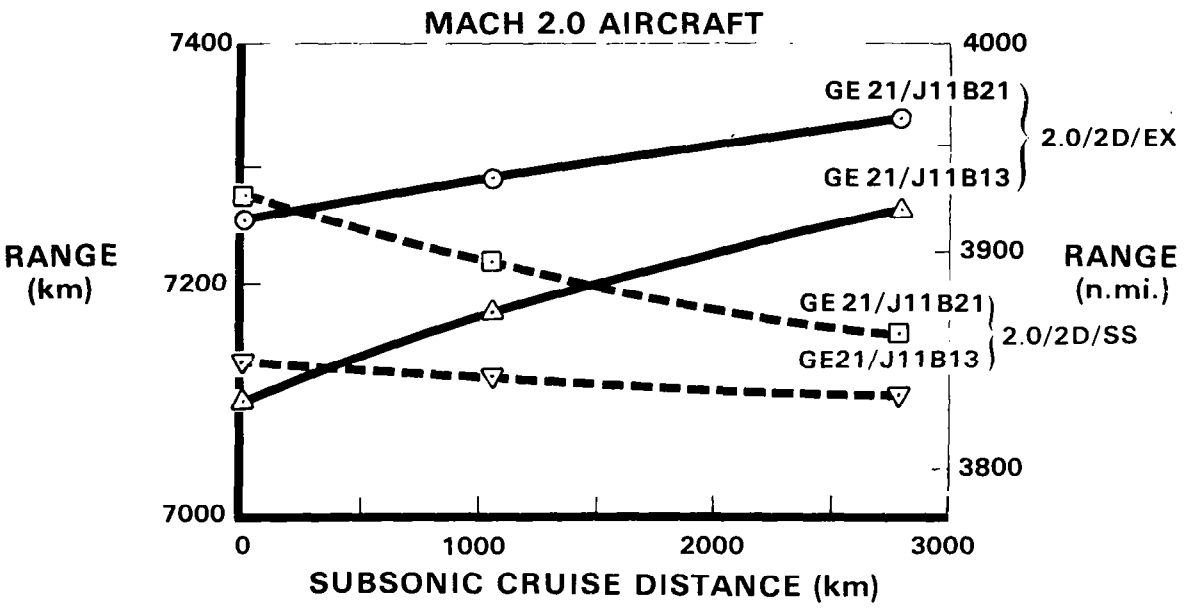

Figure 16.- Effect of subsonic cruise on range for Mach 2.0 aircraft.

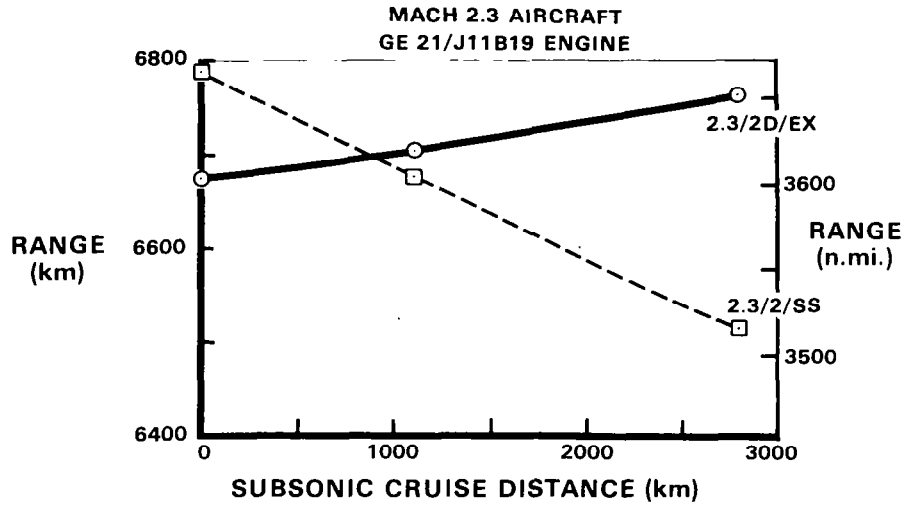

Figure 17.- Effect of subsonic cruise on range for Mach 2.3 aircraft.

SESSION IV - ENVIRONMENTAL FACTORS

INTRODUCTORY REMARKS

R. W. Schroeder
NASA Lewis Research Center

We will now proceed with the Environmental Factors Session. As all of those who have been associated with the SCR program are fully aware of, satisfying the noise and emission constraints without unduly penalizing airplane performance and economics has been, and continues to be, a major challenge. The preceding speakers clearly established that environmental considerations have a major influence on propulsion system cycle selection. Environmental factors also have a strong influence on propulsion system installation and power control/flight path optimization. In this session we will present four papers dealing with various aspects of the noise problem and two papers dealing with emissions.

VCE EARLY ACOUSTIC TEST RESULTS OF GENERAL ELECTRIC'S HIGH-RADIUS RATIO COANNULAR PLUG NOZZLE+

Paul R. Knott, J.F. Brausch, P.K. Bhutiani,
R.K. Majjigi, V.L. Doyle
General Electric Co., Cincinnati, Ohio

SUMMARY

Results of NASA Lewis Research Center/General Electric Company Variable Cycle Engine (VCE) early acoustic engine and model scale tests are presented. A summary of an extensive series of far-field acoustic, advanced acoustic, and exhaust plume velocity measurements with a laser velocimeter of inverted velocity and temperature profile, high-radius-ratio coannular plug nozzles on a YJ101 VCE static engine test vehicle are reviewed. Select model scale simulated flight acoustic measurements for an unsuppressed and a mechanical suppressed coannular plug nozzle are also discussed. The engine acoustic nozzle tests verify previous model scale noise reduction measurements. The engine measurements show 4-6 PNdB aft quadrant jet noise reduction and up to 7 PNdB forward quadrant shock noise reduction relative to a fully mixed conical nozzle at the same specific thrust and mixed pressure ratio. The influences of outer nozzle radius ratio, inner stream velocity ratio, and area ratio are discussed. Also, laser velocimeter measurements of mean velocity and turbulent velocity of the YJ101 engine are illustrated. Select model scale static and simulated flight acoustic measurements are shown which corroborate that coannular suppression is maintained in forward speed. In addition, the outlook for achieving jet noise abatement levels for high performance supersonic aircraft on the order of current subsonic commercial vehicles is discussed.

INTRODUCTION

Over the past decade, government and industry have exerted considerable research and technology efforts toward developing understanding of jet noise generation, concepts for its reduction, and practical means for suppressor implementation. In particular, the General Electric Company, under NASA-Lewis sponsorship, has undertaken extensive model scale and engine acoustic test programs (References 1,2, and work done under contract by J. Vdoviak, P.R. Knott, et al., entitled "VCE Early Acoustic Test - Forward Variable Area By Pass Injector and Coannular Acoustic Nozzle Test," to be published in 1980) to quantify the static and flight acoustic and aerodynamic characteristics for inverted velocity and temperature profile coannular plug nozzles, unsuppressed and suppressed.

+ The work reported here was sponsored by the NASA Lewis Research Center under Contracts NAS3-20582 and NAS3-21608.

This paper reviews an extensive series of static engine acoustic tests using General Electric's variable cycle engine (VCE) features tested on a modified YJ101 engine propulsion system in October of 1978. These results show that for unsuppressed high-radius-ratio coannular plug nozzles, substantial static jet mixing and shock noise reduction is obtained in engine scale. The paper also shows that for simulated flight, this level of noise reduction is maintained. In addition, a projected outlook for achieving greater jet noise reduction for SCR vehicles on the order of current subsonic commerical aircraft is briefly discussed.

The authors express their appreciation to Al Powers, Jim Stone, Orlando Gutierrez, Howard Wesoky, and Jack Whitlow of NASA-Lewis Research Center for their high interest in the word accomplished, their probing questions, and their expectancy of technical excellence.

SYMBOLS

Values are given in SI units.

A_o	ambient speed of sound; m/sec
A_r^i	nozzle system area ratio (Inner stream nozzle area/Outer stream area); dimensionless
a	speed of sound; m/sec
c_j	speed of sound of core stream, m/sec
c_{sj}	speed of sound of the thermal acoustic shield, m/sec
EPNL	effective perceived noise level, EPNdB
F	ideal total thrust, newtons
F_i	freefield SPL, dB
F_{ref}	reference thrust, newtons
G_i	ground plane measured SPL, dB
i	index of one-third octave band
$\dot{m}_j^i$	ideal inner stream (or far stream) mass flow rate, grams/sec
$\dot{m}_j^o$	ideal outer stream (or core stream) mass flow rate, grams/sec

$\dot{m}_T$	ideal total mass flow rate $(\dot{m}_j^o + \dot{m}_j^i)$, grams/sec
Pi	engine centerline measured SPL, dB
P_r^{eff}	effective pressure ratio for coannular nozzles, dimensionless
P_r^i	inner stream (or fan stream) nozzle pressure ratio, dimensionless
P_r^o	outer stream (or core stream) nozzle pressure ratio, dimensionless
PNL	perceived noise level, PNdB
PNLN	normalized perceived noise level re: $10 \log \left\{ \frac{F}{Fref} \left(\frac{\rho_j^{mix}}{\rho_o} \right)^{\omega-1} \right\}$, PNdB
R_i	ground plane microphone weighting factor (see table 1)
R_r^o	outer stream radius ratio (defined as a ratio of the radius to the throat inner diameter to the radius to the throat outer diameter of the nozzle), dimensionless
S_i	engine centerline microphone weighting factor (see table 1)
SPL	sound pressure level, dB
u'	laser velocimeter measured turbulence velocity (axial direction), m/sec
u_p	laser velocimeter measured peak mean velocity, m/sec
$\bar{U}$	laser velocimeter mean velocity (axial direction), m/sec
V_j^i	ideal inner stream (or fan stream) velocity, m/sec
V_j^o	ideal outer stream (or core stream) velocity, m/sec
V_j^{mix}	specific thrust (defined as a ratio of the ideal total thrust to the ideal total mass flow rate) $\frac{\dot{m}_j^o V_j^o + m_j^i V_j^i}{\dot{m}_T}$, m/sec
V_{sj}	velocity of the thermal acoustic shield, m/sec

V_r^i velocity ratio (V_j^i/V_j^o), dimensionless

β_j^{mix} $\left\{\left[\left(P_r^{eff}\right)^{\frac{\gamma-1}{\gamma}} -1\right] \frac{2}{\gamma-1} -1\right\}$, dimensionless

where $P_r^{eff} \equiv \frac{P_r^o + P_r^i A_r^i}{1 + A_r^i}$; $\gamma = 1.4$

TEST APPARATUS AND DATA REDUCTION PROCEDURES

The test results presented in this paper were obtained from two facilities: 1) General Electric's/Edwards Air Force Base Out Door Engine Test Facility, and 2) General Electric's Model Scale Anechoic Free-Jet Test Facility. Discussed below are brief descriptions of these facilities and the basic test arrangements and data reduction procedures used in processing the data.

General Electric/Edwards Air Force Base Out Door Engine Test Facility

For all the engine tests presented, the General Electric/Edwards Flight Test Center North Test Site was used. Figure 1 shows the general layout of the test site showing the concrete paved sound field. It has a 48.77 m (160 ft) forward quadrant radius and a 82.3 m (270 ft) aft quadrant radius with a 22.86 m (75 ft) lateral sideline connecting the two arcs. Figure 2 shows the YJ101 engine with a treated inlet for eliminating fan inlet radiated noise and a baseline conical nozzle. Figure 3 shows the inverted velocity and temperature high-radius-ratio coannular plug nozzle configuration. Figures 4 and 5 show the G.E. laser velocimeter system and a NASA Ames sideline traversing microphone systems used for diagnostic velocity profile and noise identification respectively.

A typical sound field microphone layout for the engine test results is illustrated in Figure 6. It consists of a 30.48 m (100 ft) radius microphone array at 10° increments from 10° to 160° and a 21.34 m (70 ft) lateral sideline array with ground plane microphones located at θ_i=35°, 115°, 125°, 135°, 145°, 150°, 155°, 160°, and 165°. For the 30.48 m (100 ft) radius arrangement, engine centerline height microphones and ground plane microphones were used as illustrated in Figure 7. For these measurements the farfield arc data gathered from the two-microphone system were corrected to free-field and merged using the following scheme:*

* The method selected for the two microphone merging was based on information provided by the Boeing Airplane Company in Seattle, Washington.

$$F_i = R_i\ (G_i-6) + S_i\ (P_i-3)$$

where

i = index of one-third octave band
F_i = freefield SPL
G_i = ground plane measured SPL
P_i = engine centerline measured SPL
R_i = ground plane microphone weighting factor (see Table 1)
S_i = engine centerline microphone weighting factor (see Table 1)

Figure 8 shows an illustration of this spectral merging technique for typical conical and coannular plug nozzle measurements.

General Electric Model Scale Anechoic Free-Jet Test Facility

For Model scale static and simulated flight acoustic test measurements, the General Electric Company has developed a large free-jet anechoic test facility (References 3,4, and 5). Figure 9 shows a schematic diagram of facility. The General Electric facility is one of the largest of its type in the United States. The chamber is 22 meters (72 ft) high and 13 meters (42 ft) in diameter. The anechoic characteristics are 220 Hz cut off frequency, 0.99 absorption coefficient for frequencies above 220 Hz, and the chamber ambient noise less than 40 dB. The air supply system permits scale model jet nozzles with an equivalent diameter of up to 152 millimeters (6 in.), for single or coannular jet nozzle configuration - statically and in simulated flight up to $V_{a/c} \approx 122$ m (400 fps).

TEST RESULTS AND DISCUSSION

Under two NASA-Lewis sponsored small-scale model nozzle test programs (References 1,2, and 6), substantial jet and shock noise reduction (4-6 PNdB static) at good thrust coefficients (C_{fg} = .974 at a take-off Mach number of .36) has been observed. Described below are verifications of these test results for a YJ101 engine using a unique high-radius-ratio plug nozzle exhaust system designed for an inverted velocity profile. Other engine test results and simulated flight measurements from model scale free-jet tests are also covered.

Verification of Coannular Plug Nozzle Jet and Shock Noise Reduction

Figures 10 and 11 illustrate the YJ101 engine coannular plug nozzle jet and shock noise reductions presented on a typical product engine size of .9032 m^2 (1400 in^2) and at an acoustic range of 731.5 m (2400 ft) sideline. Figure 10 shows the measured peak PNL jet noise reduction relative to the conical nozzle baseline for all the engine test results. The ordinate is peak PNL normalized with respect to ideal total thrust and static jet density, while

the abscissa is the ideal specific thrust, defined as the ideal total thrust divided by the total weight flow. The results show that in the range of 488 m/sec (1600 fps) to 701 m/sec (2300 fps), an average of 4 to 6 PNdB coannular plug nozzle jet noise reduction is realized. In the lower specific thrust range (381 m/sec (1250 fps)), the engine coannular plug nozzle jet noise benefit is observed to diminish due to engine operation at off-optimum velocity ratio.

Figure 11 shows the PNL at $\theta_i=50^o$ as a function of shock strength parameter, β_j^{mix}, for the engine tests. One notes an almost uniform 7 PNdB static shock noise reduction for the coannular plug nozzle over the conic nozzle in the range of interest (10 log β_j^{mix} = -3 to 0).

For an illustration of the typical field shape and spectral characteristics between the engine baseline conical nozzle and coannular plug nozzles, Figures 12 and 13 are presented. The results show that the inverted velocity profile coannular plug nozzle jet noise reduction is measured at all observation angles and over all frequency bands.

Influence of Coannular Plug Nozzle Geometry on Jet Noise Reduction

Two key coannular plug nozzle geometric parameters which influence the jet noise signature and which are important to the mechanical design engineer are the outer stream radius-ratio (R_r^o) and the inner stream to outer stream area (A_r^i). Engine tests included nozzles of R_r^o = .816, .853, and .875 at an A_r^i = .2, and A_r^i = .475, .2, .1, ~0 at an R_r^o = .853. Figures 14 and 15 illustrate the results of these engine acoustic measurements.

Shown in Figure 14 are the results of the radius ratio study. These engine acoustic measurements show that at high specific thrust (533 m/sec(1749 fps) to .762 m/sec (2500 fps)), the reduction of PNL at the same specific thrust is due to increasing R_r^o. The results indicate that the coannular plug nozzle jet noise reduction is close to a 6th power law on radius ratio.

Figure 15 presents the engine test results for the area ratio study. In the specific thrust range of 381 m/sec (1250 fps) to 610 m/sec (2000fps), the trend observed is that as A_r^i decreases, so does the peak PNL jet noise. At the higher specific thrusts (610 m/sec (2000 fps) to 700 m/sec (2296 fps)), the A_r^i = .2 shows the lowest noise, the A_r^i = .1 about ½ PNdB higher, and the A_r^i ~ 0 about 1.5 PNdB higher than the A_r^i = .2 data. This would correspond to a $-1.39 * \log_{10} (1+A_r^i)$ dependency for peak angle jet noise at typical takeoff sideline engine cycle conditions.

ACOUSTIC SCALING RESULTS

To illustrate acoustic scaling of typical model scale test measurements taken in General Electric's anechoic free-jet and compared with the YJ101 engine measurements for a conical nozzle and coannular plug nozzle, the following results are shown. Figures 16 and 17 show comparisons of normalized peak PNL from model and YJ101 engine tests for a conical and coannular plug nozzles (R_r^o = .853 and A_r^i = .2). All data have been scaled to typical product engine size and acoustic range. Excellent agreement is observed for both the configurations. Figures 18 and 19 show engine and model test comparisons for a coannular plug nozzle at a specific thrust of approximately 594 m/sec (1950 fps). Figure 18 compares PNL directivity whereas Figure 19 compares spectra at θ_1=50°, 90°, 130°. Again good scaling is observed.

THEORY DATA COMPARISONS AND EPNL PROJECTIONS

Theory Data Comparisons

Under NAS3-20619, a unique coannular jet and shock noise prediction method was developed (Reference 8). The prediction procedure developed was evolved from a modern theoretical acoustic point-of-view using experimentally determined information from model tests for a universal source spectrum at θ_i=90° and fluid acoustic shielding function. Figures 20 through 22 illustrate the theory/engine data comparisons for a coannular plug nozzle.

Shown in Figure 20 are engine acoustic measurements compared with predictions of OASPL for three engine conditions (typical of takeoff sideline, cut-back and approach conditions). The data/theory comparisons are at actual YJ101 engine size. Spectral data/theory comparisons for the take-off sideline condition and the cut-back condition are shown in Figure 21 and 22, respectively. The comparisons between theory and measurement are observed to be quite good.

EPNL Sensitivity Study

To assess the inflight signature of coannular plug nozzle jet mixing and shock noise, flight effects were applied to the measured engine noise data scaled to a product engine size. Several methods were used in this sensitivity study (see References 8 to 10). Figure 23 illustrates the projected EPNL's for a typical sideline noise condition. Table 2 gives the projected differences in EPNL between the conic nozzle and the coannular plug nozzle for typical sideline, cutback and approach conditions for the test points described in Table 3. This sensitivity study showed that regardless of the methods used, the projected variations in EPNL were not large at all (∿ ± 1.5 EPNL), and

that typical EPNL differences between the conic nozzle and coannular plug nozzle are about 5-6 EPNL.

VERIFICATION OF FLIGHT JET NOISE REDUCTION FROM RECENT MODEL SCALE FREE-JET TESTS

To substantiate flight jet noise reduction for coannular plug nozzles, free-jet acoustic measurements were taken at General Electric's anechoic facility. A similitude model of the YJ101 R_r^o = .853, A_r^i =.2 coannular plug nozzle was tested. Sample test results verifying coannular plug nozzle flight jet noise reduction is given in Figures 24 and 25.

Shown in Figure 24 is a comparison between a conic nozzle and a coannular plug nozzle (R_r^o =.853, A_r^i =.2) at a free jet velocity of 122 m/sec (400 fps) at typical takeoff sideline engine cycle condition. The measurements indicate that coannular jet and shock noise reduction is maintained at all observation angles. Figure 25 presents the measured flight spectral suppression trends at θ_i=60°, 90°, 140°. At all angles the coannular plug nozzle shows flight reduction of the same order as observed from previous static tests.

OTHER ENGINE TEST RESULTS

In addition to the far-field jet engine acoustic measurements described above, diagnostic measurements were performed. These measurements included sample fan inlet noise measurements, laser velocimeter measured mean velocity and turbulent velocity profiles, peak noise source locations from traversing microphone measurements, and core noise measurements. A brief summary of these results is given below.

Measurements of YJ101 Fan Inlet Turbomachinery

For one series of YJ101 conical nozzle engine tests, the treated inlet was removed and tests were performed with a standard untreated bellmouth inlet. Figure 26 illustrates these results. Although the noise signature is strongly influenced by the conic nozzle jet and shock noise (at high power settings), the fan noise tone characteristics indicate the difference tone generated from stage 1 to 2 or 2 to 3 strongly influences the forward quadrant fan spectrum and PNL. However, the YJ101 fan inlet noise for these tests were found to be within previously measured fan data sources. Figure 27 compares these YJ101 fan inlet measurements relative to several other data sources.

Laser Velocimeter Measurements of YJ101 Engine Exhaust Plumes

The General Electric Company has developed a unique velocity measurement capability for both laboratory and engine diagnostic measurements. (See Reference 1 and 11 to 13 for description of the LV system and its application to model scale jet exhaust tests). Figure 4 shows the laser velocimeter system which was used for the YJ101 engine measurements. This same laser/processor system is used for all G.E. laboratory diagnostic testing.

Figures 28 and 29 illustrate respectively typical mean velocity radial profile measurements for the conical nozzle and the coannular plug nozzle engine test measurements. The observed feature is that for the baseline conical nozzle a rather normal velocity profile was measured.* For the coannular nozzle the inner and outer stream for the coannular plug nozzle system is fully identified - at supercritical, high temperature conditions.

Figures 30 and 31 show comparisons of laser velocimeter measured mean and turbulent velocities for model scale and YJ101 engine tests. The results of Figure 30 clearly show the shock structure of the conic nozzle and the relatively low exit plane exhaust turbulence levels of the YJ101 engine. Figure 31 shows a favorable comparison for the axial mean velocity decay of the coannular plug nozzle between model and YJ101.

Sideline Traverse Test Results and Core Noise Measurements

From the sideline traverse microphone measurements (See Figure 5 for test set-up), the axial location of each 1/3 octave band peak noise source can be deduced. Figure 32 shows a comparison of the Strouhal distribution of peak noise source locations and far-field radiation angles for YJ101 conical nozzle measurements compared with other data sources. The general results obtained were that the high frequency noise sources are close to the nozzle exit and the lower frequency sources are further downstream. These results compare with previously measured test experiences using a J79 engine. Coannular plug nozzle tests showed that the higher frequency noise sources are closer to the nozzle exit than are the conic nozzle (See Reference 3 for additional details).

* An answer desired from the laser measurements was whether the YJ101 engine conic nozzle (which mixed the fan by-pass air into the core stream with a series of 24 aft variable area by-pass injectors) would have a fully mixed exit velocity profile, or some other profile which could lend to an erroneous type of baseline for acoustic measurements. The laser tests (as well as our scaling tests)show that the baseline conic nozzle was a valid baseline.

Core Engine Noise Results

From internal kulite measurements and cross-correlation techniques, YJ101 core exhaust noise measurements were performed. The results were that the internal noise sources did not contaminate any of the jet noise measurements made in the far-field or nearfield. (Reference 3 contains the detailed measurements which lead to this conclusion.)

POSSIBILITIES FOR ADDITIONAL JET NOISE REDUCTION

The acoustic measurements obtained from the YJ101 engine tests and free-jet acoustic model scale tests indicate that FAR36 (1969) type noise level technology may be possible for SCR type aircraft. There are, however, possibilities of achieving additional jet noise reductions as follows:

1. Engine cycle and engine sizing

   Fan oversizing benefit - 1-2 EPNdB reduction identifiable for the sideline.

   Engine high flow benefit - 1.5- 3 EPNdB reduction at the community measurement point is possible.

2. Advanced Aircraft Operational Procedures -

   1-2 EPNdB reduction can be expected.

3. Mechanical Suppression for Coannular Plug Nozzles - Up to 5 EPNdB reduction relative to the unsuppressed high-radius-ratio coannular plug nozzle is believed achievable; simple in mechanical design, lightweight, and with only $\sim$ 4% additional nozzle performance loss.

4. The use of Alternative Jet and Shock noise reduction schemes, such as engine mounting; application of a thermal acoustic shield or a mechanical treated ejector; enhanced exhaust mixing concepts such as coplanar mixer and tangential flow schemes; and viable combination of the above.

Tables 4 and 5 summarize some of these possibilities. Although the achievement of all the above items have not been demonstrated in a collective manner, 1979 work efforts show that the outlook for achieving noise levels approaching FAR36(1978) Stage 3 is encouraging.

As examples of recent NASA/GE contract efforts (NAS3-21608) and General Electric supported efforts, Figures 33, 34, and 35 are shown. Figures 33 and 34 show the acoustic and projected aerodynamic performance of a simple 20 shallow chute mechanical coannular plug nozzle suppressor. The results show that relative to a conical nozzle baseline, up to 11.5 PNdB reduction is possible at the sideline noise measurement location. As an example of 'alternative' jet noise suppression schemes, Figure 35 presents model scale free-jet measurements illustrating flight suppression achieved using a high-radius-ratio plug nozzle with a low velocity, high temperature thermal acoustic shield.* The results show up to 5 PNdB flight jet noise suppression relative to the core nozzle.

CONCLUDING REMARKS

The results of the YJ101 engine and model scale free-jet acoustic test results have shown that a significant amount of acoustic technology advancement has been achieved for Advanced Supersonic Cruise type aircraft.

From the Static YJ101 VCE Engine Test Program:

- For the first time anywhere, rather comprehensive advanced acoustic (far-field, nearfield, probe, and coherence) measurements were successfully and systematically performed on a high performance VCE engine test vehicle with a high-radius-ratio coannular plug nozzle.
- Significant static jet noise reduction (4-6 PNdB peak aft angle) and shock noise reduction ($\sim$ 7 PNdB) was demonstrated for General Electric's high-radius-ratio coannular plug nozzle.
- Scale model and engine jet noise scaling laws for coannular plug nozzles appeared verified.
- A unique spectral prediction method of jet and shock noise for coannular plug nozzles was successfully developed and illustrated.
- Probe and coherence measurements show no significant core noise contribution relative to the jet noise.
- Typical supersonic three (3) stage closely coupled fan noise was measured - Inlet radiated noise was approximately 5 PNdB higher than high by-pass fans under static conditions.

* The Boeing Airplane Company has done extensive prior testing of such an alternative suppression concept. These results however, are believed to be the first free-jet evaluation for a SCR type engine application.

- Extensive laser velocimeter mean velocity and turbulence velocity measurements were acquired. The YJ101 engine exhaust plane turbulence levels were measured to be relatively low (∿ 4%). Comparison of engine measurements with model scale measurements were very good.

From model scale free-jet measurements:

- Flight suppression for the unsuppressed coannular plug nozzle was verified. Up to 5 EPNdB relative to a fully mixed conical nozzle is believed to be achievable at typical take off power and cut-back conditions.

- Options for obtaining additional jet and shock noise reductions were identified:

    1. A shallow chute mechanical suppressor (up to 11.5 peak static PNdB reduction relative in baseline conic nozzle)- simple mechanical design, lightweight; ∿ 4% flight performance loss relative to the unsuppressed coannular plug nozzle.

    2. Alternative jet noise abatement schemes:

        - thermal acoustic shield

        - enhanced internal mixing schemes

        - appropriate combinations of alternative schemes and simple mechanical suppressor concepts.

Although additional work is still necessary, the outlook for achieving SCR aircraft noise levels on the order of current subsonic commercial airplanes is good. Appropriate engine and free-jet model scale programs should be continued, the goal of which should be to provide the technology to achieve FAR36(1978) Stage 3 noise levels or an appropriate equivalent (e.g., sum of three point requirements).

In terms of "next steps" for advancements in acoustic technology, the following items are recommended.

1. Establish a SCR Government/Industry noise technology goal- meet FAR36(1978) Stage 3 or an appropriate equivalent goal which properly accounts for the unique characteristics of a supersonic cruise type aircraft.

2. Continue use of the YJ101/VCE as an engine acoustic test vehicle.

- Mechanical Suppressors

- Inlet Noise Studies

- Demonstration of alternative jet noise abatement schemes

- Simulated flight tests of coannular nozzles and simple coannular suppressors, including inlet fan noise reduction devices (NASA Ames 40 X 80 Wind Tunnel).

3. Continue with aggressive and probing model scale free-jet acoustic and aerodynamic performance research investigations. Emphasis of these programs should be: to formulate appropriate suppressor theoretical prediction models; screening type testing for eventual engine evaluation; free-jet (flight) noise evaluation of all selected concepts; carry out dual paths of investigation - 1. Classical mechanical suppressors 2. Alternative schemes; research efforts which have a greater emphasis on shock noise control schemes. The end objective would be to achieve equivalent subsonic airplane noise levels without significant adverse impact on fuel and airplane economics.

REFERENCES

1. Knott, P.R., Stringas, E.J., Brausch, J.F., Staid, P.S., Heck, P.H., Lathem, D., Acoustic Tests of Duct-Burning Turbofan Jet Noise Simulation NASA CR 2966 (July 1978).

2. Knott, P.R., Blozy, J.T., Staid, P.S., Acoustic and Aerodynamic Performance Investigation of Inverted Velocity Profile Coannular Plug Nozzles, NASA CR 3149 (June 1979).

3. Savell, C.T., Stringas, E.J. et.al., High Velocity Jet Noise Source Location and Reduction Task I - Activation of Facilities and Validation of Source Location Techniques FAA-RD-76-79, I (February 1977).

4. Ibid, Task I Supplement - Certification of the General Electric Jet Noise Anechoic Test Facility FAA-RD-76-79, Ia (February 1977).

5. Clapper, W.S., Stringas, E.J. et.al., High Velocity Jet Noise Source Location and Reduction Task 5 - Investigation of In-Flight Aeroacoustic Effect on Suppressed Exhuasts, FAA-RD-76-79 V (January 1979).

6. Lee, R., Coannular Plug Nozzle Noise Reduction and Impact on Exhaust System Designs, Proceedings of the SCAR Conference November 1976, NASA CP-001, p 505, Part II.

7. Bhutiani, P.K., A Unique Coannular Plug Nozzle Jet Noise Prediction Procedure, General Electric TIS R 79 AEG 481, October 1979.

8. FAA-RD-76-79, II, High Velocity Jet Noise Source Location and Reduction - Task 2, October, 1977.

9. FAA-RD-76-79, VI, High Velocity Jet Noise Source Location and Reduction - Task 6, April, 1979.

10. Stone, J.R., An Improved Method for Predicting the Effects of Flight on Jet Mixing Noise. NASA TM-79155, 1979.

11. Benzakein, M.J., Knott, P.R., "Supersonic Jet Exhaust Noise," AFAPL - TR-82-52, August 1972.

12. Knott, P.R., et.al., "Supersonic Jet Exhaust Noise Investigation", AFAPL-TR-76-68 July 1976.

13. Knott, P.R., Scott, P.F., Mossey, P.W., High Velocity Jet Noise Source Location and Reduction Task 3 - Experimental Investigation of Suppression Principles Volume IV - Laser Velocimeter Time Dependent Cross Correlation Measurements FAA-RD-76-79, III-IV (December 1978).

TABLE 1

Band No. i	17 to 30	31	32	33	34	35	36-43
1/3 O.B. Ctr. Freq.	50Hz to 1kHz	1.25kHz	1.6kHz	2.0kHz	2.5kHz	3.15kHz	4 to 10kHz
Weighting Factors	R_i 1.0	.83	.67	.5	.33	.17	0.0
	S_i 0.0	.17	.33	.5	.67	.33	1.0

TABLE 2.- PROJECTED DIFFERENCE IN EPNL BETWEEN THE CONIC NOZZLE AND COANNULAR PLUG NOZZLE AT TYPICAL SIDELINE, CUT-BACK AND APPROACH CONDITIONS

METHOD	EPNL conic* − EPNL coannular			
	SIDELINE, EPNdB	SIDELINE, EPNdB	CUT-BACK, EPNdB	APPROACH, EPNdB
M J T SMITH	5.1	6.05	4.53	1.72
BUSHELL	5.6	6.65	4.43	2.42
HOCK (SAE)	4.8	5.85	3.93	1.82
TASK 6	4.7	5.15	4.23	1.52
MGB	5.1	6.05	4.23	2.02

*CONIC NOZZLE CONDITIONS CORRECTED TO MATCH COANNULAR PLUG NOZZLE V_j^{mix}, P_j^{mix} AND A_T.

TABLE 3.- TEST CONDITIONS FOR EPNL PROJECTIONS

TYPE CASE	Test P+	V_j^o m/sec (ft/sec)	T_t^o ^oK (^oR)	P_r^o	V_j^i m/sec (ft/sec)	T_t^i ^oK (^oR)	P_r^i	V_j^{mix} m/sec (ft/sec)	Acoustic Range m (ft)
SIDELINE	329	751.94 (2467)	1065.55 (1918)	2.87	484.63 (1590)	473.88 (853)	2.695	692.38 (2272)	731.52
	413	693.72 (2276)	992.22 (1786)	2.591	450.19 (1499)	446.67 (804)	2.45	639.56 (2098)	731.52
CUT-BACK	324	547.72 (1797)	868.88 (1564)	1.92	369.72 (1213)	415.00 (747)	1.87	508.10 (1667)	304.8 (1000)
APPROACH	288	381.00 (1250)	715.55 (1288)	1.49	277.97 (912)	371.11 (668)	1.47	368.19 (1208)	112.77 (370)

TABLE 4.- POSSIBILITIES FOR ADDITIONAL JET NOISE REDUCTION

1. ENGINE OVERSIZING; CYCLE AND HIGH FLOWING ADVANCEMENTS

   - OVERSIZING (SIDELINE) - 1-2 EPNDB REDUCTION

   - HIGH FLOW AND CYCLE OPTIMIZATION (COMMUNITY) - 1.5 - 3 EPNDB

2. ADVANCED AIRCRAFT OPERATIONAL PROCEDURES - NASA LANGLEY AND OTHERS

   - GENERALLY ACCEPTED THAT 1-2 DB BENEFIT CAN BE EXPECTED

3. GE COANNULAR PLUG NOZZLE MECHANICAL SUPPRESSORS

   - UP TO 5 EPNDB REDUCTION OVER UNSUPPRESSED COANNULAR PLUG NOZZLE IS CURRENT GOAL

4. ALTERNATIVE JET NOISE ABATEMENT SCHEMES

   - 3 TO 8 PNDB POSSIBLE

   - THERMAL ACOUSTIC SHIELDS, INTERNAL/COPLANAR MIXERS, TREATED EJECTORS

   - COMBINATIONS OF MECHANICAL SUPPRESSORS AND ALTERNATIVE SCHEMES

TABLE 5.- PROJECTED NOISE LEVELS INCORPORATING ADVANCED FEATURES[1] - 750 KLB TOGW

	BASELINE[2]	MECHANICAL SUPPRESSOR	HIGH FLOW & OVERSIZED FAN (20%)	ADVANCED A/C OPERATIONAL PROCEDURES	REDUCED NOISE LEVEL	FAR36(1978)
SIDELINE	112	-5	-1.5	-1.0	104.5	102.5
COMMUNITY	110.5	-3	-3.0	-1.5	103.0	105.5
APPROACH	104.5	-	-	-	104.5	105.5

(1) COMPLETE ENGINE/AIRPLANE SYSTEMS STUDY WITH ALL THE ABOVE ADVANCED FEATURES HAS NOT BEEN DONE.

(2) 4 GE21/J11B9 ENGINES WITH A HIGH-RADIUS-RATIO COANNULAR PLUG NOZZLE; PARTIAL CHOCKED INLET; 10% OVERSIZED FAN; MONITORING POINTS ARE FOR FAR36(1978) STAGE 3.

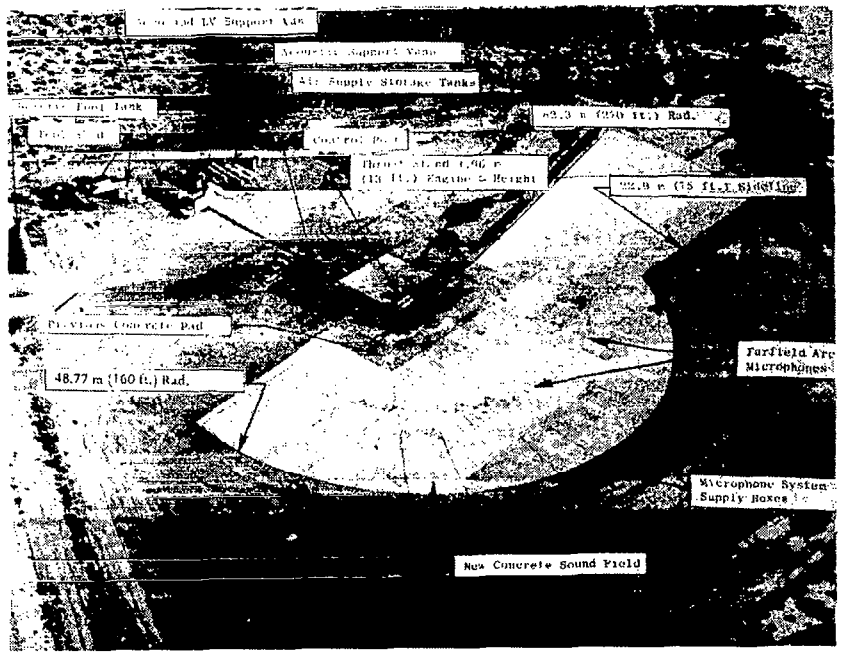

Figure 1.- Layout of Edwards test site.

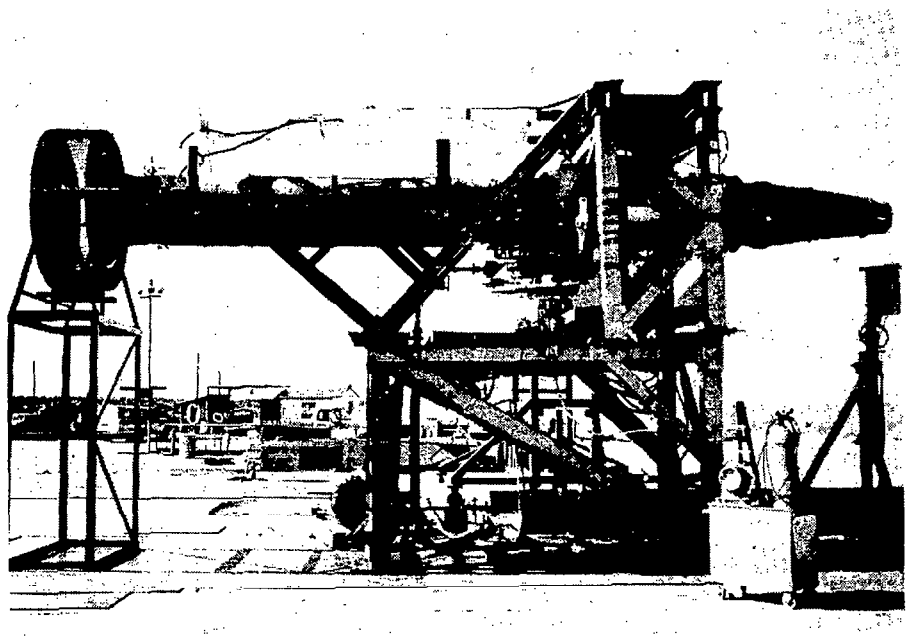

Figure 2.- YJ101 engine conic nozzle with treated fan inlet.

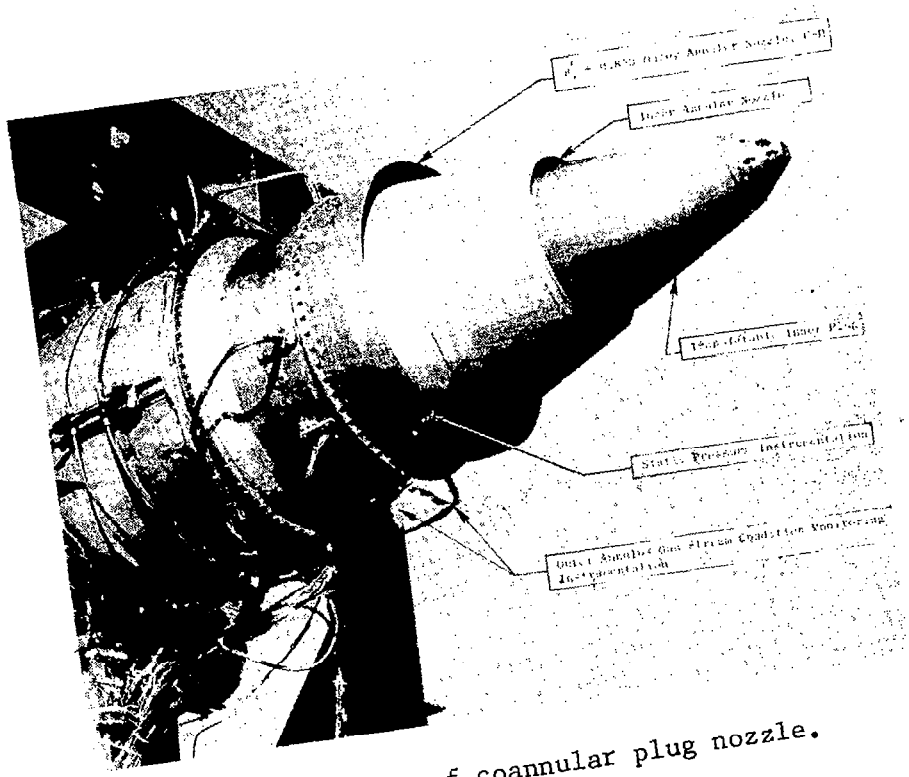

Figure 3.- Photo of coannular plug nozzle.

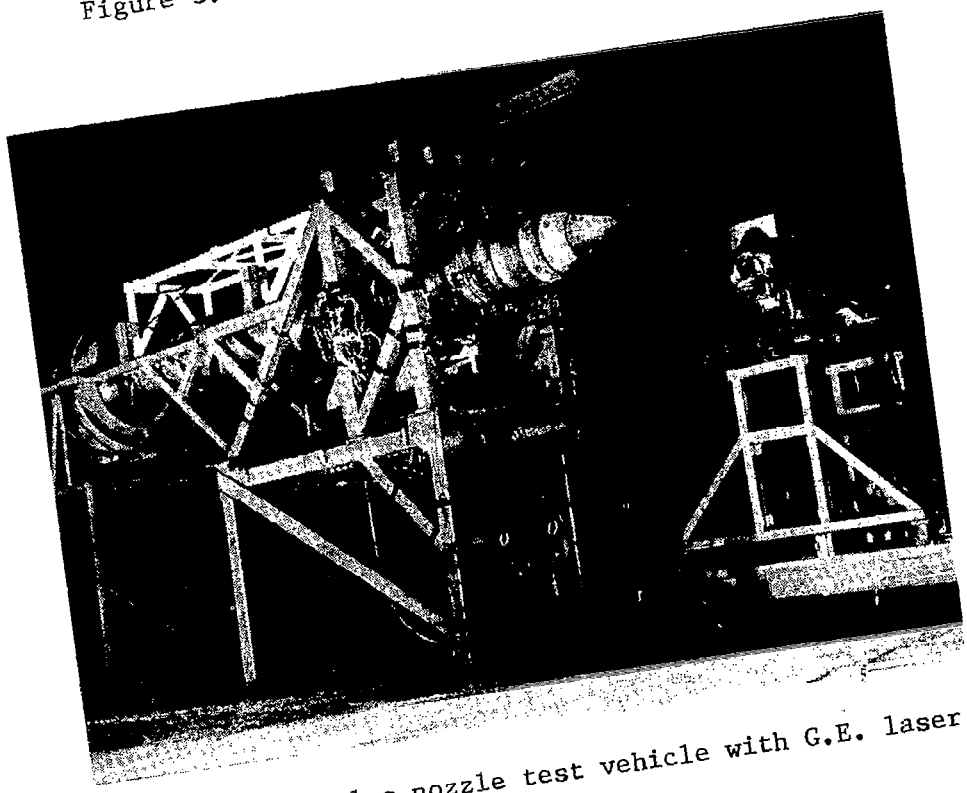

Figure 4.- YJ101 coannular plug nozzle test vehicle with G.E. laser velocimeter.

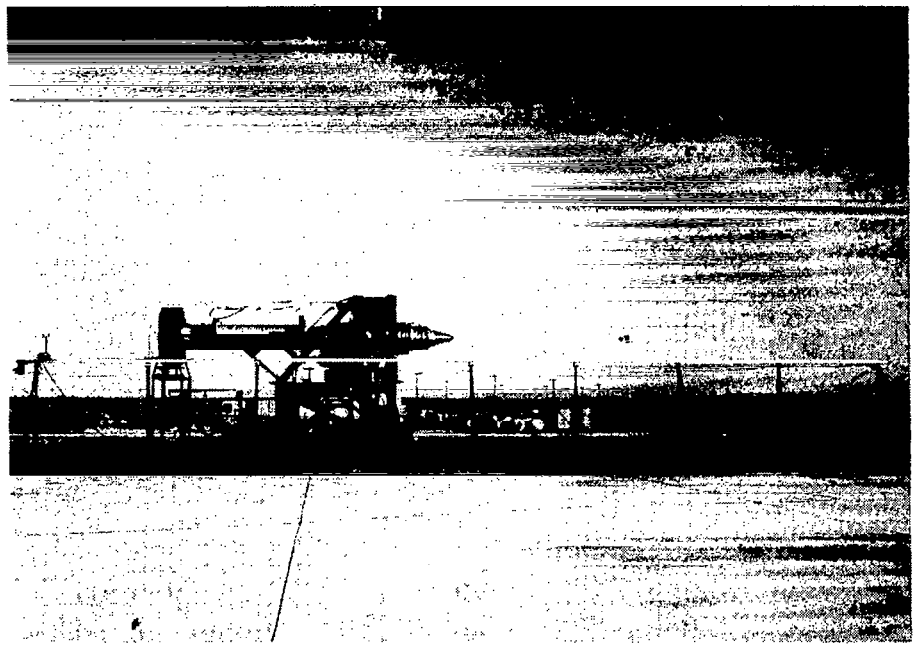

Figure 5.- YJ101 acoustic test vehicle with NASA Ames traversing microphone system.

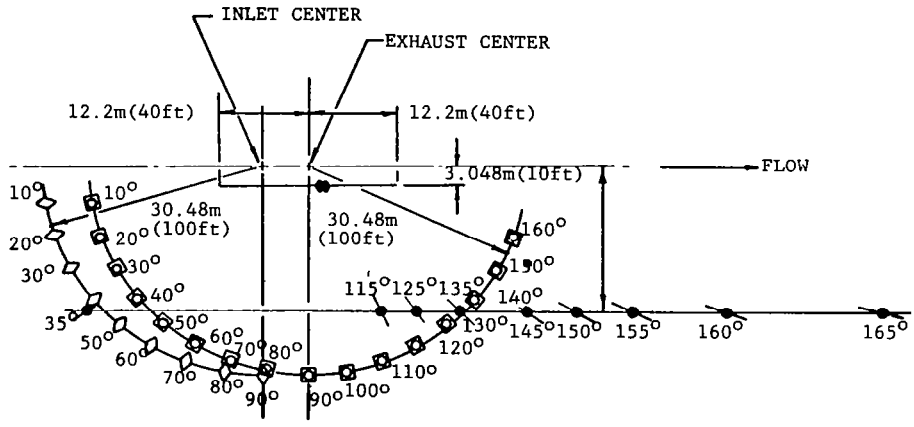

SYMBOL	MICROPHONE ORIENTATION	MEASUREMENT DISTANCE	TYPE OF MICROPHONE ARRAY	CENTER OF RADIAL MEASUREMENTS
●	GROUND	21.34m(70ft)	SIDELINE	
○	GROUND	30.48m(100ft)	ARC	EXHAUST NOZZLE
□	ENGINE CENTERLINE	30.48m(100ft)	ARC	EXHAUST NOZZLE
◊	ENGINE CENTERLINE	30.48m(100ft)	ARC	INLET
—◆—	ENGINE CENTERLINE	30.48m(10ft)	SIDELINE	

Figure 6.- Layout of Edwards test site.

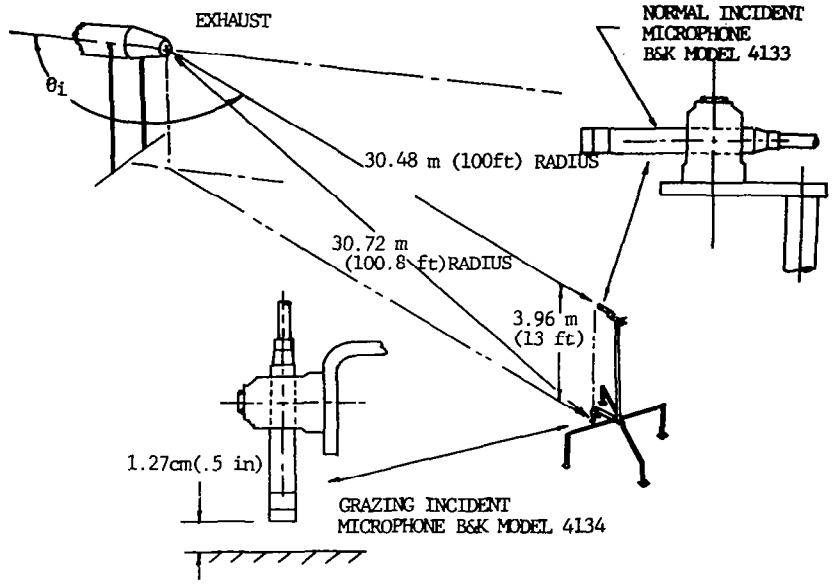

Figure 7.- Illustration of microphone setup.

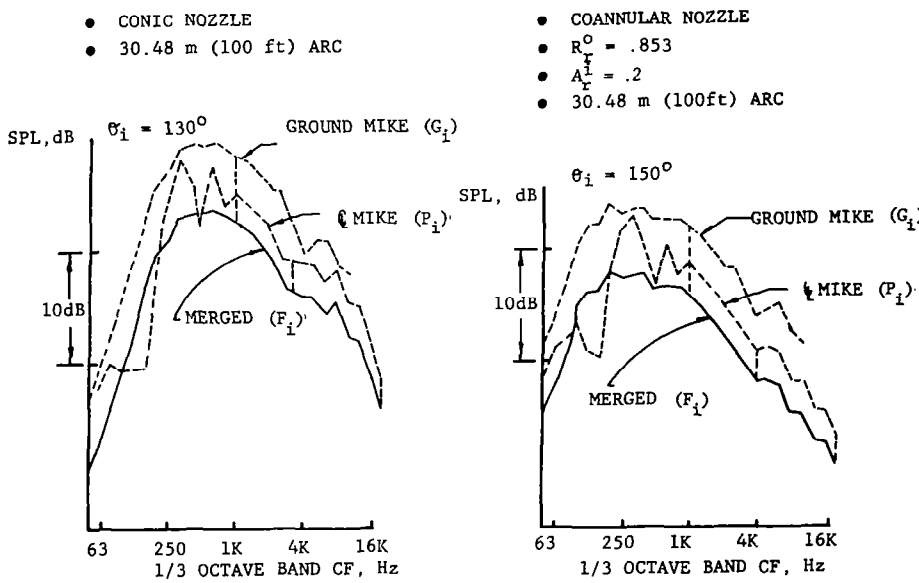

Figure 8.- Illustration of spectral merging.

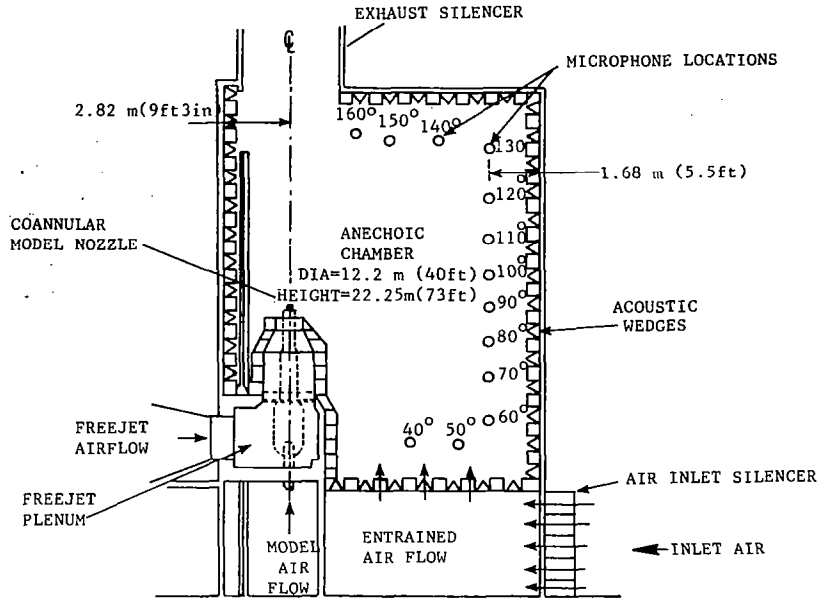

Figure 9.- Schematic of General Electric anechoic free-jet facility.

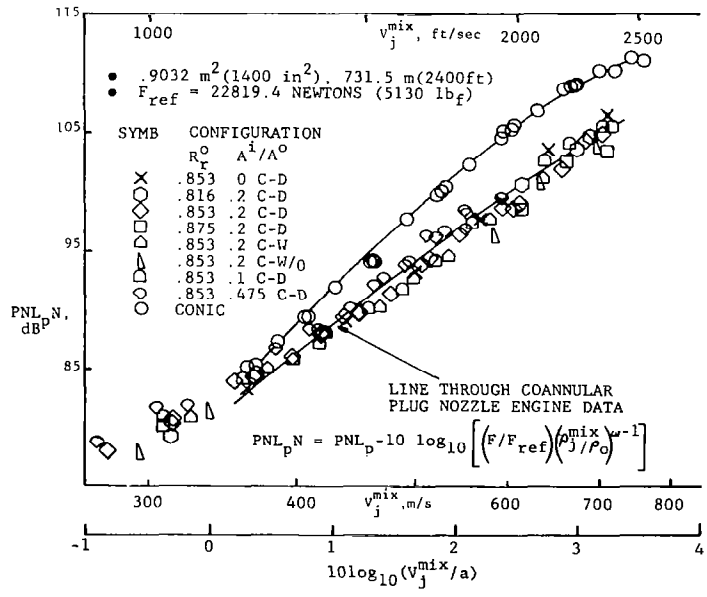

Figure 10.- Verification of coannular plug nozzle engine jet noise reduction.

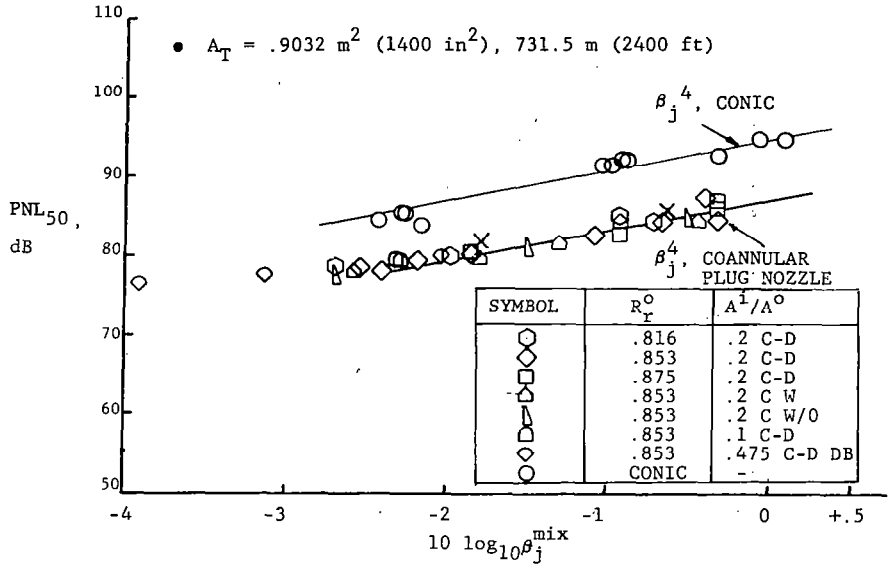

Figure 11.- Verification of coannular plug nozzle engine shock noise reduction.

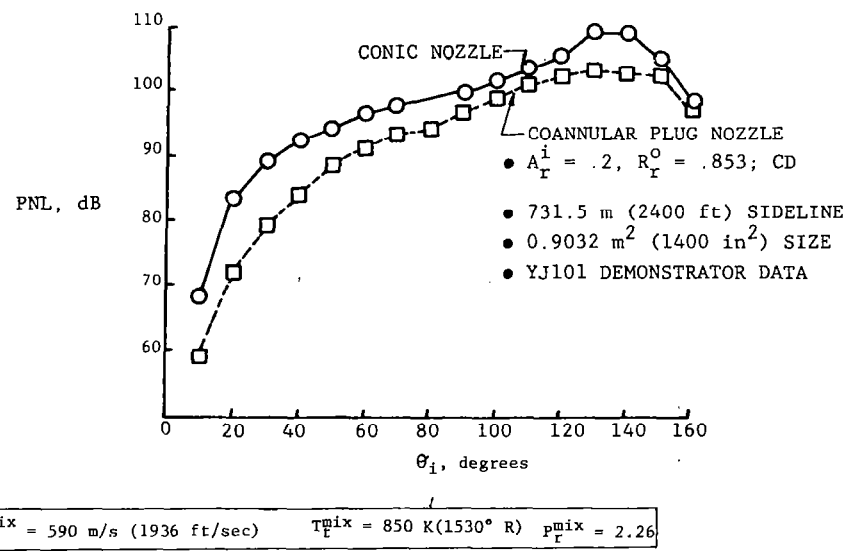

Figure 12.- Typical engine PNL directivity — conic and coannular plug nozzle.

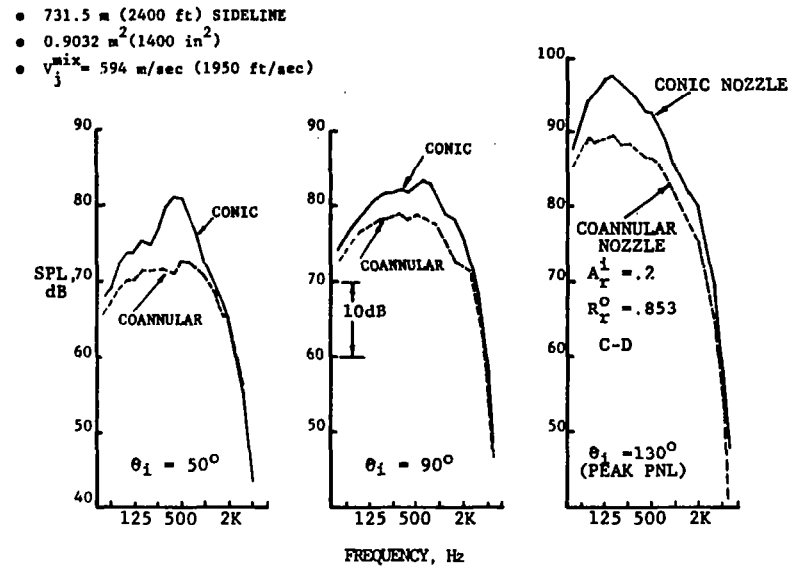

Figure 13.- Typical engine spectra characteristics — conical and coannular plug nozzle.

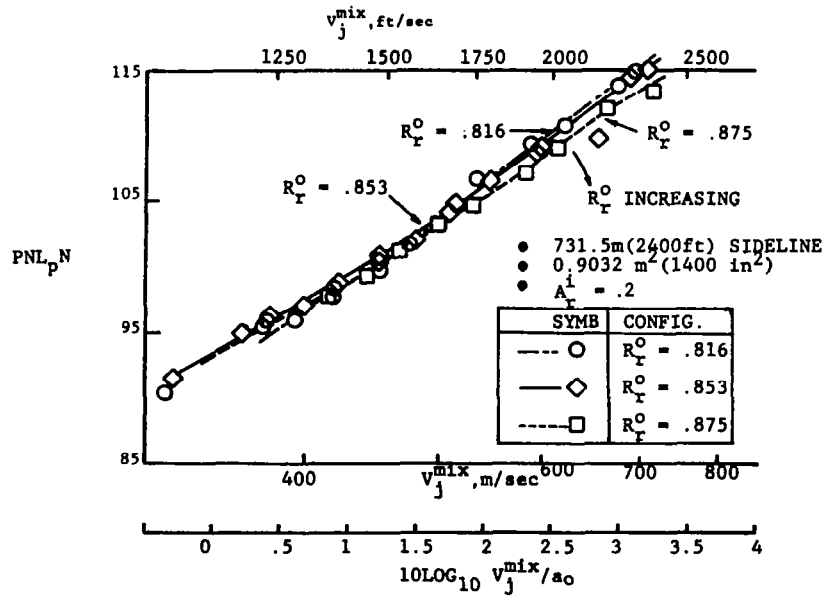

Figure 14.- Influence of radius ratio effects on coannular plug nozzle jet noise reduction.

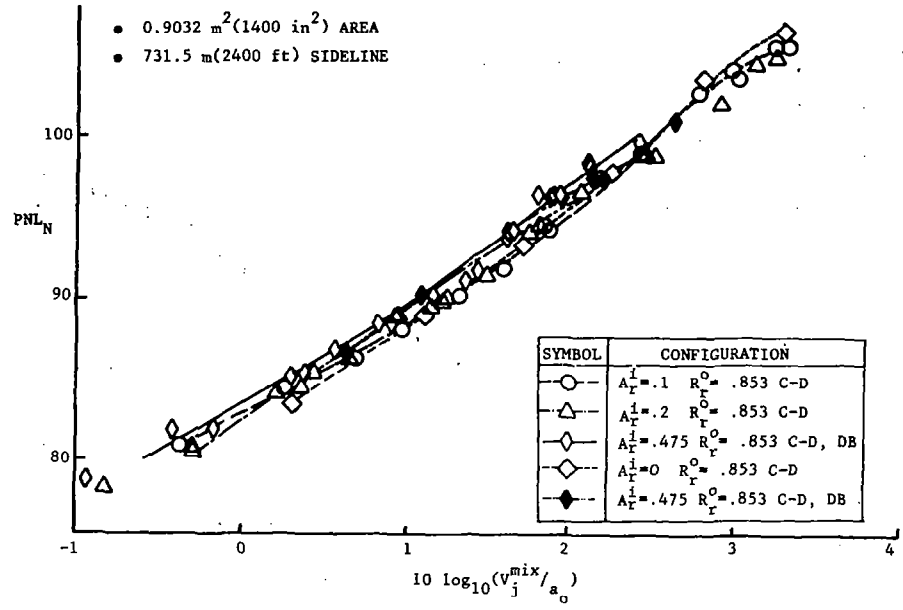

Figure 15.- Influence of area ratio effects on coannular plug nozzle jet noise reduction.

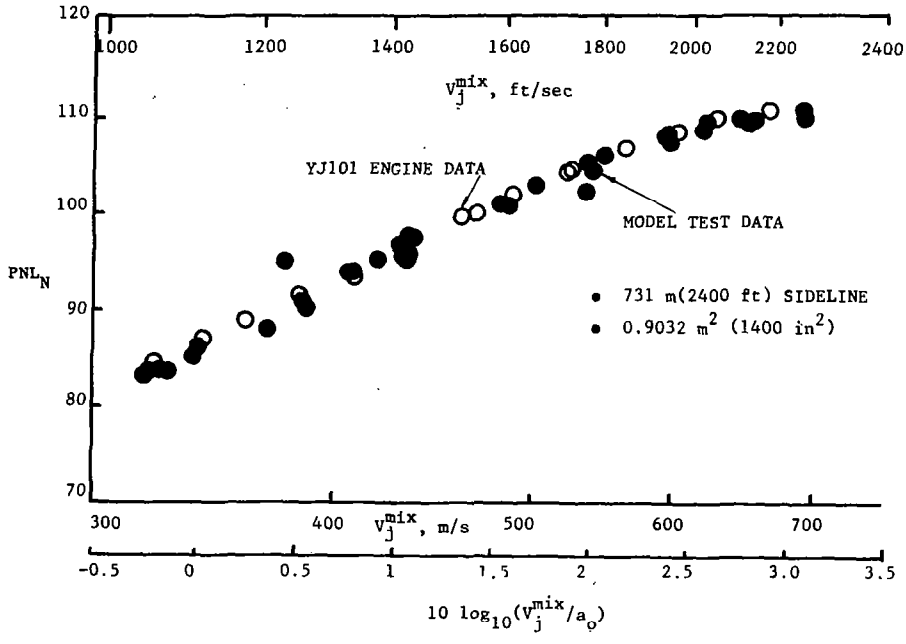

Figure 16.- Conical nozzle peak PNL acoustic scaling comparison.

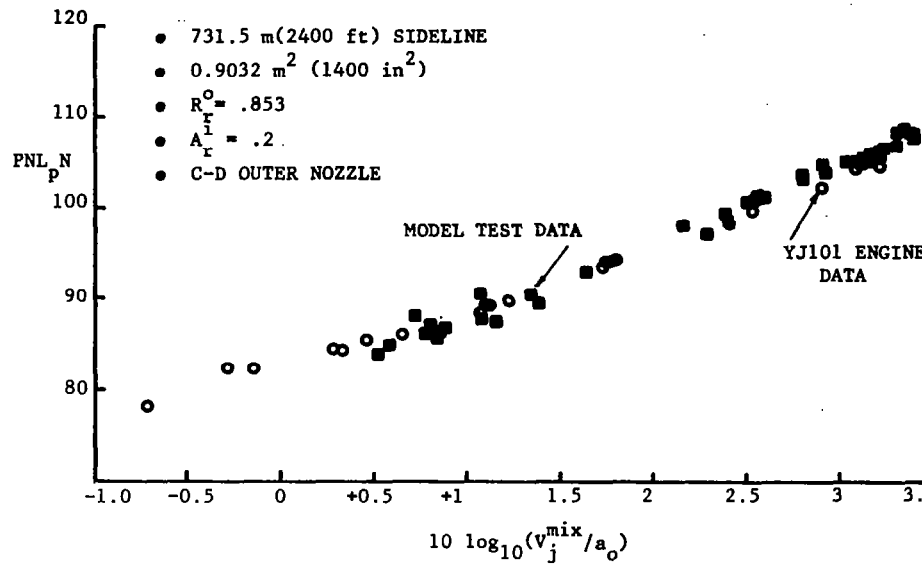

Figure 17.- Coannular plug nozzle peak PNL acoustic scaling comparison.

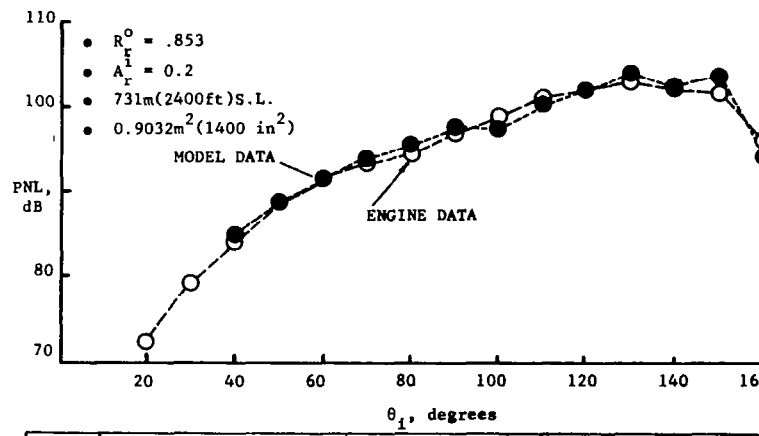

	V_j^o,m/sec (ft/sec)	T_T^{mix},K (°R)	P_r^o	V_j^i,m/sec (ft/sec)	T_T^o,K (°R)	P_r^i	V_j^{mix},m/sec (ft/sec)	T_t^{mix}K (°R)	P_r^{mix}
J101	640.38 (2101)	957 (1723)	2.278	421 (1382)	440 (793)	2.181	594 (1950)	849 (1528)	2.261
MODEL	643 (2110)	958 (1724)	2.307	389 (1276)	398 (716)	2.084	588 (1930)	678 (1220)	2.223

Figure 18.- Coannular plug nozzle scaling — PNL directivity.

	V_j^o, m/s (ft/sec)	T_T^o,K (°R)	P_r^o	V_j^i, m/s (ft/sec)	T_T^i,K (°R)	P_r^i	V_j^{mix}, m/s (ft/sec)	T_T^{mix},K (°R)	P_r^{mix}
YJ101 MODEL	640 (2101)	957 (1723)	2.278	421 (1382)	440 (793)	2.181	594 (1950)	849 (1528)	2.261
	643 (2110)	958 (1724)	2.307	389 (1276)	398 (716)	2.084	588 (1930)	678 (1220)	2.223

- 731m(2400 ft) SIDELINE
- 0.9032 m^2(1400 in^2)

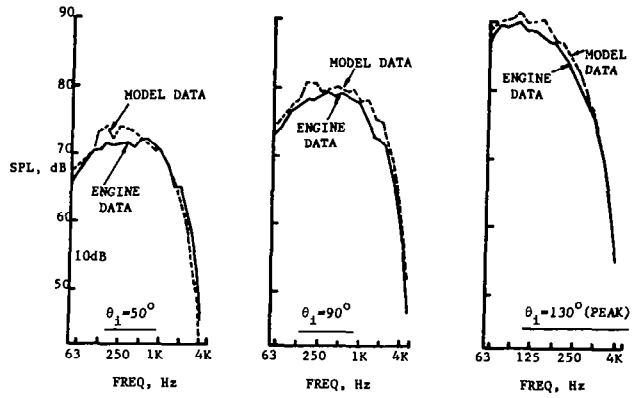

Figure 19.- Conical plug nozzle scaling — SPL spectra.

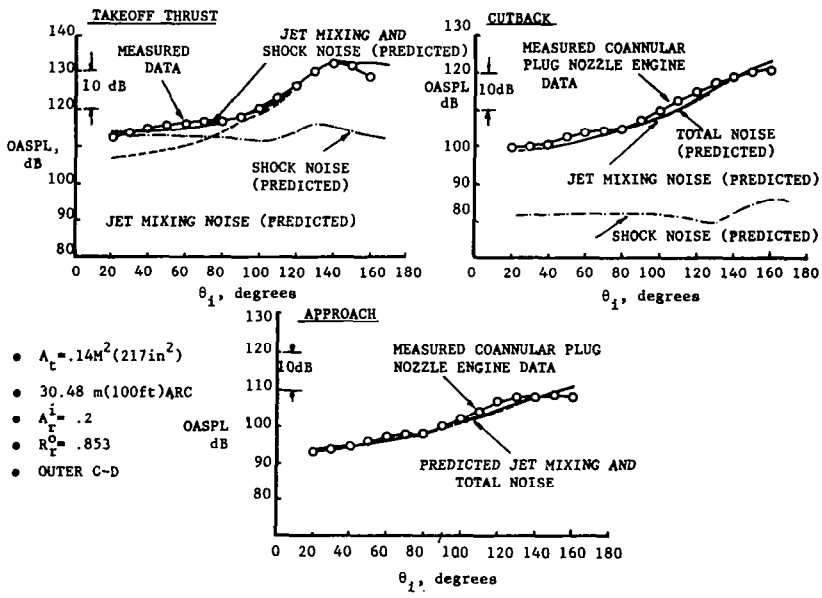

Figure 20.- Theory data comparison for engine coannular plug nozzle jet mixing and shock noise — OASPL directivity.

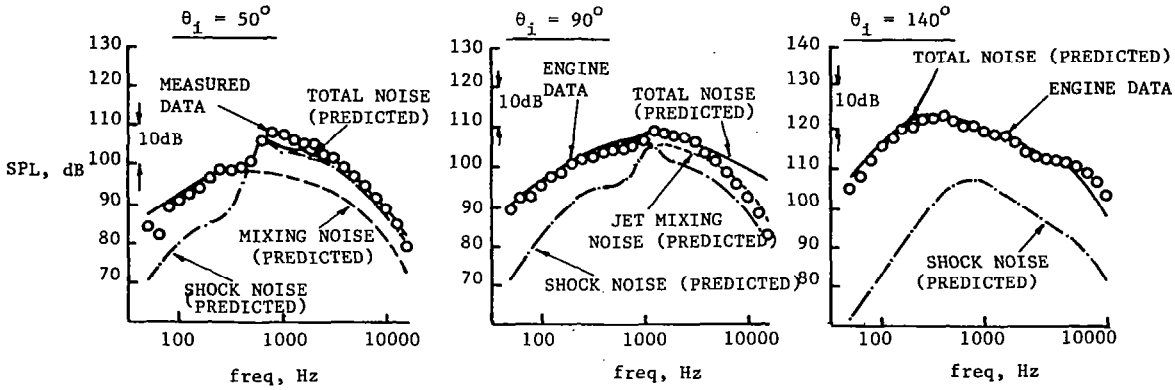

V_j^o, m/sec (ft/sec)	T_T^o, K (°R)	P_r^o	V_j^i, m/sec (ft/sec)	T_T^i, K (°R)	P_r^o	V_j^{mix}, m/sec (ft/sec)	T_T^{mix}, K (°R)	P_r^{mix}
777 (2548)	1084 (1969)	3.0	498 (1633)	478 (861)	2.84	714 (2342)	955 (1719)	2.9

Figure 21.- Theory data comparison for engine coannular plug nozzle jet mixing and shock noise — SPL spectra (typical SL condition).

- 30.48 m(100 ft)
- DEMO SIZE .14m^2(217 in^2)
- A_c^i = .2
- R_c^o = .853
- C-D OUTER NOZZLE

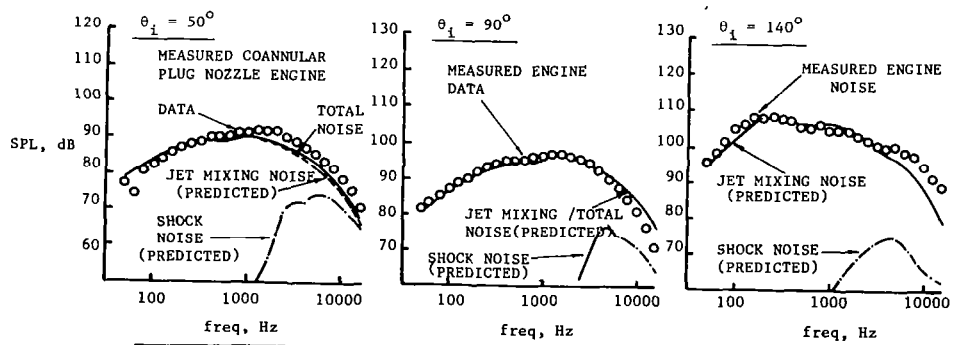

V_j^o, m/sec (ft/sec)	T_t^o, K (°R)	P_r^o	V_j^i, m/sec (ft/sec)	T_t^i, K (°R)	P_r^i	V_j^{mix}, m/sec (ft/sec)	T_t^{mix}, K (°R)	P_r^{mix}
548 (1797)	869 (1564)	1.923	370 (1213)	415 (747)	1.871	508 (1666)	767 (1381)	1.890

Figure 22.- Theory data comparison for engine coannular plug nozzle jet mixing and shock noise — SPL spectra (typical C-B condition).

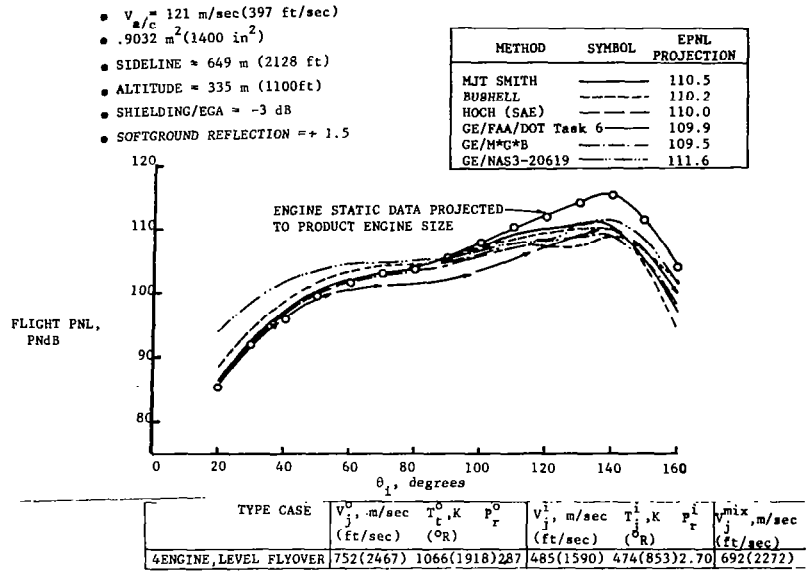

Figure 23.- Projected flight jet and shock noise for a high radius ratio coannular plug nozzle using several flight effects methods at a typical sideline condition.

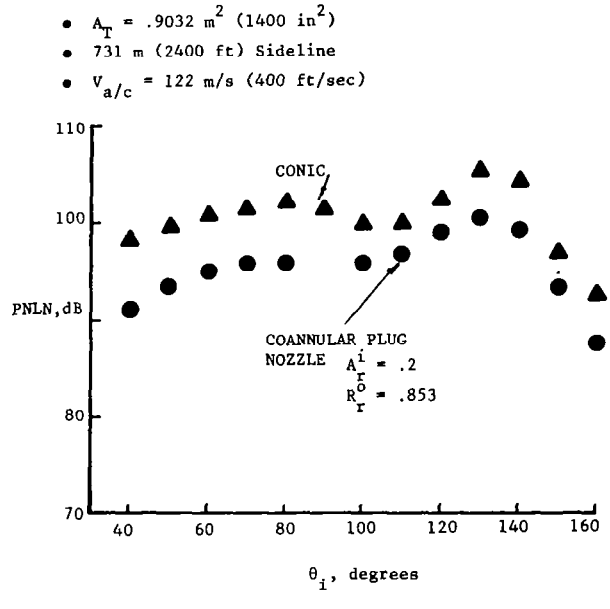

Figure 24.- Verification of flight suppression for coannular plug nozzles — PNL directivity comparison.

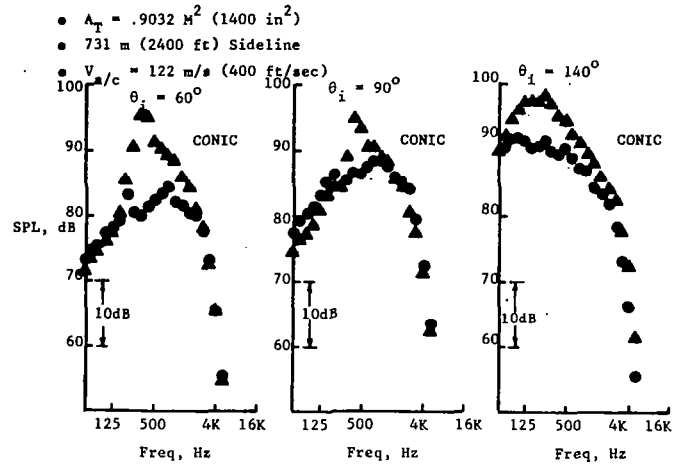

SYMB	CONFIG.	V_j^{mix}, m/s (ft/sec)	T_T^{mix}, K (°R)	P_r^{mix}
▲	CONIC	709(2327)	938(1689)	2.92
●	COANNULAR	720(2361)	941(1693)	3.02

Figure 25.- Verification of flight suppression for coannular plug nozzles — SPL spectra comparisons.

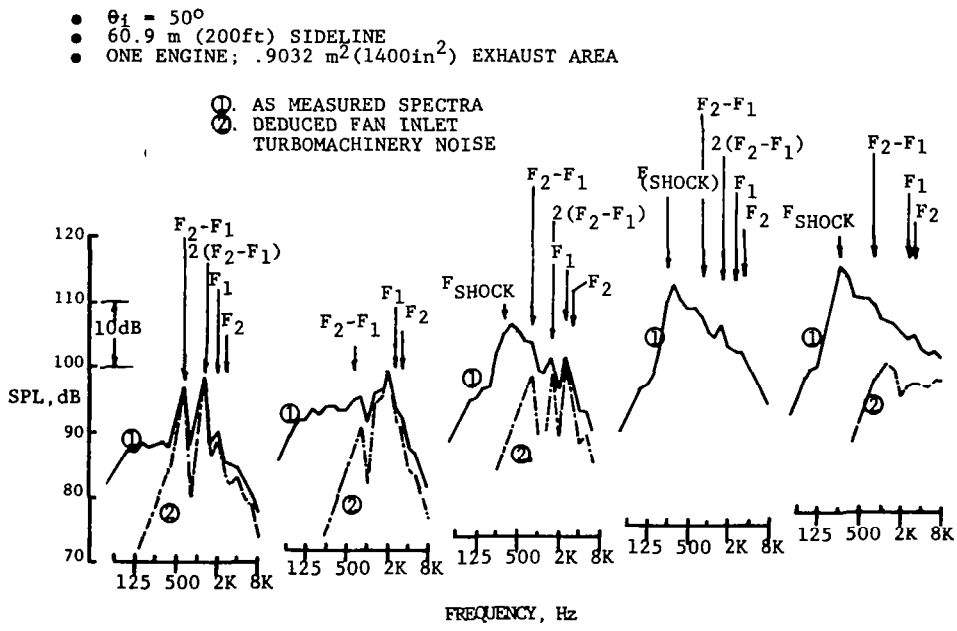

Figure 26.- Typical fan inlet turbomachinery noise.

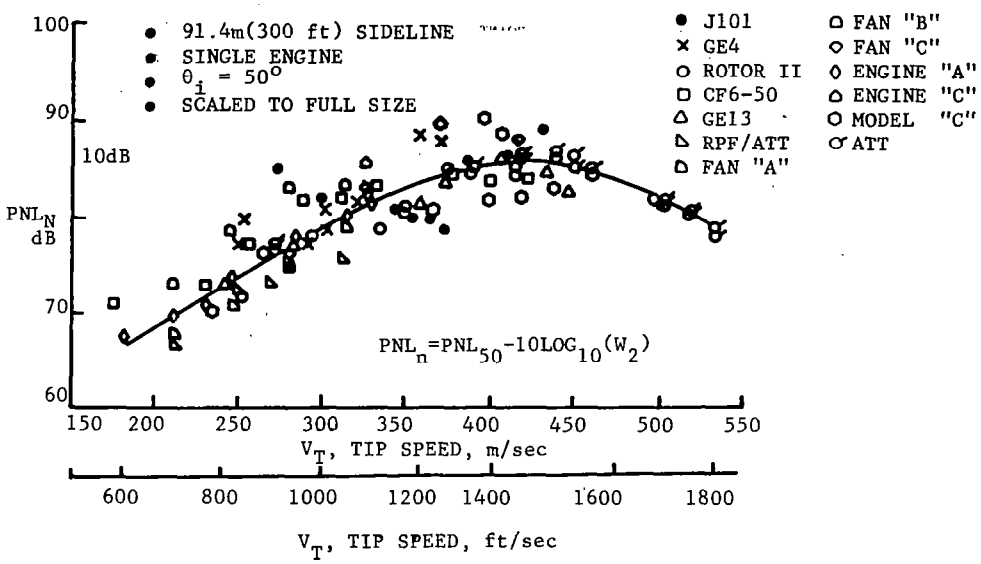

Figure 27.- YJ101 fan inlet noise relative to other data sources.

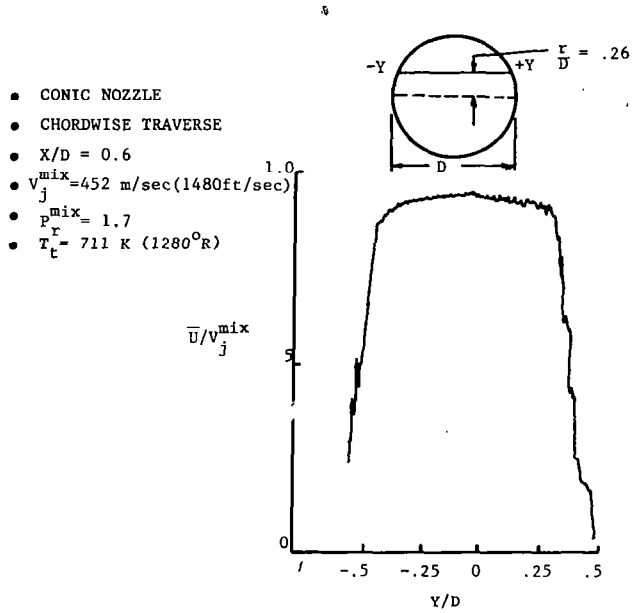

Figure 28.- Typical laser velocimeter measured mean velocity profile for engine conical nozzle tests — subsonic jet.

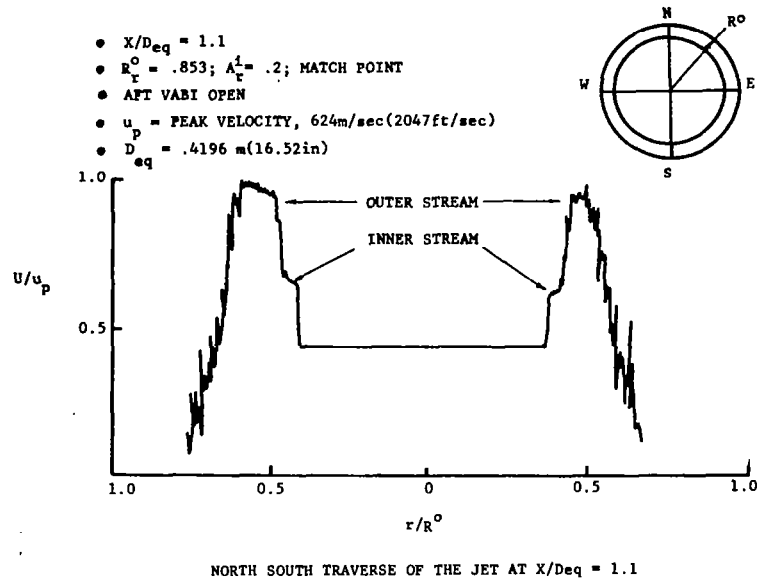

Figure 29.- Typical laser velocimeter measured mean velocity profile for engine coannular plug nozzle tests — supersonic conditions.

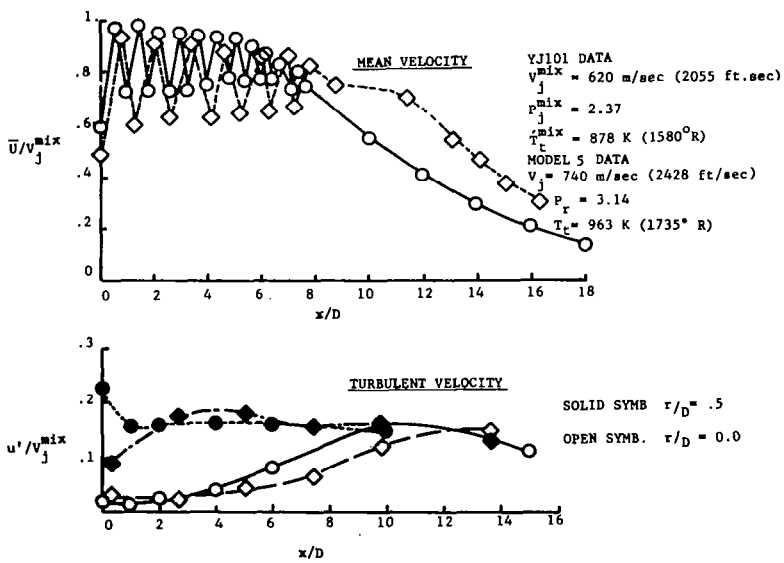

Figure 30.- Comparison of laser velocimeter measured mean velocity and turbulent velocity distributions between engine and model scale tests — conical nozzle at supersonic conditions.

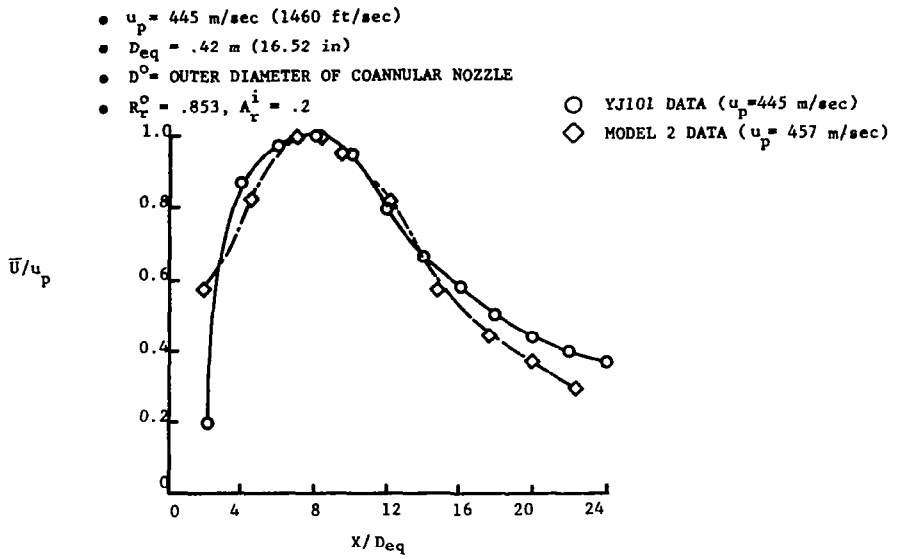

Figure 31.- Comparisons of laser velocimeter measured axial mean velocity decay for engine and model coannular plug nozzle tests — supersonic flow conditions.

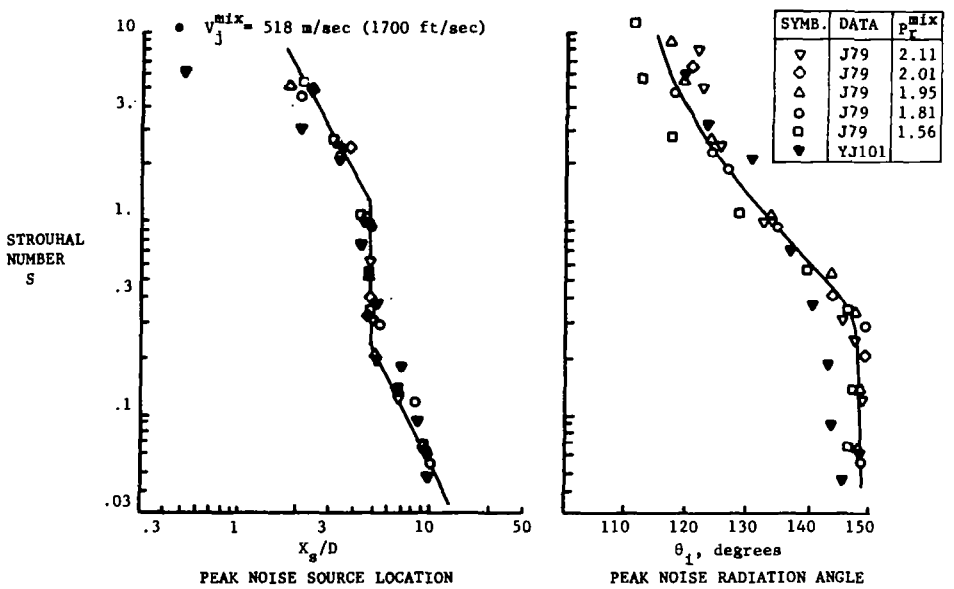

Figure 32.- Measured peak noise source locations and farfield radiation angles for J79 and YJ101/AST conic nozzles.

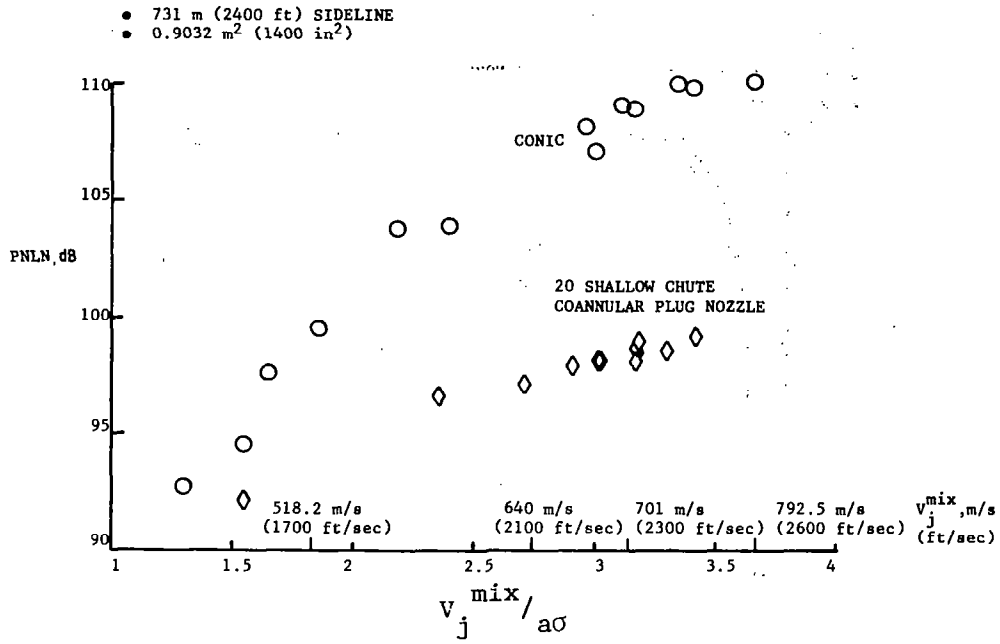

Figure 33.- Static jet noise reduction for a simple mechanical suppressor.

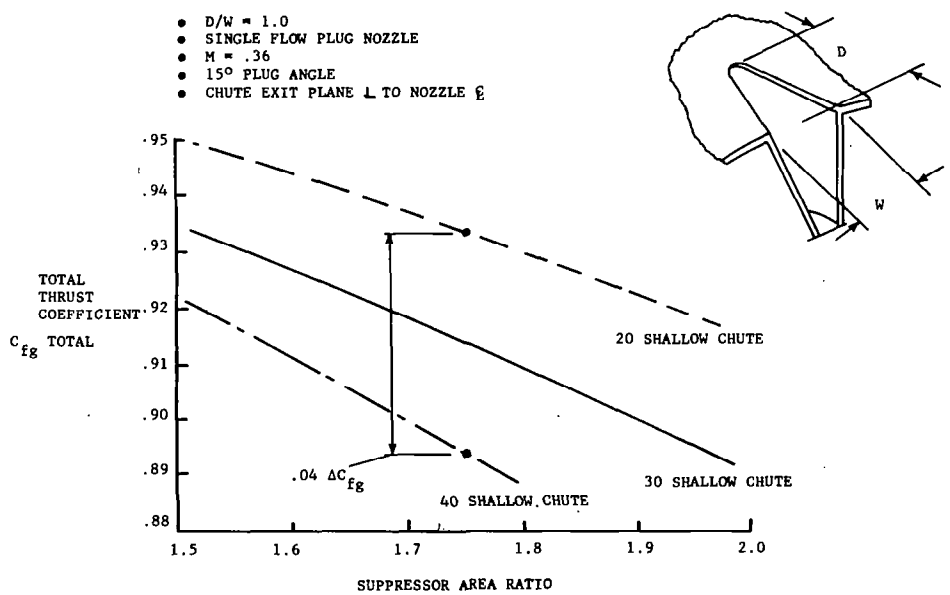

Figure 34.- Variation of total thrust coefficient with suppressor element number and area ratio.

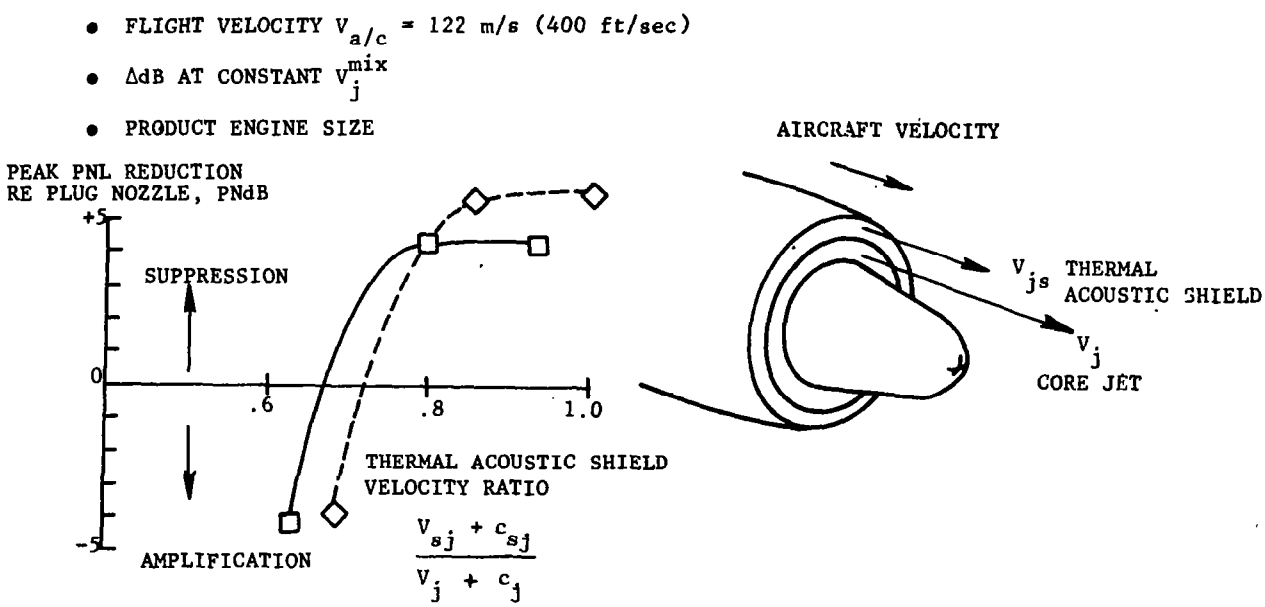

Figure 35.- Inflight thermal acoustic shield suppression.

FLIGHT AND TUNNEL TEST RESULTS OF THE MDC MECHANICAL JET NOISE SUPPRESSOR NOZZLE

R. D. FitzSimmons, R. A. McKinnon and E. S. Johnson
McDonnell Douglas Corporation

SUMMARY

A flight and wind tunnel test program to determine the acoustic and performance effects of a mechanical jet noise suppressor nozzle mounted on an engine of an HS-125 airplane has been completed.

The flight test program was jointly sponsored by McDonnell Douglas Corporation (MDC), Rolls-Royce, Ltd. (RR), British Aerospace (BAe) and the Royal Aircraft Establishment (RAE). To achieve as high an ideal jet velocity as possible to simulate a supersonic transport engine, Rolls Royce supplied a unique uprated Viper engine. Flyover noise measurements were made with microphones mounted on top of a 137.5-m (450-ft) tower of the Severn River Bridge at Bristol, England. Data were recorded from more than 400 passes of the HS-125 test aircraft over the bridge. Seven nozzle configurations - including two references nozzles, two suppressors and three ejector inlets - were tested. Acoustics results were obtained for all nozzles. The suppressor nozzle of interest for an advanced supersonic transport (AST), the MDC suppressor/treated ejector, achieved a measured noise reduction of 14 EPNdB relative to a conventional conical reference nozzle at the highest pressure ratio tested (approximately 2.5).

The wind tunnel test program was jointly sponsored by NASA, MDC, RR and BAe. The unique engine nacelle, flight hardware and nacelles from the HS-125 flight test program combined with a simulated HS-125 fuselage were tested in the NASA Ames 40 x 80 foot wind tunnel and in the outdoor Ames test facility. Both propulsion and acoustic data were recorded. Preliminary thrust data results from the wind tunnel tests are available and are summarized and compared to other mechanical suppressor test results. Nozzle performance results, including lined ejectors, are shown to be the best obtained to date in industry.

The test results indicate that a noise reduction of at least 16 EPNdB would be possible for the MDC suppressor/ejector nozzle scaled to typical AST engine size with a 5% thrust loss at a typical takeoff climb speed.

INTRODUCTION

NASA-sponsored studies of advanced engines intended for application to future AST aircraft have identified several potential engine cycles as candidates - low bypass ratio turbofan engines (leaky turbojets) and variable cycle engines. (References 1 to 4). The low bypass ratio turbofan engines require significant jet noise reductions to meet anticipated noise level requirements for a typical four engine transport configuration. The variable cycle engines employ inverted velocity profiles to reduce jet noise, but also require additional jet noise suppression to meet similar noise level requirements.

In the past, mechanical jet noise suppressors which have been designed and built have demonstrated significant levels of noise reduction statically, but dramatically lost effectiveness with forward velocity. (Reference 5). Others have shown large thrust losses in achieving significant noise reductions. (Reference 6). Designers of jet noise suppressor nozzles attempt to achieve significant noise reductions at minimum in-flight thrust losses. ICAO Working Group E Jet Suppressor Subgroup, after a careful examination of then-available test data worldwide, recommended 12 PNdB jet noise reduction for 10 percent thrust loss be used for mechanical-suppressor parametric studies (Reference 7). Previous model scale results indicated that an MDC mechanical-suppressor configuration had the potential of achieving a level of greater than 11 PNdB jet noise reduction for 5.5 percent thrust loss at AST engine design nozzle pressure ratios. However, this performance level was based on acoustic test results from the Rolls Royce (RR) spin rig at Aston Down, England (Reference 8) and unpublished thrust performance results from an MDC facility. Measured levels in the NASA Ames 40 x 80-ft wind tunnel (Reference 9) were significantly different from the measured spin rig noise reductions. To resolve the discrepancy, flight test results were required to verify the actual noise levels.

Accordingly, a joint flight test program was defined by MDC, RR, and BAe. An RAE HS-125 aircraft was modified by BAe to accept an uprated RR Viper 601 engine and an acoustically treated ejector. With NASA support, the uprated Viper 601 engine, the flight nacelle and the test nozzles were subsequently mounted on a simulated fuselage in the NASA Ames Research Center 40 x 80-ft wind tunnel to obtain thrust performance at forward velocity and also to obtain additional acoustic data. This paper presents the pertinent acoustic results from the flight test program for the AST applicable nozzles and thrust performance results from the Ames tunnel tests.

BACKGROUND

Development of an integrated engine/exhaust system meeting airport noise requirements is one of the pacing items for a new supersonic transport and it is most important to define the jet noise suppression at the earliest possible date. To expedite this activity MDC, with NASA support, since June 1974 has used a baseline configuration as the vehicle for detailed integration studies of the advanced technology engines and noise suppression schemes being derived by the major U. S. engine manufacturers under NASA contract. The analyses of the engine conceptual configurations include determination of the engine size (for noise and takeoff thrust requirements), selection of the proper inlet and nozzle design, calculation of installed engine performance, determination of structural impacts and configuration geometry changes, and determination of the overall range for each type engine/exhaust system combination. In all of these studies, noise suppresion schemes and suppression data as provided by the engine companies have been used. These studies led directly to the effort described herein which is necessary in order to provide data for the mechanical-suppressor program.

As part of the technology updating, MDC reviewed the results of the previous mechanical-suppressor testing programs prior to the design of the nozzle suppressor/ejector/reverser configuration for the conceptual MDC baseline 2.2M cruise vehicle. The design had to integrate with the airplane

without any cruise performance penalty. The design for an MDC exhaust system is shown in Figure 1. The design for the HS-125 test is an exact duplication of the design shown in the figure.

FLIGHT TESTS

The flight test program was instituted jointly to obtain in-flight acoustic data on two conical reference nozzles and two mechanical jet noise suppressor nozzles with and without a treated ejector. In any flight research program, two of the major elements are the selection of the test aircraft and the test engine.

Aircraft/Engine Selections

In the choice of an aircraft/engine combination, it was desired to choose an engine with the highest possible jet velocity to simulate as closely as possible the jet velocities projected for low bypass ratio AST engines at takeoff and cutback. Turbojet engines operate at higher jet velocities than turbofans and are therefore logical candidates for a jet-noise oriented flight test. Use of a multiengine aircraft instead of a single engine aircraft minimizes the safety and airworthiness demonstrations required for a test engine and experimental parts to be flown.

Rolls Royce was able to identify an uprated Viper 601 engine as an excellent test engine because of its high nozzle pressure ratio and the HS-125 aircraft as an attractive test vehicle. The test engine provided ideal jet velocities up to 719.3 m/s (2360 ft/sec), which compares favorably with the anticipated maximum jet velocity of 762.0 m/s (2500 ft/sec) for a projected low bypass ratio AST engine. RR had a lined tailpipe from a previous test program (Reference 10) which was available and was installed on the test engine for all flights in this program. RAE provided an HS-125 research aircraft, Figure 2, from the Bedford Systems Group which was made available for the test program and BAe agreed to modify the test aircraft as needed for instrumentation, nozzle mounting and ejector attachment.

Site

Following the selection of an RAE HS-125 research aircraft as the test vehicle, RR proposed the use of a tower on the Severn River Bridge as the microphone location based on their successful use of this location previously. (Reference 11.) One of the desirable features of this test site is the height of the microphones above the water surface (approximately 137.2 meters - 450 feet) which assures a minimum of ground surface interference and reflection. Reflections from the bridge cables, the road surface and tower roof surface have been found negligible. Figure 3 shows the test aircraft flying past the test site with one of the seven nozzle configurations installed.

Configurations

The seven nozzle configurations tested are illustrated schematically in Figure 4. Two conical reference nozzles - one with a conventional entrance

angle (RR-1) and one with a steep entrance angle (DAC-1) to simulate the primary nozzle of a supersonic cruise engine exhaust system - are included, as are two mechanical jet noise suppressor nozzles, one intended for subsonic aircraft research (RR-2) and the other for the AST (DAC-2). The suppressor nozzles can be fitted with a treated ejector to increase the noise reduction. As shown in Figure 4, three ejector inlet designs (DAC-3, DAC-4 and RR-3) are provided to achieve a total of seven configurations. Figure 2 shows the test aircraft with the uprated Viper engine and the DAC-4 nozzle configuration installed, and Figure 5 is an end view of this configuration

Instrumentation

Two acoustic recording systems are employed to provide redundancy. In each system two B&K 12.7 mm (1/2-inch) diameter type 4133 microphones are mounted vertically upward on poles about 6.1 meters (20 feet) above the roof, approximately 137.2 m (450 ft) above the water surface. Wind screens are used. Acoustic data are recorded on Nagra IV SJ portable tape recorders which are operated at a tape speed of 19 cm (7.5 inch) per second. The center track (FM) is used to record voice information between flights and IRIG B time code data during the flight recording.

Tracking of the aircraft flight path is done by an RR photographic system which is comparable to a mini kinetheodolite system. The method uses a camera to take numerous photographs of the test aircraft as it flies past the test site. Camera elevation and tilt are encoded on one channel of a Nagra IV SJ tape recorder, camera shutter contact pulses on the second channel and voice and time code (IRIG B) on the FM center track.

A second photographic method is employed as a backup for estimating the aircraft position and altitude. A camera with a lens of known focal length is mounted at the test site and the aperture pointed upward. As the aircraft flies overhead, a photographer clicks the shutter which triggers a one-half second 20 kHz pulse onto the center track of one of the Nagra IV SJ acoustic data recorders. After the film is developed, the wingspan and offset are measured. The altitude can be estimated as the aircraft wingspan in feet times the ratio of the focal length in millimeters to the measured wingspan dimension in millimeters. Similarly, the offsets - aircraft position before and after overhead and on or off line - can be estimated in feet as the aircraft wingspan in feet times the ratio of the offset in millimeters to the measured wingspan in millimeters.

Wet and dry bulb air temperatures, wind velocity and direction data are obtained at the tower test site. The air pressure is derived from measurements at the Filton Airfield nearby. Surveys of the air conditions between the test aircraft flight paths and the test site are made in a Tiger Moth aircraft in which wet and dry bulb temperatures, air pressure and wind velocity are measured. The Tiger Moth surveys are conducted before and after each flight test.

The aircraft flight recorder is programmed to record engine rpm, jet pipe temperature, jet pipe static pressure, ejector total and static

pressures and total temperature, ambient air temperature and pressure, airspeed, altitude, run number and test identification data. Synchronization between the data from the aircraft flight recorder, the Nagra IV SJ recorder of the aircraft tracking system and the Nagra IV SJ recorders of the acoustic data acquisition system is by the IRIG B time code which is recorded on all three systems.

Procedure

Prior to each flight test, the test aircraft is ferried from Bedford to Filton Airfield. At the test site, a pink noise signal (200 mV) from a pseudo random noise generator is recorded on each tape for each microphone installation. The signal is applied at the preamplifier (cathode follower) for 45 seconds. Pistonphone calibrations are conducted at the beginning and end of each test. The signal is 124 dB at 250 Hz and recorded for 30-45 seconds. Ambient noise is recorded prior to the test and at selected intervals during the test. When the noise recording crew has completed the installation and pre-test calibrations, the test aircraft is flown over the test site with a minimum of three passes for each test point. Table 1 lists the desired test conditions. The majority of the flights are made with the flight path in a direction parallel to the bridge, but a limited number of flights are made with the flight path normal to bridge. Again the majority of the flights are performed with the non-test engine operating at idle power. A limited number of "control" flights are performed with the test engine at idle power and non-test engine at takeoff power. The test passes are flown at constant airspeed and altitude to achieve a desired altitude over the test site of 152.4m, but the aircraft's altitude is allowed to increase or decrease as needed for a given power setting. Noise data recorded from the "control" flights when compared to previous data serve as a check on the validity of the recording system.

Limitations

The tests are conducted with the following weather limitations:

Precipitation	None
Wind Speed	not more than 10 knots*
Humidity	not less than 50 percent
	not greater than 90 percent

*Initial goal - subsequently modifed to 15 knots

ACOUSTIC RESULTS AND DISCUSSION

The acoustic results for the two reference nozzles, the MDC suppressor nozzle and the MDC suppressor nozzle with ram and flush ejectors, are presented in terms of the variation of peak perceived noise levels (PNLM) and effective perceived noise levels (EPNL) with ideal jet velocity, PNL directivity and one-third octave band sound pressure level (1/3 OBSPL) spectra at the peak noise angle and selected angles of 90° and 150° to the inlet.

The variation of peak PNL with relative jet velocity is shown in Figure 6 for the conventional reference and the AST applicable nozzles. The noise levels produced by the two conical nozzles (RR-1 and DAC-1) are substantially the same; therefore RR-1 is used as the reference nozzle for subsequent comparisons. The noise reductions provided by the mechanical jet noise suppressor (DAC-2) are clearly evident at high engine powers, but decrease to zero at the low end of the engine power range tested. It can be observed that the treated ejector is effective in providing additional noise reduction throughout the power range tested. It can be noted that the suppressor/ejector configuration with the ram scoop inlet (DAC-3) produced noise levels similar to the flush (flight type) inlet configuration (DAC-4). Both configurations produced measured noise reductions of approximately 14 EPNdB. Thus, previous questions of differences between the two configurations were answered. The ram scoop inlet configuration was included in the test program because all model scale tests had included the ram scoop inlet, but not the flush inlet.

The corresponding variation of EPNL with relative jet velocity is shown in Figure 7. It can be observed that the pattern of variation for the nozzles with EPNL is substantially the same as for peak PNL, which means essentially that the mechanical suppressors and the treated ejector did not have an effect on the duration correction factor component of EPNL. The beneficial effects of the treated ejector in providing additional noise reduction over the entire engine power range tested are apparent. Again, DAC-3 noise levels are not substantially different from DAC-4 noise levels.

In the analysis that follows, two typical cases are considered: one at a supercritical nozzle pressure ratio (2.2 NPR nominal) and one at a subcritical nozzle pressure ratio (1.6 NPR nominal). All data presented are for level flight 152.4m (500 ft) above the microphone and 172 knots airspeed. The tone corrected PNL (PNLT) directivity patterns are illustrated for the supercritical case in Figure 8 and for the subcritical case in Figure 9. For the sake of clarity, data are shown for the conventional reference and the AST applicable nozzles only. Since DAC-3 results are substantially the same as DAC-4, only DAC-4 results are shown. In Figure 8 the hump in the noise levels of the reference nozzle in the region of 40° to 70° is attributed to shock cell associated noise and the hump in the rear arc is jet noise. In Figure 8, the anticipated trend of the suppressor to move the angle of peak noise more forward is apparent. This trend is continued with the treated ejector attached.

From Figure 9, it can be observed that the MDC suppressor alone is ineffective in reducing the noise level below that of the reference nozzle

at subcritical nozzle pressure ratios. However, the addition of the treated ejector does provide noise reductions, particulary from 80° aft. No definite change in the peak noise angle with the ejector fitted is apparent.

One-third octave band sound pressure level spectra for the 24 center-band frequencies beginning at 50 Hertz are presented in Figures 10 to 12 for the 2.2 NPR case at selected angles of peak noise, 90° and 150° to the inlet, respectively. Similar data for the 1.5 NPR case are given in Figures 13 to 15.

From Figure 10, the reference nozzle (RR-1) spectral shape for 2.2 NPR at the peak noise angle (approximately 135°) appears to be primarily due to jet noise. Source separation techniques are available (Reference 12, for example) to separate core and jet noise, but they have not been applied to the HS-125/Viper 601 flight data to date. It can be observed that the MDC suppressor (DAC-2) reduces the low frequency noise levels. The treated ejector with the flush inlet (DAC-4) reduced the low frequency noise levels a little more, but reduced the high frequency noise levels significantly. From Figure 13, however, one can postulate the presence of core noise at 1.6 NPR influencing the reference nozzle peak SPL at 630 Hertz. The secondary peak at 315 Hertz could well be jet noise for this reduced power setting. The MDC suppressor reduced the low frequency noise levels but increased the high frequency noise levels compared to the reference nozzle. Such behavior has been demonstrated by previous mechanical suppressors. When the treated ejector with the flush inlet is added to the mechanical suppressor, noise reductions relative to the reference nozzle are provided throughout the spectrum. The beneficial effect of the treated ejector is again apparent.

At 90° to the inlet and 2.2 NPR, Figure 11 illustrates noise reduction in the low frequencies by the suppressor alone and noise reductions in the high frequencies by the treated ejector with no further reduction in low frequency noise levels. Similarly at 1.6 NPR, Figure 14 indicates modest reductions in low frequency noise levels by the suppressor but a slight increase in high frequency noise levels. Addition of the treated ejector reduced the frequency noise levels, with no change in low frequency noise levels.

At 150° to the inlet and 2.2 NPR, Figure 12 indicates significant mid-frequency noise level reductions (approximately 20 dB) and substantial high frequency noise level reductions (about 8 dB) by the suppressor and additional high frequency noise level reductions by the treated ejector. Similarly at 1.6 NPR, (Figure 15) significant low to mid-frequency noise level reductions are obtained by the suppressor but with slight increases in high-frequency noise levels which are subsequently lowered by the treated ejector.

The noise reduction provided by the DAC-4 configuration relative to the conventional reference nozzle was remarkably independent of aircraft speed, as shown in Figure 16.

WIND TUNNEL TESTS

Purpose

The purpose of the wind tunnel tests is to determine propulsion and acoustic characteristics of the seven configurations tested in flight on the HS-125 airplane. Since this HS-125 test aircraft is not instrumented to determine engine thrust, net thrust measurements of each configuration at forward speed are particularly important. These data will allow the deduction of net thrust in flight based on engine RPM. Near field acoustic measurements (in conjunction with outdoor static acoustic data) will allow a prediction and comparison of actual flight data.

Configuration

At the conclusion of the flight testing the engine, inlet, nacelle and nozzle test parts were removed from the HS-125 airplane and shipped to the NASA Ames Research Center, Moffett Field, California. The installation in the NASA Ames 40 x 80-foot wind tunnel is shown in Figure 17. A portion of the HS-125 airplane fuselage was simulated in order to provide as close a representation of the flight configuration as possible. Since all of the acoustic measurements in flight were taken below the aircraft, it was decided to rotate the engine/simulated fuselage 90° clockwise (looking forward) for the tunnel tests. In addition, the vertical and horizontal tail surfaces were simulated for test purposes, Figure 18. The engine exhaust centerline at the reference nozzle exit was located 3.96 m (13 ft) above the floor. As on the aircraft, the engine centerline is 5.5° down from the airplane centerline and 2° out from the fuselage. The entire assembly was mounted on a force table so as to obtain net thrust. Two of the configurations utilized inlet and exit fairings, Figure 19, in order to determine the drag tare. One additional configuration, only run statically, was with a calibrated bellmouth to determine engine airflow. This configuration was run at the start and at the end of the test period. The seven configurations flown on the test aircraft were run statically, at 0.2 M and 0.26 M in the wind tunnel.

Propulsion and acoustic data were obtained for a total of 13 configurations. The acoustic array consisted of two microphones (at a lateral distance of 8 and 12 nozzle diameters) on a traverse from 27° to 166° and four fixed microphones 6.1 m (20 ft) to the side as shown in Figure 20. In order to decrease the reverberant characteristics of the 40 x 80-foot test section, acoustic foam was installed on the floor and part way up to the side nearest the fixed microphones.

Instrumentation

In addition to the microphone array and thrust system described above, instruments were utilized on the engine and within the test section. Tables 2 and 3 describe this instrumentation.

Test Procedure

After calibration of the acoustic system the engine was started and stabilized at 40% RPM. The wind tunnel was started and stabilized at the

desired speed. The engine was then set at various speeds between 80% and 100% RPM. At each speed a microphone traverse from forward to aft was accomplished, recording data from the traverse and fixed microphones. Propulsion data and thrust/drag measurements were taken at the start, middle and end of the traverse cycle. After shutdown of the engine and wind tunnel a calibration of the acoustic system was accomplished.

Various critical engine parameters (RPM, JPT, JPPS, oil pressure, bearing temperatures, oil temperature, fuel flow and engine vibration) were visually monitored during each run to insure that the engine was operating satisfactorily. Engine data were printed out immediately following each run.

Results and Discussion

The data from the wind tunnel tests are presently being reduced and analyzed. Initial and final engine calibration, utilizing an instrumented bellmouth inlet and a conical nozzle, have been checked and agree with the calibration data run by RR.

Figure 21 presents the results of previous MDC tests with a 15.24 cm (6-inch) model of the 12 lobe-24 tube suppressor/treated ejector over a wide range of nozzle pressure ratios and flight Mach numbers. Predicted propulsion results for the DAC-4 configuration in the NASA Ames Viper 601 engine test are shown and preliminary test results are indicated. The agreement between the predicted and the measured test results at NASA Ames is very close at forward speeds (C_V within 0.2%). Statically, however, the agreement between predicted and measured test results varies from 0 to 1.2% lower than the previous data.

IMPLICATIONS TO ADVANCED SUPERSONIC TRANSPORTS

The results of the combined flight and wind tunnel tests should have significant implications to future advanced supersonic transports. They demonstrate that a mechanical jet noise suppressor/treated ejector nozzle exhaust system can be designed to provide large noise reductions with acceptable thrust losses. The two results - noise reductions and thrust performance are discussed in order.

The 152.4-meter, level flight data at Viper 601 engine test conditions were scaled to a nozzle size of 95.25 cm (37.5 in.) equivalent diameter and projected to typical AST anticipated flyover/cutback and sideline slant range distances of 381 m (1250 ft) and 731.5 m (2400 ft), respectively (applicable to the FAR Part 36 (Stage 2) and ICAO Annex 16 Chapter 2 takeoff and sideline measuring conditions for 4-engine aircraft). The results are presented in Figure 22, and indicate a noise level reduction of 16 EPNdB at the takeoff power setting.

Currently, only preliminary results of the thrust performance of the MDC mechanical suppressor/treated ejector nozzle are available from the Ames 40 x 80-foot wind tunnel tests (Figure 21). The thrust data taken in the wind tunnel tests are being processed and reduced to obtain the thrust coefficients for all nozzles. After the wind tunnel data reduction is complete, the in-flight thrust performance will be deduced. Based on the excellent

agreement shown in unpublished results of 15.24 cm (6 in.) equivalent diameter nozzle tests in an MDC facility, it is estimated that the in-flight thrust loss for a typical AST suppressor/ejector nozzle configuration (95.25 cm equivalent diameter) would be 5.4 percent at takeoff power and 6.6 percent at cutback power settings.

Since the deduced flight thrust performance results are not available, the increments shown in Figure 22 are for equivalent ideal jet velocities and are not at equivalent thrust levels for the two nozzles. The noise suppression levels will be adjusted to equivalent thrust levels when the flight thrust loss estimates are available.

The recommendation made by the ICAO Working Group E Jet Suppressor Subgroup, taken from Reference 7, is presented in Figure 23. The Subgroup's recommendation of the variation of noise reduction in PNdB with percent gross thrust loss is the centerline of the three. This variation was recommended for the Working Group E parametric studies. Also shown on Figure 23 is the estimate for the MDC mechanical suppressor/treated ejector configuration at a typical takeoff power setting applicable to the sideline noise measuring condition.

CONCLUDING REMARKS

Results of a joint MDC/RR/BAe/RAE flight test program in which an HS-125 research aircraft was fitted with an uprated Viper 601 engine and seven nozzle configurations show that significant noise reductions (up to 16 EPNdB) can be achieved by mechanical jet noise suppressor/treated ejector configurations relative to a conical reference nozzle. Preliminary results of thrust performance measurements taken in the NASA Ames 40 x 80-ft wind tunnel indicate good agreement of the Viper 601 size MDC mechanical suppressor/treated ejector configuration with previous unpublished results of 15.24 cm (6 in.) equivalent diameter nozzle tests in an MDC facility. Flight and tunnel test results of a mechanical suppressor have shown that a low-bypass turbofan-powered AST could be built to meet FAR Part 36 (Stage 2) noise levels.

REFERENCES

1. Allan, R. D.: Advanced Supersonic Technology Propulsion System Study - Phase II Final Report. NASA CR 134913, December 1975.

2. Allan, R. D. and Joy, W.: Advanced Propulsion System Technology Study - Phases III and IV - Final Report. NASA CR 135236, November 1977.

3. Advanced Supersonic Propulsion Study - Phase III Final Report. NASA CR 135158, December 1976.

4. Advanced Supersonic Propulsion Study - Phase IV Final Report. NASA CR 135273, November 1977.

5. Jaeck, C. L.: Static and Wind Tunnel Near-Field/Far Field Jet Noise Measurements From Model Scale Single-Flow Baseline and Suppressor Nozzles - Volume 2: Forward Speed Effects. NASA CR 137914, November 1976.

6. Burley, R. R. and Head, V. L.: Flight Velocity Effects on Jet Noise of Several Variations of a 48-Tube Suppressor Installed on a Plug Nozzle. NASA TMX-2919, January 1974.

7. Interim Report of Subcommittee on SST Noise Prediction Methods. ICAO Working Group E, 21 March 1978.

8. Rowe, W. T., Johnson, E. S. and McKinnon, R. A.: Technology Status of Jet Noise Suppression Concepts for Advanced Supersonic Transports. AIAA Paper No. 77-833, July 1977.

9. Cooperative Wind Tunnel Tests of Douglas Advanced Supersonic Technology Jet Noise Suppressor. NASA CR 158996, November 1978.

10. Brooks, J. R. and Woodrow, R. J.: Silencing an Executive Jet Aircraft. Noise Control Engineering, September-October, 1975.

11. Brooks, J. R.: Flight Noise Studies on a Turbojet Engine Using Microphones Mounted on a 450 Foot Tower. AIAA Paper No. 77-1325, October 1977.

12. Blankenship, G. L., Low, J.K.C., Watkins, J. A. and Merriman, J. E.: Effect of Forward Motion on Engine Noise. NASA CR 134954, October 1977.

TABLE 1. - HS-125 FLIGHT TESTS

SEVERN RIVER BRIDGE

ITEM	LEVELS	NOZZLE CONFIGURATIONS
NOZZLE PRESSURE RATIO	1.6, 1.8, 2.0, 2.2 AND MAX	ALL CONFIGURATIONS
FLIGHT SPEEDS:	140 KNOTS	RR-1
	172 KNOTS	ALL CONFIGURATIONS
	250 KNOTS	RR-1, DAC-4

TABLE 2. - ENGINE INSTRUMENTATION

INSTRUMENTATION	RANGE	ACCURACY
Engine RPM	0 to 110% (40% Ground Idle)	± 50 RPM
Engine JPT	0 to 900°C (436°C Ground Idle)	± 3°C
High Pressure Comp. P_{S3}	103.4 to 620.6 $\frac{kN}{m^2}$ (15 to 90 PSI)	± 0.25%
Jet Pipe Static Pressure JP_{PS}	103.4 to 310.3 $\frac{kN}{m^2}$ (15 to 45 PSI)	± 0.25%
Oil Pressure	0 to 275.8 $\frac{kN}{m^2}$ (0 to 40 PSI)	± 5%
Bearing Temp. 1	0 to 300°C	± 2%
Bearing Temp. 2	0 to 300°C	± 2%
Intake Venturi (P_S5, P_S6, P_S7, P_S8)	0-152.4 cm (0 - 60 in.) H_2O	± 0.5%
Turbine Overheat Temp	0 - 400°C	± 2%
Oil Temperature (Redlined at 117°C)	0 - 140°C	± 2%
Ejector		
Static Pressure	89.6-103.4 $\frac{kN}{m^2}$ (13 - 15 PSIA)	± 0.25%
Total Pressure	89.6-117.2 $\frac{kN}{m^2}$ (13 - 17 PSIA)	± 0.25%
Total Temperature	10 - 48.8°C (50 - 120°F)	± 2%
Ejector Acceleration	0 - 5 G	± 2%
Engine Vibration	0 - 10 MILS	± 1%

TABLE 3. - FACILITY INSTRUMENTATION

INSTRUMENTATION	RANGE	ACCURACY
Engine Thrust (Tunnel Balance System)	0 to 17793N (0 to 400 lb.) 956N (215 lb.) Ground Idle	± 0.25%
Tunnel Speed	0 to 94.5 m (0 to 310 ft)/sec	± 1.5 m (5 ft)/sec
Tunnel Temperature - Total	10° to 48.8^{o} C (50° to 120° F)	± 0.56^{o} C ± (1° F)
Tunnel Humidity	20% to 100% RH	± 5%
Fuel Inlet Pressure	0 to 310.3 $\frac{kN}{m^2}$ (0 to 45 PSI)	± 1%
Fuel Inlet Temperature	10° C to 48.8^{o} C (50° F to 120° F)	± 2.8^{o} C ± (5° F)
Tunnel Static Pressure	93.1-103.4 $\frac{kN}{m^2}$ (13.5 - 15 PSIA)	± 0.1%
Fuel Flow	0-2041 kg (0-4500 lb)/Hr. ≈ 277 kg/Hr. (500 lb/Hr) Flight Idle	± 0.25%
Tunnel Total Pressure	93.1-103.4 $\frac{kN}{m^2}$ (13.5 - 15 PSIA)	± 0.1%

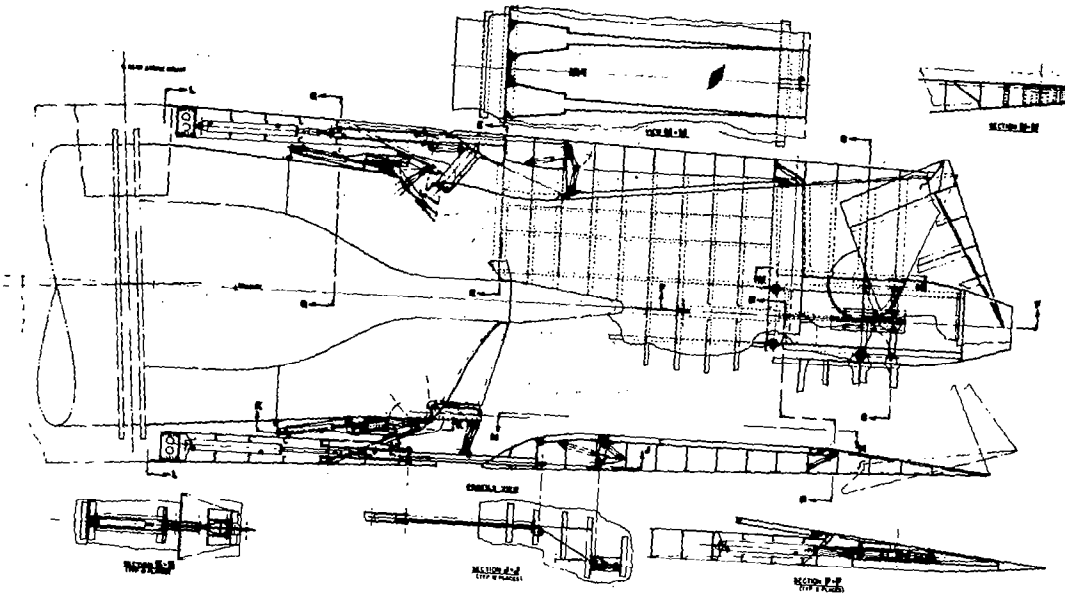

Figure 1.- MDC AST exhaust system design.

Figure 2.- HS-125 test aircraft.

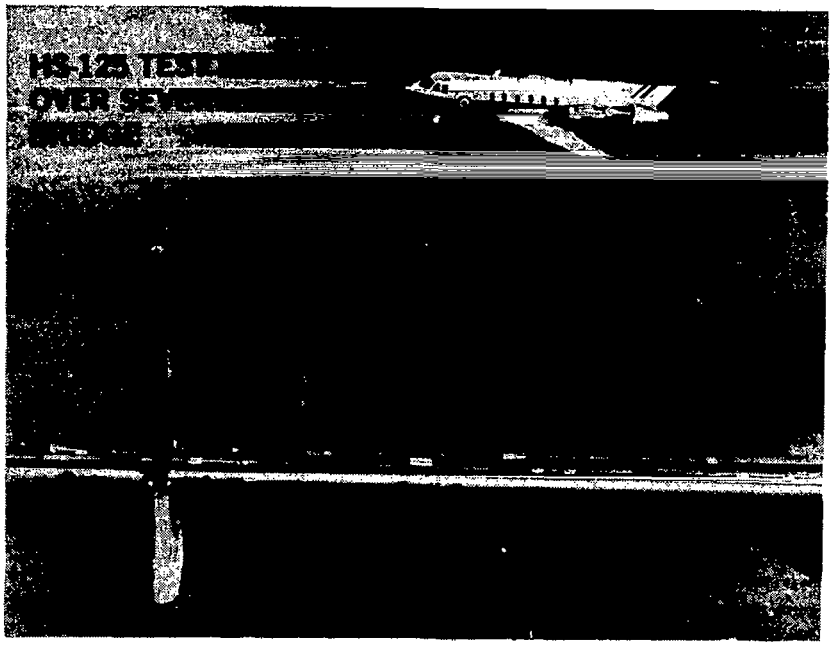

Figure 3.- HS-125 test aircraft over Severn River bridge.

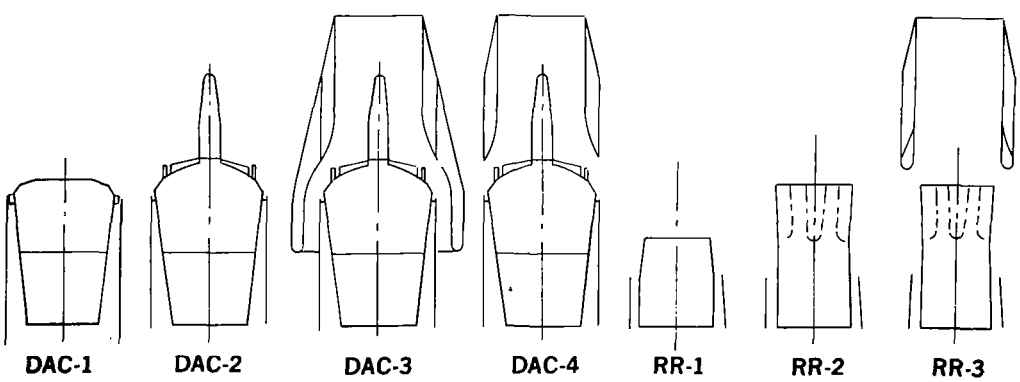

Figure 4.- HS-125 flight test configuration summary.

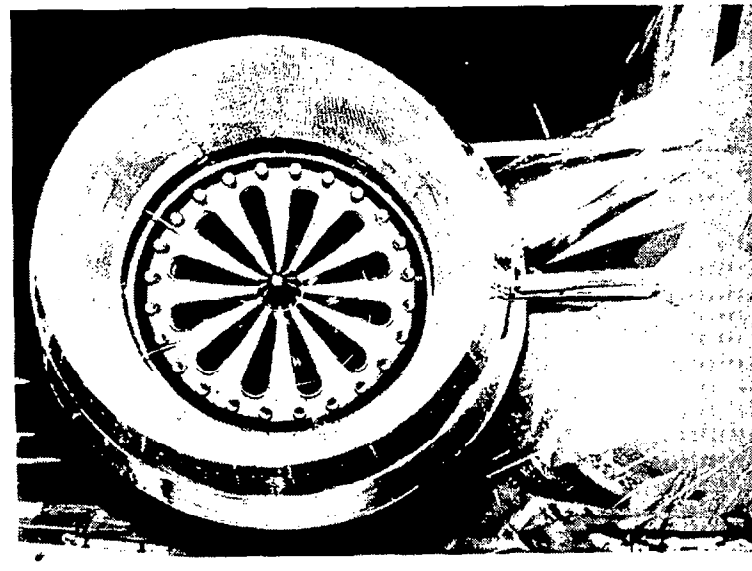

Figure 5.- Aft end view of MDC suppressor/ejector.

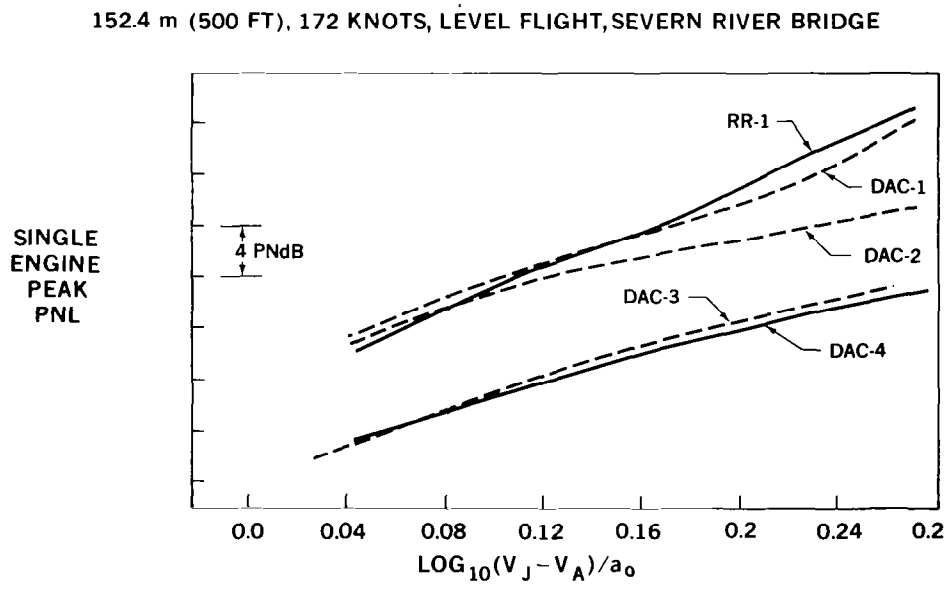

Figure 6.- Variation of peak PNL with relative jet velocity.

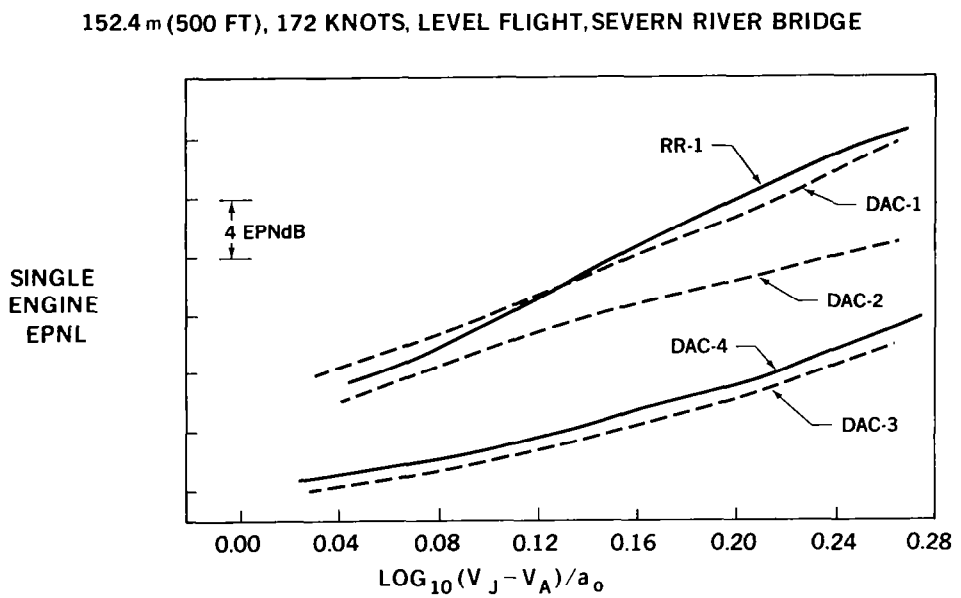

Figure 7.- Variation of EPNL with relative jet velocity.

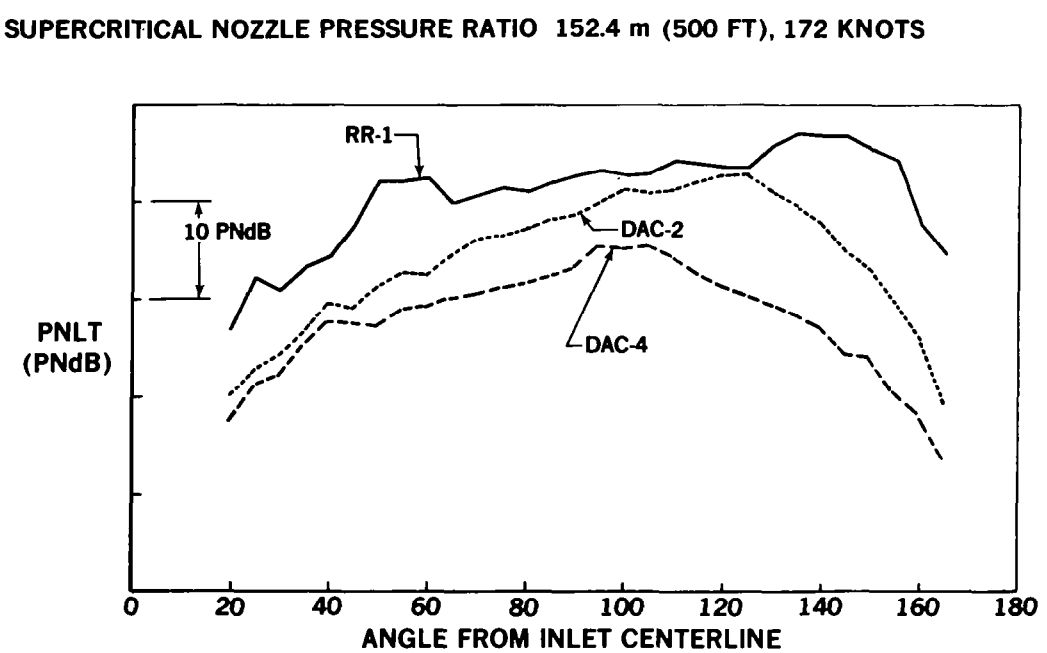

Figure 8.- PNLT directivity patterns at a typical supercritical nozzle pressure ratio.

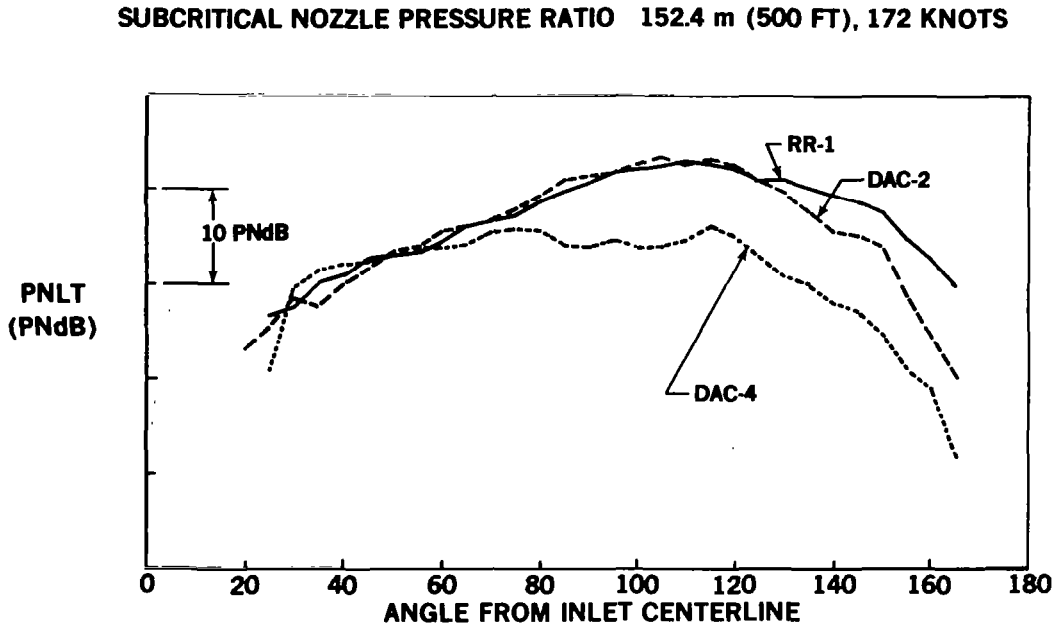

Figure 9.- PNLT directivity patterns at a typical subcritical nozzle pressure ratio.

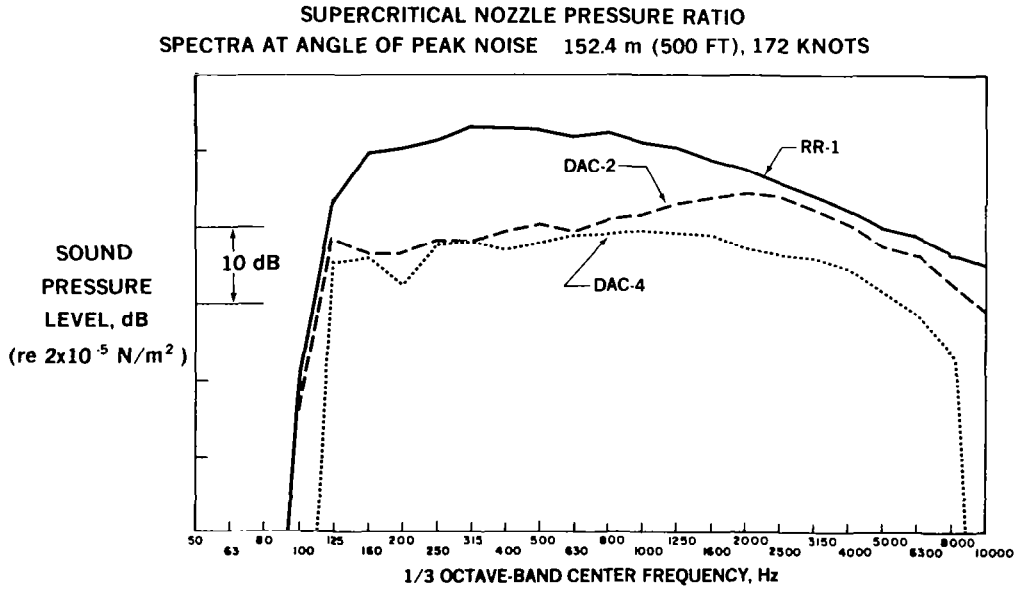

Figure 10.- Peak noise angle SPL spectra at a typical supercritical nozzle pressure ratio.

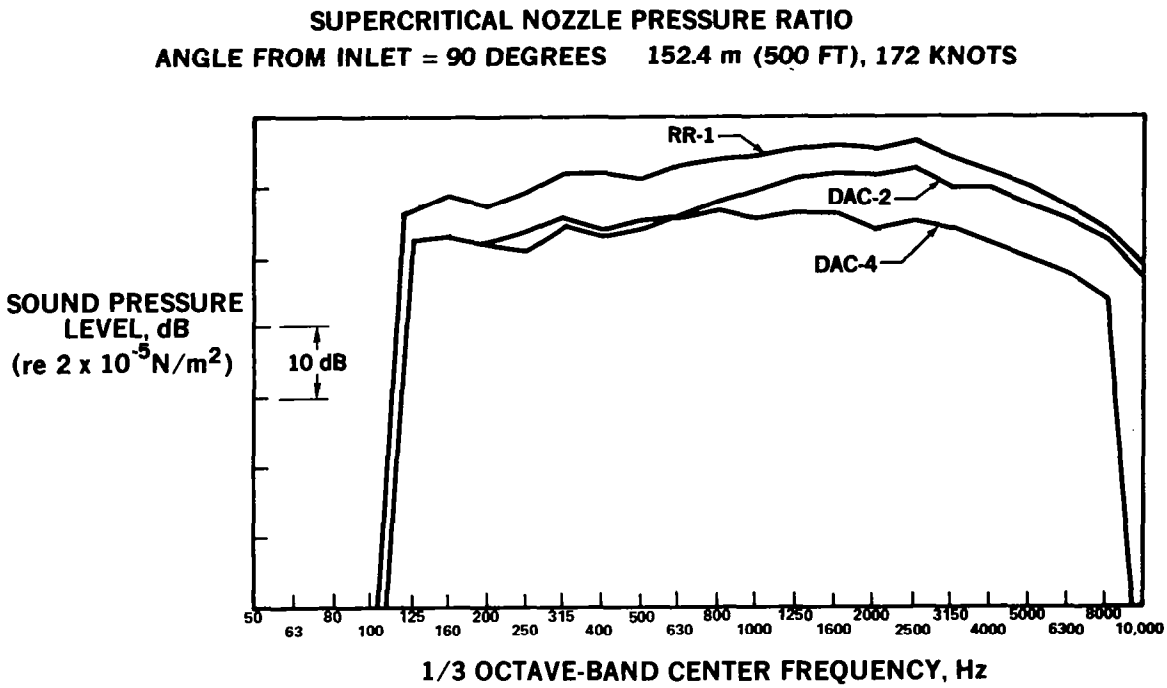

Figure 11.- SPL spectra at 90° for a typical supercritical nozzle pressure ratio.

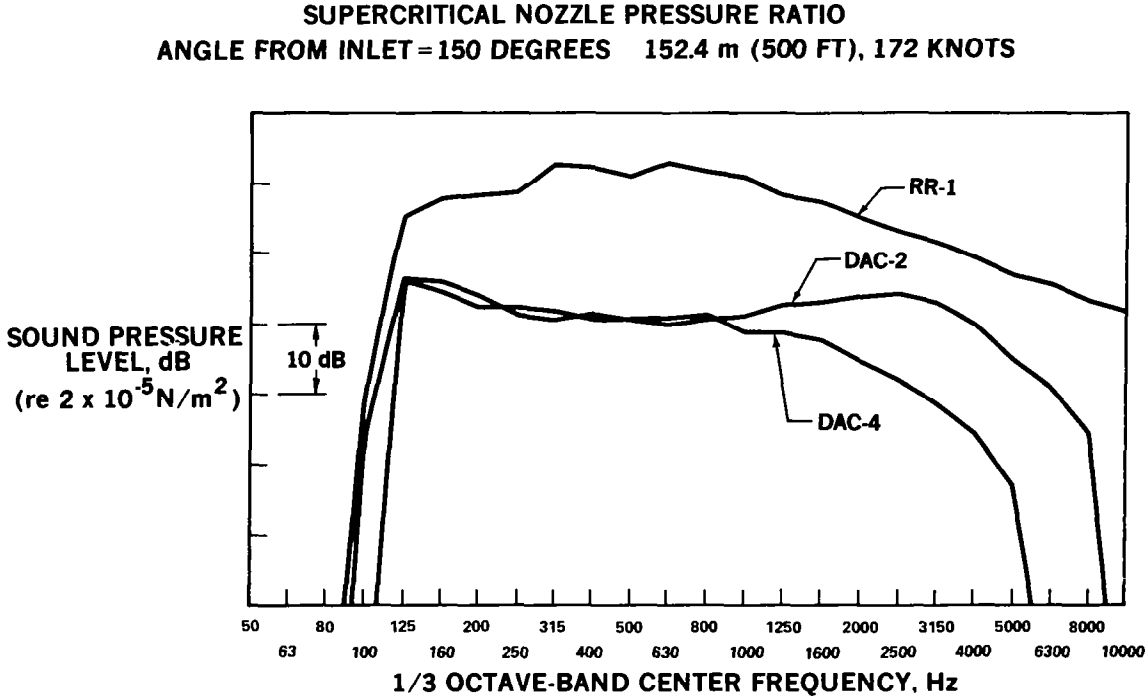

Figure 12.- SPL spectra at 150° for a typical supercritical nozzle pressure ratio.

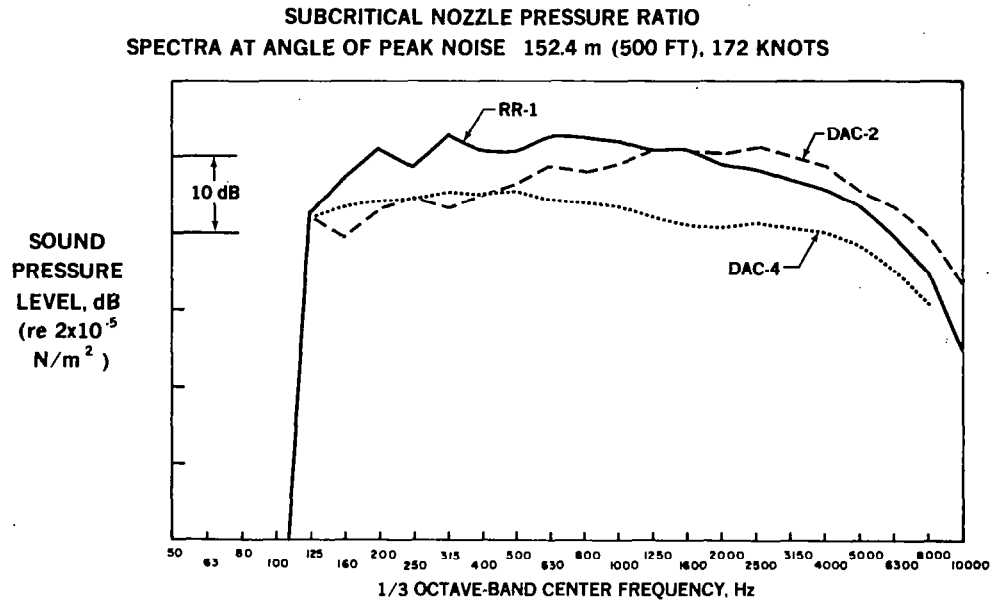

Figure 13.- Peak noise angle SPL spectra at a typical subcritical nozzle pressure ratio.

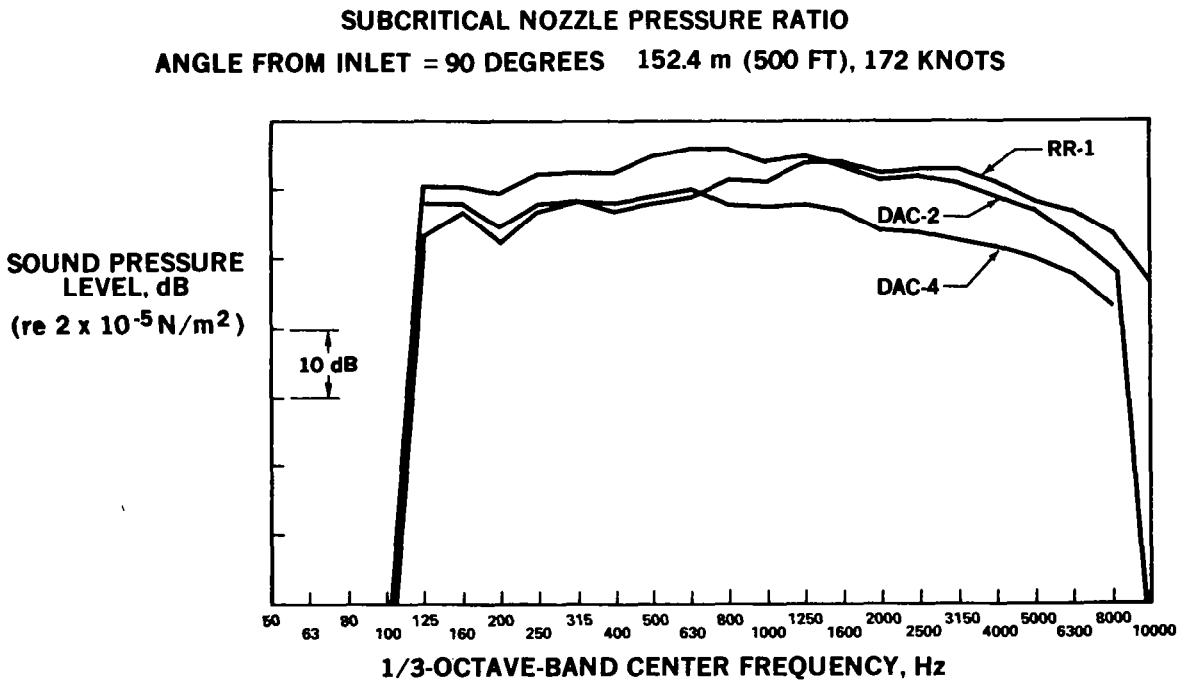

Figure 14.- SPL spectra at 90° for a typical subcritical nozzle pressure ratio.

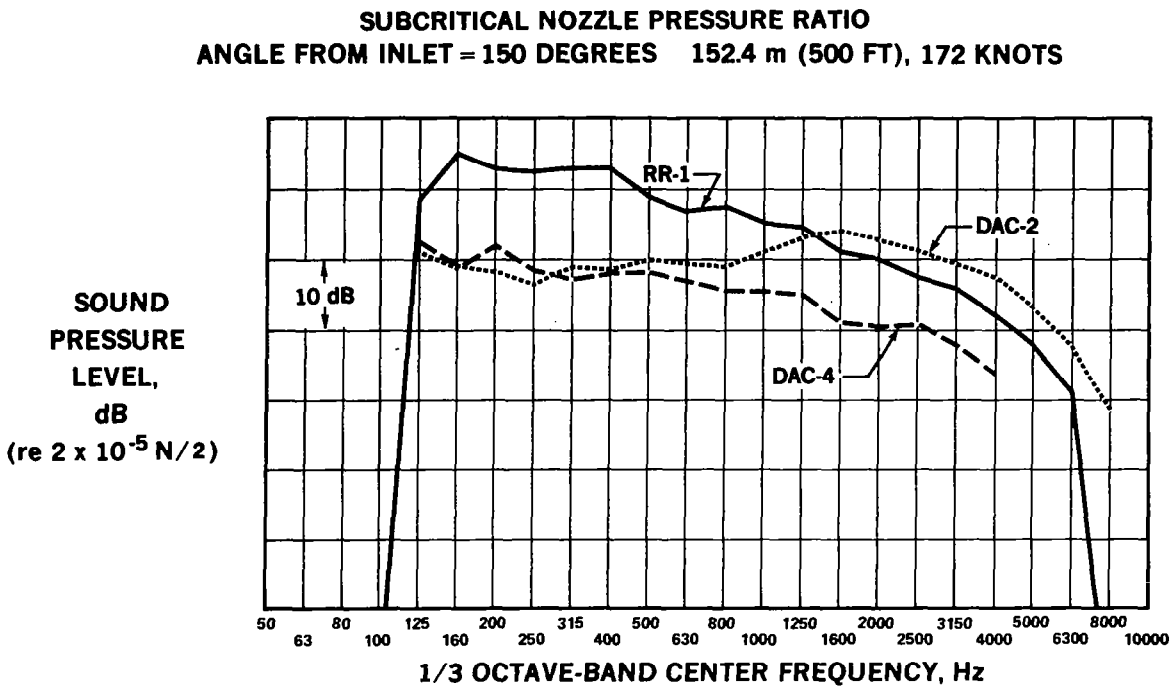

Figure 15.- SPL spectra at 150° for a typical subcritical nozzle pressure ratio.

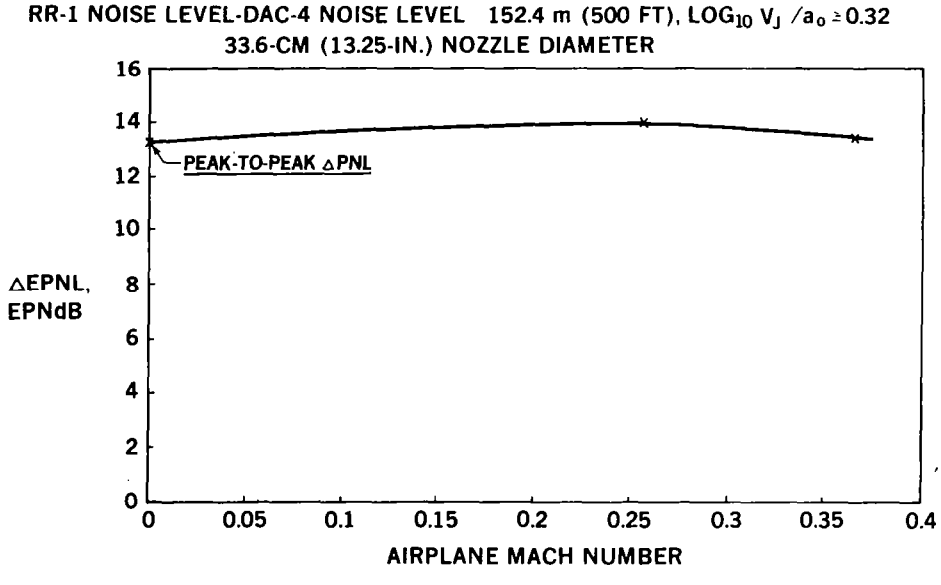

Figure 16.- Variation of noise suppression with airplane speed.

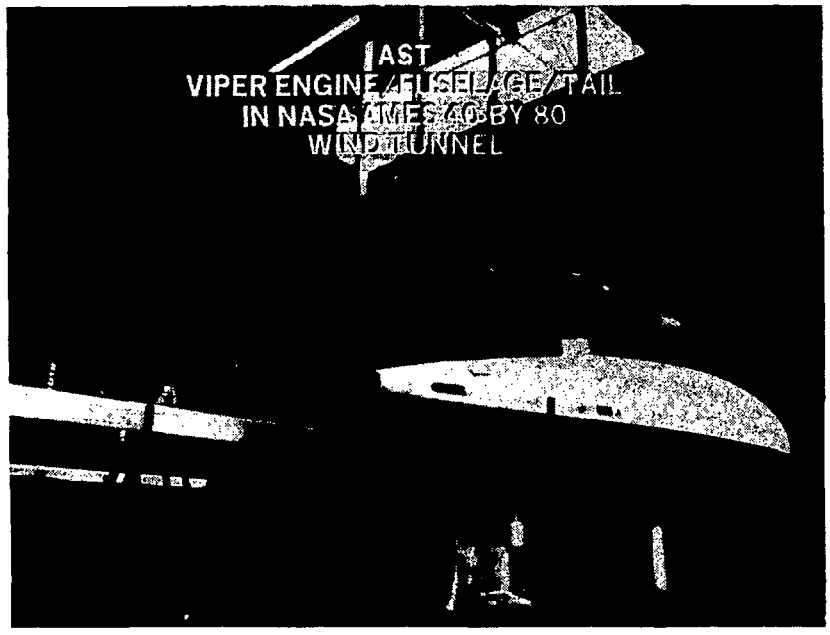

Figure 17.- Viper 601 engine and simulated HS-125 fuselage in NASA Ames 40- × 80-ft wind tunnel.

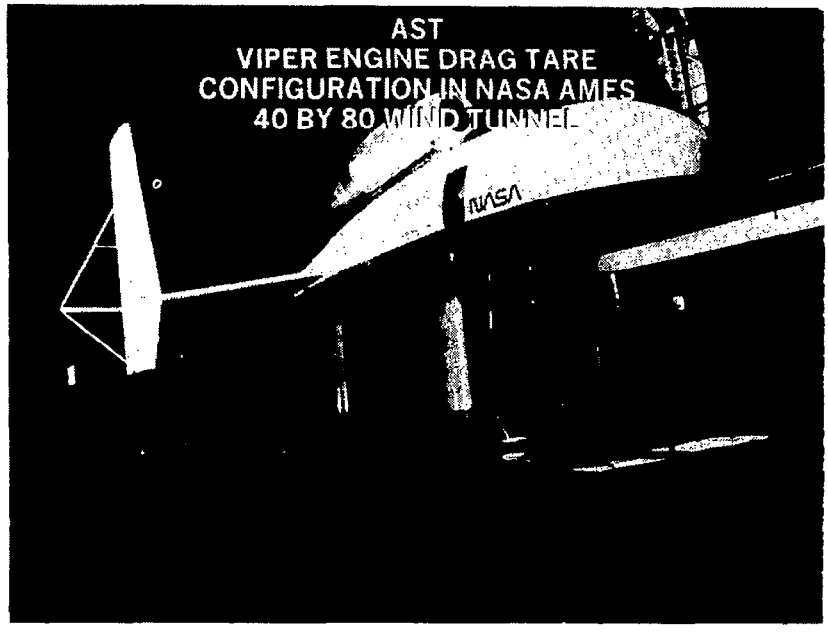

Figure 18.- NASA Ames 40- × 80-ft wind tunnel installation with simulated horizontal tail surface attached.

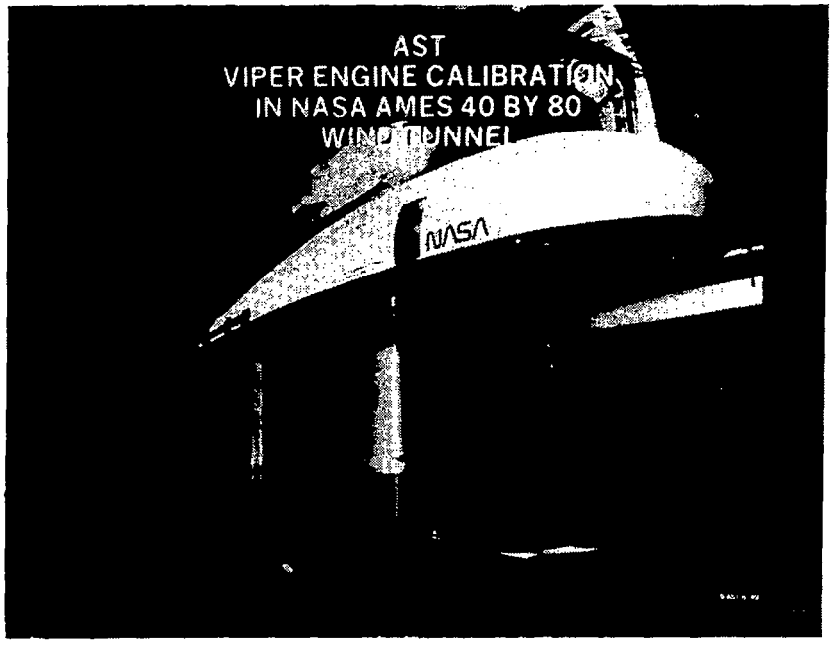

Figure 19.- Viper engine drag tare configuration, NASA Ames 40- × 80-ft wind tunnel

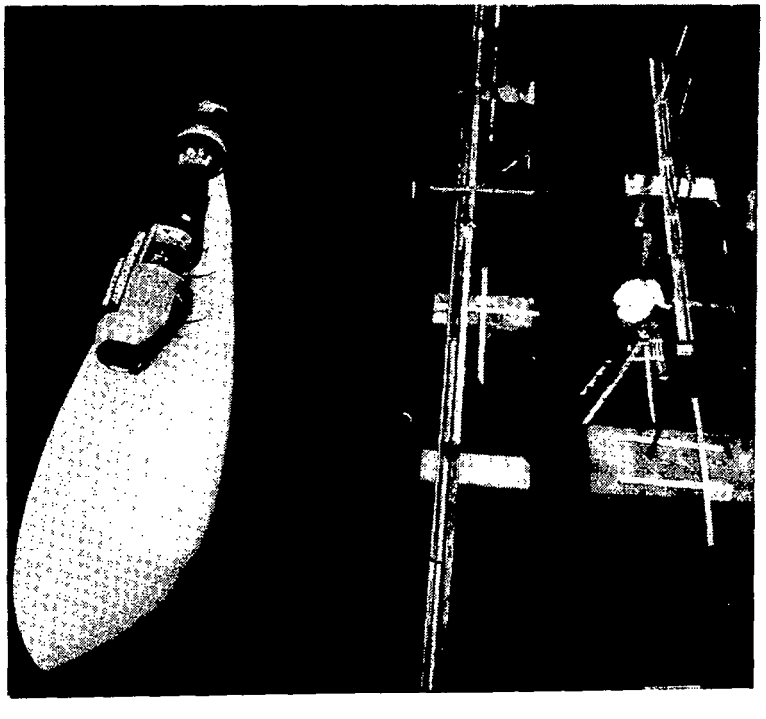

Figure 20.- NASA Ames 40- × 80-ft wind tunnel microphone array.

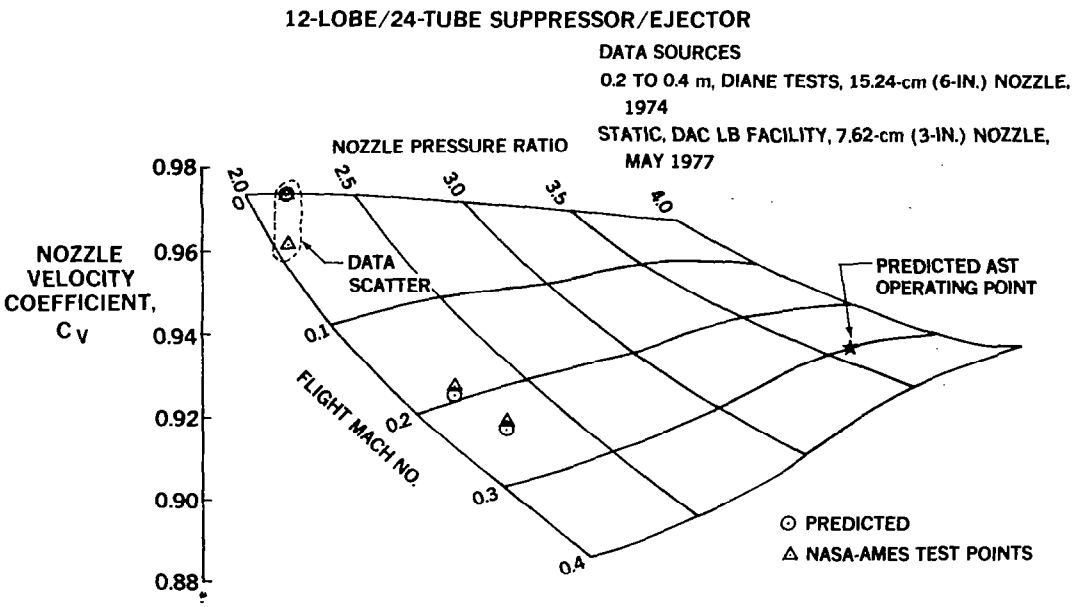

Figure 21.- MDC 12-lobe/24-tube suppressor/treated ejector nozzle performance.

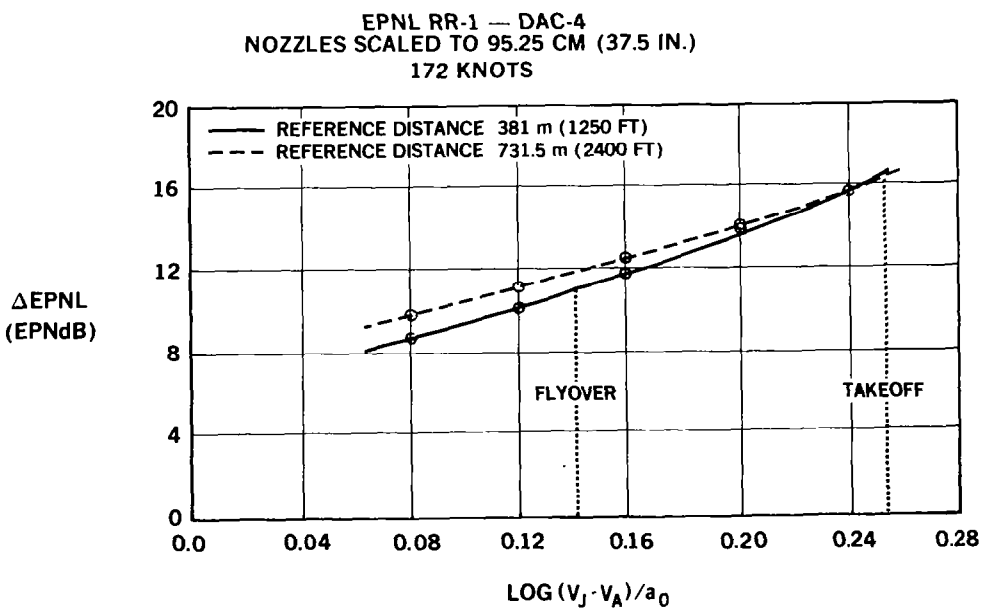

Figure 22.- Variation of noise suppression scaled to AST engine size with relative jet velocity.

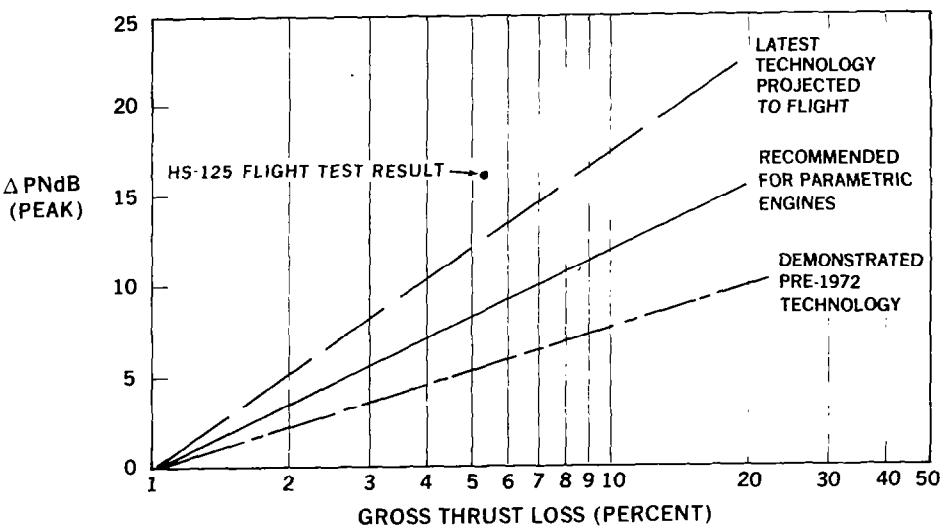

Figure 23.- Working Group E jet suppressor subgroup recommendation for trade-offs of noise suppression and thrust loss.

EFFECTS OF NOZZLE DESIGN ON THE NOISE FROM SUPERSONIC JETS

John M. Seiner, Thomas D. Norum, and Lucio Maestrello
NASA Langley Research Center

SUMMARY

The aeroacoustic supersonic performance of various internal nozzle geometries is evaluated for shock noise content over a wide range of nozzle pressure ratios. The noise emission of a Mach 1.5 and 2.0 convergent-divergent (C-D) nozzle is measured and compared to convergent nozzles. Comparisons are also made for a Mach 1.5 conical C-D nozzle and a porous plug nozzle. The Mach 1.5 conical C-D nozzle shows a small reduction in shock noise relative to the shock free case of the Mach 1.5 C-D nozzle. The Mach 1.5 C-D nozzle is found to have a wide operating nozzle pressure ratio range around its design point where shock noise remains unimportant compared to the jet mixing noise component. However it is found that the Mach 2 C-D nozzle shows no significant acoustic benefit relative to the convergent nozzle. Results from the porous plug nozzle indicate that shock noise may be completely eliminated, and the jet mixing noise reduced.

INTRODUCTION

One of the key aeroacoustic problems regarding the design of a supersonic cruise aircraft is increased acoustic emission produced by the presence of shocks in the jet exhaust plumes. This excess shock associated noise can completely dominate the jet mixing noise components in the forward quadrant of an aircraft engine that is operated with a supercritical nozzle pressure ratio. The recent theoretical work of Howe and Ffowcs-Williams[1] suggests that shock noise is an important component of the noise associated with the Concorde aircraft. The reduction of this shock noise component is important both from the standpoint of community noise and acoustic fatigue of the aircraft structure as documented by Hay and Rose[2].

A simple illustration of the physics (see Harper-Bourne and Fisher[3]) associated with the generation of shock noise is shown in figure 1. This figure depicts a standard converging nozzle operating with a supercritical nozzle pressure ratio, so that at the exit of the nozzle the static pressure is higher than that of the surrounding ambient medium. Upon leaving the nozzle exit the flow expands through the regular series of shocks in an attempt to lower the jet's static pressure to that of the surrounding medium. As the turbulent eddies convect through the shock cell system in the outer radial regions of the jet plume, intense omnidirectional broadband noise is produced with a peak frequency associated with the eddy convection velocity and shock cell spacing. The turbulence itself produces an unsteady location for the shock waves in the shear layer which, at certain nozzle pressure ratios, can cause the shock cell system to go into a resonant mode from acoustic feedback

to the nozzle lip. This condition, which was first described by Powell[4], is known as screech and has only been clearly documented for unheated model supersonic jets.

The empirical model of Harper-Bourne and Fisher adequately treats the broadband shock noise component produced by convergent nozzles up to a nozzle pressure ratio where a Mach disc begins to form. This occurs at a value of $\beta = (M_J^2 - 1)^{1/2} \sim 1.1$, where M_J is the fully expanded Mach number. The model of Harper-Bourne and Fisher was primarily developed from measurements with unheated convergent nozzles, but recently Tanna[5] has established the validity of this model for heated model supersonic convergent nozzles. The essential limitation of the Harper-Bourne and Fisher model is that it is only valid for predicting the shock content associated with convergent nozzles. It is, of course, important that a new model be developed that treats nozzle configurations which achieve a reduction or complete elimination of shock noise.

Seiner and Norum[6] have investigated the off-design performance of laboratory type convergent-divergent nozzles, and have shown that a good noise reduction benefit exists over a wide operating pressure ratio range around the nozzle's design point. While this noise reduction benefit is encouraging, of broader issue is the shock noise reduction potential that is likely to be available with the use of industrial type convergent-divergent nozzles.

This paper reports on two studies conducted at the Langley Research Center on the reduction of shock cell noise by means of convergent-divergent (C-D) nozzles and a porous plug suppressor. In the first study the noise characteristics of both convergent and convergent-divergent nozzles were documented over a wide operating nozzle pressure ratio range. The nozzle pressure ratio range was selected to span the design points of a Mach 1.5 and Mach 2 C-D nozzle. In this way the off-design performance of these various nozzle geometries could be evaluated to provide new basic understanding of the shock noise production process, and provide a data base for the development of more accurate prediction schemes.

In the second study a porous plug was introduced into the center of the jet flow from a convergent nozzle. Maestrello[7,8] has shown that the porous plug nozzle suppressor does indicate a cancellation of the shock noise component with an additional reduction in the jet mixing noise. This paper reports on the acoustic performance of a much shorter porous plug nozzle suppressor than was used in references 7 and 8. The results show that good noise reduction is still achieved.

PROPERTIES OF OFF-DESIGN CONVERGENT-DIVERGENT NOZZLES

Acoustic Facility

The acoustic facility used at the NASA Langley Research Center consists of an anechoic room with interior working dimensions of 6.71 m x 8.43 m x 7.23 m. Nozzles are supported vertically in this chamber. The far-field acoustic

measurements involve the use of 18 quarter inch free-field condenser microphones (B&K 4135) located uniformly at 7.5° intervals on a fixed radius of 3.66 m between 30° and 157.5° with respect to the upstream jet axis. The acoustic data were recorded on FM tape (DC-80 kHz). An illustration of the experimental arrangement is shown in figure 2.

For this acoustic program six nozzles were constructed whose internal contours are shown in figure 3. Of these, two are Mach 1 nozzles, one a conical convergent and the other a contoured convergent nozzle, the exit flow from the latter being parallel to the jet axis. The conical convergent nozzle represents the typical internal geometry for current commercial aircraft engine nozzles, and therefore its characteristic acoustic emission represents the reference case upon which comparisons are made. Three nozzles are convergent-divergent, and these include a Mach 1.5 C-D and Mach 2.0 C-D nozzle designed by the method of characteristics for parallel flow at the nozzle exit. These exit Mach numbers were selected on the basis that the Mach 1.5 nozzle is typical for the nozzle pressure ratio being considered for American supersonic cruise aircraft, while the Mach 2 represents a current upperbound for military type aircraft. The last C-D nozzle is a Mach 1.5 conical C-D nozzle, designed to approximate the contour of the nozzle in the F-15 airplane. The initial flow from this nozzle is divergent. The final nozzle is a contoured convergent nozzle that adapts the porous plug.

The exit diameter for each nozzle, except for the porous plug application, was chosen so that at specific points certain nozzles would exhibit the same ideal thrust. The Mach 2 nozzle was selected as the reference and constructed with an exit diameter of 5 cm. So that the Mach 1 nozzles would deliver the same thrust at the Mach 2 pressure ratio, thay were each constructed with a 3.95 cm exit diameter. The Mach 1.5 nozzles were constructed with a 4.28 cm exit diameter so that they and the Mach 1 nozzles would have the same thrust at the Mach 1.5 pressure ratio. For the above nozzles the 3.66 m microphone radius represents distances where $R/D \geq 72$.

Several pressure ratios were investigated which represent both design and off-design conditions for all nozzles. The pressure ratios under study in terms of β = 0., .2, .4, .6, .7, .8, .94, 1., 1.1, 1.34, 1.5, 1.72, 2., 2.1, and 2.15, where the values of 1.1 and 1.72 reflect the design pressure ratios of the C-D nozzles.

Experimental Results

Flow Field of a Mach 2 C-D Nozzle - A typical example of the shock structure encountered with the operation of a convergent-divergent nozzle at an off-design pressure ratio is shown in the schlieren photograph of figure 4. This photograph represents the case for the Mach 2 C-D nozzle operating in the underexpanded mode at a pressure ratio of 11.31 (β = 2). The centerline variation of Mach number for this case is shown in the lower portion of figure 4. At least 10 shock cells are evident, and these extend to a region between 25 and 30 jet diameters downstream of the jet exit. This figure shows that the supersonic core length is approximately 33 jet diameters and that the

shock cell system is extinguished several diameters upstream of the sonic point. For this pressure ratio the fully expanded Mach number is 2.24, and the average trend of the Mach number variation approaches this in the first 15 jet diameters.

As was discussed in the Introduction, unheated supersonic model jets produce high amplitude discrete frequency noise generation known as screech. This component does not appear prevalent in hot engine jet exhaust plumes, and the suppression of this component is common practice with research on model unheated jets. The general problems associated with the suppression of the screech mode in model jets are discussed by Seiner and Norum[6], and there it is shown that the stabilization of the oscillating shock structure by a tab leads to serious difficulties in interpreting acoustic data for shock noise content. Therefore the comparisons in this section are for model nozzles without screech suppression, although results from the use of a tab are presented in figures 5a and 5b.

Directivity and Power Spectra of Shock Associated Noise - The directivity of overall acoustic levels clearly indicates the degree of shock noise contamination to be observed when running a convergent nozzle relative to a C-D nozzle at its design point. Figures 5a and 5b show acoustic level as a function of angle relative to the jet flow inlet at a pressure ratio of 3.60 (β - 1.1). Results are shown for the conical convergent and conical C-D nozzles, and the Mach 1.5 C-D nozzle. Figure 5a includes the effect of the screech mode, while figure 5b displays a comparison with the screech mode suppressed by a tab. All three nozzles were designed to have the same thrust at this pressure ratio. By comparing the directivities of figures 5a and 5b it is evident that the Mach 1 conical nozzle contains strong screech tones at the Mach 1.5 design pressure ratio. With the screech mode suppressed there is little difference in the noise levels of the conical convergent and conical C-D nozzle. One can also observe that each conical nozzle still exhibits strong shock noise when compared with the shock free noise levels obtained with the Mach 1.5 C-D nozzle.

The data of figure 5 indicates that shock noise dominates the jet forward arc ($0 \leq \psi \leq 90°$). The narrowband power spectral density curves of figures 6a and 6b show the nature of this shock noise content at $\psi = 45°$ for the Mach 1 conical and Mach 1.5 conical C-D nozzles respectively. In each case the shock free contoured Mach 1.5 nozzle is shown for comparison. It is evident from these data that the broadband shock noise of both conical nozzles are relatively the same. Except for the presence of screech tones in the Mach 1 conical nozzle, the conical C-D nozzle appears to offer an insignificant acoustic benefit at these conditions relative to the conical convergent nozzle.

Shock Noise Benefit of C-D Nozzles - In order to evaluate the extent of the pressure ratio range where a C-D nozzle, designed for shock free flow, offers a noise reduction relative to a convergent nozzle the overall sound pressure level variation with β is shown in figure 7 at $\psi = 45°$. This figure indicates that there is a large range of nozzle pressure ratios around the design point of the Mach 1.5 C-D nozzle ($\beta = 1.1$) where considerably less noise is radiated compared to that produced by the strong shock cell structure of the Mach 1 conical nozzle. One can also observe with the Mach 1 conical nozzle

that beyond $\beta = 1.1$ the variation of acoustic level with the parameter β levels off and even decreases. This change in shape corresponds to the change observed in the secondary wavelength of the shock cell system resulting from the formation of a Mach disc as was reported in reference 6. Evidently as the Mach disc forms the strength of the shock cell system starting with the second shock cell, weakens in the jet's shear layer. Figure 7 also shows the variation of sound pressure with β for the Mach 1.5 conical C-D nozzle, and as expected, the acoustic benefit is much smaller than for the Mach 1.5 C-D nozzle.

In consideration of the complexity associated with integration of an engine nozzle with the optimum operating conditions of an aircraft's engine and airframe, it is difficult to prescribe what one may consider to be the best method for evaluating a jet noise benefit. Since we are attempting to compare the relative acoustic performance of convergent and C-D nozzles, a logical choice in model scale appears to be the ideal thrust. Also, the total integrated sound power of the flow appears to provide the most complete view of the dominance of the shock noise component over jet mixing noise. Hence, the total integrated sound power level is presented against ideal thrust in figure 8 for the three contoured nozzles tested.

In this figure the three darkened symbols correspond to the design points of the three nozzles. For both C-D nozzles the minimum noise point for each depression around the design point occurs in the overexpanded region, not at the design point. For the Mach 1.5 C-D nozzle, there is a 6 dB maximum difference compared to a contoured convergent nozzle with identical thrust. There is also a wide operating range where the Mach 1.5 C-D nozzle produces less noise. The case of the Mach 2 C-D nozzle is very disappointing since figure 8 shows that in comparison to a convergent nozzle it produces more noise at the same thrust almost across the entire pressure ratio range. As noted before, this primarily occurs since shock noise is relatively weak with a Mach 1 convergent nozzle at high nozzle pressure ratios, and the formation of a Mach disc produces a substantial region of subsonic flow which reduces the jet mixing noise. Figure 8 indicates that a Mach 1.5 C-D nozzle could represent an optimum selection for a design Mach number. This, of course, requires further investigation.

The results of this study are only strictly relevant to the case of unheated model jets where the dominance of the shock noise component over jet mixing noise can be clearly distinguished. With increasing jet exit velocity due to heat addition, the jet mixing noise increases but the shock noise remains relatively constant (see Tanna[5]). Thus, the results shown in this section, and particularly in figures 7 and 8, most likely indicate the maximum noise benefit available through use of a convergent-divergent nozzle.

POROUS PLUG NOZZLE SUPPRESSOR

The use of a porous plug nozzle as a means of reducing jet noise has been detailed in references 7 and 8. This section reports results for a porous plug centerbody with a shorter length than in the previous reports. Included

are shadowgraph pictures and the associated acoustic far-field spectra for the plug nozzle in comparison to a standard convergent nozzle.

Description of the Nozzle - The porous plug nozzle suppressor is shown in figure 9. This configuration has a plug/nozzle diameter ratio 0.833, with a flow exit area of 20.27 cm^2. The porous centerbody extends 24 cm from the nozzle exit, and it has a surface porosity of about 2 percent (ratio of open area to total area) which was accomplished by drilling a pattern of 0.07 cm radial holes around its periphery. The interior cavity of the plug is sealed on one end inside the nozzle and is vented to the jet stream all along its length.

A standard convergent nozzle with an exit diameter of 5.08 cm and with the same open flow exit area as the porous plug nozzle was tested to obtain comparable data as a basis for evaluating the aeroacoustic performance of the porous plug nozzle. The test was conducted over a range of pressure ratios between 1.136 - 3.72 and at ambient temperature.

Experimental Results - The shadowgraph pictures of figure 9 illustrate some of the operational features of the porous plug nozzle at a pressure ratio of 3.72. These pictures are for a longer plug, reported in references 7 and 8 and are shown here for the purpose of illustrating the concept of the flow behavior over a porous surface.

The flow of the standard convergent nozzle (figure 9, top) is underexpanded, a condition favorable for the formation of shocks in the jet. Portions of shock cells are evident, and others were observed downstream of the region shown in the photograph. The shocks are weaker further downstream and eventually disappear as the flow becomes subsonic. The interaction of these shocks with convected turbulence is the source of broadband shock noise emanating from the jet.

The flow development of a nonporous plug nozzle (a plug nozzle without venting holes) is shown in the middle photograph of figure 9. The shock pattern appears to be much weaker than in the standard nozzle, probably due to the elimination of shock focusing at the centerline. The flow from the porous plug nozzle (figure 9, bottom) looks free of shocks, indicating that the venting holes permit an adjustment of pressure gradient in the flow and hence preventing the formation of shocks.

Far-field acoustic power spectra of the porous plug and standard convergent nozzles are compared in figure 10. The data were obtained at 3.81 m from the jet exit and are presented for angles of 50°, 90°, and 160° from the inlet.

The spectra of the standard jet at angles of 50° and 90° exhibit both screech tones and broadband shock noise. A smaller tone appears at 160°, although this spectra appears to be dominated by jet mixing noise. The data from the porous plug nozzle indicate no peaks due to shock associated noise. This result is consistent with the shadowgraph of figure 9 which suggests that the shock waves are eliminated in the porous plug nozzle flow.

Note also that the porous plug nozzle spectra indicate noise reductions at essentially all frequencies at each of the angles. In particular, significant reductions are obtained at 160°, where the mixing noise dominates. This suggests that in addition to shock noise reduction, the porous plug nozzle also yields a reduction in the jet mixing noise.

Although not shown here, significant mixing noise reduction occurs even when the Mach number is subsonic, particularly at small angles from the jet axis. The differences in the noise levels between using a short porous plug and a longer one were reported in references 7 and 8. There it was shown that a longer plug produces less jet mixing noise at low frequency at angles near the jet axis. This difference reflects the trade-off between using a short versus longer plug centerbody.

CONCLUSIONS

This paper has examined the potential noise benefit offered by a convergent-divergent nozzle relative to a conical convergent nozzle over a wide range of operating pressure ratios. In the case of the shock free contoured Mach 1.5 C-D nozzle a 6 dB reduction of total integrated sound power was achieved over a Mach 1 contoured convergent nozzle operated at the same thrust. A smaller reduction of total acoustic power was found in the comparative case of the Mach 1.5 conical C-D nozzle. For the case of a Mach 2 nozzle, its benefit over a convergent nozzle is less promising unless it would be imperative to reduce the sound pressure levels slightly in the jet's forward arc as has been reported in reference 6. The data with C-D nozzles clearly indicate that current concepts regarding the design of the Mach 1.5 conical C-D nozzle is inadequate for elimination of shock noize. It is perhaps possible to emulate the shock noise reduction performance of the laboratory type C-D nozzle by considering other internal nozzle shapes that cancel internal shock waves more completely.

The results on the porous plug nozzle suppressor show that both the screech and broadband shock associated noise are eliminated with an additional decrease in the jet mixing component. The noise reduction of the plug nozzle suppressor is parametrically dependent on the plug's surface porosity and length.

REFERENCES

1. Howe, M. S. and Ffowcs-Williams, J. E.: On the Noise Generated by an Imperfectly Expanded Supersonic Jet. Phil. Trans. Roy. Soc. London, vol. 289, no. 1358, 1978, pp. 271-314.

2. Hay, J. A. and Rose, E. G.: In-Flight Shock Cell Noise. J. Sound and Vib., vol. 11, no. 7, 1970, pp. 411-420.

3. Harper-Bourne, M. and Fisher, M. J.: The Noise from Shock Waves in Supersonic Jets. AGARD-CP-131, 1973.

4. Powell, A.: On the Mechanism of Choked Jet Noise. Proc. Phys. Soc., B, vol. 66, 1953, pp. 1039-1056.

5. Tanna, H. K.: An Experimental Study of Jet Noise Part II: Shock Associated Noise. J. Sound and Vib., vol. 50, no. 3, 1977, pp. 429-444.

6. Seiner, J. M. and Norum, T. D.: Experiments of Shock Associated Noise on Supersonic Jets. AIAA Paper No. 79-1526, 1979.

7. Maestrello, L.: Initial Results of a Porous Plug Nozzle for Supersonic Jet Noise Suppression. NASA TM 78802, 1978.

8. Maestrello, L.: An Experimental Study on Porous Plug Jet Noise Suppressor. AIAA 5th Aeroacoustics Conference, Paper No. 79-0673, 1979.

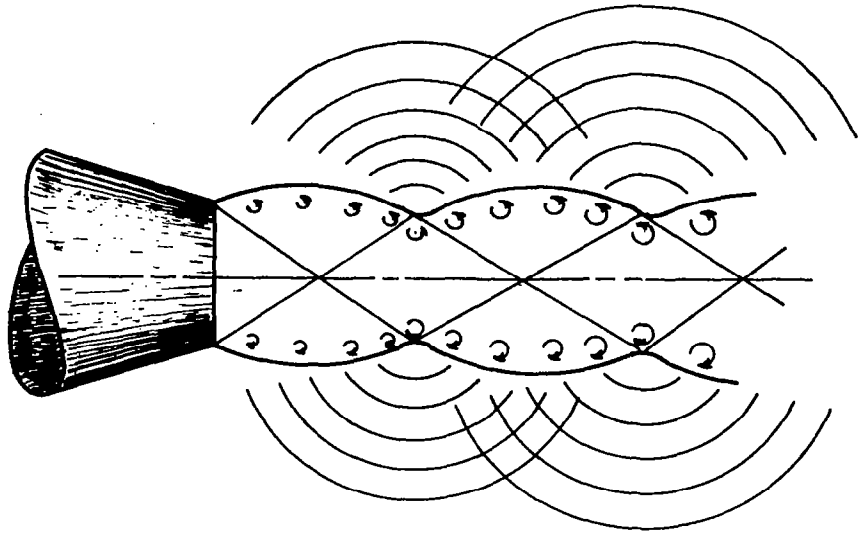

Figure 1.- Illustration of shock associated noise.

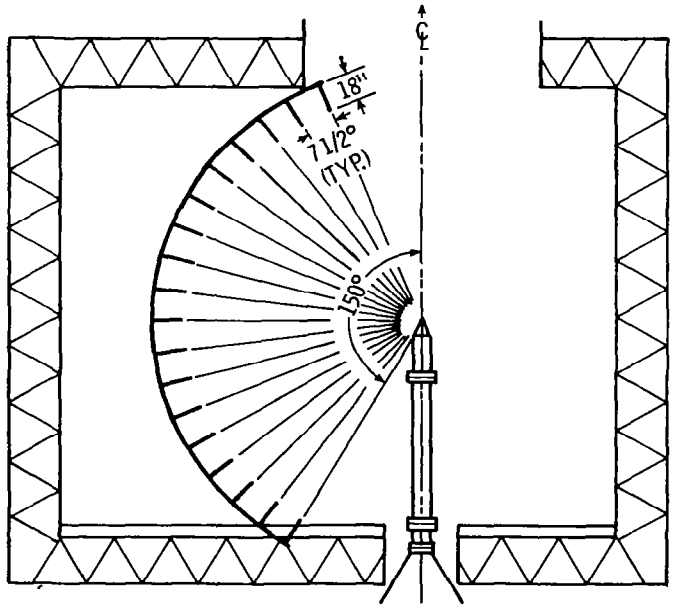

Figure 2.- Anechoic test facility.

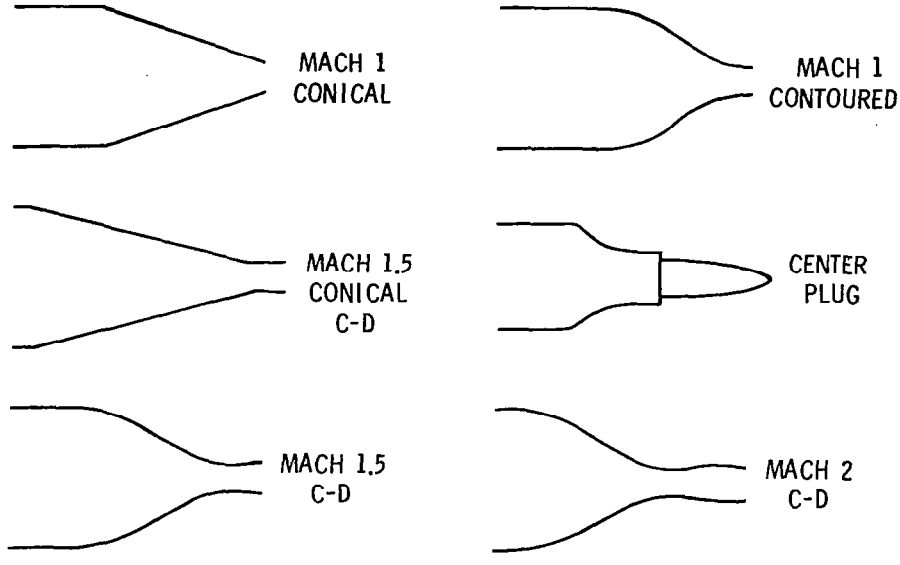

Figure 3.- Nozzle contours for shock noise study.

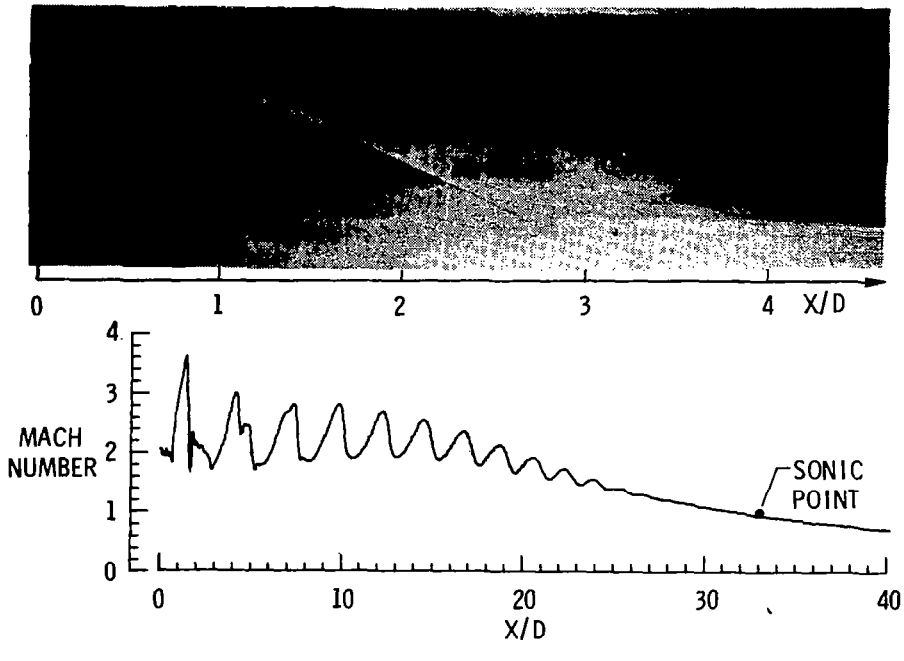

Figure 4.- Mach 2 C-D nozzle at $\beta = 2$.

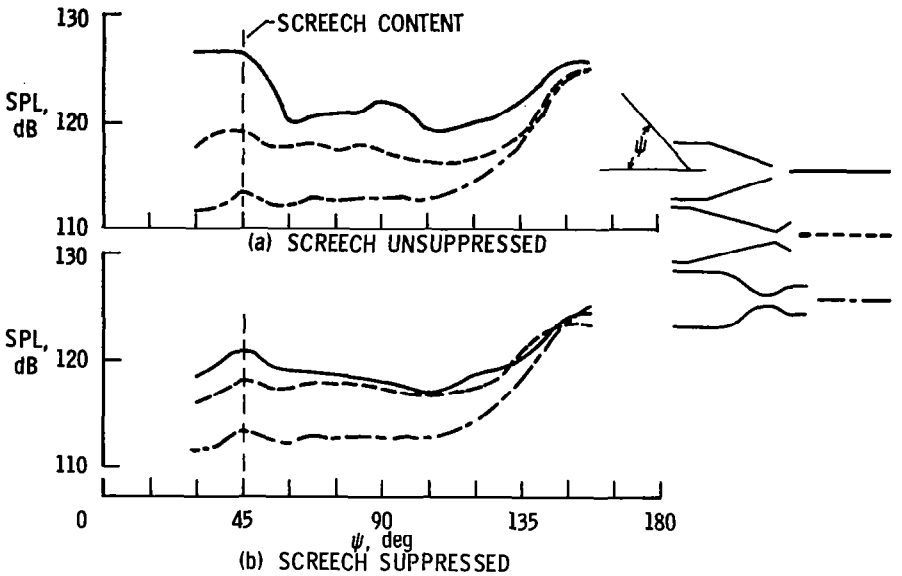

Figure 5.- Shock noise directivity at $\beta = 1.1$.

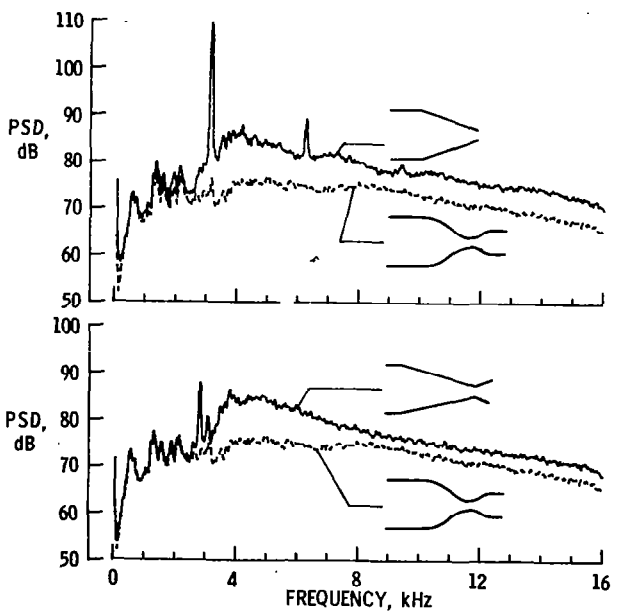

Figure 6.- Power spectral density at $\beta = 1.1$, 45° from inlet.

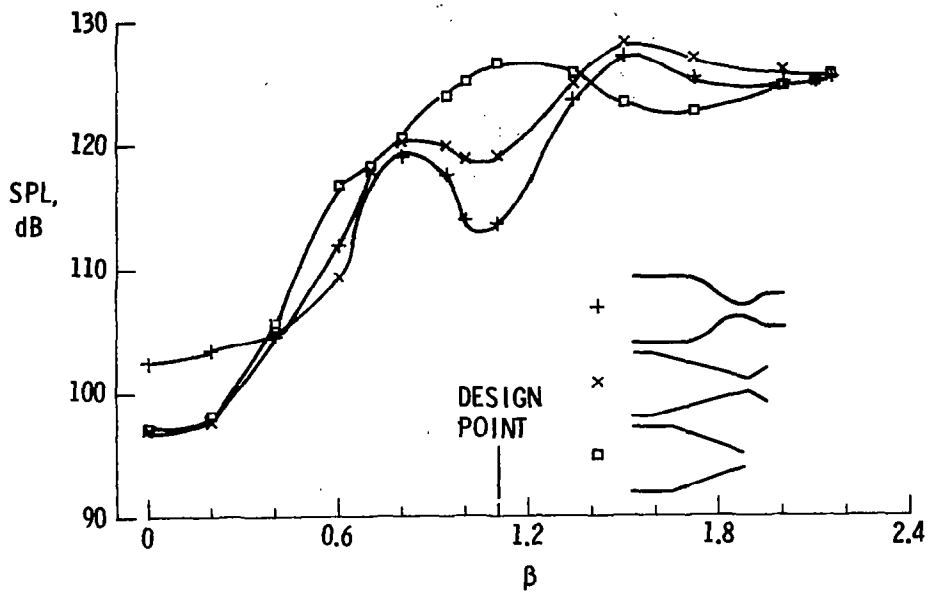

Figure 7.- Shock noise benefit of Mach 1.5 nozzles.

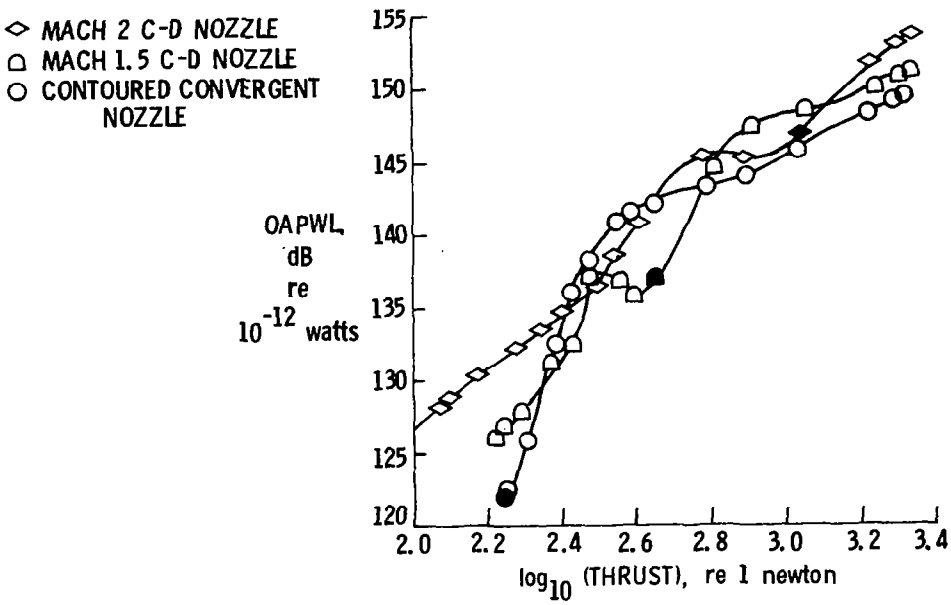

Figure 8.- Maximum overall noise benefit of C-D nozzles.

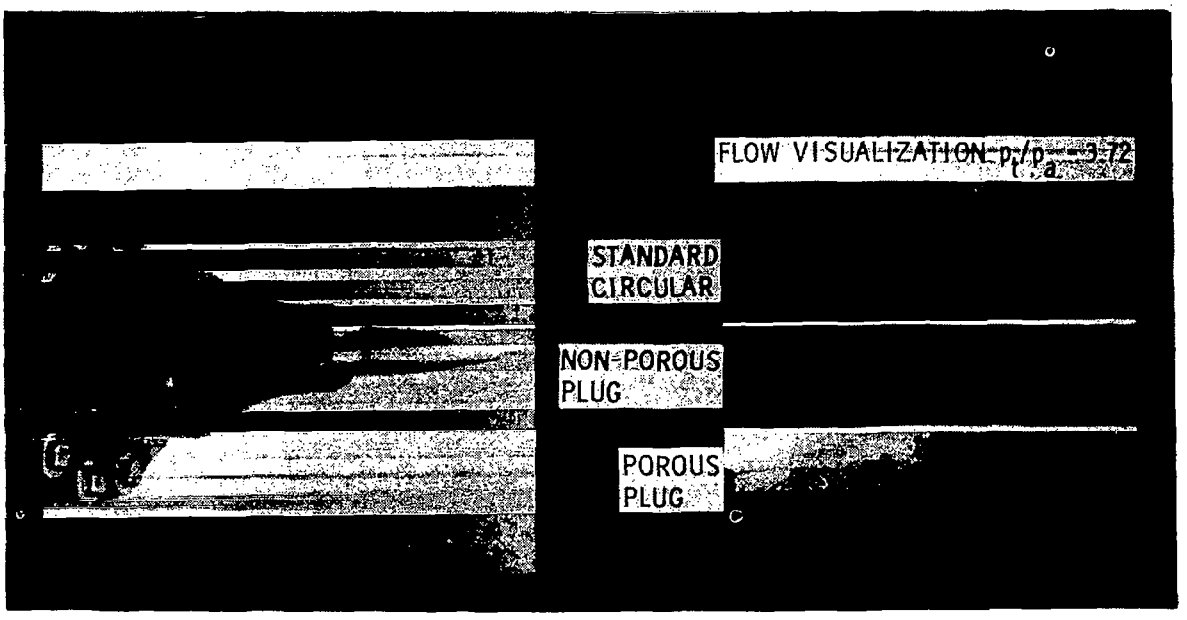

Figure 9.- Porous plug nozzle suppressor.

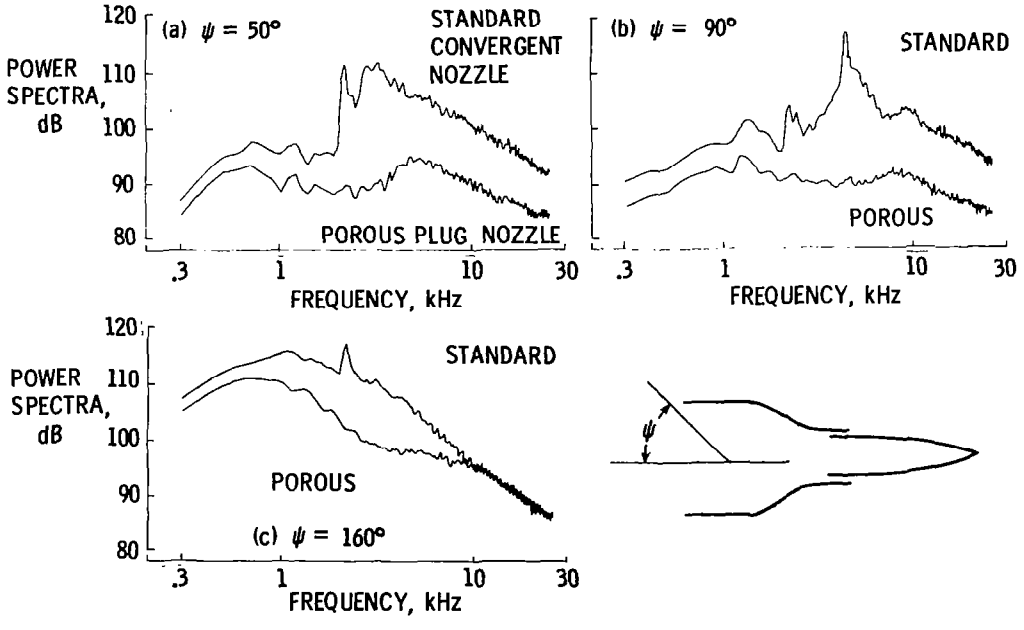

Figure 10.- Noise benefits of porous plug nozzle.

STATUS OF NOISE TECHNOLOGY FOR ADVANCED SUPERSONIC CRUISE AIRCRAFT

James R. Stone and Orlando A. Gutierrez
Lewis Research Center

SUMMARY

During the past several years, progress has been made in several areas of acoustic technology applicable to advanced supersonic cruise aircraft. This paper reviews some of the more important developments, which relate primarily to jet noise and its suppression. The noise-reducing potential of high-radius-ratio, inverted-velocity-profile coannular jets is demonstrated by model-scale results from a wide range of nozzle geometries, including some simulated flight cases.

These results have been verified statically at large scale on a variable-cycle-engine (VCE) testbed. A preliminary assessment of potential VCE noise sources such as fan and core noise is made, based on the testbed data. Recent advances in the understanding of flight effects are reviewed. The status of component noise prediction methods is assessed on the basis of recent test data, and the remaining problem areas are outlined.

INTRODUCTION

An environmentally and economically acceptable advanced supersonic cruise aircraft will require substantial advances in noise suppression technology over current, first-generation supersonic aircraft. This paper summarizes the present state of the art in noise technology applicable to supersonic cruise aircraft. Inverted-velocity-profile (IVP) coannular nozzles and mechanical suppressors, both of which show promise for jet noise reduction, receive primary emphasis. The discussion also includes the effects of flight and the influence of other (non-jet-mixing) noise sources. Throughout these discussions the status of prediction methods for the various noise sources is considered.

Inverted-velocity-profile (IVP) coannular nozzles have been identified as a major breakthrough in jet noise suppression applicable to supersonic cruise aircraft engines (e.g., ref. 1). The aeroacoustic benefits associated with IVP jets were first identified in a series of tests under NASA Lewis Research Center sponsorship (refs. 2 and 3). The results of these model-scale programs were reviewed at the 1976 SCAR Conference (refs. 4 to 6). These programs included unsuppressed configurations with and without center plugs as well as suppressed configurations. The unsuppressed IVP configurations were shown to provide noise levels near the Federal Aviation Administration guidelines, FAR-36 (1969), with good aerodynamic performance. Further noise reductions

were shown for the suppressed IVP configurations but were accompanied by significantly poorer aerodynamic performance. Thus, the emphasis of NASA-sponsored IVP noise studies for the next several years was primarily on the unsuppressed configurations, and some of the highlights of those studies are included in this paper. During this time, however, a major Department of Transportation (DOT)/FAA study (with technical support from NASA) of jet noise suppressors placed considerable emphasis on suppressors, including those for IVP configurations.

Mechanical jet noise suppressor studies during the same time period considered both dual-stream (including IVP) and single-stream concepts. Results for one promising single-stream suppressor-ejector concept are discussed in reference 7; results for a promising single-stream chute-plug design are presented in reference 8. A brief discussion of these results is included in the present paper.

The subject of flight effects on jet noise has received considerable interest and effort in recent years. According to classical jet noise theory (e.g., ref. 9), jet mixing noise should be reduced in flight because of the reduced shear on the jet. However, some experimental results for jet engines in flight have indicated apparent discrepancies; specifically, the noise in the forward quadrant was found to increase rather than decrease in flight (e.g., refs. 10 and 11). Subsequent studies conducted or sponsored by NASA have shown that these apparent anomalies can be largely resolved when the engine internal noise is accounted for (refs. 12 to 19). These studies are briefly reviewed in the present paper, and an improved flight effects procedure (ref. 20) is shown to be reasonably accurate in the high-jet-velocity range of interest for supersonic cruise aircraft. The effects of flight on IVP coannular nozzles and mechanical suppressors are also discussed.

SYMBOLS

A	exhaust area, m^2
c_a	ambient sonic velocity, m/sec
F	thrust, kN
F_{Ref}	reference thrust (arbitrary), kN
L	source-to-observer distance, m
M_0	aircraft Mach number, V_0/c_a, dimensionless
m	flight velocity exponent (eq. (1)), dimensionless
OASPL	overall sound pressure level, dB re 20 $\mu N/m^2$
PNL_N	normalized perceived noise level, $PNL - 10 \log\left[\frac{A}{L}\, 2\left(\frac{F}{F_{ref}}\right)\left(\frac{\rho_S}{\rho_0}\right)^{w-1}\right]$, PNdB

PNL_T	tone-corrected perceived noise level, PNdB
R_I	inner radius of outer stream nozzle, m
R_O	outer radius of outer stream nozzle, m
w	density exponent, dimensionless
V	velocity, m/sec
β	angle from jet axis to flightpath, deg
Δ	OASPL difference, flight minus static, dB
θ	angle referred to inlet axis, deg
ρ	density, kg/m^3

Subscripts:

a	ambient
calc	calculated
exp	experimental
F	flight
j	fully expanded isentropic jet (primary)
m	mixed
S	static
0	aircraft
1	inner stream (fully expanded)
2	outer stream (fully expanded)

JET NOISE SUPPRESSION

Jet noise is expected to be the most important noise source for advanced supersonic cruise aircraft, particularly at takeoff and cutback power. Therefore, the suppression of this noise source is of great importance to the development of an environmentally acceptable advanced supersonic cruise aircraft. Jet noise can be reduced by lowering the specific thrust at takeoff through engine-cycle modifications, by employing jet noise suppressor nozzles, or by a combination of these approaches. For example, the variable-cycle engines (VCE's) produce a relatively low specific thrust, and thereby relatively low

noise, at takeoff and provide further noise reduction when IVP coannular nozzles are incorporated. For some other engine cycles, multielement mechanical jet noise suppressors are needed and will have to provide even greater noise reductions at a given specific thrust than the IVP coannular nozzle. So that the jet noise suppression characteristics of various approaches can be compared, it has been suggested (e.g., refs. 21 and 22) that noise levels be compared with those of a mixed-flow conical nozzle at the same total mass flow and at the same specific thrust. Such comparisons are made for the various suppressor concepts discussed herein.

Inverted-Velocity-Profile Coannular Nozzles

As mentioned previously, IVP coannular nozzles have been identified as a breakthrough in jet noise suppression applicable to advanced supersonic cruise aircraft. As illustrated schematically in figure 1, this approach consists of exhausting the higher velocity stream through a high-radius-ratio annulus and the lower velocity stream through an inner nozzle. Such velocity profiles can be obtained by crossducting the fan and core streams (e.g., ref. 23) or by burning in the fan duct (e.g., ref. 24). Advances in engines incorporating these approaches were discussed at a recent NASA conference on aeronautical propulsion (ref. 25).

The noise benefits of the IVP coannular nozzle concept are shown in figure 2. Normalized peak perceived noise level is plotted against the mass-averaged jet velocity (ideal specific thrust) for several of the many configurations tested (refs. 26 and 27). A reference curve is also shown for a hypothetical, perfectly mixed conical nozzle (ref. 28). For all these coannular nozzle data, the outer-stream velocity is 1.5 to 2 times the inner-stream velocity. Noise reductions for the coannular nozzles, relative to the conical nozzle, generally improve as the ratio of the inner radius to the outer radius of the outer stream R_I/R_O increases. The bulk of the IVP data fall in a band about 6 PNdB below the conical reference, but even lower levels can be seen for some high-radius-ratio cases.

The radius ratio and velocity ratio between the two streams strongly influence the noise level at a given mass-averaged jet velocity, as illustrated in figure 3, taken from reference 27. The noise of the coannular nozzle relative to that of the perfectly mixed conical nozzle is plotted against the outer-stream to inner-stream velocity ratio V_2/V_1 over a range of mass-averaged jet velocities for radius ratios of 0.52 to 0.95. These results are in terms of the overall sound pressure level at the peak sideline noise angle, $\theta = 135^{\circ}$. The data include both conventional and inverted velocity profiles. For all four configurations a minimum noise (maximum suppression) exists for the IVP conditions. For the 0.52- and 0.62-radius-ratio nozzles, the minimum noise is only about 3 decibels below the conical nozzle prediction. As the radius ratio is increased, the minimum noise is still further reduced, to 4 decibels below the conical nozzle prediction at a 0.68 radius ratio and to over 9 decibels below the conical prediction at noncoplanar 0.95 radius ratio. The velocity ratio at which this minimum noise occurs decreases somewhat with increasing radius ratio.

IVP noise prediction. - Since the noise is a complicated function of flowfield and geometric variables, it is necessary to go beyond simple plots such as figure 2 to correlate the data. The complexity of the IVP jet noise generation processes is shown in figure 4. As many as four noise-generating regions must be considered. It is the differing trends of these different noise sources with operating conditions that leads to the existence of a minimum noise as velocity ratio increases, such as illustrated in figure 3. The low-frequency noise is generated well downstream of the nozzle where the two flows have mixed and can no longer be distinguished; this is termed the merged region. The higher frequency jet mixing noise is generated in the region near the nozzle exit where the individual jets can still be identified; this is termed the premerged region. When either or both streams are supersonic, noise can be generated by turbulent eddies passing through shock waves; thus, we must in general consider inner-stream shock noise and outer-stream shock noise.

Empirical models relating these noise-generating processes to those of a conical nozzle have been developed (refs. 21, 29, and 30). Small-scale, plugless, coannular nozzle experimental spectra (ref. 2) are compared with predictions based on the empirical models of reference 30 in figure 5. Sound pressure level is plotted against frequency for an angle of 120°, in the rear quadrant, in figure 5(a). For this case both streams are supersonic, so all four noise sources must be considered; but it is the jet mixing noises that dominate at this angle. The shock noise levels, predicted by an empirical modification to the theory of Harper-Bourne and Fisher (ref. 31), contribute somewhat in the high-frequency range but not as much as the premerged mixing noise. Results for the same conditions, but in the forward quadrant at $\theta = 75^{\circ}$, are shown in figure 5(b). It is apparent that shock noise is much more important in the forward quadrant than in the rear quadrant. The inner-stream shock noise dominates the midfrequency range and determines the peak sound pressure level. The outer-stream shock noise controls the high-frequency range. Although the relative contributions of the various sources are different in the forward and rear quadrants, the spectra at both angles are predicted with good accuracy.

Large-scale verification of IVP concept. - The acoustic characteristics of IVP coannular nozzles, originally determined from a series of model-scale tests, have now been verified on an engine, as discussed in more detail in reference 32.

Typical results are shown in figures 6 and 7 for the NASA - General Electric VCE testbed coannular plug nozzle as well as for a similar model nozzle at essentially the same conditions, with a mixed jet velocity of about 590 meters per second. For both the engine and the model, the experimental results are scaled up to a typical product-engine size (total exhaust area, 0.903 m^2) at a typical sideline distance (slant range, 731.5 m). The results are also compared with the prediction procedure of reference 30. Perceived noise is plotted as a function of angle in figure 6. The model results are verified by the engine results. The engine results are an average of 0.8 PNdB below the model results, and the standard deviation between the two data sets is 1.5 PNdB. The overall accuracy of the prediction method is also confirmed by the testbed data. The average bias of the prediction with respect to the testbed data is less than 0.1 decibel, and the standard deviation is 1.0 decibel. The predicted contributions of the combined jet mixing noises (merged plus premerged) and the shock

noises (from both streams) are also shown. Although the jet mixing noise is most important in this case, the shock noises do contribute somewhat in the forward quadrant. Although not shown here, at higher power settings and in flight, the shock noise becomes even more important and can contribute significantly to the effective perceived noise level.

Further evidence of the overall accuracy of the scaling procedure and of the prediction can be seen in more detail in figure 7, along with some indications of areas requiring improvements to the prediction procedures. Experimental data for both testbed and model scaled up to typical product-engine size are compared with the prediction on a spectral basis. The prediction procedure is accurate at low frequencies (the merged jet region) and thus gives a good estimate of the perceived noise level (PNL). It appears that improved prediction procedures are needed for premerged mixing noise and shock noise, which control the high frequencies. These sources may contribute more significantly in flight and also become more important for the shorter distances involved at the flyover noise measurement point.

Mechanical Jet Noise Suppressors

Various system studies of propulsion systems for future supersonic cruise aircraft (e.g., refs. 23 to 25) have indicated that FAR-36 (1969) noise levels can be approached with variable-cycle engines with unsuppressed IVP coannular nozzles. Other studies (e.g., ref. 33) have indicated slightly higher noise levels for such engines. In any case, FAR-36 (1969) noise levels cannot at present be predicted for such engines with any reasonable allowance for design margins without resorting to advanced operating procedures or shielding schemes. To obtain such design margins, and also to have any possibility of approaching the FAR-36 (1977) subsonic aircraft requirements, some means of suppressing jet noise will probably be needed. Therefore, although NASA's resources have been focused primarily on unsuppressed IVP coannular nozzles over the past few years, mechanical jet noise suppressor technology has continued to be advanced by the industry with some support from DOT (FAA) and more limited support from NASA. The DOT (FAA) study included a large number of single-stream and IVP-coannular suppressors; some of the most promising concepts of both types were tested in simulated flight.

Single-stream suppressors. - In addition to the variable-cycle engines, low-bypass engines with single-stream suppressors may be feasible supersonic cruise propulsion systems. Results for a promising single-stream suppressor concept developed by General Electric with support from DOT (FAA) and NASA have been reported recently in reference 8. Similarly promising results are also presented in reference 7 for a single-stream suppressor-ejector developed by McDonnell Douglas and tested with limited NASA support.

Typical results for a single-stream suppressor-ejector, in this case the McDonnell Douglas design, are shown in figure 8. Model-scale static experimental data (ref. 34) are scaled up to a typical product-engine size (exhaust area, 0.713 m^2) at a typical flyover altitude (381 m). As was done for the IVP coannular nozzles, the experimental suppressor results are compared with a predicted baseline (ref. 28) for a conical nozzle at the same ideal specific

thrust. At a relatively high jet velocity (~715 m/sec, fig. 8(a)) the peak PNL of the suppressor is 8.7 PNdB below the peak PNL of the conical nozzle according to the Rolls-Royce spin rig data, or 10.4 PNdB below the peak PNL according to the NASA Ames 40- by 80-Foot Wind Tunnel data. Thus, comparing these results with those of figure 2 shows that the suppressed low-bypass-ratio engine may be slightly quieter than a variable-cycle engine with an unsuppressed IVP coannular nozzle at the same specific thrust. However, engine weight, nozzle thrust loss, and many other factors must also be considered in choosing the best engine type for a specific application. At lower jet velocity (~490 m/sec, fig. 8(b)), the peak PNL suppression is reduced to 4.5 PNdB (spin rig) or to 6.3 PNdB (40- by 80-Ft Wind Tunnel). This reduction of suppression with decreasing jet velocity is typical of most single-stream suppressors. NASA Langley made a detailed system-noise - cost-sensitivity study of the McDonnell Douglas suppressor concept as part of an international study on the feasibility of developing noise rules for civil supersonic cruise aircraft (ref. 33). This study, based on the limited (spin rig) data available at that time, indicated that the FAR-36 (1969) noise levels might be achieved without undue cost penalties.

IVP coannular nozzles with suppressors. - Quieter variable-cycle engines may be achieveable with a suppressed IVP coannular nozzle. It was the possibility of relatively small outer-stream suppressors (small in comparison with mixed-flow, single-stream suppressors) that caused the initial interest in the IVP concept. The initial IVP model tests (refs. 2 and 3) emphasized outer-stream suppressors. With these suppressors, static peak PNL was reduced as much as 6 PNdB below that of an unsuppressed IVP coannular nozzle at the same ideal specific thrust. Because of the promise of this approach, NASA Lewis is sponsoring model-scale static and simulated flight tests (contract NAS3-21608) and large-scale VCE testbed static tests (contract NAS3-20582, exhibit C) of an outer-stream-suppressed coannular plug nozzle.

IMPORTANCE OF NON-JET-MIXING NOISES

Although it is fairly well established that jet-mixing noise is the most critical noise problem for supersonic cruise aircraft, it is necessary to develop an understanding of the other potential noise sources. For example, fan noise may well become dominant at approach, and shock-cell noise may have a significant effect on the effective perceived noise level at takeoff. Core noise contributes only slightly at low power, according to the VCE testbed results. Duct-burner combustion noise is a potential problem for which no data base yet exists. This section discusses the current status of the fan, shock-cell, and duct-burner combustion noises.

Fan Noise

Although the VCE early acoustic test was not structured to provide a definitive answer to the fan noise problem, some useful data were obtained. Tests were conducted on the testbed with a conical nozzle and two different inlets, one hardwall and one suppressed. Typical results, in terms of tone-corrected PNL directivity, are shown in figure 9 for approach and cutback power settings.

The results are scaled up to a typical product-engine size (exhaust area, 0.903 m^2) at a typical sideline distance (slant range, 731.5 m). In each case, the unsuppressed-inlet results are shown by the solid line and the suppressed-inlet results are shown by the dashed line. The fan noise can then be estimated by antilogarithmic subtraction of the suppressed, tone-corrected perceived noise level (PNL_T) from the unsuppressed value. Coannular plug nozzle data at the same power setting are shown by the circular symbols. The square symbols denote the implied total noise for an unsuppressed-inlet coannular configuration obtained by the antilogarithmic sum of the suppressed-inlet coannular plug nozzle noise and the estimated fan noise from the conical nozzle test.

At approach power (fig. 9(a)) the fan noise would apparently contribute substantially to the EPNL if it were not suppressed. In flight, with the jet-mixing noise reduced and the forward-quadrant fan noise increased, as expected, the unsuppressed fan noise might become the controlling source. It is clear that if the jet noise limit is to be achieved at approach power, an inlet suppression of approximately 15 PNdB might be required. Of course, detailed trade-off studies will be needed to determine the optimum suppression requirements. At cutback power (fig. 9(b)) the unsuppressed fan noise would still be discernible, although not as prominently as at approach power. Thus, the level of suppression required would be less than at approach power. At takeoff power, shock-cell noise makes it difficult to determine the effect of fan noise on the PNL.

The inferred fan noise from the VCE testbed is compared with predicted values from reference 35 in figure 10. Although this prediction does not apparently model the noise-generating mechanisms for this high-tip-speed split fan, such comparisons are appropriate since this method has already been used to estimate the relative importance of fan noise for such engines. Some indication of agreement between the inferred and predicted values is obtained at a typical approach power (fig. 10(a)). The agreement is not so good at cutback power (fig. 10(b)). Clearly, development of fan noise prediction procedures for high-tip-speed fans should continue in order to provide more realistic and accurate estimates. However, at typical approach power settings, the current prediction (ref. 35) does give a reasonable enough estimate of fan noise to indicate its importance relative to other noise sources.

Shock-Cell Noise

As was pointed out earlier in the discussion of the IVP coannular jet noise prediction, shock-cell noise can be a significant contributor to the takeoff flyover EPNL. In reference 36, shock noise and methods of controlling it are discussed in some detail.

Although the prediction procedure of reference 30 does include shock-cell noise calculated from a method based on modification of the Harper-Bourne and Fisher theory (ref. 31) for conical nozzles, further development is required to obtain more accurate predictions (e.g., fig. 7). Even the theoretical basis for this prediction procedure may need improvement, as indicated in reference 37.

Since shock-cell noise is of potential importance, it may be necessary to employ convergent-divergent nozzles in order to reduce or eliminate it. Noise reductions obtained by applying such an approach to single-stream circular nozzles are reported in references 36 and 37. However, for IVP coannular nozzles, the VCE testbed results and related model tests showed no benefit for a convergent-divergent, outer-stream nozzle. Because of complications involved with interacting coaxial supersonic jets (e.g., ref. 38), further research on coannular shock noise and its control is clearly needed. Incorporating a porous center plug in the nozzle exhaust also appears to offer a means of reducing shock noise (ref. 39).

Duct-Burner Combustion Noise

One variable-cycle engine concept of interest features burning in the fan duct, a method that can then produce an inverted velocity profile. Thus, the combustion noise generated in such a duct burner should be considered. However, no data base exists for such configurations. Various methods have been developed to predict combustion noise (e.g., refs. 40 to 42); however, these are based on data for core-engine combustors. In terms of the correlation parameters developed in these predictions and in more recent studies (e.g., ref. 43), the conditions expected for a duct burner fall well beyond the range of available data, and extrapolation is uncertain. Exercising these predictions for duct-burner conditions indicates that, if such extrapolation is valid, duct-burner combustion noise could be significant at takeoff. Resolution of this problem must await the development of a suitable data base.

FLIGHT EFFECTS

To assess the effect of jet noise on the environment of the airport vicinity, it is necessary to predict the effect of flight on jet engine exhaust noise. For new or proposed aircraft particularly, such predictions will be based at least in part on model and large-scale static and simulated flight experiments. Because of costs, to rely solely on full-scale flight tests would severely limit the number of configurations and concepts that could be tested. Therefore, it is of great importance to be able to predict in-flight noise from static or simulated-flight data.

The flight geometry is illustrated, and some of the key parameters are defined, in figure 11. According to classical jet noise theory (Ffowcs Williams, ref. 9), in-flight subsonic jet noise should vary with flight velocity and a flight velocity exponent m as $10 \log\left[V_j^{8-m}(V_j - V_0)^m\right]$. For the static case ($V_0 = 0$) this reduces to the well-known V_j^8 expression of Lighthill (ref. 44). Thus, by this reasoning, the difference between static and flight levels, $(OASPL)_F - (OASPL)_S$, corrected for motion effects by adding $10 \log\left[1 - M_0 \cos(\theta + \beta)\right]$, should be given by $10 \log\left[(V_j - V_0)/V_j\right]^m$.

Based on such considerations, several investigators (e.g., refs. 10, 11, and 45) have expressed their results in terms of a flight velocity exponent m defined as follows:

$$m \equiv \frac{(OASPL)_F - (OASPL)_S + 10 \log\left[1 - M_0 \cos(\theta + \beta)\right]}{10 \log\left[1 - \left(\frac{V_0}{V_j}\right)\right]} \tag{1}$$

Such data have typically been presented as plots of m versus θ, the angle from the inlet axis. Also, prediction methods for jet noise flight effects (e.g., Bushell (ref. 11)) have been proposed on the basis that m can be defined as a unique function of θ. However, it has been pointed out (ref. 17) that m is not a physical quantity but an expression based on assumed relations and that such relations do not accurately and uniquely represent the physical processes. Furthermore, it was shown in reference 17 that the exponent m is sufficiently sensitive to the measured OASPL's that the presence of even small amounts of non-jet-mixing noise can result in negative values of m. (Positive m values indicate noise reduction in flight, while negative m values indicate noise amplification in flight.) Therefore, it was indicated that prediction methods should not be formulated on the basis of m as a function of θ, as has been proposed (e.g., refs. 11 and 45).

A composite plot of typical experimental values of m available from the literature as a function of θ is shown in figure 12; the proposed prediction curves of Bushell (ref. 11) and Hoch (as given in ref. 45) are also shown. The flight data (refs. 10 and 45 to 49) show a wide range of results, including negative m values in some cases. The prediction of Bushell (ref. 11) also indicates an angular range of negative m values, primarily in the forward quadrant, as is consistent with some of the engine data (refs. 10, 11, and 45). On the other hand the simulated-flight data exhibit positive m values at all angles for shock-free jets (e.g., refs. 50 and 51, which are typical of such data), with the exception of some of the data of reference 46. The reference 46 data have a correction applied for an assumed sound absorption by the free-jet turbulent shear layer; without this correction the m values would be higher and closer to the other model data. Thus, it is apparent that improvements over the prediction of Bushell (ref. 11) are needed, and such predictions have been proposed by NASA Lewis (ref. 16) and the Société Nationale d'Etude et de Construction de Moteurs d'Aviation (SNECMA).[1] At jet velocities below approximately 520 meters per second, the earlier NASA Lewis method (ref. 16) fits the data somewhat better than does the SNECMA prediction, but the earlier NASA method is inadequate at high jet velocities. Therefore, a modified method has been developed (ref. 20) that shows better agreement with the data base than does reference 16 or SNECMA. Furthermore, the new method is more closely related to fundamental theories (refs. 9 and 52) than the earlier methods.

Plots of flight velocity exponents versus angle for the J85 turbojet engine on the Bertin Aerotrain (ref. 46) and comparisons with the prediction

[1]Method proposed to Society of Automotive Engineers A-21 Committee on Aircraft Noise by SNECMA.

method of reference 20 are shown in figure 13. The results have been corrected for Aerotrain background noise (ref. 46), for internal noise (ref. 16), and (where appropriate) for shock-cell noise (ref. 30). The results cover a range of jet velocity from 445 to 680 meters per second. The agreement is good in the rear quadrant, but the m values are consistently overpredicted for angles from 50° to 120°. The decrease in m with increasing θ at large angles and high jet velocities, a decrease that can produce negative m values (noise increase in flight), is due to supersonic convection effects and becomes more pronounced as jet velocity increases.

A statistical comparison is made in figure 14, where the distribution of the number of samples is plotted versus the experimental minus the calculated flight increment (in groupings of 0.5-dB width). The data base for this figure includes the low-bypass-ratio refanned JT8D engines on the DC-9 airplane and the higher-bypass-ratio JT9D engines on the DC-10 airplane (ref. 15). The error distribution is narrower for the present method than for the SNECMA method. The SNECMA method also has a significant peak at $\Delta_{exp} - \Delta_{calc} = -4.0$, indication of a significant problem with the SNECMA method. It is shown in reference 20 that the new method agrees better with the data base than a recently proposed SAE method. Over the data base range of jet velocity (primary) from 280 to 680 meters per second, the new method has a standard deviation of 1.5 decibels, and the proposed SAE (SNECMA) method has a standard deviation of 2.5 decibels.

IVP Coannular Nozzles

As was reported at the 1976 SCAR Conference (ref. 4), the aeroacoustic advantages of the IVP coannular nozzle concept have also been obtained under simulated flight conditions at model scale. The results of these tests are reported in detail in reference 51. Further analysis (ref. 29) of these results has shown that when the merged region and the premerged region are considered separately, the flight effects are quite similar to those of a conical nozzle at the appropriate (merged or premerged) conditions. Relative velocity exponents (eq. (1)) resulting from the analysis of reference 29 for the merged and premerged regions are shown as a function of angle in figure 15. Also shown is the range of conical nozzle mixing-noise results (ref. 51) from the same facility and over the same range of jet velocities and temperatures. The merged-region exponents are essentially in the middle of the conical nozzle range, but the premerged-region exponents tend to be on the high side (larger noise reduction in flight).

From the results discussed in the preceding paragraph it appears that the aeroacoustic advantages expected for IVP coannular nozzles should be retained in flight. However, some caution may be warranted since the tests of reference 51 were limited to two plugless coannular nozzles and were also limited to jet velocities and temperatures below those of interest for supersonic cruise application. More recent simulated flight tests conducted under contract NAS3-20619 generally confirm the trends cited in this discussion, but the final reduction of these data was not completed in time to incorporate the results in this paper.

Single-Stream Suppressors

It has been acknowledged that flight effects can be quite critical to jet noise suppressors. Therefore, recent suppressor tests (e.g., refs. 7 and 8) have emphasized flight effects. The results of reference 8 for a single-stream suppressor-ejector model are shown in figure 16 to illustrate typical trends. These results are for the same jet conditions as figure 8 but for simulated flight. The model-scale experimental data (ref. 34) are scaled up to a typical product-engine size (exhaust area, 0.713 m^2) at a typical flyover altitude (381 m), and the results are compared with those predicted (ref. 28) for a conical nozzle at the same ideal specific thrust. By comparing these results with figure 8, it can be seen that the peak noise suppression is less in simulated flight than under static conditions. The spin-rig data, particularly at low jet velocity (fig. 16(b)), appear to be contaminated by extraneous noise sources. The 40- by 80-Foot Wind Tunnel data indicate that although the flight results tend to be less favorable than the static results, peak noise suppressions of 7 PNdB at low jet velocity to 8 PNdB at high jet velocity may still be attainable in flight.

CONCLUDING REMARKS

This paper has reviewed some of the recent advances in acoustic technology applicable to advanced supersonic cruise aircraft, with emphasis on jet noise suppression and flight effects.

The noise-reducing characteristics of high-radius-ratio, inverted-velocity-profile coannular jets has been demonstrated by model-scale results from a wide range of geometries, including some simulated-flight cases. These results have now been verified statically at large scale on the variable-cycle-engine (VCE) testbed. The testbed results agree with scaled model data and with a prediction procedure based on model data.

A preliminary assessment of other potential VCE noise sources, based on the testbed data, has been presented. Unsuppressed fan noise appears to be significant and could be the controlling noise source at approach. Duct-burner combustion noise has been identified as a potentially significant problem for which no data base or acceptable prediction method is available.

An improved jet noise flight effects prediction has been developed and compared with experimental data obtained from the Bertin Aerotrain with a J85 engine, the DC-10 airplane with JT9D engines, and the DC-9 airplane with refanned JT8D engines. It has been shown that, over the data base range of jet velocity (primary) from 280 to 680 meters per second, the new method has a standard deviation of only 1.5 decibels.

REFERENCES

1. Willis, Edward: Variable-Cycle Engines for Supersonic Cruise Aircraft. Variable Geometry and Multicycle Engines, AGARD CP-205, 1976, pp. 7-1 to 7-19.

2. Kozlowski, Hilary; and Packman, Allan B.: Aerodynamic and Acoustic Tests of Duct-Burning Turbofan Exhaust Nozzle. NASA CR-2628, 1976.

3. Knott, P. R.; et al.: Acoustic Tests of Duct-Burning Turbofan Jet Noise Simulation. NASA CR-2966, 1978.

4. Gutierrez, Orlando A.: Aeroacoustic Studies of Coannular Nozzles Suitable for Supersonic Cruise Aircraft Applications. Proceedings of the SCAR Conference, NASA CP-001, Part 2, 1976, pp. 471-490.

5. Kozlowski, Hilary: Coannular Nozzle Noise Characteristics and Application to Advanced Supersonic Transport Engines. Proceedings of the SCAR Conference, NASA CP-001, Part 2, 1976, pp. 491-504.

6. Lee, Robert: Coannular Plug Nozzle Noise Reduction and Impact on Exhaust System Designs. Proceedings of the SCAR Conference, NASA CP-001, Part 2, 1976, pp. 505-524.

7. FitzSimmons, R. D.; McKinnon, R. A.; and Johnson, E. S.: Flight and Tunnel Test Results of the MDC Mechanical Jet Noise Suppressor Nozzle. Supersonic Cruise Research '79, NASA CP-2108, 1980. (Paper no. 20 of this compilation.)

8. Moore, Michael T.: Flight Effects on the Jet Noise Signature of a 32-Chute Suppressor Nozzle as Measured in the NASA Ames 40×80 Foot Wind Tunnel. (R78AEG375, General Electric Co.; NASA Contract NAS2-9312.) NASA CR-152175, 1979.

9. Ffowcs Williams, J. E.: The Noise from Turbulence Convected at High Speed. Phil. Trans. Roy. Soc. (London), Ser. A, vol. 255, no. 1061, Apr. 1963, pp. 469-503.

10. Brooks, J. R.; and Woodrow, R. J.: The Effects of Forward Speed on a Number of Turbojet Exhaust Silencers. AIAA Paper 75-506, Mar. 1975.

11. Bushell, K. W.: Measurement and Prediction of Jet Noise in Flight. AIAA Paper 75-461, Mar. 1975.

12. Stone, J. R.: On the Effects of Flight on Jet Engine Exhaust Noise. NASA TM X-71819, 1975.

13. Merriman, J. E.; et al.: Forward Motion and Installation Effects on Engine Noise. AIAA Paper 76-584, July 1976.

14. Gutierrez, O. A.; and Stone, J. R.: Developments in Aircraft Jet Noise Technology. Aircraft Safety and Operating Problems, NASA SP-416, 1976, pp. 497-512.

15. Blankenship, G. L.; et al.: Effect of Forward Motion on Engine Noise. (MDC-J7708, Douglas Aircraft Co., Inc.; NASA Contract NAS3-20031.) NASA CR-134954, 1977.

16. Stone, J. R.: Prediction of In-Flight Exhaust Noise for Turbojet and Turbofan Engines. Noise Control Eng., vol. 10, no. 1, Jan.-Feb. 1978, pp. 40-46.

17. Stone, J. R.: On the Use of Relative Velocity Exponents for Jet Engine Exhaust Noise. NASA TM-78873, 1978.

18. Ahuja, K. K.; Tester, B. J.; and Tanna, H. K.: The Free Jet as a Simulator of Forward Velocity Effects on Jet Engine Noise. NASA CR-3056, 1978.

19. Burcham, F. W., Jr.; Lasagna, P. L.; and Oas, S. C.: Measurements and Predictions of Flyover and Static Noise of a TF-30 Afterburning Turbofan Engine. NASA TP-1372, 1978.

20. Stone, J. R.: An Improved Method for Predicting the Effects of Flight on Jet Mixing Noise. NASA TM-79155, 1979.

21. Pao, S. Paul: A Correlation of Mixing Noise from Coannular Jets with Inverted Flow Profiles. NASA TP-1301, 1979.

22. Tanna, H. K.; Tester, B. J.; and Lau, J. C.: The Noise and Flow Characteristics of Inverted-Profile Coannular Jets. (Lockheed-Georgia, Co.; NASA Contract NAS1-15018.) NASA CR-158995, 1979.

23. Krebs, J. N.: Advanced Supersonic Technology Study - Engine Program Summary: Supersonic Propulsion - 1971 to 1976. Proceedings of the SCAR Conference, NASA CP-001, Part 1, 1976, pp. 353-370.

24. Howlett, Robert A.: Variable Stream Control Engine Concept for Advanced Supersonic Cruise Aircraft - Features and Benefits. Proceedings of the SCAR Conference, NASA CP-001, Part 1, 1976, pp. 341-352.

25. Powers, A. G.; et al.: Supersonic Propulsion Technology. Aeropropulsion 1979, NASA CP-2092, 1979, pp. 345-386.

26. Knott, P. R.; Blozy, J. T.; and Staid, P. S.: Acoustic and Aerodynamic Performance Investigation of Inverted Velocity Profile Coannular Plug Nozzles - Comprehensive Data Report. (R79AEG166-Vols-1, 2, 3, General Electric Co.; NASA Contract NAS3-19777.) NASA CR-159575-Vols-1, 2, 3, 1979.

27. Goodykoontz, Jack H.; and Stone, James R.: Experimental Study of Coaxial Nozzle Exhaust Noise. AIAA Paper 79-0631, Mar. 1979. (Also NASA TM-79090, 1979.)

28. Stone, James R.: Interim Prediction Method for Jet Noise. NASA TM X-71618, 1974.

29. Larson, R. S.: A Jet Exhaust Noise Prediction Procedure for Inverted Velocity Profile Coannular Nozzles. AIAA Paper 79-0633, Mar. 1979.

30. Stone, J. R.: An Empirical Model for Inverted-Velocity-Profile Jet Noise Prediction. NASA TM-73838, 1977.

31. Harper-Bourne, M.; and Fisher, M. J.: The Noise from Shock Waves in Supersonic Jets. Noise Mechanisms, AGARD CP-131, 1974, Paper 11.

32. Knott, P. R.; et al.: VCE Early Acoustic Test Results of General Electric's High-Radius Ratio Coannular Plug Nozzle. Supersonic Cruise Research '79, NASA CP-2108, 1980. (Paper no. 19 of this compilation.)

33. Mascitti, V. R.; Maglieri, D. J.; and Raney, J. P.: Preliminary Noise Tradeoff Study of a Mach 2.7 Cruise Aircraft. NASA TM-78732, 1979.

34. McKinnin, R. A.: Cooperative Wind Tunnel Tests of Douglas Advanced Supersonic Technology Jet Noise Suppressor. (McDonnell Douglas Corp.; NASA Contract NAS1-14601.) NASA CR-158996, 1978.

35. Heidmann, M. F.: Interim Prediction Method for Fan and Compressor Source Noise. NASA TM X-71763, 1975.

36. Seiner, J. M.; et al.: Effects of Nozzle Design on the Noise From Supersonic Jets. Supersonic Cruise Research '79, NASA CP-2108, 1980. (Paper no. 21 of this compilation.)

37. Seiner, J. M.; and Norum, T. D.: Experiments of Shock-Associated Noise on Supersonic Jets. AIAA Paper 79-1526, July 1979.

38. Dosanjh, D. S.; et al.: Supersonic Jet Noise Suppression by Coaxial Cold-Heated Jet Flows. AIAA Paper 76-507, July 1976.

39. Maestrello, L.: An Experimental Study on Porous Plug Jet Noise Suppressor. AIAA Paper 79-0673, Mar. 1979.

40. Huff, Ronald G.; Clark, Bruce J.; and Dorsch, Robert G.: Interim Prediction Method for Low Frequency Core Engine Noise. NASA TM X-71627, 1974.

41. Mathews, D. C.; Rekos, N. F., Jr.; and Nagel, R. T.: Combustion Noise Investigation. PWA-5478, Pratt & Whitney Aircraft Group, 1977. (FAA-RD-77-3, AD-A038154/1.)

42. Matta, R. K.; Sandusky, G. T.; and Doyle, V. L.: GE Core Engine Noise Investigation - Low Emission Engines. Final Rep. June 1975-Dec. 1976, General Electric Co., 1977 (FAA-RD-77-4, AD-A048590.)

43. von Glahn, U. H.: Correlation of Combustor Acoustic Power Levels Inferred from Internal Fluctuating Pressure Measurements. NASA TM-78986, 1978.

44. Lighthill, M. J.: On Sound Generated Aerodynamically. II. Turbulence as a Source of Sound. Proc. Roy. Soc. (London), Ser. A, vol. 222, no. 1148, Feb. 1954, pp. 1-32.

45. Brooks, J. R.: Flight Noise Studies on a Turbojet Using Microphones Mounted on a 450 Ft Tower. AIAA Paper 77-1325, Oct. 1977.

46. Clapper, W. S.; and Stringas, E. J.: High Velocity Jet Noise Source Location and Reduction, Task 4 - Development/Evaluation of Techniques for In-Flight Investigation. R77AEG189, General Electric Co., 1977. (FAA-RD-76-79-4, AD-A041849.)

47. Strout, F. G.; and Atencio, A., Jr.: Flight Effects on JT8D Engine Jet Noise as Measured in the NASA Ames 40 by 80 Foot Wind Tunnel. AIAA Paper 76-556, July 1976.

48. Munoz, L. F.: The 727/JT8D Jet and Fan Noise Flight Effects Study. D6-44145, Boeing Commercial Airplane Co., 1976. (FAA-RD-76-110, AD-A031877/4.)

49. DC-9 Flight Demonstration Program with Refanned JT8D Engines. Vol. 4: Flyover Noise. (MDC-J4518-Vol-4, Douglas Aircraft Co., Inc.; NASA Contract NAS3-17841.) NASA CR-134860, 1975.

50. Packman, A. B.; and Ng, K. W.: Effects of Simulated Forward Flight on Subsonic Jet Exhaust Noise. AIAA Paper 75-869, June 1975.

51. Kozlowski, H.; and Packman, A. B.: Flight Effects on the Aerodynamic and Acoustic Characteristics of Inverted Profile Coannular Nozzles. NASA CR-3018, 1978.

52. Goldstein, M. E.; and Howes, W. L.: New Aspects of Subsonic Aerodynamic Noise Theory. NASA TN D-7158, 1973.

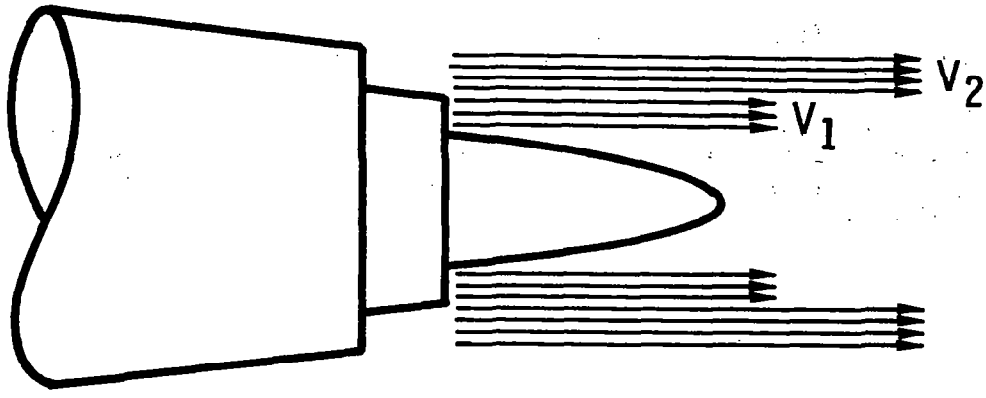

Figure 1.- Flow schematic of inverted-velocity-profile coannular jets.

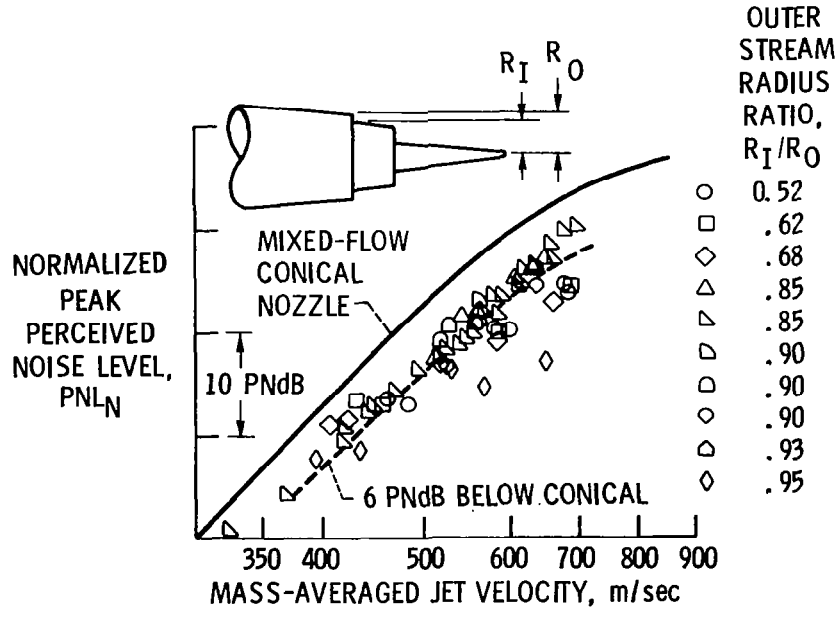

Figure 2.- Normalized peak perceived noise level for inverted-velocity-profile coannular nozzles as function of mass-averaged jet velocity.

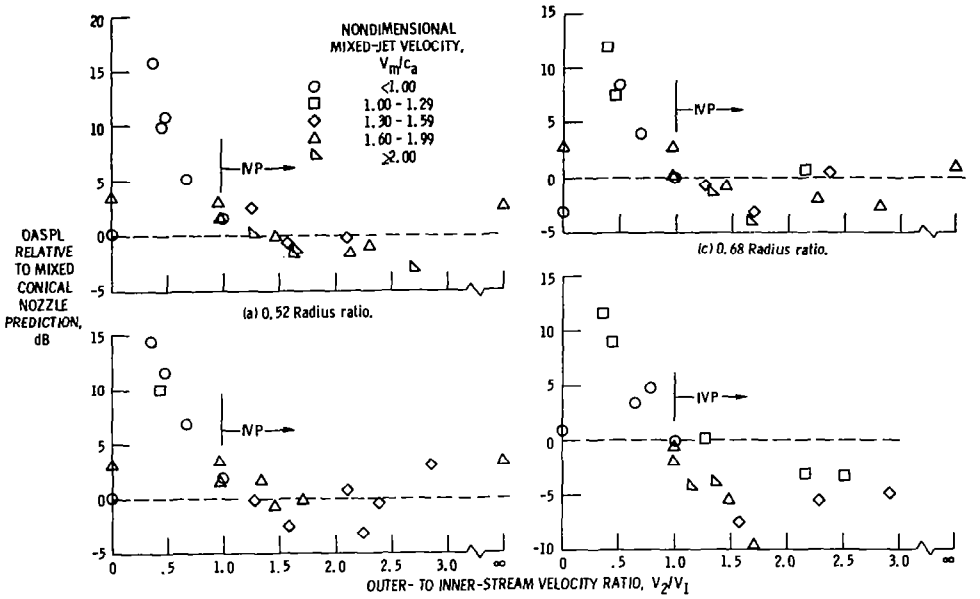

Figure 3.- Effect of velocity ratio on noise, relative to mixed-flow conical nozzle prediction, for different outer-stream radius ratio coannular nozzles. Angle referred to inlet axis, θ, 135°.

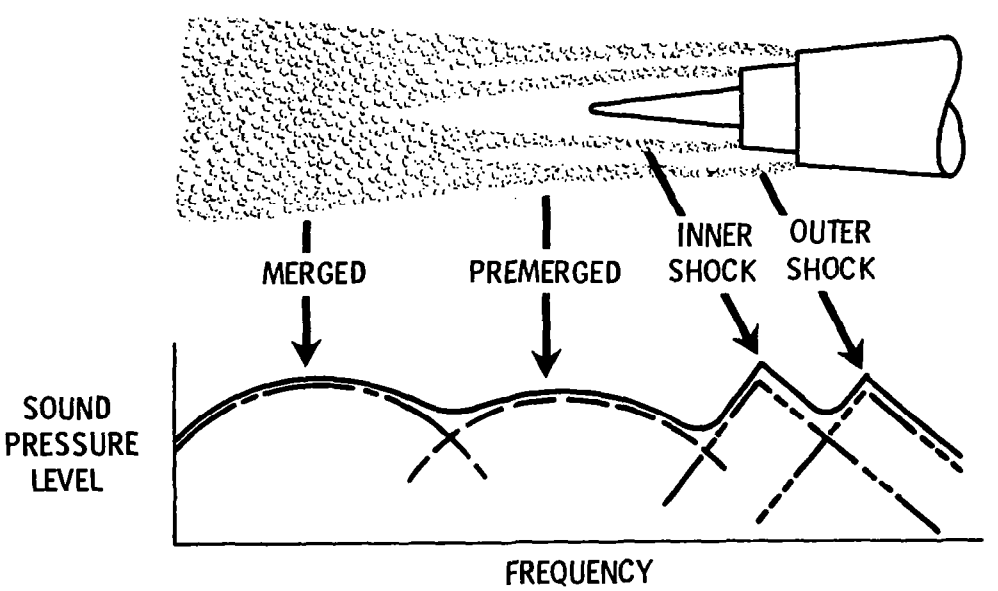

Figure 4.- Inverted-velocity-profile coannular nozzle jet noise sources.

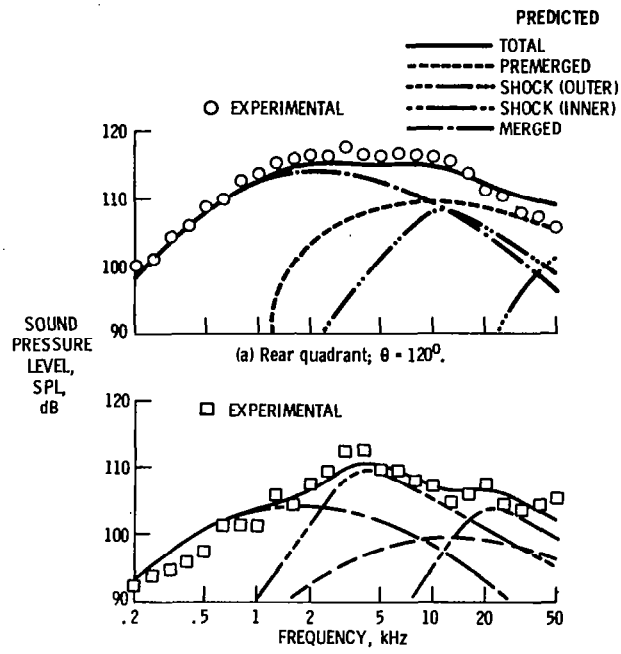

Figure 5.- Comparison of inverted-velocity-profile jet noise prediction with static model experimental data. Plugless coannular nozzle; mixed-jet velocity, $V_{j,m}$, 652 m/sec; mixed-jet temperature, 922 K; both streams supersonic.

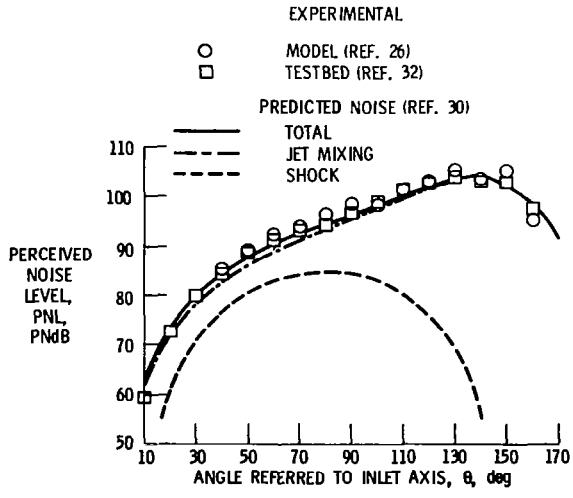

Figure 6.- Comparison of model and variable-cycle-engine-testbed experimental perceived-noise-level directivity with prediction at typical product-engine size (0.903-m^2 exhaust area) and at 731.5-m slant range. Mixed jet velocity, $V_{j,m}$, 590 m/sec; outer-stream radius ratio, R_I/R_O, 0.85.

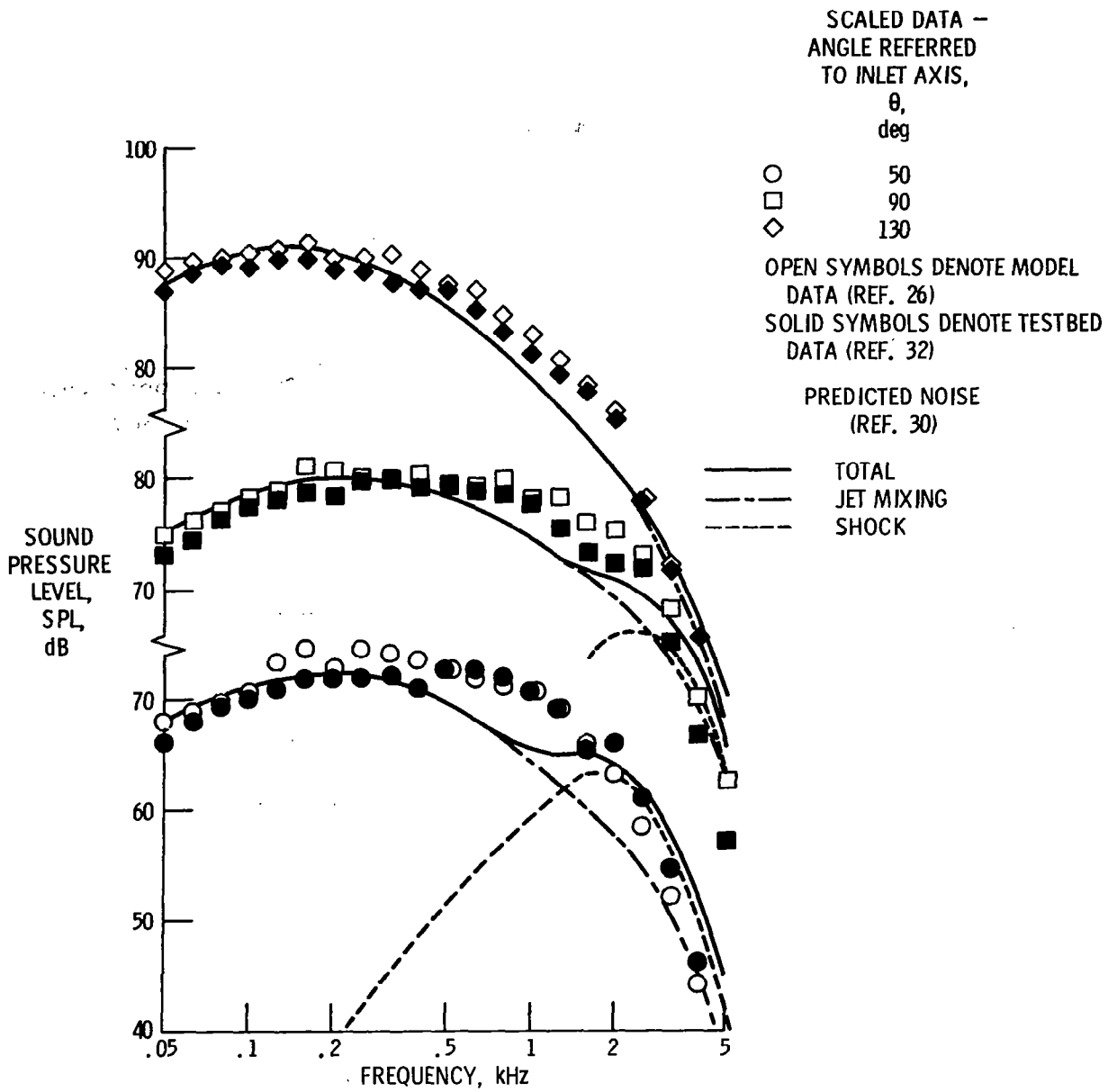

Figure 7.- Comparison of model and variable-cycle-engine-testbed experimental sound-pressure level spectra with prediction at typical product-engine size (0.903-m^2 exhaust area) and at 731.5-m slant range. Mixed-jet velocity, $V_{j,m}$, ~590 m/sec; outer-stream radius ratio, R_I/R_O, 0.85.

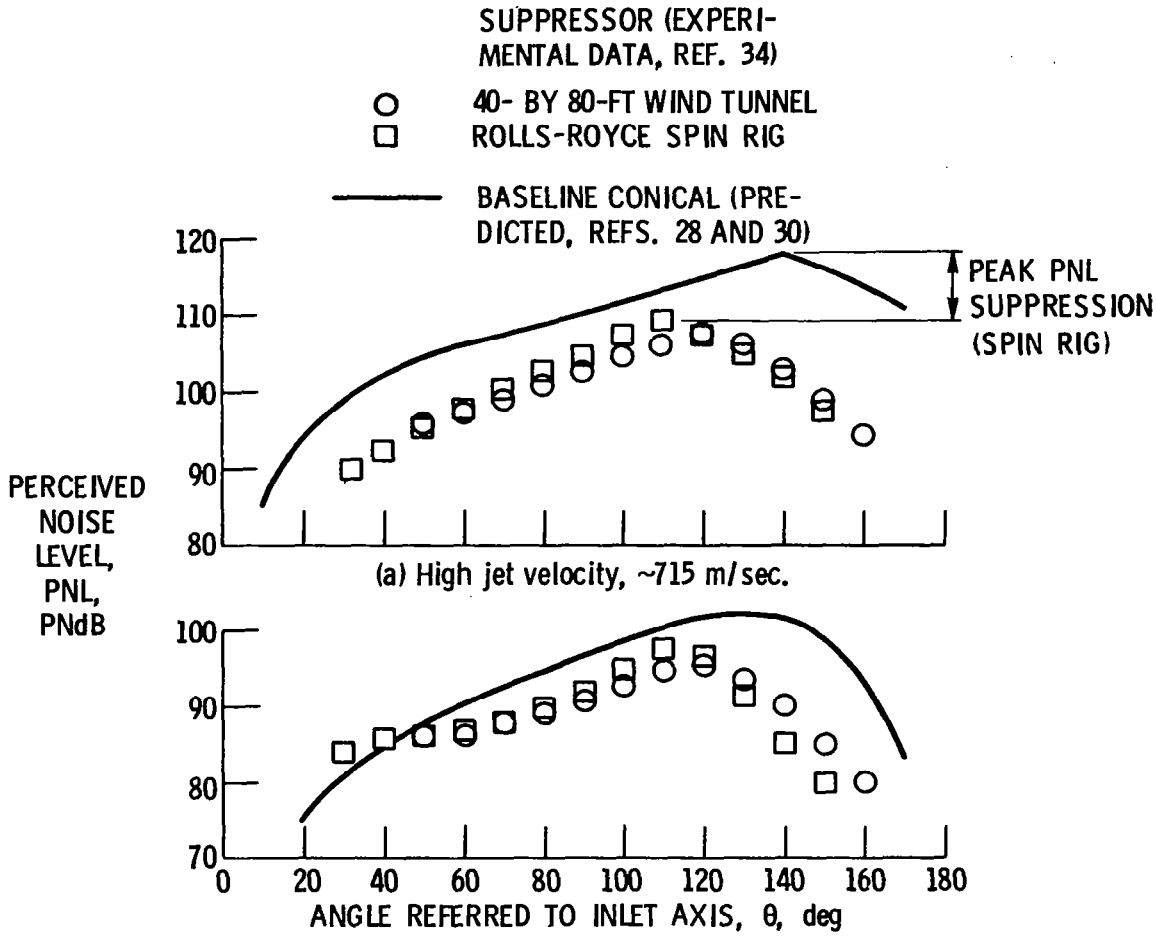

Figure 8.- Comparison of experimental, static perceived-noise-level directivity for McDonnell Douglas suppressor with lined ejector and prediction for a conical nozzle. Engine size (exhaust area), 0.713 m^2; flyover altitude, 381 m.

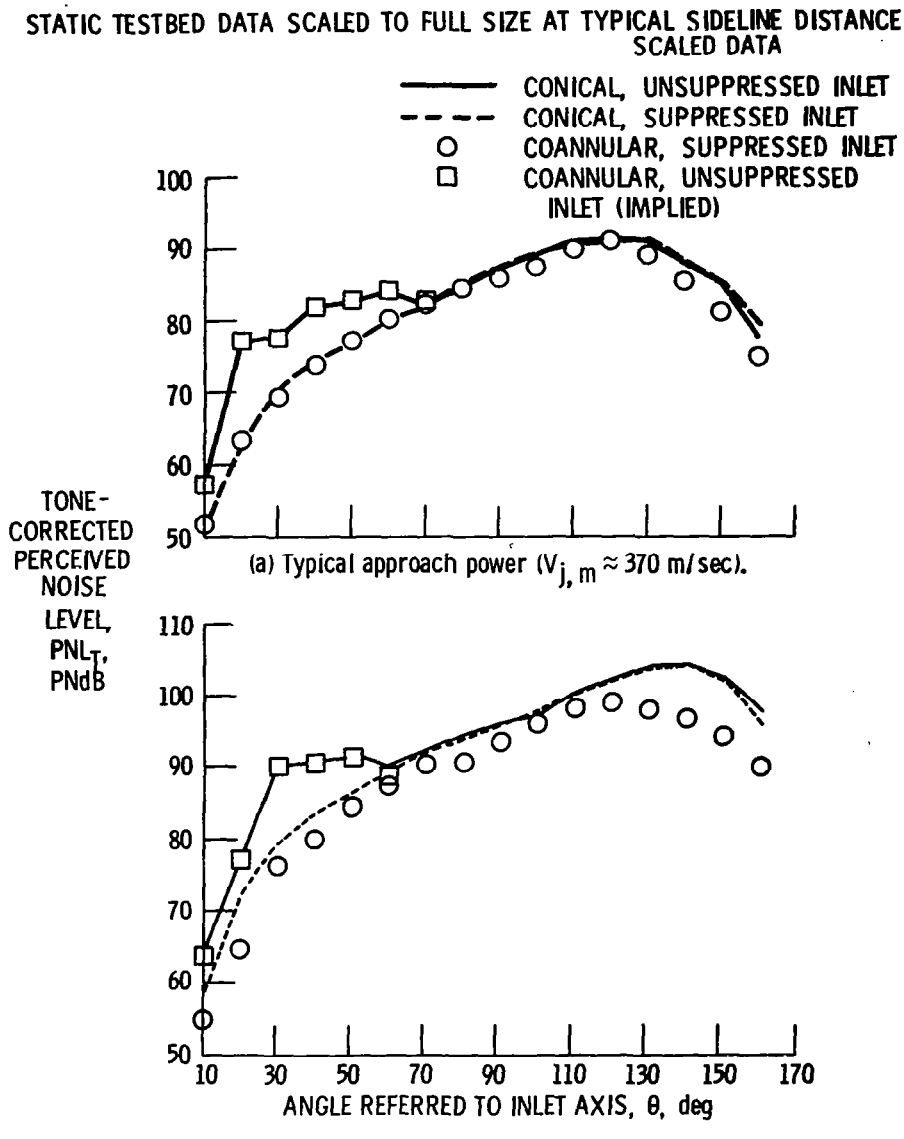

Figure 9.- Effect of fan noise on variable-cycle-engine-testbed, tone-corrected, perceived-noise-level directivity at different mission conditions. Typical product-engine size (0.903-m^2 exhaust area) at 731.5-m slant range.

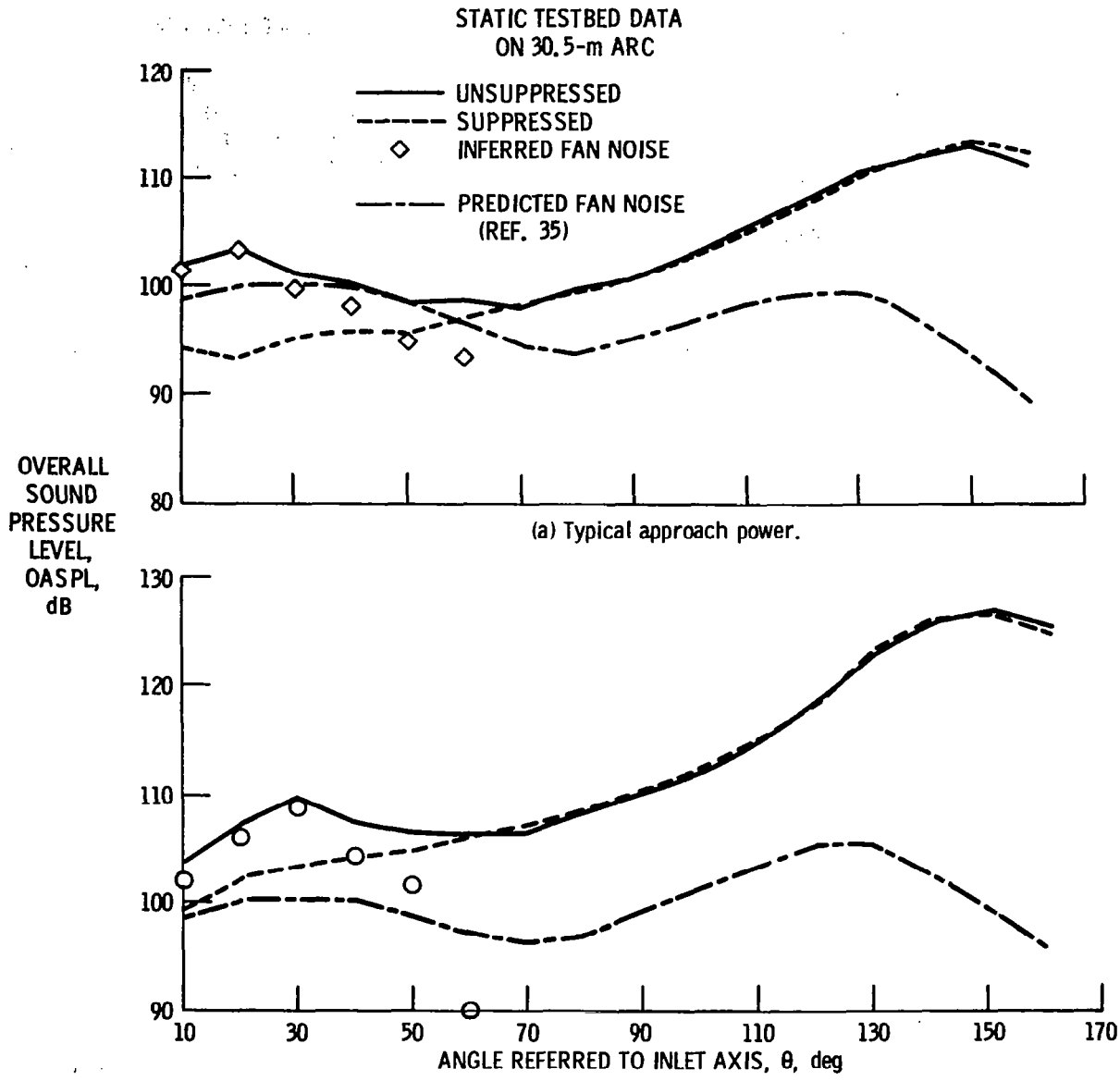

(a) Typical approach power.

Figure 10.- Comparison of variable-cycle-engine-testbed, fan-noise overall sound-pressure-level directivity with prediction.

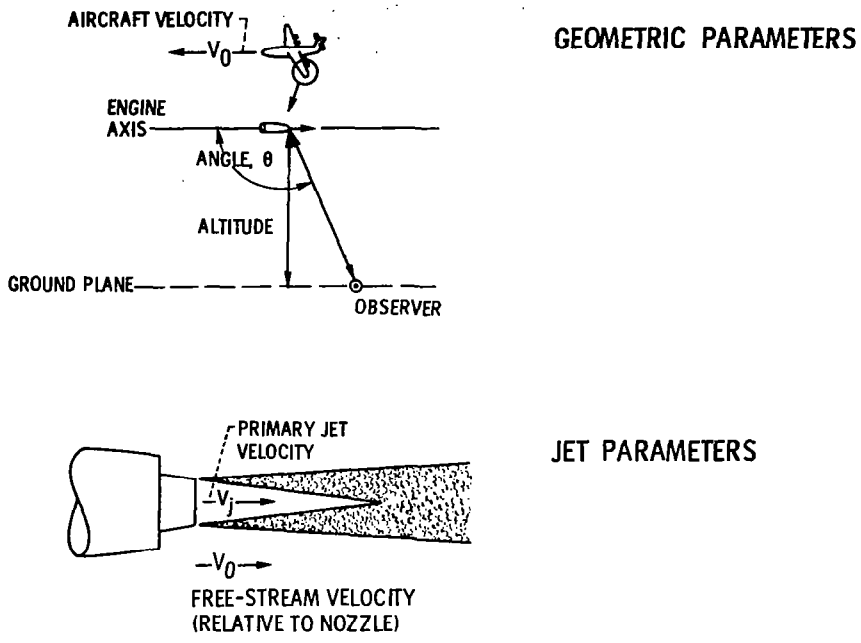

Figure 11.- Flight effects on exhaust noise (terminology for level flyover at aircraft Mach number M_0).

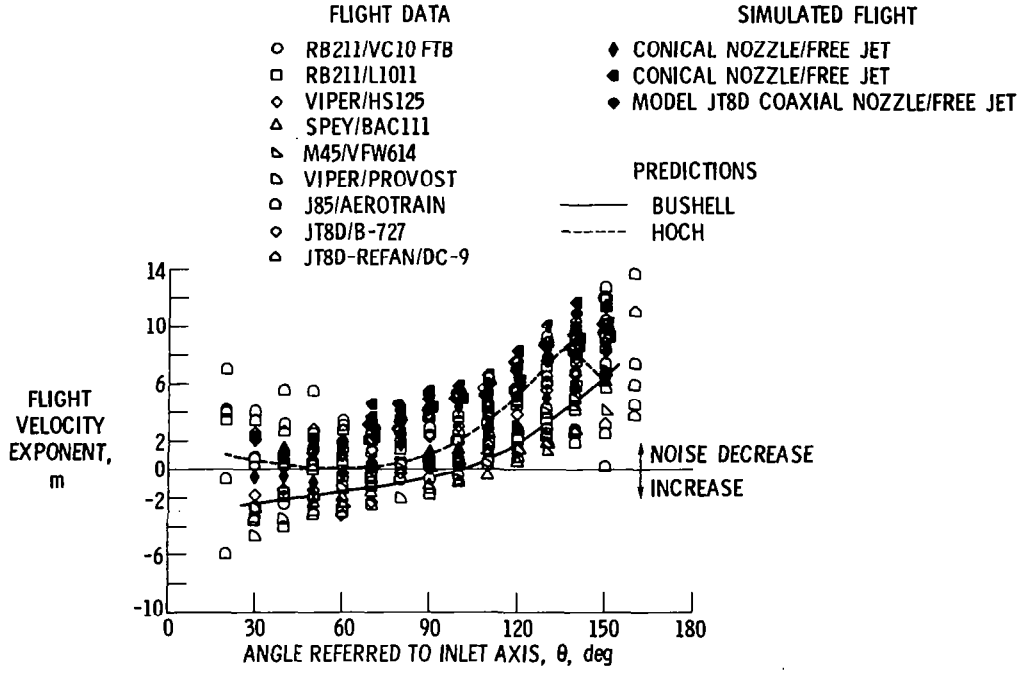

Figure 12.- Typical values of flight velocity exponents for a series of flight and simulated flight tests.

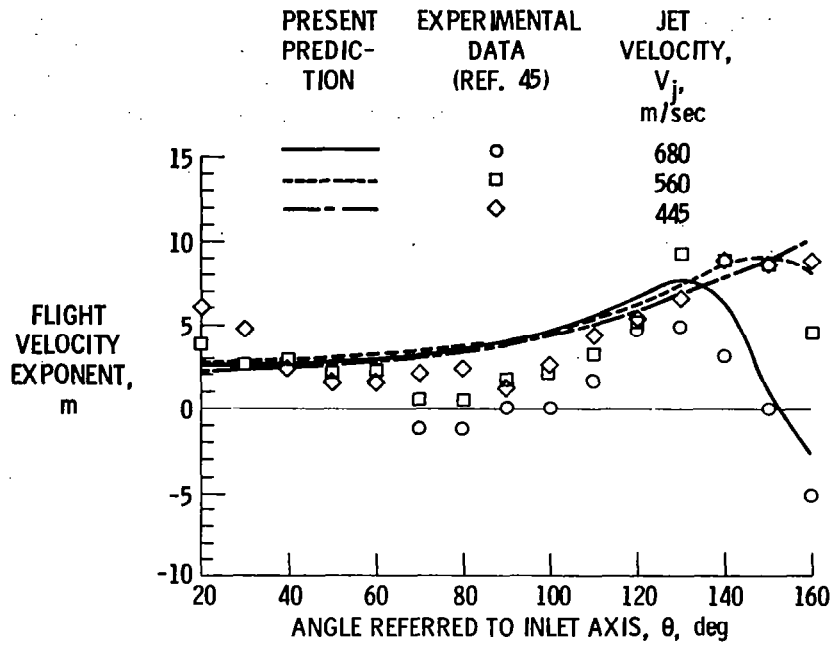

Figure 13.- Comparison of experimental and predicted flight velocity exponents for jet mixing noise of a J85 turbojet engine on the Bertin Aerotrain. Flight Mach number, M_0, 0.24.

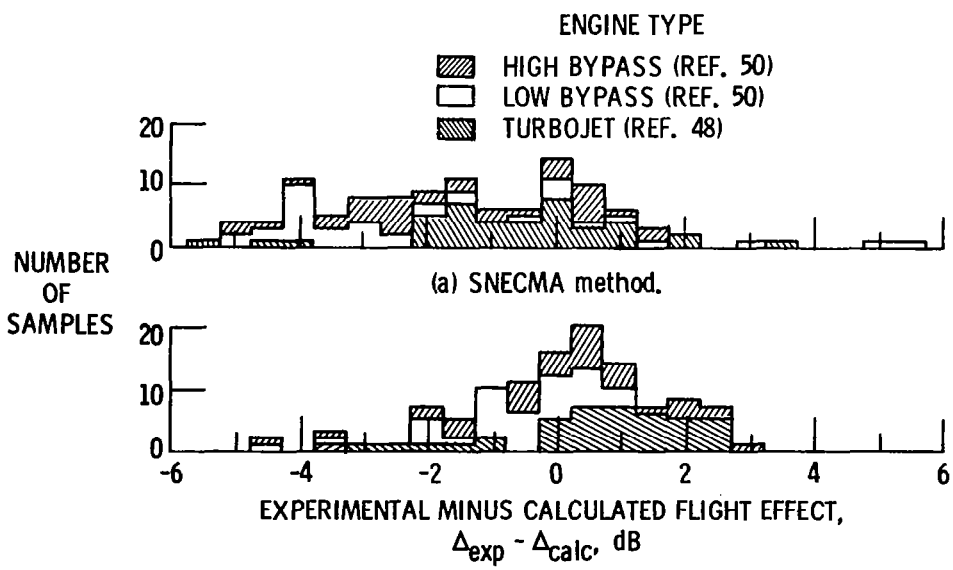

Figure 14.- Statistical comparison of prediction methods.

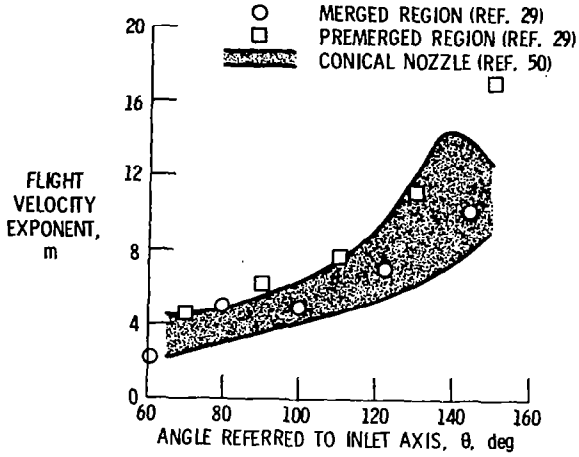

Figure 15.- Comparison of flight velocity exponents for inverted-velocity-profile coannular merged and premerged regions with conical nozzle data.

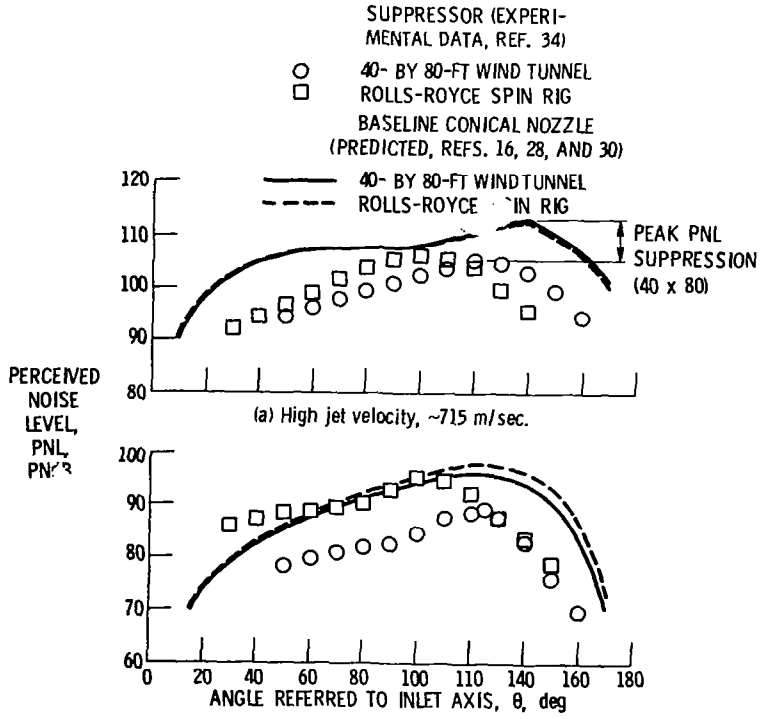

Figure 16.- Comparison of simulated flyover perceived-noise-level directivity for McDonnell Douglas suppressor with lined ejector and conical nozzle prediction. Engine size (exhaust area), 0.713 m^2; flyover altitude, 381 m.

ENVIRONMENTAL EFFECTS OF AIRCRAFT AT CRUISE: AN UPDATE

N. Sundararaman
Office of Environment and Energy
Federal Aviation Administration

SUMMARY

New laboratory determinations of chemical reaction rates and modeling refinements have shown that the effect of cruise-altitude emissions on stratospheric ozone has changed from one of ozone decrease to one of slight increase. The situation, however, is not yet fully resolved, since the uncertainties in the model predictions have not been adequately quantified. The status of the calculations of ozone change due to high altitude aircraft is critically reviewed and important areas of uncertainty identified.

HISTORICAL BACKGROUND

During 1971-1975, the U.S. Department of Transportation (DOT) completed the first comprehensive assessment of the effects of stratospheric pollution by aircraft (1). This assessment, known as the Climatic Impact Assessment Program (CIAP), was the first systematic, multidisciplinary Federal study on the stratosphere. Concurrently with CIAP, the National Academy of Sciences/ National Academy of Engineering (hereinafter referred to as NAS) in the U.S., and the British and the French governments had conducted independent studies (2, 3, 4) on the same problem; the British study was conducted by the Committee on Meteorological Effects of Stratospheric Aircraft (COMESA) and the French, by the Comite d'Etudes sur les Consequences des Vols Stratospheriques (COVOS).

Studies prior to CIAP on the pollution effects of supersonic transports (see 5 for example) had suggested that the water vapor in the exhaust could cause two effects: (1) stratospheric ozone could be depleted by a catalytic chemical reaction set involving the water-related radicals; and (2) by altering the occurrence of high cirrus and by forming persistent contrails, the injected water vapor could alter the radiation balance of the earth's surface and hence its climate. In 1971, during Congressional hearings on supersonic transport (SST) development in the United States, possible adverse health effects were for the first time linked to large scale commercial SST operations (6). The health hazard envisaged was possible increase in the incidence of skin cancer in fair-skinned humans owing to the fact that less stratospheric ozone would allow more of the biologically harmful solar ultra-violet (UV) radiation to penetrate to the ground which could induce and/or promote skin carcinomas.

The CIAP and other parallel studies had concluded that the nitrogen oxides (collectively known as NO_x and comprised of nitric oxide, NO, and nitrogen dioxide, NO_2) in the exhaust had far greater potential to deplete ozone than water vapor, despite the larger water vapor emissions (as may be seen from Table 1, adapted from (7), which lists the emission indices of various exhaust species in gm per kg of fuel burned). Thus, large scale commercial SST operations could indeed harm the environment with undesirable consequences. The CIAP Report of Findings (1) in its Executive Summary stated, in 1974:

> "Develop, within the next year, a plan for a proper program for international regulation of aircraft emissions and fuel characteristics for whatever stratospheric flight operations may evolve in the future."

> "Accelerate combustion research and engine development programs needed to make stratospheric flight possible with specified nitrogen oxide emission standards."

As may be seen from Figure 1, taken from Oliver, 1979 (8), higher Mach numbers imply higher cruising altitudes in a region of general quiescence but increasing ozone mass density (i.e., the stratosphere). The Arctic tropopause is located much lower (ca. 8 km.) than the tropical tropopause (ca. 16 km.); thus, even the current and near-future subsonics would be flying in the lower stratosphere for operations in the mid-to-high latitudes. The severity of the problem was linked to the pollutant injection altitude—the higher the altitude, the worse the effects—and not to whether the aircraft were subsonic or supersonic, with the corollary that even the subsonic fleets could pose a threat.

CIAP AND OTHER ESTIMATES

In CIAP studies, a 0.5 percent reduction in total ozone (total ozone is all the ozone contained in a column of air extending from the ground up) in the Northern Hemisphere was nominally chosen to be a "minimum-detectable" level of change (1). This change would be brought about, it was calculated, by a fleet of 120 "Concorde-like" aircraft, cruising 4.4 hours a day every day of the year (365 days) at 16.5 km using 19,100 kg of fuel per hour at cruise and emitting 18g of NO_2 per kg of fuel burned. This number is shown in Table 2 along with the numbers adapted from the NAS and other studies, for the same ozone change. Both the CIAP and the NAS calculations were predicated upon the same data base. A spread of a factor of at least 5 in these numbers is evident from Table 2.

UNCERTAINTIES IN THE CIAP AND OTHER ESTIMATES

One-dimensional (1-D) numerical models of the stratosphere were the assessment tools used by CIAP and other studies. These models, which attempt to simulate the known physics and chemistry of the stratosphere, have a severe limitation in that they assume horizontal homogeneity of stratospheric properties, especially of motion. But only 1-D models have incorporated to the satisfactory degree the treatment of stratospheric chemistry. The elements of these models include: (1) the chemistry and photochemistry of trace species of importance (e.g., ozone, nitric oxide, atomic oxygen) and (2) highly parameterized mechanisms which transport the trace species in the vertical direction.

Based upon the admittedly incomplete treatment of transport and possible inaccuracies in the laboratory chemical rate constant determination, uncertainty estimates in the model calculations were made by the CIAP and NAS studies. These estimates were subjective and are shown in Table 2. As stated earlier, even the subsonic aircraft had the potential to deplete ozone under CIAP modeling assumptions and the calculations for subsonic fleets alone are shown in Table 3.

The uncertainty ranges and the spread in the calculations were such that the Federal Aviation Administration instituted its High Altitude Pollution Program (HAPP) following CIAP to reduce them in order to formulate viable regulatory options.

CHANGES IN MODEL CALCULATIONS SINCE CIAP

In the modeling of the chemistry of the trace species, the following three changes have occurred since CIAP:

(1) Automobile exhaust containing NO_x is known to generate ozone in urban smog situations in the presence of methane and methane has been measured up to stratospheric altitudes. This "methane-oxidation" chemistry, which was not included in the CIAP model, has now been incorporated to a limited extent.

(2) Trace species other than NO_x and the water-related radicals (HO_x) have been discovered to have ozone depleting effects. The most important among these are chlorine-related ClO_x (Cl and ClO) which are anthropogenic in origin. Hence the CIAP chemistry which included only the odd oxygen (O_x), odd nitrogen (NO_x) and water-related odd hydrogen (HO_x) species has been expanded to include the odd chlorine (ClO_x) species. Thus, the treatment of chemistry has been much improved.

(3) The species in the various families such as NO_x, HO_x, and ClO_x are highly interactive; thus, changes in the rate constants of certain reactions have far-reaching consequences. Three such changes have taken place since CIAP in the following reactions:

$OH + HO_2$	About 4 times slower than the CIAP value
$HO_2 + NO$	About 40 times faster than the CIAP value
$HO_2 + O_3$	Temperature dependence different from the CIAP value.

These changes, especially the second, $HO_2 + NO$, have had profound influence on model calculations. The otherwise-very-active NO_x catalytic chain

$$NO + O_3 \Rightarrow NO_2 + O_2$$

$$NO_2 + O \Rightarrow NO + O_2$$

$$\text{Net:} \quad O_3 + O \Rightarrow 2O_2$$

is interrupted by the fast $HO_2 + NO$ reaction. The response of the model calculations to chronological changes in chemical input data is shown in Figure 2 taken from Luther et al., (9). The NO_x injection considered is equivalent to approximately 2000* "Concorde-like" CIAP aircraft, at two different altitudes (17 and 20 km). The 1975 chemistry included the revised $OH + HO_2$ rate (10), the 1977 chemistry the revised $HO_2 + NO$ rate (11), the 1979a chemistry the revised $HO_2 + O_3$ temperature dependence (12), and the 1979b chemistry the currently-accepted (13) $ClONO_2$ chemistry. ($ClONO_2$ is an example of the interactive chemistry between the NO_x and the ClO_x families. It is formed by $ClO + NO_2 \Rightarrow ClONO_2$.) In any case, without worrying about the details of the chemistry involved, one can see the profound effect of the $HO_2 + NO$ rate constant change. The unexpected feature of this figure, however, is the reversal of the trend between 1979a and 1979b.

The overall result of the three changes listed above has been a dramatic shift in the calculated aircraft effects from one of depletion to one of small increase in total ozone. However, as can be seen from Figure 3 (8), NO_x injections still deplete ozone above about 22 km while increasing it below; the sum of

* The NO_x injection considered was 1.2×10^9 kg per year as NO_2. With the "Concorde-like" CIAP aircraft as defined earlier, this corresponds to 2,245 such aircraft.

the decrease above and the increase below leads to a small net increase in total ozone. It is important to keep in mind with regard to this figure that the cross-over point from increase-below-to-decrease-above is model-dependent. Changes in the transport parameterization and in the tropospheric removal processes such as rain-out or wash-out, for example, would alter the position of this point. The calculated net effect, needless to add, will depend upon its location. The numbers (500, 1000, 1500) on the three curves in Figure 3 roughly correspond to fleets of 500, 1000, and 1500 "Concorde-like" CIAP aircraft defined earlier.

UNCERTAINTIES IN THE CURRENT CALCULATIONS

There are, despite recent improvements, still uncertainties in almost every aspect of the assessment models: those associated with atmospheric chemistry and transport, and projected fleet emissions. The High Altitude Pollution Program has identified the following specific uncertainty factors to confirm, modify or clarify the present understanding:

(1) Discrepancies in the Measured NO_x Content in the Engine Exhaust

Figure 4, from Few et al., 1977 (14), is an illustration of the measurement of NO concentration as a function of fuel-to-air (F/A) ratio obtained by different techniques. The in-situ absorption method yields values about a factor of 6 higher than the others. In a joint effort with NASA, U.S. Air Force and U.S. Navy, the FAA has undertaken to resolve the uncertainty. Preliminary data indicate that the in-situ absorption method may be in error.

(2) Two-Dimensional Models and the Distribution of Natural Ozone

It is well known that the natural (i.e., unperturbed) ozone distribution is highly seasonal and latitude dependent. The reason for this is the meridional transport in the upper troposphere and the lower stratosphere. This atmospheric region is also, coincidentally, the region of current and near-future aircraft flights. In addition, the aircraft injection is also latitude-variant (witness the transAtlantic corridor). Thus 2-D models are more appropriate for the aircraft problem. However, they suffer from lack of adequate chemistry.

The "little-change" conclusion drawn in the previous section (see Figure 4) may well be misleading in that ozone depletions may actually be occurring in certain latitude bands with increases in others. A 1-D model is inherently

incapable of addressing this issue. The consequences of the latitudinal variation in the predicted effects may be quite different in the sense that steady depletions in certain regions and steady increases in others (especially if they were to occur close to the ground) may both be harmful with no cancellation of the effects, either on climate or the biosphere.

Hence, HAPP has undertaken to refine the existing 2-D models.

An example of the shortcomings of the 2-D models in their treatment of chemistry is to be seen in Figures 5a, 5b, 6, 7 and 8 taken from Widhopf and Glatt, 1979 (15). Figure 5b is the observed seasonal and latitude variation of total ozone. Figure 5a illustrates the calculated values using CIAP (no chlorine) chemistry. Figures 6, 7, and 8 show calculated distributions with (a) HO_2 + NO reaction rate revised but with no chlorine, (b) HO_2 + NO and HO_2 + O_3 reaction rates revised and no chlorine and (c) HO_2 + NO and HO_2 + O_3 reaction rates revised and chlorine chemistry included, respectively. As may be seen, the agreement between theory and observations was good (Figures 5a and 5b), became poor (Figures 5b and 6), improved again (Figures 5b and 7) and deteriorated again (Figures 5b and 8) chronologically. This problem is being given further attention.

(3) Chemical Uncertainties

The pressure (i.e., altitude) dependence of certain reactions involving HO_x family, the temperature dependence of NO + O_3 reaction, and the uncertainties in methane oxidation chemistry, which are either unknown or poorly known, have the potential to alter the present understanding of the aircraft effects.

(4) Measurements of Background NO_x

The background concentration levels of NO, NO_2 and other members of the NO_x family in the atmosphere are not yet well known. There is a need to measure these species simultaneously, i.e., within the same air sample in order to verify the theoretical understanding of the partitioning among them. As may be seen from Figure 9 (15), which is a comparison of a 2-D model calculation against a set of simultaneous observations of NO, NO_2 and HNO_3, the situation requires further resolution. There are difficulties in the comparisons of ratios of trace species such as HNO_3 to NO_2 also (9).

CONCLUDING REMARKS

The uncertainties in the present understanding of the effects of high altitude aircraft are such as to warrant continued studies. Specific uncertainty factors have been identified and their resolution should not prove difficult.

The views expressed in this paper are solely those of the author and are not intended to reflect any policy of the Federal Aviation Administration or the U.S. Department of Transportation.

REFERENCES

1. CIAP, Report of Findings, The Effects of Stratospheric Pollution by Aircraft, Department of Transportation, Climatic Impact Assessment Program, DOT-TST-75-50, 1974.

2. NAS, Environmental Impact of Stratospheric Flight, National Academy of Sciences, Washington, D.C., 1975.

3. COMESA, The Report of the Committee on Meteorological Effects of Stratospheric Aircraft, 1972-1975, Meteorological Office, London, England, 1975.

4. COVOS, Rapport Final, Comite d'Etudes sur les Consequences des Vols Stratospheriques, Activites 1972-1976, Societe Meteorologique de France, 73-77 Rue de Sevres, 92100 Boulogne, France, 1976.

5. SMIC, Inadvertent Climate Modification, Report of the Study of Man's Impact on Climate, the MIT Press, Cambridge, MA., 1971.

6. McDonald, J.E., Statement submitted at hearings before the House Subcommittee on Transportation Appropriations, March 2, 1971.

7. English, J. M., and Guo-An Pan, Global Emissions in the Stratosphere in Propulsion Effluents in the Stratosphere, CIAP Monograph 2, Department of Transportation/CIAP, DOT-TST-75-52, 1975.

8. Oliver, R.C., Potential Effects on Stratospheric Ozone due to High Altitude Aircraft Operation, Paper to Appear in the Proceedings of the NATO Advanced Study Institute on Atmospheric Ozone, Its Variations and Human Influences, October 2-13, 1979.

9. Luther, F. M., et al., Potential Environmental Effects of Aircraft Emissions, Federal Aviation Administration, Report No. FAA-EE-79-23, Washington, D.C., 1979.

10. National Bureau of Standards, Chemical Kinetics and Photochemical Modeling for Atmospheric Chemistry, NBS Technical Note 866, National Bureau of Standards, Washington, D.C., 1975.

11. National Bureau of Standards, Reaction Rate and Photochemical Data for Atmospheric Chemistry - 1977, NBS Special Publication 513, National Bureau of Standards, Washington, D.C., 1978.

12. Jet Propulsion Laboratory, Chemical Kinetic and Photochemical Data for Use in Stratospheric Modeling, JPL Publication 79-27, Jet Propulsion Laboratory, Pasadena, CA., 1979.

13. National Aeronautics and Space Administration Reference Publication, "The Stratosphere: Present aud Future", R. Hudson (Ed.), NASA Workshop, Harpers Ferry, WV., 1979.

14. Few, J.D., et al., Evaluation of Probe Sampling vs. Optical In Situ Measurements of Nitric Oxide Concentrations in a Jet Engine Combustor Exhaust, Arnold Engineering Development Center, Tennessee, AEDC-TR-76-180, 1977.

15. Widhopf, G.F., and L. Glatt, Two-Dimensional Description of the Natural Atmosphere Including Active Water Vapor Modeling and Potential Perturbations due to NO_x and HO_x Aircraft Emissions, Federal Aviation Administration, Report No. FAA-EE-79-07, Washington, D.C., 1979.

Table 1

Typical Jet Engine Emission Indices at Cruise Altitudes. (English et al, 1975)

Exhaust Species	Emission Index, gm/kg
CO_2	3220
H_2O	1250
NO_x (as NO_2)	6-30
CO	4
SO_x (as SO_2)	1.0
Hydrocarbon (as CH_2)	0.1-0.2
Soot (as carbon)	0.1
Lubricating Oil	0.1
Trace Elements	0.01

Table 2

Number of Concorde-like Aircraft Which Would Lead to a Northern Hemispheric Ozone Reduction of 0.5%, as of 1975.

Name of Study	Number of Aircraft	Uncertainty Range (Estimate)
CIAP	120	(0.33-1.50)
NAS	79	(0.33-3.00)
COMESA	435	None given
COVOS	326	None given

Table 3
Calculated Northern Hemispheric Ozone Reduction by Subsonic Aircraft, as of 1975.

Name of Study (Reference)	Northern Hemispheric Ozone Reduction Percent	Uncertainty Range (Estimate)
1. "1974" CIAP Fleet		
CIAP	0.09	0.1-2
NAS	0.10	0.1-10
COMESA	None given	None given
COVOS	None given	None given
2. Projected Fleet of 100 B-747 SP-like Aircraft		
CIAP	0.08	0.2-2
NAS	0.16	0.1-10
COMESA	None given	None given
COVOS	None given	None given

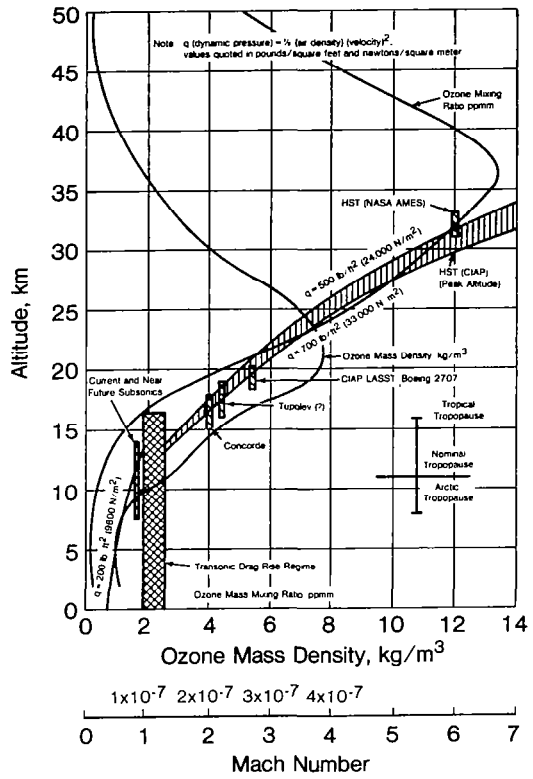

Figure 1.- Aircraft cruise altitudes and ozone data. (Oliver, 1979.)

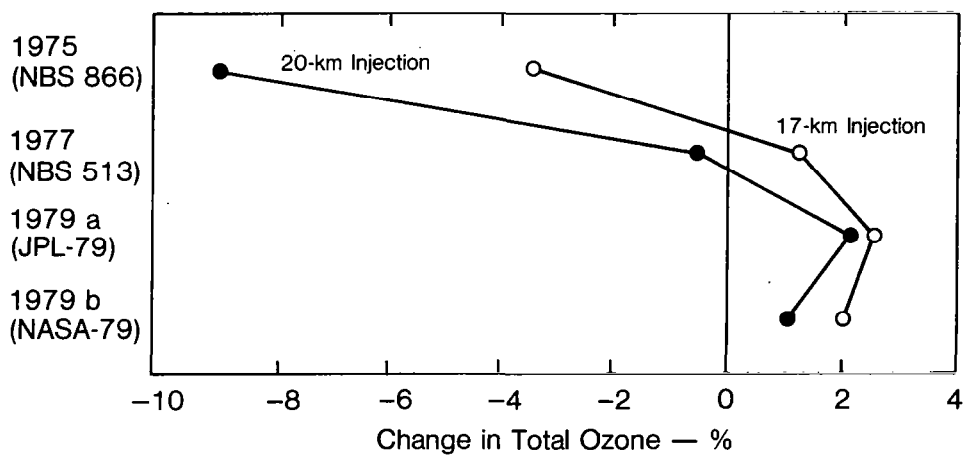

Figure 2.- Influence of changes in rate coefficients on model-predicted changes in total ozone due to NO_x injections. (Luther et al., 1979.)

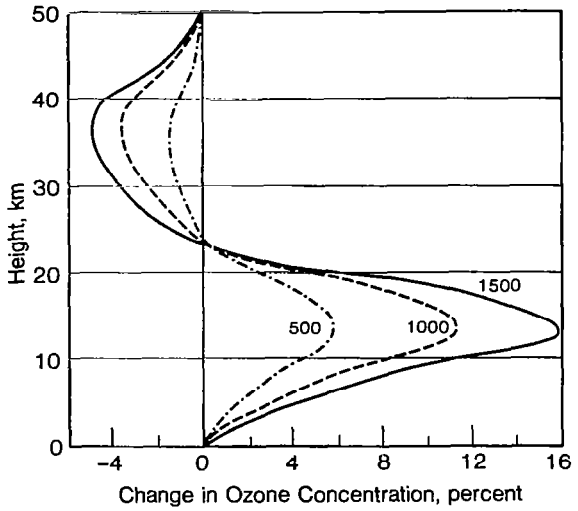

Source: Lawrence Livermore Laboratory (1978).

Figure 3.- Percentage changes in ozone versus altitude for three injection rates of NO at 20 km. Rates shown are in molecules/cm^3 sec over a 1-km band, and correspond to global injection rates of 0.62, 1.23, and 1.85×10^9 kg NO_x (as NO_2) per year. (Oliver, 1979.)

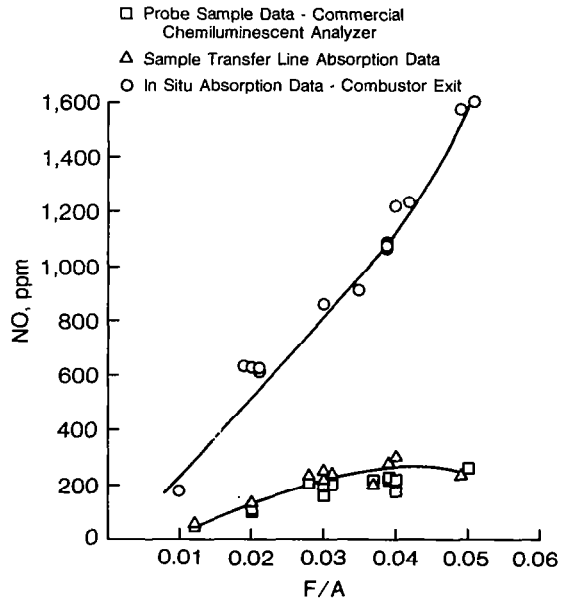

Figure 4.- NO concentration as a function of the fuel-to-air ratio for turbine engine combustor exhaust obtained by various means. (Few et al., 1977.)

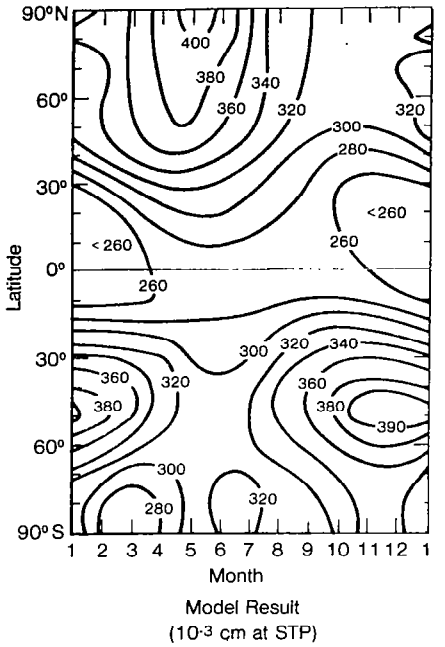

(a) Calculated, without chlorine chemistry.

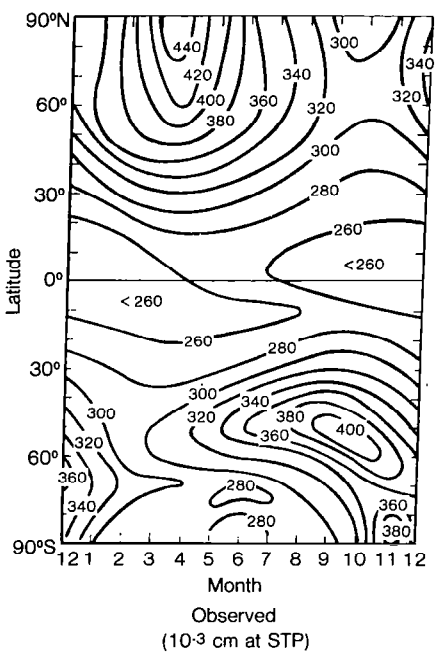

(b) Observed.

Figure 5.- Monthly variation of the total ozone column as a function of latitude (10^{-3} cm at STP). (After Widhopf and Glatt, 1979.)

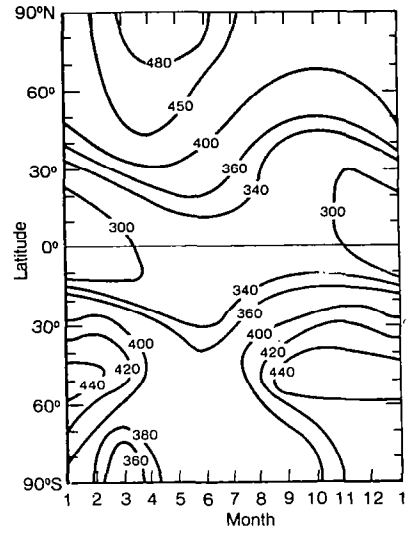

Figure 6.- Calculated monthly variation of total ozone column as a function of latitude without chlorine chemistry but with new rate coefficient for HO_2 + NO (10^{-3} cm at STP). (Widhopf and Glatt, 1979.)

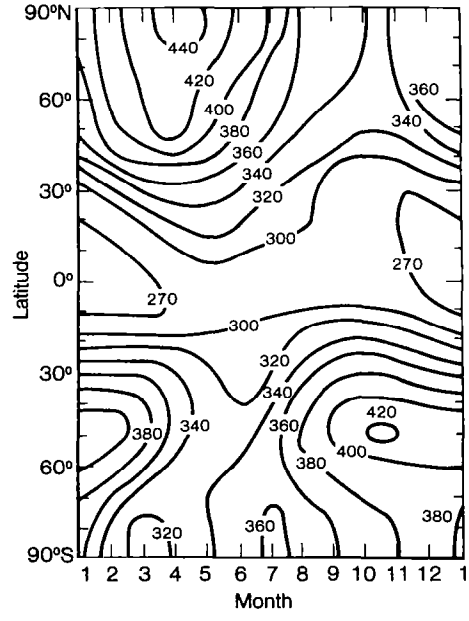

Figure 7.- Calculated monthly variation of total ozone column as a function of latitude (10^{-3} cm at STP) without chlorine chemistry but with new rate coefficients for HO_2 + NO and HO_2 + O_3. (Widhopf and Glatt, 1979.)

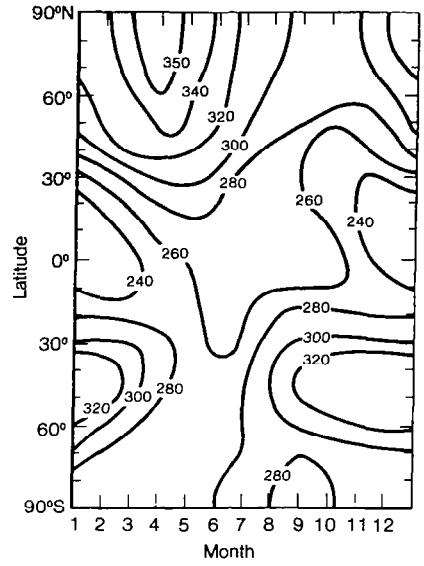

Figure 8.- Calculated monthly variation of total ozone column as a function of latitude (10^{-3} cm at STP) with chlorine chemistry and with new rate coefficients for HO_2 + NO and HO_2 + O_3 (2 ppbv CLO_x). (Widhopf and Glatt, 1979.)

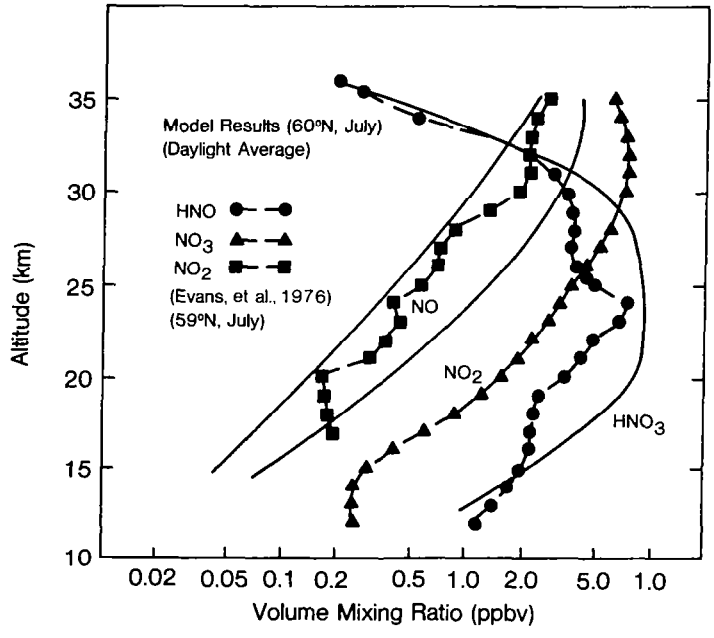

Figure 9.- Comparison of calculated and measured profiles of NO, NO_2 and HNO_3. Calculations made with the aerospace model. (Widhopf and Glatt, 1979.)

ADVANCED TECHNOLOGY FOR CONTROLLING POLLUTANT EMISSIONS FROM SUPERSONIC CRUISE AIRCRAFT

Robert A. Duerr and Larry A. Diehl
Lewis Research Center

SUMMARY

This paper presents and discusses some of the results obtained from research and development programs being sponsored or conducted by NASA. The objectives of these programs were to evolve and evaluate new gas-turbine-engine combustor technology for the reduction of pollutant emissions. Activities ranging from investigating variations of conventional combustion systems to evaluating advanced combustor concepts have been and continue to be pursued. Projected results from far-term technology efforts aimed at applying the premixed-prevaporized and catalytic combustion techniques to aircraft combustion systems indicate a potential for significant reductions in pollutant emission levels.

INTRODUCTION

This paper describes NASA-sponsored programs whose objectives were to evolve and evaluate new gas-turbine-engine combustor technology for the reduction of aircraft engine pollutant emissions.

Concern over the possibly adverse environmental effects of the first-generation supersonic transports drew attention to the exhaust pollutant emissions produced by the gas-turbine engines used to power these aircraft. Two general areas of concern were expressed: urban pollution in the vicinity of airports and pollution of the stratosphere. The principal urban pollutants were carbon monoxide and unburned hydrocarbons during idle and taxi and oxides of nitrogen and smoke during takeoff and climb. Oxides of nitrogen were also considered to be of concern during high-altitude cruise flight.

In response to growing concern over the possible undesirable effects of gaseous pollutant emissions from aircraft engines, NASA initiated in 1971 an Emissions Reduction Research and Technology program. This program and the results obtained to date are the basis for this paper. In 1973 the Environmental Protection Agency issued gaseous pollutant emission standards for aircraft engines, to be implemented by 1979. Since that time the EPA has continuously examined and studied the impact of aircraft engine emissions on air quality and has closely followed the advancing technology for control of these pollutant emissions. In March 1978, the EPA issued a Notice of Proposed Rule Making that would amend the standards. The EPA has not yet taken final action on the proposed amended standards. For the purposes of this paper we have chosen the pro-

posed EPA standards as the basis for comparing and evaluating advanced combustor concepts.

The three gaseous emissions of primary interest are carbon monoxide, unburned hydrocarbons, and oxides of nitrogen. Figure 1 illustrates schematically an aircraft engine combustor of the type used in various proposed engines for the first-generation supersonic transport (SST) aircraft. Below the sketch are bar graphs illustrating the levels of pollutants typical of these engines during landing-takeoff operation. These pollutant levels are based on an average of engine test data from the Rolls-Royce Olympus 593 and limited information obtained during prototype evaluation of the General Electric GE4 and the Pratt & Whitney JTF-17 engines. The characteristic features of the main combustor are noted in the sketch. It has a single burning zone, the primary portion of which tends to operate fuel rich. Large amounts of air bypass the combustor primary zone and are admitted further downstream to cool and dilute the combustion products. These combustors all have a step-louver-constructed, film-cooled liner; and a large portion of the total combustor airflow is used to cool the liner. The EPA has established six engine classes for gas-turbine-powered aircraft; class T5 has been designated for engines used to power supersonic commercial aircraft. The emission levels shown below the sketch are expressed as values of the proposed EPA parameter, or EPAP, and are obtained by integrating the engine emissions over a specified landing-takeoff cycle. The method of calculating the EPAP is described in the appendix. The proposed EPA standards for class T5, newly certified engines are shown as a dashed line for each of the pollutants. Levels of emissions produced by the first-generation SST significantly exceed the proposed EPA standards and thus indicate a need for reducing the pollutant emissions from this class of engines.

This paper presents and discusses some of the results obtained from research and development programs being sponsored, directed, or conducted by NASA. Although we recognize that much important work is being done at universities and in private industry, or sponsored or conducted by other government agencies (DOD, FAA, EPA, etc.), this paper concentrates on NASA programs only. Activities ranging from investigating variations of conventional combustion systems to evaluating advanced catalytic techniques are being pursued. Applications of these techniques to future aircraft engines are being considered. The results pertinent to pollutant emission reduction efforts are presented and discussed, along with an assessment of the projected development difficulties and a forecast of potential emission level reductions.

DEVELOPMENT OF CURRENT-TECHNOLOGY COMBUSTORS

The NASA Emissions Reduction Research and Technology program, as conceived in 1971, had both near-term and far-term goals. The near-term program concentrated on achieving a large and immediate reduction in pollutant emissions. It mainly addressed the then current-technology engines used to power subsonic commercial aircraft. The near-term program, conducted largely under contract, is essentially complete.

The far-term program had the overall goal of developing the technology necessary to define the minimum pollutant emission levels that aircraft gas-turbine engines could achieve. This far-term program was and continues to be conducted both in-house at the Lewis Research Center and through research grants to universities and contracts with industry.

The specific objectives of the near-term emission reduction program were to investigate new combustor concepts with the potential for significantly lower emission levels and to measure the emission reduction obtainable with these new combustors in actual engine tests. The approach taken to achieve these objectives was to let multiphase contracts with the major aircraft engine manufacturers to devise and investigate new combustor concepts. In the first phase, a variety of new combustor concepts were screened to determine those with the greatest emission reduction potential. In the second phase, those concepts were further refined, and finally the best or most "engine ready" combustor concept was tested in an engine to measure the emission reduction obtainable.

Two of the near-term programs were conducted by Pratt & Whitney and General Electric using the JT9D and CF6 engines, respectively. The results of these programs are applicable to supersonic cruise aircraft engine technology, and some elements of the resulting concepts have been incorporated into the currently proposed designs for the Pratt & Whitney Variable Stream Control Engine (VSCE) and the General Electric Double Bypass Engine (DBE).

In the figures that follow, the emission levels of advanced combustors incorporated in the P&W VSCE and the GE DBE are projected. These projections are based on standard correlating expressions developed during the JT9D and CF6 engine tests. Assuming that technology similar to that achieved in the JT9D and CF6 engine tests could be achieved in the advanced supersonic engine cycle, the JT9D and CF6 engine data have been extrapolated to the combustor conditions that would exist in the VSCE and DBE.

The Vorbix combustor concept used in the JT9D engine is illustrated in figure 2, and the combustor is shown in figure 3. (Vorbix is an acronym meaning vortex burning and mixing.) The cross-sectional sketch of this combustor (fig. 2) shows that there has been a departure from the types of combustor used in the past. This combustor has two burning stages arranged in series: The pilot stage is optimized for control of carbon monoxide (CO) and total hydrocarbons (THC) at low power, and the main stage is optimized for control of oxides of nitrogen (NO_x). The main stage becomes operational at all engine conditions beyond idle. It is separately fueled and is ignited by the pilot stage. The bar graphs shown below the sketch in figure 2 compare the emissions of the first-generaton SST engine with estimated emissions for the Vorbix combustor as contained in the VSCE. The estimates are based on projections of emission data obtained in JT9D engine tests. The advanced engine cycle used for the present versions of variable-cycle engines differs significantly from that of the first-generation SST engine. The combustor inlet pressure and temperature and combustor exit temperature are all significantly higher than in the first-generation SST engine and thus impose a much greater NO_x emissions control problem. In this case, considerable technological effort is required just to maintain the NO_x emission levels of the first-generation SST. The projected CO emissions

were reduced by over a factor of 5, THC emissions by over a factor of 40, and NO_x emissions by 10 percent.

The double-annular combustor, which was tested in an experimental CF6 engine, is illustrated schematically in figure 4 and shown in figure 5. This combustor concept is also a two-stage combustor, but here the pilot and main stages are arranged in parallel and result in a combustor with two annular burning zones. The outer or pilot zone is used at all operating conditions and is designed to minimize idle pollutants. The inner or main zone is functional at all engine conditions above idle and is designed to reduce high-power pollutants. As was done for the Vorbix combustor in figure 2, the bar graphs in figure 4 compare the first-generation SST emissions with the estimated emission levels for the double-annular combustor as contained in the DBE. The estimates are based on projections of emission data obtained in the CF6 engine tests. Projected CO emissions were reduced by 75 percent and THC emissions by a factor of 25; but estimated NO_x emissions increased by about 40 percent, a reflection of the more stringent cycle constraints mentioned earlier.

The projected engine emissions from application of these two emission-controlled combustors are summarized in figure 6. The combustor sketch shows the significant features of the typical emission-controlled combustor. Multiple burning zones are used: a pilot for engine-idle emission control, and a main zone for all higher power operating conditions. Air-blast fuel injectors are often used in the main stage to achieve fine fuel drops intimately mixed with combustion air. Since most of the air is now used in controlling the combustion process, very little air is available for dilution and temperature profile tailoring. Similarly the amount of air available for liner film-cooling is reduced, and advanced cooling schemes must be employed. The bar graphs summarize the average, estimated emission levels for the emission-controlled combustors and show significant reductions in CO and THC, but a slight increase in NO_x. The estimated THC emissions virtually disappeared, and this suggests that no further development is required to reduce levels of this pollutant. These projections prompted further work in reducing the CO and NO_x emission levels.

ADVANCED IDLE EMISSIONS CONTROL TECHNOLOGY

The results of the two programs discussed in the previous section indicated a need for reducing CO emissions over the landing-takeoff cycle by at least a factor of 2 in order to achieve the proposed EPA standards. Since CO emissions are usually most predominant at the idle power setting, an idle emissions reduction program was conducted with the objective of investigating new combustor concepts with the potential for significantly lower engine idle emissions levels.

To achieve this objective, a contract was let with industry for the investigation of three unique combustor concepts with nonconventional design features. The testing and evaluation of the concepts were confined to typical idle conditions. Application of this technology to a practical combustor system could be realized through variable-geometry schemes or by using one of these designs as the pilot stage of a multistage combustor.

All three concepts tested showed dramatic reductions in CO and THC emissions. The simplest design of the three, the hot-wall combustor, is shown in figure 7. The main feature of the hot-wall combustor is a thermal-barrier coating applied to the inside surface of the combustor liner to reduce wall quenching of the combustion gas reactions. These refractory-coated surfaces along with an impingement-cooled liner - with no film cooling whatsoever - resulted in greatly reduced quenching losses at the walls. Also, the secondary dilution air jets are placed far downstream in order to further reduce quenching for maximum reaction of the fuel and air.

The design features of the hot-wall combustor are shown in figure 8 as incorporated into the pilot stage of a hypothetical multistage combustor. The refractory surfaces of the inner liner walls and the use of impingement cooling result in minimized wall-quenching effects. The pilot combustor is designed for optimum burning rates at idle.

The projected emissions for such a combustor operating in an engine over the EPA standard landing-takeoff cycle are also shown in figure 8. Carbon monoxide emissions are significantly lower than those from the emission-controlled combustor. The NO_x emission level is essentially unchanged from that of the emission-controlled combustor since most NO_x is generated in these combustors during high-power operation.

This low-power emissions reduction program, in conjunction with the emissions-controlled combustor program, demonstrated dramatic reductions in CO and THC emissions at idle. The far-term emissions reduction program was directed toward achieving significant reductions in NO_x emissions and additionally reducing the low levels of idle pollutant emissions achieved earlier.

FAR-TERM EMISSIONS CONTROL TECHNOLOGY

At high-power operation, high flame temperature is the most important factor in the formation of oxides of nitrogen. Experimental data as well as analytical predictions indicate that NO_x emissions vary exponentially with flame temperature. Therefore, the far-term efforts have been concentrating on the technique of lean burning, in which decreasing the combustion-zone equivalence ratio lowers the flame temperature with a resultant reduction in NO_x formation.

Since the local flame temperature is a significant factor in controlling NO_x production, local fuel distributions with locally rich pockets of fuel and air must be avoided. This requires that the fuel and air be uniformly mixed throughout the combustion zone. In addition, it may be necessary to prevaporize the fuel. Large fuel droplets in the combustion zone are consumed by a diffusion flame that surrounds the evaporating droplets. This process takes place at near-stoichiometric conditions, and the high temperatures produce excessive NO_x emissions. Thus, combustors with provisions to prevaporize the fuel and to premix the fuel and air may be necessary to realize the full NO_x reduction potential of lean-burning techniques.

The concept of catalytic combustion offers the potential of even further reductions in pollutant emissions. By using a catalyst bed consisting of a ceramic honeycomb substrate impregnated with catalytic material, stable efficient combustion occurs at even leaner overall equivalence ratios.

Even though lean, premixed-prevaporized combustors and catalytic combustion appear to have the potential for achieving very low levels of pollutant emissions, considerably more effort is required before either of these technologies could be applied to aircraft engine combustion systems. These concepts then formed the basis for the far-term emission reduction program.

The objective of the far-term program is to evolve the technology needed for developing combustors with minimum pollutant levels. The approach taken to achieve this objective relies heavily on a continuing effort in basic and aplied research. The degree of risk and overall level of complexity associated with the adaptation of advanced techniques are more severe than in the near-term programs. Fundamental studies are viewed as a requirement to close gaps in our understanding of key problem areas and to provide a basis for establishing technology to a point where adaptation of a new approach to combustor hardware is practical. As mentioned earlier, two techniques appear particularly attractive in terms of their potential for reducing NO_x: the lean, premixed-prevaporized and catalytic combustion techniques. NASA has begun efforts to evolve and evaluate lean, premixed-prevaporized and catalytic combustors. It is anticipated that as these types of combustors continue to evolve, additional problem areas requiring more fundamental study and improved approaches to the adaptation of the fundamentals may be identified.

Before lean, premixed-prevaporized combustors can be applied to aircraft engines, additional research is required in several areas. Figure 9 shows a conceptual drawing of a lean, premixed-prevaporized combustor. It is a staged design, as are the previously discussed advanced combustors. The pilot stage has been configured to include features, such as a hot-wall liner, that minimize idle pollutants. The main stage contains a fuel injector, a premixing-prevaporizing section, and a flameholder. Maintaining a wide operating range while burning as lean as possible may require control of the airflow as well as the fuel-flow splits between the two stages. To achieve this required airflow control, a variable-geometry device has been included in the diffuser section.

The key areas of required research are also indicated in figure 9. Combustor inlet airflow characteristics must be known to assure uniform fuel-air distributions. Engine transient characteristics must be identified and studied to avoid autoignition and flashback in the fuel-air mixing passage. Practical schemes for varying the combustor geometry and controlling the combustor operation must be identified. For the premixing section of the main stage to operate successfully, information is needed on techniques for predicting and achieving the required fuel distribution and vaporization. Autoignition and flashback may be problems in the premixer. More data on these phenomena are needed over the range of engine operating conditions, including engine transients.

Lean stability and altitude relight capability need special attention with these systems. Because the majority of the combustor airflow must pass through the main stage to satisfy the lean-burning requirement, less air will be avail-

able to cool the combustor liner than in current-technology combustors. It, therefore, appears likely that the application of advanced liner-cooling schemes to this type of combustor will be required to avoid liner durability problems.

Digital engine controls will likely be required for the additional complexity of variable geometry. It is anticipated that full-authority digital control technology will be available in the future. However, additional study is needed to examine the control aspects of variable-geometry combustors and to establish transient response requirements.

The required research areas for catalytic combustors are listed in figure 10. In general, all the problem areas associated with premixed combustion apply equally well to the catalytic technique. Unique problems introduced with this technique include the activity of the catalytic materials over wide operating ranges, long-term degradation and poisoning of the catalyst, and thermal durability problems associated with continuous and cyclic operation of the catalyst bed. Although considerable progress has been made in the past few years on research associated with catalyst and substrate materials, considerably more effort in these areas will be required.

NASA has sponsored or conducted research programs investigating these required research areas and their application to lean, premixed-prevaporized and catalytic combustors. During the next several years combustors based on the principles of lean, premixed-prevaporized and catalytic combustion will be designed, built, and evaluated.

Estimated emission levels for lean, premixed-prevaporized and catalytic combustors operating over the EPA standard landing-takeoff cycle are shown in figure 11 and compared with the previous estimates. The cross section of the combustor shows some of the essential features of these designs. The combustor is a staged type, with variable geometry and optimized pilot-stage technology. In the main stage, lean combustion occurs downstream of the flameholder or, in the case of the catalyst shown in the inset, in the catalyst bed.

The estimated achievable CO and THC emission levels, shown in the bar graphs in figure 11, are based on the successful integration of optimized pilot-stage features as discussed previously. The emission control strategies employed here were aimed at further reducing NO_x emissions. The third set of bar graphs shows that, in terms of the integrated EPA parameter, NO_x levels may be further reduced by 55 to 60 percent. It is interesting that the pilot stage, which is necessary for engine startup and wide-range operation, may contribute more NO_x during engine idle than the main stage contributes during high-power operation. Thus the pilot stage is limiting the minimum achievable NO_x emission levels for the specified landing-takeoff cycle used in computing the EPA parameter.

The actual achievable levels may be somewhat different when these emission control techniques are developed into operational engine hardware. However, the further reduction in pollutant emissions offered by the far-term program is considerable and indicates the significant potential for reduced-pollutant-emission combustion systems for future aircraft engines.

CONCLUDING REMARKS

The advanced technology concepts described in the previous sections show potential for similar emission reductions at supersonic cruise conditions. The projected cruise emissions of oxides of nitrogen for the various programs discussed herein are compared in figure 12. The bar graphs show significant reductions in NO_x emissions as more technological advances are incorporated into the combustor design. No EPA standards have been proposed for controlling NO_x emissions at cruise.

The combustion systems in future supersonic cruise engines may well be markedly different from those presently in use if low-pollutant-emission combustion systems are found to be required. Much work, however, still remains to be accomplished before these advanced systems can be considered for actual application. Trade-offs between emissions, performance, altitude relight capability, durability, maintainability, and complexity must be evaluated in future experimental programs. In the far term, continuing research and technology programs must be pursued to validate that the minimum pollutant emission levels achieved in rig tests can in fact be realized in gas-turbine-engine combustion systems.

APPENDIX - CALCULATION OF PROPOSED ENVIRONMENTAL PROTECTION AGENCY PARAMETER (EPAP)

The proposed Environmental Protection Agency parameter is expressed as

$$EPAP = \frac{1}{F_N} \sum_{i=1}^{M} \left[(EI)_i T_i (\dot{W}_F)_i \right]$$

where

F_N installed net thrust of engine, kN

EI emission index of pollutant, g pollutant/kg fuel

T time in mode, min

W_F fuel flow rate, kg/min

M number of engine conditions (M = 7 for supersonic cruise engines)

The times in mode for the main combustor and the duct burner are given in the following table:

Combustor	Engine condition				
	Idle	Takeoff	Climb	Descent	Approach
	Time in mode, min				
Main	26.0	1.2	2.0	1.2	2.3
Duct burner	----	1.2	2.0	---	---

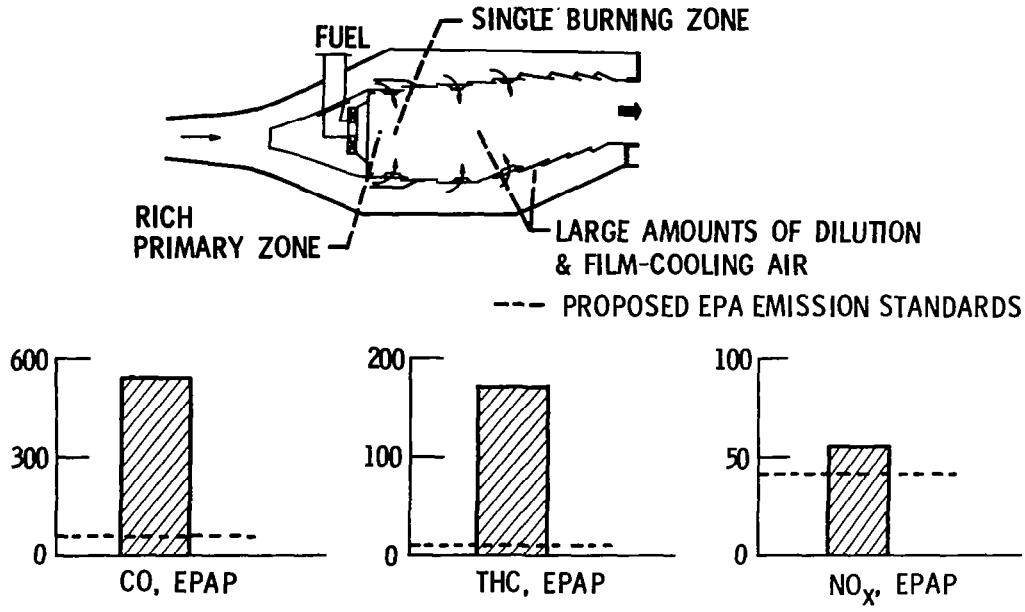

Figure 1.- First-generation SST combustor technology.

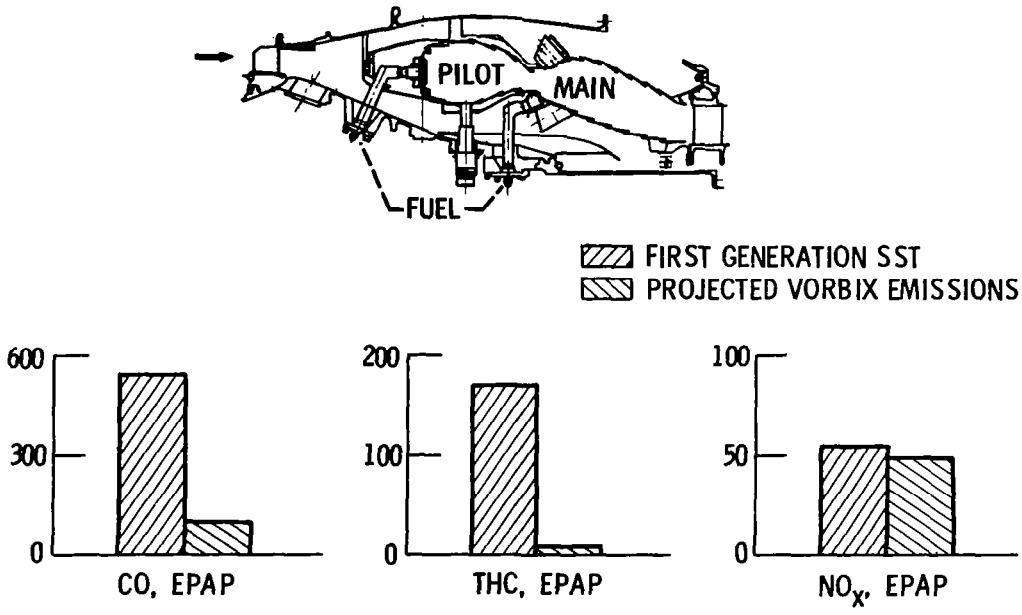

Figure 2.- Projected emission levels for advanced supersonic engine using Vorbix combustor.

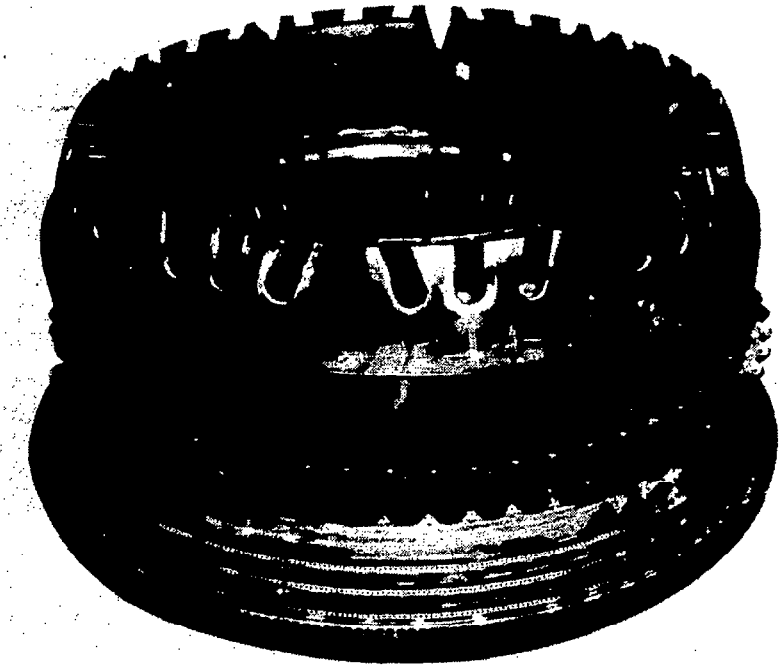

Figure 3.- Prototype Vorbix combustor.

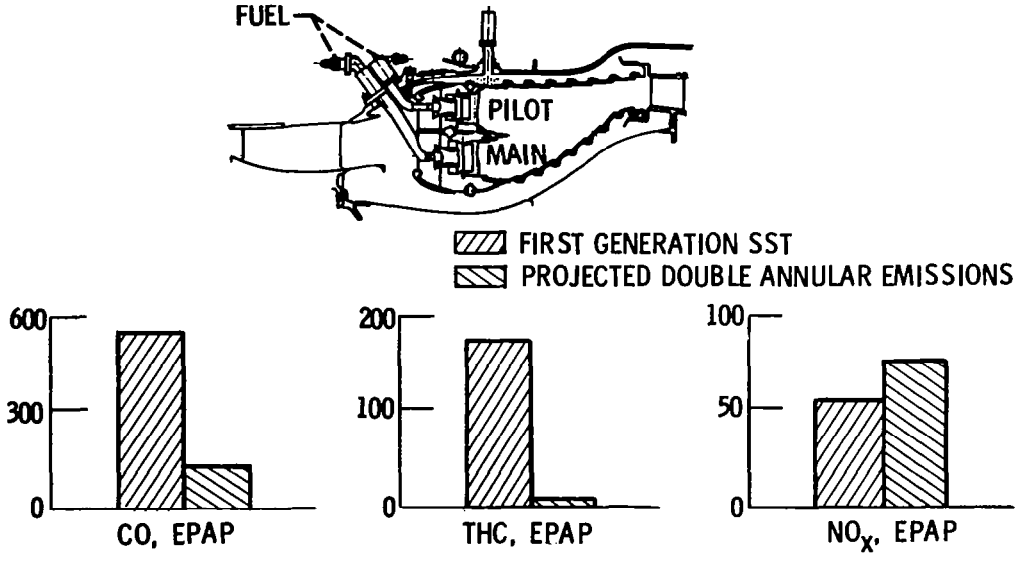

Figure 4.- Projected emission levels for advanced supersonic engine using double-annular combustor.

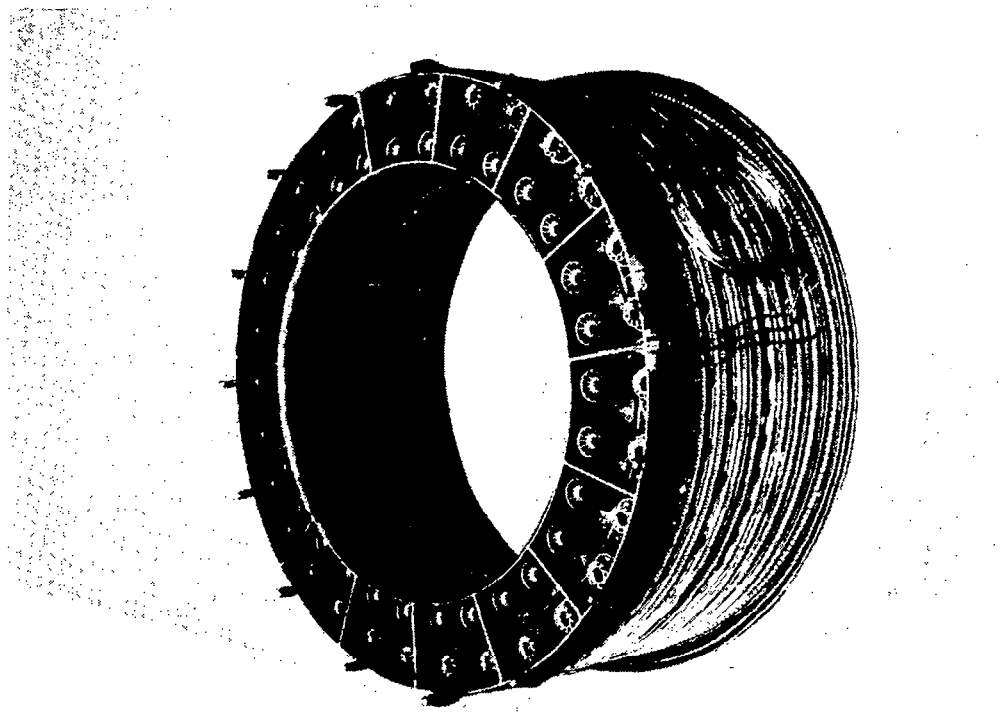

Figure 5.- Prototype double-annular combustor.

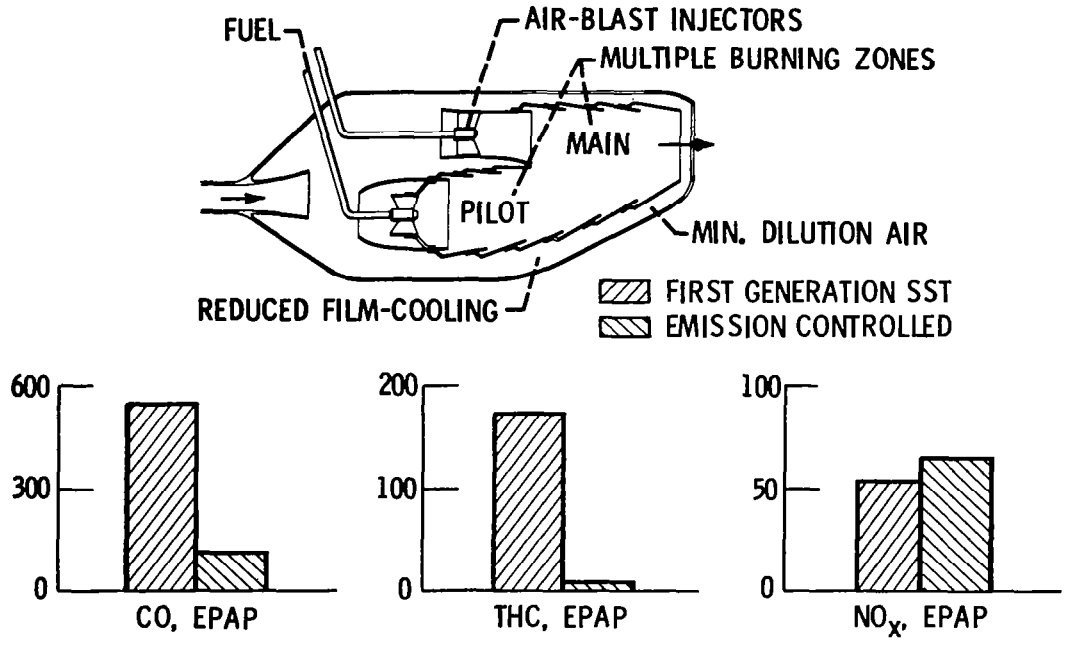

Figure 6.- Projected emission levels for advanced supersonic engine using emission-controlled combustor.

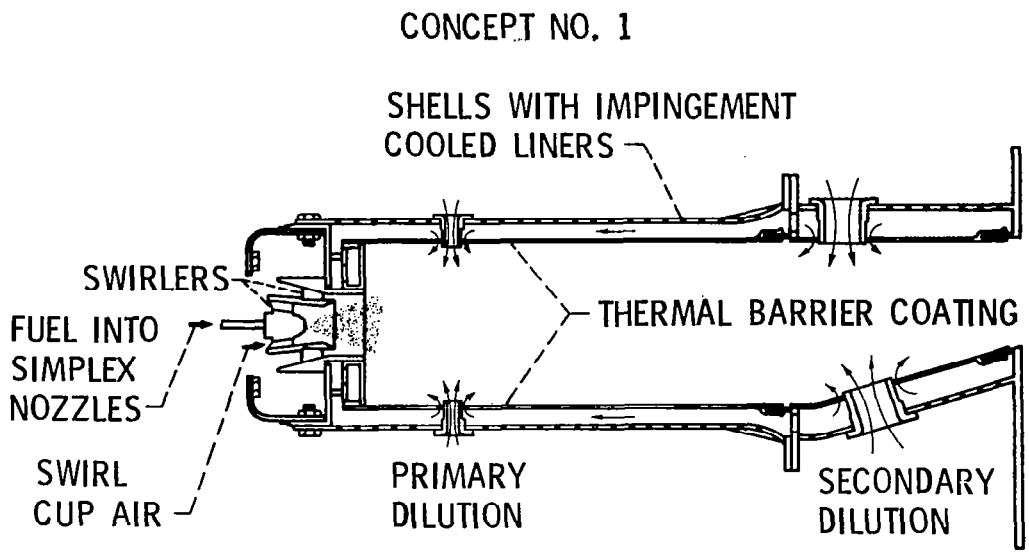

Figure 7.- Hot-wall combustor concept.

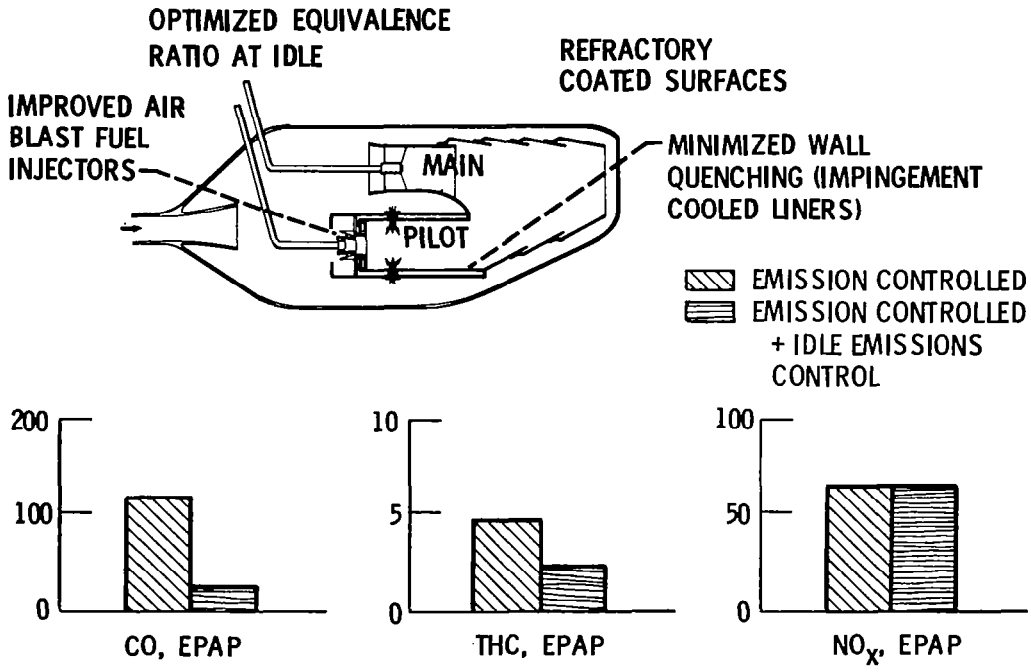

Figure 8.- Projected emission levels for advanced supersonic engine using idle-emission-controlled combustor.

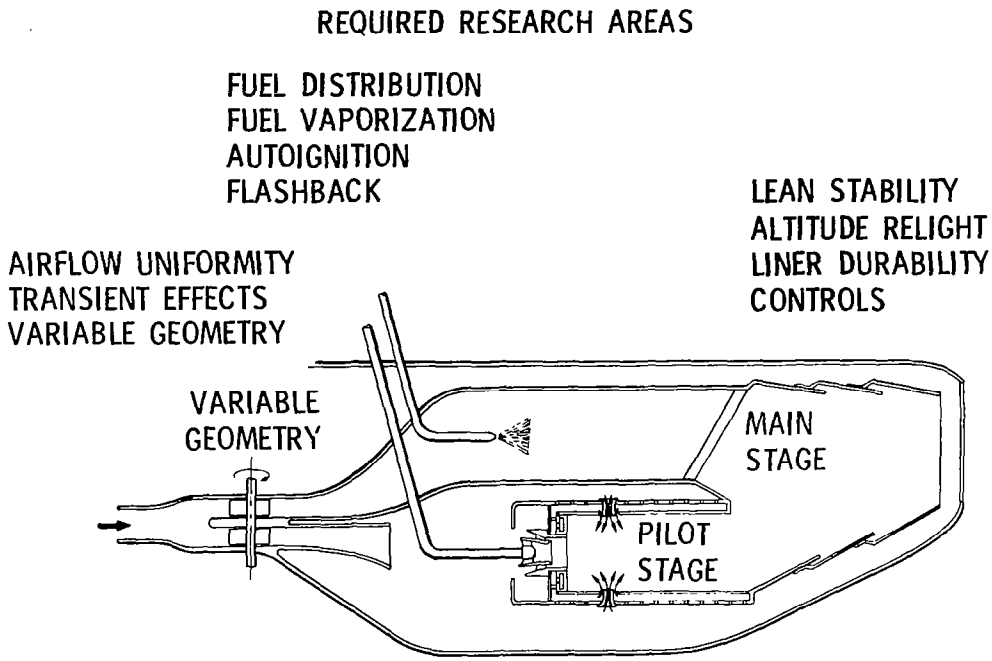

Figure 9.- Required research areas in lean, premixed-prevaporized combustor technology.

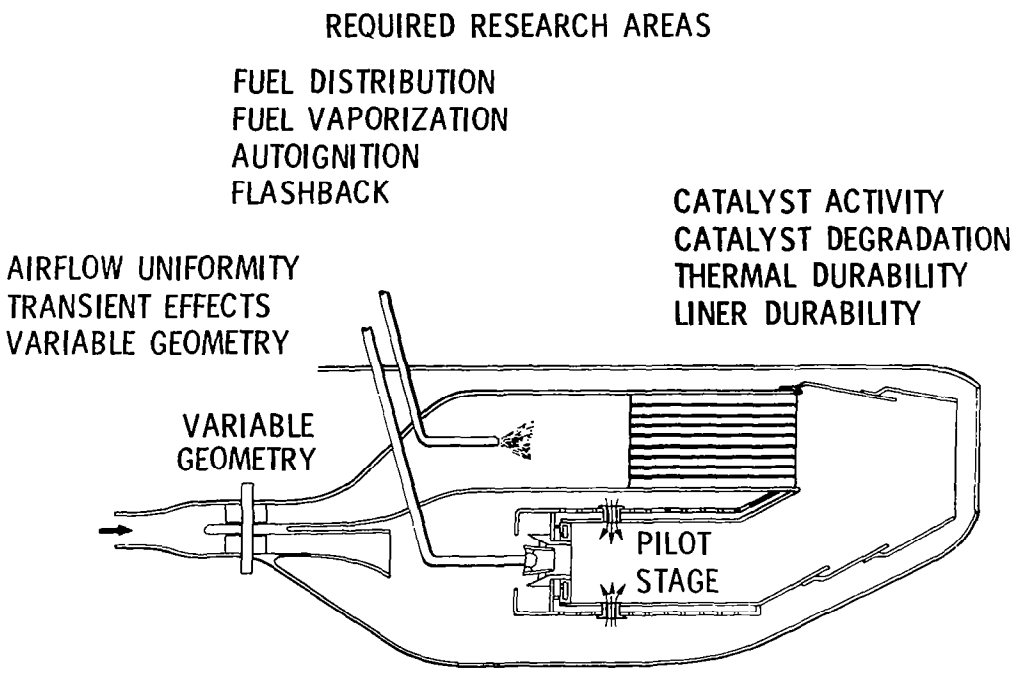

Figure 10.- Required research areas in catalytic combustor technology.

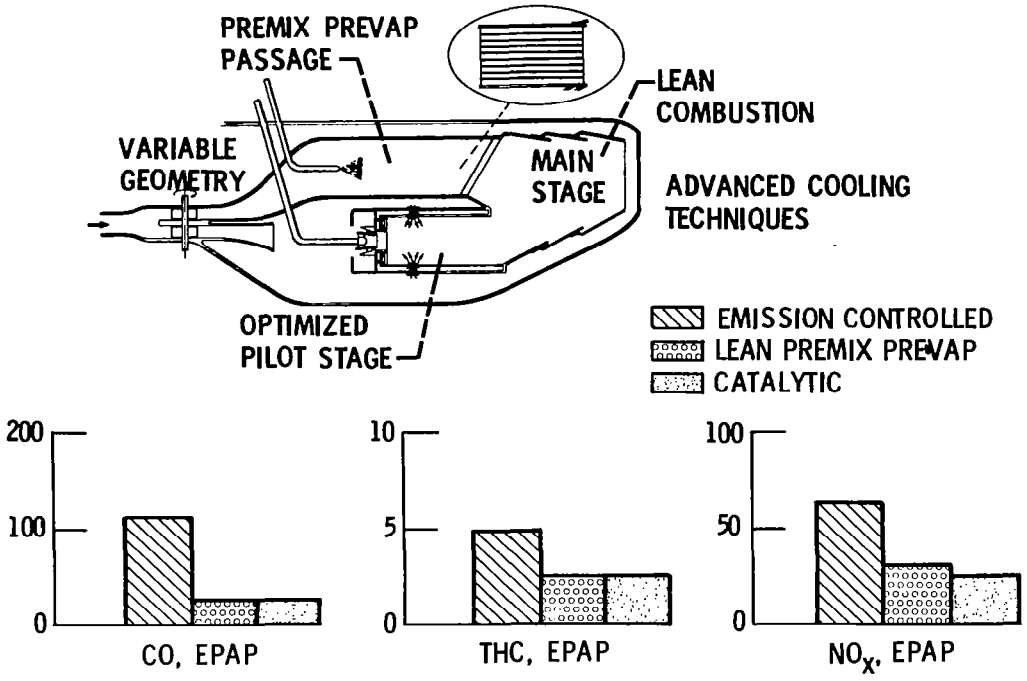

Figure 11.- Projected emission levels for advanced supersonic engine using far-term combustor technology.

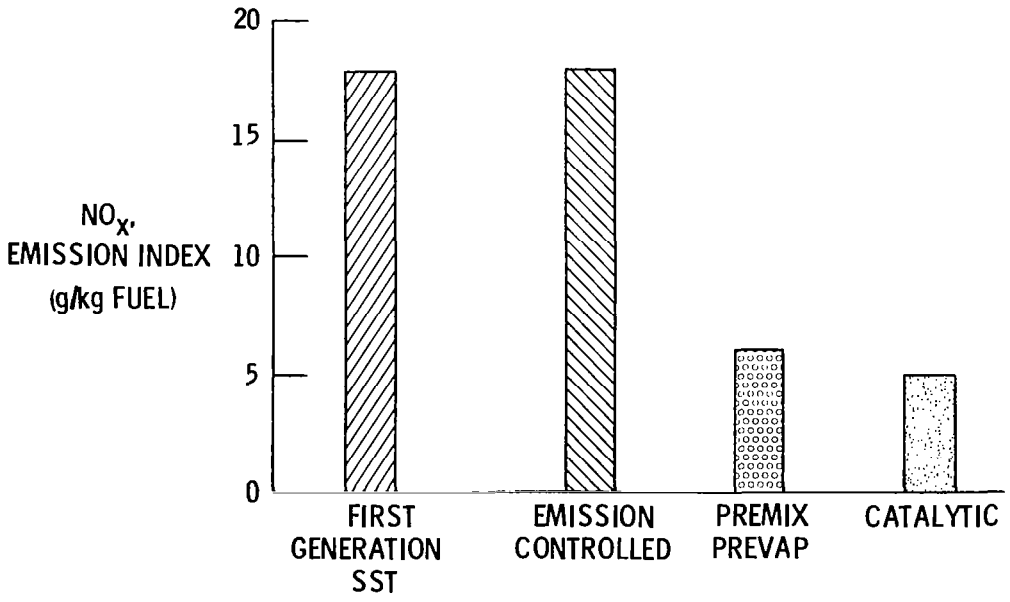

Figure 12.- Comparison of projected cruise NO_x emission levels.

*U.S. GOVERNMENT PRINTING OFFICE: 1980 - 635-050/41

1. Report No.	2. Government Accession No.	3. Recipient's Catalog No.
NASA CP-2108, Part 1		

4. Title and Subtitle	5. Report Date
SUPERSONIC CRUISE RESEARCH '79	March 1980
	6. Performing Organization Code
7. Author(s)	8. Performing Organization Report No. L-13385
9. Performing Organization Name and Address NASA Langley Research Center Hampton, VA 23665	10. Work Unit No. 533-01-43-01
	11. Contract or Grant No.
12. Sponsoring Agency Name and Address National Aeronautics and Space Administration Washington, DC 20546	13. Type of Report and Period Covered Conference Publication
	14. Sponsoring Agency Code

15. Supplementary Notes

16. Abstract

Since 1972 the Supersonic Cruise Research (SCR) Program has provided an accelerated and focused technology effort which has resulted in development of improved analytical techniques, design procedures, and an expanded experimental data base. Progress made in the first 4 years was highlighted in a conference at Langley Research Center in 1976 (see NASA CP-001, Parts 1 and 2).

Subsequent to the 1976 conference, NASA had conducted and monitored additional supersonic cruise vehicle studies and enhanced the advanced supersonic technology data base through further tests. Significant achievements in the interim since the previous conference were reported to the technical community at the SCR '79 Conference held at Langley Research Center, November 13-16, 1979. This document is a compilation of papers, authored by representatives of airframe and engine manufacturers, the Federal Aviation Administration, three NASA research centers, and the Office of Technology Assessment (Congress of the United States), which were presented at the latter Conference.

17. Key Words (Suggested by Author(s))	18. Distribution Statement
Aerodynamics Aircraft design, testing, and performance Aircraft propulsion and power Aircraft stability and control	For U.S. Government agencies and their contractors only. Date for general release March 1981. Refer questions regarding release of this report to NASA Headquarters, Code RJH-2, Jack Suddreth Subject Category 01

19. Security Classif. (of this report)	20. Security Classif. (of this page)	21. No. of Pages	22. Price
Unclassified	Unclassified	557	